NATO Science for Peace and Security Series B:
Physics and Biophysics

Quantum Nano-Photonics

Edited by
Baldassare Di Bartolo
Luciano Silvestri
Maura Cesaria
John Collins

Springer

This publication is supported by:

The NATO Science for Peace and Security Programme

Quantum Nano-Photonics

NATO Science for Peace and Security Series

This Series presents the results of scientific meetings supported under the NATO Programme: Science for Peace and Security (SPS).

The NATO SPS Programme supports meetings in the following Key Priority areas: (1) Defence Against Terrorism; (2) Countering other Threats to Security and (3) NATO, Partner and Mediterranean Dialogue Country Priorities. The types of meetings supported are generally "Advanced Study Institutes" and "Advanced Research Workshops". The NATO SPS Series collects together the results of these meetings. The meetings are co-organized by scientists from NATO countries and scientists from NATO's "Partner" or "Mediterranean Dialogue" countries. The observations and recommendations made at the meetings, as well as the contents of the volumes in the Series, reflect those of participants and contributors only; they should not necessarily be regarded as reflecting NATO views or policy.

Advanced Study Institutes (ASI) are high-level tutorial courses to convey the latest developments in a subject to an advanced-level audience.

Advanced Research Workshops (ARW) are expert meetings where an intense but informal exchange of views at the frontiers of a subject aims at identifying directions for future action.

Following a transformation of the programme in 2006, the Series has been re-named and re-organised. Recent volumes on topics not related to security, which result from meetings supported under the programme earlier, may be found in the NATO Science Series.

The Series is published by IOS Press, Amsterdam, and Springer, Dordrecht, in conjunction with the NATO Emerging Security Challenges Division.

Sub-Series

A.	Chemistry and Biology	Springer
B.	Physics and Biophysics	Springer
C.	Environmental Security	Springer
D.	Information and Communication Security	IOS Press
E.	Human and Societal Dynamics	IOS Press

http://www.nato.int/science
http://www.springer.com
http://www.iospress.nl

Series B: Physics and Biophysics

Quantum Nano-Photonics

edited by

Baldassare Di Bartolo
Department of Physics, Boston College
Chestnut Hill, MA, USA

Luciano Silvestri
Department of Physics, Boston College
Chestnut Hill, MA, USA

Maura Cesaria
IMM-CNR, Lecce, Italy
University of Florence, Sesto Fiorentino, Florence, Italy

and

John Collins
Department of Physics and Astronomy, Wheaton College
Norton, MA, USA

Springer

Published in Cooperation with NATO Emerging Security Challenges Division

Proceedings of the NATO Advanced Study Institute on Quantum Nano-Photonics
Erice, Sicily, Italy
3 July–4 August 2017

Library of Congress Control Number: 2018950399

ISBN 978-94-024-1546-9 (PB)
ISBN 978-94-024-1543-8 (HB)
ISBN 978-94-024-1544-5 (e-book)
https://doi.org/10.1007/978-94-024-1544-5

Published by Springer,
P.O. Box 17, 3300 AA Dordrecht, The Netherlands.

www.springer.com

Printed on acid-free paper

"The greatest glory in living lies not in never falling, but in rising every time we fall."

Nelson Mandela

Preface

This book presents the proceedings of a NATO Advanced Study Institute that took place at the Ettore Majorana Center in Erice, Sicily, Italy, from July 30 to August 4, 2017. The subject of the institute was Quantum Nano-Photonics.

Several lecturers presented contributions in a systematic and didactical way, each lasting several hours; others presented seminar-like talks. Many participants presented posters or short seminars. All these activities are reported in this publication.

The institute was an activity of the International School of Atomic and Molecular Spectroscopy which I preside. I have to thank several people for the success of the meeting. First of all, I like to mention Professor Sergey Gaponenko who was the efficient co-director of the institute. All the lecturers of course were of help, but I want to single out for their particularly generous contributions to the setting of the meeting: Professors Martin Wegener, John Bowen, and John Collins. The meeting also relied on the enthusiastic work of the two secretaries, Luciano Silvestri and Maura Cesaria. Antonino La Francesca, Elpidio Silvestri, and Elena Buscemi were also of notable help.

I want to acknowledge the sponsorship of the meeting by the NATO Organization, Boston College, the Italian Ministry of Scientific Research and Technology, and the Sicilian Regional Government.

At the end of this meeting, I want to look forward to the activities of the Ettore Majorana Center in years to come, including the 2019 meeting of the International School of Atomic and Molecular Spectroscopy.

Chestnut Hill, USA
December 2017

Baldassare Di Bartolo

The Co-Directors

The Team

Participants in Selinunte

Participants in Erice

Contents

Part I
Lectures

Chapter 1
Nanophotonics with and without Photons

Sergey V. Gaponenko

Abstract This chapter considers a variety of optical and light—matter interaction phenomena in the context of classical and quantum electrodynamics. All propagation phenomena are emphasized as wave-optical process where the photon notion is not necessary to be involved into consideration. All phenomena related to light emission and inelastic scattering do need photons for their interpretation. However, elastic scattering fully merges with the description based on classical electrodynamics, and spontaneous emission and inelastic scattering can be calculated using classical electrodynamics approach. Here merging of quantum and classical description is enabled by means of the operational definition of photon density of states based on the properties of a classical oscillator affected by space topology and local environment. This accordance of quantum and classical presentations is remarkably demonstrated by elaboration of the optical nanoantenna conception. The quantum-classical convergence is appreciated for new discovered phenomena of light–matter interaction in complex structures. Here the lately discovered phenomenon of changing light wavelength in a cavity is treated as possible inelastic photon scattering promoted by high photon local density of states in a tunable cavity, an analog to Purcell effect known for spontaneous emission probability.

Keywords Wave optics · Quantum electrodynamics · Nanophotonics

S. V. Gaponenko (✉)
B. I. Sepanov Institute of Physics, National Academy of Sciences of Belarus, Minsk, Belarus
e-mail: s.gaponenko@ifanbel.bas-net.by

B. Di Bartolo et al. (eds.), *Quantum Nano-Photonics*, NATO Science for Peace and Security Series B: Physics and Biophysics,
https://doi.org/10.1007/978-94-024-1544-5_1

1.1 Introduction

1.1.1 Heuristic Principles of Learning in Nanophotonics

Nanophotonics can be treated as science and technology of confined electrons and light waves. The word "photonics" in general should be identified as technologies using light rather than an instrument of managing and controlling photons as is commonly done. In this work, I keen to emphasize the purely classical, electromagnetic wave origin of many phenomena in nanophotonics and to highlight the well-known Occam razor principle ("*Among competing hypotheses, the one with the fewest assumptions should be selected"*) which has been advanced in photonics by W. Lamb [1]. It is important to understand where photons are actually involved and where only wave physics (wave mechanics and classical electrodynamics) applied to electrons and to light waves does matter. If somebody insists on necessarily photon-based description, the author believes that the new, classically unpredictable consequences should appear in this case, otherwise we should follow Occam's approach, formulated also by Isaac Newton as *"Hypotheses non fingo*" (I frame no hypothesis).

1.1.2 No Hypothesis About Light Quanta in Propagation Phenomena

All phenomena related to light propagation can be traced through analysis of wave properties of light and here the photon notion is not necessary. Notably, since Helmholtz equation used to examine light propagation, e.g. in photonic crystals, has the same form as the single particle time-independent Schrodinger equation a set of useful and meaningful analogies arise which to large extend drives many new trends in nanophotonics [2]. For example development of transmission bands in a periodic medium and localized states in a cavity are common for electromagnetic waves and for electrons. Tunneling phenomena in optics (SNOM, guide-cavity coupling) and in quantum mechanics including scanning tunneling microscopy will be considered as an insightful analogies for the local density of states notion.

Photons are involved necessarily everywhere where light—matter interaction results in light emission or inelastic scattering. Within the perturbation theory these processes can be viewed as modified due to modification of the photon density of states. Here analogies to classical electrodynamics are helpful in calculations though classical electrodynamics cannot explain the jumps resulting in photon emission and Raman scattering. Lately the nanoantenna conception has been involved in nanophotonics bridging quantum phenomena with radiophysics [5]. It is important to understand that classical consideration here appears to be very instructive though the very event of secondary photon creation remains elusive and needs consistent but cumbersome quantum electrodynamical analysis.

1.1.3 A Challenge to the Light Quantum Concept: Changing Light Color in a Tunable Cavity

A number of groups reported on a curious phenomenon when light stored in a high-Q cavity change its frequency when coming out after fast detuning of the cavity from its original resonance [3]. The phenomenon has been explained qualitatively based on a reasonable acoustical analog with a string and quantitatively based on analysis of Maxwell equations with the result that fast change in material permittivity keeps wavenumber constant whereas frequency has to change typical in proportion with relative refraction index change, i.e. by 1% or less. This phenomenon seems to have no explanation in terms of photons though such explanation bridging acoustics, wave optics and quantum electrodynamics would be important. We show that the above phenomenon can be consistently interpreted as Brillouin-Mandelstam photon scattering promoted by high local density of photon states in a tunable cavity. Scattering from the original frequency of input light to the mode of the detuned cavity is enhanced owing to high Q-factor and spatial wave confinement in accordance with the known Purcell factor [4] and extension of Purcell effect to photon scattering [5]. The issues are believed to stimulate further experiments and discussions towards understanding the quantum and classical phenomena in nanophotonics and evaluating specific quantum effects versus classical ones as well as to tracing quantum-classical convergence whenever possible.

1.2 Propagation and Elastic Scattering of Light Without Photon Concept Involved

1.2.1 Wave Phenomena in Quantum and Classical Physics: Insightful Counterparts

Photon notion is commonly used as a synonym to the word “light” without paying attention to whether a phenomenon in question or a mathematically formulated problem does really involve photons as a prerequisite for its understanding and description. Recalling the seminal work by Lamb [1] we state there is no reason to speak about *photons*, *photon* energy conversion etc. until we are not sure we actually manipulate with photons either in equations or in the labs. Recalling Lamb’s saying that ‘*radiation does not consist of particles*’ [1] and keeping on mathematical accuracy, one should avoid speaking about photons while analyzing wave equations and nobody should claim that Maxwell equations can offer knowledge about photon properties though this is, regretfully, frequently done. The typical misleading statements like, e.g. saying that a photonic crystal features energy bands for photons or photons are scattered by a nanobody should always be avoided until equations for photons are involved and phenomena cannot be understood in terms of wave optics.

Electromagnetic waves and electrons feature a number of remarkable analogies originating from the harmony of nature embodied in the notable mathematical analogy of Helmholtz equation in optics and time independent Schrödinger equation in quantum mechanics. It is reasonable to recall their simplest one-dimensional forms (Eq. 1.1) to highlight the similarity,

$$\frac{d^2\Phi(x)}{dx^2}+k^2\Phi(x)=0,\quad \Phi_{QM}\equiv\psi,\quad k_{QM}^2=\frac{2m\,(E-U)}{\hbar^2};\quad \Phi_{EM}\equiv A, k_{EM}^2=\varepsilon\frac{\omega^2}{c^2} \tag{1.1}$$

Here k is wave number, m is a particle mass, E is a particle full energy, U is a particle potential energy, A is electric field amplitude, ε is the dielectric permittivity, and ω is frequency. Subscript QM denotes quantum mechanics and subscript EM denotes electromagnetic theory.

This similarity reflects the wave properties of light and electron(s). The only difference is that Helmholtz equation describes the real electric or magnetic field that can be sensed by humans, animals or artificial detectors whereas Schrodinger equation describes special function which gives us the probability of an electron to be found at a given point of space. Material or space parameters are defined by $U(x)$ in quantum mechanics and by ε(x) in optics. Comparing quantum mechanical (subscript QM) and electromagnetic (subscript EM) counterpart, one can see that change in refractive index will result in optics in the same effect as change in potential energy U in quantum mechanics.

These analogies when applied to complex dielectric media and nanostructures consisting of non-absorbing materials allow for tracing of a number of instructive phenomena, which are pronounced in optics on a nanoscale (Table 1.1).

1.2.2 Does an Optical Tunneling Need Light Quanta?

Tunneling which is well defined in quantum mechanics has a number of counterparts in optics. Tunneling in optics occurs when evanescent electromagnetic waves penetrate over a finite distance and then convert into plane waves. It can be readily recognized as transparency of thin metal films (an analogy which is first suggested by W. Heisenberg in 1930-ies), frustrated total reflection, and imaging with near-field scanning optical microscope. There is no need to involve light quanta into consideration for optical tunneling phenomena. However, an attempt has been made to introduce ‘special’ photons, so-called virtual photons as if these are necessary to explain or understand optical tunneling [6].

Table 1.1 Analogies between electromagnetic and quantum-mechanical wave phenomena

Medium inhomogeneity	Phenomena	
	Quantum mechanics	Optics
Refraction step, potential step	Reflection/transmission	Reflection/transmission
Refraction barrier (well), potential barrier(well)	Resonant propagation, reflection/transmission	Reflection/transmission and Fabry-Perot modes in thin films
Potential well/optical cavity	Discrete energy spectrum	Resonant modes
Drop from positive to negative permittivity, high potential step ($U > E$)	Extension of wave function under barrier	Evanescence of electromagnetic field in the area with negative permittivity
A slab with negative permittivity, potential barrier with finite length	Reflection/tunneling	Reflection/tunneling, transparency of thin metal films
Two parallel mirrors, double potential barrier ($U > E$)	Resonant tunneling	Resonant transmission of optical interferometers
Periodic refractive index change in space, periodic potential in space	Energy bands formation separated by forbidden energy gaps in crystals	Development of reflection and transmission bands and band gaps in photonic crystals
Material with weak disorder of refraction index, crystalline materials with defects	Ohm's law, $1/L$ current dependence	$1/L$ transmission of opaque materials
Impurity (defect) in a crystal, a cavity or defect in a photonic crystal	Localized electron state	High-Q microcavity
Strong disorder of refraction index, highly disordered solids	Anderson localization of electrons	Anderson localization of EM-waves (hard to observe in the optical range)

1.3 Emission of Light in Terms of Photon Density of States Effects and Radiative Decay Engineering

1.3.1 Photon Density of States

In the limit of weak light–matter interaction the probability of an excited atom or a molecule to emit photon spontaneously can be described as an event which is proportional to the density of electromagnetic modes $D\,(\omega)$ which then acquires the notation of the photon density of states (DOS) by analogy with electron density of states,

$$W\,(\omega, \mathbf{r}) = W_0\,(\omega)\,\frac{D\,(\omega, \mathbf{r})}{D_0\,(\omega)} \tag{1.2}$$

For electromagnetic waves in vacuum one has $W_0(\omega)$ which is defined by

$$D_0(\omega) = \frac{\omega^2}{2\pi^2 c^3} \tag{1.3}$$

Tracing the history of this interpretation one can see that the hint to this relation can be found in the early paper by A. Einstein [7], the notion of the density of states has been introduced by S.N. Bose [8], and the very statement on proportionality between spontaneous emission probability and density of final states for photon is commonly referred to as "Fermi golden rule" in spite of the fact that E. Fermi did not derive this relation and never applied this term for photons. He introduced the label "golden rule" to the relation describing scattering of quantum particles which is also proportional to the final density of (particle) states [9], and when writing that relation he referred to the book by Schiff [10]. The earlier period of this conception is reviewed in Ref. [11].

E. M. Purcell was the first [4] to understand that for a quantum emitter in a cavity the relative weight of different modes becomes different, the dominating mode being that which is resonant to the cavity. He suggested that spontaneous decay probability would change accordingly, in proportion with the cavity Q-factor. The original Purcell factor for precise resonance between an atom emission frequency and a cavity frequency has been extended for the case of detuning by Bunkin and Oraevsky [12],

$$\frac{W(\omega)}{W_0(\omega)} = \frac{Q}{\frac{(\omega-\omega_0)^2}{\omega_0^2}Q^2 + 1}\left(\frac{\lambda^3}{V}\right), \tag{1.4}$$

where ω_0 –s the cavity resonance frequency, λ is wavelength and V is the volume occupied by the radiation mode under consideration. Eq. (1.4) is plotted in Fig. 1.1 to give an idea how radiative decay can be enhanced in a high-Q cavity. Noteworthy, large detuning results in inhibition of decay versus vacuum. This is a manifestation of the very general property known as the sum rule.

Purcell's idea is now extended to every case differing from an emitter in vacuum. For every topological situation with respect to dielectric permittivity which differs from $\varepsilon = 1$, radiative decay rate will be different from that in vacuum. This conception has become very common and got the notation "radiative decay engineering" [13]. One more representative example is given in Fig. 1.2 where photon DOS for a photonic crystal is shown. Coexistence of enhancement and inhibition of the spontaneous decay rate over the frequency axis is apparent.

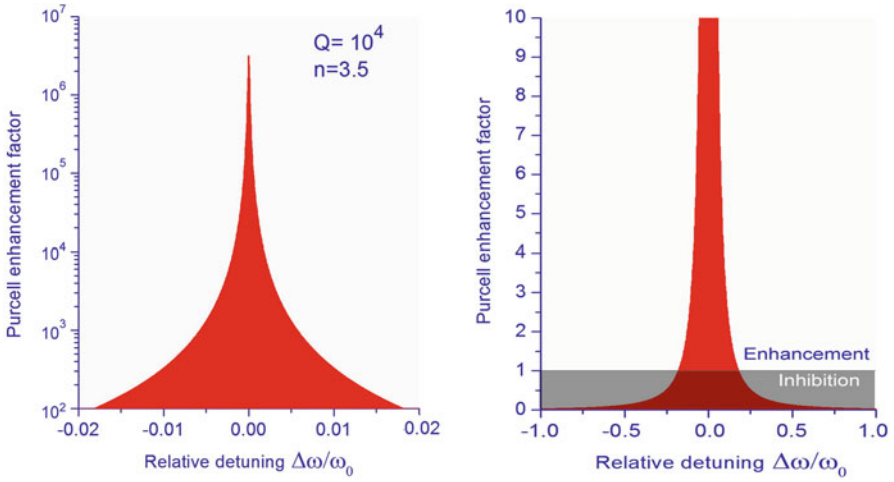

Fig. 1.1 Enhancement factor for spontaneous emission rate in a cavity according to Eq. (1.4)

Fig. 1.2 Density of states for a one-dimensional photonic crystal slab

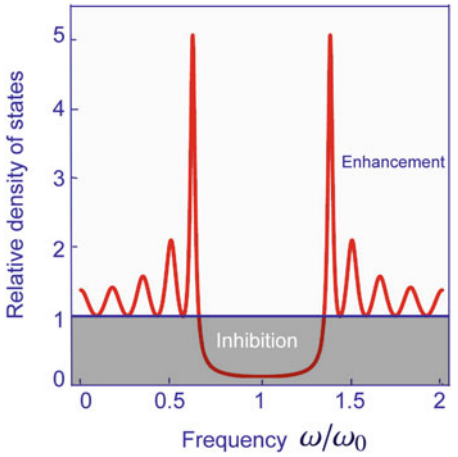

1.3.2 In the Weak Light-Matter Interaction Mode Emission of Photons Can Be Calculated Using Classical Electrodynamics

When calculating radiative decay rate for an emitter in strongly inhomogeneous space, the notion of *local* DOS is important. It can be defined as modification of a *classical emitter* rate placed at the point of interest versus free space. An atom or another quantum emitter (molecule, quantum dot etc.) is assumed to change its spontaneous decay rate accordingly. This approach was suggested in Ref. [14] and provides a bridge between classical electrodynamics and quantum theory

within the perturbational approach (weak light—matter interaction). One can see that nanophotonic phenomena immediately acquire insightful analogies in classical electrodynamics. This approach is used by many authors to calculate spontaneous emission rate for atoms, molecules and quantum dots in nanophotonics [15, 16]. It was elegantly extended towards the notion of an optical *antenna* [17]. To emphasize analogies between quantum and classical emitters we consider equations describing modification of the emitter efficiency placed near a metal nanobody in optics and in radiophysics. In optics, the efficiency is referred to as quantum yield, Q, and reads (see, e. g [18]),

$$Q(\mathbf{r},\omega) = \frac{W(\mathbf{r},\omega)/W_0(\omega)}{W(\mathbf{r},\omega)/W_0(\omega) + W_{nr}(\mathbf{r},\omega)/W_0(\omega) + (1 - Q_0(\omega))/Q_0(\omega)} \tag{1.5}$$

where Q_0 is the intrinsic quantum yield of a quantum emitter and W_{nr} is nonradiative decay rate promoted by a metal nanobody. This equation is to be compared with the radiophysical counterpart for the antenna efficiency, F [17],

$$F_{antenna} = \frac{P/P_0}{P/P_0 + P_{antenna\ loss}/P_0 + (1-\eta_i)/\eta_i} \tag{1.6}$$

where P and P_0 is power emitted with and without an antenna, respectively, $P_{\mathrm{antenna\ loss}}$ is the additional losses brought by an antenna, and η_{i} is the intrinsic efficiency of the emitter. One can see that Eqs. (1.5) and (1.6) coincide though the processes described at first glance are rather different. Both equation show that neither a metal nanobody nor an antenna can improve efficiency of an ideal emitter ($Q_0 = 1$, $P_0 = 1$) because of the losses brought.

1.4 Scattering of Photons in Terms of Density of States Effects

In quantum electrodynamics, photon scattering is viewed as a result of virtual excitation of a quantum system and instantaneous emission of another photon into the mode differing from the incident one by either of the following parameters: polarization, direction, frequency. In the case of elastic scattering (frequency does not change) scattering can be fully described based on wave scattering analysis in optics. However, one should bear in mind that in the familiar ω^4 factor defining Rayleigh scattering and blue sky color the ω^2-portion resembles a contribution from photon DOS expressed by Eq. (1.3) whereas another ω^2-portion comes as a product of an incident and scattered photon frequencies.

In the case of inelastic scattering (Mandelstam—Brillouin and Raman scattering), classical wave optics cannot be used. In this case one can treat inelastic

scattering as the process with probability (rate) proportional to the density of final states for photons, similar to spontaneous emission [5]. One can write the general relation for photon scattering rate

$$W_{\text{scatter}} \propto \left(\omega\, \omega' \frac{D\left(\omega', \boldsymbol{r}\right)}{D_0\left(\omega'\right)} \right) \tag{1.7}$$

where $\omega(\omega')$ is the incident (scattered) photon frequency.

This consideration immediately brings a wealth of phenomena and becomes very insightful in prediction of enhancement or inhibition of inelastic scattering in complex dielectric, metal-dielectric and metal nanostructures including familiar surface enhanced Raman scattering (SERS) [18–26]. High local density of photon states in photonic crystals (like that shown in Fig. 1.2) has been suggested to perform optical cooling by means of anti-Stokes Raman scattering domination over the Stokes one when photon DOS rises sharply with frequency [20]. Strong Raman scattering enhancement has been observed in a number of nanostructures with pronounced enhancement of local DOS like photonic crystals and microcavities [21–24]. Scattering contribution to extinction spectrum in plasmonic nanostructures is known to define the spectral range where radiative decay will be enhanced, and fine correlation of these two effects additionally demonstrate convergence of the DOS-based presentation of secondary photons creation both in scattering and in emission processes.

1.4.1 Tunneling Viewed as Scattering in Optics

Consideration of various wave optical phenomena in complex structures for the cases when radiation frequency does not change can be to large extent viewed as elastic photon scattering. E. g. tunneling phenomena can be interpreted as elastic photon scattering into the mode(s) having higher DOS values. Insightful examples are SNOM imaging (in many cases this is nothing but local photon DOS mapping over a surface), high transparency of Fabry—Perot cavities (so-called resonance tunneling in optics) etc. Moreover, real and imaginary experiments on optical tunneling can be purposefully used to predict modification of emission and scattering of light in complex structures. Higher tunneling probability in certain topologies will always correlate with higher photon emission and scattering rates including spontaneous emission, elastic and inelastic (Mandelstam—Brillouin and Raman scattering). Anisotropy inherent in two-dimensional photonic crystal slab will always result in angular redistribution of scattered light [26].

1.5 Purcell Effect on Photon Scattering as Possible Quantum Rationale for Adiabatic Light Frequency Shifting

1.5.1 Changing Color of Light in a Tunable Cavity

In this section, recent experiments on adiabatic light frequency shifting in tunable microcavities and photonic crystals which have been elegantly described in terms of wave optics are attempted to be explained in terms of quantum electrodynamics (QED). We suggest that photon inelastic scattering by matter enhanced by high local photon density of states (DOS) is the possible QED-based explanation of the adiabatic light frequency shifting.

Brillouin–Mandelstam light scattering by solids mediated by acoustic phonons features continuous frequency shift unlike Raman scattering and is suggested as the reasonable light-matter interaction path for the electromagnetic energy transfer from one mode to another, thus providing a material mediator in photonic transitions. The phenomenon represents then the further extension of Purcell effect to photon scattering complementing the previous reports on photon DOS effects on Raman scattering. The explanation of the observed electromagnetic energy redistribution between modes necessarily involves light-matter interaction.

In 1998 Winn et al. predicted electromagnetic energy transfer from one mode to another in a tunable photonic crystal whose parameters can by dynamically tuned by means of nonlinear permittivity effects of constituting material(s) [27]. These authors coined the notion of *photonic transition* to emphasize the novelty of the phenomenon described. Later on in 2005, Notomi and Mitsugi [28] predicted wavelength conversion in a cavity which exhibits dynamic tuning by means of fast change of refractive index of the material placed therein. In the same period, Gaburo et al. [29] suggested a photon energy lifter based on dynamical refraction index change in photonic crystal circuitry including a single cavity and coupled cavities. To meet the adiabatic regime, cavity detuning should be dynamically performed on a time scale longer than the oscillation period but definitely shorter than the time of the full release of the energy stored in a cavity, i.e. roughly $2\pi Q/\omega$ where Q is the cavity Q-factor, and ω is the light frequency. Notomi and Mitsugi ingeniously suggested sweeping sound of a guitar string with modulated tension as the acoustic-wave analog to this electromagnetic phenomenon. The relative wavelength shift almost coincides with the relative refractive index shift $\Delta n/n$, i.e. follows the cavity optical length nd where d is its geometrical size. For semiconductor multilayered photonic crystals our experiments have shown that $\Delta n/n$ can reach a few per cent in less than 10^{-12} s in the visible [30] and for the optical communication wavelength 1.5 μm [31] owing to dense electron-hole plasma generated by hard interband excitation of semiconductors with a subpicosecond laser pulse.

Changing frequency of light stored in a microcavity has been demonstrated in fine experiments by M. Lipson's group [3] where a 2.5 nm wavelength shift has been documented for light released from a cavity after rapid electro-optical detuning. Later on the same team reported on light frequency lift-up by 0.5% in

a tunable silicon ring cavity [32]. These experiments have been followed by the demonstration of "on-the-fly" wavelength shift in a photonic crystal waveguide [33]. Since then a number of groups reported on experimental performance of wavelength/frequency shifting for light stored in tunable cavities and in tunable photonic crystals in the so-called "slow light" regime ([34] and Refs, therein). An elegant electromagnetic wave theory has been elaborated by several groups [28–30], and there is no doubt that the adiabatic wavelength/frequency shift of light in dynamically tunable cavities and photonic crystals can be consistently understood in terms of classical electrodynamics.

Does it mean that the theory of this phenomenon is exhaustive? Can we speak about *photon* energy conversion?

1.5.2 Photon Energy Conversion in a Tunable Cavity

It is reasonable to look for the quantum electrodynamical (QED) counterpart to the phenomena in question. In nanophotonics, the convergence of quantum and classical approaches are often appreciated leading, e.g., to the bridge between radiophysics and quantum electrodynamics in the recently elaborated nanoantenna notion and providing efficient classical computation schemes for seemingly fully quantum phenomena like spontaneous emission of photons by excited atoms and molecules (Sect. 1.3.2). At first glance, the adiabatic frequency shifting means that photons with energy $\hbar\omega$entering a device which can be viewed as a mysterious "black box" are replaced at the output by photons with energy $\hbar\omega'$ either higher or lower than $\hbar\omega$. This looks strange, unexpected and counterintuitive. The transfer path from initial to output photons seems subtle and elusive. We suggest that this phenomenon can be treated as *spontaneous inelastic scattering of photons* by matter enhanced by high photon local density of states by analogy with Purcell effect for spontaneous photon emission in a cavity.

This approach to photon scattering in mesoscopic structures with modified photon DOS has been discussed in Sect. 1.4.

Based on the above arguments we can write for photon scattering rate W_{scatt} in a cavity the formula suggested by Purcell for exact resonance and then extended by Bunkin and Oraevsky to account for detuning of the scattered frequency ω from the cavity resonant frequency ω_0 (see Eq. 1.4),

$$\frac{W_{scatt}\,(\omega)}{\mathrm{W}_{0\ \mathrm{scatt}}\,(\omega)} = \frac{\mathrm{Q}}{\frac{(\omega-\omega_0)^2}{\omega_0^2}\mathrm{Q}^2+1}\left(\frac{\lambda^3}{\mathrm{V}}\right), \tag{1.8}$$

where $W_{0\mathrm{scatt}}$ is scattering rate in vacuum and V is the mode volume. Taking the typical $Q = 10^4$ values used in the experiments and $\mathrm{V} = (\lambda/2\mathrm{n})^3$ as the reasonable estimate for the cavity mode volume with $n = 3.5$ as a typical value for semiconductors used in photonic crystals circuitry one arrives at more than

10^6-fold enhancement. Interestingly, Eq. (1.8) reflects the common feature of every mesoscopic structure to enhance photon scattering rate in certain frequency range(s) by the expense of inhibition otherwise.

Inelastic photon scattering in solids is mediated by atomic vibrations and occurs either in the form of Raman or Brillouin-Mandelstam process. The first mechanism involves optical phonons whose frequencies (energies) lie in the range of tens THz (tens meV) and correspond to a few percent of the photon energy for the visible. The optical phonon energy in Si measures 7.8% with respect to the photon energy at the optical communication wavelength (1.5 μm). Raman scattering gives signatures of chemical bonds in solids and thus is widely used for material identification. In a dynamically tuned cavity the detuning should be equal precisely to the characteristic optical phonon energy to explain photon energy conversion. Though Raman scattering cannot be excluded and may contribute to the observed adiabatic frequency shifting in microcavities, systematic observations did not reveal manifestation of sharp resonant behavior. Probably the main reason is that the feasible shift of frequency for a tunable cavity is much lower than optical phonon frequencies. Therefore we consider the second type of inelastic scattering, namely acoustic phonons mediated one referred to as Brillouin–Mandelstam scattering. Unlike optical phonons, acoustic vibrations have no frequency cut-off and obey a continuous dispersion law starting from zero and extending to tens of THz. Therefore Brillouin scattering strongly enhanced by high photon density of states of a dynamically tuned cavity may be the reasonable candidate for a quantum process of light–matter interaction responsible for photon energy shifting. Inelastic scattering may occur with photon frequency downward (Stokes) and upward (anti-Stokes) shift.

The same approach can be applied to photonic crystals in the so-called slow light regime. It is well established for periodic structures in photonics at the edges of transmission bands and accompanied by strong enhancement of photon DOS with pronounced DOS redistribution which qualitatively corresponds to Barnett-Loudon sum rule. A representative example for a photonic crystal slab was given in Fig. 1.2. Strong enhancement of inelastic photon scattering for silicon photonic crystals near photonic band edge has been discussed recently by Chen and Bahl [20].

Thus the rationale for adiabatic photon frequency shift in tunable microcavities and photonic crystals has been proposed in terms of the Purcell effect on inelastic photon scattering in constituting material(s) promoted by photon density of states enhancement. Brillouin-Mandelstam scattering mediated by acoustic phonons in solids is suggested as the physical process in the material offering the transfer path of electromagnetic energy between two modes in microcavities and photonic crystals. The consideration complements the theory based on Maxwell equations analysis and manifests the definite convergence of quantum and classical interpretation of the phenomenon. Notably, both approaches essentially involve the matter as the necessary mediator for electromagnetic energy redistribution between different modes.

1.6 Conclusion

A brief overview of a number of common wave and quantum phenomena in optics shows that propagation phenomena including tunneling do not need light quanta in description and understanding and therefore accurate explanations of these phenomena should avoid reference to quanta. Spontaneous emission and inelastic scattering of light within the perturbational approach (weak light—matter interaction) implies emission of light quanta but calculations can be made based on classical electrodynamics considering an oscillator in a complex space (by introducing photon density of states notion). It is reasonable to consider photon-based interpretation of the known wave phenomena but in this case the photon conception should bring the new predictions otherwise impossible. If this is not the case then the Occam razor principle looks as a reasonable heuristic approach and the term 'photon' should be avoided.

Finally we show that recently predicted and observed interesting wave phenomenon, change of radiation frequency in tunable cavity can be described as inelastic photon scattering into a high-Q mode with high local density of states. This interpretation predicts enhanced effect when frequency shift coincides with phonon frequencies of materials involved in the experiments (inner substance or mirrors of a cavity).

Acknowledgements Assistance by S.V. Zhukovsky in density of states calculation for a photonic crystal is acknowledged. The work has been supported by the national program "Photonics and Electronics".

References

1. Lamb WE Jr (1995) Anti-photon. Appl Phys B 60(2–3):77–84
2. Gaponenko SV (2010) Introduction to nanophotonics. Cambridge University Press, Cambridge
3. Preble SF, Xu Q, Lipson M (2007) Changing the colour of light in a silicon resonator. Nat Photon 1(5):293–297
4. Purcell EM (1946) Spontaneous emission probabilities at radio frequencies. Phys Rev 69:681–681
5. Gaponenko SV (2002) Effects of photon density of states on Raman scattering in mesoscopic structures. Phys Rev B 65(14):140303
6. Stahlhofen AA, Nimtz G (2006) Evanescent modes are virtual photons. EPL (Europhysics Letters) 76(2):189–195
7. Einstein A (1916) Strahlungs-Emission und -Absorption nach der Quantentheorie. Deutsch Phys Ges 18:318–323
8. Bose SN (1924) Planck's Gesetz und Lichtquantenhypothese. Zs Physik 26:178–181
9. Fermi E (1950) Nuclear physics. Chicago University, Chicago
10. Schiff LI (1949) Quantum mechanics. McGraw-Hill Book Co. Inc, New York
11. Gaponenko SV (2014) Satyendra Nath Bose and nanophotonics. J Nanophotonics 8(1):087599
12. Oraevskii AN (1994) Spontaneous emission in a cavity. Physics Uspekhi 37(4):393–405

13. Lakowicz JR (2005) Radiative decay engineering 5: metal-enhanced fluorescence and plasmon emission. Anal Biochem 337(2):171–194
14. D'Aguanno G, Mattiucci N, Centini M, Scalora M, Bloemer MJ (2004) Electromagnetic density of modes for a finite-size three-dimensional structure. Phys Rev E 69(5):05760
15. Guzatov DV, Vaschenko SV, Stankevich VV, Lunevich AY, Glukhov YF, Gaponenko SV (2012) Plasmonic enhancement of molecular fluorescence near silver nanoparticles: theory, modeling, and experiment. J Phys Chem C 116(19):10723–10733
16. Rybin MV, Mingaleev SF, Limonov MF, Kivshar YS (2016) Purcell effect and lamb shift as interference phenomena. Sci Rep 6:20599
17. Bharadwaj P, Deutsch B, Novotny L (2009) Optical antennas. Adv Opt Photon 1(4):438–483
18. Guzatov DV, Gaponenko SV, Demir HV (2018) Plasmonic enhancement of electroluminescence. AIP Adv 8(1):015324
19. Alessandri I, Lombardi JR (2016) Enhanced Raman scattering with dielectrics. Chem Rev 116(24):14921–14981
20. Chen YC, Bahl G (2015) Raman cooling of solids through photonic density of states engineering. Optica 2(10):893–899
21. Thurn R, Kiefer W (1984) Observations of structural resonances in the Raman spectra of optically levitated dielectric microspheres. J Raman Spectrosc 15(3):411–415
22. Guddala S, Kamanoor SA, Chiappini A, Ferrari M, Desai NR (2012) Experimental investigation of photonic band gap influence on enhancement of Raman-scattering in metal-dielectric colloidal crystals. J Appl Phys 112(8):084303
23. Inoue K, Oda H, Yamanaka A, Ikeda N, Kawashima H, Sugimoto Y, Asakawa K (2008) Dramatic density-of-state enhancement of Raman scattering at the band edge in a one-dimensional photonic-crystal waveguide. Phys Rev A 78(1):011805
24. Sumikura H, Kuramochi E, Taniyama H, Notomi M (2013) Cavity-enhanced Raman scattering of single-walled carbon nanotubes. Appl Phys Lett 102(23):231110
25. Gaponenko SV, Guzatov DV (2009) Possible rationale for ultimate enhancement factor in single molecule Raman spectroscopy. Chem Phys Lett 477(4–6):411–414
26. Lutich AA, Gaponenko SV, Gaponenko NV, Molchan IS, Sokol VA, Parkhutik V (2004) Anisotropic light scattering in nanoporous materials: a photon density of states effect. Nano Lett 4(9):1755–1758
27. Winn JN, Fan S, Joannopoulos JD, Ippen EP (1999) Interband transitions in photonic crystals. Phys Rev B 59(9):1551
28. Notomi M, Mitsugi S (2006) Wavelength conversion via dynamic refractive index tuning of a cavity. Phys Rev A 73(5):051803
29. Gaburro Z, Ghulinyan M, Riboli F, Pavesi L, Recati A, Carusotto I (2006) Photon energy lifter. Opt Express 14(16):7270–7278
30. Stankevich VV, Ermolenko MV, Buganov OV, Tikhomirov SA, Gaponenko SV, Kuznetsov PI, Yakushcheva GG (2005) Nonlinear Bragg structures based on ZnS/ZnSe superlattices. Appl Phys B 81(2):257–261
31. Ermolenko MV, Buganov OV, Tikhomirov SA, Stankevich VV, Gaponenko SV, Shulenkov AS (2010) Ultrafast all-optical modulator for 1.5 μm controlled by Ti: Al_2O_3 laser. Appl Phys Lett 97(7):3113
32. Dong P, Preble SF, Robinson JT, Manipatruni S, Lipson M (2008) Inducing photonic transitions between discrete modes in a silicon optical microcavity. Phys Rev Lett 100(3):033904
33. Upham J, Tanaka Y, Asano T, Noda S (2010) On-the-fly wavelength conversion of photons by dynamic control of photonic waveguides. Appl Phys Express 3(6):062001
34. Notomi M (2010) Manipulating light with strongly modulated photonic crystals. Rep Prog Phys 73(9):096501

Chapter 2
Non-reciprocity in Parametrically Modulated Systems

Martin Frimmer and Lukas Novotny

Abstract A system is called reciprocal if signal propagation is identical under exchange of detector and source. Of particular technological importance are non-reciprocal devices for electromagnetic radiation. Currently available non-reciprocal technology largely relies on non-reciprocal materials. Recently, breaking reciprocity by parametric modulation has received significant attention. Here, we provide an accessible illustration of non-reciprocity in parametrically coupled two-mode systems. We use a simple mechanical oscillator picture to familiarize the reader with coherent control operations before discussing a Ramsey interferometer as the prototypical non-reciprocal device in the context of parametric mode coupling.

2.1 Introduction

Reciprocity is a key concept in electromagnetism. Stated in an oversimplified form, in a reciprocal system, the electromagnetic field generated at point B by a source at point A is equal to the field generated at point A due to a source at point B [1]. Colloquially stated, a reciprocal system has no preference for the direction of propagation of a signal. We can thus interpret reciprocity as a particular type of symmetry. For example, according to the reciprocity theorem, the radiation pattern of an antenna structure emitting electromagnetic radiation equals the angular pattern of power received by the same antenna [2]. In the context of technological applications, the breaking of reciprocity is of vital importance for the construction of isolators and circulators [3]. Most implementations of non-reciprocal devices to date rely on non-reciprocal materials. The potential of parametric effects to provide non-reciprocity has first been investigated in radio-frequency circuits [4]. In recent years, non-reciprocal devices have been demonstrated from microwave up to optical frequencies, relying on electric parameter modulation [5–10]. Furthermore,

M. Frimmer and L. Novotny (✉)
Photonics Laboratory, ETH Zürich, Zürich, Switzerland
e-mail: lnovotny@ethz.ch

B. Di Bartolo et al. (eds.), *Quantum Nano-Photonics*, NATO Science for Peace and Security Series B: Physics and Biophysics,
https://doi.org/10.1007/978-94-024-1544-5_2

parametric coupling in optomechanical systems has been exploited to realize non-reciprocal propagation of electromagnetic radiation [11–14].

A comprehensive theoretical discussion of non-reciprocity in coupled two-mode systems has been provided by Ranzani and Aumentado [15]. The purpose of this contribution is to introduce a reader unfamiliar with the dynamics of two-mode systems to the concepts necessary to understand the violation of reciprocity under parametric coupling. We use a simple mechanical picture [16] to familiarize the reader with coherent control operations and discuss a Ramsey interferometer as a prototypical non-reciprocal device.

2.2 Non-reciprocal Transmission of Signals

As a starting point, let us think about a non-reciprocal device as a "black-box" with four ports, two on the left side (labeled L_1 and L_2), and two on the right side (R_1 and R_2), as illustrated in Fig. 2.1. The signals entering and exiting these ports can be described by complex amplitudes. We denote signals propagating into (out of) the device with the superscript "in" ("out"). Let us assume that there is a simple linear relationship between the incoming and outgoing signals. If we describe the incoming signals $\mathbf{u}^{\text{in}} = [L_1^{\text{in}}, L_2^{\text{in}}, R_1^{\text{in}}, R_2^{\text{in}}]^T$ and the outgoing signals $\mathbf{u}^{\text{out}} = [L_1^{\text{out}}, L_2^{\text{out}}, R_1^{\text{out}}, R_2^{\text{out}}]^T$ as vectors, we can define the scattering matrix S of our device as

$$\mathbf{u}^{\text{out}} = S\,\mathbf{u}^{\text{in}}. \tag{2.1}$$

An example of a non-reciprocal scattering matrix would be

$$S = \begin{bmatrix} 0 & 0 & 0 & 1 \\ 0 & 0 & 1 & 0 \\ 1 & 0 & 0 & 0 \\ 0 & 1 & 0 & 0 \end{bmatrix} \tag{2.2}$$

A device characterized by this scattering matrix is illustrated in Fig. 2.1. For example, signals entering port L_1 exit at R_1. However, signals entering port R_1 do not take the reverse path and emerge at L_1. Instead, signals entering R_1 exit at L_2. Accordingly, if we have a source at L_1 and a detector at R_1, the measured signal is different from that observed upon an exchange of source and detector.

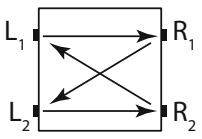

Fig. 2.1 A non-reciprocal 4-port device

2.3 Parametrically Coupled Two-Mode System

To illustrate the concept of reciprocity and its violation in parametrically modulated systems, we use a simple model of two coupled classical harmonic oscillators, whose coupling constant is time dependent. These oscillators may be implemented as modes of the electromagnetic field, or as simple mechanical oscillators. Without restricting the generality of our discussion, we choose a mechanical implementation for the purpose of this paper, as illustrated in Fig. 2.2.

Consider two identical masses m. The first mass, whose position we denote with $x(t)$, is suspended by a spring with spring constant k_x, such that the bare oscillator has a resonance frequency $\tilde{\Omega}_x = \sqrt{k_x/m}$. The second mass, whose position we denote with $y(t)$, is suspended by a spring with spring constant k_y, yielding a bare resonance frequency $\tilde{\Omega}_y = \sqrt{k_y/m}$. Both masses are coupled by a spring with spring constant G, where we assume the associated frequency $g = \sqrt{G/m}$ to be weak in comparison to both $\tilde{\Omega}_x$ and $\tilde{\Omega}_y$. We will later allow G to be time dependent to realize a parametric coupling between the two oscillators. The Newtonian equations of motion of this coupled system read

$$\ddot{x} + \Omega_x^2 x + \gamma_x \dot{x} - g^2 y = 0, \tag{2.3}$$

$$\ddot{y} + \Omega_y^2 y + \gamma_y \dot{y} - g^2 x = 0, \tag{2.4}$$

where we have defined $\Omega_x^2 = \tilde{\Omega}_x^2 + g^2$ and $\Omega_y^2 = \tilde{\Omega}_y^2 + g^2$. We describe our system in the slowly varying envelope approximation (SVEA), assuming that the motion of x and y are described by some fast oscillating carrier, whose amplitude is modulated as a function of time. To this end, we use the ansatz

$$x(t) = \mathrm{Re}\left\{\bar{a}(t)\exp\left[\mathrm{i}\Omega t\right]\right\}, \tag{2.5}$$

$$y(t) = \mathrm{Re}\left\{\bar{b}(t)\exp\left[\mathrm{i}\Omega t\right]\right\}, \tag{2.6}$$

with the carrier frequency $\Omega^2 = (\Omega_x^2 + \Omega_y^2)/2$. Inserted into Eqs. (2.3) and (2.4), we obtain the coupled mode equations for the amplitudes

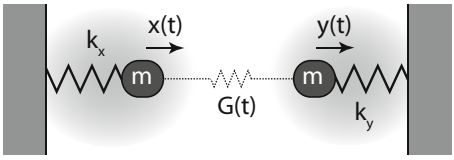

Fig. 2.2 Parametrically coupled mechanical oscillators. Each oscillator is represented by a mass m suspended by a spring with spring constant k_x or k_y, respectively. The two masses are coupled by a spring with spring constant $G(t)$ which can be modulated as a function of time

$$\mathrm{i}\begin{pmatrix}\dot{\bar{a}}\\ \dot{\bar{b}}\end{pmatrix} = \frac{1}{2}\begin{bmatrix}-\Delta - \mathrm{i}\gamma_x & \kappa\\ \kappa & \Delta - \mathrm{i}\gamma_y\end{bmatrix}\begin{pmatrix}\bar{a}\\ \bar{b}\end{pmatrix}. \tag{2.7}$$

Here, we have introduced the (renormalized) mode splitting $\Delta = (\Omega_x^2 - \Omega_y^2)/(2\Omega)$ and the coupling rate $\kappa = g^2/\Omega$. Furthermore, according to the SVEA, we have neglected terms proportional to $\ddot{\bar{a}}$ and $\ddot{\bar{b}}$, as well as terms of the type $\gamma_x\dot{\bar{a}} \ll \Omega\dot{\bar{a}}$ under the assumption of weak damping.

Equation (2.7) is a classical coupled mode equation, which has the exact form of the time dependent Schrödinger equation describing the evolution of a two-level system with level splitting Δ and coupling rate κ [17]. The complex amplitudes $\bar{a}$ and $\bar{b}$ in our classical system are amplitudes of the motion of a classical oscillator. In a quantum mechanical system, they are complex amplitudes multiplying the eigenfunction of the ground and excited state of the two-level atom, respectively [16].

A particularly interesting case to consider is that of resonant driving, where the coupling constant is varied harmonically as a function of time according to $\kappa = 2\kappa_c\cos(\omega t) + 2\kappa_s\sin(\omega t)$, where ω is chosen close to the level splitting Δ. In the rotating wave approximation [18], using the basis

$$\bar{a}(t) = a(t)\exp\left[-\mathrm{i}\frac{\omega}{2}t\right], \tag{2.8}$$

$$\bar{b}(t) = b(t)\exp\left[+\mathrm{i}\frac{\omega}{2}t\right], \tag{2.9}$$

we find the equation of motion

$$\mathrm{i}\begin{pmatrix}\dot{a}\\ \dot{b}\end{pmatrix} = \frac{1}{2}\begin{bmatrix}-\delta - \mathrm{i}\gamma_x & \kappa_c + \mathrm{i}\kappa_s\\ \kappa_c - \mathrm{i}\kappa_s & \delta - \mathrm{i}\gamma_y\end{bmatrix}\begin{pmatrix}a\\ b\end{pmatrix}, \tag{2.10}$$

where we have introduced the detuning $\delta = \Delta - \omega$ of the drive relative to the level splitting.

2.4 Bloch-Space Representation

The behavior of the parametrically coupled system can be understood graphically using a representation introduced by Felix Bloch [17]. The state of the system, described by the complex amplitudes $a(t)$ and $b(t)$, can be described in Bloch space using the transformation

$$s_x = ab^* + a^*b, \tag{2.11}$$

$$s_y = \mathrm{i}(ab^* - a^*b), \tag{2.12}$$

$$s_z = bb^* - aa^*, \tag{2.13}$$

where $\mathbf{s} = [s_x, s_y, s_z]^T$ is called the Bloch vector which can be conveniently illustrated in a three dimensional real space. Note that the amplitudes $a(t)$ and $b(t)$ offer four degrees of freedom (each has a real and an imaginary part), while Bloch space is only three dimensional. The degree of freedom separated out is the absolute phase of a and b. We can rewrite Eq. (2.10) as an equation of motion for the Bloch vector

$$\begin{pmatrix} \dot{s}_x \\ \dot{s}_y \\ \dot{s}_z \end{pmatrix} = \begin{bmatrix} -\gamma & \delta & \kappa_s \\ -\delta & -\gamma & \kappa_c \\ -\kappa_s & -\kappa_c & -\gamma \end{bmatrix} \mathbf{s}, \tag{2.14}$$

where we assumed $\gamma_x = \gamma_y = \gamma$. The equation of motion of the Bloch vector can be expressed in the form

$$\frac{\mathrm{d}}{\mathrm{d}t}\mathbf{s} = \mathbf{R} \times \mathbf{s} - \gamma \mathbf{s} \tag{2.15}$$

with the vector $\mathbf{R} = [-\kappa_c, \kappa_s, -\delta]^T$. According to Eq. (2.15), the Bloch vector rotates around the rotation vector $\mathbf{R}$ with the so-called Rabi frequency $\Omega_R = |\mathbf{R}| = \sqrt{\kappa_c^2 + \kappa_s^2 + \delta^2}$. In the absence of damping ($\gamma = 0$), the length of the Bloch vector is conserved and its tip can lie anywhere on a sphere in Bloch space, called the Bloch sphere. With appropriately normalized amplitudes, the Bloch sphere has unit radius. The orientation of the rotation vector is set by the coupling frequencies κ_s and κ_c as well as the detuning δ. The idea at the heart of coherent control is that the Bloch vector can be brought from any starting point on the Bloch sphere to any other point by generating a suitable rotation vector $\mathbf{R}$ (by turning on a parametric coupling) for the right time.

Let us discuss a few basic operations on the Bloch sphere. To ease our orientation on the Bloch sphere, we denote its poles with N and S, and intersections of the coordinate axis with the equator as illustrated in Fig. 2.3. The first operation we consider is called a $\pi/2$ pulse. Assume we initialize our system at the north pole N of the Bloch sphere, corresponding to the Bloch vector $\mathbf{s}(t = 0) = [0, 0, 1]^T$. This state has finite amplitude b, but vanishing amplitude a. After the time $\tau_{\pi/2} = \pi/(2\Omega_R)$ in the presence of a coupling with $\kappa_c > 0$ and $\kappa_s = 0$, the system has evolved to point E, corresponding to $\mathbf{s}_c(\tau_{\pi/2}) = [0, 1, 0]^T$, since the Bloch vector has been rotated by an angle $\pi/2$ around the rotation vector pointing along the negative x axis. The Bloch vector is now pointing along the y axis in Bloch space, which means that there is equal amplitude in the a mode and in the b mode. On the other hand, a $\pi/2$ pulse with coupling $\kappa_c = 0$ and $\kappa_s > 0$ takes the Bloch vector from the north pole N of the Bloch sphere to the point $\mathbf{s}_s(\tau_\pi/2) = [1, 0, 0]^T$, which we denote as F, on the equator. The difference between the points E and F is that the relative phase between a and b of these states differs by $\pi/2$. Finally, the detuning δ generates a rotation of the Bloch vector around the z axis. Accordingly,

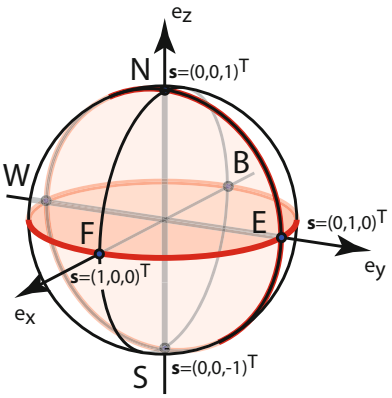

Fig. 2.3 The state of any two-mode system can be represented by the Bloch vector $\mathbf{s}$. The tip of the Bloch vector can lie anywhere on a unit sphere, called the Bloch sphere. The north pole of the Bloch sphere N corresponds to $\mathbf{s} = [0, 0, 1]^T$. In this state, all amplitude is in the mode b, while the amplitude of mode a vanishes. The south pole S corresponds to $\mathbf{s} = [0, 0, -1]^T$, where the amplitude of mode b vanishes and all amplitude is in mode a. States on the equator describe the system with equal amplitude in modes a and b, where the precise location along the equator denotes the relative phase between a and b

after a time $\pi/(2\delta)$, the Bloch vector will have rotated from the point F to the point E. To generalize operations in Bloch space, we define the operator $R_i(\theta)$, corresponding to a rotation by the angle θ around the axis i. Therefore, a rotation by an angle π around the x axis is denoted as $R_x(\pi)$.

2.5 The Ramsey Interferometer: A Non-reciprocal Device

A Ramsey interferometer is a device commonly used to characterize the coherence properties of quantum mechanical two-level and classical two-mode systems [17, 19–21]. A two-mode system traversing a Ramsey interferometer can be thought of as passing three "signal processing stations", as illustrated in Fig. 2.4a. We number these stations from left to right. In station 1, the operation $R_x(\pi/2)$ is carried out. In the station 2, a rotation $R_z(-\pi/2)$ is effected. In station 3, the Bloch vector of the system is rotated by $R_y(-\pi/2)$. Accordingly, the Bloch vector of the system leaving the Ramsey interferometer on the right $\mathbf{s}_{\text{out}}^{\text{right}}$ is related to that of the system when entering the device $\mathbf{s}_{\text{in}}^{\text{left}}$ from the left via the relation

$$\mathbf{s}_{\text{out}}^{\text{right}} = R_y(\pi/2)R_z(\pi/2)R_x(\pi/2)\mathbf{s}_{\text{in}}^{\text{left}}. \tag{2.16}$$

Let us consider the passage of a system entering the Ramsey interferometer in state S from the left, as illustrated in Fig. 2.4b. After station 1, the system is in

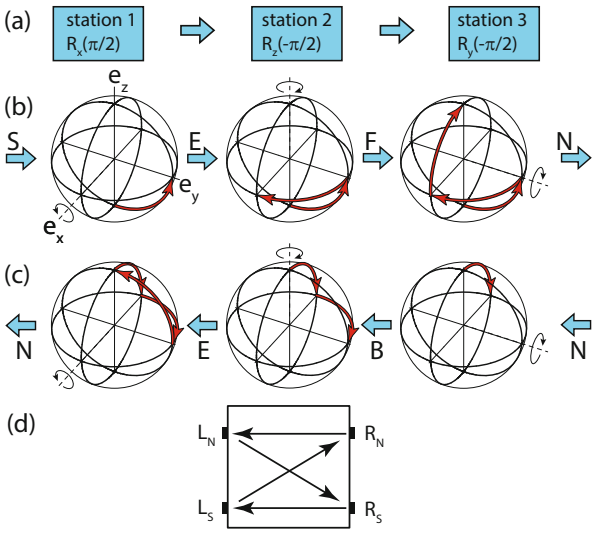

Fig. 2.4 (**a**) A Ramsey interferometer broken down into three "signal processing stations", each one carrying out a rotation on the Bloch vector of the traversing system. (**b**) System in state S entering the Ramsey interferometer from the left exits on the right in state N. (**c**) System in state N entering the interferometer from the right exits on the left in state N. (**d**) Representation of Ramsey interferometer as 4-port device

state E, followed by state F after station 2, and it leaves the interferometer in state N after station 3. Following the same reasoning, a system entering in state N is transformed via W and B to state S. In the (NS) basis, where we have $N = (1, 0)^T$ and $S = (0, 1)^T$, the transfer matrix for passage from left to right reads

$$\mathbf{s}_{\text{out}}^{\text{right}} = T_{\text{lr}}\mathbf{s}_{\text{in}}^{\text{left}} \tag{2.17}$$

with

$$T_{\text{lr}} = \begin{bmatrix} 0 & 1 \\ 1 & 0 \end{bmatrix}. \tag{2.18}$$

Importantly, when reversing the direction of passage through the Ramsey interferometer, the behavior is rather different. A system entering in state N from the right is first rotated by station 3 to B, by station 2 to E and by station 1 back to N. Furthermore, a system entering in state S from the right leaves the apparatus in the same state S when leaving on the left. Therefore, the transfer matrix for passage from right to left reads

$$T_{\text{rl}} = \begin{bmatrix} 1 & 0 \\ 0 & 1 \end{bmatrix}. \tag{2.19}$$

The Ramsey interferometer is non-reciprocal. Passing the device from left to right turns N into S and vice versa, while in the reverse direction, N remains N and S remains S. We can graphically illustrate the function provided by the Ramsey interferometer as the 4-port in Fig. 2.1d.

2.6 Discussion and Conclusion

We have realized that the Ramsey interferometer is non-reciprocal. Sending a system in state N into the interferometer from the left yields an output state S leaving the interferometer on the right. However, sending an input state S into the interferometer from the right yields the output state S leaving the interferometer on the left. The non-reciprocal nature of the Ramsey interferometer arises from the fact that rotations in a three dimensional space do not commute. Sending a two-mode system through a Ramsey interferometer from left to right does not (in general) yield the same result when sending the same system in from the right, since reversing the order of the rotations leads to a different result

$$R_x(\pi/2)R_z(-\pi/2)R_y(-\pi/2) \neq R_y(-\pi/2)R_z(-\pi/2)R_x(\pi/2). \tag{2.20}$$

For a thorough treatment of non-reciprocity in coupled mode systems from a group theoretical perspective, we refer the reader to Ref. [15].

In conclusion, we have provided an introduction the theory of parametric mode coupling. Using a system of two classical harmonic oscillators, we have introduced the concept of the Bloch sphere to discuss the Ramsey interferometer and illustrate its non-reciprocal nature.

References

1. Weng CC (1999) Waves and fields in inhomogeneous media. In: Dudley DG (ed) Wiley-IEEE Press Series on Electromagnetic Waves
2. Zangwill A (2013) Modern electrodynamics. Cambridge University Press, Cambridge
3. Saleh B, Teich M (2007) Fundamentals of photonics. Wiley series in pure and applied optics. Wiley, Hoboken
4. Kamal AK (1960) A parametric device as a nonreciprocal element. Proc IRE 48(8):1424
5. Kamal A, Clarke J, Devoret M (2011) Noiseless non-reciprocity in a parametric device. Nat Phys 7(4):311
6. Fang K, Yu Z, Fan S (2012) Photonic Aharonov-Bohm effect based on dynamic modulation. Phys Rev Lett 108:153901
7. Fang K, Yu Z, Fan S (2013) Experimental demonstration of a photonic Aharonov-Bohm effect ar radio frequencies. Phys Rev B 87:060301
8. Estep NA, Sounas DL, Soric J, Alù A (2014) Magnetic-free non-reciprocity and isolation based on parametrically modulated coupled-resonator loops. Nat Phys 10(12):923
9. Lira H, Yu Z, Fan S, Lipson M (2012) Electrically driven nonreciprocity induced by interband photonic transitions on a silicon chip. Phys Rev Lett 109:033901
10. Tzuang LD, Fang K, Nussenzveig P, Fan S, Lipson M (2014) Non-reciprocal phase-shift induced by an effective magnetic flux for light. Nat Photon 8:701
11. Ruesink F, Miri MA, Alu A, Verhagen E (2016) Nonreciprocity and magnetic-free isolation based on optomechanical interactions. Nat Commun 7:13662
12. Fang K, Luo J, Metelmann A, Matheny MH, Marquardt F, Clerk AA, Painter O (2017) Generalized non-reciprocity in an optomechanical circuit via synthetic magnetism and reservoir engineering. Nat Phys 13(5):465

13. Peterson GA, Lecocq F, Cicak K, Simmonds RW, Aumentado J, Teufel JD (2017) Demonstration of efficient nonreciprocity in a microwave optomechanical circuit. Phys Rev X 7:031001
14. Bernier NR, Toth LD, Koottandavida A, Ioannou MA, Malz D, Nunnenkamp A, Feofanov A, Kippenberg T (2017) Nonreciprocal reconfigurable microwave optomechanical circuit. Nat Commun 8(1):604
15. Ranzani L, Aumentado J (2014) New J Phys 16(10):103027
16. Frimmer M, Novotny L (2014) The classical Bloch equations. Am J Phys 82:947
17. Allen L, Eberly JH (1987) Optical resonance and two-level atoms. Dover Books on Physics, New York
18. Fox M (2006) Quantum optics: an introduction, vol 15. OUP, Oxford
19. Ramsey NF (1950) A molecular beam resonance method with separated oscillating fields. Phys Rev 78:695
20. Faust T, Rieger J, Seitner MJ, Kotthaus JP, Weig EM (2013) Coherent control of a classical nanomechanical two-level system. Nat Phys 9(8):485
21. Okamoto H, Gourgout A, Chang CY, Onomitsu K, Mahboob I, Chang EY, Yamaguchi H (2013) Coherent phonon manipulation in coupled mechanical resonators. Nat Phys 9(8):480

Chapter 3
Nanophosphors: From Rare Earth Activated Multicolor-Tuning to New Efficient White Light Sources

Maura Cesaria and Baldassare Di Bartolo

Abstract The huge and impossible to list number of publications dealing with luminescent materials demonstrates widespread interest at both fundamental and technological level in their spectroscopic properties and applications. Moreover consequences, opportunities and challenges of spatial confinement have prompted worldwide interest in nanoscale-sized luminescent materials, termed nanophosphors (n-PSPs) as a valid alternative to fluorophores and semiconductor quantum dots.

In this contribution the main classes of luminescent materials as well as spectroscopy of rare earth (RE)-activated phosphors (PSP) are first overviewed with focus on REs' transitions, luminescence mechanisms, electron-lattice dynamics, thermal line broadening and line shift. Then, the corresponding scenario for n-PSPs is presented and discussed, by providing many examples, with focus on the effects of spatial confinement and surface-to-volume ratio on luminescence efficiency, lifetime of the excited states, electron-phonon dynamics, luminescence quenching, confinement of dopants and tuning of multicolor emission. In particular, RE-activated multicolor emission is intensively investigated to produce white light for indoor and outdoor lighting. In this respect, recent reports are mentioned about a new class of efficient broadband white light emitting n-PSPs consisting of nominally un-doped RE-free oxide nanopowders and TM-doped hosts with temperature-independent emission. The novelty of this approach lies in presenting a route alternative to the presently investigated strategies to obtain WL sources that mainly include RE dopants and single-phase compounds containing REs as stoichiometric components.

Keywords Rare earths · Nanophosphors · White light

M. Cesaria
IMM-CNR Lecce, Institute for Microelectronics and Microsystems, Lecce, Italy

B. Di Bartolo (✉)
Department of Physics, Boston College, Chestnut Hill, MA, USA
e-mail: dibartob@bc.edu

B. Di Bartolo et al. (eds.), *Quantum Nano-Photonics*, NATO Science for Peace and Security Series B: Physics and Biophysics,
https://doi.org/10.1007/978-94-024-1544-5_3

3.1 Introduction

The first documented material emitting light in the dark dates to 1603, when the Italian shoemaker Vincenzo Cascariolo found that a stone (baryte) from the outskirts of Bologna was able to show persistent luminescence in the dark after being exposed by day to the Sun [1]. Since the introduction of the term "luminescence" by Eilhard Wiedemann [2], phenomena and mechanisms involving emission of photons from materials under different excitation conditions (electromagnetic, electric current, heating, charged energetic particles or chemical) have been widely studied at the fundamental level and exploited in numerous devices as well as for developing luminescence-based detection techniques. In particular the term "photoluminescence" refers to emission of electromagnetic radiation (photons) from a material following absorption of proper electromagnetic radiation (exciting source) [3, 4].

Beside conventional linear absorption, non linear absorption processes can occur that are classified as non resonant (meaning without the presence of intermediate gap states) and resonant (meaning with the assistance of intermediate gap states) multi-photon absorption. Non-resonant multi-photon interband absorption can be identified by the law $I = A\,P^n$, where I is the intensity of the emission peak, P is the pumping power, A is a constant and n stands for the number of photons involved in the multi-photon absorption [5].

Photo-luminescence phenomena can be categorized as "fluorescence" and "phosphorescence" depending on the emission time-scale: while fluorescence is associated with a short decay time (10–9 s < t < 10 ms after the excitation), phosphorescence occurs over much longer decay time (t > 0.1 s up to hours or even days) due to the involvement of spin-forbidden transitions (i.e., long lived excited state) and phonon-related processes [6]. Moreover, according to the relationship between the energy of absorption and emission processes, photoluminescence can be classified as:

- "resonant emission" whenever the photo-luminesce radiation has the same energy as the absorbed radiation,
- "up-conversion emission" if it involves the conversion of the exciting photons to higher energy emission photons and
- "down-conversion emission" if the exciting photons lead to lower energy emission photons.

In most cases, the well-known "Stokes principle" holds, i.e., down-conversion occurs, and the difference between the absorption peak and the emission peak of the same electronic transition is named "Stokes shift". On the other hand, the nomenclature "anti-Stokes photoluminescence" refers to the occurrence of photoluminescence with energy larger than the excitation energies by only a few k_BT (k_B is the Boltzmann constant, T is the absolute temperature). Instead, the term "up-conversion" (UC) technically indicates processes where the emitted photon energy exceeds the exciting photon energy by 10–100 k_BT (for example, conversion

of infrared (IR) radiation to visible and ultraviolet (UV) one) [7, 8]. Materials exhibiting UC processes are referred to as "up-converters".

Among luminescent materials (commonly termed "phosphors"(PSPs)), inorganic crystal compounds doped with one or more rare earth (RE) trivalent lanthanide ions are efficient up-converters due the richness of metastable excited states of the optical centers [9–12] that act as energy transfer bridge and/or emitting elements (donor/activator ion(s)). Indeed, due to the dipole-forbidden character of the intra-configurational 4f transitions (i.e., low absorption cross-sections and long luminescence lifetimes), direct excitation of lanthanides may be an inefficient process. As most inorganic crystals do not exhibit UC emission at room temperature, doping a well selected crystalline host with lanthanide ions and dopant-dopant interactions can enable to induce efficient UC luminescence and tunable multi-color emission [10]. Photoluminescence of RE-activated compounds is characterized by richness of energy levels, emission energy characteristic of the RE's electronic configuration, photo-stability, long-lasting luminescence lifetime, sharp emission lines, high color purity and tunable luminescence by co-doping. All of this is strictly dependent on the electronic configuration of lanthanides: crystalline field of the ligands or time variation of the crystal field have no or poor influence on the RE ions' 4f states due to their localization and shielding by the outer 5s and 5p subshells [13, 14].

Huge theoretical and experimental literature deals with physics of bulk PSPs: interplay between RE dopants and host compounds to enhance luminescence yield and efficiency, emission from optically active ions, radiative and non-radiative relaxation processes (energy-transfer (ET), UC, phonon-assisted relaxation, cross-relaxation (CR), concentration quenching, vibronic transitions) (see paragraph on bulk PSPs for details and references). The focus on bulk PSPs for more than 30 years until the late 1990s was motivated by practical limitations in preparing nanocrystals (sizes smaller than 100 nm) with high control on synthesis processes, size- and shape-dispersion, composition and surface properties. The interest in nanoscience and nanotechnology as well as the increasing trend to miniaturization have prompted the worldwide interest in applications of nanophosphors (n-PSPs) (i.e., nano-sized PSPs) as an alternative to organic fluorophores and quantum dots for biological, medical imaging and multiplexed biological labeling applications due to UC luminescence, large anti-Stokes shifts (up to 500 nm), excellent photostability, high luminescence quantum efficiency, long luminescence lifetime, narrow emission lines, high color purity, removal of UV excitation-induced photo-damage to biological samples, quantum cutting, and absence of photo-bleaching and photoblinking [15–20].

Other advantageous properties of n-PSPs are near infrared (IR) excitation with low power density (nearly 100 mW cm^{-2}), no auto-fluorescence background in biological systems under IR excitation, deep penetration lengths of the IR excitation light in biological specimens enabling large tissue penetration depth [21], minimum background noise for luminescent applications in vivo and low toxicity that make them chemically and biologically compatible as well as ideal luminescence probes in biophysics, biomedical labeling and imaging [12, 22–29]. Importantly, spatial

confinement has interesting impact on excited-state dynamics of n-PSPs, such as quantum efficiency with luminescence lifetime decreased by a few orders of magnitude for decreasing size, phonon-assisted ET, enhancement of the UC efficiency, multi-color emission [12, 30–34].

Example key-applications of lanthanide-activated nanophophors are displays [35–37], solar cells [38–42], nano-thermometry in cells [43] photodynamic therapy [44], and indoor and outdoor lighting [45, 46]. In the context of lighting strategies, the challenge of science and technology is to develop lighting sources with good efficiency, low power consumption, durability, thermal and chromatic stability, high color rendering, price competitiveness, environmental friendliness and ability to mimic the quality of the white light (WL) emitted by conventional incandescent and fluorescence lamps, which is most suitable for the human eye. Since the demonstration of WL emission by a light emitting diode (LED) based on collecting the mixed blue-yellow emission from a blue emitting ($\lambda \approx 440-460$ nm) InGaN LED chip used to excite a yellow-emitting down-converting phosphor (Ce-doped yttrium aluminum garnet YAG ($Y_3Al_5O_{12}$)) crystal [47, 48], solid-state LED WL sources have prompted interest both at the fundamental and market level thanks to their promising superior properties with respect to incandescent or white fluorescent lamps (such as improved and improvable luminous efficiency, energy-saving, long-lifetime, small volumes suitable in integrated electronics and environment-friendly features) [48–52].

White LEDs including blue-emitting GaN LEDs (450–460 nm) coated with yellow-emitting YAG:Ce^{3+} PSP suffer from poor color reproducibility, poor color-rendering index, and thermal quenching of emission at elevated temperatures with output power of the blue LED that saturates at high driving currents [53–55]. Besides mixing two complementary colors, another strategy to obtain WL emission is superposition of three primary colors (red (R), green (G) and blue (B)) by a tri-color phosphor excited by UV-LEDs. These so-called RGB PSPs, where RGB stands for Red-Green-Blue, can suffer from low luminescence efficiency because of absorption of blue emission by red and green phosphors [56]. In order to solve for the losses of RGB PSPs, single-phase WL emitting PSPs have been proposed [57].

In general, several technical drawbacks negatively affect the lighting performances of LED-based PSPs:

- blue emitters with improved efficiency and stability would be requested,
- input power-dependent emitting color and deficiency in the red component in blue LED coupled to yellow PSPs,
- improved green and yellow emission efficiency is needed,
- reabsorption of blue light from red and green PSPs in the case of RGB PSPs occurs,
- complex processing technology and careful color balance of PSP(s) emission are needed,

- luminescence spectra are unable to cover the whole visible-light range (a broad bright WL emission band (380–780 nm) or yellowish light can be observed),
- photon reabsorption and emission in multilayer architectures reduce the emission efficiency of down-converting PSPs,
- color shifts can result from driving current and chip temperature,
- the long-term stability of emitters is challenging,
- poor quantum efficiency of RE-based up-converter PSPs can result due to non-radiative loss channels,
- emission of UC WL can be quenched by CR processes in oxide and fluoride hosts triply-doped with RE ions (usually Tm^{3+}, Er^{3+}, or Yb^{3+} as sharp-line red/green/blue emitters, following absorption of Yb^{3+} and ET to Er^{3+}/Yb^{3+}levels),
- degradation of the device performance resulting from processing, packaging, and assembly of the PSPs [48–50, 56, 58–63].

Notably, most known PSPs consist of inorganic matrices doped with RE activator cations and in lesser extent TMs. Because of the lack of availability and chemical synthesis challenges of REs, whose market is dominated by China, and their environmental toxicity, scientific community is being pushed to explore novel PSPs including residual content of REs or being RE-free [64]. In this scientific scenario, the investigation of new WL emitting sources is an active field of research in both fundamental and applicative frameworks with prominent market opportunities.

In this review contribution, basics of PSP physics and spectroscopy (main classes, radiative and non radiative processes, choice of host matrix and dopants) are overviewed to provide basic information and physical insight to a reader new to the subject and to laid foundation to the discussion of the properties and advancements of n-PSPs. In this respect, discussion deals with the parameters tuning the spectroscopic response of n-PSPs with a particular focus on multi-color emission, influence of the surface-to-volume ratio and influence of the spatial confinement on dynamical characteristics (emission decay and rise time, line broadening and line shift). Many examples are provided and discussed to illustrate different issues depending on host and dopant combination as well as inherent characteristic of RE transitions and electronic configuration. At least, recently disclosed efficient broadband WL emitting n-PSPs consisting of nominally un-doped RE-free oxide nanopowders and TM-doped hosts with temperature-independent emission are mentioned [65–76]. The novelty of this approach, whose intellectual merit lies in presenting a route alternative to the presently investigated strategies to obtain WL sources, relies on presenting materials still unexplored systematically as WL lighting sources. Indeed, literature reports on optically inactive hosts at least doubly doped with different RE ions or oxides including RE ions as stoichiometric components.

3.2 Luminescence of RE-Activated PSPs: Background and Emission Mechanisms

3.2.1 Background

Based on the composition, three main classes of solid-state luminescent materials can be introduced:

- materials that inherently contain luminescent centers,
- materials consisting of an optically inactive crystal (termed host crystal) and luminescent ions termed activators (i.e. dopants acting as emitters under proper electromagnetic excitation),
- host crystals containing activator-sensitizer pairs, where the sensitizers are dopants that absorb the excitation energy and transfer it to neighboring activators.

Hereafter, a host crystal (Host) doped with one or more chemical elements (X, Y, Z) will be indicated as Host: X, Y, Z and a pair of co-dopant elements X and Y will be referred to as X/Y.

Since in general UC luminescence can't be obtained at room temperature by inorganic crystals, host materials doped with localized luminescent centers have been subject matter of intense research at the applicative level. In particular, RE-doped semiconductors or oxide host crystals show unique luminescent properties, including large Stokes shift, absence of optical blinking and photo-bleaching, UC processes (conversion of long-wavelength exciting photons into short-wavelength emission) and sharp-line emission spectra with emission lines poorly influenced by the chemical surroundings. The REs' characteristic sharp emission features are related to the REs' electronic configuration ($[Xe]4f^N$, where N refers to the number of electrons in the f-shell). Indeed, based on the periodic table of elements, the so-called "RE metals" include scandium (Sc), yttrium (Y), lanthanum (La) and the 14 lanthanide elements (cerium (Ce), praseodymium (Pr), neodymium (Nd), promethium (Pm), samarium (Sm), europium (Eu), gadolinium (Gd), terbium (Tb), dysprosium (Dy), holmium (Ho), erbium (Er), thulium (Tm), ytterbium (Yb), lutetium (Lu)) with atomic number Z ranging from 58 to 71. The most stable oxidation state of RE elements is three, meaning triply ionized or trivalent ions. Trivalent lanthanides have an outer electronic configuration $5s^25p^64f^N$ where the number N of electrons in the un-filled 4f shell ranges from 1 (Ce ion) to 13 (Yb ion) and the filling criterion of the 4f shell is dictated by the Hund rules. The $5s^25p^6$ outer less bounded configuration shields the valence electrons $4f^N$ from interactions with surrounding elements (weak electron-phonon coupling).

In contrast to RE elements, the unfilled outermost d-orbitals of transition metal (TM) elements, that are more extended and delocalized than f-orbitals, are involved in bonds with ligands leading to splitting of the atomic (unperturbed) levels from the host crystal field.

As a consequence of the screened f-states, the optical spectra of RE-activated crystals can present sharp-lines very similar in different hosts and resembling the

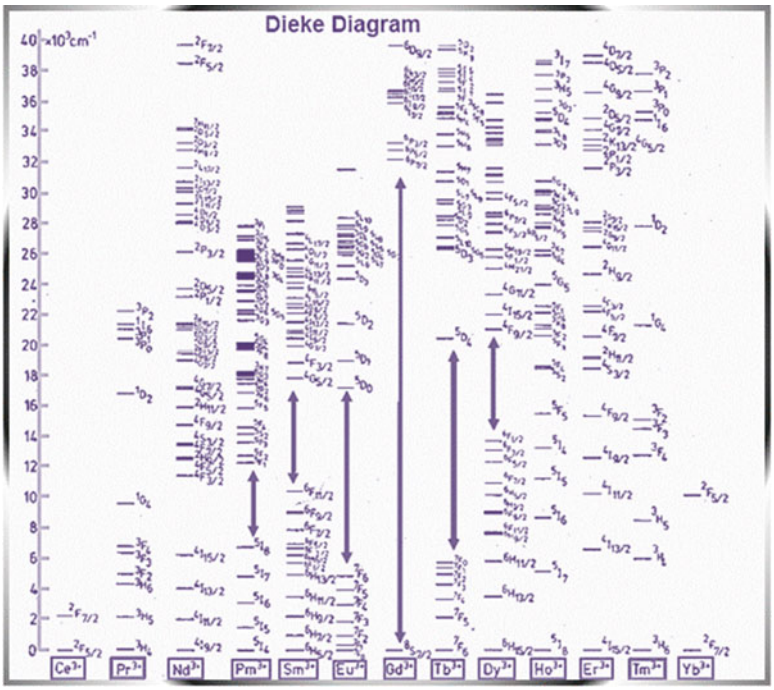

Fig. 3.1 Sketch of the Dieke diagram listing the energy levels for all lanthanides in the energy range 0–40000 cm^{-1}

counterpart RE free ions [13, 14]. This peculiarity of RE ions enables to analyze the emission spectra of crystals containing RE centers in terms of the energy level schemes of the corresponding element in a free state. This means that we can use the sets of quantum numbers classifying the energy levels of free RE ions to assign the spectral features stemming from RE optically active dopants in host crystals. Hence, the Russell-Saunders notation can be adopted: each RE dopant has multiplets of states labeled as $^{2S+1}L_J$, where S, L and J refers to spin, orbital and total (J = L−S, ... L + S) angular momentum of the N 4f electrons (N = 1, ... 13), respectively. The host-independent emission lines of all lanthanides in the range 0–40000 cm^{-1} can be easily identified or assigned based on the so-called "Dieke diagram" (Fig. 3.1), that resulted from measurements of absorption and luminescence spectra of the lanthanide series in a LaCl3 crystal [77]. It shows the energies of the states of the trivalent RE ions, indicates the magnitude of the crystal-field splitting by the width of the state and the energy level of the corresponding free-ion ($^{2S+1}L_J$, spin (S), orbital (L) and angular (J) momentum quantum numbers) given by the center of gravity of each J-multiplet.

As the Dieke diagram shows, the several chances of distribution of electrons over the seven 4f orbitals imply complex energy level structure of lanthanide dopants. In practice, radiative transitions stem form a restricted set of energy levels separated by

a large energy gap with respect to the next lower-lying level. Indeed, energy levels with large enough gap with respect to the next lowest energy levels participate more likely in radiative relaxation that in multiphonon nonradiative relaxation. Hence, the photoluminescence of lanthanide ions is dominated by the $4f^N5s^25p^6$ configuration.

Figure 3.2 depicts partial energy level diagram of lanthanides commonly used as luminescent centers in PSPs due to their space ladder-like energy levels (Ho, Er, Tm, Yb, Eu, Tb).

Typical emitting levels of lanthanides are $^4G_{5/2}$ for Sm^{3+}, $^5D_{0,1,2,3,4}$ for Eu^{3+}, $^5D_{3,4}$ for Tb^{3+}, $^5S_2$ for Dy^{3+}, $^5S_2$ and $^5S_5$ for Ho^{3+}, $^2H_{9/2}$, $^4S_{3/2}$, $^4F_{9/2}$ for Er^{3+}, and $^1D_2$, $^1G_4$ for Tm^{3+}. For example, Eu^{3+} is an excellent candidate to produce red color LED's, with its orange red/red emission arising from the characteristic $^5D_0 \rightarrow {}^7F_{1,2}$ (555 and 614 nm) electronic transitions. Yb^{3+} ions have a simple electronic energy structure and the most commonly exploited transition is $^2F_{7/2} \rightarrow {}^2F_{5/2}$ that can be excited at 980 nm. Moreover, Er^{3+}, Tm^{3+}, and Ho^{3+} have energy levels well matching the energy of the excited state of Yb^{3+} ion, which is suitable for (resonant or non-resonant) energy transfer processes from the excited state of Yb^{3+} to the excited energy levels of the energy matching lanthanides. Among other radiative transitions of trivalent lanthanides the following ones may take place: $^4G_{5/2} \rightarrow {}^6H_{5/2,7/2,9/2}$ of Sm^{3+}, $^5D_{0,1,2} \rightarrow {}^7F_{0,1,2,3,4}$ of Eu^{3+}, $^5D_{3,4} \rightarrow {}^7F_{2,3,4,5,6}$ of Tb^{3+}, $^4F_{9/2} \rightarrow {}^6H_{15/2,13/2}$ of Dy^{3+}, $^5F_4$, $^5S_2 \rightarrow {}^5I_8$ and $^5I_4 \rightarrow {}^5I_8$ of Ho^{3+}, $^2H_{11/2}$, $^4S_{3/2}$, $^4F_{9/2} \rightarrow {}^4I_{15/2}$ of Er^{3+}, as well as $^1D_2 \rightarrow {}^3F_4$ and $^1G_4 \rightarrow {}^3F_4$,$^3H_6$ of Tm^{3+}. Among triply ionized RE activators, Dy^{3+} can simultaneously emit blue (483 nm, $^4F_{9/2} \rightarrow {}^6H_{15/2}$ transition) and yellow (584 nm, $^4F_{9/2} \rightarrow {}^6H_{13/2}$ transition) radiation, which is favorable for white light emission. Upon excitation at 344 nm, Tm3+ shows strong host-dependent blue emission (488 nm, $^1D_2 \rightarrow {}^3F_4$ transition) and characteristic weak red emission (697 nm, $^1G_4 \rightarrow {}^3F_4$ magnetic dipole transition).

While the ground state configuration of a RE element is almost "pure" (i.e., the same as the RE free ions), the excited states can have L–S coupling and J mixing, meaning that a single $^{2S+1}L_J$ multiplet could describe the excited states of REs depending on the host crystal. Hence, d-like states entering in the closest excited configuration $4f^{(N-1)}5d$ of a RE element cause host-dependent radiative transitions of RE centers.

Other excited configurations of RE elements that can perturb the $4f^N$ states are $4f^{(N-1)}6s$ and $4f^{(N-1)}6p$, that however can exert less influence due to their larger energy gap than the $4f^{(N-1)}5d$ configuration with respect to the $4f^N$ states. For example, Eu^{2+} (with electronic configuration $4f^7$) in most compounds emits a broad band (from UV to yellow/red light) stemming from the $4f^65d^1$-$4f^7$ transition and the host coordination remarkably affects the emission spectrum due to the transitions involving the outer 5d- orbitals.

The interactions that contribute as perturbations in determining the ground state energy level scheme due to coupling between f and d states of trivalent lanthanide dopants are, in order of decreasing influence, Coulomb interaction, spin-orbit interaction and crystal-field interaction (Fig. 3.3) [78, 79].

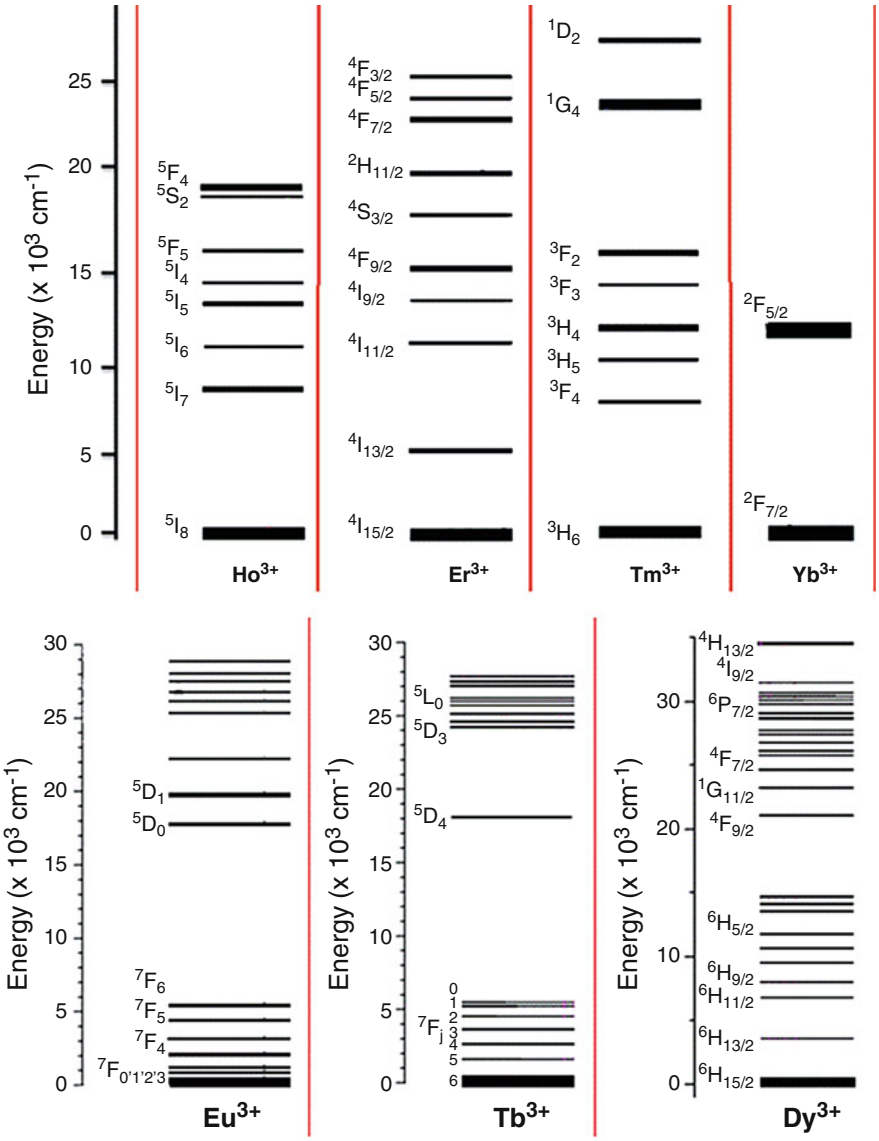

Fig. 3.2 Sketch of the partial energy level scheme of a few common trivalent RE elements (Ho, Er, Tm, Yb, Eu, Tb, Dy)

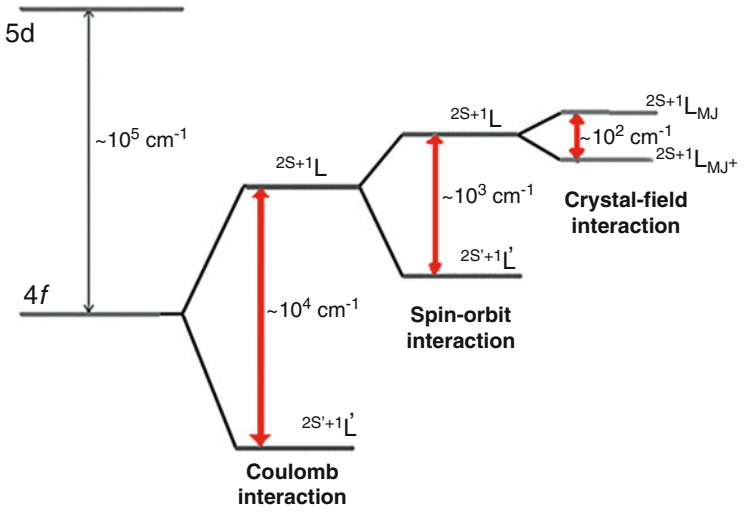

Fig. 3.3 Contributions to the splitting of the energy levels in a 4f 5d configuration of a RE-doped crystal host

Crystal field splitting (Dq) can be estimated by the following formula [80, 81]

$$D_q = \frac{Ze^2r^4}{6R^5}$$

where Z is the anion charge, e is the electron charge, r is the spatial extension of the d-like wavefunction, and R is the anion-ligand bond length. Hence, the larger energy level separation, the shorter the distance between the crystal site occupied by dopant and ligands is.

For example, in the case of $(Ca, Mg, Sr)_9Y(PO_4)_7$: Eu^{2+} phosphors, replacing Ca by Mg^{3+} (Sr^{2+}) induces a decrease (increase) of D_q due to the larger (smaller) ionic radius of the dopant that shifts the emission wavelength from 486 to 435 nm (blue-shift) with increasing Mg^{2+} content ($\leq$0.5) and from 486 to 508 nm (redshift) with increasing Sr^{2+} concentration ($\leq$0.5) [82].

The relationship between the electronic structure of RE ions and the transitions allowed by selection rules and crystal symmetry is the key to understand the luminescence properties of PSPs.

The above discussion points out that the luminescence from RE-doped hosts mainly originates from characteristic electronic transitions within the f-shell, meaning that tunable emission can be obtained based on different lanthanide dopants and their interplay, but the host lattice can exert an influence whenever excited states are involved in radiative transitions. To detail, RE emission features can be classified in two main classes: intra-configurational f–f transitions and d–f transitions. After introducing the basic characteristics of these RE-transitions, the role of the crystal

field symmetry can be better detailed in regard to the possibility to observe host-dependent energy-shifts of the RE emissions.

The f–f transitions take place between the ground state 4fN and an excited state 4fN and are characterized by a sharp emission line (FWHM < 10 nm) due to the shielding of the 4f-electrons by the outer s and p orbitals. Based on the parity conservation rule, in the case of centro-symmetric sites only magnetic dipole (i.e., $\Delta J = 0{,}1$ and when $\Delta J = 0$, only $\Delta J = |1|$ is allowed as any transition involving $J = 0$ is forbidden) f–f transitions are allowed, which are weaker than the electric dipole transitions. Whenever RE ions occupy non-centrosymmetric sites of a host crystal (for example, following removal of the inversion symmetry), f–f transitions can be observed due to the mixing between 4f states and states of different (opposite) parity belonging to a different electronic configuration (interaction of REs with crystal field or lattice vibrations) [13, 83, 84]. Although the emission energies of the f–f transitions in RE-doped crystals are unaffected with respect to the RE atomic counterpart (i.e., independent on the host lattice), the relative emission intensity depends on site symmetry and selection rules [13, 85], that is, while electric dipole transitions are also allowed in absence of inversion symmetry, magnetic dipole transitions are allowed if the RE site has inversion symmetry. While the intra-configurational f–f transitions of free lanthanide ions are inherently forbidden based on the parity selection rule, the uneven components of the crystal field can mix odd-parity configurations into the electronic configuration of RE dopants. The parity-forbidden intra f–f transitions are no longer forbidden whenever crystal field causes splitting of the energy levels of the $^{2S+1}L_J$ multiplets enabling coupling between f-states and high-energy lying unoccupied states of REs (typically, $4f^N$-$4f^{(N-1)}5d$ coupling in low symmetry (hexagonal, trigonal or lower symmetry) crystals) [86] or ligand-to-metal charge transfer configuration [87]. This issue points out the role of the host crystal (i.e., ion–ligand distance and site symmetry): strong odd crystal field components (for example, crystals with three-fold rotational axes and no inversion center) can induce splitting of the $^{2S+1}L_J$ energy multiplet and relief of the parity selection rules enables f–f transitions depending on crystal field symmetry and host-lanthanide interaction strength. The f–f transitions of RE ions show weak ion-lattice coupling strength, electric dipole oscillator strengths of 10^{-6}, and lifetimes ranging from 10^{-5} to -10^{-2} s (i.e., spin and parity forbidden transitions on RE ions are rather slow). For comparison, the d–f transitions of RE ions show strong ion-lattice coupling strength, electric dipole oscillator strengths ranging from 10^{-2} to 10^{-1}, and lifetimes ranging from 10^{-8} to 10^{-6} s. About d–f transitions, they involve the $4f^N$ ground state and $4f^{(N-1)}$-5d excited state are characterized by emission lines with FWHM from 30 to 100 nm (i.e., larger that the ones of f–f transitions) due to the influence of the crystal field on 5d-orbitals that causes $4f^{(N-1)}5d$ configurations of RE ions in solids different from those of free ions. Since the crystal-field interaction splits a d-level depending on symmetry and crystal field strength, host-dependent luminescence can be observed for RE ions showing d–f emission.

Transitions of RE elements hypersensitive to the crystal field can be observed for host crystal structure belonging to Cs, C1–6, C2v, C3v, C4v, and C6v

point groups [88, 89]. For example, typical absorption intra-4f transitions of the Dy^{3+} ions can be observed at 300, 328, 339, 355, 368, 394, 428, 455, and 475 nm as associated with the following transitions: $^6H_{15/2} \rightarrow {}^4K_{13/2} + {}^4H1_{3/2}$, $^6H_{15/2} \rightarrow {}^4K_{15/2}$, $^6H_{15/2} \rightarrow {}^4I_{9/2} + {}^4G_{9/2}$, $^6H_{15/2} \rightarrow {}^4M_{15/2} + {}^6P_{7/2}$, $^6H_{15/2} \rightarrow {}^4I_{11/2}$, $^6H_{15/2} \rightarrow {}^4M_{21/2}$, $^4I_{13/2} + {}^4K_{17/2} + {}^4F_{7/2}$, $^6H_{15/2} \rightarrow {}^4G_{11/2}$, and $^6H_{15/2} \rightarrow {}^4I_{15/2}$, $^6H_{15/2} \rightarrow {}^4F_{9/2}$ [90, 91].

The two dominant emission bands of Dy^{3+} elements appear in the blue (470–500 nm) and yellow (560–600 nm) spectral regions, respectively, stemming from the $^4F_{9/2} \rightarrow {}^6H_{13/2}$ forced electric dipole transitions and $^4F_{9/2} \rightarrow {}^6H_{15/2}$ magnetic dipole transitions. While the latter transition is hardly influenced by the crystal field strength around the Dy^{3+} ion, the former transition is hypersensitive to the crystalline environment and is the dominant emission feature for a low-symmetry host lattice with no inversion center [90, 92, 93]. The asymmetry ratio (i.e., the emission ratio of the dominant emission bands of the Dy^{3+} ion) is indicative of the degree of distortion of the inversion symmetry around the host lattice sites occupied by Dy^{3+} ions.

As a further example, the luminescence spectrum of $LiYF_4:Eu^{3+}$ n-PSPs shows sharp emission peaks in the red spectral region ($^5D_1$, $^5D_0 \rightarrow {}^7F_J$ (J = 0–6) transitions of Dy^{3+}), a peak at nearly 610–620 nm (hypersensitive $^5D_0 \rightarrow {}^7F_2$ electric dipole transition) and a peak around 590–600 nm ($^5D_0 \rightarrow {}^5F_1$ magnetic dipole transition) [94]. The electric dipole transition is very sensitive to the local environment as it is allowed only if the Eu^{3+} ion occupies a site without an inversion center. On the other hand, since the peak intensity of the $^5D_0 \rightarrow {}^5F_1$ transition is lower than that of the $^5D_0 \rightarrow {}^7F_2$ transition, Eu^{3+} ions are located at the non-inversion symmetric sites [95, 96].

Since dopants generally are required to have ionic size close to the one of the element that they replace for in the host lattice site, inorganic compounds of trivalent lanthanides are a natural choice as host materials for RE-doped phosphors. Other elements with ionic size close to lanthanides are alkaline earth ions (Ca^{2+}, Sr^{2+}, and Ba^{2+}) and TM ions such as Zr^{4+} and Ti^{4+}. As a consequence of the change in volume of the unit-cell induced by host-ion substitution, emission wavelength of RE-activated PSPs modified by changes of the strength of the crystal-field around the dopant can result [3].

The above discussion points out how doping, that inherently introduces localized lattice distortion, can be an effective method to tune the energy mismatch between levels of activator/sensitizer RE ions as well as transition probabilities by symmetry breaking/lowering. Lowered crystal symmetry can be induced by dopants with the same oxidation state of the lattice element to be replaced but different ionic radius or by changing the dopant site symmetry in different host crystal phases as well as lattice site.

About the influence of lattice sites, in most compounds Eu^{2+} (with electronic configuration $4f^7$) emits a broad band (from UV to yellow/red light) stemming from the $4f^65d^1$ $4f^7$ transition and the host coordination remarkably affects the emission spectrum due to the outer 5d-orbitals. Yellow-emission and a broad blue emission ($4f^7$-$4f^65d^1$ transition) results when Eu^{2+} ions occupy Ba sites and Sr sites,

respectively, in the $BaSrMg(PO_4)_2$ host crystal due to the presence of two kinds of lattice sites for Eu^{2+} activator centers [97]. Therefore, dopant site symmetry can be changed in a single host material yielding inherently different site symmetry without modification of chemical composition.

About the effect of different host crystal phases, an interesting example is sodium yttrium fluoride ($NaYF_4$) that can form with different phases: cubic α-$NaYF_4$, where the metal ion site has O_h symmetry, and hexagonal β-$NaYF_4$, where the metal ion site has C_{3h} symmetry. Doping $NaYF_4$ of both phases with Er^{3+} (electronic configuration $4f^{11}$) ion causes that the Er^{3+} energy level splitting due to locally distorted symmetry is no longer consistent with the site symmetry O_h and C_{3h}. Instead consistency with C_s site symmetry is induced, even if the host crystal retains its phase (cubic or hexagonal) [98]. The emission spectrum of Er^{3+} is usually dominated by the $^4S_{3/2} \rightarrow {}^4I_{15/2}$ transition (~660 nm) and $^4F_{9/2} \rightarrow {}^4I_{15/2}$ transition (~540 nm) in α-$NaYF_4$ and β- $NaYF_4$, respectively, with higher emission efficiency in the hexagonal phase host matrix. The hexagonal β-$NaYF_4$ phase activated by $Yb^{3+}$and Er^{3+} (β-$NaYF_4$:Yb/Er) or $Yb^{3+}$and Tm^{3+} (β-$NaYF_4$:Yb/Tm) ion pairs is one of the most efficient host material for RE-doped up-converters [99, 100]. In regard to Er^{3+} ion, while its ground state (i.e., a $^4I_{15/2}$ multiplet) is poorly influenced from the crystal field, the excited red-, green- and blue-emitting states of Er^{3+} in fluoride crystals (for example, $NaYF_4$) are a linear superposition of several states with less than 10% of J-mixing [9].

In general, an evaluation of the $4f^N5d^1$-$4f^N$ configuration coupling indicates that while it can induce no significant energy shift depending on the overlapping between the $4f^N5d^1$ and $4f^N$ configurations, remarkably enhanced transition probabilities can result from mixed eigenfunctions that make electric dipole transitions no longer forbidden [101]. Importantly, the weights of the $4f^N5d^1$-$4f^N$ mixed configurations depend on the energy gap between the $4f^N$ and $4f^N5d^1$ states in that larger probabilities are associated with the $4f^N$ states closer to the $4f^N5d^1$ states.

To improve the emission efficiency and reduce non-radiative losses of RE-activated phosphors, a stringent requirement on the host material is low lattice phonon frequencies, according to the multiphonon relaxation rate expressed by the exponential energy-gap law of Van Dijk and Schuurmans

$$W_0 = C \exp\left(-\alpha \frac{\Delta E}{h\upsilon_m}\right)$$

where C and α are parameters characteristic of the host crystal and $h\upsilon_m$ is the highest energy of the host lattice vibrations (phonons) that couple to the electronic transition of the RE ion [102]. Sodium rare-earth fluorides ($NaREF_4$), such as $NaYF_4$, $NaLuF_4$, and $NaGdF_4$, are chemically stable efficient host matrix due to their low photon energy, which involves a decrease in the probability of non-radiative decays and an increase of the quantum yield of UC emission [103–105]

For instance, trivalent Eu^{3+} ion (Fig. 3.2) is a red-emitting activator ($^5D_0$–^7F_J transitions (J = 0, 1, 2, 3, 4)) which can also exhibit low efficiency emissions from higher ^5D levels ($^5D_1$ (green), $^5D_2$ (green, blue), and $^5D_3$ (blue)) depending on

the host lattice (phonon frequency and crystal symmetry) and the doping content. Fluoride and oxyfluoride are suitable hosts for Eu^{3+} due to their low phonon frequencies that enable emission from the excited $^5D_{0,1,2,3}$ levels to the ^7F_J level [106, 107]. On the other hand, the probability of emission from the excited $^5D_{0,1,2,3}$ levels of Eu^{3+} ion at low doping content (x = 0.008, 0.015), is larger in $CaIn_2O_4$ than in Y_2O_3 because $CaIn_2O_4$ and Y_2O_3 crystals have vibration frequency of 475 and 600 cm^{-1}, respectively [108].

3.2.2 Luminescence Mechanisms

Depending on the energy difference with respect to the closest lower energy state, excited states can relax radiatively (i.e., by photon emission) or non-radiatively (i.e., by phonon emission as a result of ion-phonon interaction).

As overviewed, in PSPs luminescence can take place by the host lattice (i.e., band-to-band transitions or pathways involving energy levels of foreign ions) or by RE dopants classified as "activator" (A) when acting as emitting centers and "sensitizer" (S) when providing energy levels to transfer the energy (energy donor) to the emitting A ions. This latter mechanism is termed "sensitized luminescence". The lack of fully matched absorption bands between different lanthanide ions causes that different lanthanide ions cannot be excited under a single wavelength. Hence, indirect excitation via a sensitizer may act to couple transitions of different lanthanides for purposes of multicolor emission and color tuning.

The interplay between luminescence mechanisms of PSPs as well as non-radiative processes determine the resulting spectra and luminescence efficiency. The main mechanisms of luminescence in PSP materials are energy transfer (ET) and up-conversion (UC) that can take place through multistep electronic transitions driven by linear or non-linear light-matter interactions, resonant or phonon-assisted ET processes, radiative single RE ion transitions, RE-pair collective transitions, and intermediate phonon-relaxations.

Energy Transfer and Related Processes

Energy transfer refers to partial or total transfer of energy from a sensitizer center (donor ion) to a activator center (acceptor ion), i.e., a sensitizer absorbs the exciting energy and transfers it radiatively (i.e., by the emission of a photon) to the emitting activator ion. In practice, ET can take place in presence of overlap between the emission spectrum of the sensitizer S and the absorption (excitation) spectrum of the activator A and is termed " resonant ET" when the emission energy of S matches the absorption energy of A. Apart from La^{3+}, Ce^{3+}, Yb^{3+}, and Lu^{3+}, lanthanides have more than one excited 4f energy level and this richness of excited states translates in richness of possible emission colors as well as absorption of electronic excitations in ET processes. Indeed, ET is a very important process in co-doped systems, in which energy migration between sensitizers and activators and nonradiative relaxations are the primary excitation channels to observe UC luminescence.

For example, Yb^{3+} has a $^2F_{7/2}$ ground state and one excited 4f level ($^2F_{5/2}$) and the transition $^2F_{5/2} \rightarrow {}^2F_{7/2}$ has a large absorption cross-section and is associated with energy around 980 nm resonant with *f–f* transitions of Er^{3+}, Tm^{3+}, and Ho^{3+} [12]. This situation makes Yb^{3+}/Er^{3+}, Yb^{3+}/Tm^{3+} and Yb^{3+}/Ho^{3+} pairs suitable as S/A pairs for ET processes.

For anti-Stokes processes, under excitation at 980 nm Yb^{3+} is an efficient sensitizer to favor the stepwise ET to different activators (Ho^{3+}, Er^{3+},Tm^{3+}) [109] and Gd^{3+} is also used as the sensitizer to excite different lanthanide ions (Sm^{3+}, Eu^{3+}, Tb^{3+}, Dy^{3+}) under a single wavelength (275 nm) [110]. As a further example, ET from Mn^{2+} to Er^{3+} in MnF_2:Yb/Er and $KMnF_3$:Yb/Er compounds can take away the excitation energy of Er^{3+} in the $^4S_{3/2}$ level and increase the population of the $^4F_{9/2}$ state of Er^{3+}, which results in increased intensity ratio of the red-to-green emission [111, 112].

In the framework of the Dexter theory, the probability of energy transfer via multipolar interaction can be expressed by the following equation

$$P(R) = \propto \frac{Q_A}{R^b \tau_D} \int \frac{f_D(E) F_A(E)}{E_C} dE$$

where R is the donor-acceptor distance, P is the ET probability, Q_A is the total absorption cross-section of the acceptor, f_D and F_A are the probability distribution functions of donor and acceptor, respectively, τ_D is the decay time of the donor emission, and the other parameters depend on the type of ET pathway [113]. Moreover, according to Dexter's energy transfer formula, ln (η_0/η) is proportional to $C_{S/A}$ for exchange interaction and (η_0/η) is proportional to $C_{S/A}{}^{n/3}$ for multipolar interaction, where η_0 and η are the luminescence quantum efficiency of the sensitizer S without and with the activator A, respectively; $C_{S/A}$ is the total content of S and A; n = 6, 8, 10 (dipole–dipole, dipole–quadrupole, and quadrupole–quadrupole interactions, respectively) [113].

Multipolar S-A interaction is affected by the strength of the optical transitions, depends on the distance $R_{S\text{-}A}$ between S and A as $1/R_{S\text{-}A}{}^n$ (with n = 6, 8, 10 for dipole-dipole interaction, dipole-quadrupole interaction, quadrupole-quadrupole interaction, respectively) and can occur for center to center separations ranging from 2 to 10 nm (low doping concentration).

Exchange interaction is favored by high concentration of luminescent centers, large overlap integral between the electronic wave functions of S and A, small intrinsic decay time of S, large absorption strength of A, and a short distance S-A ($R_{S\text{-}A} < 0.5-1$ nm).

A critical distance of ET ($R_{ET,C}$) is defined as the distance for which the probability of occurrence of an ET process and the probability of radiative emission from S are equal. As a general rule, while ET from S to A dominates when the distance between S and A ($R_{S\text{-}A}$) is shorter than $R_{ET,C}$, radiative emission from S dominates when $R_{S\text{-}A} > R_{ET,C}$. Therefore, the efficiency of the ET process depends on spectral overlap S-A, $R_{ET,C}$ and the lifetime of S ions in absence and in presence of A ions [114].

Another contribution to ET is phonon-assisted ET that occurs whenever the difference between the transition energies of S and A is compensated by absorption or emission of phonons [115–117]. However, since phonon- assisted ET involves non radiative losses of the excitation energy, luminescence quenching may result from phonon-assisted ET.

Another process that can affect the luminescence yield in RE-activated phosphors is cross relaxation (CR), that is an ET process between two centers in which the decrease of energy of a center turns to excitation of a neighboring center. Cross relaxation may take place between the same centers (meaning that energy migration takes place without energy loss) or between two different centers having energy matched pairs of levels.

Cross-relaxation is a strongly active mechanism in Er^{3+}/Tm^{3+}co-doped upconverters [7, 118] and can take place in the intermediate states of Er^{3+} through two CR channels ($^2I_{11/2} + {}^2H_{11/2}$-$^4I_{13/2} + {}^4F_{3/2}$ and $^4F_{7/2} + {}^2H_{11/2}$-$^2H_{9/2}(^2G_{9/2}) + {}^4F_{9/2}$) that weaken the green emission resulting from $^2H_{11/2}$ and $^4S_{3/2}$ relaxing to the $^4I_{15/2}$ ground state and enhance the red emission from $^4F_{9/2}$ and blue emission from $^2H_{9/2}$.

The dopant combination $Yb^{3+}/Ho^{3+}/Ce^{3+}$ in hexagonal-phased $NaYF_4$ also leads to CR pathways. Indeed, the parity allowed *4f-5d* transitions of Ce^{3+} ions can depopulate the $^5F_4/^5S_2$ green emitting states of Ho^{3+}as well as populate the $^5F_2$ red-emitting level of Ho^{3+} by the two following CR pathways [119]:

$$
\begin{aligned}
&{}^5F_4/{}^5S_2\left(Ho^{3+}\right) + {}^2F_{5/2}\left(Ce^{3+}\right) \rightarrow {}^5F_5\left(Ho^{3+}\right) + {}^2F_{7/2}\left(Ce^{3+}\right)\\
&{}^5I_6\left(Ho^{3+}\right) + {}^2F_{5/2}\left(Ce^{3+}\right) \rightarrow {}^5I_7\left(Ho^{3+}\right) + {}^2F_{7/2}\left(Ce^{3+}\right).
\end{aligned}
$$

As a further example, the emission from the $^5D_{1,2,3}$ excited states of Eu^{3+} can be quenched by CR channels ($^5D_1$-$^7F_0$ and $^5D_0$-$^7F_3$) between neighboring Eu^{3+}ions, depending on the Eu concentration and phonon frequency of the host lattice [45]. In this respect, luminescence quenching may occur at concentrations of the localized centers above a critical value depending on the host material [92, 120]. This situation is referred to as "concentration-quenching" and includes CR and ET from one activator to another one.

For example, in host crystals doped with Dy^{3+}, for increasing Dy^{3+} concentration the intensity of the blue emission of Dy^{3+}ions, that originates from the $^4F_{9/2} \rightarrow {}^6H_{13/2}$ transition, increases up to a maximum value and then decreases due to RE-RE mutual interaction [121, 122].

In Pr^{3+}-doped inorganic crystals, mainly red emission is reported stemming from different $4f^2$-$4f^2$ transitions of Pr^{3+}, that is $^1D_2 \rightarrow {}^3H_4$ (603 nm), $^3P_0 \rightarrow {}^3H_6$ (617 nm) and $^3P_0 \rightarrow {}^3F_2$ (650 nm) transitions [123–125]. While optimized emission efficiency of the $^1D_2 \rightarrow {}^3H_4$ (603 nm) transition can be obtained at Pr^{3+} concentration ranging from 0.2 to 1.0%, a higher doping causes concentration quenching due to nonradiative ET pathways between neighboring Pr^{3+} ions [126–130].

The ion-ion critical distance (R_c) of ET can be expressed by:

$$R_c = 2\left(\frac{3V}{4\pi x_c N}\right)^{1/3}$$

where x_c is the critical concentration (for which the emission intensity and decay time begin to decrease rapidly), N is the number of RE ions in the unit cell with volume V of the host crystal [131].

Classes of UC Processes

The term UC refers to nonlinear optical processes based on the successive absorption of two or more photons followed by the emission of photons more energetic than the pump photons [7, 10]. Basically, absorption of low energy photons leads to populate excited states and if these excited states are long-lived (metastable) states then further absorption of photons for populating higher energy states is more probable than relaxation. Following multiple steps of excitation mediated by a series of metastable states, conversion of lower wavelength photons to higher wavelength radiation (i.e., UC) results due to radiative relaxation from higher energy levels. An important difference between UC and multiphoton processes is that the absorption of pump photons is sequential in the case of the UC mechanism and simultaneous in multiphoton absorption. Moreover, while a simultaneous two-photon process requires expensive high-intensity (10^6–10^9 W cm^{-2}) pump laser pulses, UC can be obtained by a low power (1–10^3 Wcm^{-2}) continuous wave laser.

In biological, label-free sensing and biomedical applications, important advantages of UC mechanisms is the possibility of using near-IR rather than UV excitation sources to minimize background auto-fluorescence, photo-bleaching, and photo-damage to biological systems while as well as to exploit the longer penetration depths of near-IR pump photons in the case of biological samples.

Among the most investigated UC host materials there are fluorides (sodium yttrium fluoride ($NaYF_4$), lithium yttrium fluoride ($LiYF_4$), sodium lutetium fluoride ($NaLuF_4$), calcium fluoride (CaF_2)), lutetium orthophosphate ($LuPO_4$), lutetium borate ($LuBO_3$), vanadium yttrium oxide (YVO_4), zirconium oxide (ZrO_2), yttrium oxide (Y_2O_3), gadolinium dioxide (Gd_2O_3) and so on.

The main classes of UC processes are "excited-state absorption" (ESA), "up-conversion by energy transfer" (ETU) and "two-photon absorption" (TPA) (Fig. 3.4).

ESA mechanism, which is the least efficient UC mechanism, involves a single center and works as follows for a three-level system. Absorption of a pump photon can lead either to an intermediate real excited state which lives long enough to let absorption of a second pump photon (excited state absorption) or to radiationless relaxations to a lower energy state. If the excitation energy matches the energy of the transition from the ground state to an excited intermediate metastable level (ground state absorption), then a subsequent absorption of a pump photon can induce a transition from the metastable state to a higher-energy lying state that relaxes radiatively with emission energy higher than the pump energy (UC luminescence process).

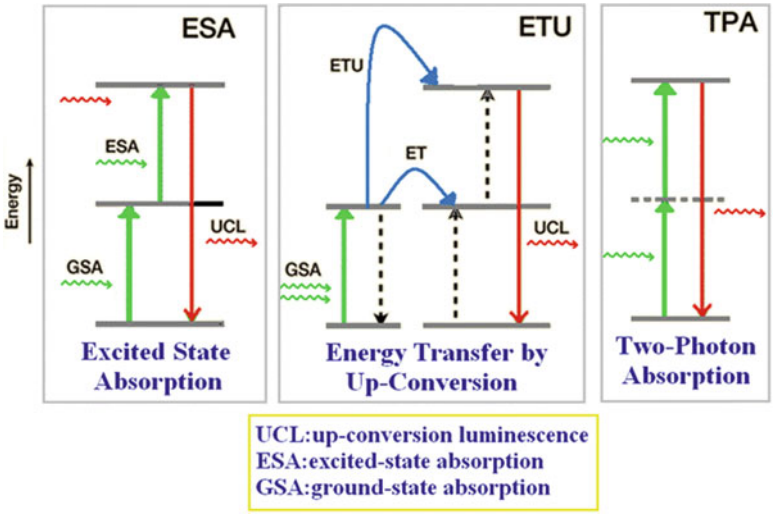

Fig. 3.4 Sketch of the dynamics of the main UC mechanisms

In the case of ETU, successive energy transfer mechanisms between centers at different sites occur starting with an A in an excited state. For instance, Fig. 3.4 shows one photo-excited center that transfers its excitation energy to a second center yielding UC luminescence. The mutual interaction between centers requires a concentration of S and A letting energy transfer processes between the localized centers. The ETU process is independent on the pumping power and two orders of magnitude more efficient than ESA [7].

About ESA and ETU mechanisms, an illustrative example is provided by Y_2O_3: Tb/Er. Upon excitation of 980 nm, the emission spectrum shows two dominant emission bands (520–570 and 650–675 nm) corresponding to $^2H_{11/2}$, $^4S_{3/2} \rightarrow {}^4I_{15/2}$ transitions (green emission) and $^4F_{9/2} \rightarrow {}^4I_{15/2}$ transition (red emission) of Er^{3+}. First, under excitation at 980 nm, Yb^{3+} ion gets excited to the $^2F_{5/2}$ state, and then relaxes back to the ground state while transferring energy to an adjacent Er^{3+} ion that populates the $^4I_{11/2}$ level of Er^{3+}. Second, the $^4F_{7/2}$ level is populated by ET from the $^4I_{11/2}$ level of Er^{3+} ion, which relaxes nonradiatively to the green-emitting levels ($^2H_{11/2}$ and $^4S_{3/2}$). On the other hand, the nonradiative relaxation of the $^2H_{11/2}$ and $^4S_{3/2}$ states can populate the $^4F_{9/2}$ level of Er^{3+} from which red emission takes place. Furthermore, the $^4I_{11/2}$ level can also decay nonradiatively to the $^4I_{13/2}$ level in Er^{3+} ion and, then absorption of a photon emitted from Yb^{3+} ion can populate the $^4F_{9/2}$.

A further process to be considered is cooperative ET involving neighboring Er^{3+} ions excited at the $^4I_{11/2}$ level in which one Er^{3+} ion de-excites to the $^4I_{15/2}$ level and the other is excited to the $^4F_{7/2}$ level.

In regard to TPA, it involves the simultaneous absorption of two photons with an intermediate virtual state, i. e. there is no real intermediate excited state.

Another UC mechanism is photon avalanche (PA) that consists of a starting non-resonant weak GSA to populate an intermediate level followed by resonant ESA to populate a higher energy visible-emitting level [132].

Notably, due to energy transfer between the excited ion and a ground state ion, the intermediate level of both ions is populated and this fact favors exponential increase of the population of the higher energy emitting level. In this picture UC luminescence occurs as an avalanche process. An efficient PA process would require metastable intermediate levels acting as carrier reservoir for the exciting source. On the other hand, PA depends on the exciting intensity and presents a slow response (of the order of seconds) to the excitation due to the multiple processes involved (excited-state absorption and cross relaxation).

Via the "hot-band absorption" UC by only a few units of thermal energy can be induced: an electron occupying a vibrational excited level of the ground state is preferentially excited and emission occurs back to a lower vibrational level again of the ground state.

The dynamics of the depicted UC mechanisms indicates that efficient UC requires the occurrence of metastable excited levels letting multiple excitation steps and population of an upper lying energy level emitting UC luminescence. Since lanthanides ions have f-levels with relatively long lifetimes and multiple excited f-levels, in principle lanthanide-doped selected host crystal are expected to be optimal candidates as up-converters. Based on the fact that efficient photon absorption and ET in the UC process would require a small enough energy difference between each excited level and its lower-energy lying intermediate, Er^{3+}, Tm^{3+}, and Ho^{3+} are optimal RE centers to generate UC emission by interplay of their levels [12].

For example, the fluoride hosts doped with Yb^{3+} and $Er^{3+}/Tm^{3+}/Ho^{3+}$ are ET visible-light emitting upconverters where the ET UC process is much more efficient than TPA because activators have real intermediate energy levels between ground and excited states. All of this lets obtain bright visible emission at low excitation power density ($1–10^3$ W/cm^2) as compared to the high power density ($10^6–10^9$ W/cm^2) exciting source needed via TPA mechanism

Another important role in affecting the UC luminescence efficiency is played by the absorption cross-section of a S center in the NIR spectral range. In practice, the small absorption cross section of RE ions resulting from the parity-forbidden *f–f* transitions negatively affects the UC emission efficiency that needs to be enhanced for useful applications of RE-based up-converters. Among lanthanides, the largest absorption cross-section is exhibited by Yb^{3+} due to the $^2F_{7/2} - {}^2F_{5/2}$ transition at 980 nm. Conveniently for collective processes, this transition is resonant with f–f transitions of the upconverting lanthanides Er^{3+}, Tm^{3+}, and Ho^{3+}.

Non-radiative Relaxation

Excited states release their energy via two decay channels depending on the energy difference with respect to the closest lower energy state, i.e., a radiative relaxation (i.e., by photon emission) or a non-radiative relaxation (i.e., by phonon emission as a result of ion-phonon interaction).

The rate of radiative relaxation from an initial state I_i to a final state I_f can be expressed as follows based on the Judd-Ofelt theory:

$$W_R\left(I_i, I_f\right) = \frac{64\ \pi^2 \Delta E^2}{3h\ (2I_i + 1)}\left(\chi F^2 + n_h^3 \overline{M}^2\right)$$

where ΔE (cm^{-1}) is the energy gap between the states involved in the transition, F^2 is the matrix element of the electric dipole moments, M^2 is the matrix element of the magnetic dipole moment, n_h is the refractive index of the host crystal, and $\chi = n_h\ (n_h{}^2+2)^2/9$ is a corrective factor (Lorentz correction) for the local field [87, 115, 133, 134]. The relaxation rate of non-radiative processes depends on the energy gap between the two electronic states, the frequencies of vibration modes and temperature [115, 134].

A typical situation can be depicted for a three-level (termed "level1", "level2" and "level3") system under the action of electromagnetic radiation with wavelength resonant with the energy-gap between the top-most (level3) and bottom (level1) levels. Under the assumption that the energy gap between level1and level3 is so large to make improbable a level3 → level1 non-radiative transition and that the intermediate level2 is closer to level3 that to level1, then a center in level3 more probably decays non-radiatively to level2 rather than radiatively to level1. This example points out that small gaps and large gaps favor non-radiative and radiative decay channels, respectively.

Quantitatively, the non-radiative relaxation rate from an initial state I_i to a final state I_f can be expressed as follows [134]

$$W_{NR}\left(I_i, I_f, T\right) = W_0\left[\frac{\exp\left(\frac{h\upsilon_m}{kT}\right)}{\exp\left(\frac{h\upsilon_m}{kT}\right) - 1}\right]^{\frac{\Delta E}{h\upsilon_m}}$$

where T is the absolute temperature, $h\upsilon_m$ is the highest fundamental phonon energy of the host lattice vibrations (phonons) coupling to the electronic transition $I_i \rightarrow I_f$ of the RE ion, ΔE is the energy gap of the transition (i.e., the energy difference between the populated state I_i and the closer low-energy state I_f) and W_0 is the transition rate at T = 0K (ground state of the phonon modes). At low temperature ($h\upsilon_m >> kT$), the multiphonon relaxation rate can be approximated by W_0 and expressed by the exponential energy-gap law of Van Dijk and Schuurmans

$$W_0 = C\ \exp\left(-\alpha \frac{\Delta E}{h\upsilon_m}\right)$$

where C and α are parameters characteristic of the host crystal [102]. Therefore, the probability of non-radiative relaxations decreases for increasing band-gap of the transition and large phonon frequencies of the host lattice favor non-radiative losses

leading to reduced luminescence quantum yield. Based on the above exponential energy-gap law, the multiphonon relaxation rate associated with *f*-levels of lanthanides decreases exponentially with increasing energy gap. At room temperature, whenever the energy-gap below the excited emitting states of RE ions is much larger than $h\upsilon_m$ (for example, the $^5D_0$ state of Eu^{3+} and $^6D_{7/2}$ state of Gd^{3+}), the relaxation is dominated by radiative relaxation. Since relatively large energy gaps are associated with the energy levels of Er^{3+} and Tm^{3+}, the probabilities of non-radiative relaxations among their excited levels are low and, as a consequence, Er^{3+} and Tm^3 can be efficient activator centers.

On the other hand, as reported while discussing the requirements on host crystals of PSPs, to reduce the non-radiative multi-phonon relaxation probability, host lattices with very low phonon energies are preferred, as low-frequency phonons can contribute significantly to radiationless decays between the closely spaced crystal-field states of RE centers.

To summarize, (i) bridging small gaps requires the interaction of few phonons, (ii) the probability of a radiative transition is proportional to the cubic power of the gap-energy and (iii) phonon density of states is proportional to the inverse of the cubic power of acoustic wave speed [135].

Another class of transitions involving ion-phonon interaction are the so-called "vibronic transitions", that is radiative emission taking place simultaneously with creation or absorption of one or more phonons when the vibrations characteristic of a host material perturb the wavefunction of an optical center yielding phonon spectral sidebands of the center [136–139]. With respect to the zero-phonon line (no excited phonon states), the vibronic features appear on the high (low) energy side in absorption (emission) at low temperatures and on both the high and low energy side at high temperatures [140].

Figure 3.5 shows the general features of a vibronic spectrum consisting of two phonon vibronic lines associated with phonon modes of frequency ω_k and $\omega_{k'}$, respectively. The top and bottom panel refers to emission and absorption vibronic spectrum, respectively. The frequency ω_0 is associated with the "zero-phonon line" and is determined by the intrinsic difference in energy levels between ground and excited states.

Since phonons can always be emitted spontaneously even at zero temperature, emission vibronic transitions can take place at very low temperature with frequencies smaller than that of the no-phonon transition according to the conservation of energy. Instead, vibronic emission at frequencies greater than the no-phonon transition cannot take place in absence of phonons, i.e. at very low temperatures. Therefore, at very low temperatures phonons can be emitted and the transitions which start from the ground state and end in an excited state can take place at frequencies higher than the no-phonon transition. For increasing temperature, emission vibronic transitions can take place at frequencies greater than the frequency of the no-phonon transition and the opposite holds for absorption vibronic transitions.

In RE-doped crystals where ion-phonon interactions are weak (such as intra $4f^N$ electronic transitions involving the lower states), vibronic bands are much weaker than the zero-phonon lines. For instance, in the case of fluoride crystals doped with

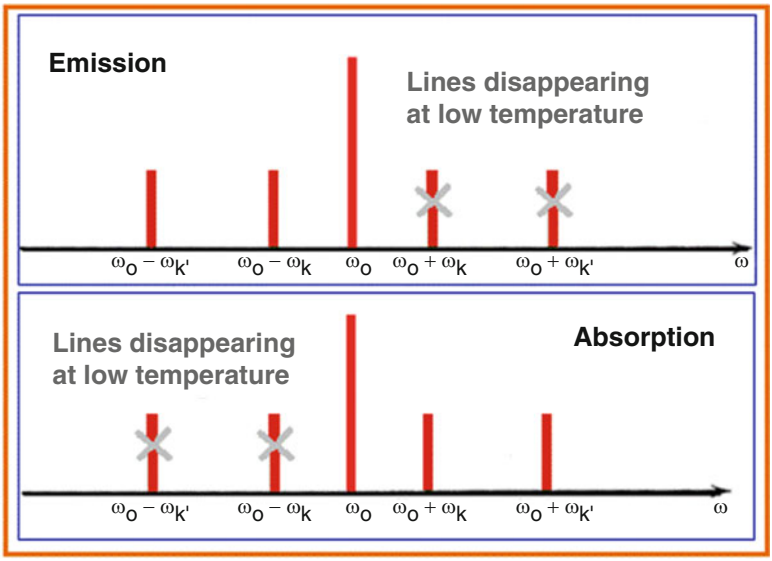

Fig. 3.5 Sketch of a vibronic spectrum in emission and absorption at low temperature

$Er^{3+}$and Ho^{3+}, weak multi-phonon side bands (vibronic coupling strength of 0.04) where measured in absorption and emission spectra [141]. Intense (comparable or stronger than the zero-phonon line) well-defined vibronic side bands can be observed in absorption and emission spectra together with the zero-phonon line in the case of *f–d* transitions of RE-ions [142] and 4f-ion activated upconverters [143].

In regard to f–f electronic transitions of RE ions, while vibronic features are not usually in presence of weak electron-phonon lattice, strong vibronic side bands may appear as related to electronic transitions involving the upper energy f-states coupled to charge transfer states. In other words, the electron-lattice vibration coupling is larger for the excited f-states than for the lower-energy lying f-states of RE ions in crystals.

For an electronic transitions between two states with energy gap E_0 and coupled to a vibration frequency υ, intensity and line shape of vibronic transitions associated to 0-n phonon lines ($n = 0, 1, 2, \ldots$) under a low-temperature approximation can be obtained based on a formula that yields a delta function for zero-phonon ($n = 0$) transition, a line width proportional to the square root of the harmonic integer n and includes the vibronic coupling strength [144]. At high temperature (i.e., $h\upsilon > kT$, which is a condition fulfilled at room temperature for most RE-doped host crystal) the formula must be modified to introduce a function of temperature T and vibration frequency υ including an activation energy of ion-lattice vibronic interactions [145]. At room temperature (i.e., $h\upsilon > kT$) the vibronic features can disappear due to broadening and overlapping effects of the spectral lines.

Vibronic transitions also influence multiphonon UC processes of RE ions because they can improve the process efficiency by increased absorption probability and compensation of energy mismatches through band width. On the other hand, in presence of vibronic coupling, non-radiative relaxations becomes more probable which means shorter lifetimes of the excited states.

Other important consequences of lattice dynamics involving RE center-phonon interactions is broadening of the linewidth of electronic transitions and/or temperature-dependent line shift. The width $\Delta\omega$ of a spectral line is influenced by several contributions: inhomogeneous broadening, homogeneous broadening, direct one-phonon processes, spontaneous decay, multi-phonon decay, Raman scattering and strain.

A spectral line is homogeneously or inhomogeneously broadened depending on whether the line is from the same center or from different but closely spaced centers. Inhomogeneous broadening is induced by structure defects and strains and shifts non-uniformly the static electronic levels [146]. Homogeneous line broadening stems from weak center–phonon interactions (temperature-dependent phonon coupling), with one-phonon and multiphonon processes that contribute mainly to line broadening and shift. The total contribution from direct one-phonon processes, multiphonon decay and radiative decay, in general, is less than 0.01 cm^{-1}. Contribution from Raman scattering amounts to a few cm^{-1} and, in bulk materials, it is the dominant contribution to the thermal broadening at temperature higher than 70 K.

The shape of a transition line is described by a Lorentzian function or a Gaussian function depending on the fact that the line is homogeneously or inhomogeneously broadened. In practice, to account for the simultaneous comparable contributions due to homogeneous and inhomogeneous broadening at room temperature, a convolution of Lorentzian and Gaussian distributions (the so-called Voigt function) is introduced to describe the resultant overall line shape.

Theoretically, under the assumption that the phonon density of states (DOS) is described by a Debye distribution (i.e., continuous DOS), the temperature-dependent line width (ΔE) and line shift (δE) can be expressed by the McCumber-Sturge formulas [147]:

$$\Delta E\,(T)\left(cm^{-1}\right) = \Delta E_o + \overline{\alpha}\left(\frac{T}{T_D}\right)^7 \int_0^{T_D/T} \frac{x^6 e^x}{(e^x - 1)^2} dx \tag{3.1a}$$

$$\delta E\,(T)\left(cm^{-1}\right) = \alpha\left(\frac{T}{T_D}\right)^4 \int_0^{T_D/T} \frac{x^3}{(e^x - 1)} dx \tag{3.1b}$$

where ΔE_0 is a residual line-width of the line at very low temperatures, $\overline{\alpha}$ and α are coefficients related to the electron-phonon coupling, and $T_D = h\upsilon_D/k$ (where υ_D is the Debye cut-off frequency of the lattice and k is the Boltzmann constant) is the effective Debye temperature of the phonon distribution. The temperature-independent quantity ΔE_0 is a measure of how widespread are the sites available

to the dopant ions and the randomness of these sites produces an inhomogeneous broadening that can be described by a Gaussian profile. The quantities $\overline{\alpha}$, α and T_D are considered as adjustable parameters to be estimated by fitting the McCumber-Sturge formulas (3.1a and 3.1b) to the experimental data. In this respect, a fitting of the temperature-dependence of the line-width ΔE in the framework of the Raman scattering model involves three adjustable parameters (ΔE_0, $\overline{\alpha}$ and T_D). Instead, a fitting of the spectral line shift δE versus temperature involves two adjustable parameters (α and T_D).

In general, the following can be observed:

- in regard to a sharp spectral line with width $\Delta\omega$ (i.e., $\Delta\omega << \omega_D$, where ω_D is the Debye frequency), $\Delta\omega$ increases with temperature and, generally, the line shape is Lorentzian,
- the dominant mechanism of line-broadening is the Raman scattering of phonons leading to homogeneous broadening and a Lorentzian-like line shape,
- for decreasing temperature, the line shape is Voigt-like (i. e., a convolution of Lorentzian and Gaussian functions) at about 77 K and Gaussian at very low temperature,
- the spectral position of a line is temperature-dependent (model based on the emission and absorption of virtual phonons) in such a way that it can in principle move towards higher or lower wavelengths for increasing temperature,

As a concluding remark in perspective of the discussion about n-PSPs, it is worth noticing that the McCumber-Sturge formulas (3.1a and 3.1b) are no longer valid at the nanoscale in the limit of discrete phonon DOS with low-frequency cut-off [135, 148–150].

Luminescence Quenching

Luminescence quenching represents loss of radiative efficiency and can be ascribed to several processes, such as:

- thermal quenching (due to non-radiative relaxation to the lowest energy ground state from excited state parabolas),
- concentration quenching (resulting from ET pathways that dominate whenever the concentration of the luminescent centers overcomes a threshold value),
- non-radiative ET through killing centers, disorder-induced states, vacancies, sensitizer or activator ions that have changed their valence,
- whenever both luminescent centers and host lattice absorb the exciting energy or the host lattice itself shows optical absorption in the spectral range where emission takes place.

For example, thermal and concentration quenching can be competitive mechanisms because, although a large Stokes shift reduces concentration quenching by reduced ET, a very large Stokes shift increases the probability for thermal quenching.

As general guidelines, the most relevant mechanisms and decay pathways resulting in degradation of the luminescence performances of PSPs are listed in the following:

- the absorbed energy does not reach the activator ion (due to competitive absorption, ET to defects or non-luminescent impurity ions, excited state absorption (ESA) and Auger processes),
- although the absorbed energy reaches the activator center, non-radiative channels dominate the radiative relaxation towards the ground state (crossing of excited and ground-state parabolas, multi-phonon relaxation, CR, photoionization, ET to quenching sites),
- the emitted radiation is re-absorbed by the luminescent material (due to self-absorption due to spectral overlap between excitation and emission bands, additional absorption bands (formation of color-center) in the spectral range where activator and sensitizer also absorb)

In order to preserve and possibly enhance the luminescence efficiency, the following requirements might be fulfilled:

- strong absorption by the optically active centers,
- host crystals with large band-gap to avoid absorption of the emitted radiation,
- dopant concentration below the threshold of concentration quenching,
- highly crystalline systems and low defect (inner and surface) density,
- high purity of the samples,
- homogeneous distribution of activators and sensitizers,
- low phonon frequencies.

3.3 Spectroscopy of n-PSPs

3.3.1 General Remarks

As overviewed, most PSPs are generally composed of a pure host material and a suitable amount of dopants (activators and sensitizers). The supplied excitation energy is absorbed by the host and transferred to the activator or directly absorbed by the activator and converted in photoemission or transferred to the activators by mediation of sensitizers. Lanthanide dopants exhibit characteristic narrow bandwidth emission peaks over all the visible spectral range that enable addressable multiple emission color from systems containing more than one lanthanide dopant and balanced contents of different lanthanides. Once the host material, the activator/sensitizer species and their concentrations are fixed, the luminescence efficiency and spectroscopy properties may strongly depend on surface-to-volume ratio, degree of crystallinity, phase, phase purity, distribution of activator/sensitizer in the host matrix as well as fabrication routes and conditions.

Spectroscopy of nanoscale-sized PSPs (n-PSPs) have been focus of worldwide interest since the demonstration and optimization of nanofabrication (chemical and physical) routes (such as, sol−gel, combustion, microemulsion, coprecipitation, laser ablation, ultrasonic spray pyrolysis, and template based strategies) able to synthesize nanocrystals with control on the synthesis protocol, size and shape, chemical composition, doping content as well as surface passivation and functionalization [26, 35, 151–156].

As it will be detailed, the advancement in nanomaterial synthesis has allowed us to finely tune the UC emission over a broad range of color output based on a few main classes of strategies, i.e., lanthanide doping with control and optimization of the dopant species and doping level, as well as morphology, size and phase control. Along with progress in nanofabrication, experimental observations have made possible to disclose a variety of modifications introduced by nanoscale resizing of RE-activated PSPs. In this respect, it is worth observing that the size-dependent spectroscopy of RE-activated n-PSPs cannot be ascribed to the size quantum effects active in semiconductor quantum dots. Instead, RE dopant choice, site symmetry, and content as well as host phase, dopant-ligand distance and surface effects play a key role.

In general lanthanide-activated PSPs exhibit sharp-line emission spectra with spectral positions weakly influenced by the chemical environment (host crystal symmetry lattice and ligands) due to the shielding of the *f*-states of RE centers from the less localized outer shells. Spatial confinement seems to cause no effects on the RE-characteristic emissions, due to the inherent localization of the RE *f*-like wave functions preventing any relevant influence from the surroundings.

Instead, host materials (i.e., ion-ligand distance and site symmetry) can influence the emission features related to the excited states of RE ions in nanocrystals because of more J-L coupling and J mixing effects with respect to the lower energy levels. Very importantly, size confinement can have consequences on spectroscopic dynamic quantities, such as probability of either radiative or non-radiative transitions, lifetime of the intermediate states provided by RE ions, thermal line broadening and thermal line shifting. Turning from bulk to nano-sized PSPs may yield enhancement in the emission intensity of a specific wavelength, improved UC efficiency, tunable luminescence color and multi-color UC.

About the size-dependence of the luminescence properties, the first observation of remarkably increased photoluminescence quantum efficiency dates to ZnS nanocrystals doped with Mn at dopant content from lower than 1% for crystal size of 70 Å to nearly 18% at crystal size of 3.5 Å [34]. Under circumstances of high radiative efficiency (∼20%), the luminescence lifetime of the transition $^4T_1 \rightarrow {}^6A_1$ of Mn^{2+} was observed to be by more than 5 orders of magnitude (ns vs. ms) faster than the corresponding radiative transition in the bulk counterpart crystals.

Further evidence of emission enhancement from lanthanide-doped nanocrystals with respect to the bulk counterparts was reported dealing with Y_2O_3:Yb/Er nanoparticles in the case of red emitting 20 nm sized nanoparticles [157] and relative emission tunable with decreasing particle size (from 55 to 13 nm), because of confinement effects related to the small Bohr radius of the exciton [158].

In nanocrystals the emission efficiency can be also enhanced by combining the energy level structure of lanthanides with dopant-induced symmetry breaking of the host material. While a dopant substituting for an inequivalent lattice site inherently causes breaking of the crystal symmetry [98], in nanocrystals site distortion can be more effectively induced by both a suitable dopant and surface lowered coordination [159].

3.3.2 Multicolor Tuning

In the applicative framework of n-PSPs, most efforts have been devoted to achieve fine tuning of the emission color in a broad range of color output and multicolor emission by single wavelength excitation. All of this is not an easy task due to the intraconfigurational energy levels of lanthanides being hardly affected by the host material. Indeed, multicolor tunable emission demands modulation of the multi-peak emission of a RE-activated n-PSPs based on dopant species and concentration-dependent dopant−dopant interaction. Host materials also play a role because they can influence the optical transitions of the dopants by lattice vibrations and crystal field. Indeed, depending on the site symmetry of lanthanides is host crystals, their luminescence properties (intensity, decay time, efficiency, relative intensity of the emission peaks) can be sensitive to the choice of the surrounding matrix.

For example, Dy^{3+} RE-ion exhibits two main emission bands, that is blue emission (470–500 nm) stemming from the $^4F_{9/2} \rightarrow {}^6H_{13/2}$ transition (single decay component between Dy^{3+} ions) and a yellow emission (560–600 nm) originating from the $^4F_{9/2} \rightarrow {}^6H_{15/2}$ transition (Fig. 3.2). While the blue emission is a characteristic luminescence of Dy^{3+}, the yellow emission is very sensitive to the host material. In fact, when a suitable content of Dy^{3+} replaces not equivalent lattice ions in oxides the yellow-to-blue intensity ratio depends on the covalency degree (bond length) between the Dy^{3+} ions and lattice ligands [160]. Therefore, in luminescent materials doped with Dy^{3+} ions tuning of the yellow-to-blue intensity ratio can enable to obtain near-WL (white-light) emission by means of a single emitting center [92, 121].

On the other hand, different dopant(s)–host combinations can allow us to produce multiple color emissions based on tunable both spectral overlap and relative ratio of different emission colors.

For instance, $NaYF_4$:Yb/Er nanocrystals with size ranging from 6 to 45 nm exhibit increased red-to-green luminescence intensity ratio and reduced luminescence lifetimes for decreasing size [31]. Under near-IR laser excitation at 980 nm, Er^{3+} yields green and red emission due to the $^2H_{11/2}, {}^4S_{3/2} \rightarrow {}^4I_{15/2}$ and $^4F_{9/2} \rightarrow {}^4I_{15/2}$ transitions, respectively (Fig. 3.2). The experimental evidence shows that, while the luminescence intensities of both emission bands get enhanced for increased nanocrystal size, the red-to green ratio is relatively larger for smaller nanocrystals due to non-radiative decays (such as intrinsic phonon modes, vibration

energy of surface ligands, solvent-mediated quenching and surface defects) more effective at the nanoscale [161–163].

About $NaYF_4$:Yb/Er, the addition of large amount of Yb (25–60 mol%) favors back-ET from Er^{3+} to Yb^{3+}, due to the reduced distance between dopants. As a consequence of back-ET processes from Er^{3+} to Yb^{3+}, the population of the excited levels of Er^{3+} ($^2H_{9/2}$, $^2H_{11/2}$. $^4S_{3/2}$) decreases, which causes a decrease in blue ($^2H_{9/2} \rightarrow {}^4I_{15/2}$) and green ($^2H_{11/2}$,$^4S_{3/2} \rightarrow {}^4I_{15/2}$) emissions and tunable emission color from yellow to red [11].

Multicolor fine-tuning of the UC emission in $NaYF_4$:Er n-PSPs can also be accomplished by the interplay of dual activators, that is $Er^{3+}$and Tm^{3+}, at precisely defined relative concentration. Efficient multicolor UC emission in solutions of lanthanide-doped cubic-structure nanocrystals was first demonstrated in $NaYF_4$:Yb/Er and $NaYF_4$:Yb/Tm nanoparticles showing strong yellow emission (that results from two main transitions of Er^{3+} ions) and blue emission (that results from transitions of Tm^{3+} ions), respectively [109, 164].

Hexagonal phase β-YF_3 nanocrystals, co-doped with suitable contents of Er^{3+}, Tm^{3+} and Yb^{3+}, under excitation at 976 nm exhibit an emission spectrum resulting from the combination of blue emission from the Yb^{3+}/Tm^{3+} pairs ($^1D_2 \rightarrow {}^3F_4$ (451 nm) and $^1G_4 \rightarrow {}^3H_6$ (478 nm) transitions), green emission from the Yb^{3+}/Er^{3+} pairs ($^3H_{11/2} \rightarrow {}^4I_{15/2}$ (530 nm) and $^4S_{3/2} \rightarrow {}^4I_{15/2}$ (550 nm) transitions), and red emission from the Tm^{3+}/Er^{3+} pairs [165].

In order to improve the efficiency of UC transitions, hexagonal and cubic $NaREF_4$ (RE = Y, Pr to Lu) nanocrystals as well as $NaYF_4$:Yb/Er/Tm nanoparticles were fabricated with several shapes (polyhedra- rod-, plate-, and dot-like) [155]. About hexagonal-phase $NaYbF_4$ nanoparticles, the Yb^{3+} ions of the host lattice can act as absorbers at 980 nm due to the $^2F_{7/2} \rightarrow {}^2F_{5/2}$ transition of Yb^{3+}(Fig. 3.2). Four different spectrally resolvable emission spectra were first demonstrated from 20 nm-sized blue- and IR-emitting $NaYbF_4$:Tm^{3+}, green (and slightly red)-emitting $NaYbF_4$:Ho^{3+}, green- and red-emitting $NaYbF_4$:Er^{3+}, and blue-, green-, red-, and IR-emitting $NaYF_4$:Yb^{3+} nanocrystals [33]. The UC levels involved in the observed spectra are the $^5F_4$, $^5S_2 \rightarrow {}^5I_8$ (540 nm) and $^5I_4 \rightarrow {}^5I_8$ (750 nm) transitions of Ho^{3+}, the $^1G_4 \rightarrow {}^3F_4$ (476 nm) and $^3F_4 \rightarrow {}^3H_6$ (800 nm) transitions of Tm^{3+}, as well as the $^2H_{11/2} \rightarrow {}^4I_{15/2}$ (520 nm), $^4S_{3/2} \rightarrow {}^4I_{15/2}$ (540 nm) and $^4F_{9/2} \rightarrow {}^4I_{15/2}$ (655 nm) transitions of Er^{3+}.

Hexagonal phase β-$NaYF_4$:Yb nanocrystals (where $NaY_{1-x}Yb_xF_4$ with x = 0.2 is a very effective UC host) and β-$NaYF_4$:Yb/Tb nanocrystals exhibit green and blueish UC photoluminescence at room temperature, respectively [33, 166–168].

As a further example, when β-$NaYF_4$:Eu (0.5 mol%) is excited at 397 nm, the exciting energy matches the strongest transition of Eu^{3+} ($^7F_0 \rightarrow {}^5L_6$) and the emission spectrum results from all the emission lines associated with the $^5D_J \rightarrow {}^7F_J$ transitions involving the excited ^5D_J states of Eu^{3+} (Fig. 3.2) (i.e., $^5D_0 \rightarrow {}^7F_1$ (590 nm), $^5D_0 \rightarrow {}^7F_2$ (614 nm), $^5D_1 \rightarrow {}^7F_0$ (525 nm), $^5D_1 \rightarrow {}^7F_1$ (536 nm), $^5D_1 \rightarrow {}^7F_2$ (555 nm), $^5D_1 \rightarrow {}^7F_3$ (563 nm), $^5D_2 \rightarrow {}^7F_{20}$ (464 nm), $^5D_2 \rightarrow {}^7F_2$ (489 nm), $^5D_2 \rightarrow {}^7F_3$ (511 nm)) [106, 107]. Since all the emission peaks have comparable intensity and their spectral overlapping covers almost the visible spectral range, white bluish emission color results.

About $NaGdF_4$ host doped with Tb^{3+}, Eu^{3+}, Dy^{3+}, and Sm^{3+} activators together with Ce^{3+} sensitizer, downshifting multicolor tuning can be obtained by ET from the sensitizer to the activator mediated by energy migration through Gd sublattice [169].

A further example of the effects of the interplay between dopants is provided by $NaYF_4$:Yb, Ho/Er-nanoparticles that yield green emission tunable from green to red and enhanced in its intensity by the addition of Mn^{2+} as a codopant able to influence crystal phase, size, and luminescence yield [170, 171].

$LiYF_4$ colloids triply-doped with Eu, Tb and Ce (with Ce and Tb acting as sensitizer ions) exhibit $Ce^{3+} \rightarrow Tb^{3+}$ and $Ce^{3+} \rightarrow Tb^{3+} \rightarrow Eu^{3+}$ ET processes that lead to intense green and red emission peaks observed for concentrations of Ce, Tb and Eu set to 13%, 14% and 1–5%, respectively. Tuning the Eu^{3+} concentration changes the intensity ratio of green-to-red emission and yields multicolor emission from green to orange for increasing Eu content [94]. Notably, the best luminescence performance of Eu-doped $LiYF_4$ colloids can be obtained at Eu concentration of 15 mol%, because a phase transformation from tetragonal-phased $LiYF_4$ to orthorhombic-phased $LiYF_4$ onsets for larger content of Eu^{3+} activator ions. Since a linear relationship occurs between the concentration of Eu^{3+} ions and the photoluminescence intensity, then the direct excitation-emission of the Eu^{3+} emission results. Due to the concentration threshold of Eu, ET from a sensitizer can be exploited to enhance the Eu^{3+} emission in $LiYF_4$ nanocrystals. The choice of Ce as a sensitizer is not decisive because both orthorhombic phase YF_3 impurities form at Eu^{3+} concentration of 15 mol% and the hypersensitive $^5D_0 \rightarrow {}^7F_2$ electric dipole transition of Eu^{3+} becomes weaker [94]. The *f–d* energy difference of Eu^{3+} activator ions in $LiYF_4$ where Ce ions are added as sensitizers, can be expressed as a sum of the energy of the first *f–d* transition of a free Ce^{3+} ion (49.340 cm^{-1}), the opposite of the crystal field depression (i.e., the lowering of this energy when $LiYF_4$ is doped by the Ce^{3+}ion) and the difference in the *f–d* energy of Eu^{3+}relative to that of the first electric dipole transition allowed in Ce^{3+} [172].

Combining Ce^{3+} and Tb^{3+} as sensitizers is a valid strategy to induce $Ce^{3+} \rightarrow Tb^{3+} \rightarrow Eu^{3+}$ ET pathways (i.e., Tb^{3+} mediated ET from $Ce^{3+}$to Eu^{3+}) [173] while blocking the corresponding metal-metal charge transfer process [174, 175].

Emission spectra can also be phase-dependent due to the site symmetry of lanthanide dopants in different host lattices [176] and the interaction of dopants in presence of presence of multiple lattice sites [98, 177]

In Pr^3-doped inorganic crystals, red emission can result from the $^1D_2 \rightarrow {}^3H_4$ (603 nm), $^3P_0 \rightarrow {}^3H_6$ (617 nm) and $^3P_0 \rightarrow {}^3F_2$ (650 nm) transitions of Pr^{3+}, green emission is associated with the $^3P_1 \rightarrow {}^3H_5$ (530 nm) and $^3P_0 \rightarrow {}^3H_5$ (547 nm) transitions of Pr^{3+}, and blue-green emission from the $^3P_0 \rightarrow {}^3H_4$ (491 nm) transition of Pr^{3+}. The emission efficiency of the $^1D_2 \rightarrow {}^3H_4$ (603 nm) red emission depends on the Pr^{3+} concentration that, in turn, exhibits an upper threshold for concentration quenching depending on the host crystal. Commonly, Pr^{3+}-doped crystals are red phosphors because red emission (in particular the

$^1D_2 \rightarrow {}^3H_4$ (603 nm) emission) shows dominant intensity compared to green blue-green emissions.

Instead of the overwhelming red emissions, $SrTiO_3:Pr^{3+}$ nanoparticles with a Pr^{3+} concentration of 0.06 can show a dominant very strong blue-green emission at 491 nm and minor two green emissions (530 nm and 547 nm) and three red emissions (603 nm, 617 nm and 650 nm) upon excitation at 325 nm Notably, at a Pr^{3+} concentration above 6% concentration quenching effect occurs for $^3P_0 \rightarrow {}^3H_4$ (491 nm) and $^3P_0 \rightarrow {}^3H_6$ (617 nm) emissions. Instead, $^1D_2$–$^3H_4$ (603 nm) emissions are strongest at a Pr^{3+} concentration in the range 0.2–1.0%. This evidence of emission properties and intensities related to the Pr^{3+} content indicates emission color of $SrTiO_3:Pr^{3+}$ compounds tunable controllably and efficiently by the amount of the optical center [178].

3.3.3 Role of Dopant Concentration in Multicolor Tuning

Another parameter that can effectively contribute to multicolor fine-tuning in the visible and near IR spectral ranges as well as affect the optical properties of n-PSPs is the dopant concentration.

Notably, in bulk PSPs, the selection of dopants and their relative contents are critical points because dopant-dopant interactions depends on the host matrix and can induce luminescence quenching. Interestingly, in n-PSPs amount of dopant much larger than the threshold amount for concentration quenching in the bulk counterpart can be added before observing concentration quenching [179].

About the role of dopant concentration in multicolor tuning, illustrative example are reported in the following.

- Y_2O_3 and ZrO_2 nanocrystals co-doped with Yb and Er, where increased percentage of Yb^{3+} induces an increase in the intensity of red emission from Er^{3+}due to enhanced back-energy transfer from Er^{3+} to Yb^{3+} [158, 159, 180],
- Y_2O_3: Er/Tm/Ho nanocrystals show relative emission intensity (red-to- green emission ratio) dependent on the particle size as well as UC emission color tunable from blue to red by changing the concentration of dopant ions (Er, Tm, and Ho) [181],
- $NaYF_4$: Tb/Er nanocrystals, where a reduction of the content of both RE dopants favors a relative decrease in the intensity of the red emission due to Yb concentration dependent back-ET from Er^{3+} to Yb^{3+} [182],
- cubic phase α-$NaYF_4$ nanocrystals doped with Yb and Tm excited by 980 nm wavelength, where high concentration of Yb decreases the contributions from blue ($^2H_{9/2} \rightarrow {}^4I_{15/2}$ transition) and green ($^2H_{11/2}$, $^4S_{3/2} \rightarrow {}^4I_{15/2}$ transitions) emissions of Er^{3+} because of back-ET from Er^{3+} to Yb^{3+} changes the relative emission intensities of the blue, green and red ($^4F_{9/2} \rightarrow {}^4I_{15/2}$ transition of Er^{3+}) emissions and tunes the color output from yellow to red at Yb^{3+} content increased from 25 to 60 mol% [11],

- $NaYF_4$:Yb/Tm nanocrystals, where increased content of Tm favors the near-IR emission with respect to the blue emission of Tm^{3+} as a result of increased population of the $^3H_4$ level induced by the $^3G_4 \rightarrow {}^3H_4$ and $^3F_2 \rightarrow {}^3F_4$ energy transitions [11],
- $NaYF_4$ colloidal nanocrystals doped with Yb, Tm and Er where, at given concentration ratio Yb/Tm of 20/0.2 mol%, changing the Er^{3+} content (0.2, 0.5, 0.8, 1.2, 1.5 mol%) lets tune the UC color output from blue emission to white emission [11],
- Tm^{3+} and Er^{3+} co-activated $LiYF_4$:Yb, Tm (0.5%), Er(0.1, 0.2, 0.3, 0.5%) n-PSPs that yield blue and green emission, respectively, under excitation with 980 nm NIR radiation with ratio of the green-to-blue photoluminescence intensity depending on the Er^{3+} concentrations [183].
- colloidal $LiYF_4$:Eu n-PSPs, containing Tb^{3+} as sensitizer ion to enhance the emission intensity, that exhibits multicolor emission from green to orange by changing the $Er^{3+}$and Tb^{3+} concentrations [94]
- $LiYF_4$:Eu n-PSPs doped with Ce (15% mol)-Tb (15% mol) sensitizer pair show efficient ET from Ce^{3+} to Eu^{3+} through Tb^{3+} resulting in Eu^{3+} emission intensity of $LiYF_4$:Ce(15%), Tb(15%), Eu(1%) three times higher than that of $LiYF_4$:Eu(15%) [94]
- single-phase $SrTiO_3$:mPr^{3+} (m = 0.01–0.1) nanoparticles, that show strong and overwhelming blue-green emission centered at 491 nm (differently from Pr^{3+}-activated phosphors that are usually dominated by red emissions) and both absolute and relative emission intensities as well as emission color tunable by Pr^{3+}-concentrations [179]
- YVO_4 nanoparticles where multicolor down-conversion tuning from blue to red was demonstrated by varying the concentrations of Dy^{3+}, Eu^{3+}, and Sm^{3+} [184].

All the above example point out that control on the doping content enables tuning of the UC luminescence and color emission as well as concentration quenching poses constraints to this control.

An interesting solution to the drawback of concentration quenching was provided based on lattice confinement of dopants. For enhancing UC emission in Er-doped n-PSPs, distribution of lanthanide ions (Yb at a content as high as 98 mol%) in arrays of well defined order and structure clusters in crystals with orthorhombic crystalline lattice was demonstrated to generate a four-photon-promoted violet UC emission from Er^{3+} with a greatly enhanced intensity [30]

3.3.4 Size and Surface Effects

Another nanoscale-related effect influencing the optical properties of lanthanide-doped nanocrystals is the increased surface-to-volume ratio that points out the role of the surface and surface-related defects and disordering. While, investigation of bulk PSPs lets gain deep understanding on many luminescence mechanisms,

nanotechnology and quantum effects have been a driving force for gaining a comprehensive picture of the luminescence processes of PSPs including the influence of surfaces [185].

Increased surface-to-volume ratio involves differences in the emission spectrum of inner versus surface dopants, increased concentration of surface dopants for decreasing size, high proportion of weakly coordinated dopant ions, changes in the coordination and bond-strength of atoms of the host, enhanced contribution from defects and solvent/surfactants.

For example, $NaYF_4$:Yb/Er (20/2 mol%) n- PSPs exhibit intense UC luminescence under 980 nm near IR excitation energy that is efficiently absorbed by Yb ions and transferred sequentially to the emitting levels of nearby Er^{3+} ions by means of the $^2F_{5/2}(Yb^{3+}) \rightarrow {}^4I_{11/2}(Er^{3+})$ pathway. Three emission bands centered at 525, 542, and 655 nm result from the $^2H_{11/2}$, $^4S_{3/2} \rightarrow {}^4I_{15/2}$ (green) transition and from the $^4F_{9/2\,2} \rightarrow {}^4I_{15/2}$ (red) transitions of Er^{3+} assisted by multiphonon relaxation processes bridging the different excited states of Er^{3+}. Turning to $NaYF_4$:Yb/Er (20/2 mol%) n- PSPs with size around 50 nm, size-dependent optical properties can be observed in that the total emission intensity and the green-to-red intensity ratio both increase for increasing size. These experimental evidences can be ascribed to the decreased influence of surface defects- and ligands-induced quenching of UC (through phonon-assisted non radiative relaxations among the excited levels of Er^{3+}) for n- PSPs getting larger [186]. Turning to ultrasmall n-PSPs, colloidal α-$NaYF_4$:Er/Yb nanoparticles show size-dependent UC emission with dominant red ($^4F_{9/2} \rightarrow {}^4I_{15/2}$ transition) and green ($^2H_{11/2}$, $^4S_{3/2} \rightarrow {}^4I1_{5/2}$ transition) color emissions for size of 5.1 nm and 8 nm, respectively [187]. Because of such a small size range, color emission and its changes are ruled mainly by surface dopants as compared with interior dopants.

In general, surface-induced effects (lowered strength of the crystal field around the surface dopants, luminescence quenching, excitation transfer from inner to surface atoms, difference between surface and core dopants, increased fraction of surface dopants as the size of the nanoparticle decreases, non radiative-losses) cause that luminescence of n-PSPs may be less efficient than the one of the bulk counterparts.

Since ultrahigh sensitive fluorescent label for biomolecule imaging demands ultrasmall (i.e., sub 10 nm-size) n-PSPs with efficient luminescence yield, synthesis approaches must face the challenging task of providing structural order over sizes smaller than 30 nm, fine control on size-dispersion and composition.

Hexagonal-phase β-$NaYF_4$ co-doped with Yb-Tm pair (blue-emitting compound) or Yb-Er pair (green-emitting compound) yields one of the most efficient UC n-PSP [11, 155, 188, 189]. However, the synthesis of smaller and smaller nanoparticles, that demands decreased reaction temperature and shortened reaction time, drives formation of cubic-phase α-$NaYF_4$ with UC emission efficiency order of magnitude lower than the hexagonal phase [35]. Sub-20-nm sized hexagonal-phase $NaYF_4$ nanocrystals were synthesized in organic solvents in presence of toxic organometallic precursors and hazardous coordinating solvents [190], which makes this wet-chemical route environmentally undesirable.

As an alternative, tuning of size (down to ten nanometres), phase (cubic or hexagonal) and UC emission color (green to blue) was demonstrated in $NaYF_4$:Yb/Er and $NaYF_4$:Yb/Tm nanocrystals by doping influencing composition and growth rate through surface charge modification at finely-defined dopant concentrations [35, 191].

To synthesize β-$NaYF_4$ nanoparticles doped with Yb/Er(18/2 mol%) and size ranging from 25 to 10 nm, doping of lanthanide ions with a size larger than Y^{3+}(r = 1.159 Å) such as Gd^{3+} (r = 1.193 Å) is effective in stabilizing pure hexagonal-phase $NaYF_4$ nanocrystals for contents up to 60% [35].

In the case of ultrasmall (sub-10 nm-sized) Yb/Tm and Yb/Er-doped $LiYF_4$ n-PSPs that yield blue and green emission, respectively, under excitation with 980 nm NIR radiation, the exciting NIR photons are efficiently absorbed by Yb^{3+} ions (due to their large absorption cross-section at 980 nm) and the excitation is transferred to Tm^{3+} and Er^{3+} ions [183]. As particle size is scaled below 5 nm, the photoluminescence intensity associated with the characteristic peaks of Tm^{3+} and Er^{3+}becomes negligible due to surface quenching. Instead, confinement of dopants by an outer $LiGdF_4$ shell enclosing sub-10 nm-sized $LiYF_4$:Yb/Tm and $LiYF_4$:Yb/Er nanocrystals lets a remarkable enhancement of the photoluminescence yield with tunable color emission (bright blue, sky blue, aqua, aquamarine, and green) depending on Tm^{3+} and Er^{3+} concentrations. In fact, in order to suppress ET to the crystal surface, spatially confine surface lanthanide ions, protect optically active dopants against surface quenching species, suppress cross-relaxation and ET interactions between lanthanide dopants and enhance the UC efficiency, a conventional effective strategy is the deposition of an inert shell of an un-doped material around the lanthanide-activated n-PSP (surface passivation) [192–196]. Among literature reports, luminescence enhancement of nearly 30 times was demonstrated for 8 nm $NaYF_4$:Yb/Tm nanocrystals after depositing a 1.5 nm thick $NaYF_4$ shell [193] as well as a two-fold increase in luminescence intensity was reported from NaYF4:Yb/Er nanocrystals coated with a $NaYF_4$ shell [194].

In general three different classes of core−shell designs have been developed: (i) dopants are entirely incorporated in the core region of the core-shell structure ("passive-shell" coating design) [192], (ii) different lanthanide dopants are used for the core and shell regions ("active-shell" coating design) [197], (iii) an optically active sublattice initiates energy migration to bridge ET processes through the core−shell interface (energy migration core−shell design) [198].

In practice, a homogeneous core/shell structure (meaning with identical material for shell and host of the core region) can be detrimental for *in vivo* bio-imaging due to possible leaking of RE ions from the host lattice. Whenever the host is a fluoride crystal, a suitable choice of the shell material can be calcium fluoride (CaF_2) thanks to its superior biocompatibility, high optical transparency, inactivity, low lattice mismatch with $NaREF_4$ nanocrystals and prevented leaking effects of RE ions.

Core/shell structures let both enhance luminescence efficiency and provide n-PSPs with better stability in water media. In this respect, the surface of RE-doped n-PSPs dispersed in aqueous solutions greatly adsorbs hydroxyl species that

enhance fluorescence quenching. Hence, the role played by a shell is shielding the core of RE-doped n-PSPs from water, that is beneficial for applications requiring the penetration of ultrasmall n-PSPs into a biomedical environment.

Other strategies of structure manipulations are assembly of nanoparticle building blocks with different chemistry and coupling of metallic nanoparticles to lanthanide-doped nanoparticles [199].

Definitively, spatial confinement of dopants combined with advances in the synthesis of nanoparticles and ability to tune their interactions and relative locations in properly designed structures open up new opportunities for multicolor tuning.

3.3.5 Excited State Dynamics

Size confinement of lanthanide dopants can remarkably affect spectroscopic dynamic quantities, such as probability of either radiative or non-radiative transitions, lifetime of the intermediate states provided by RE ions, thermal line broadening and thermal line shifting.

Turning from bulk to nanoscaled PSPs can change the radiative decay rate, i.e., the radiative lifetime, due to two effects mainly: (i) change of the refractive index by tuning of size and surrounding medium of the nanoparticles [200, 201] and (ii) field oscillations stemming from coherent interference between the exciting field and the lattice electrostatic field along the radius of the emitting nanoparticle [201–203].

About point (i), the radiative emission rate calculated by the Judd-Ofelt formula should be evaluated by considering an effective refractive index $n_{eff}(x) = xn_{NP} + (1-x)n_d$, where x is a filling factor accounting for the effective volume occupied by nanoparticles, n_{NP} is the refractive index of the nanoparticle material and n_d is the refractive index of the dielectric surrounding/embedding the nanoparticles. This approximation for calculating the radiative lifetime from the Judd-Ofelt theory is valid for nanoparticles with average size much shorter than the exciting wavelength (sub-wavelength regime). On the other hand, because of coherent interferences, inhibition of the spontaneous emission has been reported for nanoparticles with size ranging from 100 nm to 2 μm and with different dielectric surrounding media [201].Therefore, the lifetime of spontaneous emission of PSPs can be increased by scaling-down the size to the sub-wavelength regime and/or changing the surrounding medium.

Another important issue of scaling down size to the nanometer range is about the density of states (DOS) of phonons which turns from continuous (Debye approximation) to discrete with a size-dependent cutoff frequency in the low energy side, meaning that phonon modes are absent below the cutoff frequency [135, 149–151, 204].

As already discussed about the criteria to be fulfilled in selecting the host matrix of PSPs, non-radiative relaxation can be linked to the cutoff of low-frequency modes of acoustic phonons according to the modified exponential energy-gap law of Van Dijk and Schuurmans. Since spatial confinement does not change phonon DOS

at high frequencies, a non-radiative decay taking place via the emission of high-frequency phonons shouldn't be affected by size confinement. A restricted number of phonon modes implies a restriction of non radiative relaxation channels which inhibits decays between states spaced by a small energy gap. Nonradiative decays and thermalization between electronic states with energy spacing near or higher than the Debye energy of the lattice are not significantly affected by size-confinement.

On the other hand, whereas the localized nature of the 4f-shells of RE elements is not affected by spatial confinement, size-dependence of electron-phonon interaction due to modified phonon DOS is expected to influence luminescence dynamics. For example, quantum confinement has effects on ET processes. In fact, ET involves migration of electronic excitation of ions (sensitizer-activator and ions of the host lattice) by resonant ET and/or phonon-assisted ET [115] and phonon DOS enters in the calculation of phonon-assisted ET [205]. On the other hand, the rate of ET also depends on the distance between the interaction ions. As the size of the nanoparticle gets smaller and smaller, the hopping length and the probability of the donor-to-acceptor ET are lowered because the probability that a donor can find a neighboring matching acceptor decreases, the numbers of acceptors and donors are lower and defect sites can prevent efficient energy migration by trapping effects. Moreover, as a consequence of the size-dependent phonon DOS, the nonradiative relaxation of ions from excited electronic states may differ from the bulk system leading to peculiar effects such as anomalous thermalization [9].

Size-confinement can also account for the remarkably reduced UC efficiency of nanophosphors with respect to the bulk counterpart. For example, when both resonant and ET contributions are considered in Y_2O_2S:Er^{3+} nanocrystals for the $^4S_{3/2} \rightarrow {}^4I_{15/2}$ fluorescence decay of Er^{3+}, it results that the efficiency of phonon assisted ET drops for decreasing nanoparticle size and the rate of resonant ET decreases for size smaller than 20 nm [204].

Very efficient UC emission in nanocrystals was demonstrated through energy clustering at the sublattice level in Er-doped nanocrystals with orthorhombic lattice structure doped with Yb^{3+} ions ($KYb_{2-x}Lu_xF_7$: Er(2%)/Yb) distributed in arrays of tetrad clusters up to concentration of 98 mol % [30]. This particular design preserves the excitation energy because Yb^{3+}-Yb^{3+} ET is confined and minimizes ET to defects leading to an unconventional very intense four-photon-promoted violet UC emission from Er^{3+} [30].

Size and size-distribution dependence at the nanoscale is also reported in the case the emission decay-patterns. A quantity to be considered in fluorescence transitions is the lifetime of the optical center, that is the inverse of the probability of the transition under examination, which is the sum of several probabilities related to radiative and non-radiative independent processes. In general, the decay curves can be represented by a mono-exponential decay based on the following formula:

$$I = I_0 \exp\left(-t/\tau\right)$$

where I and I_0 are the luminescence intensities at times t and 0, respectively, and τ is the radiative decay time. In lanthanide-activated nanophosphors, the decay patterns of the luminescent ions can deviate from the standard exponential law of the bulk crystal and exhibit multiexponential decay ascribed to several contributions: intrinsic phonon modes, vibration energy of surface ligands, solvent-mediated quenching, different probability of nonradiative decay of near surface outer ions and ions in the core of the n-PSP, surface water, surface interactions and defects, inhomogeneous distribution of dopants throughout the nanoparticle volume [31, 32, 101].

About decay patterns, particle getting smaller and smaller may exhibit enhanced or decreased decay time depending on doping [206–208]. While single-exponential decay profiles with a lifetime comparable to the un-doped host take place in presence of large ion-ion spacing (diluted doping), increased content of the luminescent ions can result in non-exponential decay behavior of the photoluminescence intensity [209]. Also, increasing excitation intensity can promote non exponential decay time as well as shortening of the effective average decay times [210].

Also, emission line width may be size-dependent through size-dependent electron-phonon coupling.

Theoretical analysis of the size-dependence of phonon DOS and electron-phonon coupling indicates that electron-phonon coupling is not size-sensitive and size-effects on broadening and shifting of the spectral lines can be likely observed only in the limit of low temperatures and very small particles (much smaller than 50 nm) [135].

As already discussed about bulk PSPs, broadened width of a spectral line may be a direct consequence of electron-phonon coupling: while inhomogeneous broadening is related to defects and non uniform shift of the electronic energy levels, homogeneous line broadening results from temperature-dependent phonon coupling (weak ion-phonon coupling).Temperature-dependent line shifts are also related to electron-lattice interactions. Temperature-dependent line-width and shift can be expressed by the McCumber-Sturge relationships (formulas 3.1a and 3.1b) [148] that are valid for the continuous Debye approximation of phonon DOS. Therefore, the McCumber-Sturge relationships are no longer valid when size-confinement make the phonon DOS to become quantized [151] and in presence of strong and dominant vibronic effects [142, 143].

Notably, in n-PSPs the vibronic coupling strength (the so-called Huang-Rhys parameter) that accounts for the electronic-transition related lattice displacement [145] is expected to change compared to bulk PSPs with continuous phonon DOS. As a consequence, UC and relaxation dynamics become more complex and need further theoretical investigation.

Further effects of the spatial confinement and its influence on electron-phonon coupling are: (i) modified temperature-dependence (from T^7 to T^3) of the linewidth of characteristic transitions of Eu^{3+} in Y_2O_3 [211], (ii) increased lifetime (from 220 ns to 27 μs) of a multiplet of Eu^{3+} in Y_2O_3 nanocrystals as compared to the bulk counterpart [212], and (iii) size-dependent elimination of direct phonon relaxation in Y_2O_2S: Er^{3+} nanocrystals (anomalous thermalization) [149].

3.3.6 Unconventional WL Emitting n-PSPs

Over the past years most experimental efforts in multicolor tuning of the emission from n-PSPs have been devoted to obtain white light emission and implement white LED exceeding the performances of conventional incandescent or fluorescent indoor and outdoor lamps without the intense blue of pumped LEDs. Among strategies to design white LEDs, the most popular have been either combining blue LED and yellow phosphors or mixing red, green and blue emissions from phosphors excited with an UV or IR source (RGB phosphors). In this case a single host crystal is preferred and multicolor emission is provided by a single RE-dopant letting multiple emitting colors (Sm^{3+}, Eu^{3+} or Dy^{3+}), by lanthanide co-dopants (Ce^{3+}/Mn^{2+}, Ce^{3+}/Tb^{3+}, Ce^{3+}/Ho^{3+}, Tb/Sm etc.) based on ET or by multiple dopants emitting different colors ($Ce^{3+}/Li^{+}/Mn^{2+}$, $Eu^{3+}/Tb^{3+}/Tm^{3+}$,$Eu^{2+}/Tb^{3+}/Eu^{3+}$) [45].

To rationalize, WL emitting PSPs can be grouped in four main classes:

- single-phase host material singly doped with a lanthanide ion,
- a single host or different hosts containing multiple RE ions with red, green and blue emission or yellow and blue emissions,
- codoping lantahanide pairs enabling ET processes,
- defect-related luminescent materials based on optically inactive host crystals including optimal traces of activators (such as carbon impurities) [45].

An overview of the available literature demonstrates that combinations of RE dopants and single-phase compounds containing REs as stoichiometric components have been dominant classes of (nano)phosphors. In this context, the investigation of RE-free and optically active single-host new sources of broad-band WL is an interesting field of research, that can prompt interest both at the fundamental and market level as well as provide relevant progress and raise challenging fundamental and practical questions.

Recently, experimental evidence has been provided of the occurrence of warm efficient WL emission by still not understood mechanisms from a class of nanoscale materials still unexplored from the scientific community as WL emitters [65–76]. About experimental detail, a near-IR diode laser excites nanopowders of an oxide compound and, once the laser pumping power exceeds a certain threshold, the sample emits a broadband stable intense WL spectrum. Among the investigated materials, synthesized by the sol gel method, there are:

- $Gd_3Ga_5O_{12}$(GGG):Cr^{3+} nanopowders excited by a continuous wave (CW) laser diode emitting at 803.5 nm,
- undoped yttrium oxide (Y_2O_3) and Y_2O_3:Nd^{3+} nanopowders excited by a CW laser diode emitting at 803.5 and 975 nm [66, 69, 70],
- yttrium silicate (γ- $Y_2Si_2O_7$) and $Y_2Si_2O_7$:$Yb^{3+}/Er^{3+}/Tm^{3+}$excited by a CW laser diode emitting at 975 nm [71–75],
- erbium oxide (Er_2O_3) nanopowders excited by a laser diode emitting at 800 and 975 nm [76].

Notably, the originality of the obtained results resides in observing stable efficient broadband WL UC emission by nominally un-doped RE-free oxide nanomaterials and temperature-independent broadband emission in presence of a single TM (Cr) dopant for the first time. Indeed, reports on WL emitting materials deal with optically inactive hosts at least doubly doped with different RE ions or oxides including RE ions as stoichiometric components [5, 209, 213–223] as well as TM-doped garnet materials with temperature-dependent emission from TM-dopant electronic transitions and vibronic features [224–227]. In general, the emission properties of n-PSPs depend on background pressure, excitation (intensity and wavelength), composition (dopants and doping content), surface effects, size and temperature [5, 64, 209, 213, 216, 217, 219, 228–231].

Although the origin of WL emission from undoped Y_2O_3 and γ-$Y_2Si_2O_7$ is still unknown, experimental findings indicate common as well as unconventional behavior as compared to the existing literature that raise fundamental questions. Already investigated issues and key points that are worth investigation are listed in the following.

- It is worth noticing that the observed WL emission is a nanoscale phenomenon, meaning it is not detectable in the bulk counterpart materials. Hence, gaining insight in its mechanisms is critical and would be a knowledge milestone both at the fundamental and practical level. A key point is the spectroscopic properties of certain undoped nano-scaled oxides in regard to their ability to emit WL even in absence of luminescent dopant centers such as the widely used RE elements. This topic puts in evidence a change of the typical expectations in solid-state spectroscopy turning from bulk crystals to nano-sized systems.
- The primary excitation mechanism was found to be non linear versus diode power: multi-photon and multi-step absorption processes were demonstrated by the power-law dependence of the WL emission on the laser pumping power ($I = AP^n$, where I is the emission intensity, A is a constant and n is the number of incident absorbed photons leading to the observed emission intensity) [232].
- The WL emission is a threshold process with respect to the pumping power: the threshold pumping power necessary to produce WL emission decreases with decreasing the background pressure and, for given laser output power, enhanced WL emission results by lowering the pressure. These findings are consistent with the literature, in what emission can be easily observed under low pressure conditions as a threshold process with increasing intensity for decreasing pressure from atmospheric one to the vacuum and at atmospheric pressure increasing pumping power enables increasing emission intensity [5, 216, 219, 227].
- Although an appropriate dopant and doping content may increase the rate of WL intensity buildup and lower the threshold pumping power able to switch on WL emission, even in absence of optically active lanthanide dopants efficient broadband WL emission was observed. This fact indicates that WL emission cannot be ascribed to a balanced superposition of primary or complementary colors as in the case of conventional strategies.

- Unconventionally high doping levels (up to 20% of Nd and Yb) were found to cause no concentration quenching of the WL emission. Notably, bulk Y_2O_3:Nd exhibits a threshold content of Nd (a few percents) above which quenching of the emission intensity is due to ET processes involving neighboring Nd^{3+}-Nd^{3+} pairs [233]. On the other hand, an increased amount of dopant (at least doubled) can be added in nanosized phosphors as compared to the bulk counterpart before observing concentration quenching [180]. This issue, which is peculiar of the nanoworld and is consistent with our experimental evidence, however does not let account for the high (up to 20%) dopant content still compatible with efficient luminescence from Y_2O_3:Nd and $Y_2Si_2O_7$:Yb^{3+}/Er^{3+}/Tm^3.
- Interestingly, short-living versus stable broadband WL emission was measured from GGG and GGG:Cr, respectively. On the other hand, stable WL emission resulted from both undoped Y_2O_3 and Y_2O_3:Nd, with better lighting performances from Y_2O_3 and faster rising time of WL emission from Y_2O_3:Nd. Therefore, a different role is played by TM dopants as compared to RE centers in promoting WL emission in an oxide matrix that shows inherently WL emission. Importantly, once assessed that doping is not a necessary condition to observe WL emission, the role played by the dopant in the emission mechanism of WL from the host matrix is an item that definitely needs additional investigation. Therefore, dopants seem to act as additional components that can help to study emission channels to be excluded in interpreting the WL emission from the undoped matrix.
- About emission dynamics, the dependence of the WL emission intensity on dopant content, nanopowder size, pumping power, temperature and background pressure following an interruption of the excitation (decay pattern) and the excitation onset (rise pattern) was acquired. For instance, for Y_2O_3 and Y_2O_3:Nd, not single-exponential decay patterns with deviation from a mono-exponential profile enhanced for smaller size (down to 14 nm) and low temperature were observed over a temperature range from 33 to 700 K [66, 68]. About changing the pumping power, no strong dependence of the WL decay was measured. Buildup times were found of the order of seconds, shortening for increasing pumping intensity and with size-dependent profile (decreasing and steeper for decreasing size) [66, 71].
- About the influence of temperature, interestingly undoped Y_2O_3 and Y_2O_3:Nd (excited at 803.5 nm with pumping power of 2 W) exhibit broad-band (400–900 nm) WL emission spectra independent on the temperature ranging from 35 to 300 K. Instead, dynamic properties such as the decay rate were found to be temperature-dependent with faster decay for falling down temperature [66]. On the other hand, (under laser excitation at 803.5 nm and large intensity of pumping power (2 W)), GGG:Cr shows a broadband unstructured WL emission profile over a wide temperature range (from 33 to 300 K) without temperature-dependence and structural transitions [67]. This finding is unconventional by comparison with literature reports. In fact, GGG:Cr is reported to emit a featured spectrum with narrow lines stemming from the luminescence of Cr^{3+} ions and

vibronic side bands up to nearly 200–300 K. For increasing temperature, any structure is lost and the spectra become broadband-like [223–226].

3.4 Conclusions

Nanophosphors are a class of optical materials that exhibit fascinating and promising properties at both fundamental and applicative levels of knowledge. Their optical response can be engineered by size, shape, and phase control as well as composition and structure tuning. Decisive advancement in the study of n-PSPs has been possible thanks to progress in nanofabrication, enabling control on size, shape, composition, structure and surface chemistry of PSPs. In contrast to the size quantum effects active in semiconductor quantum dots, the size-dependent spectroscopy of RE-activated n-PSPs is greatly influenced by RE dopant choice, site symmetry, and content as well as host phase, dopant-ligand distance and surface effects.

The topics considered in this review contribution deal with: (i) fundamentals of luminescent bulk materials, (ii) RE-elements as activator/sensitizer centers, (iii) main classes of radiative and non-radiative mechanisms taking place in both bulk and nanoscaled PSPs, (iv) spectroscopy of n-PSPs as compared to spectroscopy of bulk PSPs (i.e., the effect of the spatial confinement on the emission dynamical quantities, such as probability of radiative and non-radiative transitions, lifetime of the excited states, thermal line broadening and thermal line shifting), (v) influence of crystal field environment and symmetry, (vi) multicolor-emission by means of RE luminescent ions in nanoscaled PSPs, and (vii) challenges in the field of white light emission. About white light sources, recent studies have been reported on efficient broadband white light emitting n-PSPs consisting of nominally un-doped RE-free oxide nanopowders and TM-doped hosts with temperature-independent emission. The novelty of this approach lies in presenting a route alternative to the presently investigated strategies to obtain WL sources that mainly include RE dopants and single-phase compounds containing REs as stoichiometric components.

References

1. Lastusaari M, Laamanen T, Malkamäki M, Eskola KO, Kotlov A, Carlson S, Welter E, Brito H, Bettinelli M, Jungner H, Hölsä J (2012) The Bologna Stone: history's first persistent luminescent material. Eur J Miner 24:885–890
2. Wiedemann E (1888) Über Fluorescenz und Phosphorescenz, I. Abhandlung (On fluorescence and phosphorescence, first paper). Ann Phys 34:446–463
3. Blasse G, Grabmaier BC (1994) Luminescent materials. Springer, Berlin
4. Ronda CR (2008) Luminescence from theory to applications. Wiley-VCH Verlag GmbH & Co, Weinheim
5. Wang J, Tanner PA (2010) Upconversion for white light generation by a single compound. J Am Chem Soc 132(3):947–949

6. Valeur B, Berberan-Santos MN (2011) A brief history of fluorescence and phosphorescence before the emergence of quantum theory. J Chem Educ 88:731–738
7. Auzel F (2004) Upconversion and anti-stokes processes with f and d ions in solids. Chem Rev 104:139–173
8. Rakovich YP, Donegan JF (2008) Anti-stokes photoluminescence in semiconductor nanocrystal quantum dots. In: Rogach AL (ed) Semiconductor nanocrystal quantum dots. Springer, Wien, pp 257–275
9. Liu G (2015) Advances in the theoretical understanding of photon upconversion in rare-earth activated nanophosphors. Chem Soc Rev 44:1635–1652
10. Suyver JF, Aebischer A, Biner D, Gerner P, Grimm J, Heer S, Krämer KW, Reinhard C, Güdel HU (2005) Novel materials doped with trivalent lanthanides and transition metal ions showing near-infrared to visible photon upconversion. Opt Mater 27:1111–1130
11. Wang F, Liu XG (2008) Upconversion multicolor fine-tuning: visible to near-infrared emission from lanthanide-doped NaYF4 nanoparticles. J Am Chem Soc 130:5642–5643
12. Wang F, Liu XG (2009) Recent advances in the chemistry of lanthanide-doped upconversion nanocrystals. Chem Soc Rev 38:976–989
13. Judd BR (1962) Optical absorption intensities of rare-earth ions. Phys Rev 127:750–761; *ibid*.: Configuration interaction of rare earth ions. Proc Phys Soc 82:874–881 (1963); *ibid.*: Handbook on the physics and chemistry of rare earths. Gschneidner Jr KA, Eyring L (eds) North-Holland, Amsterdam, pp 81–195 (1988).
14. Liu G, Bernard J (eds) (2005) Spectroscopic properties of rare earths in optical materials, Springer series in materials science. Springer, Berlin
15. Shen J, Zhao L, Han G (2013) Lanthanide-doped upconverting luminescent nanoparticle platforms for optical imaging-guided drug delivery and therapy. Adv Drug Deliv Rev 65:744–755
16. Feng W, Han C, Li F (2013) Upconversion-Nanophosphor-Based Functional Nanocomposites. Adv Mater 25:5287–5303 and references therein
17. Haase M, Schäfer H (2011) Upconverting nanoparticles. Angew Chem Int Ed Eng 50:5808–5829
18. Li XM, Zhang F, Zhao DY (2013) Highly efficient lanthanide upconverting nanomaterials: progress and challenges. Nano Today 8:643–676
19. van der Ende BM, Aarts L, Meijerink A (2009) Near-infrared quantum cutting for photovoltaics. Adv Mater 21:3073–3077
20. Park YI, Kim JH, Lee KT, Jeon K-S, Na HB, Yu JH, Kim HM, Lee N, Choi SH, Baik S, Kim H, Park SP, Park B-J, Kim YW, Lee SH, Yoon S-Y, Song IC, Moon WK, Suh YD, Hyeon T (2009) Nonblinking and nonbleaching upconverting nanoparticles as an optical imaging nanoprobe and T1 magnetic resonance imaging contrast agent. Adv Mater 21:4467–4471
21. Lu D, Cho SK, Ahn S, Brun L, Summers CJ, Park W (2014) Plasmon enhancement mechanism for the upconversion processes in $NaYF_4$:Yb($^{3+}$), Er($^{3+}$) nanoparticles: Maxwell versus Förster. ACS Nano 8:7780–7792
22. Gnach A, Lipinski T, Bednarkiewicz A, Rybka J, Capobianco JA (2015) Upconverting nanoparticles: assessing the toxicity. Chem Soc Rev 44:1561–1584
23. Arppe R, Nareoja T, Nylund S, Mattsson L, Koho S, Rosenholm JM, Soukka T, Schaferling M (2014) Photon upconversion sensitized nanoprobes for sensing and imaging of pH. Nanoscale 6:6837–6843
24. Sun LD, Wang YF, Yan CH (2014) Paradigms and challenges for bioapplication of rare earth upconversion luminescent nanoparticles: small size and tunable emission/excitation spectra. Acc Chem Res 47:1001–1009
25. Chen GY, Qiu HL, Prasad PN, Chen XY (2014) Upconversion nanoparticles: design, nanochemistry, and applications in theranostics. Chem Rev 114:5161–5214
26. Gai SL, Li CX, Yang PP, Lin J (2014) Recent progress in rare earth micro/nanocrystals: soft chemical synthesis, luminescent properties, and biomedical applications. Chem Rev 114:2343–2389

27. Jalil RA, Zhang Y (2008) Biocompatibility of silica coated $NaYF_4$ upconversion fluorescent nanocrystals. Biomaterials 29:4122–4128
28. Nyk M, Kumar R, Ohulchanskyy TY, Bergey EJ, Prasad PN (2008) High contrast in vitro and in vivo photoluminescence bioimaging using near infrared to near infrared up-conversion in Tm^{3+} and Yb^{3+} doped fluoride nanophosphors. Nano Lett 8:3834–3838
29. Yang Y, Shao Q, Deng R, Wang C, Teng X, Cheng K, Cheng Z, Huang L, Liu Z, Liu X, Xing B (2012) In vitro and in vivo uncaging and bioluminescence imaging by using photocaged upconversion nanoparticles. Angew Chem 51:3125–3129
30. Wang J, Deng R, MacDonald MA, Chen B, Yuan J, Wang F, Chi D, Hor TS, Zhang P, Liu G, Han Y, Liu X (2014) Enhancing multiphoton upconversion through energy clustering at sublattice level. Nat Mater 13:157–162
31. Zhao JB, Lu ZD, Yin YD, Mcrae C, Piper JA, Dawes JM, Jin DY, Goldys EM (2013) Upconversion luminescence with tunable lifetime in $NaYF_4$:Yb,Er nanocrystals: role of nanocrystal size. Nanoscale 5:944–952
32. Stouwdam JW, Veggel FCJMV (2002) Near-infrared emission of redispersible Er^{3+}, Nd^{3+}, and Ho^{3+} doped LaF_3 nanoparticles. Nano Lett 2:733–737
33. Ehlert O, Thomann R, Darbandi M, Nann T (2008) A four-color colloidal multiplexing nanoparticle system. ACS Nano 2:120–124
34. Bhargava RN, Gallagher D, Hong X, Nurmikko A (1994) Optical properties of manganese-doped nanocrystals of ZnS. Phys Rev Lett 72:416–419
35. Wang F, Han Y, Lim CS, Lu Y, Wang J, Xu J, Chen H, Zhang C, Hong M, Liu X (2010) Simultaneous phase and size control of upconversion nanocrystals through lanthanide doping. Nature 463:1061–1065
36. Downing E, Hesselink L, Ralston J, Macfarlane R (1996) A three-color, solid-state, three-dimensional display. Science 273:1185–1189
37. Liu XF, Dong GP, Qiao YB, Qiu JR (2008) Transparent colloid containing upconverting nanocrystals: an alternative medium for three-dimensional volumetric display. Appl Opt 47:6416–6421
38. Liu M, Lu Y, Xie ZB, Chow GM (2011) Enhancing near-infrared solar cell response using upconverting transparent ceramics. Sol Energy Mater Sol Cells 95:800–803
39. de Wild J, Rath JK, Meijerink A, van Sark WGJHM, Schropp REI (2011) Enhanced near-infrared response of a-Si:H solar cells with β-$NaYF_4$:Yb^{3+}(18%),Er^{3+}(2%) upconversion phosphors. Sol Energy Mater Sol Cells 94:2395–2398
40. de Wild J, Meijerink A, Rath JK, van Sark WGJHM, Schropp REI (2010) Towards upconversion for amorphous silicon solar cells. Sol Energy Mater Sol Cells 94:1919–1922
41. Chen D, Wang Y, Hong M (2012) Lanthanide nanomaterials with photon management characteristics for photovoltaic application. Nano Energy 1:73–90
42. Chen D, Lei L, Yang A, Wang Z, Wang Y (2012) Ultra-broadband near-infrared excitable upconversion core/shell nanocrystals. Chem Commun 48:5898–5900
43. Vetrone F, Naccache R, Zamarrón A, Juarranz de la Fuente A, Sanz-Rodríguez F, Martinez Maestro L, Martín Rodriguez E, Jaque D, García Solé J, Capobianco JA (2010) Temperature sensing using fluorescent nanothermometers. ACS Nano 4:3254–3258
44. Qian HS, Guo HC, Ho PC, Mahendran R, Zhang Y (2009) Mesoporous-silica-coated up-conversion fluorescent nanoparticles for photodynamic therapy. Small 5:2285–2290
45. Shang M, Li C, Lin J (2014) How to produce white light in a single-phase host? Chem Soc Rev 43:1372–1386 and references therein
46. Dwivedi J, Kumar P, Kumar A, Singh SVN, Singh BP, Dhawan SK, Shanker V, Gupta BK (2014) A commercial approach for the fabrication of bulk and nanophosphors converted into highly efficient white LEDs. RSC Adv 4:54936–54947
47. Fasol G, Nakamura S (1997) The blue laser diode: GaN based blue light emitters and lasers. Springer, Berlin
48. Pimputkar S, Speck JS, DenBaars SP, Nakamura S (2009) Prospects for LED lighting. Nat Photonics 3:180–182

49. Ye S, Xiao F, Pan YX, Ma YY, Zhang QY (2010) Phosphors in phosphor-converted white light-emitting diodes: recent advances in materials, techniques and properties. Mater Sci Eng R 71:1–34 and references therein
50. Xia Z, Xu Z, Chena M, Liu Q (2016) Recent developments in the new inorganic solid-state LED phosphors. Dalton Trans 45:11214–11232
51. Uchida Y, Taguchi T (2005) Lighting theory and luminous characteristics of white light-emitting diodes. Opt Eng 44:124003–124009
52. Mills A (2004) Lighting: the progress and promise of LEDs. III-Vs Review 17:39–41
53. Steele RV (2007) The story of a new light source. Nat Photonics 1:25–26
54. Lee S, Seo SY (2002) Optimization of yttrium aluminum garnet: Ce^{3+} phosphors for white light-emitting diodes by combinatorial chemistry method. J Electrochem Soc 149:J85–J88
55. Narukawa Y, Niki I, Izuni K, Yamada M, Murazaki Y, Mukar T (2002) Phosphor-conversion white light emitting diode using InGaN near-ultraviolet chip. Jpn J Appl Phys 41:L371
56. Piao XQ, Horikawa T, Hanzawa H, Machida K (2006) Characterization and luminescence properties of $Sr_2Si_5N_8$:Eu^{2+} phosphor for white light-emitting-diode illumination. Appl Phys Lett 88:161908–161910
57. Huang C-H, Liu W-R, Chen T-M (2010) Single-phased white-light phosphors $Ca_9Gd(PO_4)_7$:Eu^{2+},Mn^{2+} under near-ultraviolet excitation. J Phys Chem C 114:18698–18701
58. Cao C, Qin W, Zhang J, Wang Y, Wang G, Wei G, Zhu P, Wang L, Jin L (2008) Up-conversion white light of Tm^{3+}/Er^{3+}/Yb^{3+} tri-doped CaF_2 phosphors. Opt Commun 281:1716–1719
59. Yang LW, Han HL, Zhang YY, Zhong JX (2009) White emission by frequency Up-conversion in Yb^{3+}-Ho^{3+}-Tm^{3+} triply doped hexagonal $NaYF_4$ nanorods. J Phys Chem C 113:18995–18999
60. Kaiser W, Garrett CB (1961) Two-photon excitation CaF_2:Eu^{2+}. Phys Rev Lett 7(6):229–231
61. Wang F, Deng R, Wang J, Wang Q, Han Y, Zhu H, Chen X, Liu X (2011) Tuning upconversion through energy migration in core–shell nanoparticles. Nat Mater 10:968–973
62. Meneghesso G, Meneghini M, Zanoni E (2010) Recent results on the degradation of white LEDs for lighting. J Phys D Appl Phys 43:354007 (11 pp)
63. Chen D, Xiang W, Liang X, Zhong J, Yu H, Ding M, Lu H, Ji Z (2015) Advances in transparent glass–ceramic phosphors for white light-emitting diodes – a review. J Eur Ceram Soc 35:859–869
64. Zhu H, Lin CC, Luo W, Shu S, Liu Z, Liu Y, Kong J, Ma E, Cao Y, Liu R-S, Chen X (2014) Highly efficient non-rare-earth red emitting phosphor for warm white light-emitting diodes. Nat Commun 5:4312 (10 pp)
65. Bilir G, Di Bartolo B. Method and device for producing white light from Y_2O_3 nano-powders. Patent N.9, 209, 597. US Patent Office
66. Bilir G, Özen G, Collins J, Cesaria M, Di Bartolo B (2014) Unconventional production of bright white light emission by Nd-doped and nominally un-doped Y_2O_3 nano-powders. IEEE Photonics J 6(4):8200518 (18 pp)
67. Bilir G, Özen G, Bettinelli M, Piccinelli F, Cesaria M, Di Bartolo B (2014) Broadband visible light emission from nominally un-doped and Cr^{3+} doped garnet nano-powders. IEEE Photonics J 6(4):2201211 (11 pp)
68. Bilir G, Özen G, Collins J, Di Bartolo B (2014) Fabrication and spectral investigation of Y_2O_3:Nd^{3+} nanoparticles. Appl Phys A Mater Sci Process 115(1):263–273
69. Bilir G, Özen G, Di Bartolo B (2015) Synthesis and spectral characterization of yttrium oxide nano- powders doped with Nd^{3+} ions with a large range of concentrations. Opt Mater 42:2181–2186
70. Cesaria M, Collins J, Di Bartolo B (2016) On the efficient warm white-light emission from nano-sized Y_2O_3. J Lumin 169:574–580
71. Erdem M, Eryurek G, Di Bartolo B (2015) White light emission from sol-gel derived γ-$Y_2Si_2O_7$ nanoparticles. J Alloys Compd 639:485–487

72. Erdem M, Eryurek G, Ekmekci MK, Orucu H, Cinkaya H, Mergen A, Eryurek G, Di Bartolo B (2015) Bright white up-conversion emission from sol-gel derived $Yb^{3+}/Er^{3+}/Tm^{3+}:Y_2SiO_5$ nanocrystalline powders. Ceram Int 41:12805–12810
73. Erdem M, Eryurek G, Di Bartolo B (2015) Change of spectral output with pressure and white light generation in nanoscale $Yb^{3+}:Y_2Si_2O_7$. Opt Mater 49:90–93
74. Erdem M, Eryurek G, Mergen A, Di Bartolo B (2016) Pressure effects on the cooperative emission of $Yb^{3+}:Y_2Si_2O_7$ nano-powders. Ceram Int 42:1501–1506
75. Cinkaya H, Eryurek G, Bilir G, Collins J, Di Bartolo B (2017) Spectral characterization and white light generation by yttrium silicate nanopowders undoped and doped with Ytterbium(III) at different concentrations when excited by a laser diode at 975 nm. Opt Mater 63:167–172
76. Tabanli S, Eryurek G, Di Bartolo B (2017) White light emission from Er_2O_3 nano-powder excited by infrared radiation. Opt Mater 69:207–213
77. Dieke GH (1968) Spectra and energy levels of rare earth ions in crystals. Wiley Interscience, New York
78. Crosswhite HM, Crosswhite H (1984) Parametric model for -shell configurations. I. The effective-operator Hamiltonian. J Opt Soc Am B 1:246–254
79. Carnall WT, Goodman GL, Rajnak K, Rana RS (1989) A systematic analysis of the spectra of the lanthanides doped into single crystal LaF3. J Chem Phys 90:3443–3457
80. Robertson JM, Tol MW, Smits WH, Heyene JPH (1981) Colour shift of the Ce^{3+} emission in monocrystalline epitaxially grown garnet layers. Philips J Res 36:15–30
81. Jang HS, Im WB, Lee DC, Jeon DY, Kim SS (2007) Enhancement of red spectral emission intensity of $Y_3Al_5O_{12}$: Ce^{3+} phosphor via Pr co-doping and Tb substitution for the application to white LEDs. J Lumin 126:371–377
82. Huang C-H, Wu P-J, Lee J-F, Chen T-M (2011) $(Ca,Mg,Sr)_9Y(PO_4)_7:Eu^{2+},Mn^{2+}$: phosphors for white-light near-UV LEDs through crystal field tuning and energy transfer. J Mater Chem 21:10489–10495
83. Chang NC, Gruber JB (1964) Spectra and energy levels of Eu^{3+} in Y_2O_3. J Chem Phys 41:3227–3234
84. Buijs M, Meyerink A, Blasse G (1987) Energy transfer between eu^{3+} ions in a lattice with two different crystallographic sites:$Y_2O_3:Eu^{3+}$, $Gd_2O_3:Eu^{3+}$ and Eu_2O_3. J Lumin 37:9–20
85. Ofelt GS (1962) Intensities of crystal spectra of rare-earth ions. J Chem Phys 37:511–520
86. Liu GK, Jacquier B (2005) Spectroscopic properties of rare earths in optical materials. Springer, Berlin, pp 1–94
87. Reid MF (2000) Crystal field handbook. Newman DJ, Ng B (eds). Cambridge University Press, Cambridge, pp 190–226
88. Nieuwport WC, Blasse G (1966) Linear crystal-field terms and the $^5D_0$-$^7F_0$ transition of the Eu^{3+} ion. Solid State Commun 4:227–229
89. Kiss ZJ, Weakliem HA (1965) Stark effect of 4f states and linear crystal field in BaCIF: Sm^{2+}. Phys Rev Lett 15:457–460
90. Li YC, Chang YH, Lin YF, Chang YS, Lin YJ (2007) Synthesis and luminescent properties of Ln^{3+} (Eu^{3+}, Sm^{3+}, Dy^{3+})-doped lanthanum aluminum germanate $LaAlGe_2O_7$ phosphors. J Alloys Compd 439:371–375
91. Liu FS, Liu QL, Liang JK, Luo J, Yang LT, Song GB, Zhang Y, Wang LX, Yao JN, Rao GH (2005) Optical spectra of Ln^{3+}(Nd^{3+}, Sm^{3+}, Dy^{3+}, Ho^{3+}, Er^{3+})-doped Y_3GaO_6. J Lumin 111:61–68
92. Han SD, Khatkar SP, Taxak VB, Sharma G, Kumar D (2006) Synthesis, luminescence and effect of heat treatment on the properties of Dy^{3+}-doped YVO_4 phosphor. Mater Sci Eng B 129:126–130
93. Shannon RD (1976) Revised effective ionic radii and systematic studies of interatomic distances in halides and chacogenides. Acta Crystallogr A 32:751–767
94. Kim SY, Won Y-H, Jang HS (2014) A Strategy to enhance Eu^{3+} emission from $LiYF_4$: Eu nanophosphors and green-to-orange multicolor tunable, transparent nanophosphor-polymer composites. Sci Rep 5:7866 (1–11)

95. Won Y-H, Jang HS, Im WB, Jeon DY (2008) Red-emitting $LiLa_2O_2BO_3$: Sm^{3+}, Eu^{3+} phosphor for near ultraviolet light-emitting diodes-based solid-state lighting. J Electrochem Soc 155:J226–J229
96. Ptacek P, Schäfer H, Zerzouf O, Kömpe K, Haase M (2007) Crystal phase control of luminescing $NaGdF_4$: Eu^{3+} nanocrystals. Adv Funct Mater 17:3843–3848
97. Wu Z-C, Liu J, Hou W-G, Xu J, Gong M-L (2010) A new single-host white-light-emitting $BaSrMg(PO_4)_2$: Eu^{2+} phosphor for white-light-emitting diodes. J Alloys Compd 498:139–142
98. Tu D, Liu Y, Zhu H, Li R, Liu L, Chen X (2013) Breakdown of crystallographic site symmetry in lanthanide-doped $NaYF_4$ crystals. Angew Chem 52:1128–1133
99. Suyver JF, Grimm J, van Veen MK, Biner D, Kramer KW, Gudel HU (2006) Upconversion spectroscopy and properties of $NaYF_4$ doped with Er^{3+}, Tm^{3+} and/or Yb^{3+}. J Lumin 117:1–12
100. Suyver JF, Grimm J, Kramer KW, Gudel HU (2005) Highly efficient near-infrared to visible up-conversion process in $NaYF_4$: Er^{3+},Yb^{3+}. J Lumin 114:53–59
101. Wang W, Liu GK, Brik MG, Seijo L (2009) Orbital hybridization of trivalent uranium in crystals of hexagonal symmetry: effects on electronic energy levels and transition intensities. Phys Rev B Condens Matter Mater Phys 80:155120 (10 pp)
102. van Dijk JMF, Schuurmans MFH (1983) On the nonradiative and radiative decay rates and a modified exponential energy gap law for 4f–4f transitions in rare-earth ions. J Chem Phys 78:5317–5323
103. Yi ZG, Lu W, Liu HR, Zeng SJ (2015) High quality polyacrylic acid modified multifunction luminescent nanorods for tri-modality bioimaging, in vivo long-lasting tracking and biodistribution. Nanoscale 7:542–550
104. Yi Z, Lu W, Xu Y, Yang J, Deng L, Qian C, Zeng T, Wang H, Rao L, Liu H, Zeng S (2014) PEGylated $NaLuF_4$:Yb/Er upconversion nanophosphors for in vivo synergistic fluorescence/X-ray bioimaging and long-lasting, real-time tracking. Biomaterials 35:9689–9697
105. Xing H, Zhang S, Bu W, Zheng X, Wang L, Xiao Q, Ni D, Zhang J, Zhou L, Peng W, Zhao K, Hua Y, Shi J (2014) Ultrasmall $NaGdF_4$ nanodots for efficient MR angiography and atherosclerotic plaque imaging. Adv Mater 26:3867–3872
106. Shang M, Li G, Kang X, Yang D, Geng D, Peng C, Cheng Z, Lian H, Lin J (2012) LaOF: Eu^{3+} nanocrystals: hydrothermal synthesis, white and color-tuning emission properties. Dalton Trans 41:5571–5580
107. Li C, Zhang C, Hou Z, Wang L, Quan Z, Lian H, Lin J (2009) β-$NaYF_4$ and β-$NaYF_4$:Eu^{3+} microstructures: morphology control and tunable luminescence properties. J Phys Chem C 113:2332–2339
108. Liu X, Li C, Quan Z, Cheng Z, Lin J (2007) Tunable luminescence properties of $CaIn_2O_4$:Eu^{3+} phosphors. J Phys Chem C 111:16601–16607
109. Heer S, Kömpe K, Güdel HU, Haase M (2004) Highly efficient multicolour upconversion emission in transparent colloids of lanthanide-doped $NaYF_4$ nanocrystals. Adv Mater 16:2102–2105
110. De Vries AJ, Smeets WJJ, Blasse G (1987) The trapping of Gd^{3+} excitation energy by Cr^{3+} and rare earth ions in $GdAlO_3$. Mater Chem Phys 18:81–92
111. Zeng J, Xie T, Li Z, Li Y (2007) Monodispersed nanocrystalline fluoro-perovskite up-conversion phosphors. Cryst Growth Des 7:2774–2777
112. Xie M, Peng X, Fu X, Zhang J, Li G, Yu X (2009) Synthesis of Yb^{3+}/Er^{3+} co-doped MnF_2 nanocrystals with bright red up-converted fluorescence. Scr Mater 60:190–193
113. Dexter DLA (1953) Theory of sensitized luminescence in solids. J Chem Phys 21:836–850
114. Paulose PI, Jose G, Thomas V, Unnikrishnan NV, Warrier MKR (2003) Sensitized fluorescence of Ce^{3+}/Mn^{2+} system in phosphate glass. J Phys Chem Solids 64:841–846
115. Miyakawa T, Dexter DLA (1970) Phonon sidebands, multiphonon relaxation of excited states, and phonon-assisted energy transfer between ions in solids. Phys Rev B Solid State 1:2961–2969

116. Yen WM (1987) Spectroscopy of solids containing rare earth ions. Kaplyanskii AA, Macfarlane RM (eds). North-Holland, Amsterdam, pp 185–249
117. Huber DL (1981) Laser spectroscopy of solids. Yen WM, Selzer PM (eds). Springer, New York, pp 83–111
118. Jackson SD (2012) Towards high-power mid-infrared emission from a fibre laser. Nat Photonics 6:423–431
119. Chen GY, Liu HC, Somesfalean G, Liang HJ, Zhang ZG (2009) Upconversion emission tuning from green to red in Yb^{3+}/Ho^{3+}-codoped $NaYF_4$ nanocrystals by tridoping with Ce^{3+} ions. Nanotechnology 20:385704 (6 pp)
120. Auzel F (2002) A fundamental self-generated quenching center for lanthanide-doped high-purity solids. J Lumin 100:125–130
121. Lai H, Bao A, Yang Y, Xu W, Tao Y, Yang H (2008) Preparation and luminescence property of Dy^{3+}-doped YPO_4 phosphors. J Lumin 128:521–524
122. Su XQ, Yan B (2005) The synthesis and luminescence of $YP_xV_{1-x}O_4$: Dy^{3+} microcrystalline phosphors by in situ co-precipitation composition of hybrid precursors. Mater Chem Phys 93:552–556
123. Lazarowska A, Mahlik S, Grinberg M, Liu TC, Liu RS (2001) New Pr^{3+} sites in β-SiAlON red phosphor. Opt Mater 35:2001–2005
124. Sun H, Peng D, Wang X, Tang M, Zhang Q, Yao X (2012) Green and red emission for $(K_{0.5}Na_{0.5})NbO_3$: Pr ceramics. J Appl Phys 111:046102 (3 pp)
125. Wei Y, Wu Z, Jia Y, Wu J, Shen Y, Luo H (2014) Dual-enhancement of ferro-/piezoelectric and photoluminescent performance in Pr^{3+} doped $(K_{0.5}Na_{0.5})NbO_3$ lead-free ceramics. Appl Phys Lett 105:042902 (4 pp)
126. Zhou H, Liu X, Qin N, Bao D (2011) Strong red emission in lead-free ferroelectric Pr3+-doped Na0.5Bi0.5TiO3 thin films without the need of charge compensation. J Appl Phys 110:034102
127. Sun HQ, Peng DF, Wang XS, Tang MM, Zhang QW, Yao X (2011) Strong red emission in Pr doped $(Bi_{0.5}Na_{0.5})TiO_3$ ferroelectric ceramics. J Appl Phys 110:016102 (3 pp)
128. Zou H, Hui X, Wang XS, Peng DF, Li J, Li YX, Yao X (2013) Luminescent, dielectric, and ferroelectric properties of Pr doped $Bi_7Ti_4NbO_{21}$ multifunctional ceramics. J Appl Phys 114:223103 (4 pp)
129. Zhu G, Ci ZP, Shi YR, Wang YH (2013) Synthesis and photoluminescence properties of a red emitting phosphor $NaSr_2(NbO_3)_5$:RE^{3+} (RE=Sm, Pr) for white LEDs. J Rare Earths 31:1049–1052
130. Chen H, Lian R, Yin M, Lou L, Zhang W, Xia S, Krupa J (2001) Luminescence concentration quenching of $^1D_2$ state in YPO_4: Pr^{3+}. J Phys Condens Matter 13:1151–1158
131. Blasse G (1969) Energy transfer in oxidic phosphors. Philips Res Rep 24:131–144
132. Chivian JS, Case WE, Eden DD (1979) The photon avalanche: a new phenomenon in Pr^{3+}-based infrared quantum counters. Appl Phys Lett 35:124–126
133. Condon EU, Shortley GH (1963) The theory of atomic spectra. Cambridge University Press, Cambridge
134. Riseberg LA, Moos HW (1968) Multiphonon orbit-lattice relaxation of excited states of rare-earth ions in crystals. Phys Rev 174:429–438
135. Collins J (2016) Non-radiative processes in crystals and in nanocrystals. ECS J Solid State Sci Technol 5:R3170–R3184 and references therein
136. Blasse G (1992) Vibronic transitions in rare earth spectroscopy. Int Rev Phys Chem 11:71–100
137. Di Bartolo B, Powell RC (2014) Crystal symmetry, lattice vibrations and optical spectroscopy of solids: a group theoretical approach. World Scientific Publishing Co, Singapore
138. Hizhnyakov V, Boltrushko V, Pae K, Vaikjarv T (2011) Zero-phonon lines: novel manifestations of vibronic interactions in impurity centres of solid. Condens Matter Spectrosc Opt Spectrosc 111:377–385
139. Di Bartolo B, Peccei R (1965) Thermal effects on the fluorescence lifetime and spectrum of MgO: V^{2+}. Phys Rev 137:A 1770–A 1776

140. Auzel F (1980) Radiationless processes. Di Bartolo B (ed). New York, Plenum
141. Auzel F (1976) Multiphonon-assisted anti-Stokes and Stokes fluorescence of triply ionized rare-earth ions. Phys Rev B Solid State 13:2809–2817
142. Liu G (2014) A degenerate model of vibronic transitions for analyzing 4f–5d spectra. J Lumin 152:7–10
143. Zhou XJ, Tanner PA, Faucher MD (2007) Electronic spectra and crystal field analysis of Er^{3+} in Cs_2NaErF_6. J Phys Chem C 111:683–687
144. Huang K, Rhys A (1950) Theory of light absorption and non-radiative transitions in F-centres. Proc R Soc A 204:406–423
145. Kubo R, Toyozawa Y (1955) Application of the method of generating function to radiative and non-radiative transitions of a trapped electron in a crystal. Prog Theor Phys 13:160–182
146. Yen WM, Selzer PM (1981) Laser spectroscopy of solids. Springer, Berlin
147. McCumber DE, Sturge MD (1963) Linewidth and temperature shift of the r lines in ruby. J Appl Phys 34:1682–1684
148. Liu GK, Zhuang HZ, Chen XY (2002) Restricted phonon relaxation and anomalous thermalization of rare-earth ions in nanocrystals. Nano Lett 2:535–539
149. Meltzer RS, Hong KS (2000) Electron-phonon interactions in insulating nanoparticles: Eu_2O_3. Phys Rev B 61:3396–3496
150. Tamura A (1995) Smoothed density of states of electrons and smoothed frequency spectrum of phonons for a mesoscopic system. Phys Rev B 52:2688–2676
151. Terraschke H, Wickleder C (2015) UV, blue, green, yellow, red, and small: newest developments on Eu^{2+}-doped nanophosphors. Chem Rev 115:11352–11378
152. Que WX, Zhang QY, Chan YC, Kam CH (2003) Sol–Gel derived hard optical coating via organic/inorganic composites. Compos Sci Technol 63:347–351
153. Zhang YW, Sun X, Si R, You LP, Yan CH (2005) Single-crystalline and monodispersed LaF_3 triangular nanoplates from a single-source precursor. J Am Chem Soc 127:3260–3261
154. Mai HX, Zhang YW, Si R, Yan ZG, Sun LD, You LP, Yan CH (2006) High-quality sodium rare-earth fluoride nanocrystals: controlled synthesis and optical properties. J Am Chem Soc 128:6426–6436
155. Li Z, Zhang Y (2008) An efficient and user-friendly method for the synthesis of hexagonal-phase $NaYF_4$:Yb,Er/Tm nanocrystals with controllable shape and fluorescence. Nanotechnology 19:345606 (5 pp)
156. Li C, Lin J (2010) Rare earth fluoride nano-/microcrystals: synthesis, surface modification and application. J Mater Chem 20:6831–6847
157. Vetrone F, Boyer JC, Capobianco JA, Speghini A, Bettinelli M (2004) Significance of Yb^{3+} concentration on the upconversion mechanisms in codoped Y_2O_3: Er^{3+}, Yb^{3+} nanocrystals. J Appl Phys 96:661–667
158. Bai X, Song H, Pan G, Lei Y, Wang T, Ren X, Lu S, Dong B, Dai Q, Fan L (2007) Size-dependent upconversion luminescence in Er^{3+}/Yb^{3+}-codoped nanocrystalline yttria: saturation and thermal effects. J Phys Chem C 111:13611–13617
159. Liu G, Chen X (2007) Handbook on the physics and chemistry of rare earths. Gschneidner JKA, Bunzli JCG, Pecharsky VK (eds). Elsevier, New York, pp 99–169
160. Liang C-H, Teoh L-G, Liu KT, Chang Y-S (2012) Near white light emission of BaY_2ZnO_5 doped with Dy^{3+} ions. J Alloys Compd 517:9–13
161. Aebischer A, Heer S, Biner D, Kramer K, Haase M, Gudel HU (2005) Visible light emission upon near-infrared excitation in a transparent solution of nanocrystalline. Chem Phys Lett 407:124–128
162. Li Y, Zhang J, Zhang X, Luo Y, Ren X, Zhao H, Wang X, Sun L, Yan C (2009) Near-infrared to visible upconversion in Er^{3+} and Yb^{3+} codoped Lu_2O_3 nanocrystals: enhanced red color upconversion and three-photon process in green color upconversion. J Phys Chem C113:4413–4418
163. Lu Q, Guo F, Sun L, Li A, Zhao L (2008) Surface Modification of ZrO_2: Er^{3+} nanoparticles to attenuate aggregation and enhance upconversion fluorescence. J Phys Chem C 112:2836–2844

164. Schäfer H, Ptacek P, Kömpke K, Haase M (2007) Lanthanide- doped $NaYF_4$ nanocrystals in aqueous solution displaying strong up-conversion emission. Chem Mater 19:1396–1400
165. Chen D, Wang Y, Zheng K, Guo T, Yu Y, Huang P (2007) Bright upconversion white light emission in transparent glass ceramic embedding $Tm^{3+}/Er^{3+}/Yb^{3+}$:β-YF_3 $Tm^{3+}/Er^{3+}/Yb^{3+}$: β-YF_3 nanocrystals. Appl Phys Lett 91:251903–251905
166. Feng L, Zhang J, Wang J, Liang H, Su Q (2007) Cooperative energy transfer frequency upconversion in Tb^{3+}/Yb^{3+}- codoped oxyfluoride glasses. Spectrochim Acta Part A 67:886–889
167. Martins E, Araujo CB, Delben JR, Gomes ASL, da Costa BJ, Messaddeq Y (1998) Cooperative frequency upconversion in $Yb^{3+}Tb^{3+}$codoped fluoroindate glass. Opt Commun 158:61–64
168. Menezes LS, Maciel GS, Araujo CB, Messaddeq Y (2003) Phonon-assisted cooperative energy transfer and frequency upconversion in a Yb^{3+}/Tb^{3+} codoped fluoroindate glass. J Appl Phys 94:863–866
169. Wang F, Fan X, Wang M, Zhang Y (2007) Multicolor PEI/$NaGdF_4$: Ce^{3+},Ln^{3+} nanoparticles by single wavelength excitation. Nanotechnology 18:025701 (5 pp)
170. Reddy KL, Rai M, Prabhakar N, Arppe R, Rai SB, Singh SK, Rosenholm JM, Krishnan V (2016) Controlled synthesis, bioimaging and toxicity assessments in strong red emitting Mn^{2+} doped $NaYF_4$:Yb^{3+}/Ho^{3+} nanophosphors. RSC Adv 6:53698–53704
171. Li X, Xue Z, Liu H (2016) Hydro-thermal synthesis of pegylated Mn^{2+} dopant controlled $NaYF_4$:Yb/Er up-conversion nano-particles for multi-color tuning. J Alloys Compd 681:379–383
172. Dorenbos P (2000) The 5d level positions of the trivalent lanthanides in inorganic compounds. J Lumin 91:155–176
173. Kim SY, Woo K, Lim K, Lee K, Jang HS (2013) Highly bright multicolor tunable ultrasmall β-Na(Y,Gd)F_4: Ce, Tb, Eu/b-$NaYF_4$ core/shell nanocrystals. Nanoscale 5:9255–9263
174. Blasse G (1983) Energy transfer from Ce^{3+} to Eu^{3+} in (Y,Gd)F_3. Phys Status Solidi A 75:K41–K43
175. Zhang X, Zhou L, Pang Q, Shi J, Gong M (2014) Tunable Luminescence and $Ce^{3+}/Tb^{3+}/Eu^{3+}$ energy transfer of broadband-excited and narrow line red emitting Y_2SiO_5:Ce^{3+}, Tb^{3+}, Eu^{3+} phosphor. J Phys Chem C 118:7591–7598
176. Achatz DE, Ali R, Wolfbeis OS (2011) Luminescent chemical sensing, biosensing, and screening using upconverting nanoparticles. Top Curr Chem 300:29–50
177. Aebischer A, Hostettler M, Hauser J, Krämer K, Weber T, Güdel HU, Bürgi H-B (2006) Structural and spectroscopic characterization of active sites in a family of light-emitting sodium lanthanide tetrafluorides. Angew Chem Int Ed 45:2802–2806
178. Tang W, Sun Y, Yu M, Liu X, Yin Y, Yang B, Zheng L, Qin F, Zhang Z, Cao W (2015) White-light-emitting properties of $SrTiO_3$:Pr^{3+} nanoparticles. RSC Adv 5:27491–27495
179. Zhang W, Xie P, Duan C, Yan K, Yin M, Lou L, Xia S, Krupa JC (1998) Preparation and size effect on concentration quenching of nanocrystalline Y_2SiO_5:Eu. Chem Phys Lett 292:133–136
180. Chen G, Zhang Y, Somesfalean G, Zhang Z, Sun Q, Wang F (2006) Two-color upconversion in rare-earth-ion-doped ZrO_2 nanocrystals. Appl Phys Lett 89:163105–163107
181. Qin X, Yokomori T, Ju Y (2007) Flame synthesis and characterization of rare-earth (Er^{3+}, Ho^{3+}, and Tm^{3+}) doped upconversion nanophosphors. Appl Phys Lett 90:073104–073106
182. Wang L, Yan R, Huo Z, Wang L, Zeng J, Bao J, Wang X, Peng Q, Li Y (2005) Fluorescence resonant energy transfer biosensor based on upconversion-luminescent nanoparticles. Angew Chem 44:6054–6057
183. Hong A-R, Kim SY, Cho S-H, Lee K, Jang HS (2017) Facile synthesis of multicolor tunable ultrasmall $LiYF_4$:Yb,Tm,Er/$LiGdF_4$ core/shell upconversion nanophosphors with sub-10 nm size. Dyes Pigments 139:831–838
184. Wang F, Xue X, Liu X (2008) Multicolor tuning of (Ln, P)-doped YVO_4 nanoparticles by single-wavelength excitation. Angew Chem 47:906–909

185. Abrams BL, Holloway PH (2004) Role of the surface in luminescent processes. Chem Rev 104:5783–5801
186. Yea X, Collins JE, Kanga Y, Chenc J, Chend DTN, Yodh AG, Murraya CB (2010) Morphologically controlled synthesis of colloidal upconversion nanophosphors and their shape-directed self-assembly. PNAS 107:22430–22435
187. Mai H, Zhang Y, Sun L, Yan C (2007) Highly efficient multicolor up-conversion emissions and their mechanisms of monodisperse $NaYF_4$:Yb, Er core and core/shell-structured nanocrystals. J Phys Chem C 111:13721–13729
188. Li DD, Shao QY, Dong Y, Jiang JQ (2014) A facile synthesis of small-sized and monodisperse hexagonal $NaYF_4:Yb^{3+}$, Er^{3+} nanocrystals. Chem Commun 50:15316–15318
189. Na H, Woo K, Lim K, Jang HS (2013) Rational morphology control of β-$NaYF_4$:Yb,Er/Tm upconversion nanophosphors using a ligand, an additive, and lanthanide doping. Nanoscale 5:4242–4251
190. Yi GS, Chow GM (2006) Synthesis of hexagonal-phase $NaYF_4$:Yb,Er and $NaYF_4$:Yb,Tm nanocrystals with efficient up-conversion fluorescence. Adv Funct Mater 16:2324–2329
191. Shi F, Zhao Y (2014) Sub-10 nm and monodisperse β-$NaYF_4$:Yb,Tm,Gd nanocrystals with intense ultraviolet upconversion luminescence. J Mater Chem C 2:2198–2203
192. Kömpe K, Borchert H, Storz J, Lobo A, Adam S, Möller T, Haase M (2003) Green-emitting CePO4:Tb/LaPO4 core−shell nanoparticles with 70% photoluminescence quantum yield. Angew Chem 42:5513–5516
193. Yi G, Chow G (2007) Water-soluble $NaYF_4$:Yb,Er(Tm)/$NaYF_4$/polymer core/shell/shell nanoparticles with significant enhancement of upconversion fluorescence. Chem Mater 19:341–343
194. Mai H, Zhang Y, Sun L, Yan C (2007) Size- and phase-controlled synthesis of monodisperse $NaYF_4$:Yb,Er nanocrystals from a unique delayed nucleation pathway monitored with upconversion spectroscopy. J Phys Chem C 111:13721–13739
195. Lu Q, Guo F, Sun L, Li A, Zhao L (2008) Silica/titaniacoated $Y_2O_3:Tm^3+$, Yb3+ nanoparticles with improvement in upconversion luminescence induced by different thickness shells. J Appl Phys 103:123533 (10 pp)
196. Liu X, Kong X, Zhang Y, Tu L, Wang Y, Zeng Q, Li C, Shi Z, Zhang H (2011) Breakthrough in concentration quenching threshold of upconversion luminescence via spatial separation of the emitter doping area for bio-applications. Chem Commun 47:11957–11959
197. Qian H, Zhang Y (2008) Synthesis of hexagonal-phase core-shell $NaYF_4$ nanocrystals with tunable upconversion fluorescence. Langmuir 24:12123–12125
198. Wang F, Deng R, Wang J, Wang Q, Han Y, Zhu H, Chen X, Liu X (2011) Tuning upconversion through energy migration in core-shell nanoparticles. Nat Mater 10:968–973
199. Wang F, Liu X (2014) Multicolor tuning of lanthanide-doped nanoparticles by single wavelength excitation. Acc Chem Res 47:1378–1385 and references therein
200. Meltzer RS, Feofilov SP, Tissue B, Yuan HB (1999) Dependence of fluorescence lifetimes of $Y_2O_3:Eu^{3+}$ nanoparticles on the surrounding medium. Phys Rev B Condens Matter Mater Phys 60:R14012–R14015
201. Schniepp H, Sandoghdar V (2002) Spontaneous emission of europium ions embedded in dielectric nanospheres. Phys Rev Lett 89:257403 (4 pp)
202. Chew H (1988) Radiation and lifetimes of atoms inside dielectric particles. Phys Rev A At Mol Opt Phys 38:3410–3416
203. Benner RE, Barber PW, Owen JF, Chang RK (1980) Observation of structure resonances in the fluorescence spectra from microspheres. Phys Rev Lett 44:475–478
204. Chen XY, Zhuang HZ, Liu GK, Li S, Niedbala RS (2003) Confinement on energy transfer between luminescent centers in nanocrystals. J Appl Phys 94:5559–5565
205. Holstein T, Lyo SK, Orbach R (1976) Phonon-assisted energy transport in inhomogeneously broadened systems. Phys Rev Lett 36:891 (4 pp)
206. Hreniak D, Strek W, Gluchowski P, Bettinelli M, Speghini A (2008) The influence of the specific surface of grains on the luminescence properties of Nd^{3+}-doped $Y_3Al_5O_{12}$ nanopowders. Appl Phys B Lasers Opt 91:89–93

207. Otsuka K, Yamada T, Saruwatari M, Kimura T (1975) Spectroscopy and laser. oscillation properties of lithium neodymium tetraphosphate. IEEE J Quant Elect 11:330–335
208. Marciniak L, Stefanski M, Tomala R, Hreniak D, Strek W (2015) Size effect in luminescent properties of $LiNdP_4O_{12}$ nanocrystals. Opt Mater 41:17–20
209. Wiglusz RJ, Marciniak L, Pazik R, Strek W (2014) Structural and spectroscopic characterization of Nd^{3+}-doped YVO_4 yttrium orthovanadate nanocrystallites. Cryst Growth Des 14:5512–5520
210. Strek W, Marciniak L, Bednarkiewicz A, Lukowiak A, Hreniak D, Wiglusz R (2011) The effect of pumping power on fluorescence behavior of $LiNdP_4O_{12}$ nanocrystals. Opt Mater 33:1097–1101
211. Chen X, Di Bartolo B, Barnes NP, Walsh BM (2004) Thermal tuning and broadening of the spectral lines of trivalent neodymium in laser crystals. Phys Status Solidi 241(8):1957–1976
212. Yang H-S, Feofilov SP, William DK, Milora JC, Tissue BM, Meltzer RS, Dennis WM (1999) One phonon relaxation processes in Y_2O_3:Eu^{3+} nanocrystals. Physica B 263–264:476–478
213. Marciniak L, Strek W, Bednarkiewicz A, Lukowiak A, Hreniak D (2011) Bright upconversion emission of Nd^{3+} in $LiLa_{1-x}Nd_xP_4O_{12}$ nanocrystalline powders. Opt Mater 33:1492–1494
214. Strek W, Marciniak L, Hreniak D, Lukowiak A (2012) Anti-Stokes bright yellowish emission of $NdAlO_3$ nanocrystals. J Appl Phys 111:024305 (6 pages)
215. Marciniak L, Strek W, Bednarkiewicz A, Hreniak D, Pujol MC, Diaz F (2013) Upconversion emission of $LiNdP_4O_{12}$ and $KNdP_4O_{12}$ crystals. J Lumin 133:57–60
216. Atabaev TS, Hwang Y, Kim H (2012) Color-tunable properties of Eu^{3+}- and Dy^{3+}-codoped Y_2O_3 phosphor particles. Nanoscale Res Lett 7:556 (7 pages)
217. Wang J, Hao JH, Tanner PA (2010) Luminous and tunable whitelight upconversion for YAG ($Yb_3Al_5O_{12}$) and $(Yb,Y)_2O_3$ nanopowders. Opt Lett 35:3922–3924
218. Marciniak L, Tomala R, Stefanski M, Hreniak D, Strek W (2016) Laser induced broad band anti-Stokes white emission from $LiYbF_4$ nanocrystals. J Rare Earths 34:227–234
219. Zhu YS, Xu W, Li CY, Zhang HZ, Dong B, Xu L, Xu S, Song HW (2012) Broad white light and infrared emission bands in YVO_4:Yb^{3+},Ln^{3+} (Ln^{3+}=Er^{3+}, Tm^{3+}, or Ho^{3+}). Appl Phys Express 5:092701 (3 pp)
220. Strek W, Marciniak L, Bednarkiewicz A, Lukowiak A, Wiglusz R, Hreniak D (2011) White emission of lithium ytterbium tetraphosphate nanocrystals. Opt Express 19:14083–14092
221. Marciniak L, Strek W, Hreniak D, Guyot Y (2014) Temperature of anti-Stokes white emission in $LiYbP_4O_{12}$:Er nanocrystals. Appl Phys Lett 105:173113–173115
222. Miao C, Liu T, Zhu YS, Dai QL, Xu W, Xu L, Xu S, Zhao Y, Song HW (2013) Super-intense white upconversion emission of Yb_2O_3 polycrystals and its application on luminescence converter of dye-sensitized solar cells. Opt Lett 38:3340–3343
223. Lorbeer C, Mudring A-V (2013) White-light-emitting single phosphors via triply doped LaF_3 nanoparticles. J Phys Chem C 117:12229–12238
224. Zabiliūtė A, Butkutė S, Žukauskas A, Vitta P, Kareiva A (2014) Sol-gel synthesized far-red chromium-doped garnet phosphors for phosphor-conversion light-emitting diodes that meet the photomorphogenetic needs of plants. Appl Opt 53:907–914
225. Martın-Rodrıguez R, Valiente R, Rodrıguez F, Bettinelli M (2011) Temperature and pressure dependence of the optical properties of Cr^{3+}-doped $Gd_3Ga_5O_{12}$ nanoparticles. Nanotechnology 22:265707–265713
226. Kostyk L, Luchechko A, Zakharko Y, Tsvetkova O, Kuklinski B (2009) Cr-related centers in $Gd_3Ga_5O_{12}$ polycrystals. J Lumin 129:312–316
227. Orucu H, Ozen G, Collins J, Di Bartolo B (2009) Temperature dependence of the luminescence spectra of garnet crystals doped with chromium ions. Opt Mater 31:1065–1070
228. Strek W, Marciniak L, Gluchowski P, Hreniak D (2013) Infrared laser stimulated broadband white emission of Yb^{3+}:YAG nanoceramics. Opt Mater 35:2013–2017
229. Bednarkiewicz A, Strek W (2002) Laser-induced hot emission in Nd^{3+}/Yb^{3+}:YAG nanocrystallite ceramics. J Phys D Appl Phys 35:2503–2507
230. Sivakumar S, van Veggel FCJM, May PS (2007) Near-infrared (NIR) to red and green up-conversion emission from silica sol−gel thin films made with $La_{0.45}Yb_{0.50}Er_{0.05}F_3$

nanoparticles, hetero-looping-enhanced energy transfer (Hetero-LEET): a new up-conversion process. J Am Chem Soc 129:620–625
231. Tian Y, Tian B, Cui C, Huang P, Wang L, Chen B (2015) Size-dependent upconversion luminescence and temperature sensing behavior of spherical Gd_2O_3:Yb^{3+}/Er^{3+} phosphor. RSC Adv 5:14123–14128
232. Gamelin DR, Gudel HU (2001) Upconversion processes in transition metal and rare earth metal systems. Top Curr Chem 214:1–56
233. Hou X, Zhou S, Jia T, Lin H, Teng H (2011) Effect of Nd concentration on structural and optical properties of Nd:Y_2O_3 transparent ceramic. J Lumin 46:1953–1958

Chapter 4
Non-radiative Processes in Crystals and Nanocrystals

John M. Collins

Abstract This paper discusses non-radiative processes relevant to the luminescence characteristics of optically active ions doped into insulators or large-gap semiconductors, with particular attention to how these processes are affected as the particle size is reduced from bulk single crystals to as small as a few nanometers. The non-radiative processes discussed in this article are thermal line broadening and thermal line shifting, relaxation via phonons between excited electronic states, and vibronic emission and absorption. One prominent effect of confinement in the systems of interest is a reduction in the phonon density of states. Thus, we focus on how these non-radiative processes are altered due to the change in the phonon density of states as particle size decreases.

4.1 Introduction

Inorganic insulators doped with rare-earth ions and transition metal ions represent an important class of luminescent materials for many applications, including phosphors for lighting, scintillators, solid-state laser materials, bio-markers for imaging, and nanothermometry. Following excitation by radiation, the optical ions usually undergo some degree of non-radiative relaxation, releasing part or all of its energy to the lattice. During the non-radiative relaxation, all or part of the electronic energy initially stored in the optically active ion is converted into phonons.

The specific non-radiative processes addressed in this work are thermal line broadening, thermal line shifting, decay via a phonon from one electronic level to another, vibronic transitions, and phonon-assisted energy transfer. Generally speaking, the two main effects of going from the bulk to the nano are: (1) an increase in the surface to volume ratio, and (2) a reduction in the phonon density of states. In this paper we focus on the second point. Most non-radiative processes that play

J. M. Collins (✉)
Department of Physics and Astronomy, Wheaton College, Norton, MA, USA
e-mail: jcollins@wheatonma.edu

B. Di Bartolo et al. (eds.), *Quantum Nano-Photonics*, NATO Science for Peace and Security Series B: Physics and Biophysics,
https://doi.org/10.1007/978-94-024-1544-5_4

a significant role in the luminescent properties of these systems involve phonons, and most of those are determined in part by the phonon density of states of the lattice. One goal of this paper is to present results that demonstrate how the reduced density of states in nanoparticles affect the aforementioned processes, and under what conditions will such affects be noticeable.

To set up the problem, we first address the following question: How is the energy stored in the electronic system of the optically active ion converted into phonons? To answer this question, it is useful to first review the notion of an adiabatic process.

4.2 The Phonon Density of States in Nanoparticles

Consider a simple cubic solid with side length L and atomic spacing a. The wavelengths of the phonons vary from roughly twice the atomic spacing to twice the side length of the particle. The energy of a phonon in such a solid is given by

$$\varepsilon_{ph} = \frac{hv_s}{\lambda} = \frac{hv_s}{2L}n, \tag{4.1}$$

where v_s is the velocity of sound, $\mathrm{n} = (\mathrm{n}^2{}_\mathrm{x} + \mathrm{n}^2{}_\mathrm{y} + \mathrm{n}^2{}_\mathrm{z})^{1/2}$ and n_x, n_y, n_z are integers ranging from 1 to L/a. Note that the maximum phonon energy is determined by the interatomic spacing, and so is independent of the particle size, while the lowest frequency phonons increase in energy as the particle size, L, decreases. Thus, many low frequency phonons that exist in the bulk are no longer supported in a nanoparticle.

Calculated phonon densities of states (DOS) of cubic nanoparticles $15 \times 15 \times 15$ atoms on a side (L∼3 nm), $25 \times 25 \times 25$ atoms on a side (L∼5 nm), and that of a nanoparticle $250 \times 250 \times 250$ atoms on a side (L∼50 nm) have been calculated using the speed of sound equal to 3400 m/s and an interatomic spacing of 0.2 nm. The modes were accumulated in 1000 bins, which for the diagrams show were each approximately 0.5 cm^{-1} in width. The results are shown in Fig. 4.1. Also, Fig. 4.2 shows the same results, but with the phonon energy range between 0 and 100 cm^{-1}. We note the following:

1. For the $250 \times 250 \times 250$ atoms system, the DOS exhibits a ε^2 dependence, as expected from the Debye theory, out to a frequency at which the DOS reaches a maximum. At higher energies, the DOS is decidedly un-Debye-like, decreasing smoothly to zero. This behavior is due to the finite size of the crystal.
2. For the smaller particles, the DOS is a discrete function at lower energies, with a large energy gap between zero energy and the first mode. For 250 nm particles, the DOS appears nearly continuous at all energies, and is very similar in appearance to the DOS in a bulk cubic particle. Figure 4.2, shows the DOS at low phonon energies.

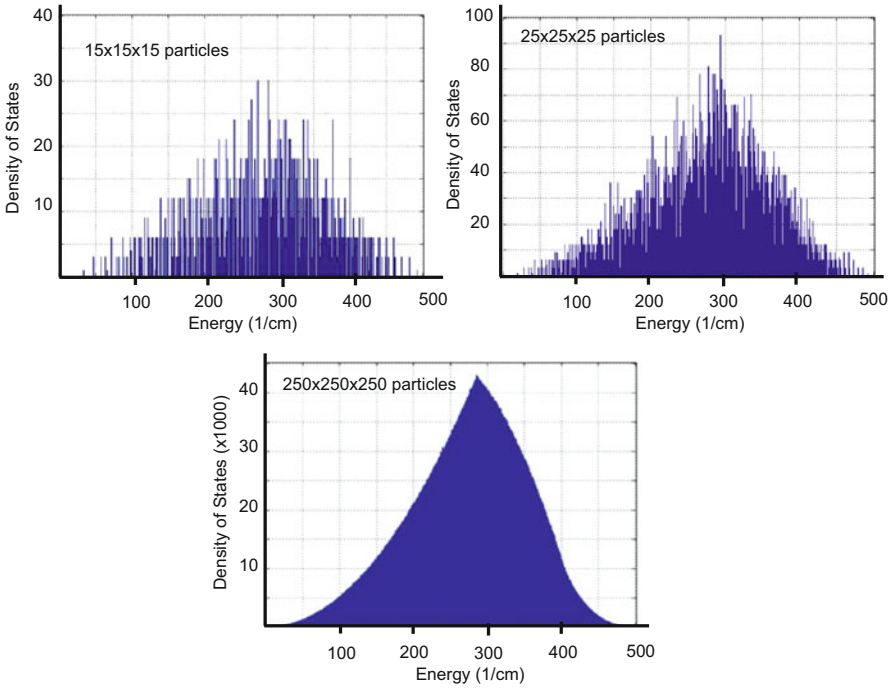

Fig. 4.1 The phonon density of states vs. phonon energy of cubic nanoparticles with (top left) 15 × 15 × 15 atoms, (top right) 25 × 25 × 25 atoms, and (bottom) 250 × 250 × 250 atoms. The velocity of sound was set to 3400 m/s

3. The results in Figs. 4.1 and 4.2 are for cubic crystals, but the discreteness of the DOS at low energies is a common feature to all very small particles. The exact shape of the DOS function, however, depends on the particle shape.

The discreteness seen in the small particle is due to the fact that in going from bulk to nano, the total number of phonon modes decreases drastically. This decrease can be shown by noting that the total number of phonon modes is simply *3 N-6*, where N is the number of atoms in the particle, and can be estimated as $N \sim (L/a)^3$. For a bulk crystal with $L = 0.3$ cm and $a = 0.2$ nm, $3N \sim 4.5 \times 10^{21}$, whereas when $L = 3$ nm, $3N \sim 4.5 \times 10^3$. Thus, going from a particle size of 0.3 cm–3 nm the total number of allowed phonon modes decreases by 18 orders of magnitude! As a result, the phonon spectrum is no longer a continuous function of energy.

Given the importance that phonon-related processes play in the luminescence behavior of ions in solids, the drastic change in the phonon DOS as one moves from the bulk to the nano-regime is likely have observable experimental effects. In the following sections, we take note of experiments that have, and in some cases have not, revealed such effects.

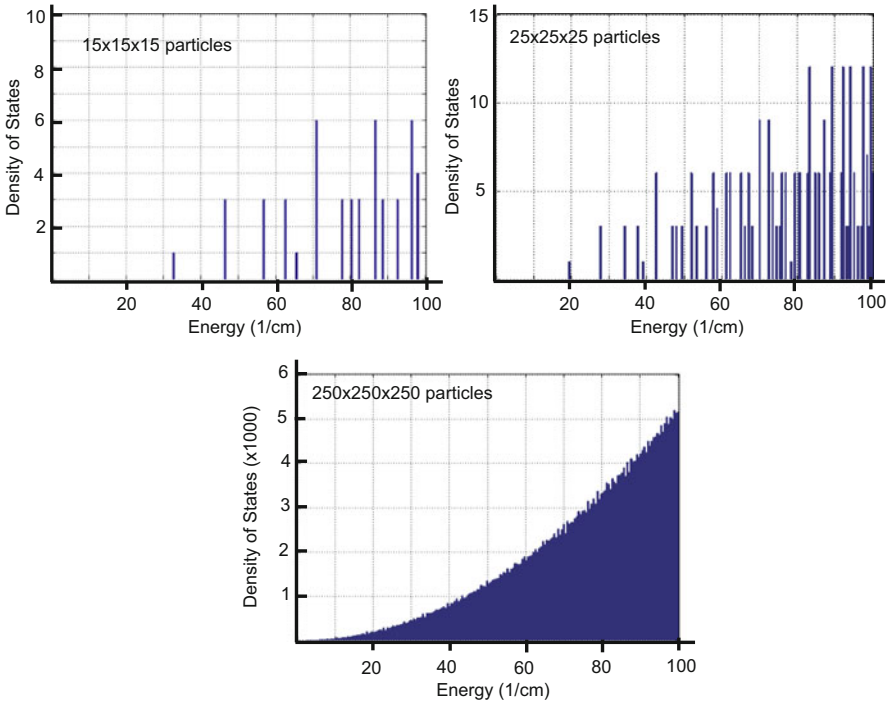

Fig. 4.2 The phonon density of states shown in Fig. 4.1 in the energy range from 0 to 100 cm^{-1}

4.3 Effect of the Phonon DOS on the Establishment of Thermal Equilibrium

Following absorption of a photon, a luminescent ion generally relaxes to a state of quasi-thermal equilibrium. The time it takes to reach this quasi-thermal equilibrium is generally on the order of picoseconds. The relaxation can be within a single electronic state or among different electronic states, the latter of which would require the breakdown of the adiabatic approximation. Even relaxation within the same electronic state requires the participation of all phonon modes and the mixing of those modes for thermal equilibrium to be established. For small particles, where the low frequency modes are discrete and well separated from one another, we may expect the establishment thermal equilibrium following excitation to be inhibited.

Experimental evidence of this effect has been observed by G. Liu et al. [1, 2], who conducted emission and excitation experiments on nanoparticles of Er-doped Y_2O_3 with radii of ~400 nm and 25 nm. Figure 4.3 shows an emission spectrum at 3 K of the $^4S_{3/2} \rightarrow {}^4I_{11/2}$ transition of Er in Y_2O_3 following excitation with a pulsed laser at energy levels into the $^4F_{7/2}$ manifold. Excitation into the $^4F_{7/2}$ levels is followed by fast relaxation to the $^4S_{3/2}$, resulting in the population of the upper crystal field level of that manifold, level (b) in Fig. 4.3. In the 400 nm particles, the

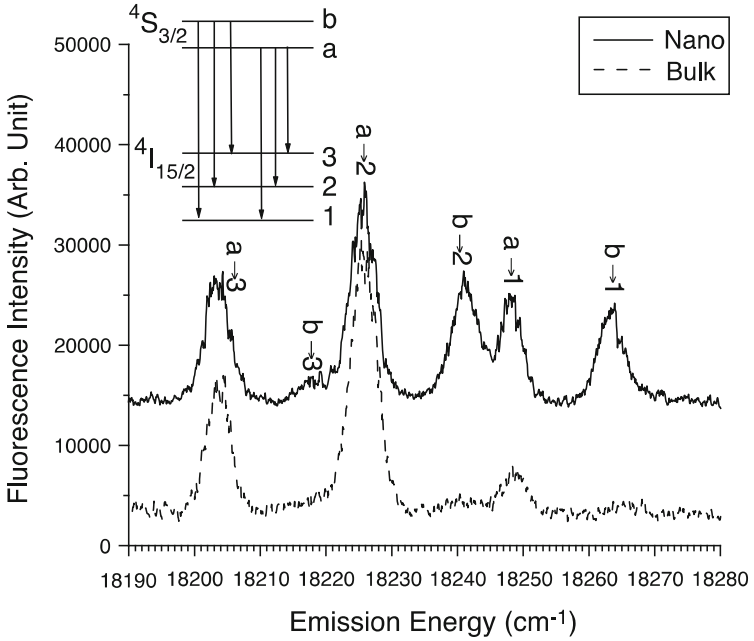

Fig. 4.3 The luminescence of the $^4S_{3/2}$–$^4I_{15/2}$ transition in bulk (dotted line) and diameter nanocrystals (solid line) of Er:Y_2O_2S at 2.6 K [1]

emission originates from only the lowest energy level of the $^4S_{3/2}$ manifold. In the 25 nm nanoparticles, however, anomalous hot emission bands are observed. This is an interesting result. Apparently, in the 400 nm particles there is fast relaxation from level (b) of the $^4S_{3/2}$ manifold to its lower metastable level (a), and so all of the emission is from level (a). In the 25 nm particles, however, there are no available modes to accept a phonon of that low frequency ($\sim$25 cm^{-1}). Consequently, the one-phonon decay process at that energy does not occur in the nanoparticle, and level (b) remains populated long enough to emit a photon. It is interesting to note, however, that above $\sim$8 K the emission from level (b) is no longer observed. It is speculated that the non-radiative decay from level (b) to level (a) can be bridged via due to two phonon (or higher-order) processes.

This experiment demonstrates the effect of the discreteness of the phonon DOS and lack of low energy phonons in small particles. However, it also hints that observing such effects may be difficult; the discreteness of the phonon DOS can be masked by second-order processes and/or by the mixing of phonons due to anharmonic contributions to the potential, even at low temperatures.

4.4 Thermal Broadening and Shifting of Sharp Spectral Lines in Nanoparticles

In this section, we focus on the changes in the density of states of nanoparticles of different sizes affects the shift thermal broadening and shifting of sharp spectral lines.

4.4.1 Broadening of a Spectral Line in a Nanoparticle

The thermal broadening of a spectral line is driven by Raman scattering, in which system in electronic state ϕ_i absorbs (emits) a phonon at frequency ω_k and then emits (absorbs) a phonon at $\omega_{k'}$. This process is shown in Fig. 4.4. The probability per unit time of this process due to modes k and k′ is:

$$(W_{Raman})_{kk'} = \frac{2\pi}{\hbar^2}\left|\alpha'\right|^2 \omega_k n \omega_{k'} n_k \left(n_{k'} + 1\right) \rho\left(\omega_f\right), \tag{4.2}$$

where $\rho(\omega_f)$ is the final phonon density of states, n_k is the occupation number of the kth phonon mode, and $|\alpha^{'}|^2$ contains information on the electron phonon coupling [3, 4]. For bulk crystals, the total contribution of the Raman process to the broadening of a spectral line usually carried out by integrating Eq.(4.2) over all

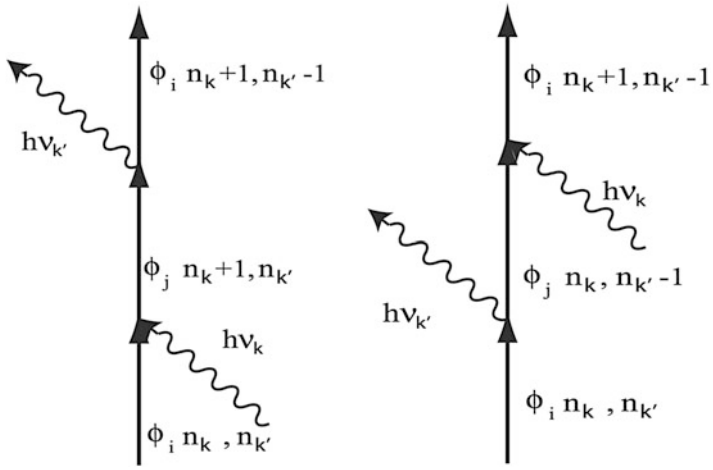

Fig. 4.4 Diagram showing the Raman processes responsible for the thermal line broadening. The left diagram shows the absorption of a phonon at frequency ν_k and the subsequent emission of a phonon a frequency $\nu_{k'}$. The right diagram shows a similar process, with the order of the emission and absorptions switched. ϕ_j represents the intermediate electronic state

phonon modes, assuming a density of states given by the Debye approximation. For nanoparticles, however, the density of phonon states is a discrete function, and the sum over states must be carried out computationally.

The total transition rate is found by summing over all final states of the lattice, subject to the condition that energy must be conserved. In nanoparticles, the density of phonon states, $\rho_{nano}(\omega)$, depends on the size and shape of the sample. Examples are shown in Figs. 4.1 and 4.2. In describing the density of phonon states, it is important to recall that each phonon mode represents a resonance peak with a particular line shape ($f(\omega)$) and line width ($\Delta\omega$). The density of states may be written as:

$$\rho_{nano}\left(\omega_i\right) = g\left(\omega_i\right) f\left(\omega_i\right), \tag{4.3}$$

where $g(\omega_i)$ is the degeneracy modes at frequency ω_i. Though the line shape is more correctly represented as a Lorentzian, we shall simplify the shape to the "top hat" function, that is:

$$f\left(\omega\right) = \begin{cases} 1/\Delta\omega & \text{for } \omega - \Delta\omega \leq \omega \leq \omega + \Delta\omega \\ 0 & \text{elsewhere} \end{cases} \tag{4.4}$$

We also assume that linewidth of each resonance, $\Delta\omega$, is independent of ω. For sharp spectral lines, we further assume that the main contribution to the broadening occurs when $|\omega_k - \omega_{k'}| \leq \Delta\omega/2$, that is, the phonons in the scattering process are of nearly the same frequency. In such a scheme, we may approximate the density of final states as

$$\varrho\left(\omega_f\right) = \rho_{nano}\left(\omega_k\right)\rho_{nano}\left(\omega_{k\prime}\right)\Delta\omega\Delta\omega'\delta\left(\omega_i - \omega_i{}'\right) \tag{4.5}$$

Summing Eq. (4.2) over phonon frequencies, and using Eqs. (4.3), (4.4) and (4.5), the total transition rate of the Raman process is

$$\begin{aligned} W_{Raman} &= \tfrac{2\pi}{\hbar^2}\left|\alpha'\right|^2 \textstyle\sum_i g^2\left(\omega_k\right)\omega_k^2 n_{\omega_k}\left(n_{\omega_k}+1\right) f^2\left(\omega\right)\Delta\omega \\ &= \tfrac{2\pi}{\hbar^2}\left|\alpha'\right|^2 \tfrac{1}{\Delta\omega}\textstyle\sum_i g^2\left(\omega_i\right)\omega_i{}^2 n_{\omega_k}\left(n_{\omega_k}+1\right) \end{aligned} \tag{4.6}$$

The degeneracy term $g(\omega)$ includes all modes within a range $\omega \pm \Delta\omega/2$. The temperature dependence is contained in the occupation numbers of the phonon modes, which is given by the Bose-Einstein distribution:

$$n_{\omega_k} = \frac{1}{e^{\hbar\omega/kT} - 1} \tag{4.7}$$

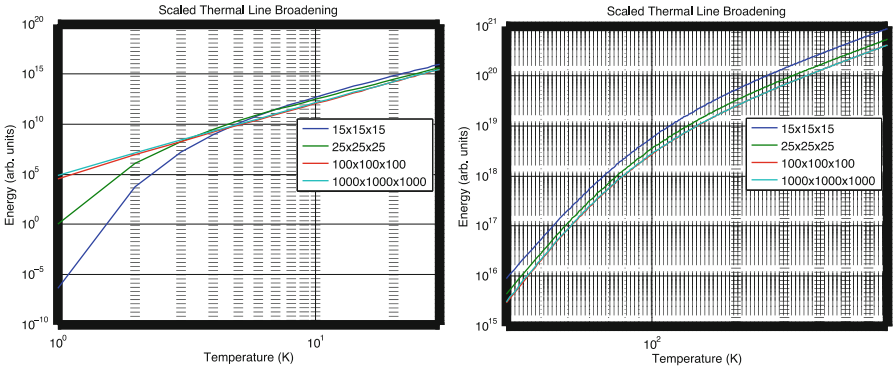

Fig. 4.5 Temperature dependence on the thermal broadening of a spectral line (given by the sum in Eq. (4.6)) for cubic nanoparticles (15 × 15 × 15-blue, 25 × 25 × 25-green, 100 × 100 × 100-red, 1000 × 1000 × 1000-cyan) for temperatures ranges 1–30 K (left) and 30–700 K (right)

The temperature dependence of the sum in Eq.(4.6) is shown in Fig. 4.5. The energy axes in Fig. 4.5 are broken up into 1000 bins, each of energy ∼ 0.5 cm^{-1}. $g(\omega_i)$ is given by the number of modes in the i^{th} bin, where ω_i is the central frequency of the bin. The sum in (Eq. 4.6), which carries the temperature dependence of the broadening, was carried out for four particle sizes (15 atoms × 15 atoms × 15 atoms, 25 atoms × 25 atoms × 25 atoms, 100 atoms × 100 atoms × 100 atoms, and 1000 atoms × 1000 atoms × 1000 atoms) at temperatures from temperatures from 1 K to 700 K.

We make the following observations regarding these results.

1. The strongest temperature dependence of the line broadening for all particle sizes occurs at temperatures below 10 K. For the 3 nm (15 × 15 × 15 atoms) nanoparticle, the temperature dependence is strong between 1 K and 10 K.
2. Above 300 K the curvature of the lines in Fig. 4.5 are independent of particle size, thus thermal dependence of the broadening should be the same for particles of all sizes.
3. Figure 4.5 also shows that above ∼10 K the expected broadening is larger for smaller particle sizes. However, this effect depends on the details of the calculation (e.g. the binning of the data and the "top hat" line shape function), and should not be taken too seriously.

To understand the strong temperature dependence of the broadening at low temperatures, it is useful to consider not just the phonon density of states, but also the phonon occupancies. Figure 4.6 shows the product $\rho_{nano}(\epsilon)n(\epsilon)$ for the 3 nm particle at T = 10 K, 100 K, and 500 K. At 10 K, only a few modes are occupied, and, in addition, the phonon occupation numbers are very small, much less than 1. At 1 K, the occupancy of the lowest mode in the 3 nm particle is $\sim 10^{-23}$. Thus, in a nanoparticle there are essentially no phonons at 1 K, so there is no broadening. This

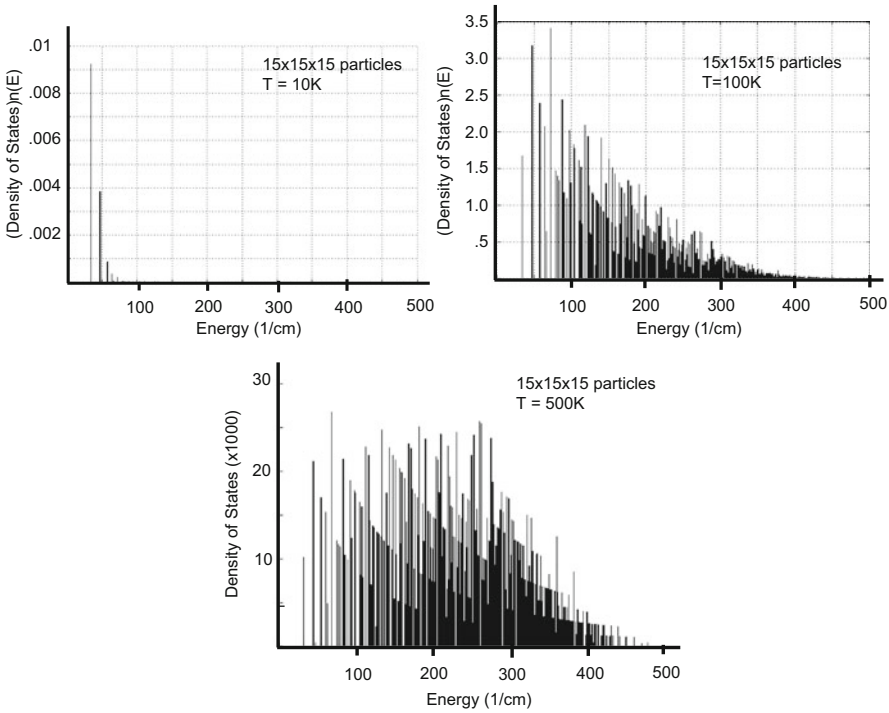

Fig. 4.6 Graphs showing the number of phonons as a function of phonon energy, i.e. $\varrho(\epsilon)n(\epsilon)$ *vs.* ϵ, for cubic nanoparticles 15 × 15 × 15 atoms (size ∼3 nm) at T = 10, 100, and 500 K

helps explain the steep slope for the 3 nm particle in Fig. 4.7 at temperatures less than a few degrees K.

Using hole-burning experiments, Meltzer and Hong [5] examined the broadening of the $^7F_0 \rightarrow {}^5D_0$ transition of Eu_2O_3 spherical nanoparticles of different diameters (5.4, 7.6, and 11.6 nm) at temperatures between 4 K and 10 K. They observed a T^n dependence, where $3 < n < 4$, for the thermal broadening of the line. This dependence is much smaller than that shown in Fig. 4.5 for the 15 nm particles, and was also much smaller than their own calculated predictions. In contradiction to the results in Fig. 4.5, the authors observed the thermal broadening increasing as the particle size decreases. To explain this they refer to calculations that posit an inverse relation between the electron-phonon coupling and particle size [6].

Erdem et al. [7] measured the linewidth of the $^2E \rightarrow {}^4T_2$ transition of Cr-doped YAG nanoparticles at temperatures from 30 K to 300 K as a function of particle size (Fig. 4.7. The results assumed a Debye phonon density of states and a Debye temperature of 550 K and where the electron-phonon coupling parameter, α', was allowed to vary. The fits to equation are reasonably good, showing that even in nanoparticles as small as 28 nm behave similar to the bulk crystal. This is consistent with the behavior shown in Fig. 4.5. Similar results were also reported by Bilir et al.

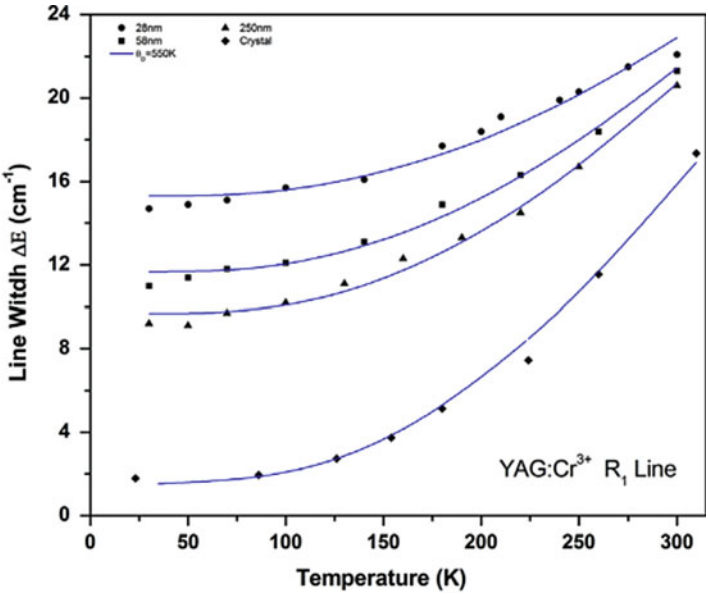

Fig. 4.7 Linewidth vs. temperature of the R_1 line in nanopowders (•28 nm, ■58 nm, ▲250 nm), and in a single crystal (♦) of Cr-doped YAG [7]

on the temperature dependence of the linewidth of Nd-doped Y_2O_3 nanoparticles ranging in diameters from 16 to 250 nm [8].

The examples above show an unresolved conflict in the behavior of the electron-phonon coupling as the particle size changes. Whereas Meltzer et al. [5] suggest an increase in the coupling as the particle size decreases, the data from Erdem et al. [6] and Bilir et al. [8] suggest a decrease in the coupling as particle size decreases. And finally, Suyver et al. [9] conclude that electron-phonon coupling is independent of particle size. These works indicate that a definitive answer as to how the electron-phonon coupling changes with particle size remains elusive.

4.4.2 Shifting of a Sharp Spectral Line in a Nanoparticle

Any interaction of a system an external agent will, in general, affect the energies of the states of the system. Thus, we expect that phonons interacting with an ion in a solid will shift the energy levels of the ion. As temperature increases, these interactions also increase, leading to the so-called thermal shift of the energy level. In a perturbation treatment, the change in energy the level found in the diagonal matrix elements containing the Hamiltonian of the perturbing interaction, i.e., matrix elements for which the initial and final states of the system are unchanged. The contribution of the electron-phonon interaction is a second-order effect. The

relevant Raman processes involve the virtual absorption and emission of phonon of the same frequency. The correction to the energy of the electronic state due to the electron-phonon interaction is given by [3]:

$$\Delta\epsilon_{i,k} = \frac{\hbar}{M v_s^2}\left[\left\langle \phi_i^0|\mathrm{V}_2|\phi_i^0\right\rangle + \sum\nolimits_j \frac{\left|\left\langle \phi_i^0|\mathrm{V}_1|\phi_j^0\right\rangle\right|^2}{\epsilon_i - \epsilon_j}\right]\omega_k\,(2n_k+1) \tag{4.6}$$

To find the total thermal shift of the particle, we neglect the contribution of spontaneous emission to Eq. (4.6) (i.e., $(2n_k + 1)$ becomes $2n_k$), and sum Eq. (4.6) over all phonon modes. Referring to Eqs (4.3) and (4.4), the total thermal shift can be written as:

$$\Delta\epsilon_i = \frac{2\hbar}{M v_s^2}\left[\left\langle \phi_i^0|\mathrm{V}_2|\phi_i^0\right\rangle + \sum\nolimits_j \frac{\left|\left\langle \phi_i^0|\mathrm{V}_1|\phi_j^0\right\rangle\right|^2}{\epsilon_i - \epsilon_j}\right]\sum\nolimits_k \mathrm{g}\,(\omega_k)\,\omega_k n_k \tag{4.7}$$

The sum in Eq. (4.7) carries the temperature dependence of the thermal line shift. Figure 4.8 shows the fit the sum in Eq. (4.7) for cubic nanoparticles ($15 \times 15 \times 15$, $25 \times 25 \times 25$, $100 \times 100 \times 100$, and $1000 \times 1000 \times 1000$ atoms) at temperatures between 1 K and 700 K. We see that, as with the line broadening, the main differences between the shift in large and small particles occurs at very low temperatures. At high temperatures, the thermal shift is nearly independent of particle size.

Erdem et al. studied the lineshift of the $^2\mathrm{E}\rightarrow{}^4\mathrm{T}_2$ emission line of Cr^{3+} in YAG in nanoparticles and in a bulk crystal [7]. The results showed that the thermal lineshift decreases as the particle size decreases. In that work, they assumed a Debye phonon

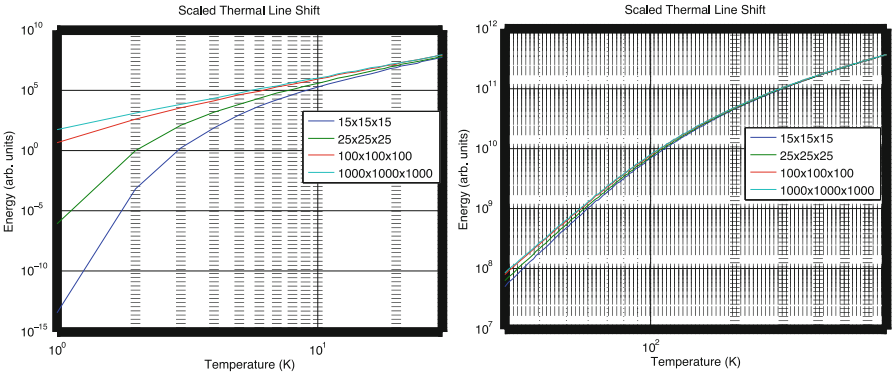

Fig. 4.8 Temperature dependence on the thermal shift of a spectral line (given by the sum in equation (78)) for cubic nanoparticles ($15 \times 15 \times 15$-blue, $25 \times 25 \times 25$-green, $100 \times 100 \times 100$-red, $1000 \times 1000 \times 1000$-cyan) for temperatures ranges 1–30 K (left) and 30–700 K (right)

density of states and a Debye temperature of 550 K, and it was found that, as with the thermal line broadening data, the electron-phonon coupling parameter decreased with particle size. Given the lack of a theoretical explanation of the electron-phonon coupling decreasing with particle size, more work is required to say definitively why the shift is less in smaller particles.

4.5 Vibronic Transitions

Following excitation, the decay of an isolated ion can occur via (1) emission of a photon, (2) emission of phonon(s), or (3) the emission of a photon concurrent with the absorption or emission of one or more phonons. This third process is referred to as a vibronic transition. In this section we discuss vibronic lines that appear as sidebands to a zero-phonon line in weakly-coupled systems [10–12].

4.5.1 Vibronic Sidebands of Sharp Lines: Theory

In the limit of weak electron-phonon coupling, the narrow zero-phonon line is accompanied by sidebands, which result from the modulation of the zero-phonon transition by the vibrations of the solid. In Fig. 4.9, one immediately notices the rich structure present in the sideband, structure that contains information of the phonon density of states. To explain such structure, we must consider the interaction of the ion with the different phonon modes of the crystal.

The transition rate of a vibronic transition involving the emission of a photon and of a phonon in the k^{th} mode is governed by terms having the following form:

$$W_k \propto \left[\left|\langle \phi_f n_{k+1}|O_{ph}|\phi_j n_k\rangle\langle \phi_j n_k|O_{rad}|\phi_i n_k\rangle\right|^2 + \left|\langle \phi_f n_{k+1}|O_{rad}|\phi_j n_k\rangle\langle \phi_j n_{k+1}|O_{ph}|\phi_i n_k\rangle\right|^2\right] \tag{4.8}$$

where O_{rad} and O_{ph} in Eq. (4.8) represent the appropriate radiative and nonradiative operators and ϕ_i, ϕ_j, and ϕ_f are the wavefunctions of the initial, intermediate and final electronic states, respectively. The first term in Eq. (4.8) represents a process whereby a photon is created in the transition from the initial electronic state to an intermediate electronic state, and then a phonon is emitted in the transition to the final electronic state. The second term reverses the order of these transitions. Figure 4.10 shows a schematic drawing of a vibronic transition that represents by the second term in Eq. (4.8).

Each of the electronic wavefunctions and the operators have a certain symmetry, and using group theory one can associate them with certain irreducible representations. We make the following definitions.

Γ_i: the irreducible representation of the initial electronic state of the transition

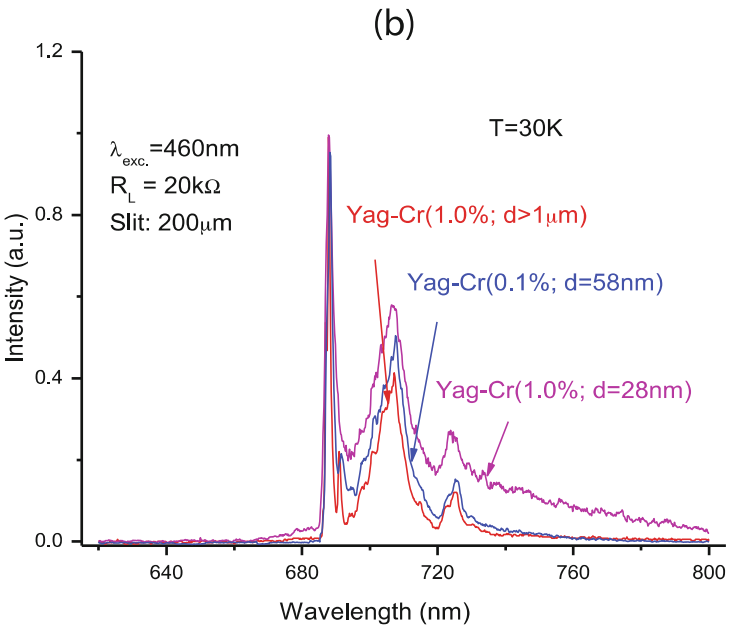

Fig. 4.9 Emission spectra at 30 K of Cr:YAG particles of 28 nm, 58 nm, and > 1000 nm. Notice the broadening of the spectral lines and an enhanced background signal as the particle size decreases

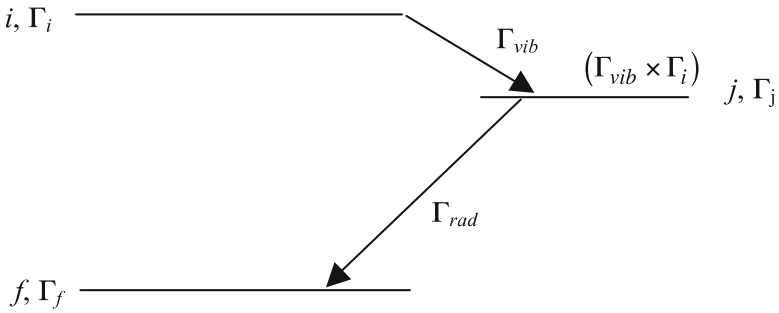

Fig. 4.10 The vibronic emission process with states and transition operators labeled according to irreducible representations

Γ_f: the irreducible representation of the final electronic state of the transition
Γ_r: the irreducible representation of the radiative operator (We will assume that this is the electric dipole operator.)
Γ_v: the irreducible representation of the vibrational mode involved in the transition

Thus, for the vibronic transition shown in Fig. 4.10 to occur the direct product Γ_i x Γ_{vib} x Γ_r must contain Γ_f:

$$\Gamma_f \in \Gamma_i \times \Gamma_v \times \Gamma_r \tag{4.9}$$

We note that Eq. (4.9) is merely a selection rule, and can only be used to determine if a particular transition can occur; it cannot be used to determine the strength of a transition.

4.5.2 *Vibronic Sidebands of Sharp Lines: The Case of MgO:V^{2+}*

Consider the case of a vibronic spectrum in emission at low temperature of MgO:V^{2+}, shown in Fig. 4.11b [12]. In MgO the V^{2+} ion sits in a site of octahedral symmetry, surrounded by six oxygen ions. Because the site has inversion symmetry, electric dipole transitions between two electronic states within the d^3 configuration are forbidden. As a result, the purely radiative transitions (accounting for the zero-phonon line) are driven by the magnetic dipole operator. Odd vibrations of the local complex destroy this inversion symmetry, so that the vibronic transitions involving such vibrations are electric dipole allowed.

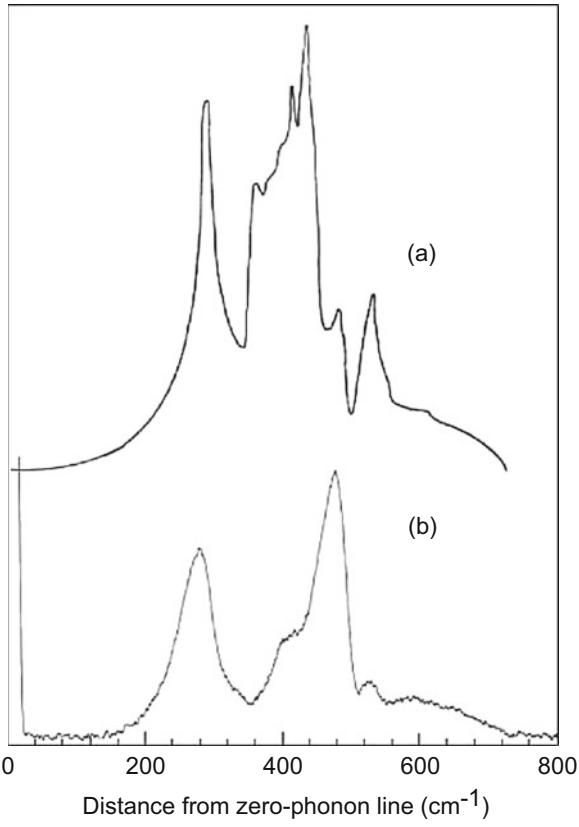

Fig. 4.11 (**a**) The density of states of MgO as determined from neutron scattering [14] shown with (**b**) the vibronic sideband of MgO:V^{2+} [12]

We now examine the relationship between theses vibronic transitions in $MgO:V^{2+}$ and the density of phonon states of the MgO lattice. First, we observe that the normal vibrational modes of the site symmetry of the octahedral group O_h are either purely even or purely odd. The representation of the final state (Γ_f) of the V^{2+} ion is known to be even. Since the electric dipole operator (Γ_{rad}) is odd, then a transition from the intermediate state via the electric dipole, according to Eq. (4.7), will be allowed only if the intermediate state is odd. The initial (excited) electronic state of V^{2+} is also even, so that only odd vibrations will be involved in the transition from Γ_i to Γ_j. Thus, Eq. (4.9) reduces to a statement of the parity selection rule.

It can be shown that of the phonons modes featured most prominently in the density of states of MgO, most of them can induce the octahedral complex to oscillate in one or more of its odd vibrational modes [13]. As a result, nearly all of the crystal phonon modes are able to participate in the vibronic transitions. The phonon spectrum of the MgO crystal (obtained by neutron scattering data [14]) is shown in Fig. 4.11a. The similarity of the shape of the low temperature vibronic sideband (Fig. 4.11b) to that of the phonon spectrum is striking, and suggests that the vibronic sideband can be closely related to the phonon spectrum of the lattice. That these two spectra show similarities and the fact that nearly all phonon modes of the MgO crystal can cause local vibrations to participate in the transition is not coincidental. However, proving a one-to-one correspondence between the peaks (and valleys) of the two spectra is not trivial, since that would require calculating the transition probabilities for each of the 3 N-6 normal modes of the crystal. Even if such a calculation could be done, it is no guarantee that such a calculation would be able to reproduce the observed vibronic spectrum. Generally, the shape of the vibronic spectrum will not exactly mimic that of the density of phonon states. It is, however, a practical way of gaining insight into the phonon density of states for some crystals.

In nanocrystals, where the confinement on the density of phonon states is most severe, one would expect that changes to the density of states would be obvious in the vibronic spectrum of the nanoparticle. In fact, such a result would represent the most direct experimental evidence of the reduced density of states in nanoparticles. Unfortunately, there is a significant amount of broadening of the zero-phonon line in small nanocrystals, due to the fact that zero phonon lines from various sites (due to the proximity of the surface) are shifted in energy with respect to one another. The sum of the contributions from various sites overlaps with a large portion of the phonon sidebands of the zero phonon line from the “normal” site. An example of this is shown in the vibronic spectra of Cr-doped YAG nanoparticles shown in Fig. 4.9. Perhaps due to the fact that this overlap is most prominent near in the low energy range of the sidebands, where the most obvious changes (i.e., discreteness of the density of states and absence of the very low energy modes) to the density of states occur, there is no reported vibronic spectrum that clearly shows the vibronic spectrum changing with particle size. The difficulty in observing this is also complicated by the fact that the emission from nanoparticles is often very weak, probably because of the large number of surface states.

4.6 Conclusions

The goal of the paper was to examine how non-radiative processes depend on particle size. Given that most non-radiative processes depend on the phonon density of states in the system under investigation, we investigated how the phonon density of states depended on particle size. This investigation consisted of calculations of the phonon density of states for cubic nanoparticle, where it was found that for very small particles, the phonon density of states becomes very different than for bulk particles. The most obvious changes in the phonon density of states between macro and nano-systems occur at the low energy end of the spectrum. The question of how non-radiative processes in doped insulators are altered as the size of the particles change from macroscopic to nano-sized was then considered.

The fact that the electronic states of optically active ions in insulators are highly localized to the site of the ion, the general theory of non-radiative transitions is largely unaltered as the particle size changes. Using the calculated densities of states for cubic nanoparticles, we examined the thermal broadening and shifting of spectral lines for various particle sizes over a wide temperature range. Initial results hint that the effects of particle size on the broadening and shifting of lines are most likely to be observed only at low temperatures and in very small particles. Even in particles on the order of 50 nm, one is unlikely to be able to discern any contribution to these processes due to confinement effects of the phonon density of states. Also discussed were how the reduced phonon density of states inhibits the system's ability to reach thermal equilibrium and should changes in the vibronic sidebands in weakly-coupled systems.

Acknowledgements The author would like to that Ryan Clair of Wheaton College for the calculations of the density of states of the nanoparticles, and also to Professor Rino Di Bartolo of Boston College for the opportunity to lecture at the Erice 2017 School. The author also acknowledges that the material presented here was supported in part by the National Science Foundation under grant number 1105907.

References

1. Liu GK, Chen XY, Zhuang HZ, Li S, Niedbala RS (2003) J Solid State Chem 171:123–132
2. Liu GK, Zhuang HZ, Chen XY (2002) Nano Lett 2:535
3. Collins J (2016) ECS J Solid State Sci Technol 5(1):R3170–R3184
4. Azumi T, Matsuzaki K (1977) Photochem Photobiol 25:315
5. Meltzer R, Hong K (2000) Phys Rev B 61(5):3396–3403
6. Takagahara T (1996) J Lumin 70:129
7. Erdem M, Ozen G, Yahsi U, DiBartolo B (2015) J Lumin 158:464–468
8. Bilir G, Ozen G, Collins J, Di Bartolo B (2014) Appl Phys A 115(1):263–273
9. Suyver J, Kelly J, Meijerink A (2003) J Lumin 104:187–196
10. Miyakawa T, Dexter DL (1970) Phys Rev B 1:2961–2969

11. Auzel F (1978) Multiphonon interaction of excited luminescent centers in the weak coupling limit: non-radiative decay and multiphonon sidebands. In: Di Bartolo B (ed) Luminescence of inorganic solids. Plenum Press, New York
12. Wall W, Di Bartolo B, Collins J, Orucu H (2009) J Lumin 129(12):1782–1785
13. W Wall (1974) Ph.D. thesis, Boston College
14. Sangster MJ, Peckham G, Saunderson DH (1970) J Phys C 3:1026

Chapter 5
Quantum Aspects of Biophotonics

Jean-Pierre Wolf

5.1 Introduction

Interestingly, while adopted for a long time in the particle physics community as a usual gauge boson, the *photon*, i.e. the quantum particle associated with light, is still sometimes debated in the *photonics* community. Some weird questions are associated, like "is this photonic process quantum?", "is it purely quantum?" or "is it non-trivially quantum?". In the present chapter, we will not enter these discussions, but rather consider processes in which the state of a system is in a quantum superposition of different states (e.g. a Schroedinger cat) or in which distinct subsystems are entangled (via non-locality).

Even more debated is the emerging field of quantum biology [1] in which some quantum pathways are supposed to be chosen in the process of natural evolution. A pivotal work was performed in 2007 by G. Fleming [2], in which he demonstrated that quantum coherent energy transfer takes place in some photosynthetic systems. More precisely, he studied by 2D-spectroscopy the light harvesting process of the green-sulphur bacteria, which has an efficiency of almost 100% for transferring the energy of an absorbed photon to the reaction center. This amazing efficiency is achieved via a specialized molecular structure called Fenna-Matthews-Olson (FMO) complex. The time resolved 2D spectra clearly showed quantum coherences between excitons from multiple pigments within the FMO structure. These results were originally obtained at 77 K, but further investigations showed that partial coherence survives, even at room temperature [3]. A major question however remains: although existing, do these quantum superpositions of states play a major

J.-P. Wolf (✉)
GAP-Biophotonics, University of Geneva, Geneva, Switzerland
e-mail: jean-pierre.wolf@unige.ch

B. Di Bartolo et al. (eds.), *Quantum Nano-Photonics*, NATO Science for Peace and Security Series B: Physics and Biophysics,
https://doi.org/10.1007/978-94-024-1544-5_5

role and are they used by Nature to enhance the efficiency of harvesting light beyond the classical limits? These questions remain open today, and are actively debated in the literature.

A particular field that uses the dynamics of quantum superpositions of states is quantum coherent control. The aim, in this case, is to optimize the efficiency of some photo-biological processes, e.g. vision, by shaping the interacting laser field. We will dedicate a significant part of this chapter to coherent control methods and applications in biophotonics.

After an introduction of the basic processes and techniques used in coherent control, such as quantum pathways interference, we will concentrate on recent achievements in the field of coherent manipulation of biological objects. Particular interest will be dedicated to the identification of biological molecules that exhibit almost identical linear spectra and the wealth of related applications, such as specific serum proteins and pathogen detection. We show that by playing with quantum interference between reaction pathways, it is possible to discriminate nearly identical cellular vitamins [4, 5] and identify selectively proteins (antibodies) in blood serum. Immunoglobulins G and M, as well as albumin, could be directly be quantified in blood serum label-free, yielding the first "Quantum Control Based Bio-assays" [6].

5.2 Basics of Coherent Quantum Control

Coherent quantum control had a significant impact on photochemistry and spectroscopy. Not only could the atomic motion be *observed* within molecules by snapshots of a few femtoseconds duration, it could also be *controlled*. The basic idea of this revolution is the use of quantum interference between different states that are in coherent superposition so that a target state is reached with maximum probability. The mechanism reminds interference in optics, where some optical paths are favored (constructive interference) while others are discarded (destructive interference), as in Young's double slit experiment. A key element for achieving this control is the transfer of coherence from the exciting light field to the atomic or molecular system via the electric dipole operator. A tailored coherent laser pulse is used to excite a molecule in a superposition of states, which drives the molecule along a specific path to obtain a targeted result.

A famous example of coherent control is the Tannor, Koslov and Rice [7, 8] "pump-dump" method (Fig. 5.1), in which many vibrational states of a molecule ABC are coherently excited for generating a vibrational wavepacket. This wavepacket explores, as a function of time, a large fraction of the electronically excited hypersurface. By firing a second laser at convenient times t1 or t2, the molecule is brought back to its ground state but onto different dissociation paths, resulting in different species AB + C or A + BC. The system can thus be driven to a specific fragment by using the quantum control of the photodissociation process.

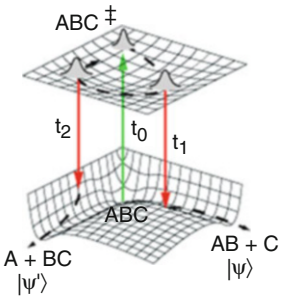

Fig. 5.1 Coherent control of the dissociation pathways of the molecule "ABC " [7, 8]

In 1992, H. Rabitz at Princeton introduced [9, 10] the concept of "optimal control", in which a feedback loop optimizes the laser pulse characteristics to reach most efficiently the desired target. For this, a large number of parameters (corresponding to the amplitude and phase of each spectral component within the exciting laser spectrum) have to be controlled. This "pulse shaping" technique is usually performed by introducing a liquid crystal array in the Fourier plane between two gratings (4f arrangement) [11]. Excellent results in terms of efficiency have been obtained using genetic-type optimization algorithms [12].

Besides the above mentioned "pump-dump" scheme, other successful control methods have been extensively applied, including stimulated Raman scattering (STIRAP), Four Wave Mixing like CARS (Coherent AntiStokes Raman Scattering), multiphoton absorption and multiphoton ionization. For more information about general quantum control aspects, a detailed review article has been published by M. Dantus et al. [13]. The controlled targets can be, for instance, specific fragments, specific isomers or specific isotopes, but also the enhancement or reduction of the fluorescence of a specific molecule (by driving it preferentially into other relaxation pathways). In this respect, a pioneering work has been performed by the group of G. Gerber [14, 15], in which the capability of distinguishing two different dyes using 2-photon absorption control was demonstrated, although the dyes had similar linear absorption and fluorescence spectra.

Experiments based on quantum control in biology have also been performed. Some striking examples are the control of the relaxation pathways in rhodopsin complexes [16, 17], the vibrational CO ladder climbing in hemoglobin [18] and pH-sensitive measurements in multi-photon microscopy [19].

An attractive application is the ability of discriminating different biological systems that are usually undistinguishable with standard linear spectroscopic approaches. One can think for instance to the early detection of cancer using the detection of specific proteins, the label-free monitoring of the cell metabolism, or the detection and identification of harmful bacteria. The aim of this chapter is to discuss these potential applications of quantum control (Fig. 5.2).

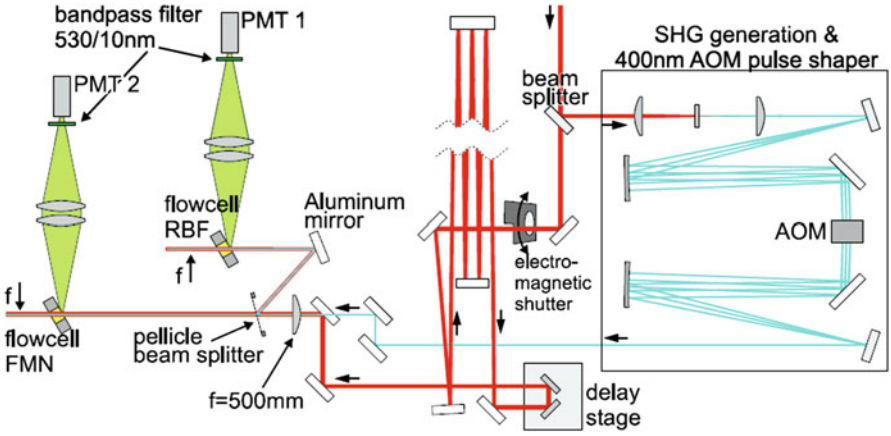

Fig. 5.2 Experimental implementation of the quantum control based optimal discrimination of two flavins (RBF and FMN). The experiment relies on fluorescence depletion with an optimally shaped excitation laser pulse. The pulse shaper uses a 4f line and an acousto-optic modulator (AOM). (From Ref. [4])

5.3 Use of Optimal Quantum Control for Discriminating Almost Identical Bio-molecules

The identification or discrimination of molecules and quantum systems that are nearly identical (proteins, bacteria, etc..) is normally an exceedingly difficult task. The conventional means of addressing this common need is through various *static* spectroscopic techniques, which can be especially difficult in complex remote environments. However, recent theoretical work showed that two or more quantum systems, even if they differ only infinitesimally, may be drawn apart to have distinct signatures through tailored control of their *dynamics*. Ultrafast broad bandwidth lasers with adaptive pulse shaping provide a means to implement this theoretical concept through controlled quantum optimal dynamic discrimination (ODD) [20]. In collaboration with the group of H. Rabitz at Princeton University, we demonstrated the capabilities of ODD by discriminating between two almost identical molecules of riboflavin (RBF) and flavin mononucleotide (FMN) in water solution, which have virtually identical linear absorption and fluorescence spectra (see Fig. 5.3a, b) [4, 5]. The successful implementation of ODD opens up numerous applications including in fluorescence microscopy, protein identification, as well as possible remote discrimination of different bacteria. A key component of ODD is operation with shaped laser pulses, which can nonlinearly interact with the molecules to fully exploit their dynamical capabilities and create discriminating signatures. The similar optical spectra of RBF and FMN arise from the common isoalloxazine ring with the only distinguishing feature being changes at the end of the side chain tail (Fig. 5.3a).

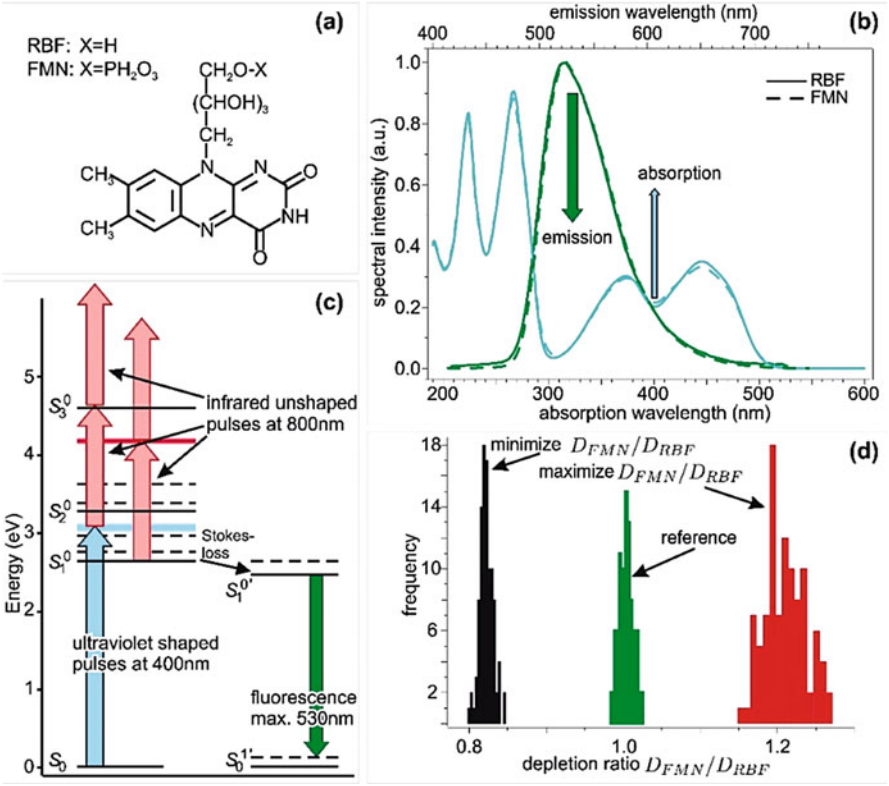

Fig. 5.3 The RBF and FMN molecules in (**a**) are very similar exhibiting nearly identical linear absorption and emission spectra in (**b**). The shaped UV control is centred at 400 nm and the flavin fluorescence signals are recorded over a window around 530 nm indicated by the respective arrows. The controlled optimal dynamic discrimination (ODD) of the flavins operates as indicated in (**c**) with a shaped UV pulse coordinated with a time delayed unshaped IR pulse to draw apart the vibronic dynamics of the flavins in the S_1 or S_2 excited states. The unshaped IR pulse serves to selectively disrupt the subsequent fluorescence signals from the two flavins and the red arrows indicate various possible means of action for the IR pulses. A typical outcome is shown in (**d**) where the ratio of flavin depletion signals, either *D(RBF)/D(FMN)* or *D(FMN)/D(RBF)*, is maximized. The reference case corresponds to the application of transform limited pulses. (From Ref. [4])

The present application of ODD utilizes a control field consisting of a shaped ultraviolet (UV) portion at 400 nm and a near infrared (IR) component at 800 nm, which is Fourier transform limited. The unshaped IR pulse follows the shaped UV pulse by a time delay τ, and the structure of the shaped UV pulse is deduced optimally under adaptive control to achieve ODD in the fluorescence signals from RBF and FMN. The primary operation of ODD relies on the shaped UV pulse coherently transferring ground state population into the flavin S_1 or S_2 excited states with the IR component likely creating further excitation of the molecules to higher lying S_n states. The IR field disrupts the vibronic excitation in S_1 or S_2 created

by the UV pulse in order to make a discriminating difference in the fluorescence spectra of RBF and FMN from S_1 recorded in the window 525–535 nm after a relaxation period of ~5 ns. Fluorescence is therefore depleted, and this fluorescence depletion value is used as measure of the molecular response to the field. The overall mechanism also may take advantage of any beneficial intra- and inter-molecular dynamical processes, and the ODD discrimination can draw on suitable coherent and incoherent aspects of the molecular dynamics.

In the first series of experiments the RBF and FMN solutions are in separate identical flow cells exposed to the same trial shaped UV pulse and time delayed unshaped IR pulse. An acousto-optic modulator is used to shape the UV pulses. A sequence of experiments $n = 1, 2,..$ was performed to record the relative depletion signal D_n

$$D_n(RBF) = \left[{F_n}^{und}(RBF) - {F_n}^{d}(RBF) \right] / {F_n}^{und}(RBF),$$

Where ${F_n}^{und}(RBF)$ is the undepleted fluorescence signal from the RBF cell (i.e., without application of the time delayed IR pulse) and ${F_n}^{d}(RBF)$ is the depleted signal in the presence of the IR pulse. An analogous expression applies to $D_n(FMN)$ for data collected from the FMN cell exposed to the same laser pulses.

The pulse shaper operated through phase modulation with 50 pixels, each on the range $0–2\pi$, over the bandwidth of the UV pulse (only 3–4 nm). A genetic algorithm of 30 individuals was used to optimize the UV pulse phases with convergence typically occurring in 100~300 generations.

Figure 5.3d demonstrates the ability of ODD to significantly draw apart the RBF and FMN fluorescence signatures in spite of their nearly identical linear optical spectra in Fig. 5.3b. For a given time delay τ, a specific optimal UV pulse is determined in the adaptive control experiment. The best discrimination was found for τ ~250–500 fs and the procedure was not able to find significant discrimination for $\tau \geq$ 1ps indicating a loss of coherence and/or insufficient overlap between the UV and IR pulses.

With a delay time τ typically around 250–500 fs, optimal pulse shapes found in different runs were very complex and showed considerable difference. They however produced exactly the same discrimination ratio when applying them, even weeks after the initial experiment. The underlying mechanisms are currently investigated, in order to identify whether this behaviour is generic or particular to this RBF/FMN system.

The assembled set of optimally discriminating laser pulses and their long-term stable performance permits exploiting ODD as a novel means for detection of nearly identical molecules when they are simultaneously present in a sample. In this work the recorded fluorescence depletion signals ${F_n}^{d}$ are utilized, as they are proportional to their respective flavin concentrations. Thus, the fluorescence signal F_n (mix) from a mixture of flavins generated with the n-th control UV-IR pulse pair is related to its

individual counterparts by

$$F_n(mix) = c(RBF)F_n{}^d(RBF) + c(FMN)F_n{}^d(FMN),$$

where *c(RBF)* is the fraction of RBF present and *c(RBF)* + *c(FMN)* = 1. The reference signals $F_n{}^d$*(RBF)* and $F_n{}^d$*(FMN)* are normalized to their respective concentrations deduced in learning the n-th control field, and similarly F_n is normalized to the total sum of the two flavins present. Two distinct ODD laser pulses could successfully determine the fractional content of the two flavins (the constrained relation between the fractions was not used in order to test the capabilities of ODD). Increasing the number of interrogating optimal pulses improves the standard deviation of the extracted component concentration fractions and a typical result using six pulses was *c(RBF)* = 0.35 ± 0.04 and *c(FMN)* = 0.68 ± 0.05 where the exact values were 0.33 and 0.66, respectively [4].

On a fundamental point of view, the exact molecular mechanisms underlying the selectivity allowed by the application of the optimally shaped pulses could be identified by quantum chemistry calculations [5]. It was shown that the optimal laser field makes use of low-frequency vibrational modes localized on the two biochromophores side chains (terminated by a phosphate group or by hydrogen) and selects the regions of their potential energy landscapes characterized by different transition dipole moments to higher excited states leading to different ionization probabilities. The resulting modulation of the excited state populations eventually controls the emitted fluorescence intensity.

5.4 Label-Free Identification of Peptides and Proteins

From the experimental standpoint, one of the major difficulties faced for the extension of the ODD scheme to proteins (or DNA) was the lack of deep UV (DUV) laser pulse shapers. This lack of ad hoc instrumentation motivated us to develop a dedicated MEMS based pulse shaper, in collaboration with CSEM-Neuchatel [21, 22]. This device proved successful for a very broad spectral range from the XUV [23] to the mid-IR.

First DUV-ODD experiments related to the fluorescing building blocks of proteins: Tryptophan and Tyrosine. The success of these experiments [24] enabled to identify tryptophan as ideal molecular target for performing ODD in proteins. In fact this bright emitting fluorophore displays a defined feature at short time-delays (<1 ps) that can be easily acted upon by an UV shaped femtosecond laser pulse and monitored by fluorescence depletion. Given tryptophan sensitivity to its local environment, it was decided to investigate the potential of ODD specifically on tryptophan-containing small peptides. We set-up a discrimination experiment aimed at the ODD fluorescence-based identification within several peptide pairs, otherwise showing identical fluorescence spectral and time-resolved response [25].

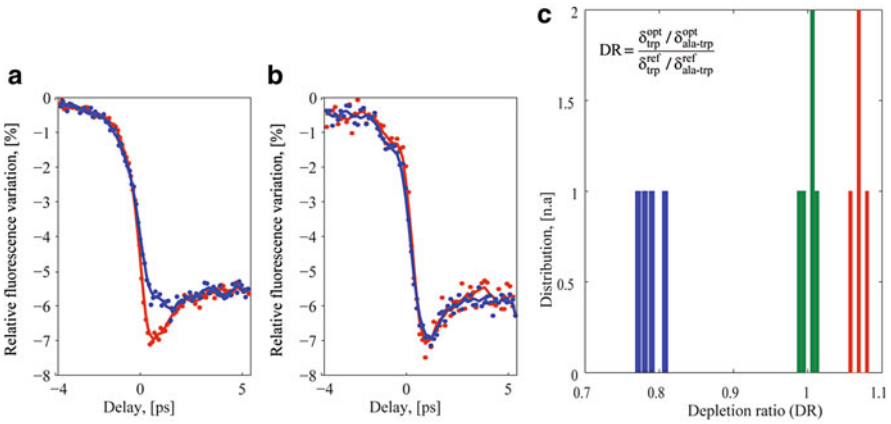

Fig. 5.4 Example of successful optimization for fluorescence depletion modulation in case of ala-trp (**a**) versus trp (**b**) with multi-objective algorithm optimization (**c**). Histogram of fluorescence depletions for ala-trp and trp. Green (middle column): reference obtained with Fourier-transform pulses, blue (left): maximization of fluorescencedepletion for ala-trp, red (right): maximization of fluorescence depletion for trp

A first series of feedback driven optimizations aimed at selectivity modifying the depletion amplitude at a given time delay (600 fs) of a defined peptide against another. An exemplary plot summarizing the outcome of an optimization run (ala-trp vs. trp) is shown in Fig. 5.4. In this case, a multi-objective optimization algorithm was launched with two independent goals: (i) increasing ala-trp fluorescence and (ii) decreasing trp fluorescence. One can appreciate the result of the procedure by applying the optimal mask on the two samples and acquiring the time resolved traces, as reported in Fig. 5.4a and b. In this example, the optimized pulse shape leads to an increase in the ala-trp time-resolved fluorescence variation by 20%, while trp remains unaffected. Optimization runs with the same objectives were repeated several times to evaluate statistical variations on the results. Note that different pulse shapes were found to lead to similar yields, pointing out the existence of multiple solutions.

The closed loop optimization procedure was then performed several times for the opposite set of goals, i.e. (i) decreasing ala-trp-fluorescence and (ii) increasing trp fluorescence. From the comparison of these traces with reference results obtained with Fourier transform pulses, we establish the histogram presented in Fig. 5.4c. The coherent manipulation of the molecular wavepacket leads to a variation of discrimination power that tears apart the trp and alatrp signatures by more than 8σ (where σ is the averaged statistical error on the results measured for a defined pulse shape).We also verified that the discrimination power DR was dependent on the time delay Δt. As expected for a coherent manipulation of the molecular wavepacket, DR decreases to zero for time delays larger than decoherence time (typically 1.5 ps).

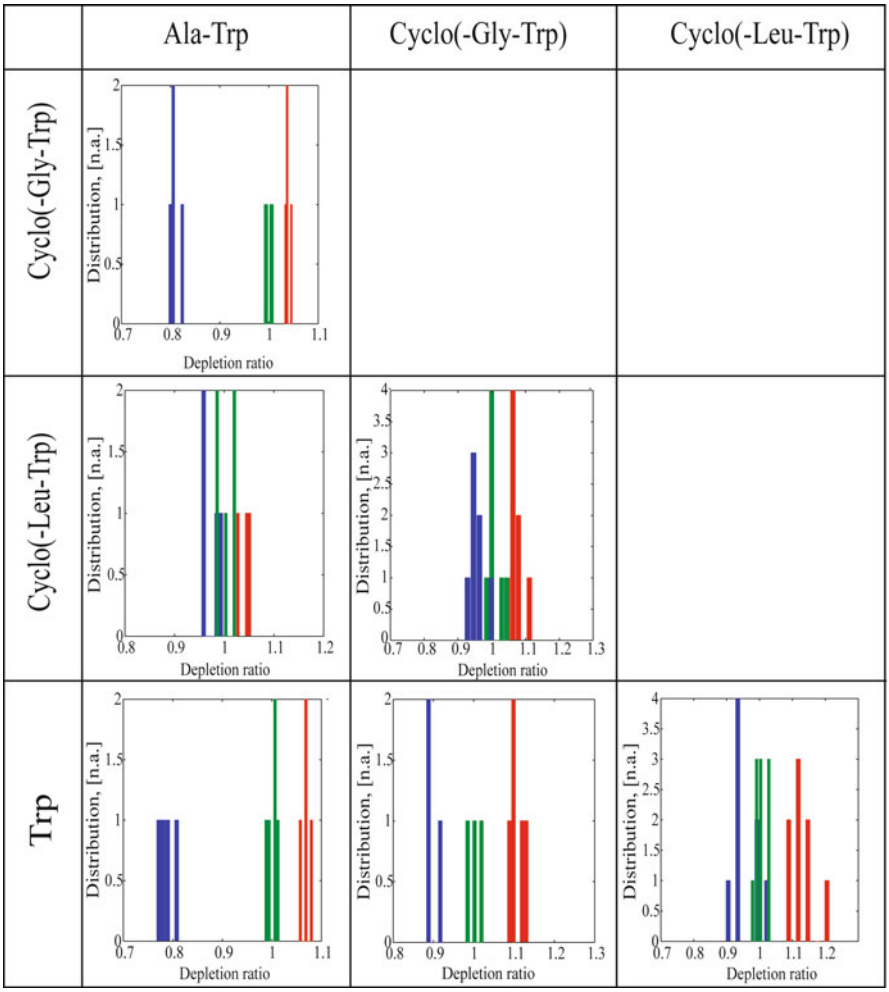

Fig. 5.5 Histograms of fluorescence depletions for various pairs of molecules. Green: reference obtained with Fourier-transform pulses, blue: maximization of fluorescence depletion for row molecule, red: maximization of fluorescence depletion for column molecule. (From Ref. [25])

The same procedure described above was applied to all pairs of dipeptides and free trp, giving rise to the matrix displayed in Fig. 5.5: In the histograms, bars indicate the ratios of the depletion values (row molecules over column molecules) obtained using phase-shaped DUV pulses retrieved by optimizations aimed at minimizing (blue) or maximizing (red) this quantity. Green bars correspond to the ratio of the depletion values measured with unshaped pulses. One can see that for several molecule pairs (trp vs. dipeptides, cyclo(-gly-trp) vs. ala-trp) the discrimination capability of the method is satisfactory, with a fluorescence difference between the optimized pulse shapes ranging from 3σ (trp vs. cyclo(-leu-

trp)) to 8σ (cyclo(-gly-trp) vs. ala-trp), which is remarkably high considering the modest bandwidth available for the shaped DUV pulse. This restricted parameter space does not allow, in opposite, to discriminate other dipeptides like cyclo(-leu-trp) vs. ala-trp.

It is clear from Fig. 5.5 that even for a group of very similar molecules addressed with identical experimental resources (laser spectral bandwidth as compared to absorption bandwidth, shaping spectral resolution), large variations do occur. No obvious reason emerged from our measurements. For instance, no correlation exists between the Stokes shifts in the static spectra and discriminability. Similarly, purely dynamical considerations, based on the time-resolved measurements, would suggest that, for instance, ala-trp should be more easily distinguished from cyclo(-leu-trp) (different relaxation time constants) than from free trp, which is not the case. No correlation with far infrared spectra was found either, stressing the importance of more complex quantum interference effects than just impulsive driving of vibrational modes.

As a natural follow up of this benchmark experiment, work is now in progress for transferring the DUV-ODD method to larger proteins with prospective applications in the field of label-free, consumable-free medical sensing. The goal of this undergoing study is currently, for instance, to quantify antibodies (such as IgG, 150 kDa) in blood serum, leading to first "quantum interference based bioassays" [6].

5.5 Quantum Controlled Vision in Live Animals?

The ultrafast investigation of the primary vision process (i.e., the rhodopsin-bound 11-cis-retinal to all-trans retinal isomerization upon photon absorption, Fig. 5.6) started with the pioneering paper by the Shank group where the arrival in the isomerization state in less than 100 fs was time-resolved using a transient absorption Scheme [26, 27]. Shortly after, Wang et al. showed wavepacket oscillations in this molecule demonstrating that coherence is preserved for at least 2 ps after photo-excitation despite the passage through the conical intersection leading to isomerization [27]. This molecular wavepacket is generated by a coherent superposition of a set of vibronic quantum states, and it evolves after excitation by the broadband femtosecond laser according to the field free Hamiltonian. The use of a second laser pulse, however, allows for the manipulation of the evolution of this wavepacket. For instance, Gerber's and Cerullo's groups demonstrated that it was possible to transfer the excited population back to the 11-cis ground state by stimulated emission before the transition through the conical emission takes place [28, 29]. These experiments can be seen as the first level of quantum control of the photo-isomerization of retinal in the rhodopsin protein.

The isomerization process can, however, be more precisely controlled by tailoring the shape of the molecular wavepacket itself. Modulating the amplitude and phase of the excitation laser spectral components allows, via the electric dipole interaction with the molecule, to modulate the phase and amplitude of the different

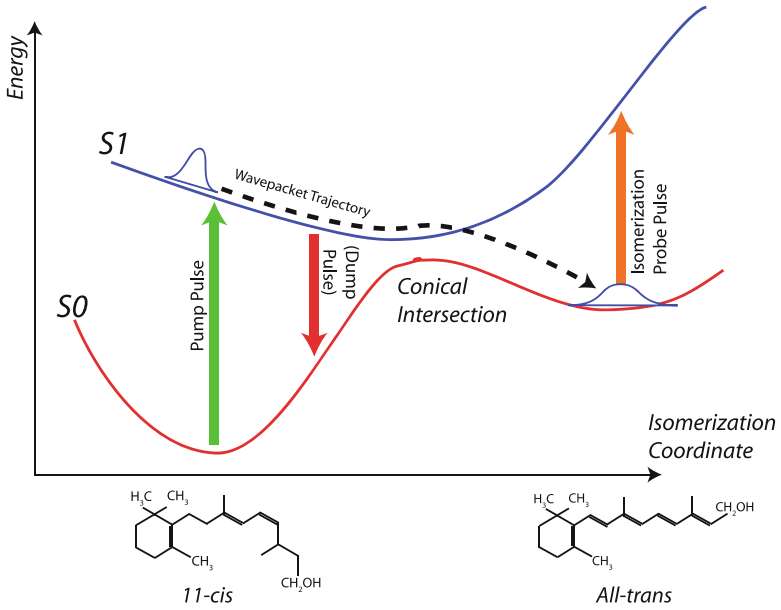

Fig. 5.6 Ultrafast manipulation of the retinal photo-isomerization in rhodopsin by pump-probe and pump-dump schemes acting on the excited states molecular wavepacket

excited wavefunctions, and thus the shape of the matter wavepacket. This concept of optimal quantum control was introduced by H. Rabitz and widely used since then for many applications in femtochemistry [10].

The first experimental demonstration of optimal quantum control of the retinal photo-isomerization in bacteriorhodopsin in solution was performed in 2005 by the group of R. Dwayne Miller [16, 30]. The experiment relied on the pump-probe scheme of Fig. 5.6 (without the dump pulse), in which the photoisomerization yield was probed by the red-shifted absorption from the isomer. The time delay between the pump and the probe during the pump pulse shape optimization procedure, was set 20 ps apart, in order to probe long term, stable isomerization. The authors showed that by applying an optimally shaped laser pulse, it was possible to increase the retinal's photo-isomerization yield by 20% as compared to a Fourier limited femtosecond pulse (Fig. 5.7 a–d). Conversely, an anti-optimal pulse shape reduced the photo-isomerization efficiency by 20%. Although a scientific debate about the linearity of the process followed these pioneering experiments, the basic concept of modulating the photo-isomerization with different pulse shapes was demonstrated. Successively, the Bucksbaum group set up a similar experiment confirming the sensitivity of isomerization to phase but only limited to pulses exceeding 10^{16} photons/cm^2 [17]. Although demonstrated on free bacteriorhodopsin in solution, these pioneering experiments set the groundwork for investigations on quantum controlling visual opsins.

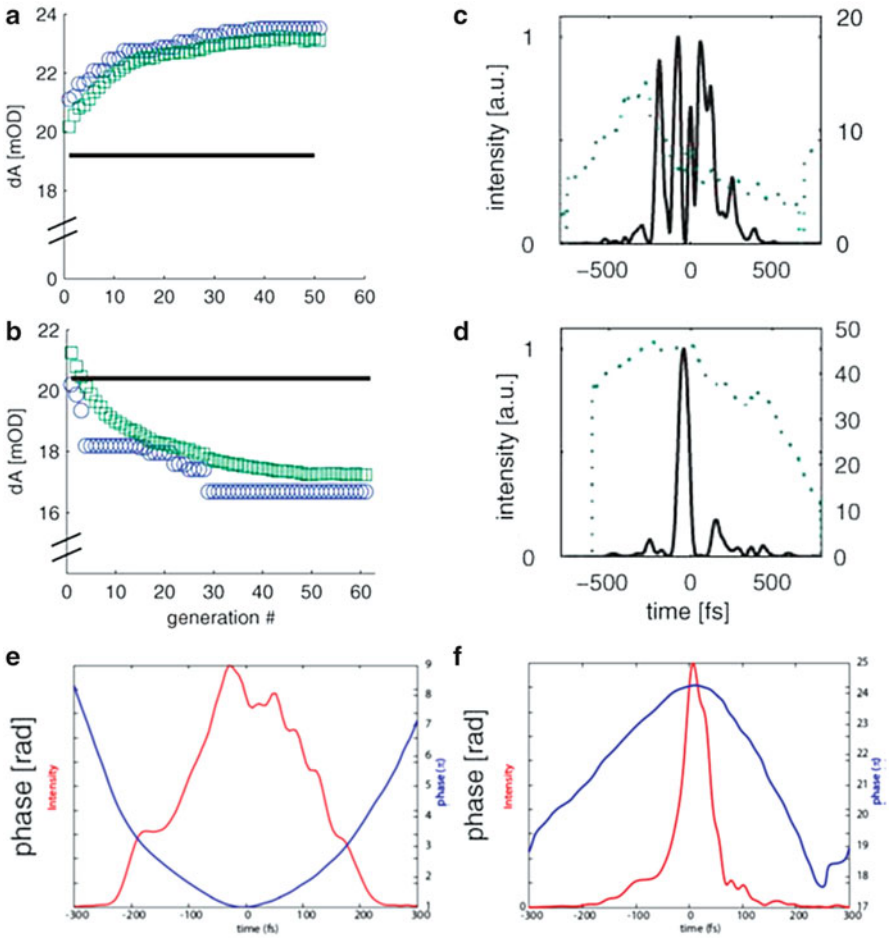

Fig. 5.7 Optimal quantum control of the photo-isomerization of retinal in bacteriorhodopsin. (**a**–**d**): Results from the original R.Dwayne-Miller paper [16]. (Adapted from Ref. 16). Optimization (**a**) and anti-optimization (**b**) procedure of the retinal photo-isomerization, leading to the pulse shapes in (**c** and **d**) respectively. These results were obtained by modifying the spectral amplitude as well. (**e**, **f**): results from our group, using different molecules, different lasers, different algorithms, and by modulating only the phase of the incoming pulse

These experiments also raised an active discussion about the possibility of controlling systems with single photon interactions, which is still ongoing [16, 31–37]. Two main topics emerged from these discussions: [1] whether, in open systems, the environment can contribute to a control in the linear regime, and [2] whether amplitude modulation and calibration flaws may lead to the original conclusions from the Dwayne-Miller group. In order to contribute to the latter part of the discussion, we reproduced the original experiment with a phase-only pulse shaper and precisely corrected for laser power fluctuations.

Interestingly, the spectral phase obtained by optimizations share several characteristics with the ones obtained by Dwayne Miller in that the pulse providing decreased isomerization bears a picosecond multi-peak structure, while the one leading to increased isomerization possess a temporal structure close to Fourier-transform.

More specifically, they realized a transient absorption measurement based on a shaped excitation pulse in the green (around 550 nm, 40 fs) and a weak probe pulse at 630 nm to measure the transition to the all-trans isomer. By using a genetic algorithm to retrieve the optimal phase-shape, the possibility to control the isomerization yield both for enhancing or decreasing the natural occurring yield (Fig. 5.7) was demonstrated [38].

However, these works were performed on bacteriorhodopsin in solution, and not rhodopsin from visiual pigments. These latter proteins are significantly different than bacteriorhodopsin, although both proteins are seven transmembrane serpentines and use retinal as their light substrate. The signaling pathways from photon absorption to neuron hyperpolarization are complex. The first step is always retinal photo-isomerization, which then induces a conformational change of rhodopsin and opsins and a cascade of reactions involving the activation of transducins (G proteins), followed by a cGMP phosphodiesterase, and eventually by the closure of cyclic nucleotide-gated Na + channels that trigger a hyperpolarization of the rod and cone cells, an ensuing depolarization of bipolar cells and the firing of retinal ganglion cells (Fig. 5.8).

A practical method to detect this activity is electroretinography (ERG), which measures electrophysiological activity of the retina (similar to electrocardiography). ERG is nowadays a widely used, noninvasive, electrophysiological assay of retinal function with well-documented methods of analysis [39]. We recently showed that it was possible to manipulate the photo-isomerization yield of photoreceptor molecules in a live mouse by modulating the spectral phase of a green femtosecond light pulse and record the electric signal generated by the retina. Our experiment is based on a kHz amplified Ti:Sapphire laser system coupled with a noncollinear parametric amplifier generating 50 fs pulses at 535 nm.

The visual response was acquired by three electrodes placed in contact with the irradiated eye, the forehead, and under skin in the tail (for ground voltage reference), respectively. First preliminary results are presented in Fig. 5.9. In these ERG traces, one can identify the characteristic A-wave (negative at early times) and B-wave (positive at later times) signals. The former is mainly attributed to cone activity and the latter to second-order retinal neurons from cones. These results unambiguously establish the possibility to efficiently acquire the visual response *in vivo* using pulsed ultra-short laser excitation, paving the way to possible quantum control of vision in living animals.

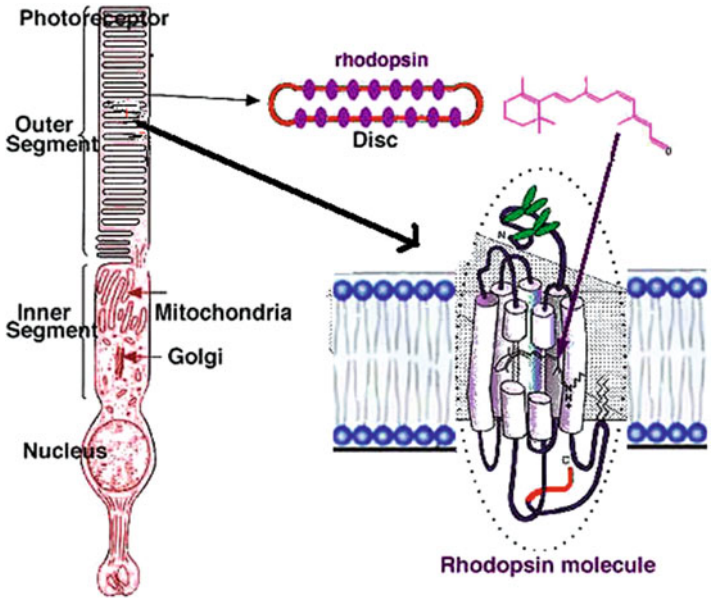

Fig. 5.8 Rod cell (left) showing a rhodopsin in outer segment disc membranes. (From webvision.med.utah.edu)

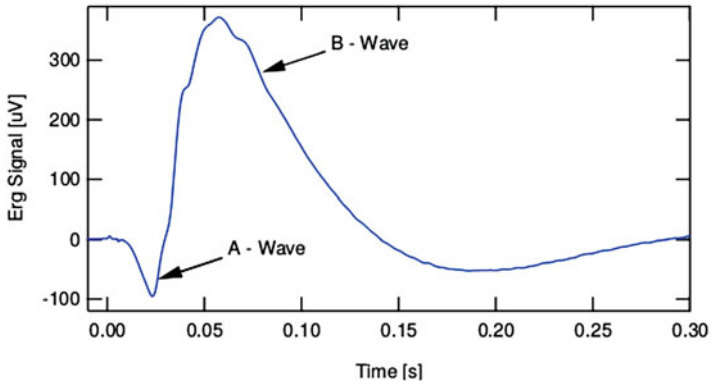

Fig. 5.9 Photopic A- and B-wave electro-retinogram (ERG) response recorded on a live C57BL/6 mouse, under illumination with a 40 fs, 535 nm laser. The A-wave amplitude and its implicit time reflect activity of M/L cones

5.6 Coherent Control of Nerve Firing in Living Brain Tissues

The photoisomerization of retinal within rhodopsin molecules acts as a photoswitch, which can be used for optically controlling nerve firing. With the advent of optogenetics, channel-rhodopsins (ChRh) of different types are expressed in cells

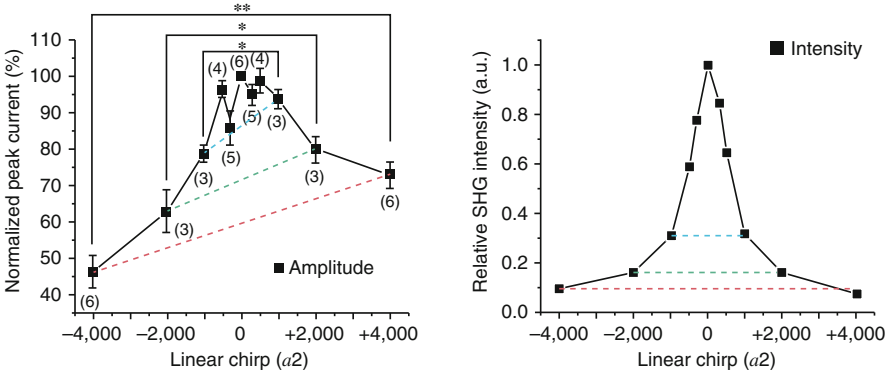

Fig. 5.10 **Left** Summary of normalized peak current amplitudes for negative and positive linear chirps. All currents were normalized to the phase-compensated condition ($a2 = 0\,\mathrm{fs}^2$). The numbers in parentheses refer to the number of neurons the currents were measured in at each linear chirp. Asterisks represent statistical significance: $^{*}p < 0.05$, $^{**}p < 0.005$. **Right**: SHG intensities at different linear chirp: $a2$ (in fs^2) $= \pm 4000$, ± 2000 and $\pm$ 1000. The SHG intensity at $a2 = 4000\,\mathrm{fs}^2$ is almost identical for PCH (0.075) and NCH (0.091); however, the peak current amplitudes in **c** are significantly different. (From Ref. [41])

from different genetically modified organisms, including mammals like mice. The optical control of brain neurons in these animals was demonstrated, e.g. for remotely controlling their muscular motion, but also for manipulating their behavior [40]. Alternatively, light stimulation and optogenetics may have significant applications in medicine, and in particular in neurodegenerative health issues, like Parkinson or Alzheimer diseases.

In 2017, a disrupting experiment was performed by the group of S. Boppart on coherent controlling living brain tissues [41]. More precisely, he induced 2-photons excitation of ChR2 and consecutive nerve firing and optimized the process while changing the spectral phase of the incoming 1 um wavelength pulses. The readout was performed electro-phisiologically with a patch clamp apparatus.

The authors observed clear asymmetry in chirp of the stimulation yield of the nerves, which is an indication of coherent effects in the photo-isomerization process in the retinal moiety (Fig. 5.10 left). Indeed, if a 2-photon excitation process is clearly favored by highest intensities, and thus short pulses, it should be equally efficient for negatively or positively chirped pulses of the same duration, as demonstrated for second harmonic generation (SHG) in Fig. 5.10 right.

The higher stimulation yield for positively chirped pulses than for negative ones points to some intra-pulse molecular processes involving the phase of the incoming field. A first interpretation attempt of this process, proposed by the authors, would be some kind of pump-dump effect for negatively chirped pulses (see Fig. 5.6) that would reduce the photo-isomerization yield by bringing back the population of the excited state to the ground state. However, in the present case, the excitation involves 2 photons, and the back stimulation would involve 2 photons as well, making this

explanation very unlikely. A clear explanation of these results is nowadays still lacking but reminds 2-photons quantum control results obtained on different dyes by the group of G. Gerber in the 2000s [14, 15].

On the practical point of view, two-photon opto-genetics is a very hot topic, as it allows targeting single cells with higher resolution and deeper stimulation as infrared radiation is much much less scattered and absorbed in tissue. The drawback of 2-photon stimulation is, however, the higher required intensity, which may be damageable for tissues. Increasing the yield of the process with quantum control is therefore particularly relevant.

5.7 Entangled Photons Microscopy

As mentioned in the introduction, another quantum signature than interference of states in the same system, is entanglement of different sub-systems. The most celebrated evidence of this process is the violation of Bell's inequalities in 1982 by the group of A. Aspect using entangled pairs of photons [42]. Since then these experiments set the ground to a "second quantum revolution", which involves all the properties of entangled states for applications like quantum cryptography, quantum telecommunications, quantum computers, or, more generally, what is called today "quantum technologies".

In entangled states, two subsystems (e.g. 2 photons) are linked in a common state, which means that if one of the subsystem is in a particular state, than the other one has to be in a particular state as well. Let's imagine 2 qubits A and B, which may have 2 values 0 and 1 (e.g. the polarization values of 2 photons A and B). Then these 2 qubits are entangled if they are represented, for example, by the following 2-particle (Bell) state:

$$\left|\Psi^{\pm}\right\rangle = \frac{1}{\sqrt{2}}\left(|0\rangle_A \otimes |1\rangle_B \pm |1\rangle_A \otimes |0\rangle_B\right).$$

These nonlocal connections between the subsystems A and B clearly have implications on the probabilities of detection, i.e. correlations, when experiments are performed. For instance, when the 2 photons cross a beamsplitter, they are known to bunch or anti-bunch, exhibiting clear non-classical statistics [43].

In microscopy, entangled states have recently been used to significantly enhance resolution and precision in phase contrast arrangements. Indeed, the minimal phase difference $\Delta\phi$ observable in a classical phase contrast microsocope scales with $N^{-1/2}$ while it scales with N^{-1} for entangled states (where N is the number of photons) [44]. Clearly, to improve phase resolution and beat the classical limit, N should be larger than 1. The above example of entangled particles above can be extended to

NOON states, where the subsystems A and B consist of N identical particles. For instance the NOON equivalent of the symmetric Bell state above writes:

$$|\psi_{\mathrm{NOON}}\rangle = \frac{|N\rangle_a|0\rangle_b + |0\rangle_a|N\rangle_b}{\sqrt{2}},$$

For a N = 2 NOON state, the quantum phase resolution would thus beat the classical limit by a factor $2^{-1/2}$. This was demonstrated by Ono et al. in their recent paper [44], as presented in Fig. 5.11, where the classical limit was experimentally beaten by 1.35 ± 0.12, i.e. close to the Heisenberg limit for 2 photons of $2^{-1/2}$. The phase object used in the experiment, a Q written on a glass plate, is only 17 nm high, demonstrating the potential of entanglement enhanced microscopy. To further improve the phase resolution, higher N "NOON state" sources would be required, which is still currently a major technological challenge.

5.8 Conclusion

Quantum inspired technologies are blooming in a wealth of domains. We presented some examples in biophotonics, covering both applicative technologies like microscopy, and more fundamental questions about the role of quantum physics in the natural evolution of organisms. There is no doubt that quantum biophotonics will represent a major field of activity in the next years. Whether purely quantum effects will be widely used for applications is unclear, but what was widely confirmed in the past, is that quantum concepts inspired groundbreaking advances in spectroscopy and photonics, even while using classical coherent light.

Acknowledgements The author gratefully acknowledge his collaborators at the Universities of Geneva and Lyon, in particular L. Bonacina, F. Courvoisier, L. Guyon, V. Boutou, E. Salmon, J. Yu, G. Mejean, J. Kasparian, C. Kasparian, A. Rondi, S. Afonina, J. Extermann, P. Bejot, S. Weber, D. Kiselev, J. Gateau, S. Hermelin and M. Moret, as well as H. Rabitz and his group at Princeton, particularly M. Roth and J. Roslund.

We also acknowledge the financial support of the Swiss National Science Foundation (contracts No. 2000021-111688 and No 200020-124689), and the Swiss NCCR MUST.

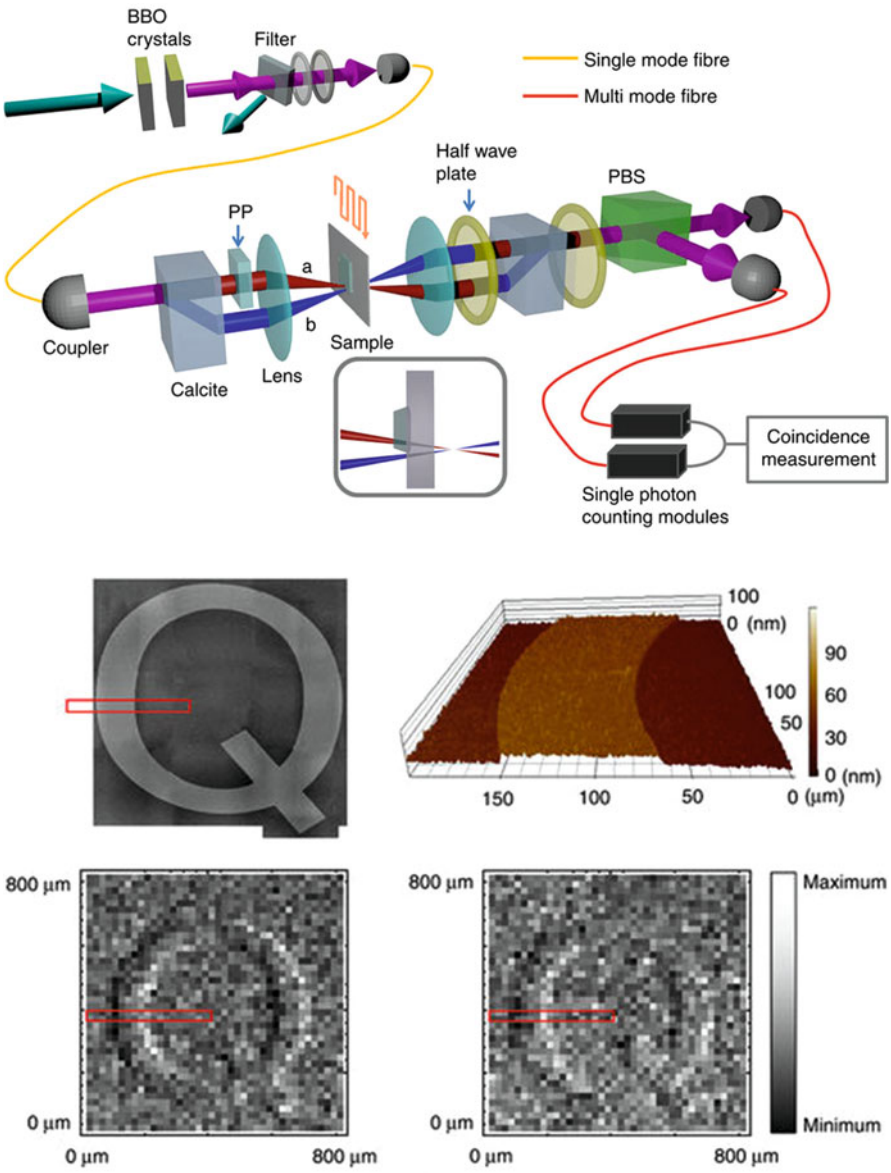

Fig. 5.11 **Upper**: Experimental set-up of the polarization entangled NOON microscope. **Lower:** results on a phase object representing a Q. The lower images clearly show the enhanced contrast as compared to classical light based phase contrast microscopy. (From Ref. [44])

References

1. Lambert N, Chen Y-N, Cheng Y-C, Li C-M, Chen G-Y, Nori F (2013) Nat Phys 9:10–18
2. Engel GS, Calhoun TR, Read EL, Ahn TK, Mancal T, Cheng YC, Blankenship RE, Fleming GR (2007) Nature 446(7137):782–786
3. Collini et al (2010) Nature 463:644–648
4. Roth M, Guyon L, Roslund J, Boutou V, Courvoisier F, Wolf JP, Rabitz H (2009) Phys Rev Lett 102:253001
5. Petersen J, Mitric R, Bonacic-Koutecky V, Wolf JP, Roslund J, Rabitz H (2010) Phys Rev Lett 105:073003
6. Afonina S, Gateau J, Staedler D, Bonacina L, Wolf J.P, in preparation (2018)
7. Tannor DJ, Kosloff R, Rice SA (1986) J Chem Phys 85:5805–5820
8. Tannor DJ, Rice SA (1985) J Chem Phys 83:5013–5018
9. Judson RS, Rabitz H (1992) Phys Rev Lett 68:1500–1503
10. Warren WS, Rabitz H, Dahleh M (1993) Science 259:1581–1589
11. Weiner AM (2000) Rev Sci Instrum 71:1929–1960
12. Bonacina L, Extermann J, Rondi A, Boutou V, Wolf JP (2007) Phys Rev A 76:023408
13. Dantus M, Lozovoy VV (2004) Chem Rev 104:1813–1859
14. Brixner T, Damrauer NH, Niklaus P, Gerber G (2001) Nature 414:57–60
15. Brixner T, Gerber G (2003) Chem Phys Chem 4:418–438
16. Prokhorenko VI, Nagy AM, Waschuk SA, Brown LS, Birge RR, Miller RJD (2006) Science 313:1257
17. Florean AC et al (2009) PNAS 106(27):10896–10900
18. Ventalon C, Fraser JM, Vos MH, Alexandrou A, Martin JL, Joffre M (2004) PNAS 101:13216–13220
19. Pastirk I, Dela Cruz JM, Walowicz KA, Lozovoy VV, Dantus M (2003) Opt Express 11:1695
20. Li BQ, Rabitz H, Wolf JP (2005) J Chem Phys 122:154103
21. Rondi A, Extermann J, Bonacina L, Weber S, Wolf J-P (2009) Appl Phys B 96:757–761
22. Weber SM, Bonacina L, Noell W, Kiselev D, Extermann J, Jutzi F, Lani S, Nenadl O, Wolf J-P, de Rooij NF (2011) Rev Sci Instrum 82:075106
23. Kiselev D, Kraus PM, Bonacina L, Wörner HJ, Wolf JP (2012) Opt Express 20(23):843–25849
24. Rondi A, Bonacina L, Trisorio A, Hauri C, Wolf J-P (2012) Phys Chem Chem Phys 14:9317–9322
25. Afonina S, Nenadl O, Rondi A, Bonacina L, Extermann J, Kiselev D, Dolamic I, Burgi T, Wolf JP (2013) App Phys B 111:541–549
26. Schoenlein R, Peteanu L, Mathies R, Shank CV (1991) Science 254(5030):412–415
27. Wang Q, Schoenlein RW, Peteanu LA, Mathies RA, Shank CV (1994) Science 266:422–424
28. Polli D et al (2010) Nature 467(7314):440–443
29. Vogt G, Nuernberger P, Brixner T, Gerber G (2006) Chem Phys Lett 433(1):211–215
30. Prokhorenko VI, Nagy AM, Miller RD (2005) J Chem Phys 122(18):184502
31. Joffre M (2007) Science 317:453
32. Liebel M, Kukura P (2017) Nat Chem 9:45
33. Brumer P, Shapiro M (1989) Chem Phys 139:221–228
34. Spanner M, Arango CA, Brumer P (2010) J Chem Phys 133: 151101(R)
35. Katz G, Ratner MA, Kosloff R (2010) New J Phys 12: 015003(R)
36. Arango CA, Brumer P (2013) J Chem Phys 138: 071104(R)
37. Weigel A, Sebesta A, Kukura P (2015) J Phys Chem Lett 6:4023–4037
38. El Hage K, Brickel S, Hermelin S, Gaulier G, Schmidt C, Bonacina L, van Keulen SC, Bhattacharyya S, Chergui M, Hamm P, Rothlisberger U, Wolf J-P, Meuwly M (2017) Struct Dyn 4:061507

39. McCulloch DL et al (2015) Doc Ophthalmol 130(1):1–12
40. Reardon S (2016) Nature News. https://doi.org/10.1038/nature.2016.20995
41. Paul K, Sengupta P, Ark ED, Tu H, Zhao Y, Boppart S (2017) Nat Phys 13:1111–1116
42. Aspect A, Grangier P, Roger G (1982) Phys Rev Lett 49:91–94
43. Hong CK, Ou ZY, Mandel L (1987) Phys Rev Lett 59(18):2044–2046
44. Ono T, Okamoto R, Takeuchi S (2013) Nat Commun 4:2426

Chapter 6
Simulations in Nanophotonics

Antonino Calà Lesina, Joshua Baxter, Pierre Berini, and Lora Ramunno

Abstract Numerical simulations of nanophotonics systems provide insight into their physical behaviour and design that provide a critical complement to experimental investigations. The finite-difference time-domain (FDTD) method is the most widely used, with its success due to its relative simplicity coupled with its broad applicability to many complex material systems, arbitrary shape configurations, time-domain visualization and, with increased computing resources, its near linear scalability for parallel computing.

The series of three lectures presented at the Quantum Nano-Photonics summer school (Erice, Italy, 2017) began with a pedagogical introduction of the fundamentals of the Yee FDTD algorithm, such as discretization of Maxwell's equations, numerical dispersion and stability criteria. Following this was a description of other necessary FDTD ingredients, such as boundary conditions, sources of excitations and material models. To demonstrate how to apply this knowledge to run an actual simulation, the lectures had an active component, wherein students received temporary access to commercial FDTD software, and a simple problem (scattering from a gold nanosphere) was simulated together in lecture. Finally, the state of art was reviewed for applications in nanophotonics, including, for example, modelling nonlinear optical processes, tightly focused sources, plasmonic metasurfaces, nonlocality, as well as some demonstrations of such applications. The role of high performance computing was also discussed [1]. Finally, the limitations of the method were described and complementary computational methods were briefly introduced to overcome some of these limitations.

A. Calà Lesina · P. Berini
Department of Physics and Centre for Research in Photonics, University of Ottawa, Ottawa, Canada

School of Electrical Engineering and Computer Science, University of Ottawa, Ottawa, Canada

J. Baxter · L. Ramunno (✉)
Department of Physics and Centre for Research in Photonics, University of Ottawa, Ottawa, Canada
e-mail: lora.ramunno@uottawa.ca

B. Di Bartolo et al. (eds.), *Quantum Nano-Photonics*, NATO Science for Peace and Security Series B: Physics and Biophysics,
https://doi.org/10.1007/978-94-024-1544-5_6

We present in this article a summary of some of the topics presented during the lectures.

6.1 Introduction

Simulations are instrumental in the field of nanophotonics, helping to shed light on light-matter interaction at the nanoscale, providing a critical complement to experimental investigations of complex systems, e.g., systems involving irregular shapes, exotic materials, or many interacting devices. Such simulations are important for many purposes, including for device design and optimization, for understanding device operation, for explaining experiments, and for discovering and predicting new phenomena. More cost effective than running multiple experiments, one can quantitatively investigate the effects of changing materials, geometries, physical effects, etc, one by one, but also gain insight through powerful visualization and movies.

Since the seminal paper on FDTD [2], the method has been applied to many areas of electromagnetism. Over the past decade, the FDTD method has become the most largely used computational technique in nanophotonics [3, 4]. A Google Scholar search of "FDTD and nanophotonics" confirms this, with double the number of hits than the next most used method, FEM (finite element method). FDTD is popular because it is relatively simple to implement, and it is extremely versatile, capable of modelling dispersive materials, nonlinearity, nonlocality, and almost any physical system that can be modeled via a macroscopic polarization field. Due to its near-linear scaling in parallel processing, it can be applied to ever larger problems, as larger and larger computational resources become available.

This paper follows the set of three lectures on simulations in nanophotonics, presented at the Quantum Nano-Photonics summer school in Erice Italy in the summer of 2017. Focusing on FDTD, the first lecture consisted of a pedagogical overview (complemented by class exercises) of the basics of the Yee algorithm and its inherent numerical dispersion and stability condition; these are reviewed for the novice in Sect. 6.2.

The next lecture focused on putting this into practice, by first discussing other ingredients needed for a successful simulation, including sources of excitation, boundary conditions, material models, and data collection/monitors in both the time and frequency domains. This was followed in the third lecture by a class exercise, in which students set up and ran an FDTD simulation on the fly, thanks to Lumerical Solutions Inc [5], which provided each participant with temporary licenses to their FDTD commercial software. This in-class example (scattering from a gold nanosphere) will be briefly described below in Sect. 6.3.

Advanced topics were introduced, such as grid limitations and convergence issues, high performance computing and scalability, advanced radiation sources such as tightly focused beams, and advanced material models (dispersive and nonlinear materials, plasmonic materials, nonlocal plasma models); a selection of

material models is presented in Sect. 6.4. Examples from our own work that illustrate why simulations can be so powerful are presented in Section 5. These include understanding why colour is generated from laser-irradiated metallic surfaces, where nonlinear emission originates in hybrid dielectric/metallic nanoantennas, and the design of a plasmonic metasurface for generating structured nonlinear light.

6.2 FDTD Basics

6.2.1 Algorithm

FDTD uses finite differencing to solve the macroscopic Maxwell's equations in the time domain. They are (in SI units):

$$\frac{\partial \mathbf{D}(\mathbf{r},t)}{\partial t} = \nabla \times \mathbf{H}(\mathbf{r},t) - \mathbf{J}_{free}(\mathbf{r},t), \tag{6.1}$$

$$\frac{\partial \mathbf{B}(\mathbf{r},t)}{\partial t} = -\nabla \times \mathbf{E}(\mathbf{r},t), \tag{6.2}$$

$$\nabla \cdot \mathbf{D}(\mathbf{r},t) = \rho_{free}(\mathbf{r},t), \tag{6.3}$$

$$\nabla \cdot \mathbf{B}(\mathbf{r},t) = 0, \tag{6.4}$$

where $\mathbf{E}$ is the electric field, $\mathbf{B}$ the magnetic field, $\mathbf{D}$ the displacement field, $\mathbf{H}$ the magnetizing fields, $\mathbf{J}_{free}$ is the free current density, and ρ_{free} the free charge density, with constitutive relations to relate $\mathbf{E}$ and $\mathbf{B}$ to $\mathbf{D}$, $\mathbf{H}$ and $\mathbf{J}_{free}$

$$\mathbf{D}(\mathbf{r},t) = \varepsilon_0 \mathbf{E}(\mathbf{r},t) + \mathbf{P}(\mathbf{r},t), \tag{6.5}$$

$$\mathbf{H}(\mathbf{r},t) = \frac{1}{\mu_0}\mathbf{B}(\mathbf{r},t) + \mathbf{M}(\mathbf{r},t), \tag{6.6}$$

where $\mathbf{M}$ and $\mathbf{P}$ are the magnetization and polarization, defined by microscopic bound charges and currents, respectively. For example, linear optical response can be written in its most general form as

$$\mathbf{P}(\mathbf{r},t) = \int \overleftrightarrow{\chi}^{(1)}(\mathbf{r}-\mathbf{r}', t-t')\mathbf{E}(\mathbf{r}',t')d\mathbf{r}'dt', \tag{6.7}$$

where $\overleftrightarrow{\chi}^{(1)}$ is the linear susceptibility tensor.

These relations are not necessarily simple, depending on the system under study. FDTD advances the electric and magnetic fields in time by finite differencing all the

derivatives in Eqs. (6.1) and (6.2) via a central difference, in order to keep second-order numerical accuracy, i.e.,

$$\frac{df}{dx} = \frac{f(x+h/2) - f(x-h/2)}{h} + O(h^2). \tag{6.8}$$

From Eqs. (6.1) and (6.2), we see that central differencing forces the electric and magnetic fields to be evaluated at different times (i.e., leap frog in time). For example, considering Eq. (6.2) evaluated at time t and discretized in time with time step Δt, for the LHS we have

$$\frac{\partial \mathbf{B}(\mathbf{r}, t)}{\partial t} \approx \frac{\mathbf{B}^{t+\Delta t/2} - \mathbf{B}^{t-\Delta t/2}}{\Delta t}. \tag{6.9}$$

The RHS must also be evaluated at time t, which means that all the $\mathbf{E}$ fields are needed at time t, unlike the $\mathbf{B}$ fields which are at $t \pm \Delta t/2$, then we get an update equation for $\mathbf{B}$ from quantities at earlier times, i.e.,

$$\mathbf{B}^{t+\Delta t/2} = \mathbf{B}^{t-\Delta t/2} - \Delta t (\nabla \times \mathbf{E})^t. \tag{6.10}$$

If we now evaluate Eq. (6.1) at time $t + \Delta t/2$ in a similar way, we then get

$$\mathbf{D}^{t+\Delta t} = \mathbf{D}^t + \Delta t (\nabla \times \mathbf{H})^{t+\Delta t/2} - \Delta t \mathbf{J}^{t+\Delta t/2}, \tag{6.11}$$

thus again, $\mathbf{D}$ at $t + \Delta t$ is updated using previous values of time. The algorithm thus proceeds as a leap frog in time, as depicted in Fig. 6.1.

Thus far we have considered the time derivatives, what about the spatial derivatives contained within the curl operator? We start with the update equation for B_x in continuous spatial coordinates

$$B_x^{t+\Delta t/2} = B_x^{t-\Delta t/2} - \Delta t \left(\frac{\partial E_z^t}{\partial y} - \frac{\partial E_y^t}{\partial z} \right), \tag{6.12}$$

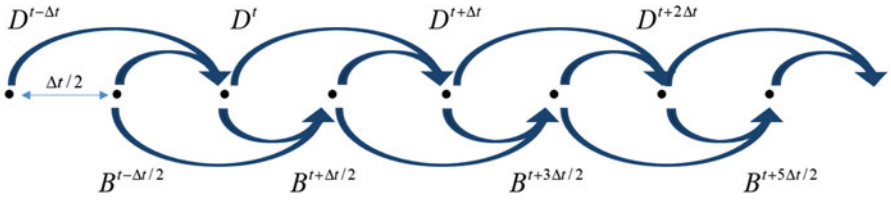

Fig. 6.1 Leap frog scheme for the temporal update of the fields

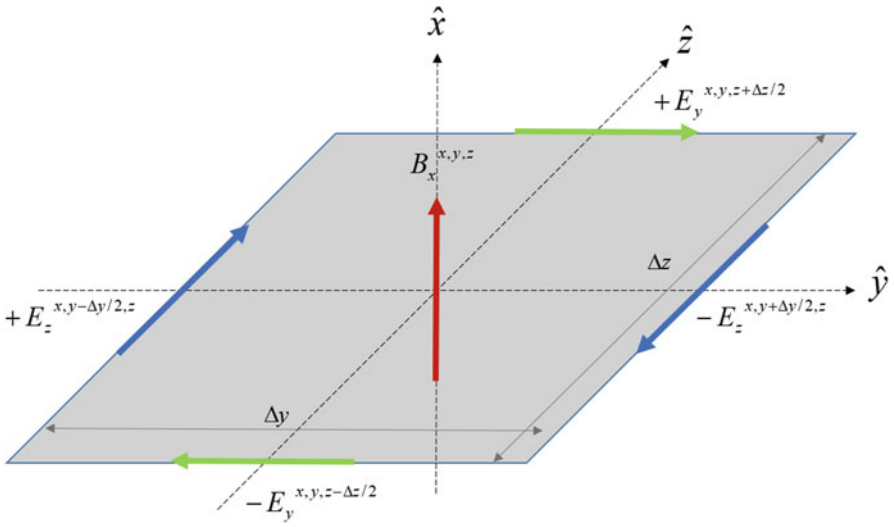

Fig. 6.2 Curl scheme for the update of one field component

and by applying the central differencing to both spatial derivatives we obtain:

$$B_x^{x,y,z,t+\Delta t/2} = B_x^{x,y,z,t-\Delta t/2} - \frac{\Delta t}{\Delta y}\left(E_z^{x,y+\Delta y/2,z,t} - E_z^{x,y-\Delta y/2,z,t}\right) + \\ + \frac{\Delta t}{\Delta z}\left(E_y^{x,y,z+\Delta z/2,t} - E_y^{x,y,z-\Delta z/2,t}\right). \tag{6.13}$$

We see that E_z and E_y need to be evaluated in "leapfrogged" spatial positions with respect to each other, and to B_x. This is depicted in Fig. 6.2, where we see that all field components are at the same x, however they are displaced from each other in y and z. This absence of colocation in space is a direct consequence of requiring the algorithm to be of 2nd order accuracy.

The computational grid cell with these field components staggered from each other was first introduced by Yee in the 1960s [2], and it is called the Yee cell. Only locally known fields are required for updating the field values on the Yee cell via the FDTD algorithm, which makes the algorithm suitable for parallelization via domain decomposition [1].

6.2.2 *Numerical Dispersion and Stability*

The Yee algorithm implementation discussed above is on a rectangular grid, which causes an inherent directionality. Thus the update equations cause a non-physical dispersion that depends on propagation direction. They also require that strict

conditions be met to ensure numerical stability. This provides fundamental limits on how large the discretization can be for a physically and numerically valid solution, and is the reason that FDTD solutions can require large computational resources to execute.

To illustrate these points, we consider the simplest case, light propagation in vacuum. The free-space dispersion relation for a plane wave of frequency ω and wavevector (k_x, k_y, k_z) is given by

$$\frac{\omega^2}{c^2} = k_x^2 + k_y^2 + k_z^2. \tag{6.14}$$

Now considering a plane monochromatic wave trial solution for the field components, and substituting these into the FDTD update equations yields [6]

$$\begin{aligned}\frac{\omega^2}{c^2}\left(\frac{\sin(\omega\Delta t/2)}{\omega\Delta t/2}\right)^2 = k_x^2\left(\frac{\sin(k_x\Delta x/2)}{k_x\Delta x/2}\right)^2 + \\ k_y^2\left(\frac{\sin(k_y\Delta y/2)}{k_y\Delta y/2}\right)^2 + \\ k_z^2\left(\frac{\sin(k_z\Delta z/2)}{k_z\Delta z/2}\right)^2,\end{aligned}$$

where in the limit of infinitely small time and space steps, we retrieve the ideal dispersion relation.

It is illustrative to neglect for the moment the discreteness in time, and consider only propagation along the x direction, with $k = k_x$. Then we obtain for the phase velocity

$$v_p = \frac{\omega}{k_x} = c\left(\frac{\sin(k_x\Delta x/2)}{k_x\Delta x/2}\right). \tag{6.15}$$

This places restrictions on how large Δx may be for a given propagation constant, and thus a given wavelength. For example, if one chooses $\Delta x = \lambda/10$, then we obtain a phase velocity of $0.984c$. This value of Δx is often used as the maximum tolerable spatial discretization.

Now consider a propagation direction that is 45 degrees in the xy plane (assuming a uniform grid) with a propagation vector of $(k/\sqrt{2}, k/\sqrt{2}, 0)$. Then the grid discretization of $\Delta x = \Delta y = \lambda/10$ yields a phase velocity of $0.992c$, which is not the same as propagation along x only, hence leading to numerical dispersion that is direction dependent, imposed by the rectangular grid.

To examine numerical stability of the Yee algorithm we extend the dispersion relation for the update equations above to the complex frequency plane, setting ω to have a real (ω_R) and imaginary (ω_I) component. Whenever there is a non-zero ω_I, there is the possibility for exponentially growing solutions, so we need to

impose $\omega_I = 0$. This provides a condition on the discretization of time, such that the maximum allowed Δt is given by the Courant stability condition [6]

$$\Delta t \leq = \frac{1}{c\sqrt{1/(\Delta x)^2 + 1/(\Delta y)^2 + 1/(\Delta z)^2}}. \tag{6.16}$$

While this condition ensures the numerical stability of solutions, it does not guarantee physical solutions. In lecture, the following question was posed to the students: using this condition, with what speed does information travel from one side of a grid cell to the other assuming a uniform 3D grid? The answer is $v = \Delta x/\Delta t = \sqrt{3}c$, faster that the speed of light! Taflove and Hagness illustrate the effects of superluminal propagation of a square pulse in one dimension [6]. While this is drastically reduced for a smooth pulse, it still does exist, though in practice is a very small error. In the example presented in lecture, these components were eight orders of magnitude smaller than the peak of the pulse.

While we discussed here the numerical dispersion and stability conditions for propagation in free space, in practice one would need the equivalent conditions for the materials being investigated. One would need to repeat the analysis on the update equations relevant for that material to obtain the new conditions, and these have been done by various authors for different materials, including plasmonic materials where one may choose $\Delta t \leq \Delta x/(\sqrt{3}c_\infty)$ [7], where $c_\infty = c/\sqrt{\varepsilon_\infty}$ and ε_∞ is the infinite frequency permittivity.

6.3 In-Class Simulation: Scattering from a Gold Nanosphere

The FDTD algorithm as discussed in the previous section, on its own is not enough for a useful simulation. One needs to add some kind of material for light to interact with, boundary conditions to terminate the simulation domain [8], a source of radiation either internal or external to the simulation, as well as monitors for data collection [1]. These topics were all touched upon in the lectures, and were put into practice in an in-class exercise: simulating the scattering of a plane wave by a gold nanosphere, and calculating its extinction cross section spectrum. Each participant in the summer school was given access to Lumerical Solutions FDTD software [5], and together we set up and performed this simulation, step by step.

This particular example was chosen for several reasons. The first is that it is important when developing and/or testing a numerical technique to begin with a simple system for verification. In the case of a single isolated sphere irradiated by a plane wave, an analytical solution exists, derived for the first time by Gustav Mie in 1908 [9, 10]. Though over a century old, this theory is still of prime importance in nanophotonics – including for example recent corrections to it for plasmonics [11] and recent interest in multipolar excitations [12]. By comparing their numerical results with the analytical model, students were able to ascertain the quality of their simulation.

In our in-class simulation, students were able to test the influence of computational parameters, such as grid size. The simulation of a sphere illustrates one fundamental drawback of FDTD: its rectangular grid. While such a grid allows relatively simple algorithms and wide applicability, it is also limiting in that there can be numerical artifacts arising from the boundaries of non-rectangular shaped objects, such as spheres. There are several work-arounds that are possible, such as: larger computational resources for smaller grid sizes [1], graded meshes where the grid size can vary along each of the three spatial dimensions if there are smaller areas that require a smaller mesh; and sub-gridding where grid cells can be divided into daughter grid cells which is much more complex to implement and may have stability issues for long runs [13].

6.4 Advanced Topics

6.4.1 High Performance Computing

High performance computing is one the best allies of computational nanophotonics because problems involving plasmonics require a fine discretization to get convergent results and this sets the need for large computational resources [1]. The FDTD method is straightforward to parallelize because the algorithm only requires the adjacent field values to run. The overall domain is decomposed into subdomains which run on different processes, and each subdomain communicates with the adjacent ones through the message passage interface (MPI) protocol [14]. Nearly linear scalability has been demonstrated, which is limited only by communication between processes. Load balancing strategies can also be implemented when some subdomains have a higher computational load which could represent a bottleneck for the overall simulation time. All the simulations we present in this paper are conducted by using an in-house parallel 3D-FDTD software [1].

6.4.2 Advanced Material Models

The FDTD method is well suited to model material properties, such as dispersion. Our group has also developed and implemented methods for materials containing nonlinearity and nonlocality which are not standard techniques, particularly the latter where almost no prior work exists.. We review here a selection of our computational approaches.

6.4.2.1 Dispersion

A dispersive material is one that exhibits a frequency dependent susceptibility, i.e.,

$$\mathbf{P}(\omega) = \varepsilon_0 \chi^{(1)}(\omega)\mathbf{E}(\omega). \tag{6.17}$$

Since FDTD is solved in the time domain a convolution is required:

$$\mathbf{P}(t) = \varepsilon_0 \int_0^t \chi^{(1)}(t-\tau)\mathbf{E}(\tau)d\tau. \tag{6.18}$$

Implementing a $\chi^{(1)}(\omega)$ model in FDTD is possible by introducing an auxiliary differential equation (ADE) in the leap frog scheme for the $\mathbf{P}$ field [15, 16]. If we consider Eqs. (6.1) and (6.5) for $\mathbf{J}_{free} = 0$, i.e.,

$$\nabla \times \mathbf{H} = \varepsilon_0 \frac{\partial \mathbf{E}}{\partial t} + \frac{\partial \mathbf{P}}{\partial t}, \tag{6.19}$$

and we discretize it, we obtain

$$\nabla \times \mathbf{H}^{t+\Delta t/2} = \varepsilon_0 \frac{\mathbf{E}^{t+\Delta t} - \mathbf{E}^t}{\Delta t} + \frac{\mathbf{P}^{t+\Delta t} - \mathbf{P}^t}{\Delta t}, \tag{6.20}$$

from which we can derive $\mathbf{E}^{t+\Delta t}$ as a function of $\mathbf{E}^t$, $\mathbf{P}^{t+\Delta t}$, $\mathbf{P}^t$ and $\mathbf{H}^{t+\Delta t/2}$. In the leap frog scheme, we need to solve for $\mathbf{P}^{t+\Delta t}$ before we can calculate $\mathbf{E}^{t+\Delta t}$.

Models for simulating complex permittivities are available, such as the Drude with two critical points (Drude+2CP) model [17] to account for the optical response of both bound and free electrons. We report as an example the case of a Drude material, for which we have

$$\chi^{(1)}(\omega) = -\frac{\omega_D^2}{\omega(\omega + i\gamma)}, \tag{6.21}$$

where ω_D is the plasma frequency and γ is the damping coefficient. Using Eqs. (6.17) and (6.21), this becomes differential form

$$\frac{\partial^2 \mathbf{P}}{\partial t^2} + \gamma \frac{\partial \mathbf{P}}{\partial t} = \varepsilon_0 \omega_D^2 \mathbf{E}, \tag{6.22}$$

which can be discretized as

$$\frac{\mathbf{P}^{t+\Delta t} - 2\mathbf{P}^t + \mathbf{P}^{t-\Delta t}}{\Delta t^2} + \gamma \frac{\mathbf{P}^{t+\Delta t} - \mathbf{P}^{t-\Delta t}}{2\Delta t} = \varepsilon_0 \omega_D^2 \mathbf{E}^{\mathbf{t}}, \tag{6.23}$$

From this we finally obtain $\mathbf{P}^{t+\Delta t}$ as a function of $\mathbf{E}^t$, $\mathbf{P}^t$ and $\mathbf{P}^{t-\Delta t}$. The scheme for the FDTD updating algorithm is in sequence

$$\begin{aligned} \mathbf{H}^{t+\Delta t/2} &= f(\mathbf{H}^{t-\Delta t/2}, \mathbf{E}^t), \\ \mathbf{P}^{t+\Delta t} &= f(\mathbf{E}^t, \mathbf{P}^t, \mathbf{P}^{t-\Delta t}), \\ \mathbf{E}^{t+\Delta t} &= f(\mathbf{E}^t, \mathbf{P}^{t+\Delta t}, \mathbf{P}^t, \mathbf{H}^{t+\Delta t/2}). \end{aligned} \tag{6.24}$$

6.4.2.2 Nonlinearity

The FDTD method is well suited for nonlinear simulations because it is a time-domain method. We show here how to implement second harmonic generation (SHG) for a dispersionless medium (ε_r is constant). We start from Eqs. (6.1) and (6.5) adapted for the nonlinear case and for one Cartesian field component

$$\nabla \times H^{t+\Delta t/2} = \varepsilon_0 \varepsilon_r \frac{E^{t+\Delta t} - E^t}{\Delta t} + \frac{P_{NL}^{t+\Delta t} - P_{NL}^t}{\Delta t}, \tag{6.25}$$

with the nonlinear polarization $P_{NL} = \varepsilon_0 \chi^{(2)} E^2$. In discretized form we have

$$\frac{\Delta t}{\varepsilon_0} \nabla \times H^{t+\Delta t/2} = \varepsilon_r (E^{t+\Delta t} - E^t) + \chi^{(2)} (E^{t+\Delta t})^2 - \chi^{(2)} (E^t)^2. \tag{6.26}$$

In order to find $E^{t+\Delta t}$ we need to solve a second-order equation, and the solution, for $\varepsilon_r^2 + 4\chi^{(2)} b > 0$, is

$$E^{t+\Delta t} = \frac{-\varepsilon_r \pm \sqrt{\varepsilon_r^2 + 4\chi^{(2)} b}}{2\chi^{(2)}}, \tag{6.27}$$

where

$$b = \frac{\Delta t}{\varepsilon_0} \nabla \times H^{t+\Delta t/2} + \varepsilon_r E^t + \chi^{(2)} (E^t)^2. \tag{6.28}$$

The auxiliary differential equation approach is very well suited for nonlinear simulations because it allows us to add extra terms in the polarization field [18]. We have implemented it by using a linear dispersive material and adding an extra term to the polarization field, which we show for one Cartesian component, i.e.,

$$P_x^t = \chi^{(3)} E_x^t |E^t|^2, \tag{6.29}$$

where $|E^t|^2 = (E_x^t)^2 + (E_y^t)^2 + (E_z^t)^2$, and we assume isotropic dispersionless nonlinearity.

6.4.2.3 Nonlocality

When describing the interaction between light and matter it is common to use the electric displacement field $\mathbf{D}(\mathbf{r}, \omega)$ which is defined by

$$\mathbf{D}(\mathbf{r}, \omega) = \varepsilon_0 \int d\mathbf{r}' \varepsilon(\mathbf{r}, \mathbf{r}', \omega)\mathbf{E}(\mathbf{r}', \omega). \tag{6.30}$$

For particles larger than 10 nm it is valid to use the local approximation, $\varepsilon(\mathbf{r}, \mathbf{r}', \omega) = \varepsilon(\omega)\delta(\mathbf{r} - \mathbf{r}')$. This states that the electric displacement field at a given point in space depends only on the electric field in that location and the dielectric function. For systems smaller than 10 nm, the local approximation can no longer be used. We therefore must include the effects of spatial nonlocality. To do so, we model the interaction between electrons and light using a hydrodynamic plasma model [19]:

$$nm\Big(\frac{\partial}{\partial t} + (\mathbf{u} \cdot \nabla) + \gamma\Big)\mathbf{u} = ne(\mathbf{E} + \mathbf{u} \times \mathbf{B}) - \nabla p. \tag{6.31}$$

This is the Euler Fluid equation with damping where the force is defined by the Lorentz force. Here $\mathbf{u}$ represents the velocity field, γ is the damping, n is the electron density, m is the electron mass, and p is the electron pressure. To use this equation for nonlocality, we need to first remove the nonlinear terms which are negligible for low field intensities [20], leaving us with

$$nm\frac{\partial}{\partial t}\mathbf{u} = -ne\mathbf{E} - nm\gamma\mathbf{u} - \nabla p. \tag{6.32}$$

For the pressure, we use the electron degeneracy pressure for p, which is

$$p = p_0\Big(\frac{n}{n_0}\Big)^{5/3}, \tag{6.33}$$

where p_0 is proportional to the Fermi energy, and n_0 is the equilibrium electron density. Using the continuity equation, $\frac{\partial n}{\partial t} = -\nabla \cdot (n\mathbf{u})$, the fact that $\mathbf{J} = -en_0\mathbf{u} = \partial\mathbf{P}/\partial t$, and only keeping the only linear terms we end up with our linear nonlocality model:

$$\frac{\partial^2\mathbf{P}}{\partial t^2} + \gamma\frac{\partial\mathbf{P}}{\partial t} - \beta^2\nabla(\nabla \cdot \mathbf{P}) = \varepsilon_0\omega_D^2\mathbf{E}, \tag{6.34}$$

where β is a constant proportional to the Fermi velocity. Notice that this is simply the aforementioned Drude material model with a spatially nonlocal term which is negligible everywhere but near the interface between the nanoparticle and the surrounding media. This is because the pressure gradient is dependent on the electron density fluctuation which disappears in the bulk [21]. This explains why

the nonlocal correction term is only required when modelling small particles, as the surface to volume ratio becomes larger.

We have devised a method to implement this model in a similar fashion to the Drude model. We show this spatial discretization of the nonlocal term is shown for the x-direction where we use the second order central-difference scheme to obtain

$$\begin{aligned}\nabla(\nabla\cdot\mathbf{P})_x^{x+\Delta x/2,y,z,t} &= \left(\frac{\partial^2 P_x}{\partial x^2}+\frac{\partial^2 P_y}{\partial x\partial y}+\frac{\partial^2 P_z}{\partial x\partial z}\right)^{x+\Delta x/2,y,z,t}\\ &= \frac{P_x^{t,x+3\Delta x/2,y,z}-2P_x^{t,x+\Delta x/2,y,z}+P_x^{t,x-\Delta x/2,y,z}}{\Delta x^2}\\ &+\frac{P_y^{t,x+\Delta x,y+\Delta y/2,z}-P_y^{t,x,y+\Delta y/2,z}-P_y^{t,x+\Delta x,y-\Delta y/2,z}+P_y^{t,x,y-\Delta y/2,z}}{\Delta x\Delta y}\\ &+\frac{P_z^{t,x+\Delta x,y,z+\Delta z/2}-P_z^{t,x,y,z+\Delta z/2}-P_z^{t,x+\Delta x,y,z-\Delta z/2}+P_z^{t,x,y,z-\Delta z/2}}{\Delta x\Delta z}.\end{aligned} \tag{6.35}$$

To test our FDTD implementation we simulated the scattering from a silver nanosphere and compared our simulation results with those calculated using the nonlocal Mie theory [22]. To show the agreement between the nonlocal Mie theory and our nonlocal implementation for FDTD, we plot the extinction spectra for three silver nanosphere sizes, 1 nm, 2 nm and 5 nm in Fig. 6.3. Here we used the Drude+2CP model [16] for silver and replaced the Drude term with Eq. (6.34)

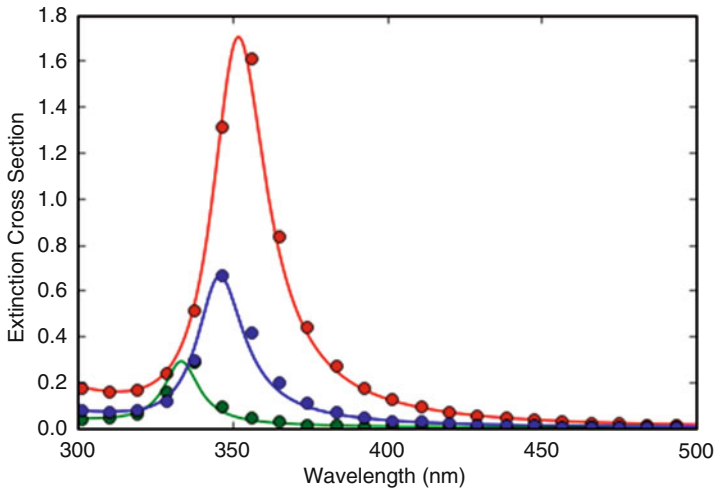

Fig. 6.3 Extinction cross sections for 5 nm (red), 2 nm (blue), and 1 nm (green) silver spheres. The dots are for the FDTD simulations and the lines for the Mie theory

for the free electrons. From the figure we see that the FDTD implementation is in agreement with Mie Theory. Also notice that there is a blue shift between the 5 nm, 2 nm and 1 nm resonances. This is a trend that can be seen experimentally but is not present in the local approximation [23].

6.5 Application to Plasmonic Metasurfaces

To illustrate the usefulness of simulations in nanophotonics, we describe here a few examples of our work on plasmonic metasurfaces. The basic element used to create a metasurface (optical surface) is called meta-atom, and it can be a nanoparticle or a more complex nanostructure. We describe here two types of optical surfaces, random and deterministic surfaces, depending on the way the meta-atoms are arranged.

6.5.1 Plasmonic Coloring

Random surfaces have been exploited for coloring coins at the Royal Canadian Mint. These surfaces are realized via a laser writing technique which is responsible for the creation of nanoparticles of different sizes and randomly distributed on an irregular surface. Understanding the color formation in such a messy configuration could not be realized without the help of a simulation. Through large-scale electrodynamics simulations we were able to qualitatively reproduce the palette of colors obtained via direct laser writing on silver [24]. More details on the simulation approach are reported in chapter "Modelling of Coloured Metal Surfaces by Plasmonics Nanoparticles" in this volume.

6.5.2 Nonlinear Plasmonics

Recently, hybrid nanostructures have been proposed to boost the nonlinear signal production at the third harmonic. These nanostructures consist of a metallic dimer nanoantenna with a highly nonlinear material in the gap (where the linear field enhancement takes place). Separating the nonlinear contributions from the metal and from the gap material in the far-field is experimentally challenging. Simulations in this case, due to the possibility of turning on and off the nonlinear emission from each part of the hybrid nanostructure, were able to identify the role each component plays in the far-field radiation [25].

Simulations also allow optimizing the design of the hybrid nanoantenna to control the phase and polarization of nonlinear optical signal generation. This led to

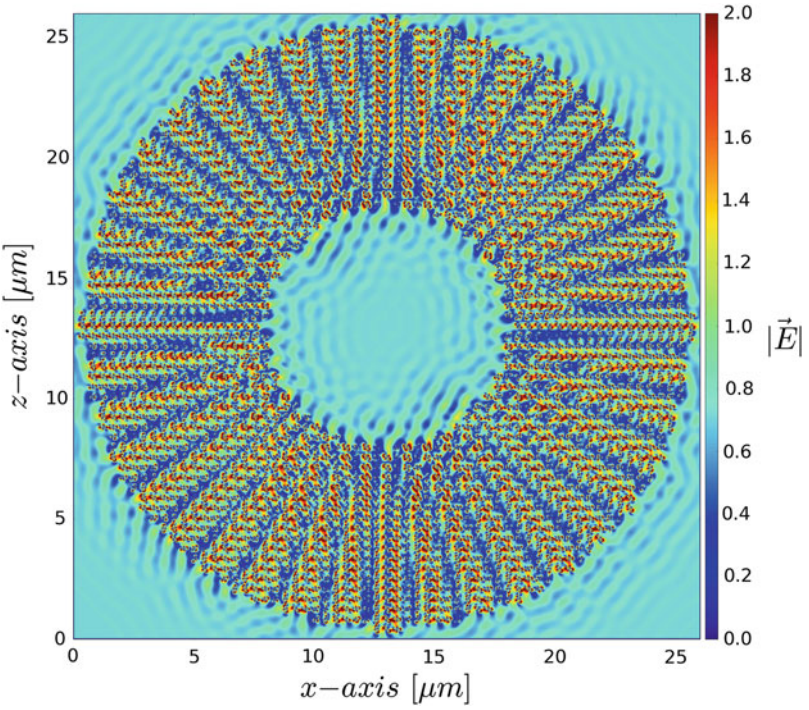

Fig. 6.4 Time frame of the FDTD simulation performed for a full metasurface of butterfly nanoantennas

the design of the so called "butterfly nanoantenna", as described in more detail in chapter "Plasmonic Metasurfaces for Nonlinear Structured Light" in this volume.

In this case, large-scale simulations were key to the design and simulation of an optical surface containing up to ∼3600 butterfly nanoantennas to generate a third harmonic far-field beam carrying an orbital angular momentum of 41. This large metasurface for its complexity could not be conceived in other ways. In Fig. 6.4 we show a snapshot extracted from the FDTD simulation for the full metasurface excited by left circular polarization.

Acknowledgements Computations were performed on the SOSCIP Consortium's Blue Gene/Q computing platform. SOSCIP is funded by the Federal Economic Development Agency of Southern Ontario, the Province of Ontario, IBM Canada Ldt., Ontario Centres of Excellence, Mitacs and Ontario academic member institutions. We acknowledge SOSCIP, the National Sciences and Engineering Research Council of Canada, and the Canada Research Chairs Program.

References

1. Calà Lesina A, Vaccari A, Berini P, Ramunno L (2015) On the convergence and accuracy of the FDTD method for nanoplasmonics. Opt Express 23:10481
2. Yee K (1966) Numerical solution of initial boundary value problems involving Maxwell's equations in isotropic media. IEEE Trans Antennas Propag 14(3):302–307
3. Taflove A, Johnson SG, Oskooi A (2013) Advances in FDTD computational electrodynamics: photonics and nanotechnology. Artech House, Boston/London
4. Agrawal A, Benson T, De La Rue R, Wurtz G (2017) Recent trends in computational photonics. Springer, Cham
5. Lumerical Solutions. www.lumerical.com
6. Taflove A, Hagness SC (2005) Computational electrodynamics: the finite-difference time-domain method, 3rd edn. Artech House, Boston/London
7. Chun K, Kim H, Kim H, Chung Y (2013) PLRC and ADE implementations of Drude-critical point dispersive model for the FDTD method. PIER 135:373–390
8. Roden JA, Gedney SD (2000) Convolution PML (CPML): an efficient FDTD implementation of the CFS-PML for arbitrary media. Microw Opt Technol Lett 27(5):334–339
9. Wriedt T (2013) The Mie theory: basics and applications. Springer, Berlin/Heidelberg
10. van de Hulst HC (1957) Light scattering by small particles. Wiley, New York
11. Fujii M (2014) Fundamental correction of Mie's scattering theory for the analysis of the plasmonic resonance of a metal nanosphere. Phys Rev A 89(3):033805
12. Smirnova D, Kivshar YS (2016) Multipolar nonlinear nanophotonics. Optica 3(11):1241
13. Vaccari A, Calà Lesina A, Cristoforetti L, Pontalti R (2011) Parallel implementation of a 3D subgridding FDTD algorithm for large simulations. Prog Electromagn Res 120:263–292
14. MPI Forum. http://www.mpi-forum.org
15. Alsunaidi MA, Al-Jabr AA (2009) A general ADE-FDTD algorithm for the simulation of dispersive structures. IEEE Photon Technol Lett 21(12):817–819
16. Prokopidis KP, Zografopoulos DC (2013) A unified FDTD/PML scheme based on critical points for accurate studies of plasmonic structures. J Lightwave Technol 31(15):2467–2476
17. Vial A, Laroche T, Dridi M, Le Cunff L (2011) A new model of dispersion for metals leading to a more accurate modeling of plasmonic structures using the FDTD method. Appl Phys A 103(3):849–853
18. Varin C, Emms R, Bart G, Fennel T, Brabec T (2018) Explicit formulation of second and third order optical nonlinearity in the FDTD framework. Comput Phys Commun 222:70–83
19. Raza S, Bozhevolnyi SI, Wubs M, Mortensen NA (2015) Nonlocal optical response in metallic nanostructures. J Phys Condens Matter 27:183204
20. McMahon JM (2011) Topics in theoretical and computational nanoscience: from controlling light at the nanoscale to calculating quantum effects with classical electrodynamics. Springer, New York
21. Ciracì C, Poutrina E, Scalora M, Smith DR (2012) Second-harmonic generation in metallic nanoparticles: clarification of the role of the surface. Phys Rev B 86:115451
22. Ruppin R (1973) Optical properties of a plasma sphere. Phys Rev Lett 31:1434–1437
23. Scholl JA, Koh AL, Dionne JA (2012) Quantum plasmon resonances of individual metallic nanoparticles. Nature 483:421–427
24. Guay J-M, Calà Lesina A, Côté G, Charron M, Poitras D, Ramunno L, Berini P, Weck A (2017) Laser-induced plasmonic colours on metals. Nat Commun 8:16095
25. Calà Lesina A, Berini P, Ramunno L (2017) Vectorial control of nonlinear emission via chiral butterfly nanoantennas: generation of pure high order nonlinear vortex beams. Opt Express 25(3):2569–2582

Chapter 7
Terahertz Nanoscale Science and Technology

John W. Bowen

Abstract The terahertz (THz) frequency range, which falls between the infrared and microwave portions of the spectrum, is rich in potential applications because the photon energies involved can open a window on physical and biological processes that are inaccessible to other wavelengths. After an introduction to the terahertz range, some example applications, and the techniques used for the generation, detection and manipulation of terahertz radiation, this chapter concentrates on the latest developments in terahertz nanoscale science and technology. Topics covered include the use of nano-structures to enhance the emission and detection of terahertz radiation; THz quantum cascade lasers; terahertz detection approaching the quantum limit; THz nanoscopy; terahertz scanning tunnelling microscopy (THz-STM); and the use of THz spectroscopy to probe biological function at the molecular level.

Keywords Terahertz technology · Nanoscale devices · Nanoscopy · Biomolecular spectroscopy

7.1 Introduction

The terahertz part of the electromagnetic spectrum, encompassing frequencies be-tween 100 GHz and 10 THz, and corresponding to wavelengths of 30 μm to 3 mm, has important properties that make it attractive for a wide range of application areas. The photon energies correlate with molecular rotations, hydrogen bonding stretches and torsions, bond vibrations and crystalline phonon vibrations, providing spectroscopic information. Furthermore, the conductivity of materials and the ultrafast motion of charge carriers can be probed using terahertz spectroscopy. Many materials that are opaque in other parts of the spectrum transmit terahertz

J. W. Bowen (✉)
School of Biological Sciences, University of Reading, Reading, UK
e-mail: j.bowen@reading.ac.uk

B. Di Bartolo et al. (eds.), *Quantum Nano-Photonics*, NATO Science for Peace and Security Series B: Physics and Biophysics,
https://doi.org/10.1007/978-94-024-1544-5_7

radiation to some degree, enabling depth-resolved imaging of their internal structure. Additionally, thermal emission peaks in this frequency range for temperatures of a few Kelvin or tens of Kelvin, enabling astronomical observation of cool objects in space, as well as of the light from rapidly receding, distant objects at the edge of the universe, which has been red-shifted into the terahertz range. On top of this, the photon energies are insufficient to cause damage to materials or harm to individuals through ionization. These factors have given rise to applications in areas as diverse as astronomy, non-destructive testing, art conservation, medical imaging, pharmacy, atmospheric science, and security screening. Despite the relatively large scale of the wavelengths involved, terahertz technology can benefit from the use of nano-structured devices and from exploiting quantum effects. Astonishingly, it can also provide the means to achieve sub-nanometer scale resolution imaging with simultaneous ultrafast time resolution and to probe biological function at the molecular level.

In order to appreciate these latest developments in terahertz nanoscale science and technology, it is helpful to have some understanding of terahertz systems in general, not just at the nanoscale, and that is where this chapter starts. It then moves on to discuss the use of nano-structures to enhance the generation and detection of terahertz radiation, terahertz quantum cascade lasers, detection approaching the quantum limit, terahertz nanoscopy, terahertz scanning tunneling microscopy, and terahertz biomolecular spectroscopy.

7.2 Terahertz Systems

7.2.1 Time Domain Systems

Many terahertz spectroscopy and imaging systems in current use are based on the generation and detection of short pulses of terahertz radiation. In order to make a spectroscopic measurement, the sample is placed in the terahertz beam so that the pulse is incident upon it and the emergent pulse is recorded as a time domain waveform. The sample will attenuate the pulse, through a combination of absorption, reflection at its surfaces and scattering, and will introduce a time delay as the pulse traverses it, which will act to broaden the width of the pulse if the material is dispersive. Because the terahertz pulse is only a few hundred femtoseconds in length, it contains a broad range of terahertz frequencies, typically spanning from 100 GHz to over 3 THz. Therefore, a complex fast Fourier transform of the time domain waveform produces its frequency domain spectrum. By taking the ratio of the spectrum of the received waveform to that when no sample is in the beam (the reference waveform), the amplitude and phase transmission coefficients at each frequency within the bandwidth may be determined.

This approach can be extended to achieve terahertz imaging by focusing the beam to a small spot at the sample and either moving the sample through the terahertz beam or scanning the beam across the sample. Typically, this is accomplished by mounting either the sample or the generation and detection heads on x–y translation stages, to allow scanning in two dimensions. Therefore, the image data is acquired pixel by pixel and consists of a full time domain waveform for each location of the beam across the sample surface. There are many ways to construct an image from this data. For example, the peak amplitude of the time domain waveform may be plotted for each pixel, or the peak amplitude integrated over different frequency ranges. Each representation can highlight different features of the sample and the most appropriate to use will depend on the application. The resulting images are usually plotted as false colour maps.

Terahertz images and spectra can be acquired in both transmission and reflection geometry by appropriate reconfiguration of the system. In reflection mode, the time domain waveform for a stratified sample will consist of a series of peaks corresponding to reflections from individual layer boundaries. Therefore, an individual peak may be isolated and an image constructed from mapping it across the sample, allowing depth-resolved imaging to be achieved. Alternatively, by stacking time domain waveforms recorded along a line across the sample so that they are side by side, and plotting a false colour map of the amplitude of each time domain point, a cross-sectional image, or B-scan, of the sample can be constructed. Signal processing techniques based on deconvolution can be used to improve the resolution, to the degree that sub-wavelength and sub-pulse width depth resolution is possible [1].

The two commonest techniques for generating the short terahertz pulses used in these systems are photoconductive generation and optoelectronic generation. Both are driven by the pulse from a near-infrared femtosecond laser. In photoconductive generation, the near-infrared laser pulse is incident on a piece of semiconductor at the feed gap between the two halves of a planar dipole antenna, which has been fabricated on a suitable dielectric substrate and is designed for radiation of terahertz frequencies. A potential difference is established between the two halves of the antenna by applying a d.c. bias voltage across them. Initially, with no near-infrared laser pulse present, the semi-conductor is non-conducting and no current flows through the antenna; hence there is no radiation. However, when the laser pulse is incident on the semiconductor, photocarriers are generated and current begins to flow. After the laser pulse has ceased, the photocarriers relax back to the conduction band and the current returns to zero. The burst of current through the antenna results in a radiated pulse of terahertz radiation. Because of the carrier lifetime, the terahertz pulse is longer than that from the near-infrared laser, typically being hundreds rather than tens of femtoseconds in duration, but it still spans frequencies up to around 3 THz.

The alternative technique of optoelectronic generation, replaces the photoconductive antenna with a non-linear crystal of material such as zinc telluride. When the near-infrared laser pulse propagates through the crystal, the non-linearity results in the generation of an emergent pulse at the difference frequencies between the

frequency components of the input pulse. Because the femtosecond input pulse has a broad frequency content spanning several terahertz about its centre frequency in the infrared, the emergent pulse covers a broad range of frequencies in the terahertz part of the spectrum. While this technique produces broader band terahertz pulses than photoconductive detection, it requires use of an amplified laser system to produce the infrared input pulse.

A gated detection system is required in order to resolve the shape of the terahertz pulse after it has interacted with the sample and to record the time domain waveform. Again, there are two detection techniques in common use, both of which use a fraction of the signal split off from the near-infrared femtosecond laser using a beam splitter as the gating or probe signal. This probe signal activates the detector for a length of time dependent on the laser pulse width, which is significantly shorter than the width of the received terahertz pulse. By introducing an optical delay line between the laser pulse which drives the generator, commonly referred to as the pump pulse, and the probe pulse, different portions of the received terahertz pulse can be detected. As the laser produces a series of pulses, each of which generates an identical terahertz pulse, the optical delay line can be scanned so that each successive probe pulse maps out the shape of the received terahertz waveform at the detector over a sequence of received terahertz pulses. This assumes that the sample does not significantly change its properties on this timescale.

Photoconductive detection uses an antenna similar to that used for photoconductive generation. However, in this case, there is no applied bias voltage and the magnitude of the current flowing through the antenna corresponds to the amplitude of the received signal. In the absence of the probe pulse, no current can flow through the antenna, even with an applied terahertz signal. However, while the probe pulse is present, photocarriers are generated in the semiconductor, enabling a current to flow through the antenna, driven by the received terahertz signal.

Alternatively, electro-optic detection utilizes the Pockels effect in an appropriately oriented crystal of a material such as zinc telluride. While no terahertz signal is incident on the crystal, an incident probe pulse from the linearly polarized near infrared laser will be converted to a circularly polarized output pulse, due to birefringence in the crystal. If a terahertz pulse is now applied co-linearly with the probe pulse, its electric field will polarize the crystal and modify its birefringence so that the emergent infrared pulse will be elliptically polarized. The amplitude of the received terahertz signal can be determined by separating the emergent infrared pulse into its orthogonal linearly polarized components, using a quarter wave plate and Wollaston prism, and detecting these with a balanced pair of photodetectors. The terahertz signal amplitude is proportional to the difference in intensities recorded at the two photodetectors.

While these time domain systems work well, there is still a desire to improve the efficiencies of terahertz generation and detection in order to increase signal-to-noise ratios and reduce data acquisition times. Section 7.3 discusses recent developments in this direction based on the use of nanostructures.

7.2.2 Frequency Domain Systems

There are many approaches to the recording of terahertz signals directly in the frequency domain, based on the use of continuous wave rather than pulsed sources. While many of these sources are sufficiently narrow band that they can be considered to produce essentially a single output frequency, some can be swept over a range of frequencies to enable spectroscopic information to be retrieved. Others are inherently broadband noise sources and frequency comb generators, which require frequency selective components or interferometric spectrometers to separate the terahertz signal into its frequency components for spectroscopic purposes.

Of particular note here, are photomixers, which use non-linear devices mounted in terahertz planar antennas to derive a terahertz output at the difference frequency between two diode lasers, which are typically operating at infrared communications wavelengths. The terahertz output frequency can be swept by sweeping the wavelength offset between the two lasers. Similar nanostructure enhancements to those described in Sect. 7.3 for photoconductive emitters and detectors are also applicable in the case of these devices.

Another class of continuous wave sources are terahertz quantum cascade lasers. As their name implies, these exploit quantum effects for their operation. They are discussed more fully in Sect. 7.4.

Quantum effects can also play an important role in terahertz detection, especially of the very small amounts of terahertz radiation received from astronomical bodies. This matter is discussed in Sect. 7.5.

7.2.3 Terahertz Optics

Lenses and mirrors are commonly used within terahertz systems in order to control the divergence and focusing of beams. However, because of the relatively large size of the wavelengths involved, the effects of diffraction cannot be ignored. This has two major consequences. Firstly, geometrical optics cannot be used for the design of terahertz systems, and secondly, there is a limitation on the minimum sized spot to which one can focus the radiation.

Figure 7.1 illustrates the propagation and focusing of a terahertz beam by a lens. Here it is assumed that the beam has a Gaussian transverse amplitude distribution, with the contour lines representing the $1/e$ amplitude level in the beam. It is clear that the beam spreads due to diffraction as it propagates and that the introduction of an optical component, such as the lens, is necessary to refocus the beam and stop it spreading to unmanageable size. The lens focuses the beam to a minimum-sized spot, known as the beam-waist, beyond which it spreads again at the same rate with which it converged. Thus a series of lenses or focusing mirrors spaced one after the other is necessary to constrain the spread of the beam within a given off-axis diameter.

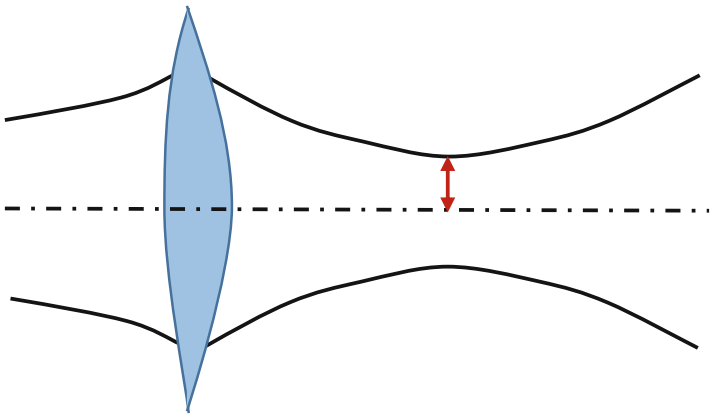

Fig. 7.1 Propagation and focusing of a terahertz beam by a lens. The solid black lines represent the 1/e amplitude contours in the beam. The dash-dot line is the optic axis. The red arrow indicates the beam-waist location

The severity of the diffraction is due to practical constraints on the size of systems, which limit the lenses and mirrors to typically only a few tens of wavelengths in diameter. Furthermore, in order to maintain the beam within that diameter, the lenses and mirrors have to be placed within the near to far field transition region of the beam, and the changing curvature of the phase-fronts at different points along the beam must be taken into account in the design of their surface profiles.

Beams with a transverse amplitude distribution which is other than Gaussian may be described by a superposition of Hermite-Gaussian or Laguerre-Gaussian beam-modes, as long as the beam can be considered paraxial. While the spreading of each of these beam-modes occurs at the same rate as the fundamental Gaussian beam-mode, they slip in phase relative to each other as they propagate, so that the resultant superposition can show a complicated changing form at different points along the beam. Fourier Optics and the angular spectrum of plane waves representation are further tools that can aid in the design of terahertz optical systems, and more details on all of these aspects are covered in [2].

Of particular concern here, is the size of the smallest spot to which the beam can be focused, as that limits the spatial resolution in conventional time domain imaging. Even with a severely non-paraxial beam, diffraction limits the minimum beam-waist size to around half a wavelength. Given the wavelengths involved, this is clearly insufficient to achieve nanoscale resolution. Ways to overcome this, which can deliver orders of magnitude improvement in spatial resolution are described in Sects. 7.6 and 7.7. Furthermore, Sect. 7.8 shows how it is possible to use terahertz spectroscopy to investigate nanoscale phenomena in biological systems, without the need to focus the beam to nanoscale dimensions.

7.3 Nanostructure Enhancement of Sources and Detectors

7.3.1 Enhancement of Photoconductive Emitters, Detectors and Photomixers

In a conventional photoconductive emitter, the size of the antenna feed gap is designed to match the diffraction limited spot size of the near infrared pump laser. However, because of the drift velocity of the photocarriers, only a small number of them reach the metal contact electrodes of the antenna on a sub-picosecond timescale that is fast enough to contribute to the terahertz pulse. Any photocarriers generated further than about 100 nm from the contact electrodes do not contribute. Often, short carrier lifetime semiconductors are used to ensure that any remaining photocarriers recombine rather than contribute to a dc current that acts to lower the bias field, which reduces the carrier acceleration between the electrodes.

However, the introduction of three-dimensional nanoscale contact electrodes in the antenna feed gap has enabled a record 7.5% optical-to-terahertz power conversion efficiency to be achieved [3]. The contact electrodes take the form of gratings of V-shaped groves cutting into the surface of the low temperature GaAs semiconductor. The grooves have metallized side-walls and are spaced apart so that the intervening regions of GaAs taper from a width of 100 nm at the surface of the GaAs slab to 160 nm over the 400 nm depth of the grooves. Thus, this structure forms an array of sub-wavelength slab waveguides for the 800 nm wavelength pump laser beam. Both of the anode and cathode contact electrodes consist of a 15 μm $\times$ 15 μm area of these gratings. The two electrodes are spaced apart by 5 μm and are connected to the arms of a logarithmic spiral terahertz antenna.

Although the slab waveguides have a sub-wavelength height, the grating structure excites surface waves that enable efficient coupling of the incident infrared laser beam into the TEM waveguide modes. The coupling is further enhanced by a 200 nm-thick SiO_2 anti-reflection coating deposited over the surface of the nanostructure gratings.

The use of these high aspect ratio grating structures results in a much larger number of photocarriers being generated within 100 nm of the contact electrodes than in conventional photoconductive emitters, and thus an increase in the number of photocarriers that can contribute to terahertz emission. This brings about a significant improvement in optical-to-terahertz conversion efficiency. The depth of the grooves in the grating structure is important because, although improvements in efficiency were seen in earlier work utilizing two-dimensional plasmonic gratings on the semiconductor surface [4], they were unable to exploit the photocarriers generated deeper within the semiconductor.

While the work described above has focused on improving photoconductive generation, similar antenna structures are used for photoconductive detectors and in photomixers, and so the use of nanostructured electrodes of a similar type should result in improvements in their efficiency too.

7.3.2 *Terahertz Generation from Plasmonic Nanoparticle and Nanohole Arrays*

Recently, there has been much interest in the emission of terahertz radiation observed when metallic nanostructures are illuminated by femtosecond infrared laser pulses, as it could prove the basis of a useful terahertz source. There has been some controversy over the mechanism involved, as different power law dependencies of the emitted terahertz intensity on the incident infrared intensity have been observed in experiments carried out by different teams, indicating different potential emission mechanisms. However, recent experiments by Polyushkin et al. [5] on plasmonic nanoparticle and nanohole arrays indicate that there are two different regimes involved.

At lower incident infrared intensities, the terahertz emission shows a slightly less than second order dependence, suggesting that the emission is due to optical rectification. At higher incident intensities, a fourth to fifth order dependence is seen, which is consistent with ejection of photo-electrons from the metal surface, caused by plasmon enhancement and multi-photon absorption of the infrared radiation, followed by pondermotive acceleration of the emitted electrons in the high electric field gradients that exist close to the metal surface due to the plasmonic enhancement, giving rise to the terahertz emission. The results presented in [5] were the first to show both regimes in the same experiment and were backed up by electron emission measurements using a time-of-flight electron spectrometer, which showed good correlation with the terahertz emission results, supporting the proposed emission mechanisms. A third regime with much reduced power dependence was seen at even higher incident intensities, which is thought to be due to the onset of tunnel ionization rather than multiphoton ionization.

It is clear that the emission depends on the local field enhancement specific to the nanostructures used. In [5], the nanoparticle arrays were designed to produce a strong plasmonic field enhancement at the incident laser wavelength and were found to have terahertz emission consistent with multiphoton ionization, but not optical rectification, within the range of incident laser intensities possible within the experimental setup. The nanohole arrays, on the other hand, were designed to have a lower field enhancement, and showed a clear transition between the optical rectification and multiphoton ionization regimes. Both samples showed the onset of tunnel ionization at very high incident intensities.

7.4 Terahertz Quantum Cascade Lasers

Conventional laser diodes, based on interband transitions between the conduction and valance bands in semiconductors, are limited to the visible and infrared portions of the spectrum, because the bandgap energy, which is of the order of electron-volts, is too high for terahertz emission. However, by exploiting intersubband

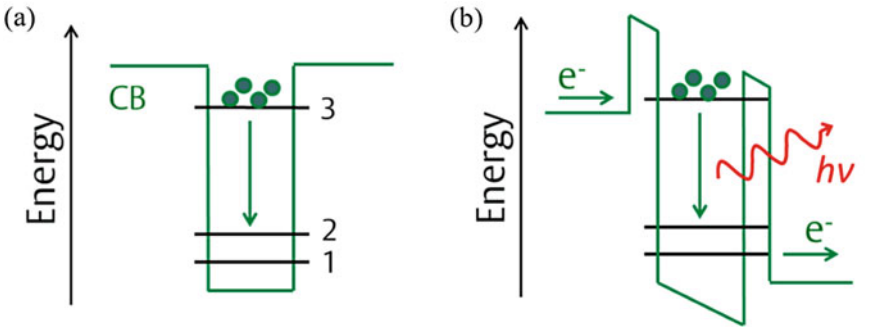

Fig. 7.2 Conduction band (CB) energy levels within a quantum well, (**a**) under zero bias. (**b**) In quantum well between two potential barriers, with applied electric field

transitions in quantum wells, with energies of milli-electron-volts, it is possible to make quantum cascade lasers operating in the terahertz range. These compact semiconductor devices are unipolar, because the emission mechanism only involves electrons, rather than electrons and holes as in interband laser diodes. Therefore, the lasing transitions occur within the conduction band. Moreover, the transition energy is dependent on the thickness of the atomic layers forming the quantum wells, and can be freely adjusted to provide a desired output frequency through bandstructure engineering.

Figure 7.2a shows three energy levels within a quantum well. For lasing to occur, it is necessary to maintain a population inversion between levels 3 and 2. Figure 7.2b shows such a quantum well formed between two potential barriers, under an applied bias voltage. Under the influence of the resulting electric field, electrons tunnel through the potential barrier into level 3, with the lasing transition occurring down to level 2. This lower state is quickly depopulated to level 1, maintaining the population inversion, with the electrons tunneling out of the quantum well through the second potential barrier.

In practical quantum cascade laser designs, multiple quantum wells separated by potential barriers are fabricated next to each other to form superlattices, in which the single well quantum states couple together to form minibands separated by a minigap [6]. This structure forms the active region of the quantum cascade laser, with the lasing transition occurring between the minibands. By cascading a series of these active regions together (typically 100 or more), with intervening injector regions which collect electrons from the lower miniband in one active region and inject them into the upper miniband in the next, each electron can produce multiple lasing transitions as it passes through the device.

In order to confine the radiation within the laser and form the laser cavity, the entire active region cascade structure forms part of a waveguide. Two types of waveguide are in use. In surface plasmon or single metal waveguides, the active region forms a ridge separated by a thin, heavily doped layer from a semi-insulating GaAs substrate, and capped with a metal contact layer. A second metal contact,

adjacent to the ridge that forms the waveguide, enables application of the necessary bias voltage. In this type of waveguide, the radiation is confined as a surface plasmon mode.

In the second type of waveguide, the metal-metal waveguide, the active region forms a ridge sandwiched between a metal layer on the surface of a substrate and second metal contact, with which it is capped. The metal-metal waveguide is better for higher temperature operation of the quantum cascade laser and for achieving operation at lower frequencies. However, it produces lower output power and, because of its tighter field confinement, gives a poorer beam profile [6].

While quantum cascade lasers are well established in the mid-infrared part of the spectrum, their realization at terahertz frequencies has been much more challenging. In part, this has been due to the challenge of developing low-loss waveguides suitable for terahertz frequencies, but also because of the difficulty in achieving population inversion for such small subband spacings. The latter requires the selective injection of electrons into the upper state and not the lower state, as well as an active region design that selectively depopulates the lower state without reducing the population of the upper state. Nevertheless, these difficulties have been overcome sufficiently for terahertz quantum cascade lasers to become available as commercial products.

Performance has been demonstrated at frequencies between 1.2–5 THz and with powers greater than 100 mW in continuous wave mode and greater than 1 W when pulsed. While tuning is limited, tuning over a 330 GHz range centred on 4 THz has been demonstrated using a micro-electromechanical plunger [7]. The greatest practical performance limitation is that of operating temperature, as the maximum operating temperature achieved is currently 199.5 K for pulsed operation and 129 K in continuous wave mode. This is primarily a consequence of thermally activated relaxation between the upper and lower radiative states based on the emission of optical phonons [8]. Alternatives to the GaAs/AlGaAs material system usually used for quantum cascade lasers are being explored, with a view to increasing the maximum operating temperature. The design of the active region is another important factor in this regard.

An alternative approach to achieving room temperature operation, is to make use of intracavity difference frequency generation in dual-wavelength mid-infrared quantum cascade lasers [9]. However, the power output from these devices is more limited, with 2 mW having been achieved in pulsed operation.

There is much current interest in producing broad-bandwidth emission from quantum cascade lasers through the generation of frequency combs. By combining four different active regions with different centre frequencies within a single laser cavity, an instantaneous bandwidth of almost 2 THz has been demonstrated, with peak power up to 10 mW in pulsed operation [10].

An alternative approach to producing broadband emission, whilst simultaneously producing a more directed beam, is the so-called random laser [11]. In this device, the laser cavity is in the form of a disc of the semiconductor layers on a metalized substrate, capped by a metal layer. The metal layers act as a metal-metal waveguide. Holes with diameter comparable to the emission wavelength are etched through

the upper metal contact and entire semiconductor structure in a random pattern. While the radiation is confined between the metal plates, it can travel in any in-plane direction and encounter the randomly placed holes, which will define the modes of the laser cavity. The holes also serve to couple the radiation out of the cavity. Because the holes are spread across the upper surface of the disc, which covers a much larger area than the end facet of a conventional quantum cascade laser waveguide, the resulting output beam is less divergent and is emitted in a direction normal to the top surface of the device. The result is a comb of frequencies, with spectral content dependent on the laser modes that are excited, and a well-directed beam.

Another recent development is the demonstration of high-resolution gas spectroscopy by self-mixing interferometry [12]. In this case, the beam from a quantum cascade laser passes through a gas cell before encountering a mirror which reflects the beam back though the gas cell to the laser, thus producing external cavity feedback. Tuning the frequency of the quantum cascade laser across a gas absorption line reduces the external feedback, which can be detected by monitoring the voltage across the laser.

7.5 Detection Approaching the Quantum Limit

The fundamental limit of detection of electromagnetic radiation of any wavelength corresponds to the detection of a single photon within the measurement interval. This is known as the quantum limit [13]. The measurement interval is related to the response time of the detection system. If the bandwidth of a given detection system is $\Delta\nu$, the corresponding measurement time will be $\Delta\nu^{-1}$. Therefore, detection of a single photon within this time, of energy $h\nu$, corresponds to a received signal power

$$P = h\nu \cdot \Delta\nu \tag{7.1}$$

Obviously, for the detection of weak sources of radiation, such as from faint astronomical objects in distant regions of the Universe, it is advantageous to have detection systems that come as close to the quantum limit as possible. While some terahertz detection systems are based on direct detection using broadband thermal detectors, others are based on heterodyne detection. The latter have the advantage of retaining all of the phase and frequency present in the input signal. They operate by diplexing the incoming signal with the signal from a local oscillator, which forms part of the detection system, or receiver, and applying this combined signal to a non-linear device known as a mixer. The output from the mixer is at the difference frequency between the input signal and that of the local oscillator. If a range of frequencies is present at the input, the result will be a range of frequencies present at the output, with the incoming signal spectrum downconverted from the terahertz range to much lower frequencies, which can be handled by conventional electronics. Inevitably, there will be noise in the detection system that will limit the smallest

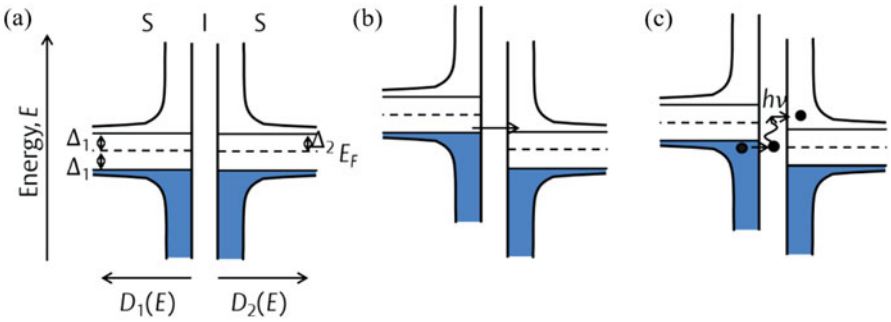

Fig. 7.3 SIS tunnel junction under different bias conditions. (**a**) Under zero bias. (**b**) Biased such that $eV_b = \Delta_1 + \Delta_2$, allowing quasiparticle tunneling. (**c**) Biased such that $eV_b = \Delta_1 + \Delta_2 - h\nu$, allowing photon-assisted tunneling

signal it can detect. In heterodyne systems, this is conventionally represented by a mixer noise temperature T_m, related to this least detectable signal power by

$$P = kT_m\Delta\nu \tag{7.2}$$

where k is Boltzmann's constant. Thus, equating (7.1) and (7.2) gives the quantum limit in terms of mixer noise temperature as

$$T_m = h\nu/k \tag{7.3}$$

Fortunately, it is possibleto approach the quantum limit in heterodyne detection at frequencies up to about 1 THz by using superconductor-insulator-superconductor tunnel junctions as mixers. These SIS mixers consist of two superconductor regions separated by a thin insulator barrier, of the order of 0.06–0.2 nm in thickness. The device is operated well below the superconducting transition temperature. The situation under different bias conditions is illustrated in Fig. 7.3. The figure represents energy on the vertical axis and density of states in the superconductors on the horizontal axis. The blue shaded regions indicate filled states, whereas unshaded regions are empty. In a superconductor, there exists a superconducting energy gap of height 2Δ, centred on the Fermi energy E_F. If different superconductors are used on either side of the insulating barrier, they will have different energy gaps, indicated in Fig. 7.3 by Δ_1 and Δ_2. Under zero bias (Fig. 7.3a), no tunneling occurs across the junction. If the bias is increased such that $eV_b > \Delta_1 + \Delta_2$, where e is the electronic charge and V_b is the bias voltage, filled states on one side of the junction line up with empty states on the other side and there is sufficient energy for Cooper pairs to break up and the resulting quasiparticles to tunnel across the junction (Fig. 7.3b). This results in a very rapid onset of current when $eV_b = \Delta_1 + \Delta_2$ because of the very large density of states close to the superconducting energy gap edge on either side of the junction. If the bias voltage is such that $eV_b < \Delta_1 + \Delta_2$, the additional

energy required for tunneling can be provided by an incoming photon (Fig. 7.3c). The resulting extreme non-linearity in response to incident radiation is the reason that SIS mixers have a performance that approaches the quantum limit.

The use of SIS mixers is now well established in terahertz astronomy. For example, SIS mixers are used in the receivers for the Atacama Large Millimeter/Submillimeter Array (ALMA), which operates at frequencies from 30 GHz – 1 THz. A receiver noise temperature corresponding to about three times the quantum limit has been achieved in the ALMA 787–950 GHz band [14].

7.6 Terahertz Nanoscopy

A number of approaches are being explored to enable sub-wavelength terahertz imaging, including the use of sub-wavelength apertures and tapered plasmonic waveguides. However, the most impressive results to date have been achieved by applying a terahertz beam to the tip of an atomic force microscope hovering over the sample to be imaged. The microscope tip acts as an antenna to concentrate the terahertz fields, with the scattered field being dependent on interaction of the evanescent field with the sample. Because of non-linearity in the field near the pointed end of the microscope tip, the scattered field contains higher harmonics of the incident terahertz frequency, which can be separated using a Michelson interferometer, enabling the scattered radiation to be distinguished from the incident radiation. Using a 2.54 THz continuous wave beam, Huber et al. [15] have demonstrated 40 nm spatial resolution imaging of nano-transistors using this technique, corresponding to a resolution of 1/3000 of the wavelength. They found that it was possible to image regions of different carrier density within single nano-transistors. Current efforts are directed towards improving the technique by replacing the atomic force microscope tip with a tip specifically designed to act as a terahertz antenna.

7.7 Terahertz Scanning Tunneling Microscopy (THz-STM)

Even finer spatial resolution is possible with THz-STM, although, in this case, the terahertz signal is used to enable ultrafast time resolution in scanning tunneling microscopy, rather than to record terahertz images directly. An incident terahertz pulse acts to provide an ultrafast modulation to the bias voltage in a scanning tunneling microscope (STM), inducing tunneling of electrons between the sample and scanning tip on a sub-picosecond timescale. This is achieved without modification to the STM, by focusing the terahertz beam so that it couples to the scanning tip of the STM, which acts as an antenna for the terahertz radiation. The non-linear current-voltage characteristic of the sample-tip tunnel junction rectifies the resulting time-dependent tunnel current, enabling it to be detected with the conventional STM electronics. In the initial demonstration of the technique [16], electron trapping in an

InAs nanodot, induced by an 800 nm optical pump pulse, was imaged in an optical pump-terahertz probe experiment. A time resolution of below 500 fs was achieved simultaneously with a 2 nm spatial resolution, corresponding to 1/150,000 of the terahertz wavelength.

Since then, the technique has been improved to the extent that it is now possible to produce a slow motion movie of the ultrafast motion of a single molecular orbital, with a spatial resolution of 0.6 Å and a time resolution of 115 fs [17]. This was demonstrated by imaging pentacene molecules, which were electronically decoupled from an underlying metal substrate by a monolayer of NaCl. Appropriate choice of the terahertz pulse amplitude opens an otherwise forbidden tunneling channel through the highest occupied molecular orbital (HOMO), enabling an electron to tunnel from the HOMO to the STM tip, and a further electron to tunnel from the metal substrate into the HOMO, resulting in a detectable ultrafast tunnel current. Removal of the electron from the HOMO abruptly changes the Coulomb and van der Waals forces between the molecule and the substrate, setting the molecule into oscillatory motion. By using an initial terahertz pulse to act as a pump to set the molecule into motion, and following it after a delay with a second terahertz pulse to act as a probe, the oscillation can be mapped out for different time delays between pairs of pump and probe pulses. The oscillation can be detected because variation of the spacing between the molecule and the scanning tip modulates the tunnel current. In the case of pentacene over a gold substrate, a 0.5 THz oscillation was observed, with an amplitude corresponding to ± 4 pm. Use of a different molecule (copper phtalocyanine) or modification of the substrate was seen to produce different oscillation frequencies, due to the dependence on the forces between the molecule and substrate. Furthermore, by appropriate choice of substrate and terahertz pulse amplitude, it is possible to selectively image the lowest unoccupied molecular orbital (LUMO) rather than the HOMO. This technique opens up new possibilities for studying the quantum motion of molecules on femtosecond timescales and with single electronic orbital resolution.

7.8 Biomolecular Spectroscopy

To gain a full understanding of the function of biomolecules, such as proteins, it is important to consider not just the molecule itself, but also the network of water molecules that surround it in a biological system. Terahertz spectroscopy can provide unique information in this regard, complementary to that provided by other techniques, as both the collective vibrational modes of biomolecules and dynamic changes in the water network that occur on sub-picosecond timescales are accessible to it. By measuring the terahertz absorption of solutions of biomolecules as a function of concentration, it has been deduced that biomolecules slow the fluctuations in the hydrogen bond network of the water molecules in their vicinity, producing a surrounding shell of hydration water with modified dynamics and

a distinct terahertz absorbance [18]. This behavior is consistent with molecular dynamics simulations, which show a shift in the vibrational density of states of the hydration water towards higher frequencies, resulting in increased absorption above about 1.5 THz and decreased absorption below this frequency [19]. Furthermore, from the profile of the absorption versus concentration curve, it is possible to determine the point at which the dynamic hydration shells begin to overlap, and thus deduce their size. In the case of proteins, it has been found that their influence on the water dynamics extends as far away as at least 10 Å; and to greater than 20 Å in some cases [18]. This is a much greater distance than had been previously assumed, based on experiments carried out using other techniques, which are insensitive to water fluctuations on the sub-picosecond timescale. Consequently, because of the separations between molecules in live cells, much of the water can be in this altered dynamic state.

Thus, because of the strong interaction between biomolecules and their surrounding water network, it is possible to make inferences about the state of the biomolecule by measuring the terahertz absorption, which tends to be dominated by the water. For example, it is possible to detect changes in molecular conformation and the presence of site-specific mutants. Terahertz spectroscopy of antifreeze proteins, which enable some animals to survive in sub-freezing temperatures by binding to nano-sized ice crystals, restricting their further growth, has suggested the existence of a gradient of hydrogen bond dynamics towards the bond site. This hydration funnel is thought to provide a long-range interaction targeting the antifreeze protein towards the ice crystal, eventually enabling it to bond to its surface through a local, short-range interaction at the antifreeze protein's ice-binding site [19]. Further terahertz measurements have indicated that a hydration funnel may play an equivalent role in enzyme-substrate catalysis [19].

Similarly, terahertz spectroscopy shows great promise for label-free detection in biomedical applications. For example, it has been demonstrated that changes in the terahertz absorption of solvation water can be used to enable the label-free detection of antibody-antigen binding in estrogen receptor alpha, which is an important biomarker for breast cancer diagnosis [20].

7.9 Conclusions

This chapter has shown how terahertz radiation can be used to provide information on nanoscale phenomena inaccessible through other means, as well as how nanoscale technology can be used to improve the performance of terahertz systems in general. This is despite the relatively long wavelengths involved. Indeed, proportionally speaking, the spatial resolution that has been achieved surpasses that in any other part of the electromagnetic spectrum. Terahertz science and technology is a relatively young field, due to the technological challenges of operating in this part of the spectrum. Nevertheless, terahertz technology has advanced dramatically in recent years and it is anticipated that new applications that make use of the unique characteristics of terahertz radiation will continue to emerge in the future.

References

1. Walker GC, Bowen JW, Labaune J, Jackson J-B, Hadjiloucas S, Roberts J, Mourou G, Menu M (2012) Terahertz deconvolution. Opt Express 20(25):27230–27241
2. Martin DH, Bowen JW (1993) Long-wave optics. IEEE Trans Microw Theory Tech 41(10):1676–1690
3. Yang S-H, Hashemi MR, Berry CW, Jarrahi M (2014) 7.5% optical-to-terahertz convesion efficiency offered by photoconductive emitters with three-dimensional plasmonic contact electrodes. IEEE Trans Terahertz Sci Tech 4(5):575–581
4. Berry CW, Jarrahi M (2012) Terahertz generation using plasmonic photoconductive gratings. New J Phys 14:105029
5. Polyushkin DK, Márton I, Rácz P, Dombi P, Hendry E, Barnes WL (2014) Mechanisms of THz generation from silver nanoparticle and nanohole arrays illuminated by 100 fs pulses of infrared light. Phys Rev B 89:125426
6. Williams BS (2007) Terahertz quantum-cascade lasers. Nat Photonics 1(9):517–525
7. Qin Q, Reno JL, Hu Q (2011) MEMS-based tunable terahertz wire-laser over 330 GHz. Opt Lett 36(5):692–694
8. Vitiello MS, Scalari G, Williams B, De Natale P (2015) Quantum cascade lasers: 20 years of challenges. Opt Express 23(4):5167–5182
9. Belkin MA, Capasso F (2015) New frontiers in quantum cascade lasers: high performance room temperature terahertz sources. Phys Scr 90:118002
10. Rösch M, Scalari G, Beck M, Süess MJ, Bachmann D, Unterrainer K, Darmo J, Faist J (2017) Terahertz quantum cascade laser based frequency comb with 1 THz spectral bandwidth and dual-comb operation. In: OTST 2017 optical terahertz science and technology abstract book. Institute of Physics, London
11. Schönhuber S, Brandstetter M, Hisch T, Deutsch C, Krall M, Detz H, Andrews AM, Strasser G, Rotter S, Unterrainer K (2016) Random lasers for broadband directional emission. Optica 3(10):1035–1038
12. Hagelschuer T, Wienold M, Richter H, Schrottke L, Biermann K, Grahn HT, Hübers H-W (2016) Terahertz gas spectroscopy through self-mixing in a quantum-cascade laser. Appl Phys Lett 109(19):191101
13. Tucker JR, Feldman MJ (1985) Quantum detection at millimetre wavelengths. Rev Mod Phys 57(4):1055–1114
14. Uzawa Y, Fujii Y, Kroug M, Makise K, Gonzalez A, Kaneko K, Kojima T, Miyachi A, Saito S, Terai H, Wang Z (2016) Development of superconducting THz receivers for radio astronomy. In: Proceedings of 41st international conference on infrared, millimeter and terahertz waves IRMMW-THz 2016, H3A.5. IEEE, Copenhagen
15. Huber AJ, Keilmann F, Wittborn J, Aizpurua J, Hillenbrand R (2008) Terahertz near-field nanoscopy of mobile carriers in single semiconductor nanodevices. Nano Lett 8(11):3766–3770
16. Cocker TL, Jelic V, Gupta M, Molesky SJ, Burgess JAJ, De Los Reyes G, Titova LV, Tsui YY, Freeman MR, Hegmann FA (2013) An ultrafast terahertz scanning tunnelling microscope. Nat Photonics 7(8):620–625
17. Cocker TL, Peller D, Yu P, Repp J, Huber R (2016) Tracking the ultrafast motion of a single molecule by femtosecond orbital imaging. Nature 539(7628):263–267
18. Leitner DM, Gruebele M, Havenith M (2008) Solvation dynamics of biomolecules: modeling and terahertz experiments. HFSP J 2(6):314–323
19. Nibali VC, Havenith M (2014) New insights into the role of water in biological function: studying solvated biomolecules using terahertz absorption spectroscopy in conjunction with molecular dynamics simulations. J Am Chem Soc 136(37):12800–12807
20. Li M, Chang T, Wei D, Tang M, Yan S, Du C, Cui H-L (2017) Label-free detection of anti-estrogen receptor alpha and its binding with estrogen receptor peptide alpha by terahertz spectroscopy. RSC Adv 7(39):24338–24344

Chapter 8
Casimir Forces: Fundamental Theory, Computation, and Nanodevice Applications

Fabrizio Pinto

Abstract Seventy years after submission to the Physical Review of the crucial quantum electrodynamical treatment of interatomic dispersion forces by Casimir and Polder, our understanding of such interactions in both the unretarded and retarded regimes has undergone a dramatic and intricate evolution. In this contribution, we explore the ultimate physical motivations leading to this fascinating trajectory rich in momentous implications for the goal of both fabrication and operation of highly integrated micro- and nano-structures. The first and most obvious development has been the growing appreciation that, far from only representing a weak, though exotic, effect, Casimir's "zero point pressure of electromagnetic waves" between two conducting parallel planes is actually a dominant interaction on the nanoscale. This resulted in Feynman's unforgettable caricature – in "There's plenty of room at the bottom" – of van der Waals forces between microparts as a "man with his hands full of molasses," which led to such forces being understood as the leading cause of undesirable stiction for several decades. However, commencing in the 1980s, the realization that such strong dispersion interactions might offer unique technological opportunities surfaced. The second thrust was connected to the discovery that, unlike expected from London's intermolecular force theory and the naive assumption of additivity, dispersion forces depend quite unpredictably on topology and on the interplay of dielectric properties of the interacting media. This may lead to drastic departures from results obtained through perturbative methods and indeed to the prediction, later verified both in the unretarded and retarded regimes, that dispersion forces may become repulsive. The challenge of computing Casimir forces in more general geometries different from that of two parallel planes has led to substantial progress from the numerical standpoint although open problems remain. Lastly, in one of the earliest and most significant discoveries in the history of the field, it was shown that dispersion forces can be modulated in time,

F. Pinto (✉)
Department of Aerospace Engineering, Faculty of Engineering, Izmir University of Economics, Teleferik Mahallesi, Balçova/İzmir, Turkey
e-mail: fabrizio.pinto@ieu.edu.tr; http://people.ieu.edu.tr/en/fabriziopinto

B. Di Bartolo et al. (eds.), *Quantum Nano-Photonics*, NATO Science for Peace and Security Series B: Physics and Biophysics,
https://doi.org/10.1007/978-94-024-1544-5_8

for instance by illumination in semiconductors. This discovery opened the way to consideration of thermodynamical engine cycles enabled by Casimir forces and to a novel, highly effective means for energy transfer on the nanoscale.

Keywords Casimir effect · Fields under the influence of external conditions · Computer algebra · History of science · Science pedagogy

8.1 Introduction

In his *Treatise on Electricity and Magnetism*, James Clerk Maxwell closes the first section on "Description of Phenomena" (Ch. 1, Experiment I, Art. 27, last paragraph) by the following two statements [1]: "No force, either of attraction or of repulsion, can be observed between an electrified body and a body not electrified. When, in any case, bodies not previously electrified are observed to be acted on by an electrified body, it is because they have become *electrified by induction*"[1] [italics in the original]. Although the former statement appears so trivial as to rarely even be explicitly stated in elementary textbooks, its correct interpretation requires extreme care.

In the following few pages of the *Treatise* (culminating with Art. 34), Maxwell recounts the methodology followed by Faraday (see Ref. [4], p. 279) "in his very admirable demonstration of the laws of electrical phenomena." After summarizing experiments conducted by means of a hollow vessel connected to a gold leaf electrometer, he logically concludes that "the electrification of a body is therefore a physical quantity capable of measurement" and "we are therefore entitled to speak of any electrified body as 'charged with a certain quantity of positive or negative electricity'." Finally, the law determining the force between electrified "bodies of dimensions small compared with the distance between them" is given as established by means of the torsion balance devised by Mitchell, used by Cavendish and "successfully applied"(Art. 38) by Coulomb. That is the relationship referred to today as Coulomb's law for the electrostatic force, $\mathbf{F}_{\mathbf{Coul}}$, between two point-like charges, $q_{1,2}$, at a mutual distance r_{12}, that is, $\mathbf{F}_{\mathbf{Coul}} = q_1 q_2 \, \hat{\mathbf{r}}_{12}/r_{12}^2$, in appropriate units. In light of this reasoning, Maxwell's cornerstone statement that "No force, either of attraction or of repulsion, can be observed between an electrified body and a body not electrified" appears irrefutable since, mathematically speaking, the force between any two point-like charges vanishes if the charge of either is zero, that is, if either body is electrically neutral (if $q_i = 0$, with $i = 1$ or 2, then $\mathbf{F}_{\mathbf{Coul}} = \mathbf{0}$).

[1] Notice that 'induction' here describes what we presently refer to as *polarization* (Ref. [2], p. 164). This quotation is from the 2nd edition (1881) of the *Treatise*. However, the entire last paragraph of Art. 27 is identical in both the 1st (1873) and 3rd editions (1892). Both statements closely paraphrase, with somewhat more familiar language, equivalent principles stated by William Thomson (Baron Kelvin) in his *On the Mathematical Theory of Electricity in Equilibrium*, indeed cited by Maxwell (see the Reprint of Papers on Electrostatics and Magnetism, p. 43, Art. 59) [3]. Also, 'electricity,' and related terms, are used where the modern term of *charge* is meant.

This might be sufficient, at least classically, if physical reality presented us only with two point-like particles. However, as Maxwell explains (Art. 28, Experiment II), charge distribution in extended objects is affected by external charges. If one *finite* body is neutral, existing charges within it will be redistributed either by moving freely on its surface (in the case of conductors), or by locally producing dipoles (in the case of insulators). Since the size of the objects involved does not vanish with respect to their mutual distances, this will produce a net force even if a body was "not previously electrified," as Maxwell indicates in his latter statement (Art. 27). These electrostatic forces due to polarization are well known even to primary and secondary school pupils, who are explained the reason they can pick up (electrically neutral) pieces of paper by rubbing a comb through their hair [5, 6]. However, such phenomena occur even on the sub-atomic scale and indeed recent computations have shown that the neutron-proton[2] (and neutron-neutron) electrodynamical Casimir-Polder interactions are expected to be "quite relevant" [9]. Despite the existence of electrostatic forces even between one charged and one neutral object, an apparently inescapable reading of Maxwell's latter statement is that, if two bodies separated by empty space are *both* electrically neutral, and if an independent means to produce polarization is absent, they should not interact with each other, that is, no electrical force should exist between them.

The present contribution is motivated by the fact that, in conflict with such an apparently straightforward conclusion, forces among neutral objects have been well known to exist for millennia from direct observation of the physical world and they have also played an early, vital role within atomistic philosophy, which obviously depends on interatomic forces in order to explain the universe as humans experience it [10]. During the emergence of modern science, the cohesion of polished marbles was reported by Boyle, [11] who conducted fascinating experiments by means of the vacuum pump he had invented [12, 13], and by Newton [14]. In 1840, as polishing technology developed, strong adhesion was reported by Whitworth also in the case of metal surfaces [15], and this phenomenon was further investigated by Tyndall, who ruled out atmospheric pressure as the cause of attraction [16]. The strong interaction of highly polished metal surfaces eventually led to the invention of the so-called Johansson gauge blocks, which are mentioned by Richard Feynman as a "fairly direct" demonstration of intermolecular forces (Ref. [17], p. 12–6) and are possibly the earliest technology enabled by engineering dispersion forces (for a full account and significance of these developments, see Ref. [18]). It is important to stress, therefore, that Casimir's discovery [19] was not, as often erroneously stated, that neutral metal plates attract but that there exists a deep physical meaning of that already well known fact [20].

[2]Therefore the statement that "neutrons have no charge and are neither attracted nor repelled by charged particles" (Ref. [6], p. 501) is obviously incorrect as neutrons, as all nucleons, are polarizable [7] (see the "Naïve picture" in Sect. 8.2.1 therein) and thus they can be "acted on by an electrified body." The erroneous statement does not appear in later editions [8].

Here we shall briefly touch on four different facets of this explosively expanding research field. Firstly, from the pedagogical standpoint, we intend to provide a relatively gentle introduction to the standard foundations of dispersion force theory. However, in order to provide motivated readers with powerful tools needed to reproduce results from the research literature, we shall pursue a computer algebra approach. The package adopted herein is *Mathematica* (v. 9.0.1.0), without any pretense whatsoever of programming expertise on the side of the author and indeed used with a fair amount of wilful unsophistication – and no guarantees – so as to leave ample room for improvement.

Secondly, we shall emphasize several aspects of the Casimir effect that are amenable to classical or semi-classical treatments. One goal of this approach is to remind readers that, unlike routinely claimed, the Casimir effect does *not* provide direct proof of field quantization such as is given by single photon detection. This may dissatisfy some purists, who repeat[3] that, for instance, since the Casimir force is proportional to Planck's constant, $\hbar$, its existence must necessarily be proof that the electromagnetic field is quantized. Such conclusion is well known to be demonstrably *incorrect* (for this debate, see Sect. 8.4 herein, Ref. [18] and Ref. [22], Sect. 8.3). The interpretation of the Casimir force in terms of radiation pressure is derived from Casimir's own original suggestion, in his foundational paper, that "This force may be interpreted as a zero point pressure of electromagnetic waves" [19]. The epistemological and ontological debates as to whether a zero-point field is compatible with classical electrodynamics are also briefly discussed below (Sect. 8.4, and References herein). A second goal of this approach, again pedagogically, is to contribute a working mental image of the physical origin of dispersion forces for use by educators as they help students at all levels develop their intuition for a concept that, as clearly shown by intense recent focus by physics and chemistry education researchers, is notoriously complex to grasp [23–25].

The third aspect, mainly left to Suggested Exercises, is concerned with application of dispersion forces to fundamental science and to technology on various scales including, of course, in nanotechnology, with an emphasis on processes leading to energy exchange by dispersion force manipulation.

Finally, as our fourth perspective, throughout this presentation we shall endeavor to provide insight into and further references regarding some historical developments surrounding the field, which is well known to be mired in multiple, hotly debated controversies.

It will become quickly apparent that dispersion force research has undergone a tremendous expansion in the last few decades. This is clearly neither the place for a technical review of the subject nor, indeed, of a review of the several reviews now available. Readers interested in becoming familiar with such reviews and the many subfields now developing may refer, for instance, to a past analysis

[3]The fact that "repetition of a plausible statement increases a person's belief in the referential validity or truth of that statement," popularly referred to as the 'truth effect,' was demonstrated decades ago by means of psychology experimentation [21].

by this author written within a space propulsion technology context [26]. Two reviews by the present author are also to appear, again considering the aerospace marketplace, especially focused on historical and future developments in the process of technology transfer of dispersion force enabled technologies – including the effect of controversies on their economic and industrial implications – with several hundred relevant references [18]. A non-mathematical introduction aimed at the level of a well-educated audience is also available [27].

8.2 Intermolecular Forces: Fundamental Results

In this section, we proceed by building a chain of arguments leading to an intuitive understanding of the physical forces between molecules as well as between macroscopic boundaries. Notice that here we follow a typesetting style similar to that used by Dubin [28], with input information (*Mathematica* `[In]` prompt) given within the LaTeX `\verbatim` environment whereas the output (*Mathematica* `[Out]` prompt) is reproduced by exporting the *Mathematica* result to LaTeX and displaying it within the {`equation`} environment. In some cases, typographical need mandated departures from such work flow without altering any results and notice also that the appearance of some characters may be different in this document than within the notebook (i.e. `\[Omega]` → ω).

8.2.1 London Expression of the van der Waals Force

Let us commence with a standard non-relativistic treatment [29, 30] of the unretarded interaction of two polarizable one-electron atoms[4] as originally given by London [32] with the further restriction to one-dimension (1D) [33, 34]. Consider two atoms arranged along, for instance, the x-axis at a mutual distance R with their electrons at a distance z_1 and z_2 from their respective nuclei. The atomic electrostatic interaction potential, V_{int}, expanded to 1st order in (z_1, z_2), is:

```
Clear["Global`*"];

Vint[z1_, z2_, R_] =
 e^2  ((1/R) + (1/(R + z2 - z1)) - (1/(R - z1)) - (1/(R + z2)))
VintExpanded[z1_, z2_, R_] =
 Normal[Series[Vint[z1, z2, R], {z1, 0, 1}, {z2, 0, 1}]]
```

$$-\frac{2e^2 z1\, z2}{R^3} \tag{8.1}$$

[4] This calculation was first attempted by S. C. Wang in 1927 [31].

so that the total electrostatic potential to the same order, V_{tot}, becomes:

```
VtotExpanded[z1_, z2_, R_]
 = (1/2) kz1^2 + (1/2) kz2^2 + VintExpanded[z1, z2, R]
```

$$-\frac{2e^2\ \text{z1}\ \text{z2}}{R^3}+\frac{k\ (\text{z1})^2}{2}+\frac{k\ (\text{z2})^2}{2} \tag{8.2}$$

This result allows us to extract the secular (or characteristic) equation [35, 36] as follows:

```
Az1z2 = {{2 SeriesCoefficient[VtotExpanded[z1, z2, R],
            {z1, 0, 2}],
           SeriesCoefficient[VtotExpanded[z1, z2, R],
            {z1 z2, 0, 1}]},
        {   SeriesCoefficient[VtotExpanded[z1, z2, R],
            {z1 z2, 0, 1}],
          2 SeriesCoefficient[VtotExpanded[z1, z2, R],
           {z2, 0, 2}]}};
Az1z2 // MatrixForm
SecularEquation[z1_, z2_, R_] = -\[Omega]^2 m IdentityMatrix[2]
     + Az1z2 ;
SecularEquation[z1, z2, R] // MatrixForm
```

$$\begin{pmatrix} k-m\omega^2 & -\dfrac{2e^2}{R^3} \\ -\dfrac{2e^2}{R^3} & k-m\omega^2 \end{pmatrix} \tag{8.3}$$

The (positive) normal mode frequencies, ($\omega 1$, $\omega 2$), are found from the determinant of the secular equation:

```
\[Omega]1[z1_, z2_, R_] =
 Solve[Det[SecularEquation[z1, z2, R]] ==0,\[Omega]][[2, 1, 2]]
\[Omega]2[z1_, z2_, R_] =
 Solve[Det[SecularEquation[z1, z2, R]] ==0,\[Omega]][[4, 1, 2]]
```

$$\frac{\sqrt{kR^3-2e^2}}{\sqrt{m}R^{3/2}} \tag{8.4}$$

$$\frac{\sqrt{2e^2+kR^3}}{\sqrt{m}R^{3/2}} \tag{8.5}$$

In order to extract the standard expression, it is necessary expand this result to 2nd order in the dimensionless parameter $\beta \equiv e^2/(k\ R^3)$ near $\beta = 0$ (the expansions to

1st order cancel each other out). For instance, for the first frequency, $\omega 1$, we find, upon remultiplying by the natural (unperturbed) frequency $\omega 0 = \sqrt{k/m}$:

```
\[Omega]1exp[z1_, z2_, R_] = Expand[(k/m)^(1/2) (Normal[
 Series[Sqrt[Apart[((\[Omega]1[z1, z2, R])^2/(k/m))]
 /. (e^2/(k R^3)) -> \[Beta]], {\[Beta], 0, 2}]]
 /. \[Beta] -> (e^2/(k R^3)))]
```

$$+\sqrt{\frac{k}{m}} - \frac{e^2\sqrt{\frac{k}{m}}}{kR^3} - \frac{e^4\sqrt{\frac{k}{m}}}{2k^2R^6} \tag{8.6}$$

and analogously for $\omega 2$, which yields a positive sign in the second term. Finally, by writing to the total energy for the two oscillators in their ground states and by introducing the classical static polarizability, $\alpha = e^2/k$, we find, for the unretarded van der Waals interaction energy, V_{vdW}:

```
Eosc[z1_, z2_, R_] =
  Expand[(1/
    2) \[HBar] (\[Omega]1exp[z1, z2, R] + \[Omega]2exp[z1, z2,
       R])] /. Sqrt[k/m] -> \[Omega]0 ;

DeltaE[z1_, z2_, R_] =
 Eosc[z1, z2, R] - \[HBar] \[Omega]0 /. e^4/k^2 -> \[Alpha]^2
```

$$-\frac{\alpha^2\,\omega 0\,\hbar}{2\,R^6} \tag{8.7}$$

Orientational averaging in the case of three dimensions replaces our numerical constant $\frac{1}{2}$ by $\frac{3}{4}$, which is the result by London [32].

8.2.1.1 Suggested Exercise 1

By building upon the above syntax (or by developing your own), generalize the above approach to three atoms. This case is treated in a pedagogical manner by Farina, Santos, and Tort [37] who, in the process, recover a very important result by Axilrod and Teller [38]. Show that, for some particular configurations of the three atoms, the mutual force is *repulsive*. This result, obtained before Casimir's papers and several years earlier than the development of the Lifshitz theory, demonstrated that unretarded, van der Waals forces are not always attractive – a finding with important technological applications [18].

8.2.2 Van der Waals Forces Between Half-Infinite Semispaces

In the assumption of pair-wise additivity, we shall now consider the van der Waals force between two parallel-plane, semi-infinite slabs separated by an empty gap of width s, as done by de Boer [39, 40]. The standard approach consists of choosing, for instance, the (x, y)-plane parallel to the two facing surfaces and of proceeding by multiple integrations. For generality and later use, we shall assume that an interatomic potential of the form:

```
U[x_, y_, z_] = -B/(x^2 + y^2 + z^2)^(\[Gamma]/2)
```

With this definition, and by identifying $s \rightarrow R$, the potential of Eq. (8.7), corresponds to $\gamma = 6$. Let us first consider one single atom at a distance s from one semi-infinite slab of atom number density $N1$. A triple integration over the entire (x, y)-plane and for $z \in [s, +\infty)$ yields the atom-slab potential, $V(s)$, as:

```
V[s_] = N1 Integrate[
 Integrate[
 U[x, y, z], {x, -\[Infinity], +\[Infinity]}, {y, -\[Infinity],
    +\[Infinity]}, Assumptions -> Re[\[Gamma]] > 2 &&
    Re[z^2] > 0], {z,s, +\[Infinity]},
 Assumptions -> Re[\[Gamma]] > 3 && Re[s] > 0 && Im[s] == 0]
```

Notice that *Mathematica* must be told specific information about all quantities involved although this may be obvious from our specific physical application. One further integration over all atoms in the second slab, assumed to have atom number density $N2$, yields the slab-slab potential, and, finally, the van der Waals force is the opposite of the derivative with respect to the gap width:

```
U[s_] = N2 Integrate[V[s + r], {r, 0, +\[Infinity]},
 Assumptions -> Re[\[Gamma]] > 4 && Re[s] > 0];

u[s_] = U[s] (Denominator[U[s]])/Factor[Denominator[U[s]]]

Fplaneplane[s_] = -D[u[s], s]
```

$$-\frac{2\pi B\,\mathrm{N1}\,\mathrm{N2}\,s^{4-\gamma}}{(\gamma-4)(\gamma-3)(\gamma-2)} \tag{8.8}$$

$$\frac{2\pi B\,(4-\gamma)\,\mathrm{N1}\,\mathrm{N2}\,s^{3-\gamma}}{(\gamma-4)(\gamma-3)(\gamma-2)} \tag{8.9}$$

By defining the de Boer-Hamaker constant, A_{dBH}, and by reading out the values of γ and B from the London potential found in Sect. 8.2.2, we find the standard expression due to de Boer [39, 40]:

```
FvdW[s_] = (Fplaneplane[s] /. {\[Gamma] -> 6,
 B -> 3 \[HBar] \[Omega]0 \[Alpha]^2 /
  4})/(N1 N2 3 \[Pi]^2 \[Alpha]^2 \[HBar] \[Omega]0/4) AdBH
```

$$-\frac{\mathrm{AdBH}}{6\pi s^3} \tag{8.10}$$

8.2.2.1 Suggested Exercise 2

(a) Extend the previous approach to the case of two macroscopic homogeneous spherical particle distributions of equal radius R and prove that the particle-particle analytical solution can be cast in a form proportional to the result given by Hamaker [41]:

```
f[x_] = (2/(x^2 - 4) ) + (2/x^2) + Log[((x^2 - 4)/x^2)];
```

(b) Demonstrate that, in the limit of distances $s \gg R$, this solution converges back to the London potential. Find the next non-vanishing term in the series expansion.

(c) Demonstrate that, in the limit for $x \to 2$, the solution converges back to the plate-plate result by de Boer given above. Find the next non-vanishing term in the series expansion.

(d) Create a plot showing your analytical solution at (a) compared to the two limits in (b) and (c). It may be helpful to create two plots, one for near range and one for far range. Due to the power-law nature of these interactions, the natural choice are log-log diagrams of the absolute value of the force.

8.2.3 The Casimir Effect

Although the first to prove that radiation pressure considerations lead to the correct expression for the Casimir force was González [42], below we adapt to the 1D case the full three dimensional (3D) mathematical treatment of Casimir's suggestion given by Milonni, Cook, and Goggin [30, 43] (note that the statement attributed to Debye by these authors in their Ref. 3 is actually due to Casimir; see footnote on p. 7 of Ref. [22]).

In the radiation pressure interpretation of the Casimir effect, the Casimir force is deemed to arise from the competing outward and inward radiation pressures acting on two parallel, ideal reflectors facing each other across a gap of width s. We recall that the expression for the classical radiation pressure [44] due to light incident at angle θ from the normal is, for a perfect reflector, $P_{\mathrm{rad}} = 2u\cos^2\theta$, where u is the radiation energy density, and the factor 2 corresponds to perfect reflection. Assuming that the energy per mode is $\frac{1}{2}\hbar\omega$, and noticing that only $\frac{1}{2}$ of such energy contributes to radiation pressure in either direction, the radiation pressure becomes:

$$P_{\mathrm{rad}} = 2\left(\frac{1}{2}\right)\left(\frac{\hbar\omega}{2}\right)\left(\frac{1}{V}\right)\left(\frac{k_z}{k}\right)^2, \tag{8.11}$$

where V is a quantization volume, k is the wave vector $k = \omega/c$, k_z is the normal component of the wave vector, and c is the speed of light.

8.2.3.1 The One-Dimensional (1D) Casimir Effect

In this 1D treatment, [45] however, radiation is assumed only to be incident at $\theta = 0$ so that no angular integrations are necessary and $k_z \equiv k$. The quantization volume can be expressed as the product of a generic square plate area of side b multiplied by the gap width, so that $V = b^2 s$. The boundary conditions corresponding to a perfect reflector require that the only modes present within the gap be those for which $k = n\pi/s$, where n is an integer. In this 1D case, the replacement of sums by integrals is not apparent but we must still include a dimensional factor, b^2, which cancels the same term in the quantization volume (see Ref. [30], Secs. 2.7 and 3.10). Therefore, by considering contributions from two independent polarizations, we find:

$$P_{\text{out}} = \frac{\pi \hbar c}{s^2} \sum_{0}^{+\infty} n \tag{8.12}$$

As for the inward pressure, the standard replacement $\sum_n (\dots) \rightarrow (s/\pi) \int (\dots)$ in Eq. (8.11) yields:

$$P_{\text{in}} = -\frac{\pi \hbar c}{s^2} \int_0^{+\infty} x \, dx \, . \tag{8.13}$$

Therefore the Casimir pressure, P_{Cas}, becomes:

$$P_{\text{Cas}} = \frac{\pi \hbar c}{s^2} \left(\sum_{0}^{+\infty} n - \int_0^{+\infty} x \, dx \right) \tag{8.14}$$

As is typical in computations of this type [46], extracting physical content requires the evaluation of the difference of two formally infinite quantities [47]. One such method is use of the Euler-Maclaurin formula, [48, 49] which we write as:

$$\Delta_0^N = \sum_0^N n - \int_0^N x \, dx = \tfrac{1}{2} \left[f(N) + f(0) \right] + \sum_{m=1}^{M(K)} \frac{B_{2m}}{(2m)!} \left[f^{2m-1}(N) - f^{2m-1}(0) \right] , \tag{8.15}$$

where $M(K) = K/2$ is K is even and to $(K-1)/2$ is K is odd. In order to obtain a finite result, we follow Casimir and multiply the integrand and summand functions by an exponential function to introduce a cutoff so that the argument in the sum and integral becomes:

```
fcas[x_, \[Lambda]_] = x Exp[-\[Lambda] x]
```

where λ is the cutoff parameter to be considered in the limit $\lambda \to 0^+$ and, in our application, $N \to +\infty$. In order to proceed with applying the Euler-Maclaurin summation formula, we evaluate the following quantity ($m = 1$), which is the only one contributing to the final result in the cutoff limit as can be verified directly:

```
Limit[D[fcas[x, \[Lambda]], {x, 1} ], x -> 0,
 Assumptions -> Im[\[Lambda]] == 0 && Re[\[Lambda]] > 0]
```

$$1 \tag{8.16}$$

Hence the final result is:

```
PCas1D[s_] = -(BernoulliB[2]/(2!)) Pi \[HBar] c/s^2
```

$$-\frac{\pi c\hbar}{12s^2} \tag{8.17}$$

which is the result given by Kupiszewska and Mostowski [45]. Notice that the result given by Bordag, Mohideen, and Mostepanenko [50] for this case refers to the potential energy and pressure per polarization hence accounting for the difference by a factor of 2 (see footnote (3) on p. 74 of Ellingsen's thesis [51]).

8.2.3.2 Suggested Exercise 3

Both the above sum and integral can be calculated analytically for the chosen analytical cutoff function and with $N \to +\infty$. Find such functions, study their difference as a function of λ and take the limit for $\lambda \to 0^+$ noticing whether any numerical instabilities arise in the numerical limit. Repeat this study considering the difference between the sum and the integral for finite N with $N \gg 1$.

8.2.3.3 Suggested Exercise 4

In the case of one infinitely conducting and one infinitely magnetically permeable plate [52, 53], the boundary conditions change and the allowed modes within the gap are defined by $k = (n + \frac{1}{2})\pi/s$. Apply the above approach to this case and discuss your conclusions.

8.2.3.4 Suggested Exercise 5

Generalize the approach of this Section to the full 3D case and recover the result found by Casimir.

8.2.4 *Electrodynamical Casimir-Lifshitz Force*

Here we present a derivation of the important result by Lifshitz [54] for the force between two semi-infinite, parallel-plane slabs without any assumption of additivity and including retardation. This calculation has been given many times by different authors but, in order to provide users with the mathematical tools to extend the validity of this treatment further, here we present a *Mathematica* formulation inspired by the matrix approach of Podgornik, Hansen, and Parsegian [55]. Unlike done originally by Lifshitz, this will enable one to later very efficiently consider the algebraically far more complex cases of slabs of finite thickness, multilayers, and even anisotropic materials [56–62]. In order to limit complications, we shall restrict ourselves to the vanishing absolute temperature limit ($T = 0$ K). Extension to the case of finite temperatures is standard, once the correct dielectric function is adopted, and it is treated in the References.

The most general geometry of the system is therefore that of two multilayer stacks described by layers of dielectric and magnetic permeability (ϵ_i, μ_i) constant within each layer separated by a gap of width s and with a semi-infinite space bounding the system to each side of the multilayers opposite to the gap. Upon choosing the (x, y) plane as parallel to the multilayer surfaces and the z-axis as perpendicular to those surfaces and oriented to the right, the Maxwell equations provide the general solutions for the bound state fields, which are assumed to exponentially decay for $z \to \pm\infty$. With this geometry, the solutions for the harmonic components of the electric field within the i-th layer can be written as (we shall assume non-magnetic media, or $\mu_i = 1$) [30, 50]:

$$\mathbf{E_i}(\mathbf{r}) = \left[e_{x,i}(z)\,\hat{\mathbf{i}} + e_{y,i}(z)\,\hat{\mathbf{j}} + e_{z,i}(z)\,\hat{\mathbf{k}} \right] e^{i(k_x x + k_y y)}\,, \tag{8.18}$$

where

$$\frac{d^2 e_{z,i}}{dz^2} - K_i e_{z,i} + 0\,, \tag{8.19}$$

and analogously for $e_{x,i}$ and $e_{y,i}$, so that the general solution is:

$$e_{z,i}(z) = A_i e^{K_i z} + B_i e^{-K_i z} \tag{8.20}$$

where

$$K_i^2 = k_\parallel^2 - \epsilon_i \frac{\omega^2}{c^2} \tag{8.21}$$

with $k_\parallel^2 = k_x^2 + k_y^2$ and ω a real quantity (clearly $i = \sqrt{-1}$ must not be confused either with the layer number index or with the x-axis versor); also notice that various layer numbering conventions exist in the literature and here we shall number all

layers in the left multistack by negative integers increasing in magnitude towards the left and by positive integers to the right, that is, $i = \cdots -2, -1 \cdots +1, +2 \ldots$ Also, from Eq. (8.20), the field to the left (right) of the leftmost (rightmost) boundary must vanish, that is, $B_{LL} = 0$ and $A_{RR} = 0$:

$$e_{z,LL}(z) = A_{LL} e^{K_{LL} z} \tag{8.22}$$

$$e_{z,RR}(z) = B_{RR} e^{-K_{RR} z} \tag{8.23}$$

8.2.4.1 Boundary Transition Matrix: Electrical Field Continuity

We can now write the electric field in two adjacent layers, generically referred as as left (L) and right (R):

```
ezL[kparal_, \[Omega]_, z_] =
  AL  Exp[KL[kparal, \[Omega]] z] + BL  Exp[-KL[kparal,
   \[Omega]] z] ;
ezR[kparal_, \[Omega]_, z_] =
  AR Exp[KR[kparal, \[Omega]] z] + BR  Exp[-KR[kparal,
   \[Omega]] z] ;
```

with obvious definitions, such as $K_{L,R} = K_{i-1,i} > 0$ and similarly for $\epsilon_{L,R}$, and `kparal`$\leftarrow k_{\parallel}$. Let us now apply the continuity condition to the normal component of the **D** field, which is guaranteed by imposing the continuity of ϵe_z and de_z/dz at the boundary.

$$\begin{pmatrix} A_R \\ B_R \end{pmatrix} = \begin{pmatrix} \mathcal{D}\mathrm{E}_{11} & \mathcal{D}\mathrm{E}_{12} \\ \mathcal{D}\mathrm{E}_{21} & \mathcal{D}\mathrm{E}_{22} \end{pmatrix} \begin{pmatrix} A_L \\ B_L \end{pmatrix} = \mathcal{D}^E_{\mathrm{LR}} \begin{pmatrix} A_L \\ B_L \end{pmatrix} \tag{8.24}$$

Requesting such continuity yields the coefficients on the right (R) of the left-most boundary, assumed conveniently placed at $z = 0$, in terms of the coefficients on the left (L), or in matrix form:

```
Solve[ \[Epsilon]L[\[Omega]] ezL[kparal, \[Omega], z]  ==
 \[Epsilon]R[\[Omega]]  ezR[kparal, \[Omega], z] &&
  D[ezL[kparal, \[Omega], z], z] == D[ezR[kparal,
   \[Omega], z], z] ,
   {AR, BR}][[1]]  /.  z -> 0
```

With these solutions, it is possible to build the boundary transition matrix, $\mathcal{D}^E_{LR}$, which yields the (A_R, B_R) coefficients on the right of the boundary by extracting the coefficients of the (A_L, B_L) constants, and we finally find:

```
\[ScriptCapitalD]E11[kparal_, \[Omega]_] =
  Expand[Coefficient[
    Solve[ \[Epsilon]L[\[Omega]] ezL[kparal, \[Omega],
           z]  == \[Epsilon]R[\[Omega]]  ezR[kparal,
            \[Omega], z] &&
```

```
        D[ezL[kparal, \[Omega], z], z] ==
       D[ezR[kparal, \[Omega], z], z] , {AR, BR}][[1, 1, 2]] /.
     z -> 0 , AL]];

\[ScriptCapitalD]E12[kparal_, \[Omega]_] =
  Expand[Coefficient[
    Solve[ \[Epsilon]L [\[Omega]] ezL[kparal, \[Omega],
           z]  == \[Epsilon]R[\[Omega]]  ezR[kparal,
            \[Omega], z] &&
        D[ezL[kparal, \[Omega], z], z] ==
       D[ezR[kparal, \[Omega], z], z] , {AR, BR}][[1, 1, 2]] /.
     z -> 0 , BL]];

\[ScriptCapitalD]E21[kparal_, \[Omega]_] =
  Expand[Coefficient[
    Solve[ \[Epsilon]L [\[Omega]] ezL[kparal, \[Omega],
           z]  == \[Epsilon]R[\[Omega]]  ezR[kparal,
            \[Omega], z] &&
        D[ezL[kparal, \[Omega], z], z] ==
       D[ezR[kparal, \[Omega], z], z] , {AR, BR}][[1, 2, 2]] /.
     z -> 0 , AL]];

\[ScriptCapitalD]E22[kparal_, \[Omega]_] =
  Expand[Coefficient[
    Solve[ \[Epsilon]L[\[Omega]] ezL[kparal, \[Omega],
           z]  == \[Epsilon]R[\[Omega]]  ezR[kparal,
            \[Omega], z] &&
        D[ezL[kparal, \[Omega], z], z] ==
       D[ezR[kparal, \[Omega], z], z] , {AR, BR}][[1, 2, 2]] /.
     z -> 0 , BL]];

\[ScriptCapitalD]ELR [
  kparal_, \[Omega]_] = {{\[ScriptCapitalD]E11[
    kparal, \[Omega]], \[ScriptCapitalD]E12[
    kparal, \[Omega]]}, {\[ScriptCapitalD]E21[
    kparal, \[Omega]], \[ScriptCapitalD]E22[
    kparal, \[Omega]]}}; MatrixForm[\[ScriptCapitalD]ELR [
  kparal, \[Omega]]]
```

$$\begin{pmatrix} \frac{\mathrm{KL(kparal},\omega)}{2\mathrm{KR(kparal},\omega)} + \frac{\epsilon \mathrm{L}(\omega)}{2\epsilon \mathrm{R}(\omega)} & \frac{\epsilon \mathrm{L}(\omega)}{2\epsilon \mathrm{R}(\omega)} - \frac{\mathrm{KL(kparal},\omega)}{2\mathrm{KR(kparal},\omega)} \\ \frac{\epsilon \mathrm{L}(\omega)}{2\epsilon \mathrm{R}(\omega)} - \frac{\mathrm{KL(kparal},\omega)}{2\mathrm{KR(kparal},\omega)} & \frac{\mathrm{KL(kparal},\omega)}{2\mathrm{KR(kparal},\omega)} + \frac{\epsilon \mathrm{L}(\omega)}{2\epsilon \mathrm{R}(\omega)} \end{pmatrix} \tag{8.25}$$

8.2.4.2 Translation Matrix

The next transformation matrix needed is a translation within a homogeneous (H) medium by a length equal to the thickness T of the generic layer so as to shift the next discontinuity placed at a generic location to the right to the origin $z = 0$:

$$\begin{pmatrix} A_{z+T} \\ B_{z+T} \end{pmatrix} = \begin{pmatrix} \Pi_{11} & \Pi_{12} \\ \Pi_{21} & \Pi_{22} \end{pmatrix} \begin{pmatrix} A_z \\ B_z \end{pmatrix} = \begin{pmatrix} \Pi_{11} & 0 \\ 0 & \Pi_{22} \end{pmatrix} \begin{pmatrix} A_z \\ B_z \end{pmatrix} = \Pi_{z,z+T} \begin{pmatrix} A_z \\ B_z \end{pmatrix} \tag{8.26}$$

Let us consider the solutions within such a homogeneous medium at generic coordinates z and at $z + T$:

```
ezH[kparal_, \[Omega]_, z_] =
 AH  Exp[KH [kparal, \[Omega]] z] + BH  Exp[-KH[kparal,
  \[Omega]] z] ezH[kparal, \[Omega], z + T]
```

where KH is equal to K_i within the layer. Therefore the translation matrix, which yields the solution at $z + T$ in terms of that at z, is, straightforwardly:

```
\[CapitalPi]11[kparal_, \[Omega]_, T_] =
  Simplify[Coefficient[ezH[kparal, \[Omega], z + T], AH]/
    Exp[KH [kparal, \[Omega]] z]] ;
\[CapitalPi]12[kparal_, \[Omega]_, T_] = 0. ;
\[CapitalPi]21[kparal_, \[Omega]_, T_] = 0. ;
\[CapitalPi]22[kparal_, \[Omega]_, T_] =
  Simplify[Coefficient[ezH[kparal, \[Omega], z + T], BH]/
    Exp[-KH [kparal, \[Omega]] z]] ;

\[CapitalPi][kparal_, \[Omega]_,
  T_] = {{\[CapitalPi]11[kparal, \[Omega], T], \[CapitalPi]12[
    kparal, \[Omega], T]}, {\[CapitalPi]21[kparal, \[Omega],
    T], \[CapitalPi]22[kparal, \[Omega],
    T]}}; MatrixForm[\[CapitalPi][kparal, \[Omega], T]]
```

$$\begin{pmatrix} e^{T\,\mathrm{KH}(\mathrm{kparal},\omega)} & 0. \\ 0. & e^{-T\,\mathrm{KH}(\mathrm{kparal},\omega)} \end{pmatrix} \tag{8.27}$$

8.2.4.3 Modes Due to Electric Field Continuity

In the archetypal case of two semi-infinite slabs, described by dielectric functions ϵ_{-1} and ϵ_{+1}, separated by a gap of medium ϵ_{Gap}, moving from left to right, the zones to consider are fewer than in the full case of stacks of finite thickness (we do not use the "0" subscript, as in ϵ_0, to avoid confusion with the SI symbol for the vacuum permittivity). Let us consider the modes associated with electric field continuity. The first boundary discontinuity is located at $z = 0$, between the left slab and the gap medium (assumed by Lifshitz to be the vacuum), described as:

$$\begin{pmatrix} A_0 \\ B_0 \end{pmatrix} = \mathcal{D}^E_{-1,0} \begin{pmatrix} A_{-1} \\ B_{-1} \end{pmatrix} \tag{8.28}$$

That is:

```
\[ScriptCapitalD]ELR1 [
  kparal_, \[Omega]_] = {{\[ScriptCapitalD]E11[
     kparal, \[Omega]], \[ScriptCapitalD]E12[
     kparal, \[Omega]]}, {\[ScriptCapitalD]E21[
```

```
      kparal, \[Omega]], \[ScriptCapitalD]E22[
      kparal, \[Omega]]}} /. {\[Epsilon]L[\[Omega]] ->
        \[Epsilon]m1 [\
\[Omega]], \[Epsilon]R[\[Omega]] ->  \[Epsilon]Gap[\[Omega]],
   KL[kparal, \[Omega]] -> Km1[kparal, \[Omega]],
   KR[kparal, \[Omega]] ->
   KGap[kparal, \[Omega]]} ; MatrixForm[\[ScriptCapitalD]ELR1 [
  kparal, \[Omega]]]
```

This is followed by translation through the gap assumed to be of width $T \to s$, that is:

$$\begin{pmatrix} A_{s+0} \\ B_{s+0} \end{pmatrix} = \Pi_{0,s+0} \begin{pmatrix} A_0 \\ B_0 \end{pmatrix} = \Pi_{0,s+0}\, \mathcal{D}^{e}_{-1,0} \begin{pmatrix} A_{-1} \\ B_{-1} \end{pmatrix} \tag{8.29}$$

and, finally, upon transforming over the boundary to the right of the gap, the overall transfer matrix is:

$$\mathcal{M}^{E}_{-1,+1} = \mathcal{D}^{E}_{0,+1}\, \Pi_{0,0+s}\, \mathcal{D}^{E}_{-1,0} \tag{8.30}$$

The conditions of field decay away from the gap demand that the (1,1) element of this result must vanish [58]. For reasons of space here we omit obvious steps and do not reproduce the unwieldy elements of the total matrix product. Standard manipulations by *Mathematica* to bring this condition into a familiar form (also omitted for brevity), yield the condition (see Ref. [30], Eq. (7.27)):

$$\frac{(\epsilon_{\text{Gap}} K_{-1} + \epsilon_{-1} K_{\text{Gap}})(\epsilon_{\text{Gap}} K_{+1} + \epsilon_{+1} K_{\text{Gap}})}{(\epsilon_{\text{Gap}} K_{-1} - \epsilon_{-1} K_{\text{Gap}})(\epsilon_{\text{Gap}} K_{+1} - \epsilon_{+1} K_{\text{Gap}})} e^{2K_{\text{Gap}} s} - 1 = 0\,. \tag{8.31}$$

The modes associated with magnetic field continuity are found in a completely analogous fashion, leading to (see Ref. [30], Eq. (7.28)):

$$\frac{(K_{-1} + K_{\text{Gap}})(K_{+1} + K_{\text{Gap}})}{(K_{-1} - K_{\text{Gap}})(K_{+1} - K_{\text{Gap}})} e^{2K_{\text{Gap}} s} - 1 = 0\,. \tag{8.32}$$

8.2.4.4 Lifshitz Expression

A reasoning in the complex plane, also due to Lifshitz, leads to consideration of an integrand for the dispersion force between two semi-infinite slabs separated by an empty gap ($\epsilon_{\text{Gap}} = 1$) as a double integral. A few standard changes of variable, also possible to implement within *Mathematica*, finally lead to the familiar expression for the Lifshitz pressure:

$$F_{\mathrm{Lif}}(s) = -\frac{\hbar}{2\pi^2 c^3}\int_1^{+\infty} dp\, p^2 \int_0^{+\infty} d\omega_I\, \omega_I^3 \times \left(\left[\frac{(s_{-1}+\epsilon_{-1}p)(s_{+1}+\epsilon_{+1}p)}{(s_{-1}-\epsilon_{-1}p)(s_{+1}-\epsilon_{+1}p)} e^{2\omega_I ps/c} - 1\right]^{-1} + \left[\frac{(s_{-1}+p)(s_{+1}+p)}{(s_{-1}-p)(s_{+1}-p)} e^{2\omega_I ps/c} - 1\right]^{-1}\right) \tag{8.33}$$

where ω_I is the imaginary part of the complex frequency, $\omega_C = \omega_R + i\omega_I$, the following variables were introduced:

$$s_{\pm 1} = +\sqrt{p^2 - 1 + \epsilon_{\pm 1}}\,, \tag{8.34}$$

and, on causality considerations, the dielectric function $\epsilon_{\pm 1}(\omega_I)$ is always real.

8.2.4.5 Suggested Exercise 6

Carry out the *Mathematica* manipulations leading to the results given above at Eqs. (8.31) and (8.32).

8.2.4.6 Suggested Exercise 7

Extend the above treatment to that of two possibly unequal slabs of finite thicknesses, a_L and a_R (compare your results to those in Ref. [50], Sec. 4.1.1.). Show that you can recover the above results in the limit of infinite thicknesses, $a_L, a_R \to +\infty$. What happens if the thickness of both slabs vanishes?

8.2.4.7 Suggested Exercise 8

Consider two bi-layers interacting across a gap. Show that you can recover the standard Lifshitz expression if the thickness of one layer vanishes while the other one diverges in each bi-layer.

8.2.4.8 Suggested Exercise 9

Recover the Casimir pressure expression by taking appropriate analytical limits ($\epsilon_{\pm 1} \to = \infty$) in the integrand at Eq. (8.33) and by using *Mathematica* to compute the integral. Show that:

$$F_{\mathrm{Cas}}(s) = -\frac{\hbar c \pi^2}{240\, s^4}\,. \tag{8.35}$$

8.2.4.9 Suggested Exercise 10

(a) Investigate the dependence of our results for the Lifshitz pressure and the unretarded Hamaker constant on the numerical values of the constants in the analytical expression of the dielectric function.
(b) How would you manipulate the dielectric function?
(c) By building upon the early treatment by Arnold, Hunklinger, and Dransfeld [63], and the more modern approach by Chen, Klimchitskaya, Mostepanenko, and Mohideen [64], formulate a model of illumination-dependent dielectric function (some possibly useful information is provided in Exercise 11).
(d) Calculate the Lifshitz pressure as a function of illumination for realistic values of parameters of interest, for instance, by using:

```
LifshitzPressure[s_] :=
 NIntegrate[
  LifshitzIntegrand[\[Omega]I, p, s], {\[Omega]I, 0,
   \[Infinity]}, {p,
    1, \[Infinity]},
  Method -> {"GlobalAdaptive",
    "SingularityHandler" -> "DuffyCoordinates"},
  WorkingPrecision -> 14, PrecisionGoal -> 10,
   MaxRecursion -> 50]
```

(e) Comment on the possibility to drive nano-oscillators by dispersion force manipulation (an example is given in Refs. [65–67]). Under what conditions can the system be driven into parametric resonance by this approach? Compare your result to that for a mechanically driven Casimir force parametric amplifier [68].

8.2.4.10 Suggested Exercise 11

Use the following naive model of the dielectric function of amorphous silicon (a:Si) (or any other Kramers-Kronig consistent one):

```
\[Epsilon]aSi[\[Omega]_] =
  1 + (\[Epsilon]1/(1 - (\[Omega] /\[CapitalOmega]1)^2 -
       I (\[Omega] /\[Gamma])));
```

with the following choices (ω is expressed in s^{-1}):

```
\[Epsilon]1 = 11.;
\[CapitalOmega]1 = 5.8 10^15;
\[Gamma] = 16.0 10^15;
```

(a) Using values of the natural constants in the MKS system, calculate the Lifshitz pressure in the $s = 0.01 - 10\,\mu$m. Identify unretarded and retarded limits and identify the onset of retardation. Use the unretarded behavior to estimate the Hamaker constant defined at Sect. 8.2.2.
(b) It has been said that the prediction that the Casimir pressure between two ideal surfaces at a distance of approximately 10 nm should be approximately equal

to 1 atmosphere is unphysical. What is the Lifshitz pressure between the two surfaces considered above across a 10 nm gap, expressed in atmospheres? What is the ratio of the Lifshitz to Casimir pressures in that case?

(c) What should the length of the side of four square pads be, if all placed within the same 10 nm distance of a highly polished ceiling, to hold the weight of one human being against the gravitational force of the earth? (assume a mass $m_{\text{human}} = 10^2\,\text{kg}$) [69].

8.3 "Perpetuum Mobile" Considerations

Given the non-trivial nature of the systems typically involved in the study of Casimir effects, it is not unusual to employ conservation arguments to uncover theoretical limitations, possible novel applications, or pitfalls leading to paradoxes connected to incompletely understood energy exchange processes in systems such as the one at Exercise 10(e) above [27, 70–72]. An additional example is the fierce debate[5] regarding the existence of "quantum friction," that is, a force expected to dampen the motion of two plane, parallel slabs moving transversally with respect to each other [74–78]. This friction can be interpreted as yet another fascinating manifestation of the electromagnetic vacuum state responsible for the *static* Casimir effect emphasized in this contribution. A suggestive description of this process is that "Qualitatively, with the inclusion of quantum fluctuations, the vacuum behaves as a complex fluid that hinders and influences the bodies moving through it" [79]. Although different viewpoints are possible [80], the fundamental origin of the friction, which requires neither roughness nor contact of any kind, can be seen to lie in the asymmetric reflection of virtual photons incident from different directions because of the relative motion of the two slabs [81]. This area of research continues to attract intense attention [82] with the earliest references cited [83] being traditionally those to the work by Teodorovich [84] and Levitov [85] along with important early contributions reported [86] to be due to Mahanti [87] and to Schaich and Harris [88].

In the most heated phase of the quantum friction debate, an appeal was made to an elementary mechanical gedanken experiment designed to logically demonstrate that the very existence of any such force would imply that "an unlimited amount of useful energy could be extracted from the quantum vacuum" [76].

The great apparent strength of this reasoning [76] lies in the fact that, if its conclusions were correct, hardly any treatment of quantum-electrodynamics would be necessary to decisively rule out the existence of quantum friction in the face

[5] The very personal ferocity surrounding Casimir effect controversies is, by itself, a subject worthy of social science study. For details about this particular exchange see, for instance, "A fraction too much friction causes physics fisticuffs" by Chris Lee [73]. For further details, and for the effect of such debates throughout the process of technology transfer, see Ref. [18].

of such strong energy conservation arguments. In fact, such proof, as presently formulated, appears to be of such broad applicability as to be able to rule out the existence of *any* friction – and even any lateral forces – between parallel moving plane surfaces in nature, regardless of their origin. However, such implications have gone completely unchallenged since the rebuttal stated: "There follows a discourse proving that there is no frictional force between two stationary media. I agree with this statement" [77].

Here we only consider this objection from an elementary mechanics standpoint and, while taking no position regarding all well known field theoretic treatments, we prove that the argument presented to show that quantum friction cannot exist [76] is logically flawed. As the entire reasoning hinges on simple mechanics and it is completely accessible to undergraduate students, appreciating this error has implications not only in our understanding of quantum electro-dynamics but also from the historical and pedagogical standpoints.

In that proof, the typical problem of a glass plate initially moving at a speed $\mathbf{u}$ with respect to a substratum held at rest in the laboratory frame is treated. A change in the reference frame is proposed on relativity grounds (Fig. 2, therein) as an artifice to expose a "paradox." Therefore it is stated that "a substrate ... assumed to be infinitely heavy" moves at a constant velocity $\mathbf{u}$ while constrained to be parallel to and under a glass plate of finite weight, initially at rest in the reference frame of the observer, and separated from the substratum by an empty gap of constant width (the author here employs the adjective "heavy" where *massive* is required).

The proposed proof is a classical *Reductio ad Absurdum* (Proof by Contradiction) [89]. If such a force as quantum friction existed, it is argued, "... the glass would be accelerated until its velocity matches the apparent velocity $\mathbf{u}$ of the substrate." This fact is employed to prove two statements: (A) "One could put an arbitrary number of cleverly designed glass pieces ... and let them become accelerated by the quantum vacuum." (B) "Quantum friction thus leads to the paradox that an unlimited amount of useful energy could be extracted from the quantum vacuum." Since (B) contradicts the principle of conservation of energy, it is concluded that quantum friction may not exist.

In order to explore the veracity of such statements, let us provide a more detailed and physically realistic description of this gedanken experiment. This can be done by assuming that the mass M_{sub} of the substratum be *finite* and possibly, but not necessarily, much larger than that of the glass plate, M_{plate}.

In principle, the quantity M_{sub} includes the entire subsystem to which the substratum is constrained, such as the Earth, or just the mass of a layer of material if the experiment is conducted in outer space. Since, as is acknowledged in the proof, Newton's Third Law applies in this case, the frictional force $\mathbf{F}_{\mathbf{fric}}$ acting on the glass plate must be at all times equal and opposite to that acting on the substratum, $-\mathbf{F}_{\mathbf{fric}}$, so that the total momentum of the system, absent any other external forces with non-vanishing horizontal component, will be rigorously conserved throughout the process.

As is well-known from the elementary mechanics treatment of one-dimensional inelastic collisions, the final speed of the substratum-glass-bar system in the new reference frame will eventually approach the asymptotic value, $\mathbf{v_{fin}} = M_{\text{sub}}\mathbf{u}/(M_{\text{sub}} + M_{\text{plate}})$ and the total energy change, ΔE, in terms of the total initial energy, E_{in}, *always negative*, will be to $\Delta E = -E_{\text{in}} M_{\text{plate}}/(M_{\text{sub}} + M_{\text{plate}}) < 0$.

These results show that, as the practically unattainable limit $M_{\text{sub}}/M_{\text{plate}} \to +\infty$ is approached, regardless of any quantum-electrodynamical details, the final velocity of the substratum-glass-bar system will indeed be $\mathbf{v_{fin}} \to \mathbf{u}^-$, consistently with (A). However, there will be no energy gain as $\Delta E \to 0^-$ in that limit, unlike claimed at (B), due to a correspondingly small, but here logically critical, negative difference in the speed of the final system with respect to the initial speed of the massive substratum.

The reasoning error may have been caused by the assumption that, in the more typical reference frame in which the glass plate is moving and the substratum is at rest, the final state of the system should correspond to a substratum-glass-bar system at rest after a long interaction. Although this assumption is practically correct in a ground-based laboratory, the final speed of the substratum-glass-bar system rigorously speaking does not vanish. In order to eliminate such mistaken assumptions, it may be helpful to visualize the substratum as a wedge-shaped "glider" of the type used in some elementary mechanics demonstrations with the glass plate represented by another glider of *finite* mass constrained to freely slide on top of it while they both ride an "airtrack" – a variation on the theme of a well-known experiment [90].

A different gedanken experiment, which adheres even more strictly to the typical theoretical treatments of quantum friction, consists of assuming that an external force $\mathbf{F_{ext}}$ be acting directly on the substratum so as to keep it at a *constant* velocity $\mathbf{u}$ in the laboratory reference frame. In this case, the substratum-glass-bar system, of total mass $M_{\text{sub}} + M_{\text{plate}}$, will, after a long interaction time, by hypothesis *already* be moving with a velocity $\mathbf{u}$. However, in order to maintain the substratum at a constant velocity, Newton's Second Law requires that $\mathbf{F_{ext}} = -\mathbf{F_{fric}}$. Therefore, although after a long interaction the final kinetic energy of the glass plate will indeed have increased by $\Delta E_{\text{plate}} = +\frac{1}{2} M_{\text{plate}} |\mathbf{u}|^2$ as claimed at (B), the total mechanical work done by the force $\mathbf{F_{ext}}$ on the substratum will equal $W_{\text{ext}} = -\frac{1}{2} M_{\text{plate}} |\mathbf{u}|^2$. Therefore, the net total energy change will be exactly $\Delta E = 0$.

Historically, powerful gedanken experiments in which requiring that an absurd state of *perpetuum mobile* be avoided to obtain the correct solution to a mechanical problem were made famous by Simon Stevin (1548/49–1620), who even placed one on the title page of his *Hypomnemata Mathematica* (1605–1608) [91–93] to the enthusiastic approval of Ernst Mach (Ref. [94], p. 24). In the present case, however, it appears that the proposed reasoning fails to allow for any conclusions against, or in favor of, the existence of frictional forces, whether they be due to quantum fields or to any other interaction.

8.4 Conclusions

It is appropriate to end by returning to the two opening statements by Maxwell quoted in the Introduction. As we have explored in this contribution, the concept that "No force, either of attraction or of repulsion, can be observed between an electrified body and a body not electrified" [1] requires a far more sophisticated interpretation. Although Coulomb's law – a cornerstone in the edifice of electrodynamics coded into our minds ever since primary school – predicts that a neutral point-like particle shall not interact with a charged point-like particle, that needs not clash with the existence of dispersion forces. In this contribution, we have explored much evidence to eliminate misconceptions so as to develop the opposite expectation, that is, that polarizable bodies *always* electrodynamically interact even if they are neutral and such interaction may well be dominant. To that end, we had to explore the profoundest implications of the latter statement by Maxwell, that "When, in any case, bodies not previously electrified are observed to be acted on by an electrified body, it is because they have become *electrified by induction*." This is the first link in the long logical chain leading to an operational understanding of the technological opportunity represented by dispersion force engineering.

An important historical question deserves to be considered at last: "Given the above statements, could Maxwell contribute to our modern understanding of intermolecular forces?" And, more explicitly: "If the existence of dispersion forces can be accommodated, or at least hypothesized, within the structure of classical electrodynamics, did Maxwell make that logical connection?" In what follows, we analyze this issue often by directly quoting from the writings of the protagonists of the period.

Our motivation in exploring this issue is the recurring theme among scientists and historians of science alike – whether implicitly or explicitly stated – as to whether Maxwell could have made further progress towards elucidating those fundamental questions by reaping a fuller harvest of the mathematical physics machinery of the *Treatise*. In the opinion of the present author, as regards Maxwell's abilities and persistence in probing difficult issues, this line of inquiry should realistically consider his death from abdominal cancer in 1879 at the relatively young age of 48 after "bringing to bear on a subject still full of obscurity the steady light of patient thought and expending upon it all the resources of a never failing ingenuity." (Ref. [95], Vol. I, Preface) Indeed, Freeman Dyson, referring to Maxwell's Presidential Address to Section A of the British Association in 1870, only points out that "It is difficult to read Maxwell's address without being infuriated by his excessive modesty ..." and, writing on *Missed Opportunities*, he turns the tables on the critics with a scorching criticism of his own: "But the mathematicians of the nineteenth century failed miserably to grasp the equally great opportunity offered to them in 1865 by Maxwell. If they had taken Maxwell's equations to heart as Euler took Newton's, they would have discovered, among other things, Einstein's theory of special relativity, the theory of topological groups and their linear representations, and probably large pieces of the theory of hyperbolic

differential equations and functional analysis. A great part of twentieth century physics and mathematics could have been created in the nineteenth century, simply by exploring to the end the mathematical concepts to which Maxwell's equations naturally lead" [96].

However, apart from the temptation to engage in counterfactual history [97] speculations – what Carr referred to as "parlour games" [98] – about Maxwell's alleged omissions, there is merit in investigating classical electrodynamics as a logical tool to clarify the role of quantization in dispersion force theory, to strengthen semi-classical arguments and to develop new expository approaches. The logical pathways presented herein suggestively illustrate that Coulomb's law with point-like, *non-polarizable* neutral particles does *not* imply that *polarizable* neutral particles should not interact. A description of dispersion forces as a natural consequence of classical electrodynamics can greatly aid to provide much needed pedagogical devices for use by educators [25], to dispel the widespread concept of the Casimir effect as a "mystery," to enhance effective communication with investors, the media and the public, and to stimulate confidence in the viability of dispersion force engineering startup and spin-off companies [18].

Chronologically, it is relevant to notice that the first edition of the *Treatise* dates to 1873, or thirty-three years after Whitworth's report at the Glasgow meeting of the British Association (Ref. [99], p. 4) and only two years before Tyndall's paper read at the Royal Institution [16], which means that the contemporary state of the art in cohesion experimentation had to be well known to Maxwell. As far as atomistic theory – regarded as the indispensable framework of dispersion force physics – in the words of Maxwell's early biographer, "we are indebted for all the modern developments of the molecular theory of gases, as well as for its establishment on a sound dynamical basis," [100] mainly to Clausius, Boltzmann, and Maxwell. More specifically about molecular interactions, as shown even just by his famous entry on *Capillary Action* in the 9th edition of the *Encyclopædia Britannica* (Ref. [95], Vol. II, p. 541), Maxwell's contribution to early explorations in the nature of molecular forces was nothing short of substantial and is, by itself, the subject of extensive studies [101]. Coulson, also cited by El'yashevich and Prot'ko [102], provides a list of related "problems advanced by Maxwell: (1) What is a molecule and what is the nature of the aggregate of atoms of which it consists? (2) What is the origin of intermolecular or interatomic forces? And what is their law of dependence on distance and orientation? (3) Why are molecules so invariable in character with no evolutionary or continuously varying properties? (4) How does a molecule form?" [103].

Coulson summarizes the situation by stating that "Maxwell had almost got to the limit of what he could have done in the discussion of interatomic forces" and he names a formidable list of items unavailable to Maxwell including "the discovery of the electron... the nuclear atom, ... electron shells, ... stationary states, ... the wave equation, and ... the Pauli exclusion principle" [103]. Use of the adverb "almost" is due to the opinion that "Maxwell could have been expected to make further progress than he did" only in the latter of items (2), that is, in ascertaining the "form of the interatomic and intermolecular force ... by making more use of Clausius' virial

theorem." If so, what can be said about "the origin of intermolecular or interatomic forces" by means of Maxwell's equations? Coulson reflects on "how impossible it was that Maxwell should have been able to describe either the dispersion attractive forces, or the spin repulsion and attractions." The assessment is that accounts of interatomic force physics before and after the development of modern quantum theory "appear to have almost nothing in common" [103].

This peremptory position is justifiable from the standpoint of modern quantum electrodynamics but it fails to capture the subtler mathematical implications of Maxwell's equations. For instance, shortly after Maxwell's early death, Lebedev could already discern such connections with extraordinary clarity and rare intuition in his doctoral dissertation: "Hidden in Hertz's research, in the interpretation of light oscillations as electromagnetic processes, is still another as yet undealt with question, that of the sources of light emission ... such a problem leads us ... quite unexpectedly as it were, to one of the most complicated problems of modern physics – the study of molecular forces. Adopting the point of view of the electromagnetic theory of light, we must state that between two radiating molecules, just as between two vibrators in which electromagnetic oscillations are excited, there exist ponderomotive forces: They are due to the electrodynamics interaction between the alternating electric current in the molecules (according to Ampere's laws) or the alternating charges in them (in accord to Coulomb's laws); we must therefore state that there exist between the molecules in such a case molecular forces whose cause is inseparably linked with the radiation processes ..."[6] The obvious modern objection to any argument based on the "radiation process" is that atoms, in their stationary states, are in fact *not* radiating. This same severe limitation is mentioned much later by Casimir in his critique of Overbeek's intuitive, but "misleading" [107, 108] model – an imperfect model that, as Casimir nevertheless generously repeats, provided the initial impetus towards the expression for the Casimir-Polder force. Disregarding this issue of principle, in order to anticipate the connection to dispersion forces, Maxwell would have had to speculate about the inner structure of the atom to conclude that their charged constituents, if driven from their positions of equilibrium, will oscillate, radiate, and interact as Lebedev suggested. In the present work, we took advantage of Lorentz atomic models "to go further than Maxwell" (Ref. [109], §122) but, as remarked by Coulson, [103] Maxwell's description of polarized matter had to be formulated prior to the discovery of the electron by J. J. Thomson in 1897 [110, 111]. Although the historical development of our understanding of molecular structure following Maxwell is a complex subject [2, 112–114], Yaghjian judges that "the closest he seems to approach the idea of dielectrics containing dipoles is ... in explaining the theory of Mossotti that a dielectric contains small conducting elements insulated from one another and capable of charge separation (forming dipoles)" [115].

[6]This is a translation into English quoted in Ref. [104]; see also Ref. [105] (in German) and Ref. [106] (in Russian).

Mossotti's results [116, 117] regarding atomic structure "were based on an ether concept typical of his epoch, and are hence difficult to follow for the modern reader" [118]. Remarkably, however, Mossotti "utilised a mathematical method which had been developed by Poisson for the examination of a similar question in magnetism." (Ref. [119], §142–151; see also Ref. [112], pp. 188–189). As explained much later by Van Vleck, "this concept of the polarization of the molecule as the cause of the departures of ϵ and μ from unity is by no means a purely twentieth-century concept, and was intimated by Faraday" [120]. Indeed, Mossotti's starting point had been Faraday's conclusion that "it is the molecules of the substances that polarize as wholes ... and that however complicated the composition of a body may be, all those particles or atoms which are held together by chemical affinity to form one molecule of the resulting body, act as one conducting mass or particle ..." (Ref. [121], §1699–1700). Van Vleck continues: "In 1836, Mossotti pictured the molecule as a conducting sphere of radius a, on which the charge would, of course, readjust or 'polarize' itself under the influence of an applied field, thus making the molecular moment different from zero. If the electric susceptibility χ_e is small compared to unity, he thereby showed that $\chi_e = Na^3$. It seems almost too hackneyed to mention that the values of a obtained from this simple equation (together with the observed N and χ_e) are comparable in magnitude with the molecular radii in kinetic theory" [120] (N is the number of atoms in the unit volume; see also Ref. [122], Sec. 10.12).

Maxwell was obviously deeply affected by Mossotti's work, which he repeatedly cites and critiques over a period of several years, somewhat appearing to vacillate between acceptance and doubt but never fully endorsing it. For instance, in 1841, in a short communication devoted to that subject, Maxwell writes that "although M. Mossotti's general view may be correct, I believe it will be found that his analysis is erroneous" [123]. In 1864, in *A dynamical theory of the electromagnetic field*, Maxwell lucidly explains that "in a dielectric under the action of electromotive force, we may conceive that the electricity in each molecule is so displaced that one side is rendered positively and the other negatively electrical, but that the electricity remains entirely connected with the molecule, and does not pass from one molecule to the other"[7] [95] (Vol. I, p. 526). In 1869, in his paper *On the Mathematical Classification of Physical Quantities*, he judges rather ungenerously that "Mossotti ... was enabled to make use of the mathematical investigation of Poisson relative to magnetic induction, merely translating it from the magnetic language into the electric, and from French into Italian" [95] (Vol. II, p. 258). Finally, in the *Treatise*, Maxwell comments that "This theory of dielectrics is consistent with the laws of electricity, and may be actually true." (Vol. I, §62).

The early proof by Mossotti [117], recast by Jeans in modern notation (Ref. [119], §149), remains a standard textbook calculation in the electrostatics of dielectric media to this day. Of particular interest in our case are the even simpler model with one central, point-like positive charge surrounded by a cloud

[7] Here "a molecule is the smallest possible portion of a particular substance." [123] (Vol. II, p. 46).

with homogeneous negative charge density [122] and that of two homogeneously, opposite charged spheres superimposed to each other in the absence of an external field [124]. In both cases, the polarizability of the system is shown to be $\alpha \approx a^3$. As pointed out by Lorentz (Ref. [109], §124), such results are only rigorously valid for the static polarizability, which was extended to include the dynamic polarizability by treating the time-dependent case first by Lorenz [125] and, independently, by Lorentz himself – "certainly a curious case of coincidence" [109].

In the Introduction, we stated that two neutral, polarizable particles will not interact "if an independent means to produce polarization is absent." In fact, Spruch considered the dipole-dipole interaction of two particles of dynamic polarizabilities $\alpha_{1,2}(\omega)$ within a volume $\mathcal{V}$ much larger than the size of the particles, and immersed within a background *classical* field $\mathbf{E_0}(\omega, \mathbf{r})$, where $\mathbf{r}$ is the position vector [126]. On realizing that – consistently with Lebedev's and Overbeek's intuitions – only the "radiation" term proportional to $1/r$ contributes to the potential, $V^{\text{class}}_{\text{pol pol}}(r)$, and by introducing the energy density $u(\omega) = |\mathbf{E_0}(\omega, \mathbf{r})|^2$ of the mode of frequency ω of the smoothly varying electric field, this treatment leads to the following result:

$$V^{\text{class}}_{\text{pol pol}}(r) = \frac{\mathcal{V}}{c^5 r} \int_0^{c/r} \alpha_1(\omega)\alpha_2(\omega)\, u(\omega)\, \omega^4\, d\omega\,. \tag{8.36}$$

Crucially, Spruch comments that the above is "a result that Maxwell could have derived, and perhaps did" [126]. The first part of this statement – once again in the tradition of results Maxwell allegedly missed – is correct but quite bold given the logical chain we have seen is needed to reach the concept of dynamic polarizability even if just with a rudimentary model for a "molecule." The latter part of the statement, although an effective 'narrative hook,' is probably fictional.

The connection between the above equation and quantum electrodynamics takes place by simply writing the energy density per mode of the zero-point field as $\mathcal{V}u(\omega) = \frac{1}{2}\hbar\omega$, thus leading to the Casimir-Polder potential, V_{C-P}, only as "the last step" [126]:

$$V_{C-P} \sim -\frac{\hbar c \alpha_1(0)\alpha_2(0)}{r^7} \tag{8.37}$$

However, the presence of this random field of intensity proportional to $\hbar$ in Spruch's approach does *not* imply that quantization of the electromagnetic field is needed to reach the Casimir-Polder expression. In fact, simply the introduction of a fluctuating *classical* field of appropriate specific energy density leads to the same mathematical results obtained by the methods of QED. This was stressed by Casimir, who, writing one year before his death in 2000, commented on this approach that "The problem in quantum electrodynamics is then reduced to a problem in classical electrodynamics" [20].

As Spruch and Kelsey explained: "Why vacuum-fluctuation arguments worked in the past in the problems to which they were applied is, to our knowledge, not completely understood, but the simplicity of the approach gives it considerable

appeal, as a means of providing physical insight into known results and as a means of suggesting new results" [127]. Consequently, a very extensive literature reporting dispersion force calculations now exists based not on standard field quantization but on the injection into the system of an appropriate classical field – an approach sometimes referred to as 'random' or 'stochastic' electrodynamics (SED) [128–132].

A succinct and lucid presentation of the logical premises of SED has been given by Milonni (Ref. [30], Sec. 8.12; see also Ref. [133], Sec. 5). He explains: "In QED we cannot arbitrarily set to zero the homogeneous, source-free solution of the Maxwell operator equations in the Heisenberg picture. This "vacuum" field is necessary for the formal consistency of QED... Classically, however, we generally assume implicitly that the homogeneous solution of the Maxwell equations is that in which the electric and magnetic fields vanish identically. That is, we assume that there are no fields in the absence of any sources... This difference between classical and quantum electrodynamics, together with the evident importance of the fluctuating vacuum field in QED, suggests the adoption of a different boundary condition in classical electrodynamics: instead of assuming that the classical field vanishes in the absence of sources, we can assume that there is a fluctuating *classical* field with zero-point energy $\frac{1}{2}\hbar\omega$ per mode. Whether it is a better working assumption than the standard, "obvious" one is a matter to be ultimately decided by comparison with experiment" [30]. From this point of view, important parallels and connections exist with the cosmological constant problem, which has been speculated to be connected to gravitating zero-point energy affecting the expansion of the universe [134–136].

Fascinatingly, as first shown by Marshall [128], any classical zero-point field of spectral energy density $\rho_0(\omega) \propto \omega^3$ is Lorentz invariant; furthermore, the specific choice $\rho_0(\omega) = \hbar\omega^3/2\pi^2c^3$, well known from QED, causes a mean square displacement fluctuation in a classical charged harmonic oscillator equal to that of the corresponding quantum problem. Shortly after these findings, Boyer proposed to elevate the Lorentz invariance of the zero-point spectrum to the role of an SED postulate [137, 138]. Therefore, "...we require that the spectrum of the radiation shall look the same to all observers moving at constant relative velocity with respect to each other" [137] and "... $\hbar$ enters our theory, not as any quantum of action, but solely as the constant setting the scale of the zero-point electromagnetic radiation spectrum" [139].

As Boyer reported, "Some readers of this classical electromagnetic analysis are distressed, even indignant at the idea of a "classical" electromagnetic zero-point radiation. They insist that zero-point radiation is a "quantum" idea which can not be used as part of classical physics. However, surely this objection is without merit" [131]. Such strong opinions also transpire from scientific language usage. For instance, Boyer judges that "The idea of quanta forms a subterfuge for what is a natural part of a theory of classical statistical thermodynamics including electromagnetism," [139] using the noun *subterfuge* three more times in the course of the same paper. As though in direct response, Milonni, typically quite impartial, turns the same terminology against random electrodynamics, which he describes

as "at best an interesting subterfuge" (Ref. [133], Sec. 5.2) before using the same term twice more in the same paper (Ref. [133], Sec. 5.5). The sometimes acrimonious debate as to the reasons non-fully quantum theories of dispersion forces lead to correct results – only partially within our scope herein – continues unabated to this day [18, 140] as this approach is now also being tested to probe spacetime fluctuations in the weak field limit of the gravitational field, for which no quantization scheme is yet known [22, 141].

The adoption of a classical random field described by $\hbar$ "...as a multiplicative constant chosen by comparison of theoretical predictions with experiment" [30] changes none of the mathematical findings by Spruch. In the fully retarded regime in which the only significant contribution to the integral at Eq. (8.36) comes from the static polarizabilities $\alpha_{1,2}(0)$ – provided by experimental measurements – we finally recover the quantum electrodynamical Casimir-Polder expression, $V_{\mathrm{C-P}}$, from completely classical considerations (see Ref. [142], Sec. IV). The classical picture of dispersion forces to emerge is therefore that of an interaction caused by a Lorentz invariant stochastic field postulated to fill the universe and driving the process of mutual atomic polarization.[8]

On the one hand, from the historical point of view, we can now ask: "Was such a description within Maxwell's hypothetical reach?" As we have seen, this would have required both a model for the dynamical polarizability – or at least its static limit – and the concept referred to today as the Lorentz covariance of Maxwell's equations as the framework to accommodate a classical zero-point field. Strictly speaking, covariance would not be understood till after Maxwell's death, that is, at the very earliest, till the little cited discovery of the "Voigt transformations," [143–146] in 1887 and the later critical re-elaborations by Lorentz and Poincaré [147, 148]. Even with such machinery, however, the existence of homogeneous solutions of Maxwell's equations different than the "true vacuum" (all fields equal to zero) was not truly appreciated till the use by Lifshitz [54] of Rytov's "random field" [149] and the much later work by Marshall cited above. Of course, an appreciation of the fact that any external field, invariant or not, could "drive" dispersion forces as shown by a rudimentary model of polarizability was within Maxwell's potential reach, and that might have led to further speculations as to the form of the intermolecular potential even earlier than the discovery of invariance. In fact, as we have explored in this work, introduction of external fields is a common strategy to engineer dispersion forces [132]. If the existence of random fields had been speculated and if dynamical polarization had been at least tentatively modeled, Maxwell could have logically connected electromagnetism to the existence of dispersion forces and to cohesion. All such suppositions, however, must deal with the reality of Maxwell's early death and one is left speculating the many ways in which he would have further contributed to physics if, as for Casimir, his life had spanned 90 years, or till 1921.

[8] This concept might be a provocative solution of 'double-starred' Prob. 10.31, "Mutually induced dipoles" in *Electricity and Magnetism* by Purcell and Morin [122].

Acknowledgements I am grateful to Professor Di Bartolo, Director, for his gracious invitation to participate – as a humble student – in the NATO Advanced Study on "Quantum Nanophotonics," and for much more. I was particularly touched by the splendid atmosphere created by the Organizers, Maura Cesaria and Luciano Silvestri, and wish to thank many fellow-students for their great interest in Casimir forces and for their inspiring comments to the lectures I presented. I dedicate this contribution to my father, Italo Pinto (1928–2017), who passed away before the Proceedings could appear in print, for a lifetime of steadfast encouragement and support in the pursuit of my dreams to investigate the secrets of the universe and communicate that enthusiasm and curiosity to others.

Bibliography

1. Maxwell JC (1954) A treatise on electricity and magnetism (vol I and vol II), 2nd edn. Dover Publications, Inc., New York
2. Darrigol O (2000) Electrodynamics from Ampère to Einstein. Oxford University Press, Oxford
3. Thomson W (1st Baron Kelvin) (1884) Reprint of papers on electrostatics and magnetism, 2nd edn. Macmiillan & Co., London
4. Faraday M (1844) Experimental researches in electricity (vol II). Richard and John Edward Taylor, London
5. Hirsch EDJ (1992) What your third grader needs to know. Dell Publishing, New York
6. Hewitt PG (1999) Conceptual physics, 3rd edn. Addison-Wesley, San Francisco
7. Hagelstein F, Miskimen R, Pascalutsa V (2016) Prog Part Nucl Phys 88:29
8. Hewitt PG (2006) Conceptual physics, 10th edn. Addison-Wesley, San Francisco
9. Babb JF, Higa R, Hussein MS (2017) Eur Phys J A 53:126
10. Pinto F (2016) In: Third IEEE international workshop on metrology for aerospace. IEEE, Florence, p. (Paper ID: 4292221)
11. Boyle R (1669) A continuation of new experiments. Henry Hall printer to the University, Oxford
12. Shapin S, Schaffer S (1985) Leviathan and the air pump: Hobbes, Boyle, and the experimental life. Princeton University Press, Princeton
13. Sparnaay MJ (1989) In: Sarlemijin A, Sparnaay MJ (eds) Physics in the making, essays on developments in 20th century physics in honour of H. B. G. Casimir. North-Holland, Amsterdam, pp 235–246
14. Newton I (1704) Opticks, 4th edn. William Innys at the West-End of St. Paul's
15. Whitworth J (1858) Miscellaneous papers on mechanical subjects. Longman, London
16. Tyndall J (1875) Proc R Inst Great Britain 7:524
17. Feynman R, Leighton RB, Sands M (1963) Feynman's lectures on physics. Caltech, Pasadena
18. Pinto F (2018) In: Schulz MJ, Shanov VN, Yin J, Cahay M (eds) Nanotube superfiber materials, science to commercialization, chap 30. Elsevier
19. Casimir HBG (1948) Proc Kon Ned Akad Wetenshap 51:793
20. Casimir HBG (2000) In: Babb JF, Milonni PW, Spruch L (eds) Comments on atomic and molecular physics, comments on modern physics. Part D (Special issue: Casimir forces), vol 1. Gordon and Breach Science Publishers, Malaysia, pp 175–177
21. Hasher L, Goldstein D, Toppino T (1977) J Verbal Learning Verbal Behav 16:107
22. Pinto F (2016) Class Quantum Grav 33:237001
23. Cooper MM (2015) J Chem Ed 92:1273
24. Underwood SM, Reyes-gastelum D, Cooper MM (2016) Chem Educ Res Pract 17:365
25. Becker N, Noyes K, Cooper M (2016) J Chem Ed 93:1713
26. Pinto F (2012) 48th AIAA/ASME/SAE/ASEE joint propulsion conference (JPC) & exhibit, July. AIAA, Atlanta, pp 1–31. https://doi.org/10.2514/6.2012-3713

27. Pinto F (2014) Am Sci 102:280
28. Dubin D (2003) Numerical and analytical methods for scientists and engineers using mathematica. Wiley-Interscience, Hoboken
29. Cohen-Tannoudji C, Diu B, Laloë F (1977) Quantum mechanics. pp 1130–1140
30. Milonni PW (1994) The quantum vacuum. Academic Press, San Diego
31. Wang SC (1927) Phys Z 28:663
32. London F (1937) Trans Faraday Soc 33:8
33. Karplus M, Porter RN (1970) Atoms & molecules. The Benjamin/Cummings Publishing Company, Menlo Park
34. Kleppner D (1990) Phys Today 43(10):9
35. Landau LD, Lifshitz EM (1976) Mechanics, 3rd edn. Pergamon Press, Oxford
36. Goldstein H, Poole C, Safko J (2002) Classical mechanics, 3rd edn. Addison Wesley, San Francisco
37. Farina C, Santos FC, Tort AC (1999) Am J Phys 67(4):344
38. Axilrod BM, Teller E (1943) J Chem Phys 11(6):299
39. de Boer JH (1936) Trans Faraday Soc 32:10
40. Verwey EJW, Overbeek JTG (1948) Theory of the stability of lyophobic colloids. Elsevier Publishing Company, Inc., New York
41. Hamaker H (1937) Physica 4(10):1058
42. González AE (1985) Physica 131A:228
43. Milonni PW, Cook RJ, Goggin ME (1988) Phys Rev A 38(3):1621
44. Landau LD, Lifshitz EM (1975) The classical theory of fields, 4th edn. Pergamon Press, Oxford
45. Kupiszewska D, Mostowski J (1990) Phys Rev A 41(9):4636
46. Pinto F (2009) Phys Rev A 80:042113
47. Dowling JP (1989) Math Mag 62(5):324
48. Hardy GH (1949) Divergent series. Oxford University Press, London
49. Arfken G, Weber HJ (2013) Mathematical methods for physicists. Elsevier Academic Press, Amsterdam
50. Bordag M, Mohideen U, Mostepanenko VM (2001) Phys Rep 353:1
51. Ellingsen SA (2006) Casimir effect in plane parallel geometry. Ph.D. thesis, Norwegian University of Science and Technology
52. Boyer TH (1974) Phys Rev A 9(5):2078
53. Hushwater V (1997) Am J Phys 65(5):381
54. Lifshitz EM (1956) Sov Phys JETP 2(1):73
55. Podgornik R, Hansen PL, Parsegian VA (2003) J Chem Phys 119:1070
56. Abelès F (1950) Ann Phys Paris 5:596
57. Born M, Wolf E (1970) Principles of optics, 4th edn. Pergamom Press, Oxford
58. Ninham BW, Parsegian VA (1970) J Chem Phys 52(9):4578
59. Zhou F, Spruch L (1995) Phys Rev A 52(1):297
60. Bendickson J, Dowling JP, Scalora M (1996) Phys Rev B 53(4):4107
61. Parsegian VA (2006) Van der Waals forces. Cambridge University Press, Cambridge
62. Veble G, Podgornik R (2009) Phys Rev B 80:075422
63. Arnold W, Hunklinger S, Dransfeld K (1980) Phys Rev B 21(4):1713
64. Chen F, Klimchitskaya GL, Mostepanenko VM, Mohideen U (2007) Phys Rev B 76:035338
65. Pinto F (2014) Int J Mod Phys D 23(12):1442001
66. Pinto F (2016) TAUP 2015: proceedings of the XIV international conference on topics in astroparticle and underground physics. J Phys Conf Ser 718, Fornengo N, Regis M, Zechlin HS (eds) IOP Publishing, Turin, p 072004
67. Pinto F (2017) In: Proceedings of the fourteenth Marcel Grossmann meeting on general relativity Bianchi M, Jantzen RT, Ruffini R (eds) (World Scientific, Singapore, pp 3175–3182
68. Imboden M, Morrison J, Campbell DK, Bishop DJ (2014) J Appl Phys 116:134504
69. Hawkes EW, Eason EV, Christensen DL, Cutkosky MR (2015) J R Soc Interface 12(102):20140675. https://doi.org/10.1098/rsif.2014.0675

70. Forward RL (1984) Phys Rev B 30(4):1700
71. Pinto F (1999) Phys Rev B 60(21):14740
72. Maclay G (2010) Phys Rev A 82(3):032106
73. Lee C (2009) Ars Technica 11(3). http://arstechnica.com/science/news/2010/06/a-fraction-too-much-friction-or-not-who-knows.ars
74. Philbin TG, Leonhardt U (2009) New J Phys 11(3):033035
75. Pendry JB (2010) New J Phys 12(3):033028
76. Leonhardt U (2010) New J Phys 12(6):068001
77. Pendry JB (2010) New J Phys 12(6):068002
78. Volokitin A, Persson BNJ (2011) New J Phys 13(6):068001
79. Kardar M, Golestanian R (1999) Rev Mod Phys 71(4):1233
80. Maghrebi MF, Golestanian R, Kardar M (2013) Phys Rev A 88(4):042509
81. Pendry JB (1997) J Phys Condens Matter 9:10301
82. Silveirinha MG (2014) New J Phys 16(6):063011
83. Milton KA (2011) Am J Phys 79(7):697
84. Teodorovich EV (1978) Proc R Soc Lond A 362(1708):71
85. Levitov LS (1989) Europhys Lett 8(6):499
86. Kyasov AA, Dedkov GV (2000) Surf Sci 463(1):11
87. Mahanty J (1980) J Phys B At Mol Opt Phys 13(22):4391
88. Schaich W, Harris J (1981) J Phys F Met Phys 11:65
89. Solow D (2009) How to read and do proofs. Wiley, New York
90. Keig WE (1985) Am J Phys 53(11):1084
91. Ord-Hume AWJG (1977) Perpetual motion: the history of an obsession. San Martin's Press, Inc, New York
92. Sorensen RA (1991) Am Sci 79(3):250
93. Sorensen RA (1992) Thought experiments. Oxford University Press, New York
94. Mach E (1919) The science of mechanics: a critical and historical account of its development. The Open Court Publishing Co., Chicago/London
95. Maxwell JC (1965) The scientific papers of James Clerk Maxwell. Dover Publications, Inc., New York
96. Dyson FJ (1972) Bull Am Math Soc 78(5):635
97. Bunzl M (2004) Am Hist Rev 109(3):845
98. Carr EH (1961) What is history? Cambridge University Press, Cambridge
99. Goodeve TM, Shelley CPB (1877) The Whitworth measuring machine. Longmans, Green, and Co., London
100. Campbell L, Garnett W (1882) Life of James Clerk Maxwell. Macmiillan & Co., London
101. Rowlinson JS (2002) Cohesion – a scientific history of intermolecular forces. Cambridge University Press, Cambridge
102. El'yashevich MA, Prot'ko TS (1981) Sov Phys Usp 24:876
103. Coulson CA (1962) Nature 195:744
104. Derjaguin BV (1967) Sov Phys Usp 10:108
105. Lebedev P (1894) Annalen der Physik und Chemie 52:621
106. Lebedev P (1963) Collected works. Izdatel'stvo Akademii Nauk S.S.S.R., Moscow-Leningrad
107. Casimir HBG (1998) Essays in honour of Victor Frederick Weisskopf (Physics and society). Springer, New York, pp 53–66
108. Casimir HBG (1987) In: Greiner W (ed) Physics of strong fields. Springer, pp 957–964
109. Lorentz HA (1916) The theory of electrons. B. G. Teubner, Leipzig
110. Thomson JJ (1897) Philos Mag 90:S1:25
111. Falconer I (1987) BSHS 20:241
112. Whittaker ET (1910) A history of the theories of Aether and electricity, vol I. Longmans, Green, and Co., London
113. Knudsen O (1978) Centaurus 2:53
114. Buchwald JZ (1985)From Maxwell to microphysics: aspects of electromagnetic theory in the last quarter of the nineteenth century. University of Chicago Press, Chicago

115. Yaghjian AD (2014) Prog Electromagn Res 149:217
116. Mossotti OF (1837) In: Taylor R (ed) Scientific memoirs, vol I, chap. Article XX, pp. 448–. Richard and John. E Taylor, London
117. Mossotti OF (1850) Memorie di Matematica e di Fisica della Societá Italianà delle Scienze 24(Pt. 2):49
118. Pelosi G, Selleri S (2015) Radio Sci Bull 355:79
119. Jeans JH (1911) The mathematical theory of electricity and magnetism, 2nd edn. Cambridge University Press, Cambridge
120. Van Vleck JH (1932) The theory of electric and magnetic susceptibilities. Oxford University Press, London
121. Faraday M (1839) Experimental researches in electricity, vol I. Bernard Quaritcii, London
122. Purcell EM, Morin DJ (2013) Electricity and magnetism, 3rd edn. Cambridge University Press, New York
123. Maxwell JC (1841) Philos Mag Ser 3 LVII,19:125, 384
124. Griffiths DJ (2012) Introduction to electrodynamics. Addison-Wesley
125. Lorenz L (1880) Ann Phys Chem 1:70
126. Spruch L (1986) Phys Today 39(11):37. https://doi.org/10.1063/1.881043
127. Spruch L, Kelsey J (1978) Phys Rev A 18:845
128. Marshall TW (1965) Proc Cambridge Philos Soc 61:537
129. Henry LL, Marshall TW (1966) Il Nuovo Cimento B XLI(2):188
130. Boyer TH (2001) In: Squeezed states and uncertainty relations, held at Boston university, Boston, U.S.A. on 4–8 June (2001), ed. by A.V.S. D. Han, Y. S. Kim, B. E. A. Saleh, Teich, M. C. Boston, U.S.A., pp. 1–6
131. Boyer TH (2010) Found Phys 40(8):1096. https://doi.org/10.1007/s10701-010-9436-0
132. Brügger G, Froufe-Pérez LS, Scheffold F, Sáenz JJ (2015) Nat Commun 6:7460
133. Milonni PW (1976) Phys Rep 25:1
134. Weinberg S (1989) Rev Mod Phys 61:1
135. Rugh SE, Zinkernagel H (2002) Stud Hist Philos M P 33:663
136. Wang Q, Zhu Z, Unruh WG (2017) Phys Rev D 95:103504
137. Boyer TH (1969) Phys Rev 182:1374
138. Boyer TH (1985) Sci Am 253(2):70
139. Boyer TH (1969) Phys Rev 186:1304
140. Simpson WM (2014) Stud Hist Philos Mod Phys 48:84
141. Ross DK, Moreau W (1995) Gen Relativ Gravit 27:845
142. Boyer TH (1972) Phys Rev A 5:1799
143. Voigt W (1887) Nachr Ges Wiss Gottingen 2:41
144. Ernst A, Hsu JP (2001) Chin J Phys 39(3):211
145. Heras R (2015) ArXiv pp 1–13
146. Chashchina O, Dudisheva N, Silagadze Z, Voigt SW (2016) ArXiv pp 1–32
147. Macrossan AMN (1986) BJPS 37(2):232
148. Darrigol O (2005) In: Einstein, 1905–2005 (Progress in mathematical physics, vol 47), chap. 1. Birkhäuser, pp 1–31
149. Rytov SM Theory of electric fluctuations and thermal radiation (AFCRC-TR-59-162)

Chapter 9
Nanomaterials and Nanotechnologies for Photon Radiation Enhanced Cancer Treatment

Diana Adliene

Abstract Nanotechnology plays an increasingly important role in the diagnostics, prognostics, theranostic and management of targeted cancer treatments. Radiotherapy is a golden standard for cancer treatment: it requires high accuracy in delivering treatment to cancer patients to reduce toxicity to surrounding tissues and relies on both adequate imaging technologies and precise treatment dose calculations. Since the positive outcome of cancer treatment depends on a proper radiation dose delivery to the target, theoretical dose planning for each patient verified by experimental dose assessment is absolutely necessary. Introduction of the innovative nanotechnologies requires new improved dose delivery concepts that relay on utilization of new nanoscale materials. Materials on the nanoscale such as quantum dots, metal nanoparticles, combined core-shell nanoparticles, drug carriers provide many unique properties and are emerging with promising applications for their implementation in the development of the new cancer treatment strategies.

A quantum physical approach on how nanotechnology and nanomaterials are contributing to the improvement of cancer treatment and monitoring including some development tendencies of nanomaterials for radiation detection and imaging are discussed in this paper with the aim of providing some insights and ideas on future development of photon radiation based nanomedical applications for cancer treatment.

Keywords Photons · Nanomaterials · Photosensitizers · Cancer treatment

9.1 Introduction

Through last decades nanomaterials and nanotechnologies became a part of every day's life. Nanotechnology is defined as the "intentional design, characterization,

D. Adliene (✉)
Kaunas University of Technology, Kaunas, Lithuania
e-mail: diana.adliene@ktu.lt

B. Di Bartolo et al. (eds.), *Quantum Nano-Photonics*, NATO Science for Peace and Security Series B: Physics and Biophysics,
https://doi.org/10.1007/978-94-024-1544-5_9

production and application of materials structures, devices and systems by controlling their size and shape in the nanoscale range (1–100 nm)" [1]. Having high scientific potential nanotechnology plays an increasingly important role also in nanomedical applications. Nanomedicine is defined as the "monitoring, repair, construction and control of human biological systems at the molecular level, using engineered nanodevices and nanostructures" [2]. Nanomaterials used in in medicine may have different sizes, shapes, chemistries, and surface characteristics thus exhibiting tunable optical, electrical magnetic and biological properties. Also they may have some unique characteristics compared to conventional micron-size materials: (1) high ratio of surface area to volume, which enables high loading of drugs on nanomaterial carriers; (2) size dependent properties such as quantum confinement in semiconductor particles (quantum dots) and (3) superparamagnetism of magnetic particles that are used for the improvement of medical imaging techniques. A big variety of different passive and active nanostructures and systems are being used in medical field however the highest scientific priority is addressed to the development of nanomedical systems with enhanced functionality and established multitasking [3].

In this chapter only small area of nanomedicine-application of nanomaterials and nanotechnologies for radiation sensitization, assessment and evaluation in radio-/phototherapy and diagnostics will be discussed with the emphasis on quantum mechanical aspects of photon (X-rays, gamma -rays, UV-VIS-IR light) interaction processes.

9.2 Some Quantum Physical Aspects of Photon Interaction with Matter

The discovery of X-rays by W.C. Röntgen in 1895 contributed significantly to the development of light duality theory. It was shown, that high energy X-rays were behaving similar to light waves and were following the same laws of optics. However the explanation based on the wave propagation theory was not sufficient enough to describe such phenomena as photo effect or Compton scattering and many others. Postulations made by M. Planck and A. Einstein regarding energy quantification and existence of energy quants (photons) provided an elegant solution of this problem, however required the recognition of the dual nature of the light (X-rays). The theory of particulate (photons) nature of light was not recognized by scientific community for a long time after the first indicative experiments were performed. The scientists are discussing A. Einstein's mysterious idea of "smallest packet of energy" until now. Despite of heavy debates, the overall consensus regarding the existence of a photon as a particle is not achieved yet.

In this chapter the photon will be treated in terms of energy quantum due to the fact that the main concern in radiation medicine is energy transfer/absorption in the target object.

Let us assume that electromagnetic radiation penetrating absorbing medium consists of photons that may interact with the atoms in medium, with atomic nuclei or with atomic electrons. Interaction in which electrically charged particles are released from or within a material when it absorbs the energy transferred by electromagnetic radiation is one of the fundamental phenomena of quantum physics. The radiant energy may be infrared, visible, or ultraviolet light, X- rays, or gamma rays; the material may be a solid, liquid, or gas; and the released particles may be ions (electrically charged atoms or molecules) as well as electrons. The probability of each interaction depends on the photon energy and characteristic nature of material. We will focus on photon interactions that play an important role in medical radiation field covering application of nanotechnologies and sensors and nanomaterials for radiation treatment and diagnostics and radiation protection.

Ionization and excitation are two most important processes of photon – electron interactions [4]:

- Excitation of an atom is present when an electron gains sufficient amount of energy and moves from a given shell to a higher n shell which is empty or is not filled by the corresponding number of electrons. Excitation energy (excitation potential) is a minimum energy required to excite an atom from its ground state to a higher state.
- Ionization of an atom occurs when atom bound electron gains sufficient energy to overcome its binding energy in the shell and releases from the atom. Ionization energy (ionization potential) is a minimum energy required to release electron from atom or ion.

9.2.1 High Energy Photon Interactions with Matter

Depending on the amount of energy which is transferred by X-rays or gamma radiation to the electron it will be removed from a given shell in the atom and immediately begin to transfer its energy to the surrounding material. Because the electron carries an electrical charge, it can interact with other electrons via distance pushing them away from its path thus exciting or ionizing the atom (Fig. 9.1).

Most of the ionization produced by X- and gamma radiation is not a result of direct photon interactions, but rather of interactions of the energetic electrons with the material.

The energy loss by electron travelling in matter is well-defined by mass stopping power, $S_e(E_K)_{el}/\rho$ using corrected Bethe formula for electrons [5, 6], which accounts electron and proton energy loss by soft collisions with atomic electrons (radiation or Bremsstrahlung) plus those hard collisions resulting in δ-rays (Eq. 9.1):

$$S_e(E_K)_{el}/\rho = \left(2\pi r_e{}^2 m_e c^2/\beta\right) * (Z/uA) * \left(\ln (E_K/I)^2 + \ln (1+\tau/2) + F^{\pm}(\tau) - \delta\right), \tag{9.1}$$

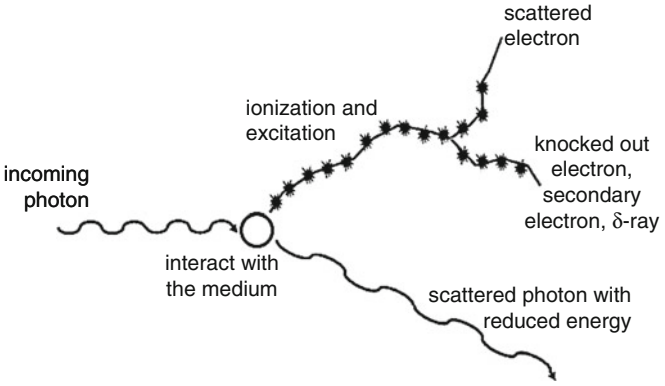

Fig. 9.1 Schematic presentation of high energy photon interaction with electron [4]

where for electrons:

$$F_{el} = \left(1 - \beta^2\right) * \left(1 + \tau^2/8 - (2\tau + 1)\ \ln 2\right), \tag{9.2}$$

and for positrons:

$$F_{pos} = 2\ln 2 - \left(\beta^2/12\right) * \left(23 + 14/\left(\tau + 2\right) + 10/(\tau + 2)^2 + 4/(\tau + 2)^3, \tag{9.3}$$

where r_e is the classical electron radius, c is the speed of light in vacuum ($m_e c^2$ is the electron rest energy), β is the velocity of the incident particle, v, divided by the speed of light, Z is the charge of the incident particle in units of the charge of the electron, and I is the mean excitation energy of the medium, u is the atomic mass constant, 1/12 of the mass of ^{12}C atom, A is atomic mass number, $\tau = E_K/m_e c^2$).

Photoelectric effect, Compton scattering and pair production are the main photon interaction processes in which photon energy is transferred to electrons (positrons).

A photoelectric interaction is a two-step energy deposition process (Fig. 9.2). In the first step X-ray or gamma photon transfers all its energy to a tightly bound electron of absorber (electrons from inner shells of atom mainly) and disappears, while the orbital electron is ejected from the atom as a photoelectron. The depositing of the energy in the surrounding matter by the electron is the second step. This interaction is possible when photon's energy is only slightly higher than the binding energy of the electron: a portion of photon's energy is used to overcome the electron's binding energy and to remove it from the atom as well as the remaining energy is transferred to the electron as kinetic energy and is deposited near the interaction site. Such interaction creates a vacancy in one of the electron shells, typically the K or L, which is filled by the electron from the outer shell followed by characteristic (fluorescent) radiation. The energy of the characteristic radiation

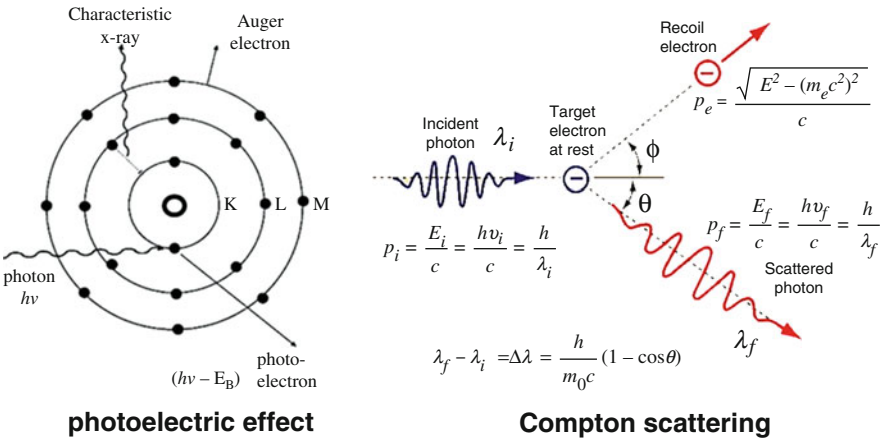

Fig. 9.2 Photon-electron interaction processes: Photoelecric effect (L); Compton effect (R) [4]

depends on the binding energy of the electrons involved. Fluorescence, in general, is a process in which some of the energy of X-ray or gamma photon is used to create a second photon of the same type but with less energy. In some cases the conversion of X-rays into light photons is also possible. It is to notice that characteristic X-rays themselves may be absorbed in the atom resulting in emission of Auger electrons.

The average energy, $(E_K)_{tr}$, transferred by a photon to an electron of the X-shell (K, L, ... X) is given as [7]:

$$(E_K)_{tr} = h\nu - P_x \omega_x (E_B)_x, \tag{9.4}$$

where $(E_B)_x$ is the binding energy of the X-shell (photoelectron), P_x is the fraction of all photoelectric interactions in the X-shell, as compared to the total number of photoelectric events in the whole atom and ω_x is the fluorescent yield for the X-shell which is defined as the number of photons emitted per vacancy in a given atomic shell. The fraction of Auger electrons equals to: $1 - \omega$. The photoelectric effect is the dominant photon interaction in tissue below 30 keV.

A Compton interaction (incoherent scattering) is characteristic for medium and high energy photons interacting with loosely bound electron (from the outer shells of the atom) (Fig. 9.2).

Part of the incident photon energy is transferred to a "free" orbital electron which is emitted from the atom as the Compton (recoil) electron under the angle ϕ. The photon is scattered through a scattering angle θ and its energy $h\nu'$ is lower than the incident photon energy $h\nu$ resulting in the photon wavelength change after interaction:

$$\Delta\lambda = \lambda_C \ (1 - \cos\theta)\,, \tag{9.5}$$

with $\lambda_C = 0.024$ Å as the Compton wavelength of the electron.

Taking into account energy and momentum conservation in the Compton process the scattered photon energy $h\nu'$ and the kinetic energy of Compton electron E_K are given as follows:

$$h\nu' = h\nu / \left(1 + h\nu/m_e c^2 \ (1 - \cos\theta)\right), \tag{9.6}$$

$$E_K = h\nu \left(h\nu/m_e c^2 \ (1 - \cos\theta) / \left(1 + h\nu/m_e c^2 \ (1 - \cos\theta)\right), \tag{9.7}$$

where m_e is the rest mass of electron.

Photon interaction in the nuclear Coulomb field of the atom results in creation of **the electron-positron pair** with a combined energy [7]:

$$(E_K)_{tr} = h\nu - 2m_e c^2. \tag{9.8}$$

Since this is an energy to mass conversion process, pair production has an energy threshold of $2m_e c^2 = 1.022$ MeV. The process is followed by positron annihilation with a "free" and stationary electron, producing two annihilation quanta, most commonly with energies of 0.511 MeV each and emitted at 180° from each other to satisfy the conservation of charge, momentum and energy (Fig. 9.3).

When pair production occurs in the field of an orbital electron, triplet (an electron – positron pair and the orbital electron) production is possible. The threshold for this effect is $4m_e c^2$.

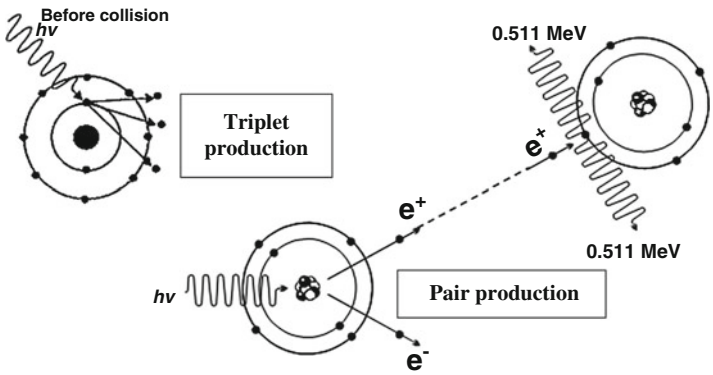

Fig. 9.3 Pair /triplet production. (Adapted from Miglierini [8])

9.2.2 *Interaction of High Energy X-Rays and Gamma Photons with Biological Tissue*

Radiation therapy uses ionizing radiation as a tool for the cancer treatment. It aims at killing the cancerous cells in a treated volume via energy transport to the targeted biological tissues by energetic electrons and positrons produced in photon interactions. Cell killing is a multi-step process. It depends on the energy absorption in some critical volume of the biological tissue. The energy absorbed in unit mass of a certain volume is defined as the absorbed dose and is the main quantity in radiation medicine.

$$D = dE/dm. \tag{9.9}$$

Deposition of the energy as a result of ionization or excitation processes in biological tissue may lead to the damage of the cellular constituents of biological tissue, particularly deoxyribonucleic acids (DNA), thus preventing normal DNA replication and cell division. Two types of ionization events – direct and indirect are possible, when ionizing radiation interacts with the target objects – DNA macromolecules residing in the cells. These molecules regulate cellular activity and contain genetic information needed for cell replication. If the amount of transferred radiation energy is sufficient to directly ionize DNA, the interaction results in DNA damage and even lead to the death of the cells. Other molecules that contribute to the cell function, such as RNA, proteins and enzymes may also be affected by the direct ionization effect (Fig. 9.4).

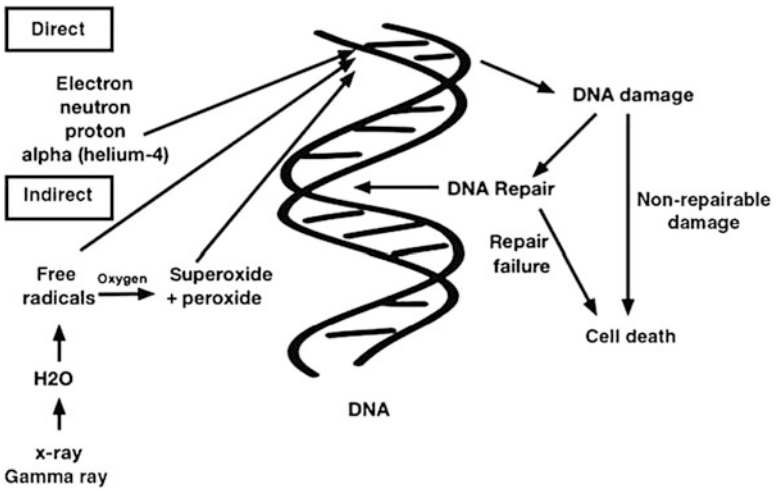

Fig. 9.4 Radiation induced ionization processes in biological tissue. (Direct ionization of DNA by charged particles is included for the comparison)

However, it is to notice that photon induced direct ionization of DNA is a rare process. More than two thirds of radiation induced biologic damages result from indirect ionization in which the initial radiation firstly interacts with water molecules in the cell and generates free radicals and ions, such as hydroxyl OH•, hydrogen H•, water H_2O+, H_3O+, superoxide O_2^-. Photons that exceed ~7 eV are capable of ionizing water. Interaction of radiolysis products and their reactive derivatives with DNA molecules contributes significantly to DNA damages, such as change or loss of base, disruption of hydrogen bonds between DNA strands, breakage of one or both DNA strands, cross-linkage of DNA strands within the helix to other DNA or proteins.

Depending on the energy absorbed, ionization may not have any negative effect on cell or, in contrary, may cause: (1) sub-lethal damage of the cell (cells are damaged, but it is reparable); (2) mutation of the cell (cell damage may be incorrectly repaired and the cell function is altered, or the cell reproduce at an uncontrolled rate (cancer), and (3) cell death (cell damage is so extensive that the cell is not able to reproduce).

The biological response of cells is dependent on the total absorbed dose, dose rate, on presence of the oxygen in media and linear energy transfer, which is defined as the amount of energy deposited per unit path length by photons or electrons travelling through biological tissue. All these parameters are taken into account improving radiative medical procedures and are subject of further investigations. For example, a recent study [9] revealed how ionizing radiation damages DNA and causes cancer. The explanation of carcinogenic potential of ionizing radiation was based on identification of two genomic imprints in human cancers: an excess of deletions and of an exceedingly rare type of rearrangement balanced inversions that are generated by ionizing radiation. These findings related to generation of distinctive mutational signatures by ionizing radiation lead to the explanation of carcinogenic potential of radiation.

9.2.3 Photon Induced Electron Excitation –Relaxation Mechanisms

If the energy of interacting electromagnetic radiation is too low to ionize the atoms excitation is possible in which electron at the ground state may be excited to the higher electronic state, due to the absorbed radiation energy. Molecular excitation is more likely related to low energy irradiation (UV, VIS, IR light) as compared to the ionization. High energy radiation however may cause atomic excitations in crystalline solids. In both cases direct emissive relaxation (fluorescence) is possible but also two- step relaxation via additional excited energy level (excited triplet level in molecules, impurity levels in solids) is possible. Crystalline structures characterized by three- level relaxation scheme are well explored in sensor applications, such as thermo-luminescence and optically stimulated dosimeters. X-ray fluorescence plays also an important role in radiological imaging.

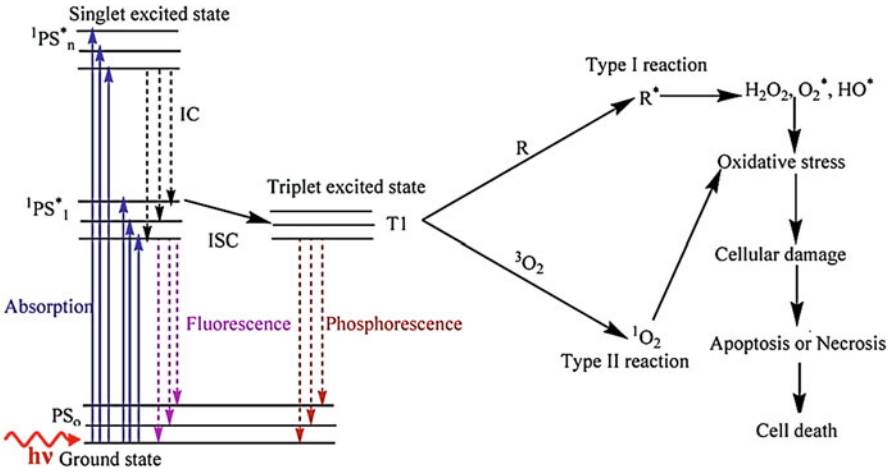

Fig. 9.5 Modified Jablonski energy level diagram of photosensitized molecule and indication and chemical processes that are activated in cellular environment due to molecule excitation by light [12]

Despite of the variety of relaxation mechanisms in different materials, physical principles of electron excitation – relaxation processes in triplet energy level structures will be discussed on the basis of process analysis in molecular system of light illuminated photosensitizer – agent used in photodynamic therapy of cancer. Explanative extension to chemical processes, responsible for generation of reactive oxygen structures needed to kill cancerous cells will be also provided.

Photosensitization is a process applied in photodynamic therapy (PDT) when a special fluorescent material (photosensitizer) is introduced into the target (cancerous) cells and the cancer site is illuminated to the light from the therapeutic window ($\lambda = 600 \div 900$ nm). In the presence of oxygen molecules, the light illumination of photosensitizer (PS) can lead to the generation of cytotoxic reactive oxygen species (ROS, singlet oxygen) and consequently destroy the cancerous cells through apoptosis and/or necrosis pathways [10, 11]. It is to notice that light up to only $\lambda = 800$ nm can generate $^1O_2$, since longer wavelengths radiation has insufficient energy to initiate photodynamic reaction.

Jablonski energy level diagram of molecular structure which includes excited triplet state (Fig. 9.5) [12] might be used for more detailed explanation of the physical and chemical processes explored in photodynamic therapy.

Let us assume that photosensitizer's (e.g. porphyrin) molecule is illuminated to the light from the therapeutic window ($\lambda = 600 \div 900$ nm). Molecule absorbs the radiation energy very fast (10–15 s) and the electrons from the singlet ground state PS_0 are transferred to the one of the excited singlet states $^1P^*(S_1 - S_n)$. Electron at the higher orbital has the opposite spin orientation relative to electron at the lower orbital. Since the excited electron moves to another orbit, in which the electron is less tight bond to the atom, it occupies higher vibrational level than the level at which it was in the ground state. Vibrational relaxation takes $10^{-14} - 10^{-11}$ s and is realized through intermolecular collisions.

The emissive return of the molecule from the lowest vibrational energy level of the excited singlet state $^1P^*(S_1-S_n)$ to a vibrational level of the ground state PS_0 without changing of spin orientation is called fluorescence. The energy of fluorescent photons is lower than that of incident photon. The short life – time (10^{-9} s) of the singlet excited state is sufficient to be used for diagnostic purposes, however it is too short to induce intermolecular energy transfer or electron transfer. Moreover, singlet-triplet energy transfer is usually forbidden process due to the spin conservation rule (the ground state of dioxygen, O_2, which plays an important role in generation of ROS, is in a triplet state).

Time extension for the electron in the excited state is realized via intersystem crossing to produce the triplet energy state T_1. The exited triplet state is produced via inversion of the spin (spin flip) of the excited electron resulting in existence of two unpaired electrons with the same spin orientation. Since transition from T_1 to ground level PS_0 is a forbidden process (due to the different multiplicity of the states), the excited triplet state tends to have a longer lifetime of (10^{-3}–10^{-2} s) as compared with the excited singlet state [13]. Photosensitizers with a long living T_1 state are often used to stimulate biologically relevant photochemistry in two competing pathways, the Type-I and Type-II reactions. Both types of reactions cause oxidation of various cellular molecules and can induce cell death via apoptosis, necrosis and autophagy.

The Type I reaction involves electron/proton transfer directly from the PS to cellular organic substrates (lipids, proteins, nucleic acids, etc.), yielding free radicals or radical ions that interact with molecular oxygen (O_2) to produce reactive oxygen species (ROS), such as hydrogen peroxide (H_2O_2), the superoxide anion (O_2^-) and the hydroxyl radical (OH•). The last one is strong electrophile which is able to chemically attack a very wide range of biomolecules [14].

The ground electronic state of oxygen is also triplet, whereby the two outermost orbitals are unpaired but spin parallel. This triplet can undergo energy transfer upon collision with the excited PS triplet. Type II process involves “flipping the spin” of the outermost O_2 electron and shifting it into the orbital containing the other electron, which in turn leaves one orbital entirely unoccupied. Generated singlet oxygen $^1O_2$ is not considered as radical, since its electron configuration is instable due to the presence of spin paired electrons. In particular, short- lived (10–320 ns) and extremely reactive singlet oxygen $^1O_2$ produced through the Type-II reaction is thought to be responsible for the cell death induced by PDT [9]. It is to notice that the energy of the excited state in PS should be higher, then 94 kJ/mol (0.97 eV, energy of singlet oxygen). The most important photosensitizers are characterized in [15, 16].

9.3 The Role of Nanomaterials and Nanotechnologies in Cancer Treatment Strategies

Nanomaterials can bridge the gap between the bulk and molecular levels and lead to new applications in different fields, including also biomedical field. In this frame, various applications of nanostructures for the development of new cancer treatment methods are of great importance. However it is to notice, that this chapter is aimed to provide rather rough insights and ideas to different possibilities of nano-applications in cancer treatment than discussions on the topic in very details, which could be found in different review articles provided by other authors [17–19].

Let us assume that the solid exhibiting distinct variation of optical and targeting properties with a variation of particle size <100 nm can be called as nanostructure. Nanostructures may be in a form of pure materials, mixtures, composites and alloys, may have differently engineered structure, different shape and size, and be defined as three-dimensional, e.g. nanoparticle, two-dimensional, e.g. thin film or quantum wells, one-dimensional, e.g. nanowires and zero-dimensional, e.g. quantum dots, objects.

Quantum dots are most interesting and extremely important semiconductor (mainly) nanostructures that exhibit three dimensional quantum confinement. Quantum confinement effect occurs sizing down the semiconductor crystal, which usually has fixed bandgap between its valence and conductance bands, to less than Bohr radius (1–5 nm [20]) due to the response of electronic excitation states to the particle boundaries by adjusting their energy states [21]. Three different material specific Bohr radii can be estimated:

$$a_e, a_h, a_{exc} = \varepsilon \left(m/m^*\right) a_0, \tag{9.10}$$

where m is the rest mass of a particle such as electron (e), hole (h) or electron-hole pair (exciton, exc), m* is the reduced mass ("effective" inertial mass) of the particle, ε is the material's dielectric constant, and a_0 is the Bohr radius of hydrogen (5.291772×10^{-11} m).

Solving the Schrödinger equation for a spherical approximation of QDs, the energy gap can be defined as [22]:

$$E_g\,(QD) = E_{g,0} + \left(h^2 \alpha_{n,l}\right) / 8\pi^2 m_{eh} R^2, \tag{9.11}$$

where E_{g0} is an energy bandgap of bulk semiconductor, $m_{eh} = m_e \times m_h/(m_e + m_h)$ is effective mass of an electron-hole pair (exciton), m_e and m_h are effective masses of an electron and a hole, respectively.

Due to the wave function symmetry [23] energy levels are described like atomic orbitals labelled by the quantum numbers $\alpha_{n,l}$ (n = 1, 2, 3, etc., l = s, p, d, etc.). Decreasing or increasing size of QDs lead to corresponding increase or decrease in energy gap and introduces color changes in absorption spectra followed by the emission of light of corresponding wave length.

Like Jablonski's diagram (Fig. 9.5) indicating electronic energy levels of organic molecules and photochemical reactions occurring from their excited states [24, 25], a three level model can similarly outline energy states of QDs. Three level energetic scheme of QD contains a "trap" or "dark" excitonic state, which is populated from the first excited state through non-radiative transition [26] is comparable with the long lived triplet excited state T1 (Fig. 9.5) of usual photosensitizer and thus can generate singlet oxygen [27]. Photoexcited quantum dots and ground-state triplet oxygen have to be in contact to undergo triplet energy transfer (TET), as in the case of conventional PDT photosensitizers [28, 29].

Different aspects of QDs development, fabrication and application are being explored due to the big potential of these nanostructures in technological applications, many excellent reviews and articles have been published during the last years [17, 18, 30]. However the applicability of quantum dots for cancer therapies and radiation medicine especially exploring radiosensitization and conjugate mechanisms is not thoroughly discussed yet [27, 31, 32].

9.3.1 Photodynamic Therapy for Cancer Treatment

Photodynamic therapy (PDT) is a promising therapeutic modality for the treatment of oncological diseases. Photodynamic therapy involves three key components: a photosensitizer, localized in target tissue, light used to illuminate target and molecular oxygen which is necessary to produce ROS and singlet oxygen that are responsible for cell damage leading to the cell death (see photosensitization in the previous subchapter). It has the advantage of dual selectivity, due to the preferential localization of the photosensitizer by the malignant tissue and restriction of photo activation to the tumor site due to localized light irradiation. It introduces and controls important cell death mechanisms and being minimal invasive is attractive as an alternative to surgery. The evident advantage of PDT over other conventional cancer treatments such as chemotherapy and radiotherapy is its minimal side effects, selective targeting, reduced toxicity that allows for repeated treatment. However it is to notice, that due to a small penetration depth of light photons, PDT may be applied for the treatment of surface or shallow located cancers [33–36].

A very detailed review on PDT applications for different cancer treatment is provided in [14] in which also novel strategies in PDT are outlined:

Two Photon PDT Excitation of sensitizer by short (∼100 fs) laser pulses with very high peak power enables simultaneous absorption of two light photons. Since each photon only contributes half the excitation energy, near-infrared light can be used to achieve deeper tissue penetration [37]. Alternatively, if the laser beam is strongly focused, then the activation volume may be extremely small [38].

Metronomic PDT Low dose rate delivery of both drug and light over an extended period (hours-days). This can result in tumor cell-specific apoptosis, with minimal tissue necrosis [39].

Nanotechnology in PDT Nanoparticles (NPs) have several potential roles in PDT: as PSs *per se*, for PS delivery [40] and as energy transducers [41].

Nanoparticles selected for photosensitizer enhancement must meet the following requirements [19]:

- The nanoparticle emission spectrum must match the photosensitizer's absorption spectrum, which guarantees efficient activation of the photosensitizers and production of singlet oxygen. It is easy achievable because a nanoparticle's emission spectrum is dependent on the diameter of the nanoparticle.
- The nanoparticles must have high luminescence efficiency, i.e., excitation should result in strong emission by the nanoparticle. For example, if a scintillation nanoparticle is used, luminescence is produced as a result of excitation by radiation (scintillation luminescence), and the nanoparticle should emit strongly.
- The nanoparticles must be easily attached to or linked with photosensitizers.
- The nanoparticles must be non-toxic, water soluble, and stable in biological environments.

The potential advantage of NPs is that a high 'payload' can be delivered and they can be 'decorated' with multiple targeting moieties such as antibodies or peptides. Other approaches [42] include: biodegradable polymers, ceramic (silica) and metallic (gold, iron oxide) NPs; magnetic NPs, in which an applied magnetic field enhances localization to the tumor; and hybrid NPs that allow both PDT and either another therapeutic strategy such as hyperthermia or an imaging technique such as magnetic resonance imaging. Materials that themselves generate $^1O_2$ upon photoexcitation include silicon NPs and quantum dots [43]. Quantum dot conjugates with photosensitizers may have some advantages, in particular because of the large absorbance cross-section and the tunable optical properties enabling flexible utilization of variable excitation wavelengths to activate the photosensitizer molecule.

These concepts illustrate a general advantage of NP-based PDT: photophysical and photochemical properties of the PS can be uncoupled from the delivery and activation processes and potential of PDT alone or in combination with approved or experimental therapeutic approaches as a promising antitumor strategy [40].

9.3.2 Nanoparticles for Radiation Therapy Enhancement

Taking into account that radiation therapy is not selective antitumor treatment the main challenge for this treatment is the enhancement of the therapeutical efficacy without increasing damages to the surrounding organs at risk (OAR). Combination of nanoparticles and radiation therapy opens the possibility to increase differentiation between healthy and cancerous tissues. The treatment efficacy can be expressed in terms of dose modifying factor (DMF), which is relies on cell survival evaluation [17]:

$$\mathrm{DMF} = \mathrm{D}_{\mathrm{sensi}}/\mathrm{D}_0, \tag{9.12}$$

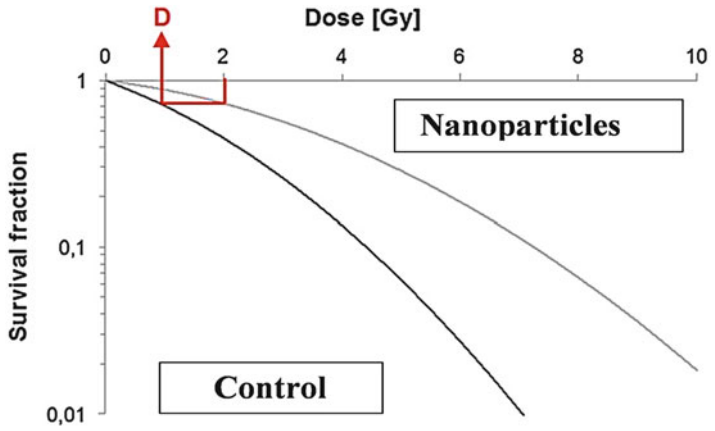

Fig. 9.6 Survival curve example. (Illustration adapted from DMF assessment strategy [17])

where D_{sensi} is the dose required to produce an effect in the cell with radiosensitizer/radioprotector and D_0 is the dose required to produce the same effect without radiosensitizer/radioprotector.

This definition is similar to that of the relative Biological Effectiveness (RBE) [44], which allows adapting of the delivered dose according to the performance of the improved/new therapeutic system or strategy, in comparison to the dose of conventional treatment. The radiosensitizing effect on survival of cells is provided in Fig. 9.6 [17]. It is shown, that introducing nanoparticles into the cells allows achieving of the same radiobiolgical effect with a lower X-ray irradiation dose as compared to the dose to the cell colonies without NPs and thus reduce the treatment dose by DMF.

There are several mechanisms of photon (X-ray) interaction with nanoparticles introduced into the tumor: (1) NPs that enhance photoelectric effect and Compton scattering (and thus the subsequent emissions of secondary electron, explained in the sub-chapter 2.1) to increase conventional radiation therapy efficacy; (2) X-ray triggered drug-releasing NPs [45], that represent capsule loaded with drugs, which is destroyed due to irradiation and the drug is released inside the targeted tissues; (3) Self-lighting photodynamic NPs that are usually made of a lanthanide-doped high-Z core [46]. Once irradiated by X-rays, the scintillator core emits a visible light and activates a photosensitizer that generates singlet oxygen ($^1O_2$) and ROS for tumor destruction (combination of photodynamic therapy and enhanced radiation therapy) [47].

Radiosensitization by Quantum Dots and Nanoparticles Radiation sensitizers are drugs that enhance the effects of single or fractionated radiation therapy. Metallic nanoparticles can be used as adjuncts to radiotherapy. Tightly packed metal nanoparticles may increase therapeutic efficiency of radiotherapy by selectively scattering and/or absorbing X-rays or gamma rays causing localized damage to

DNA and other targeted organelles of cancer cells and thus decreasing total radiation dose to minimize side effects of ionizing radiation on cancer patients [27, 48]. Dose enhancement is believed to occur due to transport of photoelectrons scattered on these heavy metals [49]. This approach of using nanomaterial radiosensitizers (NMRS) is termed Nanoparticle Enhanced X-ray Therapy (NEXT) [50, 51].

There is considerably increasing interest in effective dose enhancement of ionizing radiation by particles, including not only metallic particles but also other promising candidates, such as: CaF, LaF, ZnS or ZnO quantum dots, carbon dots, nanoparticle-photosensitizer conjugates [52] and many others.

The most studied and also in some cases implemented into clinical practice NPs are gold-based NPs [48, 53], but also the use of lanthanide-based NPs, titanium oxide nanotubes or cadmium selenide quantum dots [54–57] is possible. NPs usually have a simple structure composed of a core, a shell and a surface [58]. In the case of radiosensitizing NPs, the core is usually made of high-Z materials such as silver, lanthanides and most extensively of gold, in order to exploit the increased photon absorption. Also the irradiation energy plays an important role, since the most effective X-ray energy absorption resulting in the ejection of electron happens at low energy where photoelectric effect is dominant [59]. This effect is prevailing until the photon energy reaches a medium energy (e.g. 500 keV for Au) with a cross-section varying with Z^4 or Z^5 depending on the material and is enhanced by an increased absorption by electron shells (K, L, M, etc.) at low energies. It is to notice, that due to the ionization of atom, a characteristic X-ray or an Auger [60] electron emission is following the emission of photoelectron. Taking into account that conventional radiotherapy is a high energy (MeV) cancer treatment, which explores poly-energetic X-rays, the medium- and high-energy components are more likely to interact by Compton effect. Generated Compton, photo- or Auger-electrons can induce the emission of secondary electrons (also called delta rays) that are believed to be responsible for the majority of cells damages via production of ROS in radiotherapy. It is to notice that X-ray induced ROS generation mechanisms in cells in the presence of NPs depend on NPs composition, size and some other parameters [61].

One of the excellent demonstrations regarding increased ROS generation in X-ray irradiated cells might be paper published by Klein et al. [62], which describes the in vitro formation of ROS in SuperParamagnetic Iron Oxide nanoparticles (SPIONs) loaded MCF-7 cells exposed to X- rays. According to the authors, the impact of X-rays on generation of ROS in cells loaded with citrate-coated SPIONs can be enhanced by 240% as compared with X-ray irradiated cells without NPs.

Application of NPs may contribute to the targeted enhanced radiation sensitivity, however it is extremely important to achieve, that introduced NPs a concentrating mainly in the tumor, not in the healthy organs at its vicinity. Otherwise it may lead to the opposite effect (Fig. 9.7) as it was illustrated by Retif et al. [17].

Heavy metal-based NPs have also been suggested as effective **tumor-targeting theranostic agents** with dual functions. An efficient targeted system for tumor imaging and irradiation dose amplifier for radiotherapy under the guidance of

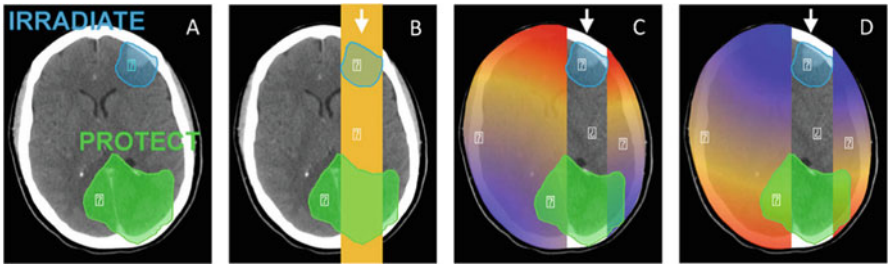

Fig. 9.7 (**a**) Illustration of a clinical scenario where a tumor volume (blue) has to be irradiated while a part of an organ (green) has to be protected. (**b**) A simple anterior beam is irradiating the blue volume. (**c**) The maximum beam energy (indicated in red) is delivered to the tumor with a reduced energy to the out of the target region. (**d**) Given that the interaction probability is higher for low-energy photons, the radiosensitization in presence of NPs should be higher out of the target area. In this case, the green volume that has to be protected would be in the most radiosenzitized area (indicated in red). (Illustration adapted from [17])

computed tomography imaging has been introduced [63] in which application of $BaYbF_5$: 2% Er^{3+} NPs was discussed. The method explores NPs features to emit upconversion luminescence with greatly suppressed auto fluorescence and contribute to the photo damage and toxicity of cells when excited to near red laser light, thus showing potential for cell or even tissue tracking during radiotherapy procedure. Working in parallel with imaging procedure megavoltage photon beam interaction with NPs contributes to the enhanced efficacy of radiation treatment.

It is also to notice, that radioisotope-labeled nanoparticles have been developed to increase tumor accumulation and reduce undesired biodistribution. Intratumoral injection of these particles might be even more effective as compared to brachytherapy [64].

9.3.3 Combined Cancer Treatment Strategies

Surgery, chemotherapy, radiotherapy and to less extent photodynamic therapy are main cancer treatment strategies. Since no one strategy is perfectly adjusted to meet the challenge (kill the cancer), combination of all possible methods is requested including also development of new ones. Implementation of nanotechnologies contributes significantly to the simultaneous applications of cancer treatment modalities.

Radiotherapy and Chemotherapy The combination of chemotherapy and radiotherapy is one of the most effective ways to improve clinical treatment of locally advanced cancers. The concurrent chemoradiotherapy outperforms sequential therapies because chemotherapy sensitizes the tumor cells to radiation-induced killing and treatment; meanwhile the concurrent therapy avoids the repopulation of cancer

cells which will occur during the course of sequential treatment [65]. Nanotechnology can facilitate the chemoradiotherapy in two ways. One is to deliver chemotherapeutics by nanoparticles combined with external irradiation for combination therapy due to the radiosensitizing effect of some chemotherapeutic drugs, such as cisplatin, doxorubicin, and paclitaxel [66–68]. Second is to co-deliver both, chemotherapeutics and radiosensitizers/radioisotopes in the same nanoparticle, which achieves the simultaneous delivery of agents at lesion as well as concise ratio control. Both nanotechnology approaches benefit from decreased toxicity in normal tissues and preferential accumulation in tumors [69].

Photodynamic Therapy and Radiotherapy In PDT concept certain photosensitizers (PS) are localized in neoplastic tissue and are subsequently activated with the appropriate wavelength of light to generate active ROS and $^1O_2$ that are toxic to tumors. Due to the limited penetration range of light PTD is most appropriate for small or superficial lesions. In order to treat deep located tumors X-rays as excitation source might be used instead of light. In such a case activation of the photosensitizer within tumors would be performed using ionizing radiation. This new modality will allow treatment of deep tumors using lower radiation dose than conventional radiotherapy. Potential of simultaneous radiation and photodynamic treatment was disclosed by W. Chen and J. Zhang [47, 70, 71]. They described the synthesis of LaF_3:Tb^{3+}-meso-tetra (4-carboxyphenyl) porphine (MTCP) NP conjugated to folic acid and investigated the energy transfer as well as the formation of $_1O^2$ following X-ray irradiation. It was found [71] that upon X-ray irradiation, the porphyrin alone is a radiosensitizer but the effect is enhanced when MTCP is coupled to LaF_3:Tb^{3+} NPs targeted or not with folic acid. The average energy transfer rate in the MTCP conjugates is 56.7%. The same team realized also ZnO-MTAP (meso-(o-amino-phenyl porphine) conjugate in which the energy transfer was around 89 % [17]. The advantages of the new PDT-radiation therapy are: (1) two effective treatments (radiation therapy and PDT) are combined; (2) the modality is capable and efficient for deep cancer treatment; (3) the risk of radiation damage to healthy tissue is lower; and (4) the treatment is simple, relatively inexpensive and efficient.

Synchronous Radiotherapy and Deep Photodynamic Therapy with Diminished Oxygen Dependence Strong oxygen dependence and limited penetration depth are the two major challenges facing the clinical application of photodynamic therapy (PDT). In contrast, ionizing radiation is too penetrative and often leads to inefficient radiotherapy (RT) in the clinic because of the lack of effective energy accumulation in the tumor region. As a next step to overcome these problems integration of a scintillator and a semiconductor as an ionizing-radiation-induced PDT agent was proposed [72], which allowed achieving synchronous radiotherapy and depth-insensitive PDT with diminished oxygen dependence (Fig. 9.8).

The goal is achieved applying Ce^{3+}- doped $LiYF_4$@SiO_2@ZnO core-shell structure (SZNPs) as an agent for ionizing radiation induced PDT. SZNP consists of Ce^{3+}-doped $LiYF_4$ scintillator, which is used to downconvert high energy

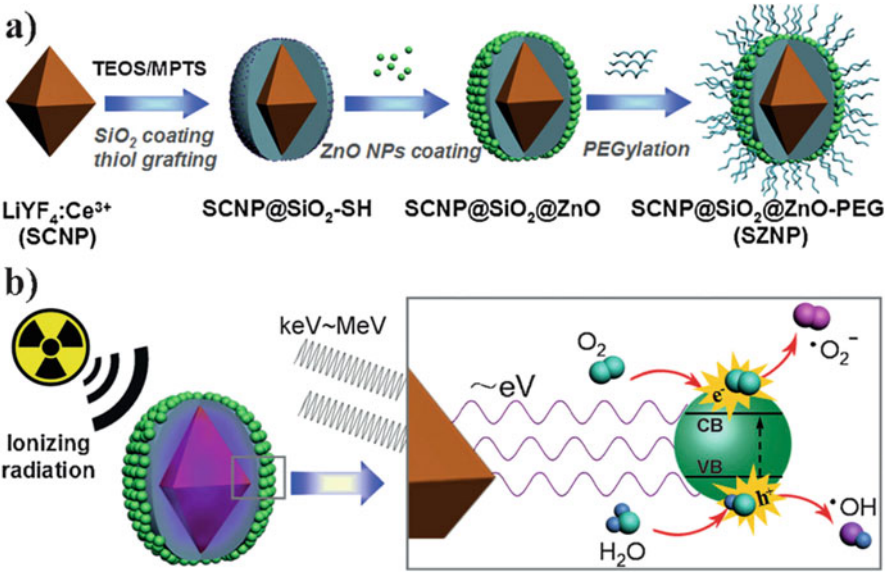

Fig. 9.8 (**a**) Schematic illustration of the synthetic route to monodisperse SZNPs; (**b**) the mechanism of ionizing radiation-induced photodynamic therapy [72]

radiation to luminescence in the UV/Vis region of the spectrum. After conversion in scintillator emitted low energy photons are absorbed by NPs surface bound ZnO NPs. It is important to notice, that the emission band of scintillator under X-ray excitation must match the absorption band gap of ZnO. The subsequently formed excitons (the electron–hole pairs) interact with water and oxygen molecules to form free radicals [73, 74]. The highly reactive hydroxyl radicals (OH) are derived from the reaction between the hole (h+) and the absorbed water instead of O_2 [75], which essentially minimizes the oxygen-tension dependency for the generation of reactive oxygen species [76, 77].

These and other very encouraging results are the basis of new NPs developments, however it is to notice, that all NPs are more or less toxic [78, 79]. Nanotoxicity problem should be taken into account when implementing new nano-based cancer treatment strategies.

9.4 Summary

Based on quantum physical approach of photon interaction with matter two main radiative cancer treatment strategies have been introduced: low energy (UV/VIS light) photon exposure related Photodynamic therapy and medium and high energy (X-ray, gamma ray) photon irradiation related radiation therapy. It was shown, that

both therapies have big potential for their future use in oncology, however significant improvements in their applications can be achieved implementing nanotechnology concept and synergy of at least two different cancer treatment strategies. Some insights and ideas for future developments in photon radiation based nanomedical applications highlighting also the problems of nanotoxicity have been also introduced.

References

1. COMA (2007) Publicly available specification 136: terminology for nanomaterials. British Standards Institute, London
2. Freitas RA (1999) Nanomedicine, Volume 1: Basic capabilities. Landes Bioscience, Austin
3. Yao C, Lu J (2012) Introduction to nanomedicine. In: Webster T (ed) Nanomedicine: technologies and applications. Woodhead Publishing Limited, Cambridge
4. Adlienė D (2017) Radiation interaction with condensed matter. In: Sun Y, Chmielewski AG (eds) Applications of ionizing radiation in materials processing, vol 1. Institute of Nuclear Chemistry and Technology, Warsaw, pp 33–54
5. Bethe H, Ashkin J (1953) In: Segré E (ed) Experimental nuclear physics. Wiley, New York, p 253
6. Report 90: Key data for ionizing-radiation dosimetry: measurement standards and applications. J Int Comm Radiat Unit Measure 14(1), 21–30 (2014)
7. Podgorsak EB (2010) Radiation physics for medical physicists. Springer, Berlin/Heidelberg/New York
8. Miglierini M (2017) Detectors of radiation. Lecture for the E. Wigner course. http://www.nuc.elf.stuba.sk/bruno/presentations/detectors/htm. Last accessed 2017/10/05
9. Behjati S et al (2016) Mutational signatures of ionizing radiation in second malignancies. Nat Commun 7:12605. https://doi.org/10.1038/ncomms12605
10. Lukšienė Ž (2003) Photodynamic therapy: mechanism of action and ways to improve the efficiency of treatment. Medicina 39(12):1137–1150
11. Hu Z, Oleinick N, Hamblin MR (2014) Photodynamic therapy as an emerging treatment modality for cancer and non-cancer diseases. J Anal Bioanal Tech S1(e001). https://doi.org/10.4172/2155-9872.S1-e001
12. Debele TA, Peng S, Tsai H-C (2015) Drug carrier for photodynamic cancer therapy. Int J Mol Sci 16(9):22094–22136
13. Majumdar P, Nomula R, Zhao J (2014) Activatable triplet photosensitizers: magic bullets for targeted photodynamic therapy. J Mater Chem C 2:5982–5997
14. Agostinis P et al (2011) Photodynamic therapy of cancer: an update. CA Cancer J Clin 61(4):250–281
15. Food and Drug Administration (FDA) – Center for Drug Evaluation and Research. Approved Drug Products. http://www.accessdata.fda.gov/scripts/cder/drugsatfda/index.cfm. Last accessed 2017/09/30
16. European Medicines Agency (EMA). Human Medicines. http://www.ema.europa.eu/ema/index.jsp?curl=pages/medicines/landing/epar_search.jsp&mid=WC0b01ac058001d124. Last accessed 2017/09/30
17. Retif P et al (2015) Nanoparticles for radiation therapy enhancement: the key parameters. Theranostics 5(9):1030–1044
18. Bera D et al (2010) Quantum dots and their multimodal applications: a review. Materials 3:2260–2345
19. Juzenas P et al (2008) Quantum dots and nanoparticles for photodynamic and radiation therapies of cancer. Adv Drug Deliv Rev 60(15):1600–1614

20. Hardman R (2006) A toxicologic review of quantum dots: toxicity depends on physicochemical and environmental factors. Environ Health Perspect 114:165–172
21. Hollingsworth JA, Klimov VI (2004) Soft chemical synthesis and manipulation of semiconductor nanocrystals. In: Klimov VI (ed) Semiconductor and metal nanocrystals: synthesis and electronic and optical properties. Marcel Dekker, New York, pp 1–64
22. Kippeny T, Swafford LA, Rosenthal SJ (2002) Semiconductor nanocrystals: a powerful visual aid for introducing the particle in a box. J Chem Educ 79:1094–1100
23. Norris DJ (2004) Electronic structure in semiconductor nanocrystals. In: Klimov VI (ed) Semiconductor and metal nanocrystals: synthesis and electronic and optical properties. Marcel Dekker, New York, pp 65–102
24. Lakowicz JR (2006) Introduction to fluorescence, principles of fluorescence spectroscopy. Springer, New York, pp 1–26
25. Juzeniene A, Nielsen KP, Moan J (2006) Biophysical aspects of photodynamic therapy. J Environ Pathol Toxicol Oncol 25:7–28
26. Bawendi MG et al (1992) Luminescence properties of CdSe quantum crystallites: resonance between interior and surface localized states. J Chem Phys 96:946–954
27. Samia AC, Chen X, Burda C (2003) Semiconductor quantum dots for photodynamic therapy. J Am Chem Soc 125:15736–15737
28. Schweitzer C, Schmidt R (2003) Physical mechanisms of generation and deactivation of singlet oxygen. Chem Rev 103:1685–1757
29. Krasnovsky AA (2007) Primary mechanisms of photoactivation of molecular oxygen. History of development and the modern status of research. Biochemistry (Mosc) 72:1065–1080
30. Petryayeva E et al (2013) Quantum dots in bioanalysis: a review of applications across various platforms for fluorescence spectroscopy and imaging. Appl Spectrosc 67(3):215–252
31. Bakalova R et al (2004) Quantum dots as photosensitizers? Nat Biotechnol 22:1360–1361
32. Park YS et al (2006) X-ray absorption of gold nanoparticles with thin silica shell. J Nanosci Nanotechnol 6:3503–3506
33. Diamond I et al (1972) Photodynamic therapy of malignant tumours. Lancet 2:1175–1177
34. Kochevar IE (2004) Singlet oxygen signaling: from intimate to global. Sci STKE 2004:e7
35. Moan J (1990) On the diffusion length of singlet oxygen in cells and tissues. J Photochem Photobiol B Biol 6:343–344
36. Clo E et al (2007) Control and selectivity of photosensitized singlet oxygen production: challenges in complex biological systems. Chembiochem 8:475–481
37. Starkey JR et al (2008) New two-photon activated photodynamic therapy sensitizers induce xenograft tumor regressions after near-IR laser treatment through the body of the host mouse. Clin Cancer Res 14:6564–6573
38. Collins HA et al (2008) Blood vessel closure using photosensitisers engineered for two-photon excitation. Nat Photonics 2:420–424
39. Lilge L, Portnoy M, Wilson BC (2000) Apoptosis induced in vivo by photodynamic therapy in normal brain and intracranial tumour tissue. Br J Cancer 83:1110–1117
40. Luo D et al (2017) Chemophototherapy: an emerging treatment option for solid tumors review. Adv Sci 4:24
41. Wilson BC (2006) Photonic and non-photonic based nanoparticles in cancer imaging and therapeutics. In: Dubowski J, Tanev S (eds) Photon-based nanoscience and nanobiotechnology. Springer, Dordrecht, pp 121–151
42. Chatterjee DK, Fong LS, Zhang Y (2008) Nanoparticles in photodynamic therapy: an emerging paradigm. Adv Drug Deliv Rev 60:1627–1637
43. Kim S et al (2007) Organically modified silica nanoparticles co-encapsulating photosensitizing drug and aggregation-enhanced two-photon absorbing fluorescent dye aggregates for two-photon photodynamic therapy. J Am Chem Soc 129:2669–2675
44. Valentin J (2003) Relative biological effectiveness (RBE), quality factor (Q), and radiation weighting factor (Wr). International Commission on Radiological Protection
45. Starkewolf ZB et al (2013) X-ray triggered release of doxorubicin from nanoparticle drug carriers for cancer therapy. Chem Commun 49:2545–2547

46. Carter JD et al (2007) Nanoscale energy deposition by X-ray absorbing nanostructures. J Phys Chem B 111:11622–11625
47. Chen W, Zhang J (2006) Using nanoparticles to enable simultaneous radiation and photodynamic therapies for cancer treatment. J Nanosci Nanotechnol 6:1159–1166
48. Herold DM et al (2000) Gold microspheres: a selective technique for producing biologically effective dose enhancement. Int J Radiat Biol 76:1357–1364
49. Guo T. Nanoparticle radiosensitizers. 2006WO2006037081
50. Praetorius NP, Mandal TK (2007) Engineered nanoparticles in cancer therapy. Rec Pat Drug Deliv Formul 1:37–51
51. Chen W (2008) Nanoparticle fluorescence based technology for biological applications. J Nanosci Nanotechnol 8:1019–1051
52. O'Donoghue JA, Wheldon TE (1996) Targeted radiotherapy using Auger electron emitters. Phys Med Biol 41:1973–1992
53. Hainfeld JF et al (2008) Radiotherapy enhancement with gold nanoparticles. J Pharm Pharmacol 60:977–985
54. Townley HE, Kim J, Dobson PJ (2012) In vivo demonstration of enhanced radiotherapy using rare earth doped titania nanoparticles. Nanoscale 4:5043–5050
55. Mirjolet C et al (2013) The radiosensitization effect of titanate nanotubes as a new tool in radiation therapy for glioblastoma: a proof-of-concept. Radiother Oncol 108:136–142
56. Takahashi J, Misawa M (2007) Analysis of potential radiosensitizing materials for X-ray-induced photodynamic therapy. Nanobiotechnol 3:116–126
57. Yang W et al (2008) Semiconductor nanoparticles as energy mediators for photosensitizer-enhanced radiotherapy. Int J Radiat Oncol Biol Phys 72:633–635
58. Fukumori Y, Ichikawa H (2006) Nanoparticles for cancer therapy and diagnosis. Adv Powder Technol 17:1–28
59. Butterworth KT et al (2012) Physical basis and biological mechanisms of gold nanoparticle radiosensitization. Nanoscale 4:4830–4838
60. Martin JE (2013) Physics for radiation protection. Wiley, Chichester
61. Klein S et al (2013) Oxidized silicon nanoparticles for radiosensitization of cancer and tissue cells. Biochem Biophys Res Commun 434:217–222
62. Klein S et al (2012) Superparamagnetic iron oxide nanoparticles as radiosensitizer via enhanced reactive oxygen species formation. Biochem Biophys Res Commun 425:393–397
63. Xing H et al (2013) Computed tomography imaging-guided radiotherapy by targeting upconversion nanocubes with significant imaging and radiosensitization enhancements. Sci Rep 3:1751
64. Zhou M et al (2015) Radio-photothermal therapy mediated by a single compartment nanoplatform depletes tumor initiating cells and reduces lung metastasis in the orthotopic 4T1 breast tumor model. Nanoscale 7(46):19438–19447
65. Lawrence TS, Haffty BG, Harris JR (2014) Milestones in the use of combined-modality radiation therapy and chemotherapy. J Clin Oncol 32(12):1173
66. Jung J et al (2012) Polymeric nanoparticles containing taxanes enhance chemoradiotherapeutic efficacy in non-small cell lung cancer. Int J Radiat Oncol Biol Phys 84(1):e77–e83
67. Werner ME et al (2013) Preclinical evaluation of Genexol-PM, a nanoparticle formulation of paclitaxel, as a novel radiosensitizer for the treatment of non-small cell lung cancer. Int J Radiat Oncol Biol Phys 86(3):463–468
68. Xiong H et al (2015) Doxorubicin-loaded carborane-conjugated polymeric nanoparticles as delivery system for combination cancer therapy. Biomacromolecules 16(12):3980–3988
69. Mi Y et al (2016) Application of nanotechnology to cancer radiotherapy. Cancer Nanotechnol 7(11):1–16
70. Chen W (2008) Nanoparticle self-lighting photodynamic therapy for cancer treatment. J Biomed Nanotechnol 4:369–376
71. Liu Y et al (2008) Investigation of water-soluble x-ray luminescence nanoparticles for photodynamic activation. Appl Phys Lett 92(4):043901

72. Zhang C et al (2015) Marriage of scintillator and semiconductor for synchronous radiotherapy and deep photodynamic therapy with diminished oxygen dependence. Angew Chem Int Ed 54:1770–1774
73. Zhang H et al (2011) A strategy for ZnO nanorod mediated multi-mode cancer treatment. Biomaterials 32(7):1906–1914
74. Chen Z et al (2014) A multi-synergistic platform for sequential irradiation-activated high-performance apoptotic cancer therapy. Adv Funct Mater 24(4):522–529
75. Li W et al (2012) Mechanism of photogenerated reactive oxygen species and correlation with the antibacterial properties of engineered metal-oxide nanoparticles. ACS Nano 6:5164–5173
76. Allison RR, Sibata CH (2010) Oncologic photodynamic therapy photosensitizers: a clinical review. Photodiagn Photodyn Ther 7:61–75
77. Fuchs J, Thiele J (1998) The role of oxygen in cutaneous photodynamic therapy. Free Radic Biol Med 24:835–847
78. Tsuji JS et al (2006) Research strategies for safety evaluation of nanomaterials. Part IV: Risk assessment of nanoparticles. Toxicol Sci 89(1):42–50
79. Fu PP et al (2014) Mechanisms of nanotoxicity: generation of reactive oxygen species. J Food Drug Anal 22:64–75

Chapter 10
Fundamental Experiments and Quantum Technology Applications with Defect Centres in Diamond

Oliver Benson

Abstract The observation of single quantum objects has been a challenging task requiring advanced experimental techniques. With improved microscopy methodology it is nowadays possible to observe such objects in the solid state with compact setups even at room temperature. In this contribution we introduce defect centres in diamond and discuss two recent experiments. One concerns the direct observation of the quantum nature of light with not more but a single detector. The second one shows how to use defect centres as a valuable light source for quantum key distribution.

Keywords Diamond defect centre · Single photons · Light quantization · Superconducting detectors · Quantum key distribution · Quantum information

10.1 Introduction

Defect centers in diamond are stable atom-like objects, that emit light. This simple feature has nevertheless allowed for a large number of experiments and applications. The reason is that the very nature of light emitted from a single quantum system has quantum features as well. On the other hand, light, i.e. an electromagnetic field in the visible special range, is easy to detect, even at an ultra-low level of intensity. In this way the state of the emitter can be detected and even manipulated with light.

In this contribution we discuss two experiments with a defect centre in diamond, more precisely with a single nitrogen vacancy centre. Both experiments utilize the quantum nature of the emitted light. A first one is of fundamental nature [1], whereas a second one deals with an application in quantum information processing [2].

O. Benson (✉)
Nano-Optics, Institute of Physics, Humboldt-University, Berlin, Germany
e-mail: oliver.benson@physik.hu-berlin.de; https://www.physik.hu-berlin.de/de/nano

B. Di Bartolo et al. (eds.), *Quantum Nano-Photonics*, NATO Science for Peace and Security Series B: Physics and Biophysics,
https://doi.org/10.1007/978-94-024-1544-5_10

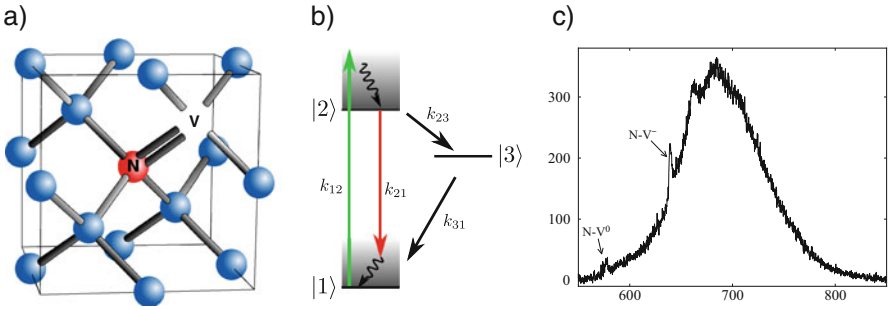

Fig. 10.1 Nitrogen vacancy (NV) centre in diamond: (**a**) structure, (**b**) level scheme, (**c**) emission spectrum

10.2 Single Photon Emitters Based on Defect Centres in Diamond

Defect centres in diamond are the subject of intense research due to their exceptional role as single-photon sources at ambient condition [3]. Among the different defects, nitrogen vacancy (NV) centres are the best studied, a nitrogen replacing a carbon atom with an adjacent vacancy in the diamond lattice (Fig. 10.1a). A charged NV^- and an uncharged NV^0 configuration of this defect could be identified, with zero phonon lines (ZPL) at 638 nm and 575 nm. At room temperature, single-photon emission around 700 nm with count rates up to 10^6 counts/s can be observed from the NV^-. The spectrum of a single NV centre in a nanodiamond is shown in Fig. 10.1c. In nanodiamonds, we always observe both ZPLs attributed to (de-)charging effects. The optical transition occurs between two spin-triplet states ($|1\rangle \rightarrow |2\rangle$), but at least one singlet state is also present (Fig. 10.1b) and can be filled by intersystem crossing, which results in an additional bunching feature in the $g^{(2)}$-function. The presence of NV centres in nanodiamonds down to sizes of 5 nm make them superior fundamental building blocks in more complex, hybrid assembled photonic and plasmonic structures.

10.3 The Most Fundamental Experiment to Show the Quantum Nature of Light

10.3.1 Concept of the Experiment

The first experiment based on an NV centre single photon source concerns non-classicality, i.e. a proof that light consists of photons. Many properties of a light emitter can be studied only by analysing auto-correlation functions of the electric field. Firstly, this holds for revealing the non-classical character of a quantum light

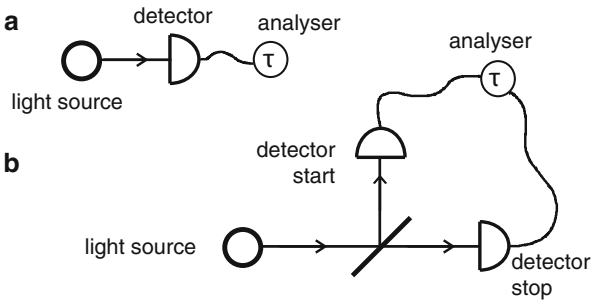

Fig. 10.2 Scheme of setups to measure the second-order auto-correlation function of the electric field of a light source. (**a**) Measurement scheme with a single fast detector. (**b**) Conventional HBT-setup. (Reproduced from [1])

source. The quantum nature of an emitter can be demonstrated only by measuring temporal intensity correlations (or photon statistics) of the emitted light, i.e. the second-order auto-correlation function of the electric field, given by

$$g^{(2)}(\tau) = \frac{\langle E^{\dagger}(t)E^{\dagger}(t+\tau)E(t+\tau)E(t)\rangle}{\langle E^{\dagger}(t)E(t)\rangle^2} = \frac{\langle : I(t)I(t+\tau) : \rangle}{\langle I(t)\rangle^2} \tag{10.1}$$

where : : denotes normal ordering of the operators [4]. For totally uncorrelated light, as from a laser, $g^{(2)}(\tau) = 1$ for all τ. However, for a number state $|n\rangle$, at $\tau = 0$ the second-order auto-correlation function drops to $g^{(2)}(0) = 1 - \frac{1}{n} < 1$ while for classical light sources $g^{(2)}(\tau) \geq 1$ for all τ [4]. Such a measurement of the $g^{(2)}$-function is used to prove non-classical light emission from single-photon sources.

For classical sources analysis of the photon statistics also provides useful information. For example, fluorescence correlation spectroscopy (FCS) [5–7] is widely used to characterize particle dynamics. In particular, diffusion coefficients, average concentrations, chemical reaction rates, molecular rotational Brownian motion, singlet-triplet dynamics, and spectral dynamics can all be observed using FCS [8–10].

When measuring the $g^{(2)}$-function with a single detector placed after the light source (Fig. 10.2a), photon arrival time differences τ shorter than the detector's dead time t_d cannot be measured. Thus a measurement of the $g^{(2)}$-function can only be performed for time differences larger than the detector's dead time, any features for time differences $\tau < t_d$ cannot be resolved. This is crucial for the demonstration of non-classical light emission since here the task is to measure an antibunching feature at $\tau = 0$. If t_d is of the same order or larger than the width of the antibunching dip, non-classical photon emission cannot be demonstrated with such a simple setup. This is the reason why the typical experimental setup for measuring the intensity auto-correlation function is the Hanbury-Brown and Twiss (HBT) setup [11], which is shown in Fig. 10.2b. In each of the outputs of a 50:50 beam splitter a detector is placed and time differences between clicks in detector start and detector stop are recorded. The $g^{(2)}$-function can be obtained from the distribution of these time differences for all photon arrival time differences τ.

However, disadvantages of this configuration are the facts that the setup cannot be built as compactly as the one with a single detector and that more equipment is needed. Furthermore, for the setup with a single detector in principle one can obtain a higher count rate than for the one with a time difference measurement between a start and a stop detector. Last but not least, sometimes the HBT configuration gives rise to misleading interpretations of the experimental process. It may suggest that the photon has to "decide" at the beam splitter which way to take, rather than that the projection on one of the two possible paths is made when the photon is detected at either of the detectors.

Here, we present our experimental data for observing non-classical photon statistics with a single detector. As single-photon source we utilized a nitrogen vacancy (NV) centre in a diamond nanocrystal [3].

10.3.2 Experimental Results

The lifetimes of NV centres in diamond nanocrystals are around 30 ns, which is very large compared to other single-photon sources as e.g. quantum dots. For resolving the interesting features of the corresponding $g^{(2)}$-function with a single detector that its dead time must be well below this value.

As a detector we utilized a fiber-coupled superconducting single-photon detector (SSPD). It consists of a 100 nm wide and 5 nm thick NbN meandering wire. This meander structure is fabricated on a sapphire crystal and covers an area of $10\,\mu\text{m} \times 10\,\mu\text{m}$ (Fig. 10.3a). The fabrication procedure is described elsewhere [12]. A fixed fiber-coupling to the detector area was implemented (Fig. 10.3b). For that purpose the sapphire was thinned to a thickness of $100\,\mu\text{m}$ and its back side was polished. The end facet of a single-mode fiber was aligned on the detector area and glued directly on the back side of the sapphire crystal. Figure 10.3d shows a scheme of the detector chip. For operation the detector was cooled to 4 K and biased at 90% of its critical current. Photon absorption in the detector causes a breakdown of the superconductance and thus a voltage pulse across the wire [12]. Figure 10.3c shows a scheme of the detector setup. The detector chip is mounted on a dip stick an immerged in liquid helium. These pulses from the detector are amplified by 76 dB at two 2 GHz bandwidth amplifiers. The inset in Fig. 10.4 shows a typical voltage curve for a photon absorption recorded with an oscilloscope of 2 GHz bandwidth. There was always a small reflection of the pulse observed after 14 ns which might be due to impedance mismatch. The dead time of the detector is $\leq$5 ns, the dark count rate is $<50\,\text{s}^{-1}$ and the quantum efficiency at 630 nm around 10%. The temporal resolution of the whole detector system was measured by applying femtosecond optical pulses from a titanium-sapphire laser. The voltage pulses of the SSPD and the trigger signal from the laser were connected to a time interval counter with 4 ps resolution. Such the time resolution of our system could be determined to 100 ps.

Figure 10.5 shows the experimental setup for measuring the $g^{(2)}$-function. Nanodiamonds were spin-coated on a coverslip and a single NV^- centre was located

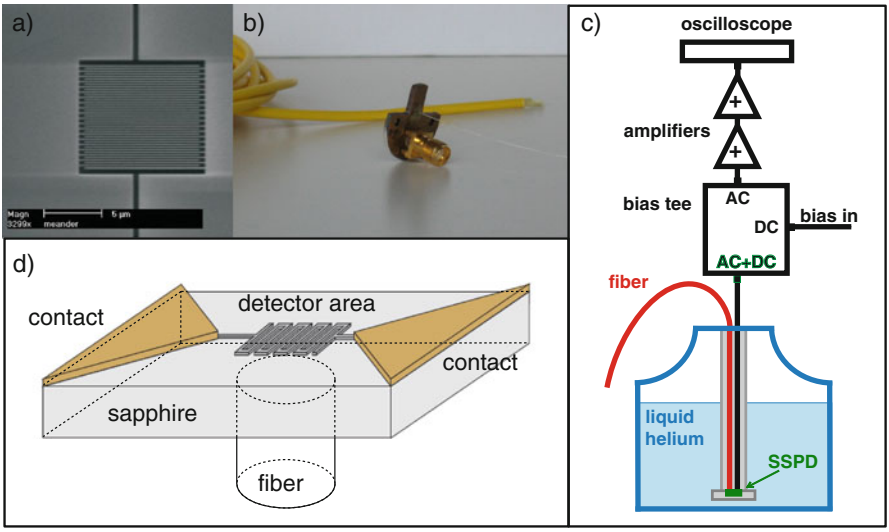

Fig. 10.3 (**a**) STM picture of the detector area, which covers an area of $10\,\mu\text{m} \times 10\,\mu\text{m}$. (**b**) Fiber-coupled detector, mounted on a circuit board. (**c**) Detector System: The fiber-coupled chip is mounted on a dip-stick and immerged in liquid helium. It is connected to a bias-tee through which the bias current is provided. The short voltage pulses from the detector are amplified an fed to an oscilloscope. (**d**) Scheme of the fiber-coupled detector chip. (Reproduced from [1])

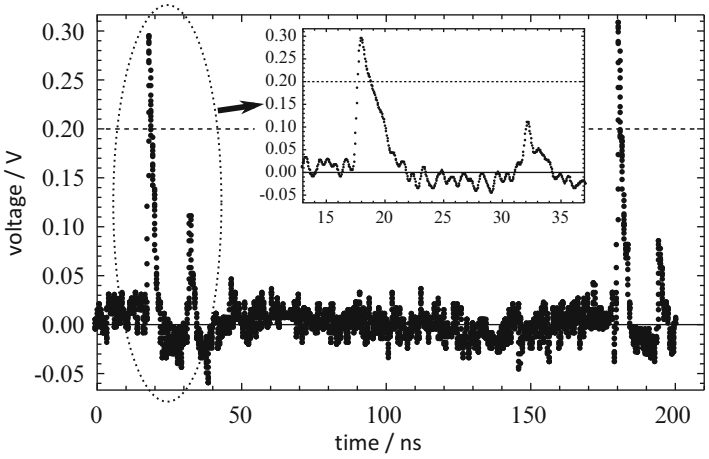

Fig. 10.4 Typical trace with two detection events within a time window between 4 ns and 200 ns. The inset is a zoom of the first pulse

in a home-made inverted microscope as described elsewhere [13]. The excitation light was filtered out before the emission was coupled into a single mode optical fiber. Via the optical fiber the light was sent directly to the SSPD (Fig. 10.5a) or coupled to a standard free beam HBT-setup (Fig. 10.5b) with two avalanched

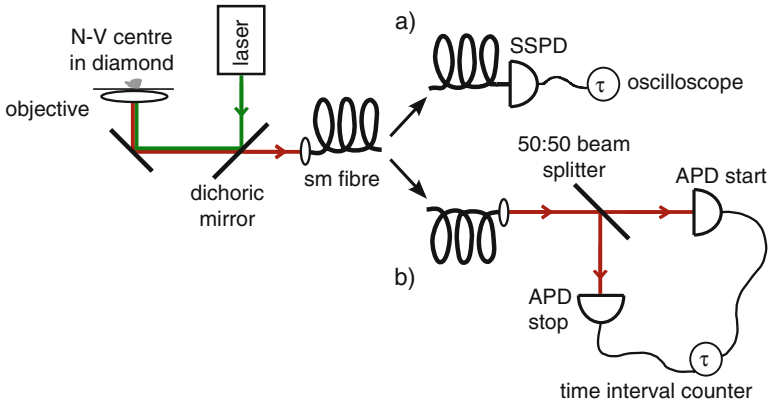

Fig. 10.5 Experimental setup. Light from a single NV centre in a diamond nanocrystal is coupled to (**a**) a single fiber-coupled SSPD or (**b**) a free space HBT setup. (Reproduced from [1])

photodiodes (APDs) in the beam splitter outputs. In case (a) the voltage pulses from the SSPD were fed to an oscilloscope with 2 GHz bandwidth. The oscilloscope was programmed to save a pulse trace whenever a trigger level of 200 mV was exceeded twice with a time difference of between 4 ns and 200 ns. For this trigger level the reflections are neglected. A typical trace is shown in Fig. 10.4. For measuring the $g^{(2)}$-function, 30,000 traces were recorded and analysed. The distribution of the time differences between two trigger events was determined. In case (b) the time differences between signals from the APDs were recorded with a time interval counter.

The experimental results for the non-classical light source are shown in Fig. 10.6. For the same NV centre two different measurements were performed, one with a single SSPD and for comparison another one with a usual HBT setup with APDs in the beam splitter outputs. For the latter events from stray light due to the free beam operation were subtracted. The distributions of time differences for both experiments overlap very well. Single-photon statistics is clearly proven by both measurements. The black line is a fit to the APD measurement.

To summarize this section, we have shown experimentally that it is possible to prove non-classical light emission with only one detector. The required temporal resolution of the $g^{(2)}$-function was achieved because we utilized a superconducting single-photon detector with a short dead time compared to the lifetime of our single-photon source.

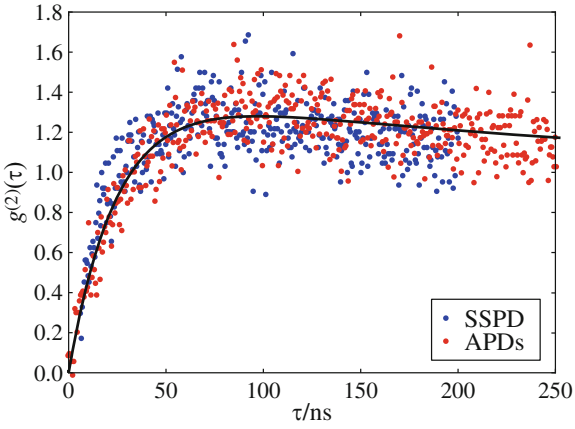

Fig. 10.6 Measurement of the distribution of time differences between photon arrivals for a nonclassical light source (single NV centre), measured with a single detector (blue) and a HBT setup with two APDs (red). The black line is a fit to the data. (Reproduced from [1])

10.4 Application of a Room-Temperature Single Photon Source for Quantum Key Distribution (QKD)

The most promising candidates for practical true single photon sources (SPS) today are solid-state emitters, such as quantum dots (QDs) [14, 15] or defect centres in diamond [16, 17]. The latter have the tremendous advantage that they operate at room temperature and show now photo bleaching or blinking. This makes them ideal sources for non-classical light in a number of applications. For the nitrogen vacancy (NV) centre single photon rates exceeding 2 Mcps [18] were reported under continuous laser excitation. Other, presumably Cr-related centres with potentially even higher count rates have been investigated [19, 20], but their reliable fabrication is problematic and a full understanding of their structural properties is missing. Here we concentrate on the use of NV centres as SPS in quantum key distribution (QKD) [21, 22].

In QKD, high key rate and/or long distance experiments have been successfully implemented without true single photons using weak coherent laser pulses (WCP) [23, 24] together with the decoy state protocol [25, 26]. Although this protocol is secure against photon number splitting (PNS) attacks, it has the disadvantage of producing some overhead, because one explicitly uses vacuum and very low intensity pulses together with the signal pulses and also operates with faint pulses with a mean photon number per pulse of around 0.5. In addition, long-range QKD requires quantum repeaters where sources of single indistinguishable photons are advantageous over photon pair sources [27]. A true single photon source with high efficiency could therefore still be favourable in quantum information processing compared to WCP. Efficiency means that it emits a single photon into a well defined spectral and spatial mode with a probability near unity each time a trigger is applied. A practical SPS should also have a stable emission rate, be easy-to-use, should operate at room temperature and at high repetition frequencies.

In order to evaluate the applicability of the NV centre as reliable source for quantum information processing, in particular for QKD, it is desirable to use testbeds that allow for long-term measurements, implementation of different protocols, as well as straightforward integration of different defect centres. In this section, we report the realization of such a testbed. It consists of a short free-space transmission line combined with a compact SPS based on defect centres. The source relies on a specialized confocal setup for stable optical excitation and efficient collection of single photons from defect centres. Furthermore, it is designed in a way that it is easy to replace one kind of defect centre by another.

10.4.1 Compact and Versatile Design of a Single Photon Source Based on Defect Centres in Diamond

The design of the source relies on a compact, portable and ready to use confocal setup. A ZrO_2 solid immersion lens (SIL) can be utilized to enhance the collection of single photons emitted from defect centres in nanodiamonds spin-coated directly on the SILs. Details of the fabrication of SILs with NV centres are provided in [18]. The source is built for single photon emitters with a wavelength range from 600 to 800 nm. With this it allows for the implementation of SPS using NV, SiV as well as Cr-based defect centres. Figure 10.7 shows a schematic (a) and a photograph (b) of the source which fits completely on an aluminum plate and has dimensions of only 22.5 cm $\times$ 19 cm $\times$ 9 cm. In this way the SPS is mobile and can easily be integrated in different experimental setups. The setup is robust against mechanical vibrations and thermal drifts due to its small size and compact mounting of all optical components. The generated single photon beam can either be freespace or fiber coupled by removal/addition of a single mirror which is equipped with a magnetic base. The sample unit holding the defect centres can either be the SIL with spin-coated defect centres or another substrate due to a removable sample holder. The setup is equipped with broadband optics and thus suitable for various defect centres, provided their emission wavelength is in the range of 600–800 nm. Only the exchangeable dichroic mirror has to be adapted together with the suitable excitation source. The sample holder is mounted on a 3-axes piezo stage. In order to keep track of the absolute position of the stage, sensors capable of detecting changes on a nanometer scale are used (SmarAct System). With this system it is possible to focus on a well defined position on the sample with very high accuracy and stability.

In principle, any kind of colour centre can be employed in the source described.

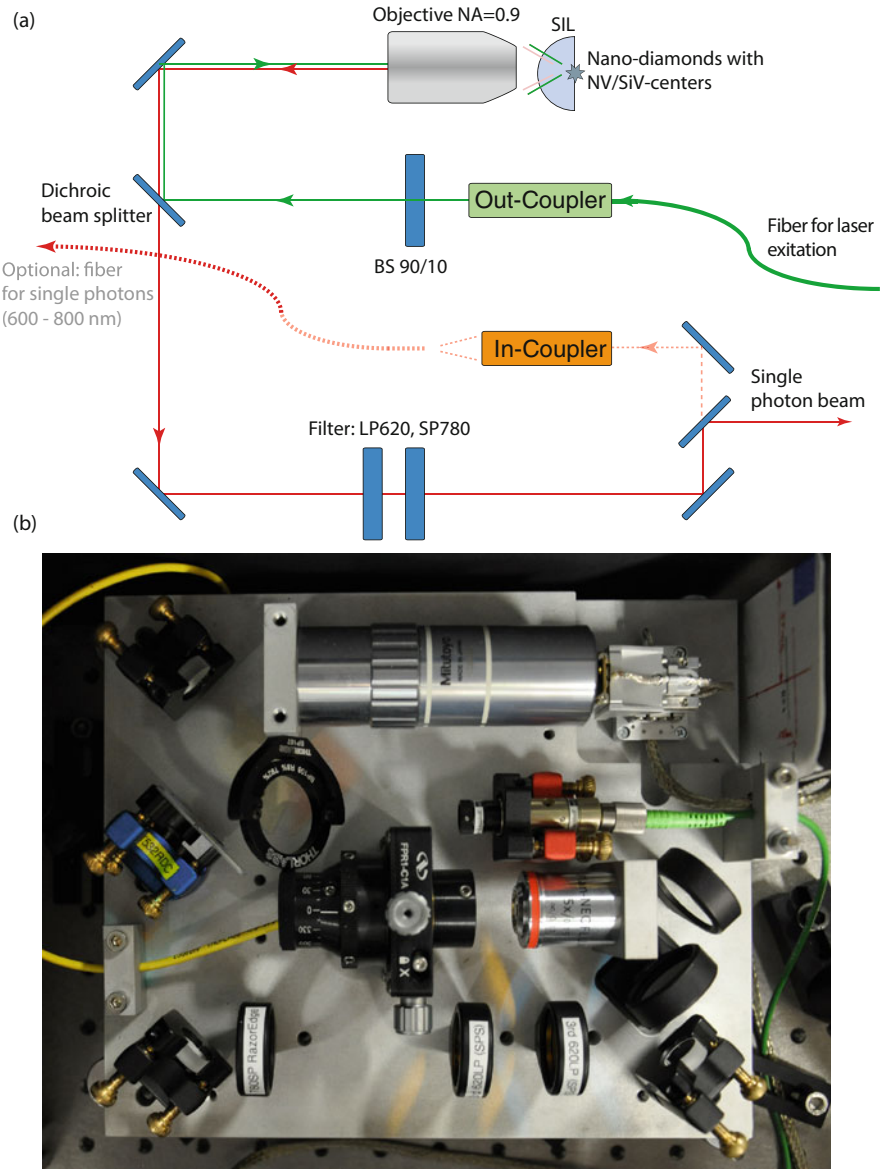

Fig. 10.7 (**a**) Scheme and (**b**) photo of the compact confocal setup. The excitation laser is focused with a high NA objective onto the sample which is either one of several diamonds spincoated on a solid immersion lens (SIL) or grown on a substrat. The emission is collected by the same objective and then filtered by a dichroic beam splitter (exchangeable) and longpass (LP) and shortpass (SP) filters to clean it from residual laser light or fluorescence of the SIL or the substrate. (Reproduced from [2])

10.4.2 Properties of the NV Centre for QKD Applications

The quality of single photon emission, in particular the contribution of multi-photon events is routinely determined by measuring the second order autocorrelation function ($g^{(2)}(\tau)$) in a Hanbury-Brown Twiss (HBT) setup [11]. Although in the ideal case $g^{(2)}(\tau = 0) = 0$, a value of $g^{(2)}(\tau = 0) < 0.5$ is generally accepted as a criterion for single photon emission. Values below 0.12 have been reported with NV defect centres [18]. In QKD it is favourable to have photons at a well defined instant of time, thus pulsed excitation of the defect centres is of interest. In such a pulsed excitation scheme, using a green diode laser (PicoQuant LDH-P-FA-530 [28], 531 nm, pulse width <100 ps), we achieved count rates of 8900 cps at an excitation rate of 1 MHz for an NV centre in a nanodiamond which was spincoated on a SIL. This corresponds to an overall photon yield of 0.89% and a source efficiency of 2.9%. The latter is defined as the ratio of excitation pulses resulting in a single photon without background in the desired optical mode, here the freespace beam of the QKD experiment. This value is determined for a given overall photon yield by taking the overall transmission η_{setup} of 0.31 of our setup, including the efficiency of ∼65% of the avalanche photodetectors (APDs), into account. For the QKD experiment, the maximal excitation rate was limited to frequencies up to 1 MHz by the modulation rate of the electro optic modulators (EOMs) (see section Fig. 10.4.3). A $g^{(2)}(0)$ value under pulsed excitation of 0.09, clearly indicating high purity single photon emission, is measured (Fig. 10.8a) using high resolution time-correlation electronics (PicoHarp 300 from PicoQuant). A lifetime of 28.5 ± 1.5 ns is calculated from the pulse shape.

10.4.3 Setup of QKD Testbed

The setup is shown in Fig. 10.9. The emitted freespace photons from the SPS are initially prepared in a linear polarization state by passing through a linear polarization filter after a $\lambda/2$ plate which is adjusted to maximize the count rate. After passing through a pinhole for further spatial mode cleaning, the photons impinge on the first EOM which is controlled by Alice. The EOM acts as a $\lambda/2$ and $\lambda/4$ plate, respectively, depending on the applied voltage. In this way two orthogonal linearly polarized photon states as well as two orthogonal circular polarization states can be encoded on the incoming photons, compliant to the BB84 protocol [29]. After passing through a lens system for recollimation, the photons pass through a second EOM, which is controlled by Bob. Bob randomly chooses a measurement basis by setting the voltage such that the EOM either does not modify the photons or acts as a $\lambda/4$ plate. A circular polarization is thus transformed into a linear one or vice versa. The linear polarization state can then be deterministically analyzed in a system consisting of a polarizing beam splitter (PBS), a linear polarization filter, compensating the non-perfect contrast of the PBS in reflection, and two avalanche

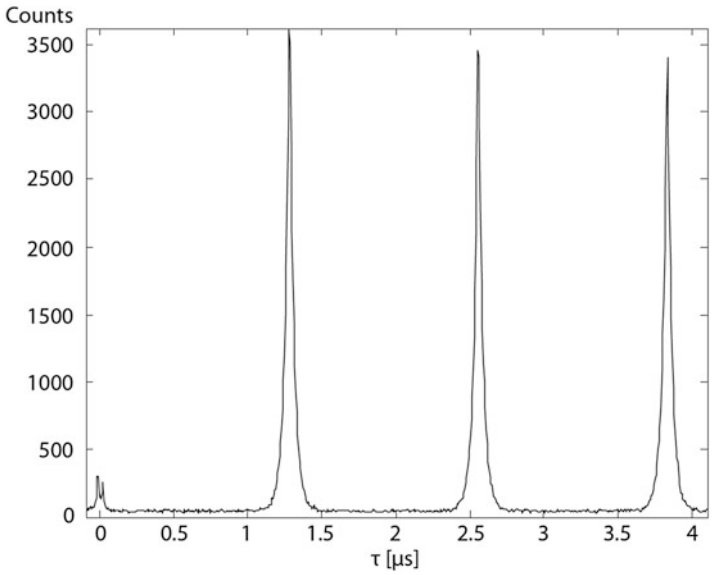

Fig. 10.8 Measured intensities as a function of time for NV centre emission under pulsed excitation to calculate $g^{(2)}(\tau)$. The excitation rates were 800 kHz. The missing pulse at $\tau = 0$ indicates single photon emission. From the pulse shape we calculated al lifetime of the excited state of 28.5 ± 1.5 ns. (Reproduced from [2])

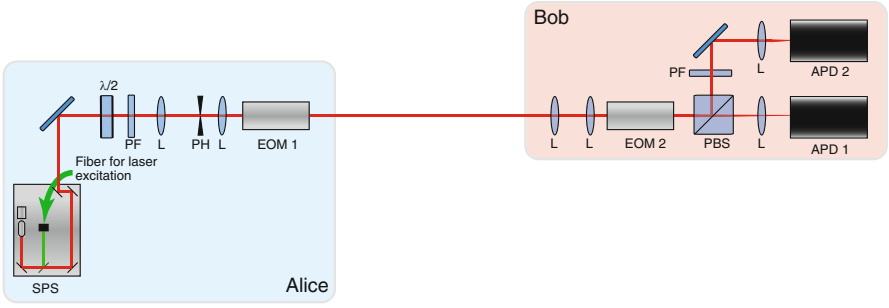

Fig. 10.9 Schematics of the QKD testbed. Single photons are emitted from the source (SPS) and prepared in a well defined polarization state by the $\lambda/2$ plate and a polarization filter (PF). After collimation and spatial mode cleaning by two lenses (L) and a pinhole (PH), they pass through an electro-optical modulator (EOM 1). On Bob's side, the beam is recollimated by two lenses and then passes through a second modulator (EOM 2). Then, the polarization is analyzed by a polarizing beam splitter (PBS) and a polarization filter in the reflected mode of the PBS, which has a slightly reduced contrast compared to the transmitted mode. After passing through a lens for focusing, the photons are detected on one of two APDs. (Reproduced from [2])

Table 10.1 Results of the QKD experiments in a test run for 300 s

NV	
Repetition rate	1 MHz
Count rate	8.9 ± 0.1 kbit/s
Sifted keyrate	3.99 ± 0.05 kbit/s
QBER	$3.0 \pm 0.2\%$
Secured keyrate	2.6 kbit/s

photodiodes (APDs) (Perkin Elmer AQR). For the random bit and basis choice of Alice and Bob, quantum random numbers from the online random number service of HU Berlin and PicoQuant GmbH (http://qrng.physik.hu-berlin.de/), see also [30] are used.

The EOM is constructed in a way that it acts as a zero order waveplate. This minimizes its wavelength dependency during the modulation of different polarization states. However, especially when using the broadband NV centre as light source, possible dependencies between wavelength and transmitted polarization state could open the door to side-channel attacks which would have to be analyzed in way similar to the analysis of multiphotons (cf. Fig. 10.4.4 below, especially the notion of "tagged" photons).

10.4.4 Experimental Results

In order to test the suitability of SPS based on the NV centre we ran the BB84 protocol in the QKD setup. The experimentally obtained parameters are summarized in Table 10.1. With the brightest NV centre, emitting at a count rate of 8.9 kcps, a sifted keyrate of 3.99 kbit/s at a quantum bit error rate (QBER) of 3% was achieved. The raw key was then further processed using the CASCADE protocol [31], resulting in a secure keyrate of 2.6 kbit/s. The CASCADE protocol is an efficient postprocessing protocol for the sifted key aiming at minimizing discrepancies between Alice and Bobs keys while at the same time minimizing Eves possible information about it. It consists of two steps: error correction by parity comparison between Alice and Bob and subsequent dilution of Eves information in the so-called privacy amplification. This privacy amplification is realized by a randomly chosen function belonging to a special class of hash functions. The observed QBER can be explained by the limited contrast of the polarization optics and the EOMs. The experiment ran with a stable emission rate over several hours, which was the necessary time to find the right EOM settings for transmission. This shows the long-term stability of our setup.

It is interesting to have a look at the source efficiencies and the $g^{(2)}(0)$ values of the SPS and their consequences on security concerning multiphoton events. An upper bound on the probability p_{m} to have multiphoton events in pulses emitted from a sub-Poisson light sources is given by [32],

$$p_{\mathrm{m}} \leq \frac{\mu^2 g^{(2)}(0)}{2}, \tag{10.2}$$

where μ is the mean photon number per pulse which is identical to the efficiency of the SPS to emit a single photon into the desired mode. This upper bound can then be used to calculate a lower bound on the secure keyrate R, which takes the unsecurity of having multiphoton events into account [33]:

$$R \geq q\{-Q_\mu f(E_\mu)H_2(E_\mu) + Q_\mu(1-\Delta)(1-H_2(E_\mu/(1-\Delta))\} \quad (10.3)$$

q is an efficiency factor depending on the exact protocol and expressing the randomness of the base choice, here it is 1/2, Q_μ, the signal gain, is the fraction of detection events at Bob's side which is related to the signal with mean photon number μ (For an exact definition of Q_μ, see i.e. [26]), f is the error correction efficiency of the postprocessing protocol, E_μ is the error rate of a signal with mean photon number μ, and $H_2(x) = -x \cdot log_2(x) - (1-x) \cdot log_2(1-x)$ is the binary Shannon information function [34]. Δ is the ratio of "tagged" photons. "Tagged" photons are photon qubits emitted by a faulty source, wearing a "tag" with readable information for the eavesdropper revealing the actual basis of the qubit, cf. [33]. When more than one photon is emitted at a time, it carries the same information as its partner photon and can be regarded as a "tagged" photon when exploited by Eve in a PNS attack. For a single photon source $\Delta = p_\mathrm{m}/p_\mathrm{click}$, with the detection probability of a signal $p_\mathrm{click} \approx \mu \cdot \eta_\mathrm{total} + p_\mathrm{dc}$ [32]. η_total contains, besides the setup transmission η_setup (cf. Sect. 10.4.2), the transmission of the quantum channel. The darkcount probability p_dc is in our setup 2.4×10^{-5}.

Figure 10.10 shows the results of these secure keyrate calculations as a function of the channel loss. The secure key generation rate at 0 dB roughly reproduces our measured keyrate after postprocessing. For comparison we also plotted the secure

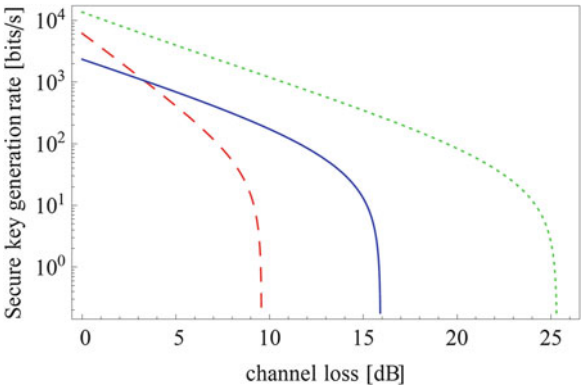

Fig. 10.10 Secure key rates as a function of channel loss achieved with the BB84 protocol utilizing a true SPS with an NV centre. For comparison, the keyrate when using an attenuated laser without the decoy state protocol at the optimized mean photon number $\mu \sim \eta_{total}$, where η_{total} is the overall transmission of the setup, is shown in red and dashed. Also shown in green and dotted is the secure keyrate when using WCP together with the decoy state protocol with a mean photon number of 0.5. (Calculated as in [36]; reproduced from [2])

keyrate of a potential experiment with identical parameters (please note that for lasers repetition rates might be chosen to be higher than particularly for the NV SPS), but with an attenuated laser instead of a single photon source with a mean photon number of $\mu \sim \eta_{\text{total}}$, which is approximately optimal for an attenuated laser without the decoy state protocol and when considering possible PNS attacks [35]. The keyrate is calculated as in Eq. 10.3, taking the multiphoton probability of a Poissonian lightsource into account. Also, the keyrate of an identical experiment with an attenuated laser source together with the decoy state protocol (the used mean photon number of 0.5 is calculated as in [36]) is shown. At low loss, attenuated laser pulses without the decoy state protocol have relatively high signal intensities and thus outperform our SPS, but at a certain channel loss (>3.3 dB) for the NV, cf. Fig. 10.10, translating into distances >8 km using a typical transmission of light through air in sea level of 0.4 dB/km the SPS provides higher secure keyrates and longer achievable transmission distances. This is due to a lower number of multiphoton events in a true SPS compared to an attenuated classical pulse of the same mean photon number. However, for the parameters achieved with single photon sources based on defect centres an attenuated laser together with the decoy state protocol is still favourable over our SPS regarding maximum keyrates and achievable distances. This is because the obtained efficiencies of the SPS is not high enough and at the same time the $g^{(2)}(0)$ value not low enough to outperform WCP together with the decoy state protocol (cf. Sect. 10.5). In this context, it is also interesting to note that even SPS sometimes have to be attenuated to reduce the small, but in a real source still existing fraction of multi-photon events to achieve the maximal possible transmission distance [32]. Even with high source efficiency, thus high mean photon number per excitation, security can be compromised at certain distances if the $g^{(2)}(0)$ value is not low enough. In fact for every $g^{(2)}(0)$ value and a given darkcount rate of the detectors, the maximal mean photon number to realize the longest distances can be estimated after the following formula, taken from [32]:

$$\mu_{\text{c}} = \sqrt{\frac{2p_{\text{dc}}}{g^{(2)}(0)}} \tag{10.4}$$

The ideal case would be to have a SPS which is above this critical mean photon number and to attenuate it in order to achieve the best rates at any distance. For our NV centre, we have an efficiency of 0.029 and a $g^{(2)}(0)$ of 0.09 (cf. Sect. 10.4.2). The critical mean photon number for this value of $g^{(2)}(0)$ is 0.039, a little above the given efficiency. There are examples of NV centres with higher efficiencies [18] which would surpass their critical mean photon number.

To summarize this section, single photon sources based on defect centres in diamond could outperform attenuated light sources in the future under optimistic but not unrealistic assumptions [2].

10.5 Conclusion

Defect centres in diamond have found many applications in the last years. On the one hand there are fundamental studies to learn about the quantum nature of electromagnetic field as we discussed in Sect. 10.3. More recently, we could also demonstrate the observation of the quantum Zeno effect using measurements on a single NV centre [37].

One the other hand, there are already true applications of single NV centers. In Sect. 10.4 we described a task in optical quantum technologies, i.e. quantum key distribution. Another direction is the use of NV centres in sensing. Aside from fundamental optical sensing, such as single emitter fluorescence lifetime imaging [38], there is by now a large activity on using NV centers as ulra-sensitive nanomagnetometer [39].

References

1. Steudle G, Schietinger S, Höckel D, Dorenbos SN, Zadeh IE, Zwiller V, Benson O (2012) Measuring the quantum nature of light with a single source and a single detector. Phys Rev A 86:053814
2. Leifgen M, Schröder T, Gädeke F, Riemann R, Metillon V, Neu E, Hepp C, Arend C, Becher C, Lauritsen K, Benson O (2014) Evaluation of nitrogen- and silicon-vacancy defect centres as single photon sources in quantum key distribution. New J Phys 16:023021
3. Jelezko F, Wrachtrup J (2006) Single defect centres in diamond: a review. Phys Status Solidi A 203:3207–3225. https://doi.org/10.1002/pssa.200671403
4. Walls DF, Milburn GJ (2008) Quantum optics. Springer. https://doi.org/10.1007/978-3-540-28574-8
5. Magde D, Elson EL, Webb WW (1972) Thermodynamic fluctuations in a reacting system – measurement by fluorescence correlation spectroscopy. Phys Rev Lett 29:705–708. https://doi.org/10.1103/PhysRevLett.29.705
6. Elson EL, Magde D (1974) Fluorescence correlation spectroscopy. I. Conceptual basis and theory. Biopolymers 13:1–27. https://doi.org/10.1002/bip.1974.360130102
7. Magde D, Elson EL, Webb WW (1974) Fluorescence correlation spectroscopy. II. An experimental realization. Biopolymers 13:29–61. https://doi.org/10.1002/bip.1974.360130103
8. Schwille P (2001) Fluorescence correlation spectroscopy and its potential for intracellular applications. Cell Biochem Biophys 34:383–408. https://doi.org/10.1385/CBB:34:3:383
9. Webb WW (2001) Fluorescence correlation spectroscopy: inception, biophysical experimentations, and prospectus. Appl Opt 40:3969–3983. https://doi.org/10.1364/AO.40.003969
10. Marshall LF, Cui J, Brokmann X, Bawendi MG (2010) Extracting spectral dynamics from single chromophores in solution. Phys Rev Lett 105:053005. https://doi.org/10.1103/PhysRevLett.105.053005
11. Hanbury-Brown R, Twiss RQ (1956) Correlation between photons in two coherent beams of light. Nature 177:27–29. https://doi.org/10.1038/177027a0
12. Goltsman GN, Okunev O, Chulkova G, Lipatov A, Semenov A, Smirnov K, Voronov B, Dzardanov A, Williams C, Sobolewski R (2001) Picosecond superconducting single-photon optical detector. Appl Phys Lett 79:705. https://doi.org/10.1038/177027a0
13. Schietinger S, Barth M, Aichele T, Benson O (2009) Plasmon-enhanced single photon emission from a nanoassembled metal-diamond hybrid structure at room temperature. Nano Lett 9:1694–1698. https://doi.org/10.1021/nl900384c

14. Intallura PM, Ward MB, Karimov OZ, Yuan ZL, See P, Shields AJ, Atkinson P, Ritchie DA (2007) Quantum key distribution using a triggered quantum dot source emitting. Appl Phys Lett 91:161103. https://doi.org/10.1063/1.2799756
15. Heindel T, Kessler CA, Rau M, Schneider C, Fürst M, Hargart F, Schulz W-M, Eichfelder M, Rübach R, Nauerth S, Lermer M, Weier H, Jetter M, Kamp M, Reitzenstein S, Höfling S, Michler P, Weinfurter H, Forchel A (2012) Quantum key distribution using quantum dot single-photon emitting diodes in the red and near infrared spectral range. New J Phys 14:083001
16. Kurtsiefer C, Mayer S, Zarda P, Weinfurter H (2000) Stable solid-state source of single photons. Phys Rev Lett 85:290–293. https://doi.org/10.1103/PhysRevLett.85.290
17. Neu E, Steinmetz D, Riedrich-Möller J, Gsell S, Fischer M, Schreck M, Becher C (2011) Single photon emission from silicon-vacancy colour centres in chemical vapour deposition nano-diamonds on iridium. New J Phys 13:025012. https://doi.org/10.1088/1367-2630/13/2/025012
18. Schröder T, Gädeke F, Banholzer MJ, Benson O (2011) Ultrabright and efficient single-photon generation based on nitrogen-vacancy centres in nanodiamonds on a solid immersion lens. New J Phys 13:055017. https://doi.org/10.1088/1367-2630/13/5/055017
19. Aharonovich I, Castelletto S, Johnson BC, McCallum JC, Simpson DA, Greentree A, Prawer S (2010) Chromium single-photon emitters in diamond fabricated by ion implantation. Phys Rev B 81:121201. https://doi.org/10.1103/PhysRevB.81.121201
20. Aharonovich I, Castelletto S, Simpson DA, Greentree AD, Prawer S (2010) Photophysics of chromium-related diamond single-photon emitters. Phys Rev A 81:043813. https://doi.org/10.1103/PhysRevA.81.043813
21. Beveratos A, Brouri R, Gacoin T, Villing A, Poizat J-P, Grangier P (2002) Single photon quantum cryptography. Phys Rev Lett 89:187901. https://doi.org/10.1103/PhysRevLett.89.187901
22. Alléaume R, Treussart F, Messin G, Dumeige Y, Roch J-F, Beveratos A, Brouri-Tualle R, Poizat J-P, Grangier P (2004) Experimental open-air quantum key distribution with a single-photon source. New J Phys 6:92. https://doi.org/10.1088/1367-2630/6/1/092
23. Dixon AR, Yuan ZL, Dynes JF, Sharpe AW, Shields AJ (2010) Continuous operation of high bit rate quantum key distribution. Appl Phys Lett 96:161102. https://doi.org/10.1063/1.3385293
24. Schmitt-Manderbach T, Weier H, Fürst M, Ursin R, Tiefenbacher F, Scheidl T, Perdigues J, Sodnik Z, Kurtsiefer C, Rarity JG, Zeilinger A, Weinfurter H (2007) Experimental demonstration of free-space decoy-state quantum key distribution over 144 km. Phys Rev Lett 98. https://doi.org/10.1109/CLEOE-IQEC.2007.4386755
25. Hwang W-Y (2003) Quantum key distribution with high loss: toward global secure communication. Phys Rev Lett 91. https://doi.org/10.1103/PhysRevLett.91.057901
26. Lo H-K, Ma X, Chen K (2005) Decoy state quantum key distribution. Phys Rev Lett 94:230504. https://doi.org/10.1103/PhysRevLett.94.230504
27. Sangouard N, Simon C, Minar J, Zbinden H, de Riedmatten H, Gisin N (2007) Long-distance entanglement distribution with single-photon sources. Phys Rev A 76:050301. https://doi.org/10.1103/PhysRevA.76.050301
28. Schönau T, Riecke SM, Lauritsen K, Erdmann R (2011) Amplification of ps-pulses from freely triggerable gain-switched laser diodes at 1062 nm and second harmonic generation in periodically poled lithium niobate. Proc SPIE 7917:791707–791707. https://doi.org/10.1117/12.872114
29. Bennett CH, Brassard G (1984) Quantum cryptography: public key distribution and coin tossing. In: Proceedings of the IEEE international conference on computers, systems, and signal processing, Bangalore, vol 175. https://doi.org/10.1016/j.tcs.2014.05.025
30. Wahl M, Leifgen M, Berlin M, Röhlicke T, Rahn H-J, Benson O (2011) An ultrafast quantum random number generator with provably bounded output bias based on photon arrival time measurements. Appl Phys Lett 98:171105. https://doi.org/10.1063/1.3578456
31. Brassard G, Salvail L (1994) Secret-key reconciliation by public discussion. In: Helleseth T (ed) Advances in cryptology – EUROCRYPT 93, LNCS 765. Springer, Berlin/Heidelberg, pp 410–423. ISBN: 978-354057600-6

32. Waks E, Santori C, Yamamoto Y (2002) Security aspects of quantum key distribution with sub-Poisson light. Phys Rev A 66:042315. ISSN: 10502947
33. Gottesman D, Lo H-K, Lütkenhaus N, Preskill J (2004) Security of quantum key distribution with imperfect devices. Quantum Inf Comput 4:325–360. ISSN: 15337146
34. Shannon CE (1948) A mathematical theory of communication. Bell Syst Tech J 27:379–423, 623–656. https://doi.org/10.1002/j.1538-7305.1948.tb01338.x
35. Lütkenhaus N (2000) Security against individual attacks for realistic quantum key distribution. Phys Rev A 61:052304. ISSN:10502947
36. Ma X, Qi B, Zhao Y, Lo H-K (2005) Practical decoy state for quantum key distribution. Phys Rev A 72:012326. https://doi.org/10.1103/PhysRevA.72.012326
37. Wolters J, Strau M, Schoenfeld R-S, Benson O (2013) Quantum Zeno phenomenon on a single solid-state spin. Phys Rev A 88:020101. https://doi.org/10.1103/PhysRevA.88.020101
38. Schell AW, Engel P, Werra JFM, Wolff C, Busch K, Benson O (2014) Scanning single quantum emitter fluorescence lifetime imaging: quantitative analysis of the local density of photonic states. Nano Lett 14:2623–2627. https://doi.org/10.1021/nl500460c
39. Hong S, Grinolds MS, Pham LM, Le Sage D, Luan L, Walsworth RL, Yacoby A (2013) Nanoscale magnetometry with NV centers in diamond. MRS Bull 38:155–161. https://doi.org/10.1557/mrs.2013.23

Chapter 11
Emerging Fields of Colloidal Nanophotonics for Quality Lighting to Versatile Lasing

Hilmi Volkan Demir

Abstract Solution-processed semiconductor nanocrystals have attracted increasingly greater interest in optoelectronics including color conversion and enrichment in quality lighting and display backlighting. Optical properties of these colloidal nanocrystals can be conveniently controlled by tailoring their shape, composition, and size in an effort to realize high-performance light generation and lasing. We now witness the expanding deployment of semiconductor nanocrystals in consumer products being adapted by giant electronics companies. Based on the rational design and control of excitonic processes in these nanocrystals, it is possible to achieve highly efficient light-emitting diodes and optically pumped lasers. In this chapter, we introduce an emerging field of nanocrystal optoelectronics with applications from quality lighting to versatile lasing. We look into the performance limits of color conversion using colloidal nanocrystals. Here we introduce a new concept of all-colloidal lasers developed by incorporating nanocrystal emitters as the optical gain media intimately into fully colloidal cavities. As an extreme case of solution-processed tightly-confined quasi-2D colloids, we also show that the atomically flat nanoplatelets uniquely offer record high optical gain coefficients and ultralow threshold stimulated emission. Given the recent accelerating progress in colloidal nanophotonics, solution-processed quantum materials now hold great promise to challenge their conventional epitaxial counterparts in the near future.

Keywords Colloidal nanophotonics · Colloidal quantum dots · Colloidal quantum wells · Semiconductor nanocrystals · Nanoplatelets · All-colloidal lasers

H. V. Demir (✉)
LUMINOUS! Center of Excellence for Semiconductor Lighting and Displays, NTU – Nanyang Technological University, Singapore, Singapore

UNAM – Institute of Materials Science and Nanotechnology, Bilkent University, Ankara, Turkey
e-mail: volkan@stanfordalumni.org

B. Di Bartolo et al. (eds.), *Quantum Nano-Photonics*, NATO Science for Peace and Security Series B: Physics and Biophysics,
https://doi.org/10.1007/978-94-024-1544-5_11

Fig. 11.1 Evolution of light sources: from candles as blackbody radiators to light-emitting semiconductor devices of LEDs as the next-generation light engines

11.1 Color Conversion and Enrichment with Colloidal Nanocrystals

11.1.1 LED Lighting and Photometric Benchmarking

Artificial lighting uses about one fifth of the global electricity generation worldwide. This consumption is even higher in developing parts of the world, exceeding one third of the electricity generation locally. This can be reduced by over 50% (and in fact in principle much more depending on the level of improvement in photon management) with the performance levels to be met using semiconductor light-emitting diodes (LEDs) [1]. To this end, the LED-based light engines are targeted to serve as the next-generation lighting sources (Fig. 11.1). However, for a large-scale deployment of LEDs, it is not only about the energy efficiency and the optical output power per unit cost; the quality lighting also critically matters. Increasing visual acuity and color perception is hence key to the wide-scale penetration of LEDs into the general lighting market.

For visual acuity, in addition to the efficiency of a light source, the perceived level of efficiency is important. This is related to the sensitivity curves of the human eye, which show the spectrally-varying sensitivity level given the lighting condition (Fig. 11.2). The luminous efficacy of optical radiation (LER) quantifies the perceived optical efficiency (in lumens per optical Watt), while the luminous efficiency (LE) gives the electrical one. LE is basically the perceived optical output power per electrical input power (in lumens per electrical Watt). When there are sufficiently many photons making to a human eye, like on a sunny day, we have the photopic sensitivity curve, which corresponds to the photon-adapted vision, peaking at about 555 nm. As we have fewer and fewer photons collected by the eye, however, the sensitivity curve shifts toward shorter wavelengths, going through the mesopic region. When very few photons are available to the eye, like at a full-moon night, we lose the color perception but can still see – this is where we have the scotopic curve in effect, peaking at about 505 nm. This corresponds to the dark-adapted vision. Between the photopic and scotopic peaks, there is a major shift

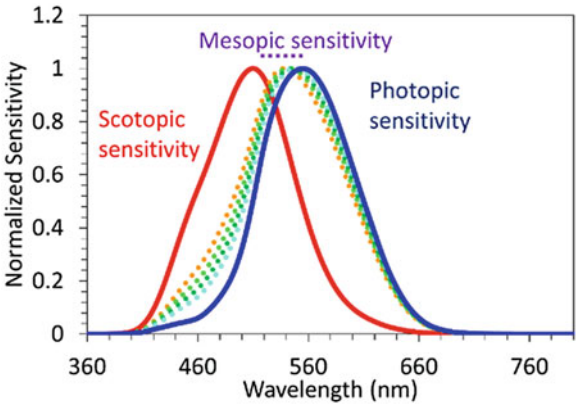

Fig. 11.2 Human eye sensitivity, shifting with the lighting intensity level: photopic, mesopic and scotopic sensitivity curves

of about 50 nm, which makes a substantial difference for the spectral content of a light source in terms of the perceived efficiency given the amount of photons available. In between these two extremes there is the transition region of mesopic curves. Because the sensitivity curves move with the lighting level, once can achieve spectrally enhanced lighting with careful spectral management of the lighting for the same of level optical power.

In addition to the visual acuity, we have equally important the visual performance, which is related to the shades of white light. This is quantified by the correlated color temperature (CCT). The weaker bluish tint in the white shade, the warmer white light is, corresponding to the lower CCT. This is essential to avoid disrupting biorhythm (circadian cycle) of the human clock (day-night). Finally, as another important aspect of quality lighting, the visual comfort requires good color rendition. This is related to the capability of a light source to reflect the true colors of an illuminated object. There are various metrics that have been defined to represent the level of color rendering including color rendering index (CRI) and color quality scale (CQS). This family of figure-of-merits is closely linked to human emotions triggered by light.

There are two mainstream strategies of generating white light using LEDs. In one approach, commonly known as the multi-chip approach, there are multiple LED chips, typically comprising of red-, green- and blue-emitting LEDs used together to make a white LED platform. Multiple LED chips emitting in different colors age at different rates. To keep the operating color point the same over time, the driving circuitry is typically complicated and there is a cost issue related with such complex drivers. On top of that, there is a green gap problem: green LEDs suffer efficiency, making it challenging to cover the green spectral region.

On the other hand, an easy and convenient approach for white light generation with LEDs is the so-called 'color conversion', which allows for using color-converting phosphors together with a pump LED emitting at a short wavelength, for example, more commonly in blue or cyan and possibly in near-UV. Typical color-converting materials contain rare earth elements as the emission centers doped in

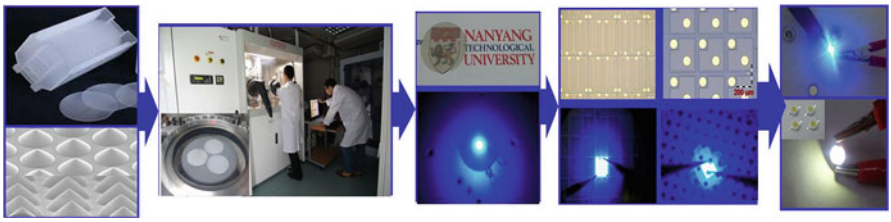

Fig. 11.3 Making a color-conversion white LED from the MOCVD growth to chip fabrication and packaging with the color convertors

a host matrix. This approach is a low-cost alternative to the multichip approach. However, there is a fundamental energy loss associated with conversion from the high-energy photons to the low-energy ones in the process of color conversion. Today the white LEDs most commonly found in the market are the color conversion LEDs. Figure 11.3 shows the processing steps of making a color-conversion LED starting with epitaxial growth of III-nitride epitaxy on sapphire using metalorganic chemical vapor deposition (MOCVD), continuing with the chip fabrication, and finally integrating with the color convertors at the chip level.

In color conversion, typically broad emitters of phosphors are used. They are easy to generate white light. However, it is difficult to control their spectral features precisely. For example, yellow phosphors are often employed, which would typically result in a low color rendering index of ~70. Using yellow phosphors, one would commonly achieve cool white appearance due to high correlated color temperature in the range of ~4000–8000 K. To address this difficulty, red-green phosphors can be preferred. Surely, this will allow for improved color rendering, exceeding 80 and even possibly reaching 95 in CRI while the CCT can be kept <3500 K; but, this comes at the penalty of a reduced luminous efficacy level of optical radiation due to the inevitable red tail, typically falling below 300 lm/W_{opt}. In addition, there are other problems related to the phosphor host and dopants including the granularity of their powder form and the resulting undesired scattering, the narrow absorption band of their rare earth dopants, and finally the supply security of the rare earth elements, which has become a major problem more recently.

11.1.2 Paradigm Shift with Narrow Quantum Emitters of Nanocrystals

Solution-processed semiconductor nanocrystals have been attracting increasingly a greater deal of interest in color conversion and enrichment for quality lighting and display backlighting. Optical properties of these colloidal materials can be conveniently controlled by tailoring their shape, composition, and size [2]. As

an alternative to broad emitters, narrow emitters of these nanocrystals offer the possibility to obtain photometrically ultimate performance. This is enabled by the fact that it is possible to control precisely the spectrum of such narrow quantum emitters.

Using various combinations of semiconductor quantum dot nanophosphors, it is possible to achieve warm white light with CCT < 3500 K, CRI > 80, and LER > 300 lm/W_{opt}, all at the same time [3]. This is a superior level of photometric performance compared to what can be possibly achieved with rare earth phosphors. Previously, there were concerns about their large scale production. Now this type of difficulties has been addressed. We now witness the expanding deployment of semiconductor nanocrystals in consumer products being adapted by electronics companies.

High optical quality white LEDs using quantum dot based nanophosphors with a carefully designed spectral content of emission has been widely investigated and a detailed review can be found in Demir, H.V., et al. Nano Today 6, 632 (2011) [3]. This is indeed a paradigm shift from continuous broad emitters to discontinuous narrow emitters of the right strategic combination.

With semiconductor nanocrystals, we can now routinely achieve high crystal quality. This is fast and low-cost solution-based processing. Using colloidal synthesis, shape, size and composition control and tuning are possible to target specific excitonic properties. Among the important advantages of semiconductor nanocrystals that are relevant to white light generation are the tunable absorption edge/emission peak, broadband absorption spectrum, narrow emission spectrum, high photoluminescence quantum efficiency, and stability against photobleaching (compared to organic counterparts). With semiconductor nanocrystals, one can reach reasonably high levels of quantum yield exceeding 95% in solution (using Cd-containing dots) with adjustable optical spectrum. In addition to being easy to tune, these nanocrystals offer color purity as a result of their spectrally narrow emission. They provide strong absorption, which is broad-band, whereas phosphors possess narrow absorption bands. This means that it is not only the emission band that one needs to get it right for white light generation, but it is also the absorption band that has to be right to match the emission wavelength of the pump LED.

As a result, semiconductor nanocrystal color convertors, with a careful design of the spectral content, enable high-quality white light having high color rendering index (for most natural objects) above 90, warm white shade at a low correlated color temperature below 3500 K, and a high luminous efficacy of optical radiation above 350 lm/W_{opt}. They also allow for high scotopic-to-photopic ratio (S/P) above 2.5 for spectral enhanced lighting. Therefore, photometrically, the nanocrystals provide the ability to outperform the phosphors. Furthermore, semiconductor quantum dots materials are abundant, whereas the rare-earth elements used in the conventional phosphors of LEDs are scarce. To date examples of commercialization and prototypes for general lighting and backlighting include the remote phosphor for general lighting and the backlighting unit for liquid crystal displays (LCD), which has been indeed commercially successful. In fact, in addition to white light generation, color enrichment has become also very important in the LCD

backlighting. Here the color purity (with a full-width half-maximum of 30 nm) is the key and using saturated red, green and blue color components is necessary to span a larger color space than that required by the national TV standards.

When integrated with blue LEDs, at least the red- and green-emitting nanocrystals are needed to make reasonable quality white light source. Adding in also the yellow nanocrystals is essential to make it ultimately high quality. In operation, these nanocrystals are optically pumped by the electroluminescence of their integrated LED, which is electrically driven. In this process, the physical mechanisms involved are the optical absorption and emission in the nanocrystals. The photoluminescence from the nanocrystals together with the electroluminescence form the LED collectively generates the white light. In addition, there are the undesired processes including the reabsorption of the photons emitted by the nanocrystals and dipole-dipole interaction (Förster-type energy transfer – FRET) between the nanocrystals. The reabsorption basically decreases the optical output power, while this type of FRET process among nanocrystals makes photo-generated excitons to be quickly zipped into nearby nanocrystals. If there are defected subpopulations of neighbor nanocrystals, then these transferred excitons are trapped and can undergo nonradiative recombination process and these defected nanocrystals thus act as exciton sinks that quench emission. In other words, their effective volume to trap excitons widely expands a result of the FRET process. In summary, in the process of while light generation collectively with the nanocrystal, the journey of an exciton in the nanocrystals includes exciton generation, exciton recombination, exciton transfer (FRET), and exciton trapping. Figure 11.4 illustrates the desired photoluminescence from nanocrystals in addition to the adverse energy transfer between them.

One important challenge with using semiconductor nanocrystals is that they are in dispersion. This means that, as they are synthesized, they are naturally available in solvents. This is not compatible with the existing backend process lines in LED packaging, which uses phosphors in the powder form. For that, the phosphors powder is dispersed in host organics, which is typically silicone, and then this mixture is dispensed directly and cured on the top of LED chips. To adopt

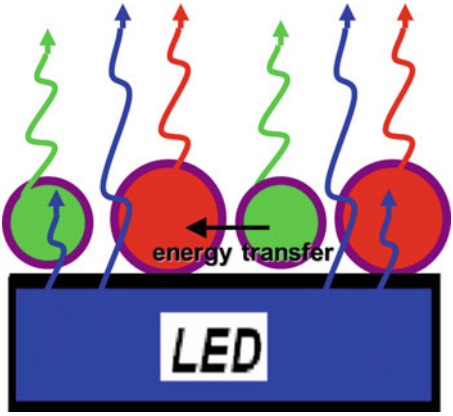

Fig. 11.4 Simple illustration of the concept of color-conversion white LEDs integrating the red- and green-emitting nanocrystals, which depicts the optical pumping by a blue LED chip and the resulting red and green photoluminescence from the nanocrystals, along with the undesired energy transfer from a green nanocrystal to a red one

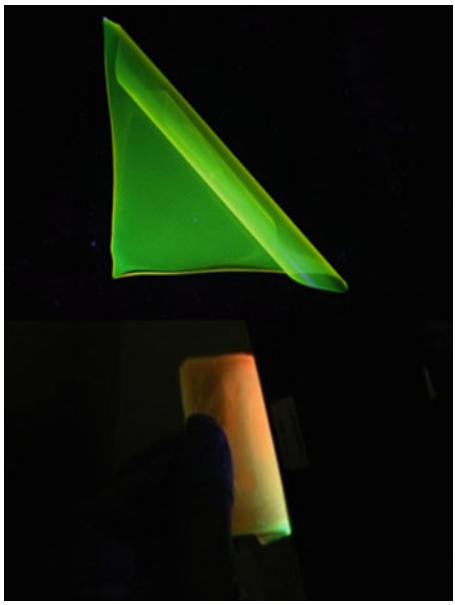

Fig. 11.5 Examples of nanocrystal sheets (monocolor and bi-color)

this process, we developed macrocrystals of nanocrystals that allow to embed the semiconductor nanocrystals into the large size crystals wrapping around the tiny nanocrystals and protecting them. These macrocrystals can then be grinded into micro-powder to be mixed with silicone and conveniently dispensed in the available process line.

Another approach is to make standalone nanocrystal films to be used as remote color convertors (Fig. 11.5). This type of nanocrystal sheets can be made quite large in size, in the range of over half a meter by over half a meter, and can be directly used as surface emitters for color conversion in lighting and color enrichment in LCD electronic displays. They can be mono-color or can be made in multiple colors, for example, integrating two layers on top of each other. Figure 11.5 shows proof-of-concept demonstrations of a green-emitting standalone nanocrystal sheet along with a bi-color (red and green) version – here one can see the dual color emission from a corner of the bent region.

11.1.3 Limits of Color Conversion with Nanocrystals

It is clear that nanocrystals provide us with the ability to carefully engineer the emission spectra to generate white light and optimize the photometric figure of merits, which would otherwise be impossible in the case of broadly-emitting phosphors. This is simply owing to the unique narrow emission of nanocrystals. However, the scientific questions remain: how well can we can do in practice

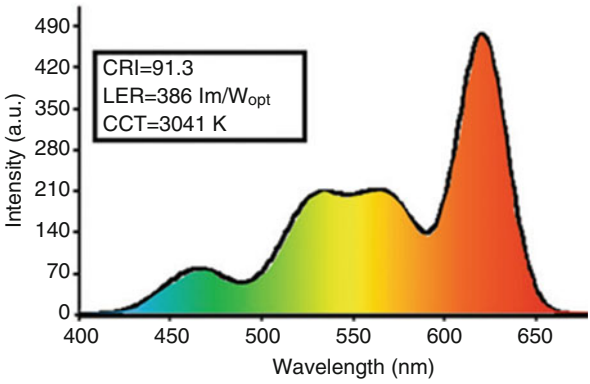

Fig. 11.6 Photometrically high-performance color-conversion white LED generated with using nanocrystal emitters

and what are the fundamental limits and trade-offs in terms of the photometric performance when using nanocrystal integrated LEDs? To this end, we investigated what is doable and how, and what is the ultimate performance level that we can realize. To systematically study this problem, we set an ambitious set of photometric targets including CRI $\geq$ 90, LER $\geq$ 380 lm/W_{opt}, and CCT < 4000 K [3]. What we found is that surprisingly only a very small fraction (only 0.001%) of over 230 million designs reach this performance levels. Obtaining highly efficient white light sources requires spectra that are carefully tuned and precisely controlled.

Extraordinarily high photometric performance is possible using nanocrystals (Fig. 11.6). This first necessitates a strong red component, which needs to be sharp in emission. It turns out that the red component has a critical emission wavelength at 620 nm, which is as far as possible into the red to make it warm white light but not too much to avoid reduction in the spectral efficiency. This color component has to hit the target peak emission with a precision of 1–2 nm, which is reproducibly doable for colloidal synthesis of nanocrystals. Otherwise, the penalty paid in terms of the reduction in photometric performance is the highest compared to all other color components. In contrast to the red, the blue component should be the weakest, and the green and blue can fill in the mid-gap at the middle level. With these, using nanocrystal emitters, it is possible to exceed CRI over 90 and LER over 385 lm/W_{opt} for a quite warm white shade at about 3000 K, as depicted in Fig. 11.6.

To further explore the performance limits and trade-offs, we systematically studied the CRI versus LER for the photopic (photon-adapted) vision (Fig. 11.7). We found that CRI above 90 is feasible within a relatively large window of LER. However, we discovered that this comes at the cost of decreasing LER: the higher LER is, the more CRI is to be traded off. Moreover, this fundamental trade-off becomes steeper with decreasing color temperature (for warmer white shades), as seen in Fig. 11.7.

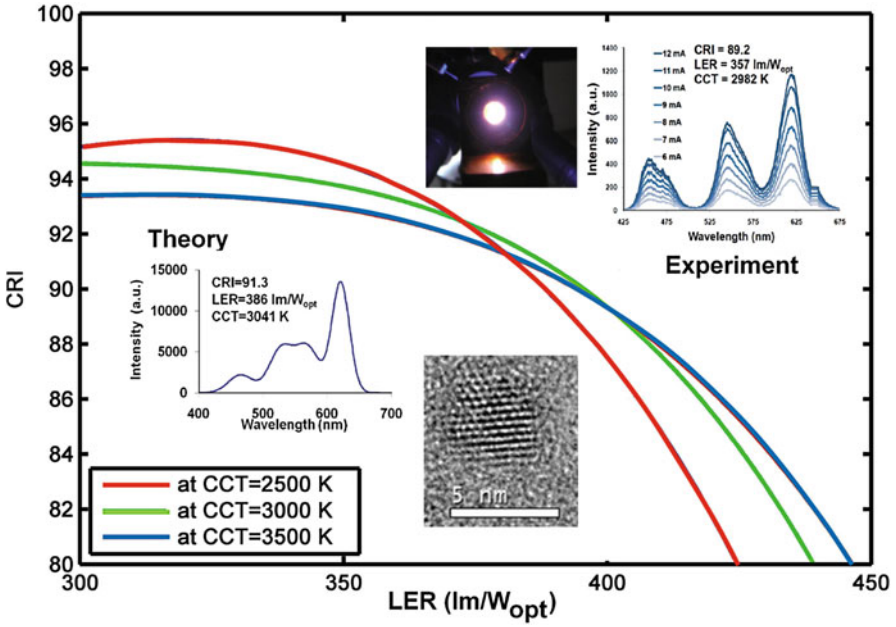

Fig. 11.7 Photometric vision performance limits: CRI vs. LER parametrized with respect to CCT, along with the theoretical and experimental implementations

11.2 All-Colloidal Lasers of Colloidal Nanocrystals

11.2.1 Colloidal Quantum Dots for Lasing

Based on the rational design and control of excitonic processes in semiconductor nanocrystals, in addition to color-conversion light-emitting diodes, it is possible to achieve highly efficient optically pumped lasers. These provide versatile lasing as a low-cost solution, in principle, essentially on any substrate. In the future, this type of versatile colloidal lasers is considered to find applications for general lighting, among other applications. This is because laser-based lighting is indistinguishable to human eyes compared to other light sources including the LEDs.

For this purpose, we introduce a new concept of all-colloidal lasers developed by incorporating nanocrystal emitters as the optical gain media intimately into fully colloidal cavities [4]. To this end, we use highly efficient CdSe/CdS core/shell nanocrystals synthesized with monolayer growth technique. These are polytypic lattice CdSe/CdS quantum dots, starting with zinc blende CdSe core and sequentially growing thick CdS shell in wurtzite. Therefore, the crystal lattice changes from zinc blende to wurtzite. The resulting nanocrystals have highly crystalline structure with a highly monodisperse size distribution (Fig. 11.8). They are almost non-blinking and exhibit near-unity quantum yield.

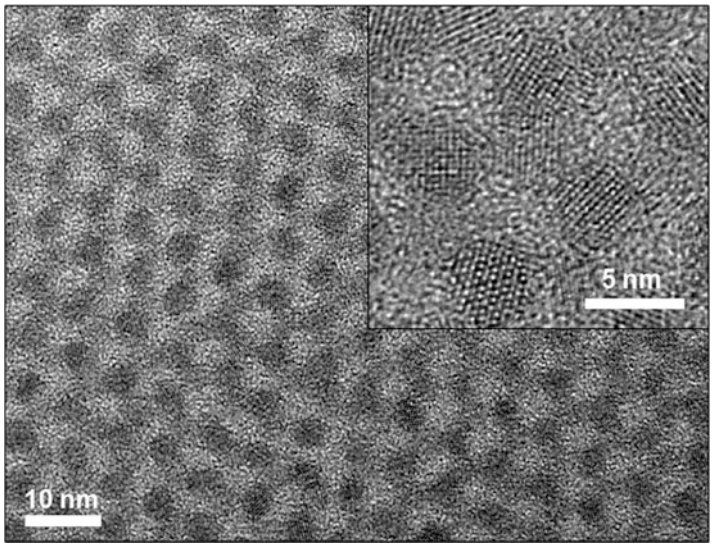

Fig. 11.8 Transmission electron microscopy images of CdSe/CdS core/shell nanocrystals (scale bars: 10 and 5 nm)

Figure 11.9 illustrates the concept of all-colloidal lasers that integrate quantum dot emitters as the optical gain medium intimately into a fully colloidal cavity. The cavity consists of alternating layers of titania and silica nanoparticles, as can be seen in the cross-sectional scanning electron microscopy image of the colloidal reflectors in the cavity. This laser is made of only solution-processed films including both the colloidal cavity and the colloidal gain. This implies that these lasers can be implemented basically on any platform of any type in principle (flexible, stretchable, etc.) Fig 11.10 shows the emission spectra collected from the all-colloidal laser of quantum dots parameterized with respect to the pump intensity, along with the characteristic spectral narrowing that can be seen in Fig. 11.10a. In Fig. 11.10b the integrated intensity distinctly exhibits the threshold and the stimulated emission region taking over after the threshold. A quality laser beam is observed to come out of this optically pumped all-colloidal laser of quantum dots. To the best of our knowledge, this is the first example of all-colloidal lasers.

Although the lasing performance obtained with this all-colloidal laser of quantum dots is one of the best in its class, there are fundamental barriers that stem from the intrinsic properties of this type of colloidal quantum dots. Among them is the large optical gain thresholds (in the range of several 100 s $\mu J/cm^2$ under pulsed excitation), which is due to the small optical gain coefficients ($\sim 100\ cm^{-1}$) possible. The root cause for their limited gain is the ultrashort gain lifetimes (typically shorter than 50 ps), which is constrained by the dominant Auger recombination and small absorption cross-sections. Therefore, an improved colloidal gain medium is required to overcome these barriers.

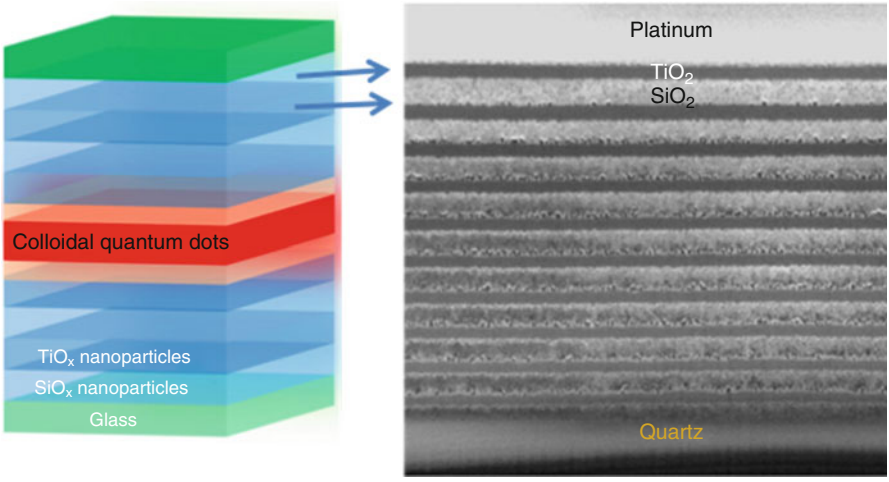

Fig. 11.9 Concept of all-colloidal lasers incorporating quantum dot emitters as the optical gain medium intimately into a fully colloidal cavity made of alternating layers of titania and silica nanoparticles: a simple sketch and a cross-sectional scanning electron microscopy image showing the colloidal reflectors as part of the cavity

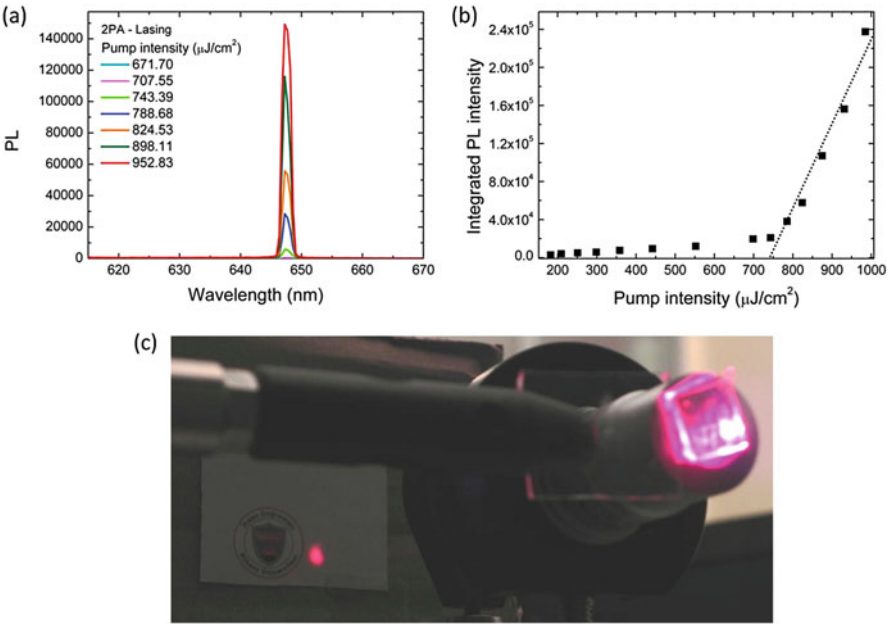

Fig. 11.10 (**a**) Emission spectra from the all-colloidal laser of quantum dots parameterized with respect to the pump intensity, (**b**) integrated intensity as a function of the pump intensity, and (**c**) quality laser beam coming out of the optically pumped all-colloidal laser of quantum dots

11.2.2 A New Paradigm Shift with Flat Nanocrystals of Nanoplatelets and Future Outlook

The need for improved colloidal gain medium brings us to a recent family of semiconductor nanocrystals: colloidal nanoplatelets, which are quasi-two dimensional nanocrystals [5]. These nanoplatelets are basically 'atomically flat'. They do not exhibit size distribution in the vertical thickness; they all have a single "magic" size in the vertical direction. As a result, they exhibit extremely narrow photoluminescence spectrum (with a full-width-at-half-maximum of 7–8 nm at room temperature). As an extreme case of the solution-processed tightly-confined quasi-2D colloids, what we find is that these atomically flat nanoplatelets uniquely offer record high optical gain coefficients and ultralow threshold stimulated emission.

This is indeed a new paradigm shift from colloidal quantum dots to wells possessing flat surfaces and extremely tight confinement. They only suffer homogeneous broadening, enabling their narrow emission. Thanks to their tight confinement, they feature giant oscillator strength and giant absorption cross-section with the lateral area that can be extended over 100 s of nanometers on each side. These extraordinary properties translate to the reduced optical gain thresholds (in the range of $\sim$10 μJ/cm^2 under pulsed excitation) and large optical gain coefficients ($\sim$1000 cm^{-1}), accompanied with long gain lifetimes ($\sim$150 ps).

There properties motivate us for all-colloidal laser made of nanoplatelets [6]. Figure 11.11 shows the characteristic emission spectra from such an all-colloidal laser of quantum wells parameterized with respect to the pump intensity and the integrated intensity as a function of the pump intensity. This is one of the first demonstrations of lasing using core/crown nanoplatelets by single photon absorption pumping. For another demonstration, also see another independent report from Talapin et al. [6]. Two photon absorption based pumping is also possible. This has thus led to also the first demonstration of lasing in the nanoplatelets using two-photon absorption pumping. In operation, record high optical gain was observed, which is 4$\times$ larger than the best in quantum dots and 2$\times$ larger than the best in quantum rods. Systematic variable stripe length study revealed that, while in colloidal dots $\sigma_{gain} = \sim$150 cm^{-1} and in colloidal rods $\sigma_{gain} =$ 300–350 cm^{-1}, the colloidal wells achieve $\sigma_{gain} >$ 1000 cm^{-1}.

The future outlook includes the advanced heterostructures of nanoplatelets, as visioned in Fig. 11.12. This kind of advanced heteronanoplatelets offers a great deal of photo- and thermal-stability, along with further enhanced gain capabilities. With such an accelerating progress, such solution-processed quantum wells now hold great promise to challenge their conventional epitaxial counterparts in the near future.

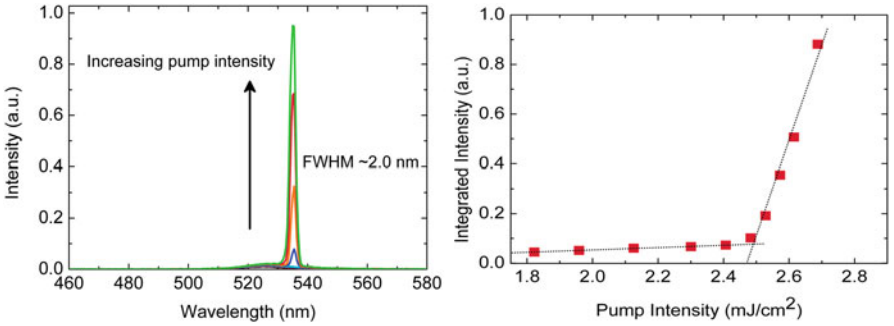

Fig. 11.11 Emission spectra from the all-colloidal laser of quantum wells parameterized with respect to the pump intensity, together with integrated intensity as a function of the pump intensity

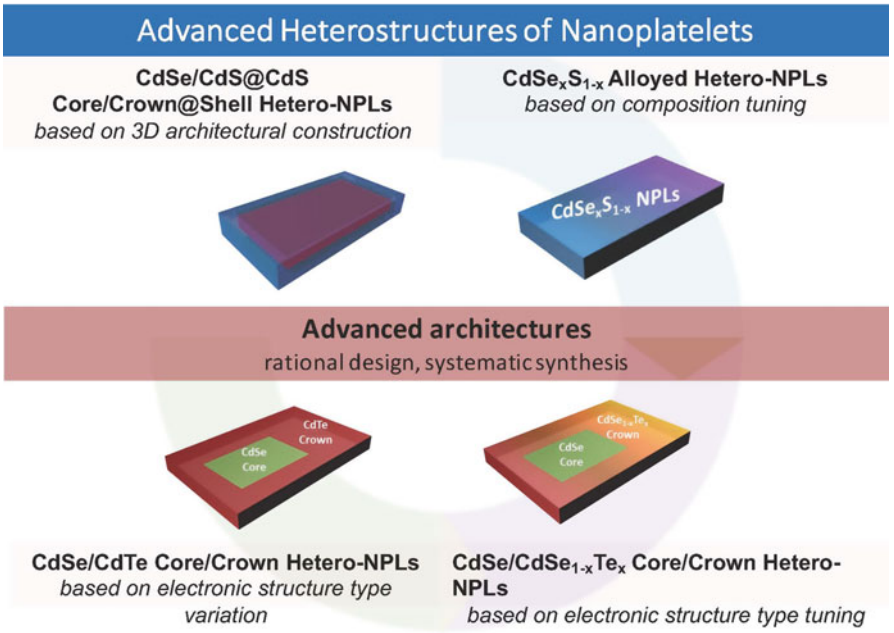

Fig. 11.12 Outlook for advanced heterostructures of nanoplatelets

References

1. Shubert EF (2006) Light-emitting diodes. Cambridge University Press, Cambridge
2. Gaponenko SV (1998) Optical properties of semiconductor nanocrystals. Cambridge University Press, Cambridge
3. Demir HV et al (2011) Nano Today 6:632; Erdem T, Demir HV (2011) Nat Photonics, 5(3):126
4. Guzelturk B et al (2015) Adv Mater 27:2741
5. Ithurria S et al (2008) J Am Chem Soc 130:16504; and Ithurria S et al (2011) Nat Mater 10:936
6. Guzelturk B et al (2014) ACS Nano 8:6599; also, C. She et al Nano Lett (2014) 14:2772–2777

Chapter 12
Semiconductor Nanophotonics Using Surface Polaritons

Thomas G. Folland and Joshua D. Caldwell

The properties of crystalline materials are dictated by the physical arrangement and behaviour of their constituent atoms. The behaviour of electrons and phonons (lattice vibrations), generally dominate the optoelectronic properties of a material. Electrons typically occupy either bound states, where they are unable to move and contribute to charge transfer, or in a delocalised state, where they can propagate through the lattice and carry electric current. These states form energy bands, called valence and conduction bands (see Fig. 12.1a), and the energies of these bands are one of the key ways of classifying materials. In a metal, these bands of energies overlap, and as a result, electrons are always able to freely propagate throughout the material. On the other hand, in an insulator these bands are separated by an energy difference (the band gap) and there is a small electronic density of states near the valence and conduction band edges. Semiconductors exist in-between these two extremes. They possess a band gap, but charge carriers can be moved between bands through either external stimuli or during the growth process via doping. This means that whilst semiconductors intrinsically behave as insulators, perturbations induced by thermal energy, light, dopants, or an electric field can switch them into acting as a conductor. Furthermore, in polar semiconductors the charge separation between the ionic lattice sites allow for crystalline vibrations (phonons) to couple with infrared to terahertz light. This broad range of interactions is what has made semiconductors an integral part of electronics, light emitting diodes, lasers, detectors and photovoltaics.

Whilst conventional optical design approaches are limited by the diffraction limit to occur on the scale of the wavelength of light in a material, nanophononics can exploit quasi-particles called polaritons to shrink the wavelength of light to deeply sub-diffractional scales, allowing optical energy to be confined to essentially

T. G. Folland (✉) · J. D. Caldwell
Department of Mechanical Engineering, Vanderbilt University, Nashville, TN, USA
e-mail: josh.caldwell@vanderbilt.edu

B. Di Bartolo et al. (eds.), *Quantum Nano-Photonics*, NATO Science for Peace and Security Series B: Physics and Biophysics,
https://doi.org/10.1007/978-94-024-1544-5_12

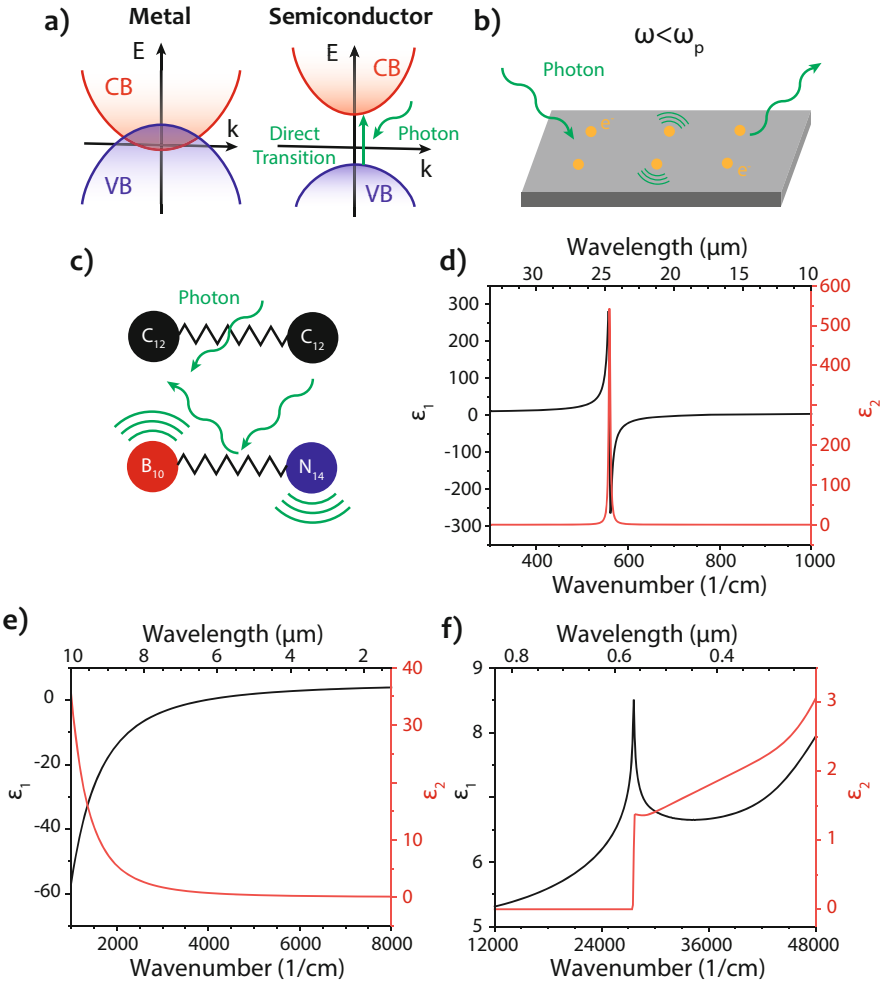

Fig. 12.1 The optical properties of semiconductors. (**a**) A schematic of the band structure of electrons in a metal and a semiconductor illustrating both conduction and valence bands. When the energy of an incident photon is of sufficient energy to excite a free carrier across the band gap, carrier conduction is enabled. (**b**) Free electrons are able to coherently oscillate out of phase in response to an incident electromagnetic field and reflect the incident waves (**c**) Optic phonons in a polar material are also capable of coherently oscillating out of phase with incident IR or THz light, inducing similar reflections in a narrow frequency band. (**d**–**f**) shows the corresponding change in the dielectric function for a semiconductor (here GaN) (**d**) optic phonon effects (TOLO) (**e**) free-carrier effects (Drude) and (**f**) bandgap, and interband transitions

nanometric volumes. This is particularly useful for making compact, flat and efficient optical components such as emitters [1–3], lenses [4, 5] and absorbers [6]. Beating the diffraction limit is of importance for designing optoelectronic devices in the infrared, where the wavelength of light is long and optical materials are less well

developed. This chapter will describe the optical properties of semiconductors, and how these can be exploited in the field of nanophotonics. First, we will show how the material properties of semiconductors are uniquely suited for creating infrared optical devices. Secondly, we will describe the diffraction limit, and how it can be surpassed using polaritons, and examples of their use based on semiconductor systems. Finally, we will go on to present one advanced topic in semiconductor nanophotonics, regarding exotic materials which exhibit very large anisotropy [7], leading to unusual phenomena such as hyper lensing [8, 9].

12.1 The Optical Properties of Semiconductors

12.1.1 The Dielectric Function

The dielectric function is the mathematical description of how a material behaves in the presence of a electromagnetic field. While a full discussion can be found in several textbooks [10–12], here we present the fundamental concepts as they pertain to semiconductor materials. When an electric field is applied to a material, this induces some change in the localized and delocalized charge in the atomic lattice. This consequentially generates its own electromagnetic field, the so-called polarization field $\overline{\boldsymbol{P}}$. The electric field $\overline{\boldsymbol{E}}$ can be described as the superposition of the applied electric field (the so-called displacement field $\overline{\boldsymbol{D}}$) and this polarization field.

$$\overline{\boldsymbol{E}} = \overline{\boldsymbol{P}} + \overline{\boldsymbol{D}} \tag{12.1}$$

As $\overline{\boldsymbol{P}}$ will be a function of $\overline{\boldsymbol{D}}$, we describe the relationship by the electric susceptibility χ, which can be expanded as a Taylor expansion:

$$\overline{\boldsymbol{P}} = \chi(\boldsymbol{D}) = \overline{\overline{\chi}}^{(1)}\overline{\boldsymbol{D}} + \cdots. \tag{12.2}$$

For simplicity, here we will only consider the first-order term in this expression, which describes the linear response of electromagnetic materials. Combining the above two equations, we get:

$$\overline{\boldsymbol{E}} = \left(1 + \overline{\overline{\chi}}^{(1)}\right)\overline{\boldsymbol{D}} = \overline{\overline{\varepsilon}}\,\overline{\boldsymbol{D}}. \tag{12.3}$$

This defines our dielectric function $\overline{\overline{\varepsilon}}$ (hereafter we drop matrix notation; ε). The $\overline{\overline{\chi}}^{(n)}$ terms of this Taylor expansion are matrices that can have different values for different crystallographic axes. This can give rise to many useful phenomena such as birefringence.

For this chapter, we are interested in how the dielectric function effects the propagation of electromagnetic waves. It is easy to show that Maxwell's equations in the absence of an external source takes the form of the wave equation:

$$\nabla^2 \overline{\boldsymbol{E}} - \frac{\epsilon\mu}{c^2} \frac{\partial^2 \overline{\boldsymbol{E}}}{\partial t^2} = 0, \tag{12.4}$$

where $c^2 = 1/\sqrt{\mu_0 \varepsilon_0}$. This has a solution of the form $\overline{\boldsymbol{E}}(\overline{\boldsymbol{r}}, \boldsymbol{t}) = \overline{\boldsymbol{E}}_{\boldsymbol{0}} e^{i\left(\overline{\boldsymbol{k}} \bullet \overline{\boldsymbol{r}} - \omega t\right)}$, a wave propagating with velocity $v = c/\sqrt{\mu\varepsilon}$. This provides the important link between the refractive index and the dielectric function $n^2 = \mu\varepsilon$; note that in general both values are complex numbers, which allows for both periodic (real) and evanescent (imaginary) solutions. From the above equations we see that the dielectric function provides a complete description of how an electromagnetic wave will propagate through and interact with a given medium. The dielectric function for a given material must be derived from the frequency dependent properties of the electrons and atoms within that material. For semiconductors there are four major types of interactions between light and matter which dictate the dielectric function within the optical frequency regime. These are the excitation of electrons from one energy band to another (interband transitions), electron excitation to higher energy states within the same energy band (intraband transitions), excitation of free electron motion, and excitation of lattice vibrations (so called phonons), which we will now examine each effect on a case by case basis.

12.1.2 The Band Gap

As outlined in the introduction of this chapter, in a semiconductor with no free carriers, all electrons are confined to atomic lattice sites – e.g. the valence band is full and the conduction band is unoccupied. However, if electromagnetic energy (e.g. light) greater than the direct bandgap is incident on the semiconductor, then spectral absorption occurs (see Fig. 12.1a). It is important to note that for many semiconductors that this direct bandgap transition is not always the lowest possible interband transition from the valence to conduction band. In these cases, the band alignments of the lowest unoccupied conduction band and the highest filled valence band are offset in the Brillouin zone, and therefore, such transitions require the assistance of optic phonons to overcome the momentum mismatch between the two states. Such semiconductors are referred to as indirect bandgap semiconductors, and tend to exhibit recombination lifetimes substantially longer than those for direct gap semiconductors. Examples of these different types are Si and SiC (indirect) and GaAs and GaN (direct). In devices such as light emitting diodes (LEDs) the strong valence to conduction band absorption can be exploited to induce narrowband spectral emission resulting from the recombination of the electron-hole

pair generated. The effect the band gap has on the dielectric function is to introduce a strong absorption edge that is dependent on the density of states of electrons and holes close to the conduction and valence band edges – visualized in Fig. 12.1f for GaN. There are two other important effects that also have significant effects on the dielectric function in the spectral range near the bandgap – excitonic and intraband transitions. A detailed discussion of these topics, as well as the exact form of the dielectric function for these transitions is beyond the scope of this chapter.

12.1.3 Free Charge Carriers

While a completely pure semiconductor inherently has no free charge carriers, as introduced above, it is possible to introduce charges by including defects and/or impurities in the crystal lattice. This is achieved systematically by doping. For example, phosphorous or boron can be introduced into silicon to achieve this effect. In the case of the former, one excess electron per phosphorus atom results in a donor band that is located just below the conduction band edge and can offer sufficient carriers to populate the conduction band with significantly lower applied bias or available thermal energies. Similarly, if boron impurities are introduced, the fact that it has one less valence electron results in a band of empty acceptor states just above the valence band, which through thermal or low field excitation can induce valence electrons to populate these acceptor states, allowing for sufficient conduction. This gives rise to electronic transitions in the energetic vicinity of the bandgap such as acceptor-to-donor, valence-to-donor and acceptor-to-conduction band transitions, all of which induce a strong absorption and thus a inflection in the real and peak in the imaginary part of the dielectric function, similar to the bandgap effects observed in Fig. 12.1f.

The presence of free charge carriers also has significant implications on the dielectric function in spectral regions removed from the bandgap energy. This results from the local screening field that occurs when electrons with density n are stimulated to move coherently, thereby forming a plasma against a background of positive ions (or hole plasma against a background of negative ions) [13]. In essence the free carriers respond to incident electromagnetic fields by coherently oscillating out of phase with the field, screening out the incident radiation, inducing a high reflectivity (see Fig. 12.1b). This can be well-defined by the Drude-Lorentz formalism, which takes the functional form:

$$\varepsilon(\omega) = \varepsilon_\infty - \frac{\omega_p^2}{\omega^2 + i\gamma\omega} \tag{12.5}$$

where ω_p is the the plasma frequency, and is defined by $\omega_p^2 = ne^2/\varepsilon_0 m_e$ (n is the carrier concentration, m_e is the electron mass, e is the electronic charge), and ε_∞

is the high frequency dielectric constant, and γ represents the free carrier damping. The plasma frequency sets the upper limit in frequency where the free carriers can coherently respond to the incident radiation and effectively screen it out. Above this, the carriers cannot keep up with the incident electromagnetic field and the screening effect is lost, and therefore so is the high reflectivity. Therefore, at frequencies below ω_p, the real part of the permittivity will be negative, quite literally 'not permitting' the electromagnetic energy into the material. The latter term is determined by the scattering of the free charge carriers with other electrons, defects or phonons, with a scattering rate $\tau = 1/\gamma$. For metals, this is typically on the order of tens of femtoseconds, [14] whilst for high quality semiconductors it can approach, and in many cases exceed 100 femtoseconds [15]. One major advantage of the free electron plasma in semiconductors, as opposed to metals, is that the carrier concentration can be continuously varied using doping [16–18], electrostatic gating [19–21] or optical pumping [5, 22]. This means that the dielectric function can be effectively controlled during the growth process or dynamically using external stimuli. An example of the dielectric function for the semiconductor GaN when doped to 2×10^{20} is shown in Fig. 12.1e.

12.1.4 Lattice Vibrations

All crystalline materials exhibit coherent vibrations of the atomic lattice called phonons, some of which will interact with light. In general these can be split into two classes – acoustic and optical phonons. Acoustic phonons have low energy (typically less than a meV) and correspond to the displacement of both atoms in the same direction. Optical phonons have higher energy (typically on the order of 1–100 meV), and correspond to oscillations of the atoms in opposing directions. Both exhibit longitudinal modes [oscillation in the direction of propagation, with the frequency ω_{LO} for the longitudinal optic (LO) phonon] and transverse modes [oscillation occurs perpendicular to the direction of propagation with ω_{TO}, for the transverse optic (TO) phonons]. For nonpolar materials, such as silicon, the longitudinal and transverse phonons are degenerate and infrared inactive, and therefore do not play a significant role in the infrared dielectric function. However, for polar materials, such as GaN (Fig. 12.1c, d), such oscillations result in a charge separation, inducing an energy separation between TO and LO phonons, with longitudinal modes shifting to higher energies with respect to the transverse modes. In addition, this provides a net polarizability to the TO phonon, making it interact with light. Thus, resonant absorption of light results in the coherent oscillation of the ionic charges on the lattice (optic phonon) that is opposite in phase with the incident electromagnetic field. Therefore, much like the free carriers in a metal or highly doped semiconductor, this creates a screening field reflecting the incident

light. Correspondingly, this will result in the real part of the permittivity becoming negative, mathematically expressed using the well known "TOLO" formalism:

$$\varepsilon(\omega) = \varepsilon_\infty \frac{\omega_{LO}^2 - \omega^2 - i\gamma_{LO}\omega}{\omega_{TO}^2 - \omega^2 - i\gamma_{TO}\omega} \tag{12.6}$$

The functional form of this dielectric function is shown in Fig. 12.1d for GaN. Similar to electrons, each of these modes also has a characteristic scattering time τ, and thus an equivalent damping constant γ_j, where j represents either the LO or TO values and ε_∞ refers to the high frequency dielectric function that is dominated by intraband transitions, for full details see [23]. One important distinction between the free carrier plasma and polar phonons, resides in the corresponding scattering lifetime of the two oscillations with the latter generally on the order of picoseconds, therefore significantly reducing losses in the material, which has significant implications for any resulting polaritons [24, 25].

12.2 The Diffraction Limit and Polaritons

Conventional optics use materials with positive dielectric constants to manipulate plane waves. Plane waves have the advantage that they propagate large distances and are relatively easy to manipulate, however, they are limited by diffraction and thus the scale of the optics must be commensurate with the wavelength of light in the material. If one tries to focus plane waves onto a small spot, using either an aperture or lens, one finds that light will form the so called Airy disk – which has a width (D) dependent on the free-space wavelength [26].

$$D \sim 0.61 \frac{\lambda_0}{n \sin(\theta)} \tag{12.7}$$

where λ_0 is the free space wavelength, n is the refractive index in which light is propagating, θ is the half angle subtended by the lens and 0.61 is a geometry dependent numerical factor. Note that $n \sin(\theta)$ is also referred to as the numerical aperture of a lens. In a similar sense, any structures on a scale much below this limit will be invisible to light at these free-space wavelengths. Now the obvious question is "why is this such a problem?". If we approximate $D\ \lambda_0/2$, our minimum spot size is of the order of a few hundred nanometers in the visible, but rises to micron- to tens-of-micron-scale in the mid-infrared and of the order of 100 μm in the terahertz. Now say we want to optically identify a thin film of polymer – or paint – which could be on the order of 1 μm in physical thickness. It's obvious that visible light will be able interact with the layer, as the film is on the order of, or larger than λ_0. This will enable us to directly observe any absorption features clearly. However, for mid- and far-infrared measurements, we are going to have significant issues due to a large $\lambda_0$of the excitation compared with thickness. This problem propagates into

many other areas of optics, such as grating, filter and absorber designs, where optics at long wavelengths are inherently much larger.

There has been great progress in recent years in using a range of dielectric materials that have inherently high refractive index to more tightly confine light [27–30]. For many practical purposes such structures are sufficient to improve device performance and confine light more tightly [30, 31] However, these structures are still fundamentally diffraction limited. On the other hand, evanescent waves are subject to no such limit. In a material where the dielectric function is negative, the refractive index becomes imaginary and the electromagnetic fields will decay evanescently, with no restriction on how rapidly they will decay. As a result, light doesn't propagate within the material and therefore the usefulness of these materials in bulk form is limited to reflective optics. The solution to broaden the application of such materials is found in the formation of polaritons – quasiparticles that arise from the coupling between light and an oscillating charge in the material. In particular – we are interested in surface polaritons, which are supported at the boundary between a material with a negative real part of the permittivity and a dielectric (positive, real permittivity). Polaritons can exhibit arbitrarily high confinement of the electromagnetic fields at interfaces, making them applicable for nanoscale confinement and manipulation of light, which gave rise to the fields of nanophotonics and metamaterials.

The formation of polaritons is a direct solution of Maxwell's equations at the boundary [13]. The field decays evanescently away from the interface on both sides, with a characteristic wavevector k, which is related to the compressed wavelength of the polariton through its reciprocal. The relationship between k and the dielectric function at the two boundaries is provided by the expression:

$$k = k_0 \sqrt{\frac{\varepsilon_m \varepsilon_d}{\varepsilon_m + \varepsilon_d}} \tag{12.8}$$

where ε_m is the relative permittivity of the polaritonic material, ε_d is the relative permittivity in the dielectric and k_0 represents the free-space wave vector of the incident light. This function is plotted in Fig. 12.2a for the boundary between a free electron material and vacuum. Note that as real part of the permittivity in the material approaches $Re(\varepsilon_m) = -Re\,(\varepsilon_d)$ ($Re(\varepsilon_d) = 1$ in vacuum or air) k diverges and becomes infinitely large. As k is inversely proportional to the λ, this implies λ becomes infinitely small, thus, at this point the light can become confined to essentially arbitrarily small sizes in a lossless medium. Whilst the form plotted in Fig. 12.2a assumes a Drude-Lorentz dielectric function, this can also serve as a good approximation for the dielectric function of any polaritonic material.

One of the challenges associated with surface polaritons is that they propagate much more slowly than free-space electromagnetic radiation. This means that it is impossible to directly excite polaritons with normal plane waves (which lie on the light line, red line in Fig. 12.2a). This is referred to as the 'momentum mismatch' and can be visualized by the separation between the red 'light line' and the 'surface plasmon polariton' dispersion relation (lower energy black line)

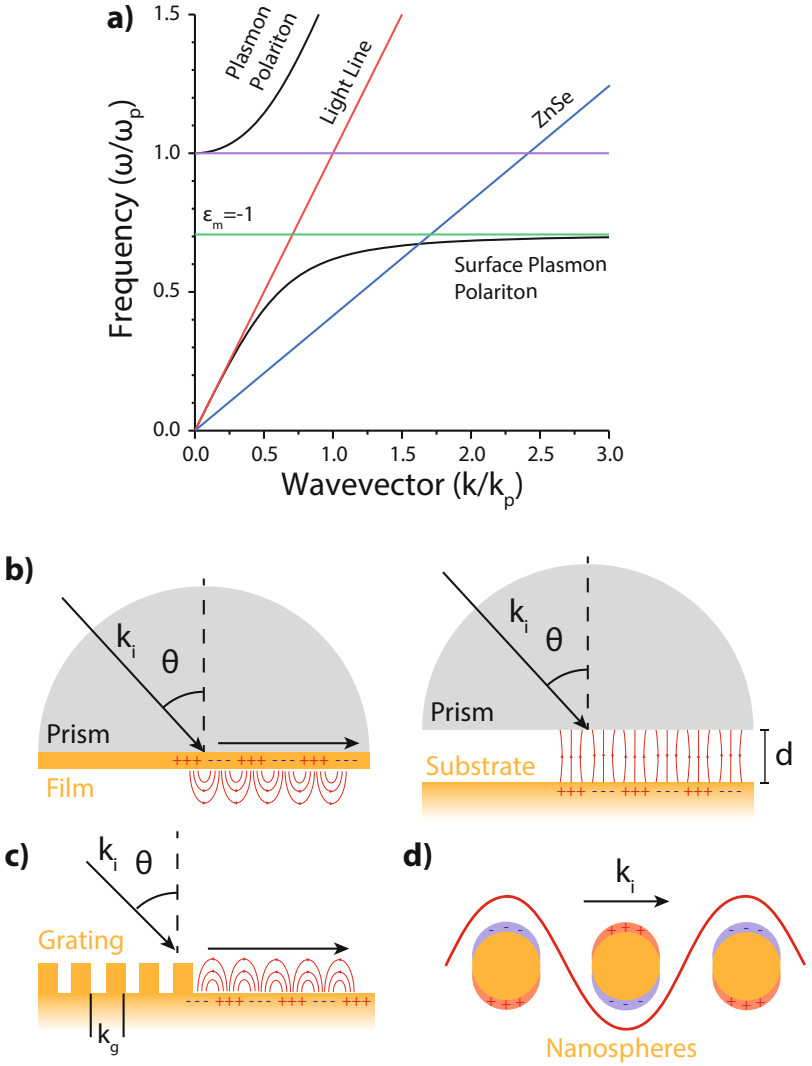

Fig. 12.2 (**a**) Dispersion of surface plasmon polaritons shows the change in the wavevector (reciprocal of the wavelength) for a SPP with respect to light in a vacuum and light in a ZSe prism. To stimulate polaritons, the momentum mismatch between the polariton and incident light must be overcome. This can be realized via a number of methods such as (**b**) prism coupling, (**c**) grating coupling, and (**d**) scattering by subwavelength or subdiffractional nanoparticles

in Fig. 12.2a. This momentum mismatch can be compensated for in a number of ways, by slowing down the incident light, therefore enabling the excitation of SPPs with incident electromagnetic waves (light). One of the easiest ways to do so is via prism coupling (shown in Fig. 12.2b [32]). Prism coupling exploits

the evanescent wave at the boundary of a high refractive index prism, either in contact with a thin film of a metal (Fig. 12.2b left), or a small spacing away (Fig. 12.2b right). The result allows coupling into polaritons with wavevectors up to that which can be achieved in the prism material (shown as blue line in Fig. 12.2a for ZnSe). A second route is by exploiting grating structures, where additional momentum is provided by the periodicity of the grating (Fig. 12.2c). This is essentially a form of Bragg scattering, that is light hits the grating and is slowed when it is coupled into the diffractive modes. By changing the angle of incidence θ, the momentum of a given incident frequency can be tuned to match the momentum offset between the free-space light and the polariton mode. The final method of exciting surface plasmons is by coupling to nanoparticles, where the additional momentum is provided by Mie scattering from the small particle size [33]. This can be visualized for spherical particles in Fig. 12.2d, but is more typically observed in the form of resonant nanoparticles fabricated via top-down [34, 35] or bottom-up approaches [36, 37]. This is also the methodology behind the stimulation of polaritons within the scattering-type scanning near-field optical microscopy (s-SNOM) [2, 22, 38–43] and photothermal induced resonance (PTIR) [44–49] approaches, where scattering from a typically metalized atomic force microscope (AFM) tip can be used to directly probe the polaritonic evanescent near-fields on flat slabs or in nanostructured polaritonic materials. While this effect is presented here for SPPs, this general formalism is equally applicable to other types of polaritons, such as SPhPs [50] and exciton polaritons [51]. Two recent reviews of the various types of polaritons within two dimensional van der Waals materials offer an overview of the various types [52, 53]. While focusing on 2D materials, these same concepts are equally applied to bulk materials as well.

12.3 Surface Plasmon Polaritons in Semiconductors

As stated above, while metals such as silver and gold have provided the predominant materials for SPPs within the visible spectral range, the high plasma frequency of metals limits their use for polaritonic applications in the infrared. This is because the continuous dispersion of the permittivity with reducing frequency in metals causes the real part of the dielectric function to become progressively more negative [54]. As the extent of the evanescent field becomes larger as the permittivity becomes more negative, this implies that the confinement (e.g. k) decreases, effectively eliminating the potential benefits of these optical modes. Therefore, for infrared applications, materials with lower plasma frequencies are required.

The most suitable materials for IR SPPs are the highly doped semiconductors. The benefits of these materials are that by changing the material of interest, frequency of operation can be dictated. Looking to the Drude formalism of the dielectric function for guidance (Eq. 12.5), we note that the permittivity is directly related between the squares of the plasma and incident frequencies. The plasma

frequency is itself dependent upon the carrier density, mobility and effective mass of the free carriers:

$$\omega_p^2 = \frac{ne^2}{\varepsilon_0 m_e} \tag{12.9}$$

Note, that for the purposes of gaining broad tuning control of the material dielectric function with changing carrier density, a small effective mass is desired. This typically occurs within narrow gap semiconductors with low energy conduction and valence bands, thus identifying the appropriate material in a given spectral band is necessary. Beyond this, within a given material, the operational frequency can be tuned through doping, [16, 55, 56] or even actively modulated [5, 20, 22, 57] by dynamically modifying the carrier density within the material. This offers significant flexibility in the design of active optical components.

Perhaps the first investigations highlighting the use of highly doped semiconductors for near-infrared SPPs, focused on degenerately doped transparent conducting oxides (TCOs) [58, 59]. A vast amount of research has focused on such materials, including the demonstration of the PlasMOStor with indium tin oxide [60] and tunable SPPs with picosecond response times [59] within doped ZnO films. In addition, there is the potential to utilize the spectral position where the real part of the permittivity become negative, the so-called 'epsilon near zero' or ENZ condition, [61] to pin the resonant frequency of gold antennas regardless of their length [62]. However, further discussion of ENZ modes is out of the scope of this chapter.

A broad array of impactful work has also been more recently reported from numerous groups using more traditional epitaxially grown semiconductor materials and nanostructures. For instance, through nanowire growth, the Filler group at Georgia Tech has demonstrated the ability to spatially locate highly doped regions within silicon nanowires, essentially creating plasmonic barcodes in the process [63]. A great deal of work has also been demonstrated by the concerted efforts of the Wasserman, Law, Brener and Hoffmann groups (among others) in the realization of highly doped semiconductors [64, 65]. This has resulted in the demonstration of highly localized SPPs within InAs nanostructures for chemical sensing [66] and infrared beam steering via direct control of SPPs in highly doped GaAs [67]. However, for most of these materials, the SPPs are limited to the long-wave to far-IR. Alternatively, wider bandgap semiconductors such as Ge-doped GaN [68] can also be utilized to realize SPPs in the mid-wave IR, but tend to suffer from high optical losses at high carrier concentrations.

A recently identified plasmonic semiconductor that seems to bypass issues with high optical losses for mid-wave IR is CdO. The work of Sachet et al. demonstrated that within the CdO semiconductor, that *increased doping* up to the 10^{20} cm^{-3} level actually resulted in an *increase* in mobility, and thus a *reduction* in SPP-based optical losses. This effect, when coupled with the relatively low effective mass of

CdO ($m^* = 0.2–0.25$) [69] results in a broadly tunable plasma frequency offering SPP spectral coverage from approximately 2–9 μms with low optical losses [70].

Perhaps one of the most dynamic and exciting of IR-active SPP materials is the 2D material grapheme [52, 53, 71–74]. A single atomic sheet of hexagonally bonded carbon atoms, graphene offers a broad range of exciting physical phenomena of interest, for instance, the linear Dirac dispersion in the electronic band structure. It is this linear dispersion that provides linear control of the free sheet charge density with changing doping, bias or optical fluence that offers a linearly tunable plasma frequency over much of the mid-IR to terahertz spectral range. Interestingly, SPPs supported by graphene charge carriers are effectively confined to a one-atom thin surface, offering unprecedented confinement of the incident optical fields. Initially probed by s-SNOM by the Basov [21] and Hillenbrand/Koppens [19] groups, graphene plasmons have stimulated a research field unto their own, [53] offering the demonstration of perfect absorbing structures [75], plasmon-based photodetectors [76] and optical modulators [77].

As shown here, SPPs can offer a broad range of opportunity for the design and realization of IR nanophotonic components. However, the scattering rates for these materials is still typically in the hundred femtosecond regime [78]. While acceptable for many applications, this does result in broad resonance linewidths for nanostructures that in many cases are not suitable for optical sources, beacons, antennas or for enhanced infrared spectroscopies. Thus another polariton type can also be exploited.

12.4 Surface Phonon Polariton in Semiconductors

As introduced above, surface phonon polaritons (SPhPs) are derived from optic phonons within a polar crystal lattice. Due to the long scattering lifetimes of optic phonons, they exhibit significantly reduced optical losses when compared to SPPs [50]. These reduced losses are directly observed in reductions in the resonance linewidths of SPhP-based antennas, resulting in quality factors (Q) that are about an order of magnitude higher than plasmonic counterparts, while offering similar or better field confinements [2, 41, 50, 79, 80]. The quality factor can be thought of as a measure of efficiency, effectively describing the number of oscillations the dipolar field will make within the antenna before it decays to $1/e$ of the original intensity. Work by the Caldwell [2, 50, 57, 79, 81–83] and Taubner [2, 41, 83–85] groups have demonstrated that quality factors ranging from 40–305 have been realized experimentally, while calculations based on the dielectric function of the best polar materials, such as silicon carbide, infer $Q > 1000$ are indeed possible [86]. As shown in Fig. 12.3, a broad range of polar materials exist that can be used to support SPhPs from the mid-wave IR out into the terahertz spectral range. However, any given material can only support SPhPs within a narrow spectral window bounded by that materials LO and TO phonon frequencies, referred to as the Reststrahlen band [33, 50, 87].

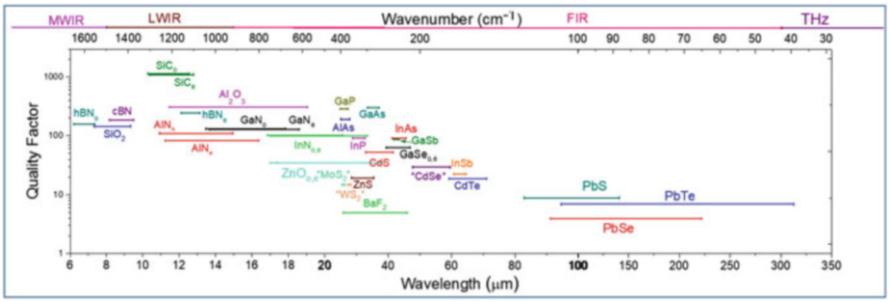

Fig. 12.3 Spectral ranges of the Reststrahlen bands for different polar materials illustrating the spectral range where any given material can support SPhPs

A recent review article by the Caldwell group [50] demonstrated where SPhPs could provide advancements over the state of the art. It has been demonstrated that similar to SPPs that the resonant frequency can be tuned throughout the Reststrahlen band of a given material by changing the size [2, 41, 79, 80], shape [81] and array periodicity [83]. Also similar to SPPs, the crossing of the real part of the permittivity from positive to negative values near the LO phonon frequency also gives rise to the ENZ condition [62]. However, there still remains the question of whether SPhPs and their corresponding increased lifetimes offer significant benefits in the realization of long-propagating polaritons desired for optical waveguides and photonic interconnects.

Within the same review article mentioned above, [50] the potential of SPhPs for propagating polaritons was also discussed. With the long intrinsic polariton lifetimes, one might instinctually infer that the SPhPs would propagate significant distances, well in excess of SPPs. However, a close look at the dielectric function of polar dielectric materials demonstrates that the real part of the dielectric function varies quite rapidly with changing frequency. This fast dispersion can be visualized in Fig. 12.4 where the normalized dispersion of the real part of the permittivity for silver and 4H-SiC are provided. Here the ω_p refers to either the ω_p of the metal or ω_{LO} for the polar dielectric. As the group velocity, v_g, which is the velocity at which the polariton will propagate, is the slope or derivative of this frequency-dependent dispersion of the dielectric function, it can be quickly observed from this plot that despite the long lifetimes, that the propagation will occur at drastically slower velocities for SPhPs with respect to SPPs. This has been recently experimentally demonstrated by Yoxall et al. [88] for phonon polaritons within hexagonal boron nitride (hBN) and can be expressed in a propagating figure of merit that is nominally equivalent with standard SPP metals and doped semiconductors as discussed in the literature [50].

One significant limitation beyond the limited spectral range and slow v_g results from the inability to easily tune optic phonon frequencies. While the realization of ternary and quarternary semiconductors (such as AlGaN) offers some flexibility in this regard, the frequency of the optic phonons and therefore of the SPhP cannot

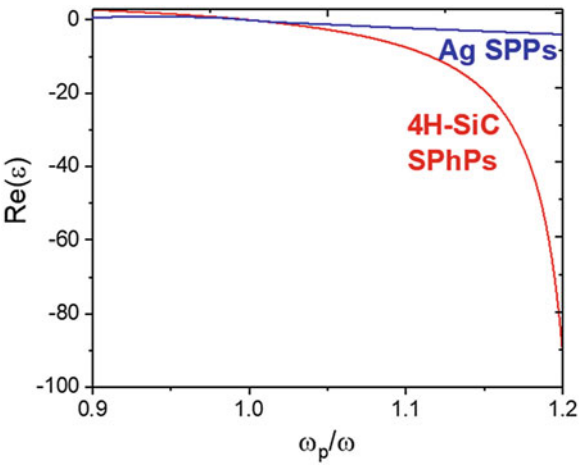

Fig. 12.4 Normalized dispersion in the dielectric functions for a metal (Ag, blue) and polar crystal (4H-SiC, red) illustrating the much fast dispersion, and thus, much slower group velocities of polaritons within the polar crystals (SPhPs) in comparison to those in metals and highly doped semiconductors (SPPs)

be changed in-situ. However, opportunities to dynamically tune do indeed exist. For instance, it was recently demonstrated by the Taubner group that through the incorporation of the phase change material GST, which is widely used in rewritable data storage technologies, that the infrared optical response of SPhP materials could be modulated by transitioning between the amorphous and crystalline states of the material [89]. Another approach can be realized through the incorporation of free carriers into polar semiconductors through optical pumping or electrostatic gating. This can be realized through the LO-phonon plasmon coupling effect, whereby the overlapping polarization fields of a free carrier plasma and the LO phonon can be coupled to induce a spectral blue shift in the apparent LO phonon frequency and broadening [90, 91]. By doing this dynamically through optical pumping or modulated gating, one can dynamically tune the dielectric function [22, 57]. As the resonant frequency of a polaritonic antenna is tied to a given magnitude of the real part of the dielectric function, [33, 92] this dynamic spectral shift in the dielectric function will also result in a commensurate shift in the SPhP resonance [22]. This was recently demonstrated by Dunkelberger et al. [57] and demonstrates the potential feasibility for realizing next generation active infrared optics.

12.5 Hyperbolic Polaritons in Semiconductors

As briefly mentioned in Sect. 1, it is possible for the dielectric function to behave differently between the crystallographic axes of a material. An extreme case arises where the dielectric function along orthogonal axes are not just different (birefringent), but actually opposite in sign. A material that has these properties is called ‘hyperbolic’ and supports polaritons with highly unusual properties. Quite how unusual these properties are is best discussed by the concept of iso-frequency surfaces. In an anisotropic material [7, 93], one can express the relationship between

ω and k in the following form:

$$\frac{k_x^2 + k_y^2}{\varepsilon_z} + \frac{k_z^2}{\varepsilon_{x,y}} = \left(\frac{\omega}{c}\right)^2 \tag{12.10}$$

Where x, y, and z represent the different axes of the crystal [94]. For a given frequency the solutions to this equation can be represented in k-space by a surface detailing the possible values of k (polariton wavelengths) that can be supported at that single frequency within that material. An example is shown in Fig. 12.5a for an isotropic material – it is simply an empty spherically shaped surface. This means that within such a material that at a single frequency, only a single k or polariton wavelength can be supported at any given propagation direction. This can also be observed by drawing a horizontal line at a given frequency in the dispersion relationship presented in Fig. 12.2a for an SPP. In an anisotropic material, where all the axes exhibit permittivities that are of the same sign, then the spherical surface is simply distorted into an ellipsoidal surface. However, something unusual happens when the signs of $\varepsilon_{x,y}$ or ε_z are opposite. In these cases the surface flips from being a closed to an open hyperbolic surface – as shown in Fig. 12.5b, c. The difference between these two isofrequency surfaces is dictated by whether one axis (in this case the z-axis) or two axes (here, x and y) are negative in sign, respectively. This gives rise to the corresponding Type I and II hyperbolic response. This drastic change in the isofrequency response has two important consequences for the propagation of light; (1) an infinite slab of the material can support a polariton with any k (polariton wavelength) at any given frequency, but this comes at the (2) cost of the direction of propagation for that wavevector becoming fixed [8, 42, 95, 96]. That is, unlike in normal materials the polariton cannot propagate in any direction, but instead only at a defined angle with respect to the z-axis. This angle is dependent upon the square root of the ratios between the in and out of plane dielectric functions as follows:

$$\theta(\omega) = \arctan\left(\frac{1}{i}\frac{\sqrt{\varepsilon_t(\omega)}}{\sqrt{\varepsilon_z(\omega)}}\right). \tag{12.11}$$

Whilst hyperbolic materials were first demonstrated artificially, by using metal/dielectric stacked metamaterials with repeated unit cells that are structured well below the wavelength of light, [7, 97, 98] inherently high losses from the SPP layers remain a problem. An alternative is that certain anisotropic crystals exhibit this behaviour naturally due to differences in the phonon energies between in and out of plane directions [71, 99, 100]. Perhaps the most remarkable crystal in this regard, which was also the first to be experimentally exploited for nanophotonics, is the 2D material hBN (See dielectric function in Fig. 12.5d) [38, 80]. Due to its layered structure the in and out of plane optic phonon energies are significantly different, meaning that both Type I and II hyperbolic behaviour is observed in these crystals. Indeed, hyperbolic modes have been directly observed in hexagonal boron nitride using both s-SNOM and nanoparticle structures [8, 20, 38, 42, 44, 80,

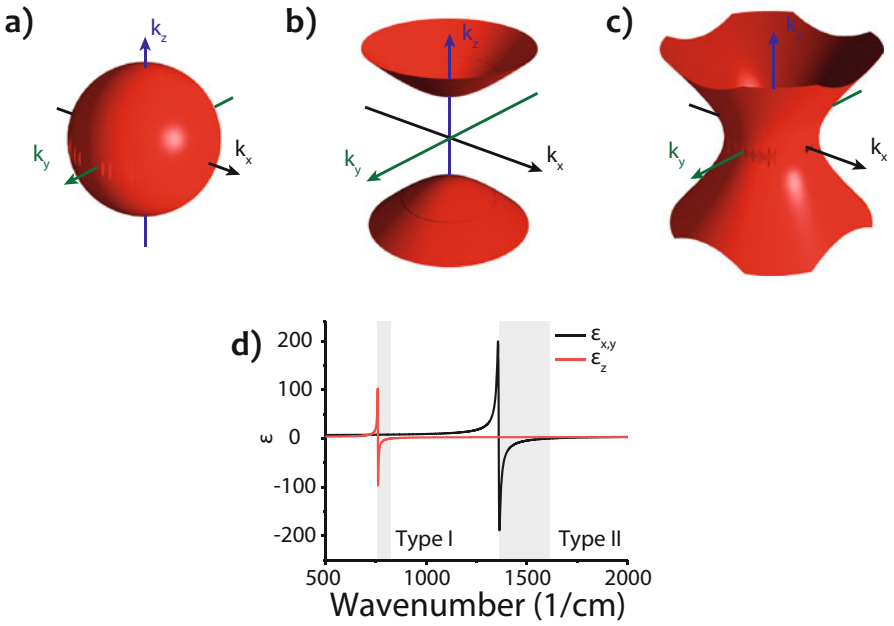

Fig. 12.5 Isofrequency surfaces for (**a**) isotropic, (**b**) Type I and (**c**) Type II hyperbolic materials. (**d**) Shows the dielectric function of hexagonal boron nitride, revealing the extreme anisotropy of these crystals

101–103]. This has allowed for the demonstration of the concept of a hyper-lens – a flat lens which exploits the angled propagation of light in hyperbolic materials to directly image objects much smaller than the diffraction limit [8, 95].

12.6 Conclusions

As detailed in this chapter, semiconductor materials offer a broad range of flexibility in the design of nanophotonic devices and offer unique material properties that dramatically expand their functionality with respect to metals or insulators. Presented in this chapter is just a brief overview of some of the predominant advantages of semiconductor materials in the realm of nanophotonics. However, this work focused entirely on the use of polaritons to realize nanophotonics. While outside of the scope of this chapter, it should be noted that the use of quantum confined structures such as quantum wells and dots, photonic crystals, dielectric Mie cavities and metamaterials also offer substantial opportunities. It is the hope of the authors that this chapter can provide some initial insight into the highly intriguing properties of polaritons and the various types that can be supported within semiconductor materials; including surface plasmon, surface phonon and hyperbolic polaritons. The authors anticipate

that these types of sub-diffractional optical modes will form the basis for the next generation of optical components, providing compact, active and tunable devices that will drastically change the functionality of our optical systems.

Acknowledgements Both JDC and TGF acknowledge support from the School of Engineering at Vanderbilt University.

References

1. Greffet J-J et al (2002) Coherent emission of light by thermal sources. Nature 416(6876):61–64
2. Wang T et al (2017) Phonon-polaritonic bowtie nanoantennas: controlling infrared thermal radiation at the nanoscale. ACS Photonics 4(7):1753–1760
3. Schuller JA et al (2010) Plasmonics for extreme light concentration and manipulation. Nat Mater 9:193–204
4. Yu N, Capasso F (2014) Flat optics with designer metasurfaces. Nat Mater 13:139–150
5. Ferrera M et al (2016) Dynamic nanophotonics. J Opt Soc Am B 34(1):95–103
6. Watts CM, Liu X, Padilla WJ (2012) Metamaterial electromagnetic wave absorbers. Adv Opt Mater 24:OP98–OP120
7. Poddubny A et al (2013) Hyperbolic metamaterials. Nat Photonics 7:948–957
8. Li P et al (2015) Hyperbolic phonon-polaritons in boron nitride for near-field optical imaging and focusing. Nat Commun 6:7507
9. Liu Z et al (2007) Far-field optical hyperlens magnifying sub-diffraction limited objects. Science 315:1686
10. Yariv A, Yeh P, Yariv A (2007) Photonics: optical electronics in modern communications. In: The Oxford series in electrical and computer engineering, 6th edn. New York, Oxford University Press xii, 836 p
11. Jackson JD (1999) Classical electrodynamics, 3rd edn. Wiley, New York xxi, 808 p
12. Kittel C (2005) Introduction to solid state physics, 8th edn. Wiley, Hoboken xix, 680 p
13. Maier SA (2007) Plasmonics: fundamentals and applications. Springer, New York xxiv, 223 p
14. Scharte M et al (2001) Do Mie plasmons have a longer lifetime on resonance than off resonance? Appl Phys B 73:305–310
15. Woessner A et al (2015) Highly confined low-loss plasmons in graphene-boron nitride heterostructures. Nat Mater 14:421–425
16. Law S et al (2014) Mid-infrared designer metals. Opt Express 20:12155–12165
17. Law S, Liu R, Wasserman D (2014) Doped semiconductors with band-edge plasma frequencies. J Vac Sci Technol B 32:52601
18. Law S et al (2014) All-semiconductor negative index plasmonic absorbers. Phys Rev Lett 112:17401
19. Chen J et al (2012) Optical nano-imaging of gate-tunable graphene plasmons. Nature 487:77–81
20. Dai S et al (2015) Graphene on hexagonal boron nitride as a tunable hyperbolic metamaterial. Nat Nanotechnol 10:682–686
21. Fei Z et al (2012) Gate-tuning of graphene plasmons revealed by infrared nano-imaging. Nature 487:82–85
22. Spann BT et al (2016) Photoinduced tunability of the reststrahlen band in 4H-SiC. Phys Rev B 93:085205
23. Stroscio MA, Dutta M (2001) Phonons Nanostruct. Cambridge University Press
24. Khurgin JB, Boltasseva A (2012) Reflecting upon the losses in plasmonics and metamaterials. MRS Bull 37:768–779

25. Caldwell JD et al (2016) Atomic-scale photonic hybrids for mid-infrared and terahertz nanophotonics. Nat Nanotechnol 11:9–15
26. Born M, Wolf E (1999) Principles of optics: electromagnetic theory of propagation, interference and diffraction of light. 7th expanded ed. Cambridge University Press, Cambridge/New York, xxxiii, 952 p
27. Moitra P et al (2013) Realization of an all-dielectric zero-index optical metamaterial. Nat Photonics 7:791–795
28. Valentine J et al (2009) An optical cloak made of dielectrics. Nat Mater 8:568–571
29. Bezares FJ et al (2013) Mie resonance-enhanced light absorption in periodic silicon nanopillar arrays. Opt Express 21(23):27587–27601
30. Spinelli P, Verschuuren MA, Polman A (2012) Broadband omnidirectional antireflection coating based on subwavelength surface Mie resonators. Nat Commun 3:692
31. Brongersma ML, Kik PG (2010) Surface plasmon nanophotonics. Springer, New York, p 268
32. Raether H (1988) Surface plasmons on smooth and rough surfaces and on gratings. Springer tracts in modern physics. Springer-Verlag, Berlin/New York x, 136 p
33. Bohren CF, Huffman DR (2004) Absorption and scattering of light by small particles. Wiley, Weinheim
34. Caldwell JD et al (2011) Large-area plasmonic hot-spot arrays: sub-2 nm interpillar spacings with plasma enhanced atomic layer deposition of ag on periodic arrays of Si nanopillars. Opt Express 19(27):26056
35. Caldwell JD, et al (2011) Surface enhanced raman scattering enhancements from silver atomic layer deposition coated nanowires, in CLEO:2011 – laser applications to photonic applications. Optical Society of America. p. paper CMX2
36. Adams SM et al (2012) Non-lithographic SERS substrates: tailoring surface chemistry for au nanoparticle cluster assembly. Small 8(14):2239
37. Fontana J et al (2013) Large surface-enhanced Raman scattering from self-assembled gold nanosphere monolayers. Appl Phys Lett 102:201606
38. Dai S et al (2014) Tunable phonon polaritons in atomically thin van der Waals crystals of boron nitride. Science (Washington) 343(6175):1125–1129
39. Hillenbrand R, Taubner T, Keilmann F (2002) Phonon-enhanced light-matter interaction at the nanometre scale. Nature 418(6894):159–162
40. Taubner T, Keilmann F, Hillenbrand R (2004) Nanomechanical resonance tuning and phase effects in optical near-field interaction. Nano Lett 4(9):1669–1672
41. Wang T et al (2013) Optical properties of single infrared resonant circular microcavities for surface phonon Polaritons. Nano Lett 13(11):5051–5055
42. Giles AJ et al (2016) Imaging of anomalous internal reflections of hyperbolic phonon-polaritons in hexagonal boron nitride. Nano Lett 16(6):3858–3865
43. Giles AJ et al (2017) Ultra-low-loss polaritons in isotopically pure materials: a new approach. Nat Mater 17:134
44. Brown LV et al (2017) Nanoscale mapping and spectroscopy of non-radiative hyperbolic modes in hexagonal boron nitride nanostructures. To be submitted
45. Centrone A (2015) Infrared imaging and spectroscopy beyond the diffraction limit. Annu Rev Anal Chem 8:101–126
46. Chae J et al (2017) Nanophotonic atomic force microscope transducers enable chemical composition and thermal conductivity measurements at the nanoscale. Nano Lett 17: 5587–5594
47. Katzenmeyer AM, Aksyuk V, Centrone A (2013) Nanoscale infrared spectroscopy: improving the spectral range of the Photothermal induced resonance technique. Anal Chem 85(4):1972–1979
48. Katzenmeyer AM et al (2015) Absorption Spectrosocyp and imaging from the visible through mid-infrared with 20 nm resolution. Anal Chem 87(6):3154–3159
49. Lahiri B et al (2013) Nanoscale imaging of plasmonic hot spots and dark modes with the photothermal-induced resonance technique. Nano Lett 13(7):3218–3224

50. Caldwell JD et al (2015) Low-loss, infrared and terahertz nanophotonics with surface phonon polaritons. Nano 4:44–68
51. Lagois J, Fischer B (1978) Dispersion theory of surface-exciton polaritons. Phys Rev B 17(10):3814–3823
52. Basov DN, Fogler MM, García de Abajo FJ (2016) Polaritons in van der Waals materials. Science 354(6309):195
53. Grigorenko AN, Polini M, Novoselov KS (2012) Graphene plasmonics. Nat Photonics 6(11):749–758
54. Palik ED (1985) Handbook of optical constants of solids. Academic, Orlando
55. Boltasseva A, Atwater HA (2011) Low-loss plasmonic metamaterials. Science (Washington) 331(6015):290–291
56. Law S, Yu L, Wasserman D (2013) Epitaxial growth of engineered metals for mid-infrared plasmonics. J Vac Sci Technol B 31:03C121
57. Dunkelberger AD, et al (2017) Active tuning of surface phonon polariton resonances via carrier photoinjection. ArXiv Condensed Matter e-prints, **under review Nature Photonics**: p arXiv:1705.05980
58. Traviss D et al (2013) Ultrafast plasmonics using transparent conductive oxide hybrids in the epsilon near zero regime. Appl Phys Lett 102(12):121112
59. Kim J et al (2014) Optical properties of gallium-doped zinc oxide – a low-loss plasmonic material: first principles theory and experiment. Phys Rev X 3:041037
60. Dionne JA et al (2009) PlasMOStor: a metal-oxide-Si field effect plasmonic modulator. Nano Lett 9(2):897–902
61. Silveirinha MG, Engheta N (2006) Tunneling of electromagnetic energy through sub-wavelength channels and bends using epsilon-near-zero (ENZ) materials. Phys Rev Lett 97:157403
62. Kim J et al (2016) The role of epsilon-near-zero substrates in the optical response of plasmonic antennas. Optica 3(3):339
63. Boyuk DS, Chou L-W, Filler MA (2016) Strong near-field coupling of plasmonic resonators embedded in Si nanowires. ACS Photonics 3(2):184–189
64. Law S et al (2013) All-semiconductor plasmonic nanoantennas for infrared sensing. Nano Lett 13(9):4569–4574
65. Jun YC et al (2012) Active tuning of mid-infrared metamaterials by electrical control of carrier densities. Opt Express 20(2):1903
66. Offermans P, Crego-Calama M, Brongersma SH (2010) Gas detection with vertical InAs nanowire arrays. Nano Lett 10(7):2412–2415
67. Adams DC et al (2010) Plasmonic mid-infrared beam steering. Appl Phys Lett 96:201112
68. Kirste R et al (2013) Ge doped GaN with controllable high carrier concentration for plasmonic applications. Appl Phys Lett 103(24):242107
69. Jefferson PH et al (2008) Bandgap and effective mass of epitaxial cadmium oxide. Appl Phys Lett 92:022101
70. Sachet E et al (2015) Dysprosium-doped cadmium oxide as a gateway material for mid-infrared plasmonics. Nat Mater 14(4):414–420
71. Low T et al (2017) Polaritons in layered two-dimensional materials. Nat Mater 16:182–194
72. Basov DN et al (2014) Colloquium: graphene spectroscopy. Rev Mod Phys 86:959–994
73. Vakil A, Engheta N (2011) Transformation optics using graphene. Science (Washington) 332:1291–1294
74. Yao Y et al (2013) Broad electrical tuning of graphene-loaded plasmonic antennas. Nano Lett 13(3):1257–1264
75. Jadidi MM et al (2015) Tunable terahertz hybrid metal-graphene plasmons. Nano Lett 15:7099–7104
76. Koppens FHL et al (2014) Photodetectors based on graphene, other two-dimensional materials and hybrid systems. Nat Nanotechnol 9:780–793
77. Sun Z, Martinez A, Wang F (2016) Optical modulators with 2D layered materials. Nat Photonics 10:227–238

78. Khurgin JB, Sun G (2011) Scaling of losses with size and wavelength in nanoplasmonics and metamaterials. Appl Phys Lett 99:211106
79. Caldwell JD et al (2013) Low-loss, extreme sub-diffraction photon confinement via silicon carbide surface phonon Polariton Nanopillar resonators. Nano Lett 13(8):3690–3697
80. Caldwell JD et al (2014) Sub-diffractional, volume-confined polaritons in the natural hyperbolic material hexagonal boron nitride. Nat Commun 5:5221
81. Ellis CT et al (2016) Aspect-ratio driven evolution of high-order resonant modes and near-field distributions in localized surface phonon polariton nanostructures. Sci Rep 6:32959
82. Razdolski I et al (2016) Resonant enhancement of second-harmonic generation in the mid-infrared using localized surface phonon polaritons in subdiffractional nanostructures. Nano Lett 16:6954–6959
83. Chen Y et al (2014) Spectral tuning of localized surface phonon polariton resonators for low-loss mid-IR applications. ACS Photonics 1(8):718–724
84. Michel A-KU et al (2013) Using low-loss phase-change materials for mid-infrared antenna resonance tuning. Nano Lett 13(8):3470–3475
85. Li P, Taubner T (2012) Multi-wavelength superlensing with layered phonon-resonant dielectrics. Opt Express 20(S3):A11787
86. Tiwald TE et al (1999) Carrier concentration and lattice absorption in bulk and epitaxial silicon carbide determined using infrared ellipsometry. Phys Rev B 60(16):11464–11474
87. Adachi S (1999) The reststrahlen region. In: Optical properties of crystalline and amorphous semiconductors: materials and fundamental principles. Springer Science+Business Media, LLC, New York, pp 33–61
88. Yoxall E et al (2015) Direct observation of ultraslow hyperbolic polariton propagation with negative phase velocity. Nat Photonics 9:674–678
89. Li P et al (2016) Reversible optical switching of highly confined phonon-polaritons with an ultrathin phase-change material. Nat Mater 15:870–875
90. Caldwell JD et al (2007) Free carrier distribution profiling of 4H-SiC substrates using a commercial optical scanner. J Appl Phys 101:093506
91. Harima H, Nakashima S, Uemura T (1995) Raman-scattering from anisotropic LO-phonon-plasmon-coupled mode in n-type 4h-SiC and 6h-SiC. J Appl Phys 78:1996–2005
92. Maier SA (2007) Plasmonics: fundamentals and applications, 1st edn. Springer, Berlin
93. Noginov M et al (2013) Focus issue: hyperbolic metamaterials. Opt Express 21(12): 14895–14897
94. Fisher RK, Gould RW (1969) Resonance cones in the field pattern of a short antenna in anisotropic plasma. Phys Rev Lett 22:1093–1095
95. Dai S et al (2015) Subdiffractional focusing and guiding of polaritonic rays in a natural hyperbolic material. Nat Commun 6:6963
96. Ishii S et al (2013) Sub-wavelength interference pattern from volume plasmon polaritons in a hyperbolic medium. Laser Photonics Rev 7:265–271
97. Shalaev VM et al (2005) Negative index of refraction in optical metamaterials. Opt Lett 30(24):3356–3358
98. Jacob Z et al (2010) Engineering photonic density of states using metamaterials. Appl Phys B 100(1):215–218
99. Sun J, Litchinitser NM, Zhou J (2014) Indefinite by nature: from ultraviolet to terahertz. ACS Photonics 1(4):293–303
100. Korzeb K, Gajc M, Pawlak DA (2015) Compendium of natural hyperbolic materials. Opt Express 23(20):25406–25424
101. Ambrosio A et al (2017) Mechanical detection and imaging of hyperbolic phonon polaritons in hexagonal boron nitride. ACS Nano 11(9):8741–8746
102. Xu XG et al (2014) One-dimensional surface phonon polaritons in boron nitride nanotubes. Nat Commun 5:4782
103. Xu XG, Tanur AE, Walker GC (2013) Phase controlled homodyne infrared near-field microscopy and spectroscopy reveal inhomogeneity within and among individual boron nitride nanotubes. J Phys Chem A 117:3348–3354

Chapter 13
Waveguide Integrated Superconducting Single Photon Detectors

Wolfram H. P. Pernice

Abstract Nanophotonic circuits employ waveguiding devices to route light across quasi-planar integrated optical chips in analogy to electrical wires in integrated electrical circuits. Using materials with high refractive index allows for confining light into sub-wavelength dimensions as efficient optical wires. Interaction with the environment is possible through near-field coupling to the evanescent tail of propagating optical modes, given that the measurable system is close to the waveguide surface. The interaction length can then be conveniently tailored by simply choosing a sufficiently long waveguide. This approach is particularly interesting for designing highly sensitive detectors which are able to register individual photons. Because nanophotonic circuits are well-suited for the study of single photon effects on chip, such detectors constitute a fundamental building block for emerging quantum photonic technologies. Here I introduce the concept of waveguide integrated single photon detectors, with a focus on superconducting nanowire single photon counters. The chapter covers the basics of single photon threshold detection, as well as advanced designs for multi-photon and coherent detection. The co-integration with nanophotonic circuits to realize hybrid systems enables advanced on-chip platforms for emerging applications in integrated quantum photonics.

Keywords Nanophotonics · Single photon detection · Superconducting devices

13.1 Introduction

Nanophotonic circuits have been an invaluable resource for implementing complex optical functionality on a chip. By employing individually optimized photonic building blocks custom integrated optical devices can be realized for applications in telecommunication, optical signal processing and filtering. Traditionally, integrated

W. H. P. Pernice (✉)
Institute of Physics, University of Münster, Münster, Germany
e-mail: wolfram.pernice@uni-muenster.de

B. Di Bartolo et al. (eds.), *Quantum Nano-Photonics*, NATO Science for Peace and Security Series B: Physics and Biophysics,
https://doi.org/10.1007/978-94-024-1544-5_13

photonic components are realized from dielectric materials which often do not provide active functionality, such as devices for light generation or detection. Therefore heterogeneous integration schemes in which passive waveguide devices are afterwards equipped with additional source and detection elements are emerging as attractive solutions to arrive at fully integrated systems. In particular, for demanding applications in non-classical optics, heterogeneous integration is a viable option because of existing incompatibilities between different material platforms for fabricating sources of non-classical light, waveguide modulation approaches and photon detection systems.

Highly efficient low noise single-photon detectors are key to the realization of numerous applications, both classical as well as quantum technological [1, 2]. While classical applications such as optical time domain reflectometry and optical coherence tomography show a need for improved signal-to-noise ratio and detector timing characteristics [3, 4], quantum applications in quantum metrology and optical quantum computing crucially depend on high efficiency, low-noise performance and minimal timing jitter [5–11]. The implementation of numerous linear optics quantum information processing schemes, most prominently quantum key distribution, is currently limited by the availability of suitable quantum detectors in large numbers [1, 6–8, 12].

In order to be compatible with the existing telecommunication infrastructure it is desirable to operate in the near-infrared wavelength regime around 1550 nm. In this regime predominantly avalanche photo diodes (APDs) based on the InGaAs material systems are employed [13]. Such detectors are, however, plagued by high dark count rates and detection efficiency below 30%. Furthermore, gated mode operation is prerequisite, thus limiting available detection rates and secure transmission distances. As an alternative, superconducting nanowire single-photon detectors (SNSPD) have emerged as a promising detector architecture when ultra-low noise is required [14]. SNSPDs are operated at cryogenic temperatures below the critical temperature where the material is in its superconducting phase. The absorption of photons incident on the superconducting nanowire locally destroys the superconductivity which leads to a stark change in detector resistance which, in turn, can be registered electronically.

The detection mechanism of nanowire SSPDs can be understood in the framework of the quasi-static vortex (QSV) model, combined with quasi-particle diffusion. The absorption of a photon increases locally the temperature of electrons, thus forming a hot-spot inside the nanowire. Suppression of the order parameter in the spot and the corresponding enhancement of the kinetic inductivity lead to redistribution of the supercurrent density. If the suppression of the order parameter and supercurrent are sufficient, the supercurrent density exceeds the depairing current density in the center of the spot or at the edge of the strip, depending on whether the spot was formed near the center of the strip or near the edge. Immediately after this, a vortex-antivortex pair or a single vortex is nucleated and crosses the strip and locally heats it up, which leads to a further reduction of the depairing current density and also the nucleation of new vortices. Model calculations show that for films with high resistivity like NbN crossing of the strip by just several

vortices or pairs completely destroys the superconductivity in the narrow belt across the strip. The breakdown of the superconductivity corresponds to the appearance of resistance and thus a detection event. Then the supercurrent is reduced, heating stops and the superconducting state is recovered on a picosecond timescale through thermalization with the cold bath.

For applications in the telecommunication range SNSPDs have provided favorable performance characteristics, including timing jitter below 20 ps and dark count rates of only a few Hertz [15–17]. Traditional SNSPDs are coupled to optical fibers under normal incidence. Because the nanowires are prepared from ultra-thin films with thicknesses below 5 nm, the available absorption length is limited by the film thickness, which allows a large portion of the incident photon flux to permeate the detector region without being absorbed. Absorption under normal incidence is furthermore not compatible with an integrated optical platform where out-of-plane optical access is typically avoided. By using multi-layer thin-film architectures the absorption efficiency can be increased to 93%, as recently demonstrated at detectors made from tungsten silicon (WSi) [15].

To overcome existing limitations in detector design, waveguide integrated nanowire [16] superconducting detectors have been suggested as an alternative route [17–20]. In this design, photons are no longer absorbed under normal incidence, but rather by evanescent coupling to the superconducting nanowire which is situated directly atop an optical waveguide. The available coupling length over which photons are absorbed can in principle be increased arbitrarily to achieve near-unity absorption efficiency. More importantly, however, such a design is directly compatible with integrated optical circuits and thus ideally suited to complement integrated quantum optical platforms. In the visible wavelength regime, detectors made from NbTiN have shown characteristic plateau behavior and thus high internal quantum efficiency [20]. High internal quantum efficiency is required in order to be able to operate the single photon detector far from the critical current which in turn provides low noise-equivalent power (NEP). This has been achieved in the visible wavelength regime, where silicon APDs are available.

In analogy, highly efficient waveguide integrated SNSPDs with plateau behavior in the telecommunications wavelength range can be achieved with niobium nitride (NbN) SNSPDs on top of silicon nitride (Si3N4) waveguides. Such devices show on-chip detection efficiencies above 80% with NEPs at the 10^{-19} W/Hz$^{1/2}$ level. Waveguide integrated SNSPDs are fully scalable and thus allow for convenient combination with on-chip quantum optical circuits.

13.2 Multi–Photon Detection in SNSPDs

Waveguide integrated nanowire SSPDs not only provide single-photon counting capability, but can also be used to discriminate larger numbers of photons when operated under different biasing conditions. Superconducting nanowire detector devices are realized with a three steps lithography process for integration with

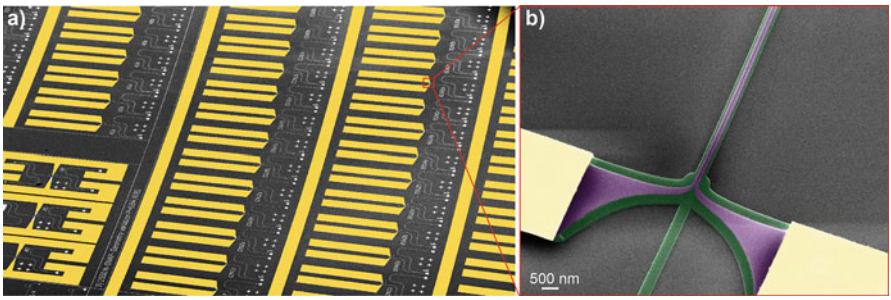

Fig. 13.1 (**a**) Section of a nanophotonic chip with several circuits for single photon detection. Each device is equipped with two grating couplers for coupling light into the waveguides, as well with an electrically contacted SNSPD. (**b**) False-color scanning electron microscope image of a SNSPD (purple) atop a silicon nitride waveguide (green)

nanophotonic circuitry. Typical nanophotonic circuits after fabrication are shown in Fig.13.1a, where many detector devices are realized in parallel. We use nanophotonic circuits into which light is injected and collected from waveguides which support transverse-electrical (TE) mode propagation using an optical fiber array and a pair of optical grating couplers, designed for 1550 nm wavelength (white triangular structures in Fig. 13.1a). The integrated optical circuit consists of a 50:50 waveguide splitter that routes half of the coupled light to the detector region and the other half to a reference grating coupler port which is used to determine the amount of photons travelling to the detector. The SNSPDs are fabricated directly on top of the waveguide so that for sufficiently long nanowires the incoming photons are almost fully absorbed. Therefore the detection probability is mostly limited by the internal quantum efficiency of converting an absorbed photon into a detection event. In addition, the detection regime can be controlled by varying the biasing condition of the nanowires as well as the nanowire geometry. By design, this most easily involves changing the nanowire width which influences the probability to generate a detection event upon absorption of individual photons.

If the value of the supercurrent is not sufficiently large or the width of the strip is too large, after the formation of the hot spot the redistributed supercurrent density will not exceed the depairing current density, and the absorption of a single photon is insufficient to generate an output signal. Instead, simultaneous absorption of multiple photons in a small region of the wire is needed to lead to a breakdown of the superconductivity. In addition, the multi-photon absorption events must occur within the original hotspot lifetime. At high bias current ingle photon detection regime is predominant. However, when applying a current lower than 0.5 Ic, multi-photon detection is enhanced.

For high bias currents, the detection probability grows linearly with the number of incoming photons. By reducing the bias current, this proportionality becomes non-linear which on a log-log scale translates into a change of the slope of the detection curve. A similar behavior occurs when applying identical bias condition

to detectors with different nanowire widths. For a large number of incoming photons the detection probability saturates, meaning that all the incoming pulses are detected. This saturation occurs at lower photon numbers for narrower wires and also at higher bias currents. For wider wires biased far away from the critical current, the absorption of a single photon is insufficient for breaking the superconductivity. Therefore in order to produce a voltage signal the absorption of multiple photons in the same region of the nanowire is needed. By investigating the different detection regimes it is thus possible to arrive at suitable designs of the SSPDs which are capable of detecting the simultaneous arrival of a specific number n of photons rather than single photons. This property may be of particular interest for the detection of Fock or NOON states.

For a number of photons less than one photon per pulse on average, the one photon detection regime is always predominant. When increasing the number of photons per pulse, the multi-photon regime dominates instead. We observe that the incoming photon number has to be increased at low bias current in order to register a real signal. This is partially due to an overall device sensitivity reduction at lower currents. In addition, the simultaneous presence of multiple photons rapidly declines with decreasing optical input powers which, in turn, reduces the detection probability.

Model calculations allow determining the internal quantum efficiency in waveguide integrated SSPDs. The model is in agreement with the QSV theory and shows that wider nanowires are better candidates for simultaneous multiphoton detection. From the internal quantum efficiency calculation, they show in fact a wider bias current range in which pure two or three photon detection regimes are more efficient than the single photon detection regime. Narrow wires represent an efficient solution for single photon detection. A plateau in the 80 nm and 100 nm nanowires internal quantum efficiency for single photon detection indicates that narrower wires can operate as single photon detectors at lower currents where the signal to noise ratio is very high without any loss in the efficiency [21].

13.3 Cavity Enhanced SNSPDs

In order to enhance the absorption efficiency, the interaction length of the coupled system can be increased by elongating the nanowire. This, however, also increases the detector footprint and reduces the speed. Upon a detection event, the time needed for a complete recovery of the original detection efficiency is limited by the kinetic inductance. This quantity is proportional to the nanowire length. Therefore, a longer nanowire raises the absorption efficiency, but increases the recovery time as well. This trade-off between detector speed and absorption efficiency is inherent to SNSPDs. Different approaches to enhance the detection speed have been adopted, including the use of superconducting materials with low kinetic inductances or parallel nanowire geometries. In the former concept, the fundamental limit for the recovery time is imposed by the material properties of the superconducting film. The

latter approach, based on a cascade-switching mechanism, suffers from operation instabilities and signal after-pulsing; imposing a limit on the attainable recovery time.

The trade-off between absorption efficiency and detector speed can be overcome by aligning the superconducting nanowire perpendicular to the waveguide and not parallel, as described in the previous sections. Together with the contact pads this gives the detector a microbridge geometry. Such a design renders the detector fast; but because of a strongly reduced interaction length it only provides low absorption efficiency. To nullify this drawback, we capitalize on a coherent perfect absorber (CPA) concept [22] and integrate the nanowire into a suitably designed optical cavity [23].

The cavity is made from photonic crystal (PhC) elements consisting of air holes etched into the waveguide. The back mirror of the cavity is perfectly reflecting at the frequency of operation. The front mirror is only partially reflecting. Thereby, the entire cavity is designed such that directly reflected light at the front mirror destructively interferes with light that experience multiple round trips in the cavity. Since the only escape path for the photon energy is dissipation in the nanowire, the absorption is strongly enhanced thanks to CPA. The entire device is a part of a silicon-on-insulator (SOI) nanophotonic circuit and thus fully integrated. The small footprint of the nanowire leads to low kinetic inductance compared to traditional U-shape designs and governs the timing characteristics of our cavity-integrated microbridge nanodetectors. We experimentally verified the high detection rate using a GHz pulsed laser source in combination with single-shot measurements recorded at a fast oscilloscope. From evaluating the number of events in a certain time span exceeding a selected threshold level, we obtain a maximum count rate of 1.20 GHz, corresponding to the repetition rate of the light source. It has to be noted that in this measurement the number of photons per pulse is high in order to reliably trigger in a detection event. Therefore these measurements, do not corresponding to single-photon sensitivity. Correspondingly, the bias current has to be reduced in order to maintain superconductivity in the nanowire.

Besides detector speed, the timing accuracy or timing jitter is a crucial aspect of single-photon detection, particularly for correlation measurements and time-correlated single-photon counting. Using a picosecond pulsed laser source in combination with a digital sampling oscilloscope in histogram mode, the arrival time of detection pulses are measured with respect to the excitation pulse. The full width of half maximum (FWHM) of the histogram, as obtained from a Gaussian fit, is a measure of the detector's timing jitter. We find a best value of 32 ps among the examined cavity-integrated microbridge detectors (Fig. 13.2).

Combining photonic crystal cavity and compact nanowire geometry culminates in a strong enhancement of the detection efficiencies on resonance compared to stand-alone nanodetectors, exhibiting outstanding decay and recovery times. The small detector footprint leads to dark count rates below 1 Hz and the efficient detection of multi-photon states as a threshold detector. The latter enables the realization of efficient autocorrelation detectors at adaptable threshold levels while the small decay times allow to establish time-multiplexed single-photon detection

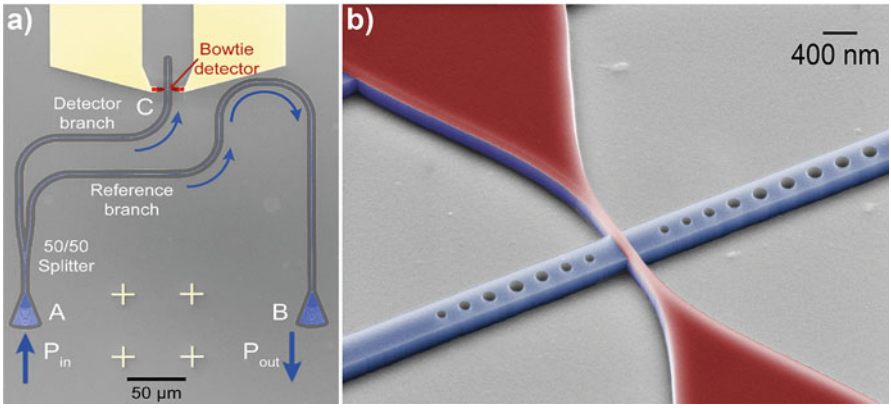

Fig. 13.2 (**a**) False-color SEM micrograph of a photonic circuit used to characterize ultrafast cavity enhanced SNSPDs in bow-tie geometry. (**b**) Zoom into the cavity region where the SNSPD is aligned across the silicon waveguide between photonic crystal mirrors

schemes. These results pave the way towards arrays of compact waveguide-coupled detectors, providing a monolithic scalable platform for applications in on-chip quantum optics and time-correlated single-photon counting [24].

13.4 Multi–Detector Devices

The detection of individual photons by SNSPDs is an inherently binary mechanism, revealing either their absence or presence while not providing their spectral information. For multi-color imaging techniques, such as single photon spectroscopy, fluorescence resonance energy transfer microscopy, and fluorescence correlation spectroscopy, wavelength discrimination is essential and necessitates spectral separation prior to detection. Spectral discrimination of the incoming single photon signal can be efficiently achieved with nanophotonic circuits. The waveguide integrated detector design outlined in the previous sections enables the seamless integration of multiple SNSPDs with advanced on-chip photonic circuitry while maintaining the detectors' efficiency and temporal precision. The co-integration of multiple SNSPDs with wavelength-separating photonic circuitry therefore offers a convenient approach to on-chip single photon spectroscopy with high timing accuracy and fast data acquisition rates. Beside pure spectroscopic analysis at the single photon level, the concept enables advanced techniques such as fluorescence lifetime imaging in a single device.

We realize fully integrated single photon spectrometers (SPSs) by co-integrating eight SNSPDs with an arrayed waveguide grating (AWG) on a silicon-nitride on insulator substrate. An optical micrograph of an exemplary device is shown in Fig. 13.3a, where the photonic circuitry is placed in the upper half and the

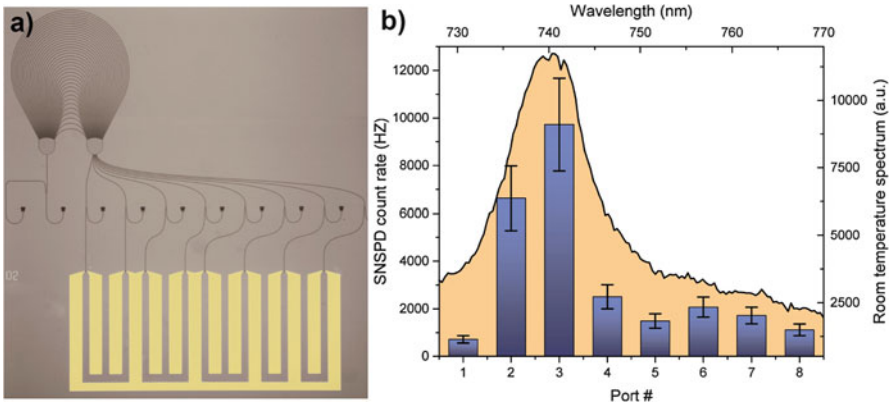

Fig. 13.3 (**a**) Optical micrograph of an arrayed waveguide grating device combined with eight on-chip SNSPDs. (**b**) Spectral analysis of light emission from diamond nanoclusters with silicon vacancy color centers using a visible light single photon spectrometer

electrically contacted SNSPDs are shown in the bottom half. The silicon nitride photonic platform enables broadband optical operation, filtering and multiplexing combined with highly efficient on-chip single photon detection. In particular, the platform allows for harnessing long efforts in developing photonic components which perform a wide range of optical functionality on chip. SNSPDs provide the aforementioned active detection functionality to these circuits. As an illustrating example, in Fig. 13.3b the detection of light emission from diamond nanoclusters which contain silicon vacancy color centers is shown. In this case the photonic circuits are designed for operation in the red wavelength regime which resides well within the detection optical bandwidth of SNSPDs. Analogous designs for the telecommunication wavelength regime allows for wavelength discrimination in the near-infrared wavelength region [25].

The adoption of a quantum photonic approach to sensing and imaging holds the potential to herald a new level of experimental fidelity. By integrating multiple SNSPDs with wavelength-discriminating on-chip circuitry spectrally resolved single photon detection with high timing precision can be realized in a single photonic device. The two circuit devices presented here serve as prototypes of a rich class of hybrid nanophotonic-superconducting systems. AWGs with tens of output waveguides provide room for large SNSPD arrays similar to CCD arrays in conventional spectrometers. Such devices could enable the live monitoring of numerous fluorophores over a wide spectral range. In particular, highly precise infrared and thermal imaging become possible owing to the SNSPDs' enormous spectral range.

The presented SPS operated in the telecommunication wavelength regime at 1550 nm hold promise for serving as receiver elements in wavelength-division multiplexed (WDM) optical networks with low signal strengths and, in particular, for quantum optical implementations which require the reliable detection of individual photons on tailored wavelengths. Owing to the SNSPDs' high temporal accuracy and good on-chip detection efficiency even more advanced protocols involving quantum cryptography and quantum key distribution on multiple wavelength channels and thus with high bandwidth are brought within reach.

13.5 Coherent Detection

An alternative way of determining the spectrum of unknown radiation with higher spectral resolution is to use coherent detection [26] instead of photonic circuit components. Using coherent detection, the detector absorbs radiation from two different sources (a source signal S and a local oscillator LO) which are frequency-shifted relatively to each other. The resulting response signal is then the difference (intermediate) frequency (IF), corresponding to the beating frequency of the two fields. Knowing the LO frequency and measuring the IF allows thus to determine the frequency and phase of the unknown signal S.

While analog detectors are normally used for coherent detection, single photon counters such as InGaAs avalanche photodiodes have also been used for heterodyne detection [27]. This approach allows to combine the detection of photons as well as heterodyne mixing and is of interest for Doppler shift detection of specular and diffused targets during LiDAR investigation. Furthermore, using photon counters in the coherent detection allows to reduce LO power by more than 9 orders of magnitude from a MilliWatt to PicoWatt level. Combining mixing techniques with the superior sensitivity of SNSPDs on an integrated platform thus enables on-chip heterodyne detection with high spectral resolution (Fig. 13.4).

By using waveguide-integrated SNSPDs near quantum limited sensitivity is feasible with a chip-based device [28]. We demonstrated single-photon counting with on-chip detection efficiency up to 86% and a coherent mixing with a spectral resolution ($f/\Delta f$) greater than 10^{11} at telecom wavelengths. These devices thus operate close to the shot-noise limit. Interestingly, they allow for heterodyne detection at ultra-low local oscillator powers (10^5–10^9 photons /s) and only require an extremely weak signal photon flux of the incident test signal (10^3–10^9 photons/s). In particular short SNSPDs show wide conversion bandwidth and can thus be used for coherent detection applications where narrow-line observations are required over a broad bandwidth.

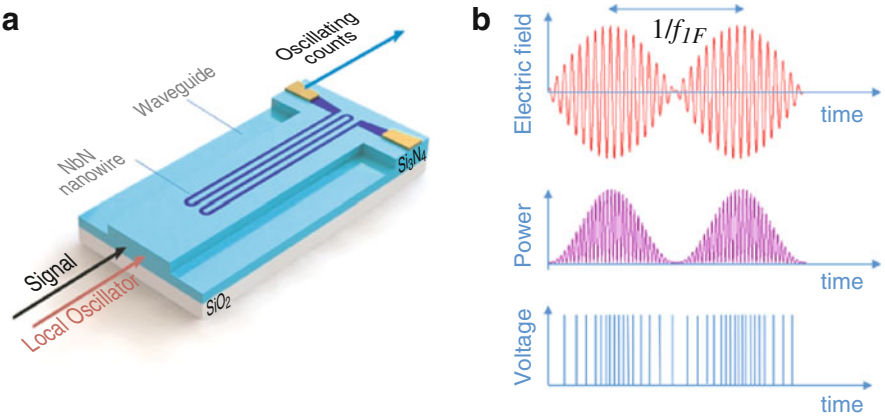

Fig. 13.4 (**a**) Schematic of coherent detection with waveguide integrated SNSPDs illuminated by a signal and local oscillator field. (**b**) Operation principle of the device. The superposition of both fields yields a time varying beating signal (top). The beating fields translates to an oscillating power at the inverse IF. This power fluctuation yields a time dependent count rate at the SNSPD

13.6 Conclusions

Waveguide integrated SNSPDs provide passive waveguide circuits with advanced detection capability on a single photon level. In comparison to fiber coupled detectors, waveguide integrated devices can be fabricated with drastically reduced dimensions which provides opportunities for ultrafast detection and dense integration. Through evanescent coupling to propagating modes such SNSPDs can be seamlessly integrated with photonic circuitry and thus allow for building on years of development efforts in this field. Superior performance in terms of noise and efficiency further allows for implementing advanced measurement schemes to extend the functionality of pure single photon counters. This on the one hand enables multi-photon threshold detection, as well as providing wavelength discrimination to otherwise broadband detectors. In combination with scalable fabrication for multi-detector devices, waveguide SNSPDs thus offer an attractive platform for quantum photonic applications.

References

1. Hadfield RH (2009) Single-photon detectors for optical quantum information applications. Nat Photonics 3:696–705
2. Eisaman MD, Fan J, Migdall A, Polyakov SV (2011) Single-photon sources and detectors. Rev Sci Instrum 82:071101
3. Eraerds P, Legré M, Zhang J (2010) Photon counting OTDR: advantages and limitations. J Light Technol 28:952–964

4. Stellari F, Song P, Weger A (2011) Single photon detectors for ultra low voltage time-resolved emission measurements. IEEE J Quantum Electron 47:841–848
5. O'Brien JL (2007) Optical quantum computing. Science 318:1567–1571
6. Knill E, Laflamme R, Milburn G (2001) A scheme for efficient quantum computation with linear optics. Nature 409:46
7. Takesue H et al (2007) Quantum key distribution over a 40-dB channel loss using superconducting single-photon detectors. Nat Photonics 1:343–348
8. Gisin N, Ribordy G, Tittel W, Zbinden H (2002) Quantum cryptography. Rev Mod Phys 74:145–195
9. Korneev A et al (2007) Single-photon detection system for quantum optics applications. IEEE J Sel Top Quantum Electron 13:944–951
10. Giovannetti V, Lloyd S, Maccone L (2011) Advances in quantum metrology. Nat Photonics 5:222–229
11. Gaggero A et al (2010) Nanowire superconducting single-photon detectors on GaAs for integrated quantum photonic applications. Appl Phys Lett 97:151108
12. Natarajan CM et al (2010) Operating quantum waveguide circuits with superconducting single-photon detectors. Appl Phys Lett 96:211101
13. Itzler M a et al (2011) Advances in InGaAsP-based avalanche diode single photon detectors. J Mod Opt 58:174–200
14. Gol'tsman GN et al (2001) Picosecond superconducting single-photon optical detector. Appl Phys Lett 79:705
15. Marsili F et al (2013) Detecting single infrared photons with 93% system efficiency. Nat Photonics 7:210–214
16. Hu X, Holzwarth CW, Masciarelli D, Dauler EA, Berggren KK (2009) Efficiently coupling light to superconducting nanowire single-photon detectors. IEEE Trans Appl Supercond 19:336–340
17. Sprengers JP et al (2011) Waveguide superconducting single-photon detectors for integrated quantum photonic circuits. Appl Phys Lett 99:181110
18. Gerrits T et al (2011) On-chip, photon-number-resolving, telecommunication-band detectors for scalable photonic information processing. Phys Rev A 84:060301
19. Tanner MG et al (2012) A superconducting nanowire single photon detector on lithium niobate. Nanotechnology 23:505201
20. Schuck C, Pernice WHP, Tang HX (2013) NbTiN superconducting nanowire detectors for visible and telecom wavelengths single photon counting on Si3N4 photonic circuits. Appl Phys Lett 102:051101
21. Ferrari S, Kahl O, Kovalyuk V, Goltsman GN, Korneev A, Pernice WHP (2015) Waveguide-integrated single- and multi-photon detection at telecom wavelengths using superconducting nanowires. Appl Phys Lett 106:151101
22. Liu N, Mesch M, Weiss T, Hentschel M, Giessen H (2010) Infrared perfect absorber and its application as plasmonic sensor. Nano Lett 10(7):2342–2348
23. Akhlaghi MK, Schelew E, Young JF (2015) Waveguide integrated superconducting single-photon detectors implemented as near-perfect absorbers of coherent radiation. Nat Commun 6:8233
24. Vetter A, Ferrari S, Rath P, Alaee R, Kahl O, Kovalyuk V, Diewald S, Goltsman GN, Korneev A, Rockstuhl C, Pernice WHP (2016) Cavity-enhanced and ultrafast superconducting single-photon detectors. Nano Lett 16:7085
25. Kahl O, Ferrari S, Kovalyuk V, Vetter A, Lewes-Malandrakis G et al (2017) Spectrally multiplexed single-photon detection with hybrid superconducting nanophotonic circuits. Optica 4:557–562
26. Jacobs SF (1988) Optical heterodyne (coherent) detection. Am J Phys 56:235–245
27. Luu JX, Jiang L (2006) Saturation effects in heterodyne detection with Geiger-mode InGaAs avalanche photodiode detector arrays. Appl Opt 45:3798–3804
28. Kovalyuk V, Ferrari S, Kahl O, Semenov A, Shcherbatenko M et al (2017) On-chip coherent detection with quantum limited sensitivity. Sci Rep 7(4812):4812

Chapter 14
Whispering Gallery Mode Resonators as Opto-Mechanical Probes to Nanoparticle-Microcavity Interaction and Charge

Stephen Arnold, J. R. Lopez, E. Treasurer, K. M. Snyder, and D. Keng

Abstract Whispering Gallery Mode (WGM) resonators demonstrate nearfield interactions that sensitively shift resonance frequencies with interaction lengths less than 200 nm. This range is ideal for observing the effect that double layers have on the motion of protein, virus, and artificial nanoparticles. In exploring the measurement possibilities we were immediately drawn to the opportunity for determining physical parameters that have not revealed themselves through microcavity experiments in the past. The first example of this general interest is the measurement of charge. Charge significantly influences the binding of virus and other nano-particles to microcavity bio-sensors, although surprisingly there have been no reports of the determination of either cavity charge density σ_w or nanoparticle charge q_p using these sensors. In this paper we review our recent progress in experimentally demonstrating an approach for the determination of both. We use an opto-mechanical Whispering Gallery Mode (WGM) *Carousel trap* to extract the electrostatic interaction energy versus separation s between the cavity surface and an orbiting nanoparticle of know charge, from WGM frequency fluctuations induced by the particle. Next we fit this interaction energy to wall-colloid theory (first *Debye-Hückel*, and then *Gouy-Chapman* theory) and determine σ_w. This charge density on a just-prepared silica microsphere is far less than literature values. With this microcavity charge density in hand, a larger particle having unknown charge and orbiting the same microcavity has its charge measured from its associated electrostatic interaction energy. This charge is in agreement with independent measurements.

S. Arnold (✉) · J. R. Lopez · E. Treasurer · K. M. Snyder · D. Keng
Microparticle Photophysics Lab (MP3Lab), NYU School of Engineering, Brooklyn, NY, USA
e-mail: sa1577@nyu.edu

B. Di Bartolo et al. (eds.), *Quantum Nano-Photonics*, NATO Science for Peace and Security Series B: Physics and Biophysics,
https://doi.org/10.1007/978-94-024-1544-5_14

14.1 Introduction

The stimulation of Whispering Gallery Modes (WGMs) in microspheres in aqueous solution through fiber coupling in 1995 [1], along with the estimated extreme sensitivity of the resonance frequency shift to the binding of a biological layer in 1995 and 2001 [1, 2], has led to an explosion in the use of this device for bio-sensing [3]. In 2003 it was estimated that single aqueous borne biological nano-particles could be detected [4], a prediction that was validated in 2008 with the detection of InfluenzaA virus [5]. To date single particle size has been measured to better than $\pm 2\%$ through WGM frequency shifts [6, 7], and antibody recognition of virus has also been demonstrated [8], however the one physical parameter that has eluded experimenters is the nano-particle charge q_{p}. Although a recent scheme has been proposed for determining the charge of a nano-particle upon binding to a high Q WGM resonator in air [9], there actually have not been any demonstrations published using this proposal. Our interest is in the aqueous phase where applications abound (e.g. charge controls the efficiency of nanoparticle drug bio-uptake and distribution [10, 11]). In what follows we demonstrate a method for using the perturbation of a WGM's resonance frequency by an orbiting nanoparticle to determine the microcavity's surface charge density σ_w [12]. With this charge density in hand the determination of the charge of an arbitrary nano-particle orbiting the same microcavity is straight-forward [12].

14.2 Theoretical Approach

Figure 14.1 illustrates the idea behind WGM Coulometry. A nano-particle is caught in equatorial orbit around a WGM microcavity by the near balance between an attractive optical gradient force $\underline{F}_{\mathrm{g}}$, and a repulsive electrostatic force $\underline{F}_{\mathrm{es}}$, while being driven longitudinally by a dissipative scattering force $\underline{F}_{\mathrm{s}}$. The gradient force is conservative, whereas the scattering force is not. The electrostatic repulsion that is generated between the negative silica surface and the negative charge of the nanoparticle is radial and conservative. Knowledge about the charge on the particle q_p or the charge density on the microcavity surface σ_w can only be obtained through the measurement of this electrostatic force. This force is determined from the electrostatic potential U_{es}, by measuring the overall potential $\mathrm{U} = \mathrm{U}_{\mathrm{g}} + \mathrm{U}_{\mathrm{es}}$, and subtracting the well-known optical gradient potential U_{g} [13]. The particle is driven by thermal fluctuations that are much more effective in changing its gradient interaction in the radial direction than along the polar direction. This is due to the fact that the gradient potential is proportional to the local intensity seen by the particle. For the microcavity used in our experiments changing the radial separation from 200 nm to 10 nm produces an increase in intensity by $\sim$170%, whereas motion along a meridian upward from the equator by the same 190 nm, produces a decrease in intensity by about 1%. In addition, a particle in an equatorial orbit is constrained

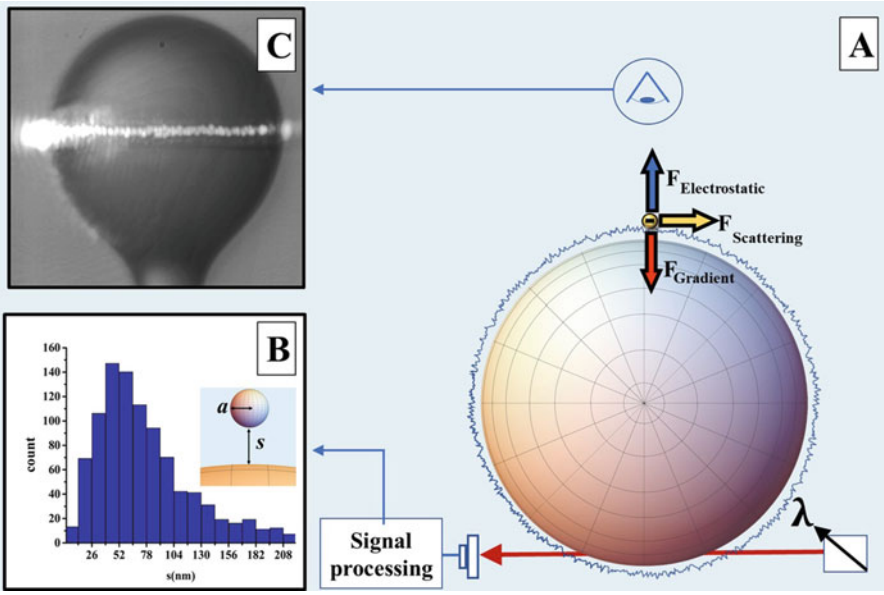

Fig. 14.1 Principle behind WGM Coulometry. (**a**) Polar illustration of a nano-particle orbiting a spherical microcavity. It undergoes nanoscopic Brownian fluctuations within a radial potential well due to a near balance between an attractive optical gradient force $\underline{F}_g$ and a repulsive electrostatic force $\underline{F}_{es}$ that are revealed through the frequency shifts of the associated WGM. By extracting the electrostatic potential energy U_{es} for a nanoparticle of known charge, the microcavity surface charge is estimated. A particle of unknown charge orbiting the same sphere has it charge revealed from its interaction potential energy; (**b**). Frequency shifts translated into interfacial separation *s*. (**c**) Time lapse image perpendicular to the symmetry axis reveals that the particle is caught in an equatorial mode around a spherical micro-cavity ~40 microns in radius

latitudinally by other dissipative parts of the Maxwell stress tensor, thereby keeping it on an equatorial track as shown in Fig. 14.1c even though they cannot be described by a potential. All of this points to constructing a physical model that is radial. Since the radial motion of the nano-particle is driven by thermal fluctuations, U may be extracted from fluctuations in the interfacial separation s of the nano-particle from the microcavity surface using Boltzmann's probability equation. A neat thing about the WGM microcavity is that s fluctuations may be monitored from the resonance frequency shifts of the cavity.

The link between resonance frequency shift $\Delta\omega$ and separation s is through the *Reactive Sensing Principle* (RSP) which states that the shift in the resonant frequency by a perturbing particle is in proportion to the energy with which the particle is polarized by the evanescent field [4]. Since the evanescent intensity drops off exponentially with separation, the ratio of the shift that a particle induces at separation s to that at $s = 0$ is $\Delta\omega(s)/\Delta\omega(0) = e^{-s/L}$, where L is the characteristic evanescent intensity length. This can be written for small perturbations in terms of the free space wavelength; $\Delta\lambda(s)/\Delta\omega(0) = e^{-s/L}$. Consequently, from the measured

shift, one gains information about the separation. This allows a histogram of separations to be built up (Fig. 14.1b). Once normalized the probability to be at a certain separation $P(s)$ allows the overall potential to be determined;

$$\frac{\mathrm{U\,(s)}}{\mathrm{k_B T}} = -\ln\left(\frac{\mathrm{P\,(s)}}{\mathrm{P\,(s_{ref})}}\right) \tag{14.1}$$

where s_{ref} is a reference separation for which $\mathrm{U(s_{ref})} \approx 0$. The gradient potential is attractive and decays exponentially $\mathrm{U_g(s)/k_B T} = -|\mathrm{Ag}|\ \mathrm{e}^{-\mathrm{s/L}}$, so that the electrostatic potential is given by

$$\frac{\mathrm{U_{es}\,(s)}}{\mathrm{k_B T}} = -\ln\left(\frac{\mathrm{P\,(s)}}{\mathrm{P\,(s_{ref})}}\right) + |\ \mathrm{A_g}\ |\ \mathrm{e}^{-\mathrm{s/L}} \tag{14.2}$$

The electrostatic interaction energy between the nanoparticle and the silica surface of the microcavity in its simplest linearized form (*Deybe-Hückel* theory) is described by [14].

$$\mathrm{U_{es}\,(s)} \simeq \frac{\mathrm{q_p \sigma_w \lambda_D}}{\varepsilon_0 \varepsilon_\mathrm{r}\left(1 + \frac{\mathrm{a}}{\lambda_\mathrm{D}}\right)} \mathrm{e}^{-\mathrm{s}/\lambda_\mathrm{D}} \tag{14.3}$$

where λ_D is the Debye length, and ε_r is the relative permittivity of the environment at zero frequency ($\varepsilon_\mathrm{r} = 80.2$ for water at 20 °C). On this basis our expectation is that the U_{es} arrived from our experimental protocol (Eq. 14.2) should fall off exponentially with a characteristic length λ_D.

14.3 Experimental Approach

One can readily see from Eq. 14.3 that once λ_D is determined from experiment for a nanoparticle of known radius a and charge q_p, the microcavity charge density σ_w can be determined. With σ_w in hand, other particles having unknown charge, can have their charge determined. A complete non-linear theory can be introduced for more accurate results (*Gouy–Chapman* theory) [14], as we will discuss later in this paper, however the basic measurement idea is not changed. In what follows we will describe our experimental setup, and display some results that verify the exponential decay in the electrostatic interaction energy U_{es}.

Experiments were carried out using a slightly prolate micro-spheroid of fused silica having an equatorial radius of approximately 40 μm. The micro-spheroid is formed in air by melting the end of an optical fiber with a CO_2 laser, and used directly and within minutes in a microfluidic cell (Fig. 14.2).

The cell is controlled to ±0.001°C, which reduces the wavelength drift to less than 5 fm in the absence of the orbiting particle, but over an equivalent period used in

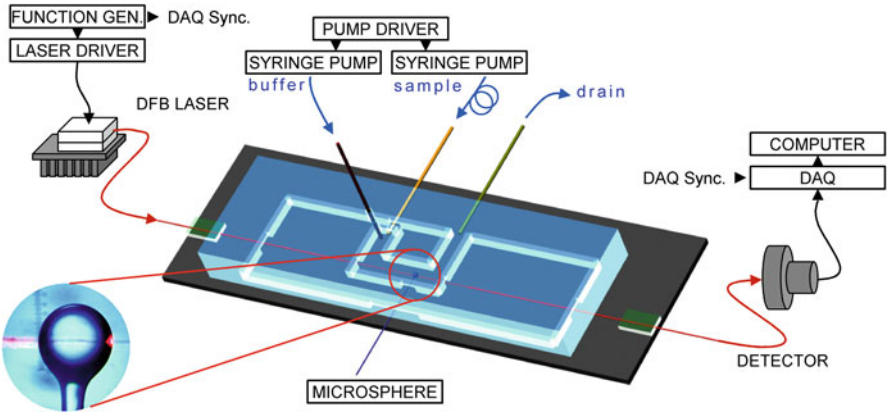

Fig. 14.2 Microfluidic system

the nanoparticle orbiting experiments. By comparison the fluctuations experienced in the presence of the orbiting nanoparticles at their peak were as much as 100× this drift, which rendered the drift relatively unimportant for our experiments.

This microcavity is coupled evanescently to a tapered fiber driven near a wavelength of 1060 nm, and excited into a first order equatorial mode (i.e. m = l, see time lapsed photograph, Fig. 14.1c) by selecting the shortest wavelength resonance within a group having angular momentum near $l = 340$ (Fig. 14.3) [6].

The fluid in the cell contains a dilute aqueous concentration of polystyrene nanoparticles along with 0.5 mm NaCl at a pH of 5.7 [6]. The polystyrene particles develop a negative charge in solution due to anionic sulfonate ($R\text{-}SO^{-}_{3}$) groups on their surface. After a particle is caught in orbit, fluctuations of the WGM resonance frequency are recorded, and processed to produce a separation histogram, as displayed in Fig. 14.1b. The results in Fig. 14.1b were for a nano-particle taken from a sample with a mean radius $< a > = 140$ nm. The microcavity WGM was driven with injected power of 230 μW and had a Q factor 7.2×10^5.

Figure 14.4a shows results arrived at by applying Eq. 14.1 to the histogram in Fig. 14.1b. The interaction energy U is clearly discerned as having generated a radial trap ~5 k_BT deep. The long tail in this potential is due to the optical gradient potential U_g which drops off exponentially with s with a characteristic length $L \sim 190$ nm in agreement with Mie theory. By applying Eq. 14.2 and subtracting the gradient potential from the overall potential we arrive at the electrostatic potential U_{es}, as shown in Fig. 14.4b. Here we see an exponential decay as expected from Eq. 14.3, revealing both the extrapolated electrostatic interaction potential at the surface $U_{es}(0)$, and the Debye length λ_D. Furthermore, examining this equation reveals the means by which it can be used to obtain both the microcavity charge density σ_W and subsequently the charge of the orbiting nanoparticle q_p. All that is needed is to repeat the experiment using a standard nanoparticle of known size a,

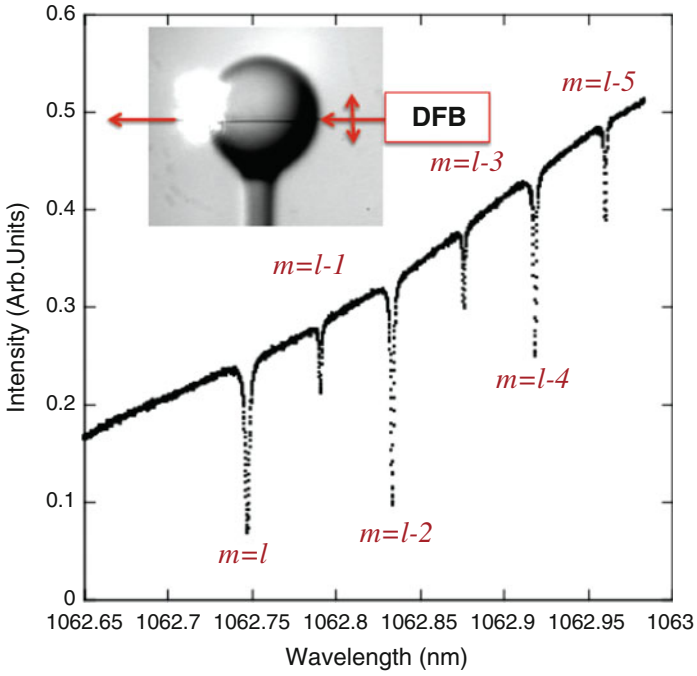

Fig. 14.3 Spectrum of resonance with $l = 340$. Orbit in Fig. 14.1c is induced by tuning laser to $m = l$ mode

and charge q_p. Since the statistical experiment yields $U_{es}(0)$, and λ_D, the addition of a and q_p allows the surface charge density σ_W to be determined,

$$\sigma_w \simeq \frac{\varepsilon_0 \varepsilon_r U_{es}(0)}{q_p \lambda_D} \left(1 + \frac{a}{\lambda_D}\right) \tag{14.4}$$

Next we set about to do this.

The orbiter's charge q_p can be obtained from independent zeta potential measurements [15]. Reproducible measurements were obtained on PS particles having a mean radius $< a > = 178$ nm. At our experimental salt concentration of 1.0 mM NaCl, the mean charge obtained from the zeta potential measurement $<q_{pz}> = -1.88 \times 10^{-15}$ C. A particle from this sample was then forced into carousel motion in order to obtain $U_{es}(0)$ and λ_D: $U_{es}(0)/k_BT = 31.7 \pm 1.6$, $\lambda_D = (8.9 \pm 0.8)$ nm. Given the measured values previously mentioned, Eq. 14.4 gives $\sigma_W = -(1.1 \pm 0.2) \times 10^{-4} C/m^2$. For a series of experiments spaced apart by hours this number remained of similar magnitude even though the charge densities in the literature for the same pH and salt concentration are about one to two orders of magnitude greater [16]. The reason for this disparity stems from the way in which silica microcavities are typically prepared.

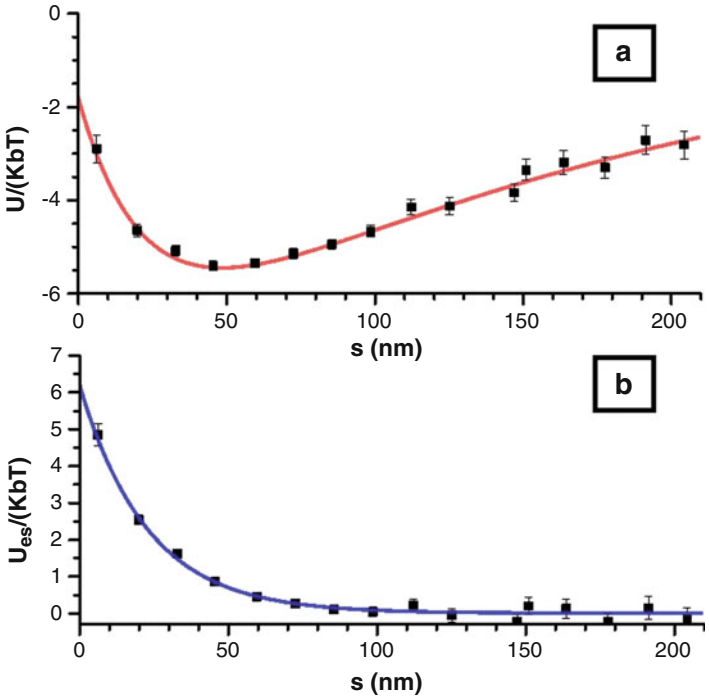

Fig. 14.4 (**a**) Potential energy of interaction extracted from fluctuations of an orbiter 140 nm in radius (Fig. 14.1b) using Eq. 14.1. The error bars are based on assuming Poisson statistics. (**b**) Electrostatic potential found after subtracting the gradient potential ($|A_g| = 8.1$, $L = 190$ nm) from Fig. 14.4a. The electrostatic potential is fit to an exponential decay with $U_{es}(0)/k_BT = 6.2 \pm 0.3$, and $\lambda_D = 21.5 \pm 2.0$ (solid blue curve uses the mean values of these parameters)

In the preparation of silica micro-cavities the temperature is raised above 1600 °C in order to soften the silica, either to form a microsphere, or in the reflow used in toroidal cavities. This eliminates charge sites, which are principally silanol groups, Si-OH. The extreme heat replaces these with siloxane groups, Si-O-Si, having various forms. Whereas silanol groups are readily ionized by de-protonation at a near neutral pH, siloxanes are not ionizable unless they are converted to silanols. Once having cooled this surface to room temperature and submerging the microsphere in water as we do, the conversion process can take weeks [16]. As a test of this hypothesis we introduced microcavities into high temperature steam at 3 atmospheres and 120 °C for 1 h, in an attempt to reconstruct the silanols [17, 18]. As a result when the same microcavity that gave the results in Fig. 14.4 was used as in Fig. 14.1, the repulsive interaction was too great to form a carousel trap for the same conditions. So far as we know our experiment represents the first charge density measurements on a pre-melted silica microcavity. We conclude that pre-melting a silica microcavity leaves the surface with far less charge density in water than silica pretreated and hydroxylated with high temperature steam [17].

The weakly charged microcavity prepared by pre-melting silica can be used for nano-particle charge measurements by inverting Eq. 14.4,

$$q_p \simeq \frac{\varepsilon_0 \varepsilon_r U_{es}(0)}{\sigma_w \lambda_D} \left(1 + \frac{a}{\lambda_D}\right) \tag{14.5}$$

The form of this equation is quite simple in as much as the particle charge is directly proportional to the value of the electrostatic interaction potential at $s = 0$. If we choose now to inject a particle of unknown charge q_x into a solution having the same monovalent NaCl concentration as we used for the 178 nm standard particle, the Debye length will remain unchanged (i.e. $\lambda_D = (8.9 \pm 0.8)$ nm). In addition, we will use the same microcavity within about 10 min of the standard experiment, so that σ_w is constant, consistent with our measurements of charge density, and reports in the literature that the time constant for such change is on the order of weeks [16, 19]. Consequently, the unknown charge

$$q_x \simeq \frac{U_{es,x}(0)}{U_{es,s}} \left[\frac{1 + \frac{a_x}{\lambda_D}}{1 + \frac{a_s}{\lambda_D}}\right] < q_{pz,s} > \tag{14.6}$$

where we have relabeled the standard particle's charge as $<q_{pz,s}> = -1.88 \times 10^{-15}$ C. We next proceed to apply Eq. 14.6.

After clearing the standard particle from solution by a flush of solvent of the same salt concentration, larger particles were injected into the solvent with a mean size of $<a_x> = 228$ nm, but having an unknown charge. One of these particles was forced into a carousel orbit while recording the fluctuations. Using the same fitting procedure as in Fig. 14.4, the electrostatic interaction potential was determined to be $U_{es}(0)/k_BT = 48.0 \pm 2.4$, from which Eq. 14.6 gives its charge to be $-(3.6 \pm 0.3) \times 10^{-15}$ C. Following this evaluation, we made a separate measurement of the zeta potential on the 228 nm particles and obtained a charge $<q_{pz,s}> = -4.0 \times 10^{-15}$ C. The mean for our carousel determined charge in an absolute sense (3.6×10^{-15} C) is about 10% less than arrived at from zeta potential measurements, however the uncertainty within a standard deviation does not bridge this gap.

At this point it is appropriate to return to the possible limitations of applying *Debye-Hückel* theory (D-H) to our experiments. This theory relies on a linearization within the Poisson-Boltzmann equation, which requires that the charge be small enough such that *R,* the ratio of the interaction energy with a monovalent ion just outside the Stern layer to the thermal energy, be less than one. Although this is indeed the case for the microcavity surface, for which the estimated charge density gives $R \sim 0.05$, for our nano-particles the ratio R_p is considerably larger due to their larger charge densities, and thus it is more accurate to use *Gouy-Chapman* (G-C) theory [14] instead. For the nano-particles having a radius of 228 nm, R_p estimated from its measured zeta potential is about 2, causing the charge inferred from *Debye-Huckel* theory to underestimate what the *Gouy-Chapman* theory would yield. We

observe this to be in line with our findings as well, in as much as *Debye-Huckel* theory as applied to our carousel experiment underestimates the charge.

14.4 Nonlinear Approach

In the interest of completeness, we describe the computational approach to using the *Gouy-Chapman theory* for obtaining the particle charge. With the charge density on the cavity small enough to be linearized, we simply need to change q_p in Eq. 14.3 to a non-linear expression [14]. This involves substituting for q_p

$$q_p^* = 4\pi a_p^2 B \tanh\left[\frac{1}{2} sinh^{-1}\left(\frac{2q_p}{B4\pi q_p^2}\right)\right] \tag{14.7}$$

where $B = q_e/(\pi\ \lambda_D\ \lambda_B)$, q_e is the electron charge, and λ_B known as the Bjerrum length, is the distance between electrons in aqueous medium that results in an interaction energy equal to the thermal energy k_BT and $\lambda_B = 0.715$ nm. For our Debye length ($\lambda_D = 8.9$ nm), $B = 7.9 \times 10^{-3}$ C. For the standard parameters associated with the 178 nm experiment (i.e q_p, λ_D, and $U_{es,s}(0)$), and the interaction parameter for the 228 nm particle (i.e the associated $U_{es,x}(0)$) we find the charge of the 228 nm particle to be $-(4.0 \pm 0.5) \times 10^{-15}$ C, for which the mean agrees with the zeta potential measurement.

14.5 Concluding Remarks

We have shown that not only is it possible to determine the charge density of a glass microsphere from the orbiting properties of a nanoparticle of known charge, but also use the measured charge density of the microsphere to estimate the charge of other particles undergoing carousel motion about the same microsphere. Our method is a new experimental approach to Coulometry of single nanoparticles using resonance frequency shift fluctuations of a microcavity. The experimental uncertainties can be reduced by acquiring more counts in a given histogram, and by reducing noise. Laser noise reduction through the use of a reference interferometer should allow for charge measurements on considerably smaller particles (e.g. Small virus, protein, etc.) [20]. Since the nanoparticle does not bind, the method is non-destructive, thereby enabling it to be used to determine the native (isolated) charge of a bio-nanoparticle (e.g. Virus, protein). Its non-binding nature allows the same particle to be passed on for further characterization. It also extends the multitude of sensing measurements that the WGM resonance shifts can accomplish on single nanoparticles (i.e. Size, potential mapping [13], polarizability, charge, and for a specifically adsorbed virus, genotype).

Acknowledgements We doubly thank David Keng for providing the MP3Laser system used in taking the measurements in this paper, and for contributing his time without charge. We also thank Prof. Rasti Levicky at NYU Tandon for valuable discussions.

References

1. Serpengüzel A, Griffel G, Arnold S (1995) Excitation of resonances of microspheres on an optical fiber. Opt Lett 20:654–656
2. Arnold S (2001) Microspheres, photonic atoms and the physics of nothing. Am Sci 89:414–421
3. Sun Y, Fan X (2011) Optical ring resonators for biochemical and chemical sensing. Anal Bioanal Chem 399:205–211
4. Arnold S, Khoshsima M, Teraoka I, Holler S, Vollmer F (2003) Shift of whispering-gallery modes in microspheres by protein adsorption. Opt Lett 28:272–274
5. Vollmer F, Arnold S, Keng D (2008) Single virus detection from the reactive shift of a whispering-gallery mode. Proc Natl Acad Sci 105:20701–20704
6. Keng D, Tan X, Arnold S (2014) Whispering gallery micro-global positioning system for nanoparticle sizing in real time. Appl Phys Lett 105:071105
7. Foreman MR, Keng D, Lopez JR, Arnold S (2017) Whispering gallery mode single nanoparticle detection and sizing: the validity of the dipole approximation. Opt Lett 42:963–966
8. Arnold S, Ramjit R, Keng D, Kolchenko V, Teraoka I (2008) MicroParticle photophysics illuminates viral bio-sensing. Faraday Discuss 137:65–83
9. Chen YL, Jin WL, Xiao YF, Zhang X (2016) Measuring the charge of a single dielectric nanoparticle using a high-Q optical microresonator. Phys Rev Appl 6:044021
10. Ayala V, Herrera AP, Latorre-Esteves M, Torres-Lugo M, Rinaldi C (2013) Effect of surface charge on the colloidal stability and in vitro uptake of carboxymethyl dextran-coated iron oxide nanoparticles. J Nanopart Res 15:1874
11. He C, Hu Y, Yin L, Tang C, Yin C (2010) Effects of particle size and surface charge on cellular uptake and biodistribution of polymeric nanoparticles. Biomaterials 31:3657–3666
12. Lopez JR, Treasurer E, Snyder KM, Keng D, Arnold S (2018) Whispering gallery mode coulometry of the nanoparticle-microcavity interaction in aqueous solution. Appl Phys Lett 112 (in press)
13. Arnold S, Keng D, Shopova SI, Holler S, Zurawsky W, Vollmer F (2009) Whispering gallery mode carousel–a photonic mechanism for enhanced nanoparticle detection in biosensing. Opt Express 17:6230–6238
14. von Grünberg HH, Helden L, Leiderer P, Bechinger C (2001) Measurement of surface charge densities on Brownian particles using total internal reflection microscopy. J Chem Phys 114:10094–10104
15. Strubbe F, Beunis F, Neyts K (2006) Determination of the effective charge of individual colloidal particles. J Colloid Interface Sci 301:302–309
16. Bolt GH (1957) Determination of the charge density of silica sols. J Phys Chem 61:1166–1169
17. Zhuravlev LT (2000) The surface chemistry of amorphous silica. Zhuravlev model. Colloids Surf A Physicochem Eng Asp 173:1–38
18. Zhuravlev LT (1987) Concentration of hydroxyl groups on the surface of amorphous silicas. Langmuir 3:316–318
19. Iler RK (1979) The chemistry of silica. Wiley-Interscience, New York, p 661
20. Lu T, Lee H, Chen T, Herchak S, Kim JH, Fraser SE, Flagan RC, Vahala K (2011) High sensitivity nanoparticle detection using optical microcavities. Proc Natl Acad Sci 108: 5976–5979

Chapter 15
Novel Aspects of the Fabry-Pérot Resonator

Markus Pollnau and Nur Ismail

Abstract We systematically characterize the Fabry-Pérot resonator. We derive the generic Airy distribution of a Fabry-Pérot resonator, which equals the internal resonance enhancement factor, and show that all related Airy distributions are obtained by simple scaling factors. We verify that the sum of the mode profiles of all longitudinal modes generates the Airy distribution. Consequently, the resonator losses are quantified by the linewidths of the underlying Lorentzian lines and not by the measured Airy linewidth. We introduce the Lorentzian finesse which provides the spectral resolution of the Lorentzian lines, whereas the usually considered Airy finesse quantifies the performance of the Fabry-Pérot resonator as a scanning spectrometer.

15.1 Introduction

The Fabry-Pérot resonator which was invented in 1899 [1] has proven very useful as a high-finesse interferometer in uncountable spectroscopic applications. Since 1960, it has also formed the fundamental basis for a large class of open resonators that have enabled laser oscillation. The Fabry-Pérot resonator has been extensively investigated, experimentally as well as theoretically. However, when the losses become high, discrepancies between the theoretical approaches surface, common approximations turn invalid, and even the definitions of typical parameters break down or prove inappropriate.

M. Pollnau (✉)
Department of Electrical and Electronic Engineering, Advanced Technology Institute, University of Surrey, Guildford, UK

Department of Materials and Nano Physics, KTH—Royal Institute of Technology, Electrum 229, Kista, Sweden
e-mail: m.pollnau@surrey.ac.uk

N. Ismail
Department of Materials and Nano Physics, KTH—Royal Institute of Technology, Electrum 229, Kista, Sweden

B. Di Bartolo et al. (eds.), *Quantum Nano-Photonics*, NATO Science for Peace and Security Series B: Physics and Biophysics,
https://doi.org/10.1007/978-94-024-1544-5_15

We analyze the performance and relevant parameters of the Fabry-Pérot resonator, with reference to the book on the Fabry-Pérot resonator by Vaughan [2] and the standard text books by Siegman [3], Svelto [4, 5], and Saleh and Teich [6–8]. We demonstrate that the sum of the mode profiles of all longitudinal modes, which are Lorentzian-shaped in case of frequency-independent losses, is the fundamental spectral function that characterizes the Fabry-Pérot resonator. It physically generates the Airy distribution of the Fabry-Pérot resonator. The resonator losses are quantified by the linewidths of the underlying Lorentzian lines. We define the Lorentzian finesse which provides the resolution of the Lorentzian lines, whereas the usually considered Airy finesse describes the performance of the Fabry-Pérot resonator as a scanning spectrometer.

15.2 Resonator Losses and Outcoupled Light

Throughout this paper, we assume a two-mirror Fabry-Pérot resonator of geometrical length ℓ, homogeneously filled with a medium of refractive index n_r. Both, ℓ and n_r are assumed to vary insignificantly over the frequency range of interest. The round-trip time t_{RT} of light travelling in the resonator with speed $c = c_0/n_r$, where c_0 is the speed of light in vacuum, is given by

$$t_{RT} = \frac{2\ell}{c}. \tag{15.1}$$

Outcoupling losses occur due to non-perfect reflectivity of the two mirrors,

$$\begin{gathered} r_i^2 = R_i = 1 - t_{out,i}^2 = 1 - T_{out,i} = e^{-t_{RT}/\tau_{out,i}} \quad \Longleftrightarrow \\ \frac{1}{\tau_{out,i}} = \frac{-\ln(R_i)}{t_{RT}} = \frac{-\ln(1-T_{out,i})}{t_{RT}}. \end{gathered} \tag{15.2}$$

Here, $r_i(\nu)$ and $R_i(\nu)$ are the electric-field and intensity reflectivities, respectively, $t_{out,i}(\nu)$ and $T_{out,i}(\nu)$ are the electric-field and intensity transmissions, respectively, and $\tau_{out,i}(\nu)$ is the exponential decay time resulting from the outcoupling loss at mirror i. All other losses shall be neglected. The photon-decay time $\tau_c(\nu)$ of the resonator is then given by

$$\frac{1}{\tau_c} = \sum_i \frac{1}{\tau_{out,i}} = \frac{\sum\limits_i \delta_{out,i}}{t_{RT}} = \frac{\sum\limits_i -\ln(R_i)}{t_{RT}}. \tag{15.3}$$

The number $\varphi(t)$ of photons at frequency ν, present inside the resonator at time t, is described via the photon-decay time $\tau_c(\nu)$ by the differential rate equation

$$\frac{d}{dt}\varphi(t) = -R_{decay}(t) = -\frac{1}{\tau_c}\varphi(t). \tag{15.4}$$

$R_{decay}(t)$ is the photon-decay rate per unit time. With a number φ_s of photons present at the starting time $t = 0$, integration delivers

$$\varphi(t) = \varphi_s e^{-t/\tau_c}. \tag{15.5}$$

With $\phi(\nu)$ quantifying the single-pass phase shift between the mirrors, the round-trip phase shift at frequency ν accumulates to

$$2\phi\,(\nu) = 2\pi\,\nu t_{RT} = 2\pi\,\nu\frac{2\ell}{c}. \tag{15.6}$$

We have assumed above that the refractive index n_r of the medium and, thus, the speed of light c are independent of frequency. Consequently, also the round-trip time t_{RT} becomes independent of frequency. Resonances occur at frequencies at which light exhibits constructive interference after one round trip. The difference in phase shift per round trip between adjacent resonance frequencies amounts to 2π, from which the free spectral range $\Delta\nu_{FSR}$ then derives as [2].

$$\frac{d}{d\nu}\,(2\phi) = \frac{d}{d\nu}\,(2\pi\,\nu t_{RT}) = 2\pi\,t_{RT} \quad \Rightarrow \quad \frac{2\pi}{\Delta\nu_{FSR}} = 2\pi\,t_{RT} \quad \Rightarrow \quad \Delta\nu_{FSR} = \frac{1}{t_{RT}}. \tag{15.7}$$

Each resonator mode with its mode index q, where q is an integer number in the interval $[-\infty,\ \ldots,\ -1,\ 0,\ 1,\ \ldots,\ \infty]$, is associated with a resonance frequency ν_q and wavenumber k_q,

$$\nu_q = q\,\Delta\nu_{FSR} = q/t_{RT} \quad \Rightarrow \quad k_q = \frac{2\pi\,q\,\Delta\nu_{FSR}}{c}. \tag{15.8}$$

Two modes with opposite values $\pm q$ and $\pm k$ of modal index and wavenumber, respectively, physically representing opposite propagation directions, occur at the same absolute value $|\nu_q|$ of frequency.

According to Eq. (15.5), light at frequency ν oscillating inside the resonator decays out of the resonator with a time constant of $\tau_c(\nu)$. If the resonator losses are independent of frequency, the photon-decay time $\tau_c(\nu)$ is the same at all frequencies. The decaying electric field at frequency ν_q is represented by a damped harmonic oscillation with an initial amplitude of $E_{q,s}$ and a decay-time constant of $2\tau_c$. In phasor notation, it can be expressed as

$$E_q(t) = \begin{cases} E_{q,s}e^{i2\pi\nu_q t}e^{-t/(2\tau_c)} & t \geq 0 \\ 0 & t < 0 \end{cases}. \tag{15.9}$$

Fourier transformation of the electric field in time provides the electric field per unit frequency interval,

$$\begin{aligned}\tilde{E}_q(\nu) &= \int_{-\infty}^{+\infty} E_q(t) e^{-i2\pi\nu t} dt = E_{q,s} \int_{0}^{+\infty} e^{-[1/(2\tau_c)+i2\pi(\nu-\nu_q)]t} dt \\ &= E_{q,s} \frac{1}{(2\tau_c)^{-1}+i2\pi(\nu-\nu_q)}.\end{aligned} \tag{15.10}$$

Each mode has a normalized spectral line shape per unit frequency interval given by [9].

$$\begin{aligned}\tilde{\gamma}_q(\nu) &= \frac{1}{\tau_c}\left|\frac{\tilde{E}_q(\nu)}{E_{q,s}}\right|^2 \\ &= \frac{1}{\tau_c}\left|\frac{1}{(2\tau_c)^{-1}+i2\pi(\nu-\nu_q)}\right|^2 = \frac{1}{\tau_c}\frac{1}{(2\tau_c)^{-2}+4\pi^2(\nu-\nu_q)^2} \\ &= \frac{1}{\pi}\frac{1/(4\pi\tau_c)}{1/(4\pi\tau_c)^2+(\nu-\nu_q)^2} \quad \text{with} \quad \int \tilde{\gamma}_q(\nu)\, d\nu = 1,\end{aligned} \tag{15.11}$$

in units of (1/Hz). Introducing the full-width-at-half-maximum (FWHM) linewidth $\Delta\nu_c$ of the Lorentzian spectral line shape, we obtain

$$\Delta\nu_c = \frac{1}{2\pi\tau_c} \;\Rightarrow\; \tilde{\gamma}_q(\nu) = \frac{1}{\pi}\frac{\Delta\nu_c/2}{(\Delta\nu_c/2)^2+(\nu-\nu_q)^2} \quad \text{with} \quad \int \tilde{\gamma}_q(\nu)\, d\nu = 1. \tag{15.12}$$

Calibrated to a peak height of unity, we obtain the Lorentzian lines, in units of (1):

$$\gamma_{q,L}(\nu) = \frac{\pi}{2}\Delta\nu_c\tilde{\gamma}_q(\nu) = \frac{(\Delta\nu_c)^2}{(\Delta\nu_c)^2+4(\nu-\nu_q)^2} \quad \text{with} \quad \gamma_{q,L}(\nu_q) = 1. \tag{15.13}$$

When repeating the above Fourier transformation for all the modes with mode index q in the resonator, one obtains the full mode spectrum of the resonator.

15.3 Airy Distributions of the Fabry–Pérot Resonator

In this Section, we derive the generic Airy distribution, show that it represents the spectral dependence of the internal resonant enhancement factor, and demonstrate that all other Airy distributions describing the circulating, back-circulating, transmitted, and back-transmitted intensity (Fig. 15.1) only include simple scaling factors, depending on whether the light incident upon mirror 1 or its fraction

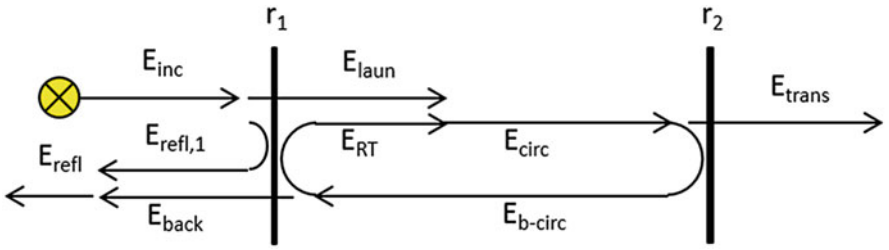

Fig. 15.1 Fabry-Pérot resonator with electric-field mirror reflectivities r_1 and r_2. Indicated are the characteristic electric fields produced by an electric field E_{inc} incident upon mirror 1: $E_{refl,1}$ initially reflected at mirror 1, E_{laun} launched through mirror 1, E_{circ} and $E_{b\text{-}circ}$ circulating inside the resonator in forward and backward propagation direction, respectively, E_{RT} propagating inside the resonator after one round trip, E_{trans} transmitted through mirror 2, E_{back} transmitted through mirror 1, and the total field E_{refl} propagating backward. Interference occurs at the left- and right-hand sides of mirror 1 between $E_{refl,1}$ and E_{back}, resulting in E_{refl}, and between E_{laun} and E_{RT}, resulting in E_{circ}, respectively. (Figure taken from Ref. [10])

launched into the resonator is considered as a reference. We verify that the physical origin of the Airy distribution is the sum of mode profiles of the longitudinal resonator modes.

15.3.1 Generic Airy Distribution: The Internal Resonance Enhancement Factor

The response of the Fabry-Pérot resonator is most easily derived by use of the circulating-field approach [3], as displayed in Fig. 15.1. This approach assumes a steady state and derives the Airy distributions via the electric field E_{circ} circulating inside the resonator. In fact, E_{circ} is the field propagating in the forward direction from mirror 1 to mirror 2 after interference between the field E_{RT} that is circulating after one round trip, i.e., after having suffered outcoupling losses at both mirrors, and the field E_{laun} launched through the first mirror.

With the phase shift 2ϕ of Eq. (15.6) accumulated in one round trip, the field E_{circ} can be related to the field E_{laun} that is launched into the resonator in the situation of Fig. 15.1a by

$$E_{circ} = E_{laun} + E_{RT} = E_{laun} + r_1 r_2 e^{-i2\phi} E_{circ} \quad \Rightarrow \quad \frac{E_{circ}}{E_{laun}} = \frac{1}{1 - r_1 r_2 e^{-i2\phi}}. \tag{15.14}$$

Exploiting the identities

$$\left|e^{-i\phi}\right|^2 = |\cos(\phi) - i\sin(\phi)|^2 = \cos^2(\phi) + \sin^2(\phi) = 1$$
$$\cos(2\phi) = 1 - 2\sin^2(\phi) \tag{15.15}$$

yields

$$\begin{aligned}\left|1-r_1r_2e^{-i2\phi}\right|^2 &= |1-r_1r_2\cos(2\phi)+ir_1r_2\sin(2\phi)|^2\\ &= [1-r_1r_2\cos(2\phi)]^2+r_1^2r_2^2\sin^2(2\phi)\\ = 1+R_1R_2-2\sqrt{R_1R_2}\cos(2\phi) &= \left(1-\sqrt{R_1R_2}\right)^2+4\sqrt{R_1R_2}\sin^2(\phi)\,,\end{aligned} \tag{15.16}$$

$$\begin{aligned}\left|r_1-r_2e^{-i2\phi}\right|^2 &= |r_1-r_2\cos(2\phi)+ir_2\sin(2\phi)|^2\\ &= [r_1-r_2\cos(2\phi)]^2+[r_2\sin(2\phi)]^2\\ &= R_1+R_2-2\sqrt{R_1R_2}\cos(2\phi)\\ &= R_1+R_2-2\sqrt{R_1R_2}\left[1-2\sin^2(\phi)\right]\\ &= \left(\sqrt{R_1}-\sqrt{R_2}\right)^2+4\sqrt{R_1R_2}\sin^2(\phi)\,.\end{aligned} \tag{15.17}$$

The generic Airy distribution, which considers solely the physical processes exhibited by light inside the resonator, then derives as the intensity circulating in the resonator relative to the intensity launched, which by use of Eqs. (15.15) and (15.16) yields

$$\begin{aligned}A_{circ} &= \frac{I_{circ}}{I_{laun}}=\frac{|E_{circ}|^2}{|E_{laun}|^2}=\frac{1}{\left|1-r_1r_2e^{-i2\phi}\right|^2}\\ &= \frac{1}{\left(1-\sqrt{R_1R_2}\right)^2+4\sqrt{R_1R_2}\sin^2(\phi)}.\end{aligned} \tag{15.18}$$

Physically, A_{circ} represents the spectrally dependent internal resonance enhancement which the resonator provides to the light launched into it. It is displayed for different mirror reflectivities in Fig. 15.2. At the resonance frequencies ν_q, where $\sin(\phi)$ equals zero, the internal resonance enhancement factor is

$$A_{circ}\left(\nu_q\right)=\frac{1}{\left(1-\sqrt{R_1R_2}\right)^2}. \tag{15.19}$$

15.3.2 Other Airy Distributions

Once generic Airy distribution of Eq. (15.18), is established, all other Airy distributions, i.e., the observed light intensities relative to the launched or initial intensity from the light source (Fig. 15.1) can then be straight-forwardly deduced by simple scaling factors. Since the intensity launched into the resonator equals the transmitted fraction of the intensity incident upon mirror 1,

$$I_{laun}=(1-R_1)\,I_{inc}, \tag{15.20}$$

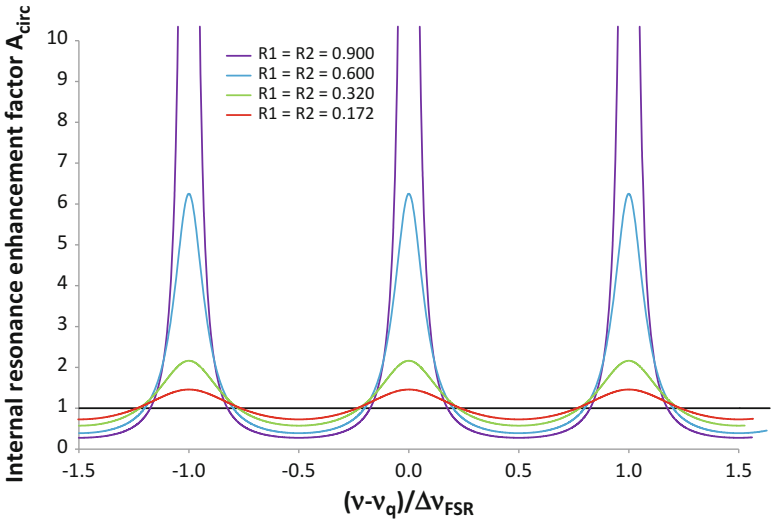

Fig. 15.2 Generic Airy distribution A_{circ}, equaling the spectrally dependent internal resonance enhancement which the resonator provides to light that is launched into it. For the curve with $R_1 = R_2 = 0.9$, the peak value is at $A_{circ}(\nu_q) = 100$, outside the scale of the ordinate. (Figure taken from Ref. [10])

and the intensities transmitted through mirror 2, reflected at mirror 2, and transmitted through mirror 1 are the transmitted and reflected/transmitted fractions of the intensity circulating inside the resonator,

$$I_{trans} = (1 - R_2)\, I_{circ},\, I_{b-circ} = R_2 I_{circ},\, I_{back} = (1 - R_1)\, I_{b-circ} \tag{15.21}$$

respectively, one obtains the following Airy distributions:

$$A_{b\text{-}circ} = \frac{I_{b\text{-}circ}}{I_{laun}} = R_2 A_{circ}, \tag{15.22}$$

$$A_{trans} = \frac{I_{trans}}{I_{laun}} = (1 - R_2)\, A_{circ}, \tag{15.23}$$

$$A_{back} = \frac{I_{back}}{I_{laun}} = (1 - R_1)\, R_2 A_{circ}, \tag{15.24}$$

$$A_{emit} = A_{trans} + A_{back} = \frac{I_{trans} + I_{back}}{I_{laun}} = (1 - R_1 R_2)\, A_{circ}, \tag{15.25}$$

$$A'_{circ} = \frac{I_{circ}}{I_{inc}} = (1 - R_1)\, A_{circ}, \tag{15.26}$$

$$A'_{b\text{-}circ} = \frac{I_{b\text{-}circ}}{I_{inc}} = (1 - R_1)\, R_2 A_{circ}, \tag{15.27}$$

$$A'_{trans} = \frac{I_{trans}}{I_{inc}} = (1 - R_1)\,(1 - R_2)\, A_{circ}, \tag{15.28}$$

$$A'_{back} = \frac{I_{back}}{I_{inc}} = (1 - R_1)^2 R_2 A_{circ}, \tag{15.29}$$

$$\begin{aligned} A'_{emit} &= A'_{trans} + A'_{back} = \tfrac{I_{trans}+I_{back}}{I_{inc}} \\ &= (1 - R_1)\,(1 - R_1 R_2)\, A_{circ}. \end{aligned} \tag{15.30}$$

The index "emit" denotes Airy distributions that consider the sum of intensities emitted on both sides of the resonator. The prime denotes Airy distributions with respect to the incident intensity I_{inc}.

The back-transmitted intensity I_{back} cannot be measured, because also the initially back-reflected light adds to the backward-propagating signal. The measurable case of the intensity resulting from the interference of both backward-propagating electric fields is derived as follows. The back-transmitted electric field is

$$E_{back} = it_1 r_2 E_{circ} e^{-i2\phi} \quad \Rightarrow \quad \frac{E_{back}}{E_{inc}} = \frac{-t_1^2 r_2 e^{-i2\phi}}{1 - r_1 r_2 e^{-i2\phi}}. \tag{15.31}$$

Including the initially back-reflected electric field, $E_{refl,1} = r_1 E_{inc}$, the total electric field propagating backward from mirror 1 is

$$\frac{E_{refl}}{E_{inc}} = \frac{E_{refl,1} + E_{back}}{E_{inc}} = r_1 + \frac{-t_1^2 r_2 e^{-i2\phi}}{1 - r_1 r_2 e^{-i2\phi}} = \frac{r_1 - r_2 e^{-i2\phi}}{1 - r_1 r_2 e^{-i2\phi}}. \tag{15.32}$$

Exploiting Eqs. (15.15, 15.16, and 15.17), the total relative intensity propagating backward from mirror 1 amounts to

$$\begin{aligned} A'_{refl} &= \tfrac{I_{refl}}{I_{inc}} = \tfrac{|E_{refl}|^2}{|E_{inc}|^2} = \tfrac{|r_1 - r_2 e^{-i2\phi}|^2}{|1 - r_1 r_2 e^{-i2\phi}|^2} = \tfrac{(\sqrt{R_1} - \sqrt{R_2})^2 + 4\sqrt{R_1 R_2}\sin^2(\phi)}{(1 - \sqrt{R_1 R_2})^2 + 4\sqrt{R_1 R_2}\sin^2(\phi)} \\ \Rightarrow \quad A'_{trans} + A'_{refl} &= \tfrac{I_{trans}+I_{refl}}{I_{inc}} = 1, \end{aligned} \tag{15.33}$$

as expected for a resonator that exhibits only outcoupling losses. At the resonance frequencies, the back-emitted electric field E_{back} destructively interferes with the electric field $E_{refl,1}$ initially back-reflected.

A'_{circ} of Eq. (15.26) represents the external resonance enhancement factor with respect to I_{inc}. The external resonance enhancement factor at the resonance frequencies is

$$A'_{circ}\left(\nu_q\right) = \frac{(1-R_1)}{\left(1-\sqrt{R_1 R_2}\right)^2} = (1-R_1)\, A_{circ}\left(\nu_q\right). \tag{15.34}$$

In experimental situations, often light is transmitted through a Fabry-Pérot resonator in order to characterize the resonator or to use it as a scanning interferometer (see later in Sect. 15.4). Therefore, an often applied Airy distribution is A'_{trans} of Eq. (15.28). It describes the fraction I_{trans} of the intensity I_{inc} of a light source incident upon mirror 1 that is transmitted through mirror 2, see Fig. 15.1. A'_{trans} is displayed in Fig. 15.3 (solid lines) for different values of the reflectivities $R_1 = R_2$. Its peak value at the resonance frequencies ν_q is

$$A'_{trans}\left(\nu_q\right) = \frac{(1-R_1)\,(1-R_2)}{\left(1-\sqrt{R_1 R_2}\right)^2} \overset{R_1=R_2}{=} 1. \tag{15.35}$$

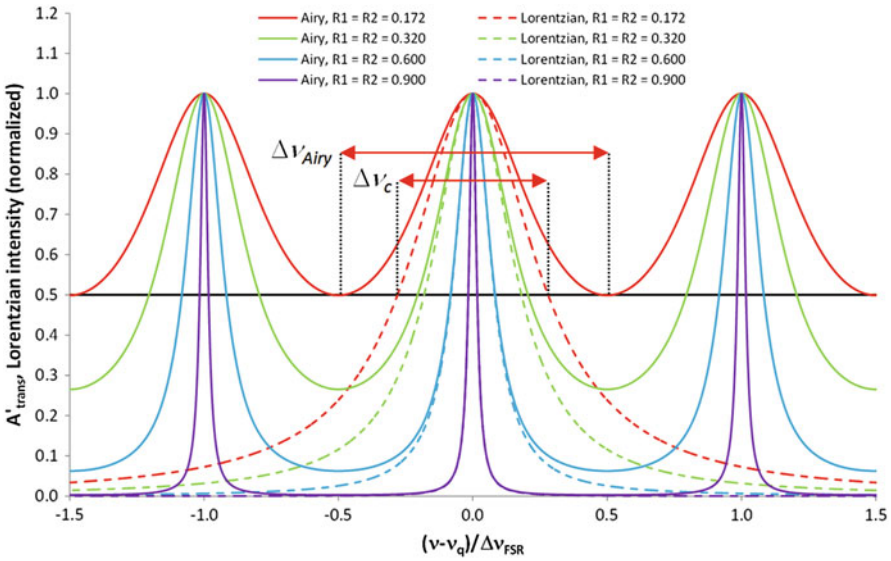

Fig. 15.3 Airy distribution A'_{trans} (solid lines), corresponding to light transmitted through a Fabry-Pérot resonator, calculated from Eq. (15.28) for different values of the reflectivities $R_1 = R_2$, and comparison with a single Lorentzian line (dashed lines) calculated from Eq. (15.13) for the same $R_1 = R_2$. At half maximum (black line), with decreasing reflectivities the FWHM linewidth $\Delta\nu_{Airy}$ of the Airy distribution broadens compared to the FWHM linewidth $\Delta\nu_c$ of its corresponding Lorentzian line: $R_1 = R_2 = 0.9, 0.6, 0.32, 0.172$ results in $\Delta\nu_{Airy}/\Delta\nu_c = 1.001, 1.022, 1.132, 1.717$, respectively. (Figure taken from Ref. [10])

15.3.3 Airy Distribution As a Sum of Mode Profiles

In Fig. 15.3 one observes that, at high reflectivity, there is almost perfect agreement between the spectral shape of the Airy distribution (solid purple line) and its underlying Lorentzian lines (dashed purple line), i.e., the former is rather well represented by the latter. This fact has prompted Saleh and Teich [6] to propose that in this case the Airy linewidth $\Delta\nu_{Airy}$ of a Fabry-Pérot resonator is similar to the linewidth $\Delta\nu_c = 1/(2\pi\tau_c)$ of its underlying Lorentzian lines, both defined as FWHM (black line). However, as is generally well known, with decreasing reflectivity the linewidth of the Airy distribution (solid lines) broadens faster than that of the underlying Lorentzian lines (dashed lines).

Svelto [5] attributes this discrepancy to Eq. (15.5) being only an approximation, thereby implicating that also Eq. (15.11) is only an approximation, such that the Airy linewidth $\Delta\nu_{Airy}$ of a Fabry-Pérot resonator can only at high reflectivity be approximated by the linewidth $\Delta\nu_c$ of its underlying Lorentzian lines. We will demonstrate that the discrepancy has a different reason.

According to Koppelmann [11], Bayer-Helms [12] "showed that the Airy distribution can be represented exactly" by the sum of Lorentzian spectral line shapes times a calibration factor. Firstly, while being literally correct, this statement is physically misleading, secondly, the calibration factor used in [11] remains unexplained, thirdly, the equivalence is shown only for equal reflectivities, $R_1 = R_2$, and finally, the equivalence is not investigated for non-Lorentzian spectral line shapes.

Here we verify that the Airy distribution is nothing else but the sum of the mode profiles of the longitudinal resonator modes, thereby revealing the physical origin of the Airy distribution. Our approach starts from the electric field E_{circ} circulating inside the resonator, considers the exponential decay in time of this field through both mirrors of the resonator, see Fig. 15.1, Fourier transforms it to frequency space according to Eq. (15.10) to obtain the normalized spectral line shapes $\tilde{\gamma}_q(\nu)$ of Eq. (15.11), divides it by the round-trip time t_{RT} to account for how the total circulating electric-field intensity is longitudinally distributed in the resonator and coupled out per unit time, resulting in the emitted mode profiles,

$$\gamma_{q,emit}(\nu) = \frac{1}{t_{RT}}\tilde{\gamma}_q(\nu), \tag{15.36}$$

in units of (1), and then sums over the emitted mode profiles of all longitudinal modes at positive, zero, and negative frequencies. Consequently, the sum of emitted mode profiles describes an experiment that must result in the Airy distribution A_{emit} of Eq. (15.25). Exploiting the derivation given in Appendix C of [10], the sum of emitted mode profiles of Eq. (15.36) yields

$$\sum_{q=-\infty}^{\infty}\gamma_{q,emit}(\nu) = \frac{1-R_1R_2}{\left(1-\sqrt{R_1R_2}\right)^2 + 4\sqrt{R_1R_2}\sin^2(\phi)} = A_{emit}, \tag{15.37}$$

which is indeed equal to Eq. (15.25), with Eq. (15.18) inserted. Each spectral line shape $\tilde{\gamma}_q(\nu)$ of Eq. (15.11) and mode profile $\gamma_{q,\,emit}(\nu)$ of Eq. (15.36) is extended over the infinite frequency range, consequently light at a specific frequency ν inside the resonator excites all longitudinal modes of the resonator. However, the contributions from different longitudinal modes to the light at frequency ν do not interfere with each other, because all optical modes are orthogonal with each other. For this reason, the sum in Eq. (15.37) is over the intensity mode profiles $\gamma_{q,\,emit}(\nu)$ rather than over the electric fields. Because of resonant enhancement of the launched light the peak value of A_{emit} at the resonance frequencies ν_q,

$$A_{emit}\left(\nu_q\right) = \frac{1 - R_1 R_2}{\left(1 - \sqrt{R_1 R_2}\right)^2} = \frac{1 + \sqrt{R_1 R_2}}{1 - \sqrt{R_1 R_2}} > 1, \tag{15.38}$$

becomes larger than unity. Nevertheless, because of Eqs. (15.20) and (15.33) the energy of the system is conserved.

The observation that with decreasing R_1 and R_2 the linewidth of the resulting Airy distribution in Fig. 15.3 is increasingly broader than the linewidth of the underlying Lorentzian lines simply arises from the fact that one sums up mode profiles (with the same linewidth as the Lorentzian lines) that resonate at different frequencies. It does not constitute a discrepancy, as has often been proposed.

The derivation shown here demonstrates that—from a physical point of view—the spectral line shapes and mode profiles are the fundamental spectral functions that characterize the Fabry-Pérot resonator and their sum quantifies its spectral response. As we will see in Sect. 15.4, this fundamental understanding has direct consequences for the definitions of linewidth and finesse.

The same simple scaling factors of Eqs. (15.20) and (15.21) that provide the relations between the individual Airy distributions, see Eqs. (15.18) and (15.22, 15.23, 15.24, 15.25, 15.26, 15.27, 15.28, 15.29, 15.30), also provide the relations among $\gamma_{q,\,emit}(\nu)$ and the other mode profiles:

$$\begin{aligned}
\gamma_{q,circ} &= \tfrac{1}{R_2}\gamma_{q,b\text{-}circ} = \tfrac{1}{1-R_2}\gamma_{q,trans} = \tfrac{1}{1-R_1}\gamma_{q,back} = \tfrac{1}{1-R_1R_2}\gamma_{q,emit} \\
\gamma'_{q,circ} &= \tfrac{1}{R_2}\gamma'_{q,b\text{-}circ} = \tfrac{1}{1-R_2}\gamma'_{q,trans} = \tfrac{1}{1-R_1}\gamma'_{q,back} = \tfrac{1}{1-R_1R_2}\gamma'_{q,emit} \\
&= (1 - R_1)\,\gamma_{q,circ}.
\end{aligned} \tag{15.39}$$

The various mode profiles $\gamma_q(\nu)$ and $\gamma'_q(\nu)$ are calibrated with respect to the launched and the incident intensity, respectively, and the sum over one of these mode profiles at all resonance frequencies generates the corresponding Airy distribution.

15.4 Lorentzian Linewidth and Finesse Versus Airy Linewidth and Finesse

A commonly accepted definition of spectral resolution the Taylor criterion [13]. It proposes that two spectral lines can be resolved if the individual lines cross at half intensity. In the case of two identical, symmetric spectral lines their peaks would then be separated by their FWHM. The Taylor criterion is utilized in the following.

15.4.1 Characterizing the Fabry–Pérot Resonator: Lorentzian Linewidth and Finesse

When launching light into the Fabry-Pérot resonator in a non-scanning experiment, i.e., at fixed resonator length (and fixed angle of incidence), the Fabry-Pérot resonator becomes the object of investigation. The spectral line shapes, Lorentzian lines, and mode profiles are the fundamental functions. By measuring the sum of mode profiles, the Airy distribution, one can derive the total loss of the Fabry-Pérot resonator via recalculating the Lorentzian linewidth $\Delta\nu_c$ of Eq. (15.12), displayed (blue line) relative to the free spectral range in Fig. 15.4a, c.

The underlying Lorentzian lines can be resolved as long as the Taylor criterion is obeyed (Fig. 15.5). Consequently, one can define a parameter which we call the Lorentzian finesse of a Fabry-Pérot resonator:

$$F_c := \frac{\Delta\nu_{FSR}}{\Delta\nu_c} = \frac{2\pi}{-\ln(R_1 R_2)}. \tag{15.40}$$

It is displayed as the blue line in Fig. 15.4b, d. The Lorentzian finesse F_c has a fundamental physical meaning: it describes how well the Lorentzian lines underlying the Airy distribution can be resolved when measuring the Airy distribution. A Fabry-Pérot resonator generating single-longitudinal-mode laser light is characterized by its Lorentzian linewidth and finesse.

Since $\Delta\nu_c$ exists for any mirror reflectivity, the definition of the Lorentzian finesse does not break down at a critical value. However, at the point where

$$\Delta\nu_c = \Delta\nu_{FSR} \quad \Rightarrow \quad R_1 R_2 = e^{-2\pi} \approx 0.001867, \tag{15.41}$$

equivalent to $F_c = 1$, the Taylor criterion for the spectral resolution of a single Airy distribution is reached. For equal mirror reflectivities, this point occurs when $R_1 = R_2 \approx 4.32\%$. Therefore, the linewidth of the Lorentzian lines underlying the Airy distribution of a Fabry-Pérot resonator can be resolved by measuring the Airy distribution, hence its resonator losses can be spectroscopically determined, until this point. Obviously, the Lorentzian finesse according to the definition of

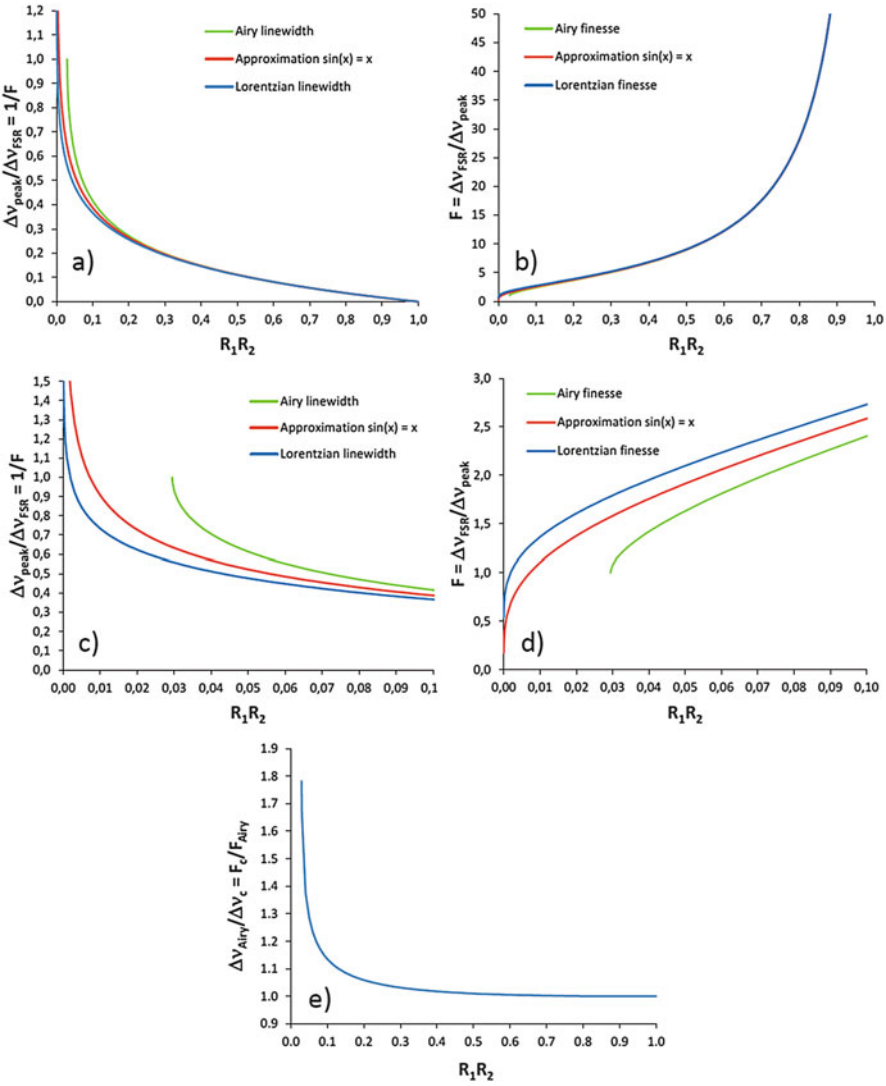

Fig. 15.4 (**a**) Relative Lorentzian linewidth $\Delta\nu_c/\Delta\nu_{FSR}$, with $\Delta\nu_c$ from Eq. (15.12) (blue curve), relative Airy linewidth $\Delta\nu_{Airy}/\Delta\nu_{FSR}$, with $\Delta\nu_{Airy}$ from Eq. (15.43) (green curve), and its approximation of Eq. (15.46) (red curve), and (**b**) Lorentzian finesse F_c of Eq. (15.40) (blue curve), Airy finesse F_{Airy} of Eq. (15.45) (green curve), and its approximation of Eq. (15.47) (red curve) as a function of reflectivity value R_1R_2. (**c** and **d**) Zoom into the low-reflectivity region. The exact solutions of the Airy linewidth and finesse (green lines) correctly break down at $\Delta\nu_{Airy} = \Delta\nu_{FSR}$, equivalent to $F_{Airy} = 1$, whereas their approximations (red lines) incorrectly do not break down. (**e**) Ratio between the Airy linewidth $\Delta\nu_{Airy}$ of Eq. (15.43) and the Lorentzian linewidth $\Delta\nu_c$ of Eq. (15.12), equaling the ratio between the Lorentzian finesse F_c of Eq. (15.40) and the Airy finesse F_{Airy} of Eq. (15.45), as a function of reflectivity value R_1R_2. (Figure taken from Ref. [10])

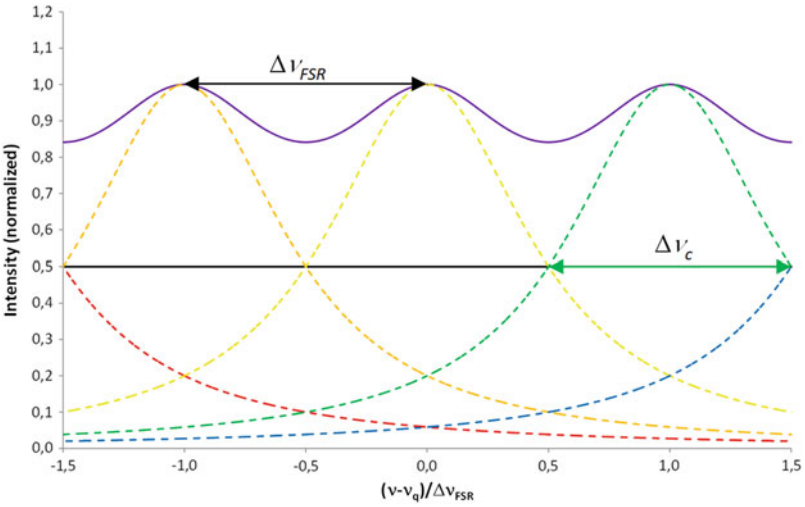

Fig. 15.5 Illustration of the physical meaning of the Lorentzian finesse F_c of a Fabry-Pérot resonator. Displayed is the situation for $R_1 = R_2 \approx 4.32\%$, at which $\Delta\nu_c = \Delta\nu_{FSR}$ and $F_c = 1$, i.e., two adjacent Lorentzian lines (dashed colored lines, only 5 lines are shown for clarity) cross at half maximum (solid black line) and the Taylor criterion for spectrally resolving two peaks in the resulting Airy distribution (solid purple line) is reached. (Figure taken from Ref. [10])

Eq. (15.40) plays an essential role in the characterization of low-reflectivity or otherwise high-loss Fabry-Pérot resonators.

15.4.2 Scanning the Fabry-Pérot Resonator: Airy Linewidth and Finesse

A different situation occurs when the Fabry-Pérot resonator is used as a scanning interferometer, i.e., at varying resonator length (or angle of incidence), to spectroscopically distinguish spectral lines at different frequencies within one free spectral range. In this case several Airy distributions, each one created by an individual spectral line, must be resolved. Therefore, now the Airy distribution becomes the underlying fundamental function and the measurement delivers a sum of Airy distributions. The parameters that properly quantify this situation are the Airy linewidth $\Delta\nu_{Airy}$ and the Airy finesse F_{Airy}.

On either side of the peak of Eq. (15.35) located at ν_q, the transmitted intensity decreases to $A'_{trans}\left(\nu_q\right)/2$ when the phase shift ϕ changes by the amount $\Delta\phi$ and, accordingly, $\sin^2(\phi)$ changes from 0, such that in the denominator of A_{circ} of Eq. (15.18)

$$4\sqrt{R_1R_2}\sin^2(\Delta\phi) = \left(1-\sqrt{R_1R_2}\right)^2 \quad \Rightarrow \quad \Delta\phi = \arcsin\left(\frac{1-\sqrt{R_1R_2}}{2\sqrt[4]{R_1R_2}}\right). \tag{15.42}$$

Exploiting Eqs. (15.6) and (15.7) to calculate $\phi = \pi\nu/\Delta\nu_{FSR}$, resulting in $\Delta\phi = \pi(\Delta\nu_{Airy}/2)/\Delta\nu_{FSR}$, then provides the FWHM linewidth $\Delta\nu_{Airy}$ of the Airy distribution [3],

$$\Delta\nu_{Airy} = \Delta\nu_{FSR}\frac{2}{\pi}\arcsin\left(\frac{1-\sqrt{R_1R_2}}{2\sqrt[4]{R_1R_2}}\right). \tag{15.43}$$

The Airy linewidth $\Delta\nu_{Airy}$ is displayed as the green curve in Fig. 15.4a, c in direct comparison with the Lorentzian linewidth $\Delta\nu_c$. The ratio between $\Delta\nu_{Airy}$ of Eq. (15.43) and $\Delta\nu_c$ of Eq. (15.12) is displayed in Fig. 15.4e.

The concept of defining the linewidth of the Airy peaks as FWHM breaks down at $\Delta\nu_{Airy} = \Delta\nu_{FSR}$ (solid red line in Fig. 15.3), because at this point the Airy linewidth instantaneously jumps to an infinite value. For lower reflectivity values R_1R_2, the FWHM linewidth of the Airy peaks is undefined and other definitions or concepts would have to be utilized to describe the situation. The limiting case occurs at

$$\Delta\nu_{Airy} = \Delta\nu_{FSR} \quad \Rightarrow \quad \frac{1-\sqrt{R_1R_2}}{2\sqrt[4]{R_1R_2}} = 1 \quad \Rightarrow \quad R_1R_2 = 17-12\sqrt{2} \approx 0.02944. \tag{15.44}$$

For equal mirror reflectivities, this point is reached when $R_1 = R_2 \approx 17.2\%$ (solid red line in Fig. 15.3).

The finesse of the Airy distribution of a Fabry-Pérot resonator, which is displayed as the green curve in Fig. 15.4b, d in direct comparison with the Lorentzian finesse F_c, is properly defined as

$$F_{Airy} \overset{!}{:=} \frac{\Delta\nu_{FSR}}{\Delta\nu_{Airy}} = \frac{\pi}{2}\left[\arcsin\left(\frac{1-\sqrt{R_1R_2}}{2\sqrt[4]{R_1R_2}}\right)\right]^{-1}. \tag{15.45}$$

When scanning the length of the Fabry-Pérot resonator (or alternatively the angle of incident light), the Airy finesse lucidly quantifies the maximum number of Airy distributions created by light at individual frequencies ν_m within the free spectral range of the Fabry-Pérot resonator, whose adjacent peaks can be unambiguously distinguished spectroscopically, i.e., they do not overlap at their FWHM (Fig. 15.6). Consequently, this definition of the Airy finesse is consistent with the Taylor criterion of the resolution of a spectrometer and is, therefore, denoted by an exclamation mark in Eq. (15.45). Since the concept of the FWHM linewidth breaks

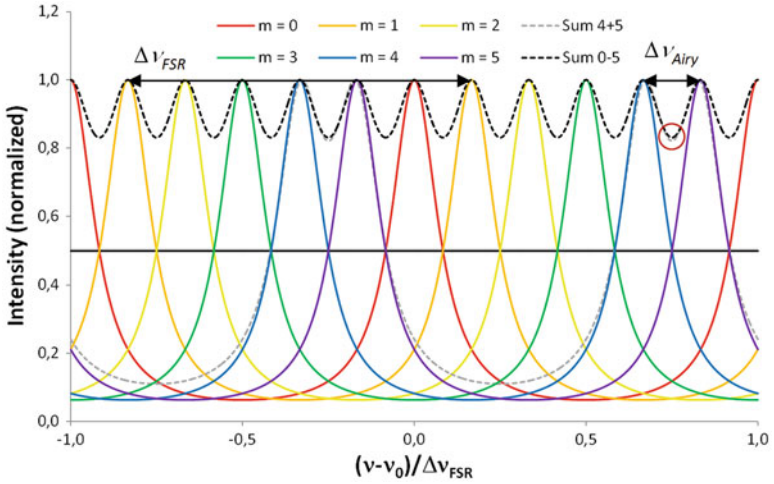

Fig. 15.6 Illustration of the physical meaning of the Airy finesse F_{Airy} of a Fabry-Pérot resonator. When scanning the Fabry-Pérot length (or alternatively the angle of incident light), Airy distributions (solid lines) are created by signals at individual frequencies. If the signals occur at frequencies $\nu_m = \nu_q + m\Delta\nu_{Airy}$, where m is an integer starting at q, the Airy distributions at adjacent frequencies are separated from each other by the linewidth $\Delta\nu_{Airy}$, thereby fulfilling the Taylor criterion for the spectroscopic resolution of two adjacent peaks. The maximum number of signals that can be resolved is F_{Airy}. Since in this specific example the reflectivities $R_1 = R_2 = 0.59928$ have been chosen such that $F_{Airy} = 6$ is an integer, the signal for $m = F_{Airy}$ at the frequency $\nu_q + F_{Airy}\Delta\nu_{Airy} = \nu_q + \Delta\nu_{FSR}$ coincides with the signal for $m = q$ at ν_q. In this example, a maximum of $F_{Airy} = 6$ peaks can be resolved when applying the Taylor criterion. However, the sum of two adjacent "resolvable" peaks (dashed gray line) exhibits a deeper dip between the adjacent peaks to be resolved, i.e., a better resolution, than the sum of all "resolvable" peaks (dashed black line), see the difference highlighted in the red circle. (Figure taken from Ref. [10])

down at $\Delta\nu_{Airy} = \Delta\nu_{FSR}$, consequently the Airy finesse is defined only until $F_{Airy} = 1$, see Fig. 15.4d, because the arcsin function in Eq. (15.45) cannot produce values above $\pi/2$.

Generally, one can argue that the Taylor criterion leaves some ambiguity to the definition of the limit of spectral resolution, because it does not state whether it requires the absence or allows for the presence of additional resolvable spectral lines. In the example of Fig. 15.6, the sum of two adjacent "resolvable" Airy distributions (dashed gray line) is better resolvable than the sum of all "resolvable" Airy distributions (dashed black line), because in the latter case additional Airy distributions contribute, see the dashed lines within the red circle in Fig. 15.6. If either of the two options defines the limit of spectral resolution, the other cannot.

15.4.3 Questionable Approximations and Definitions

Often the unnecessary approximation $\sin(\phi) \approx \phi$ is made when deriving from A'_{trans} of Eq. (15.28) the Airy linewidth [2, 4]. In contrast to the exact Eqs. (15.42) and (15.43), it leads to

$$\begin{aligned} &4\sqrt{R_1 R_2}(\Delta\phi)^2 \approx \left(1-\sqrt{R_1 R_2}\right)^2 \quad \Rightarrow \\ &\Delta\nu_{Airy} \approx \Delta\nu_{FSR}\frac{2}{\pi}\Delta\phi = \Delta\nu_{FSR}\frac{1}{\pi}\frac{1-\sqrt{R_1 R_2}}{\sqrt[4]{R_1 R_2}}. \end{aligned} \tag{15.46}$$

This approximation of the Airy linewidth, displayed as the red curve in Fig. 15.4a, c, deviates from the correct curve at low reflectivities and incorrectly does not break down when $\Delta\nu_{Airy} > \Delta\nu_{FSR}$. This approximation is then typically also inserted into Eq. (15.45) to calculate the Airy finesse [4], resulting in

$$F_{Airy} \overset{!}{:=} \frac{\Delta\nu_{FSR}}{\Delta\nu_{Airy}} \approx \pi\frac{\sqrt[4]{R_1 R_2}}{1-\sqrt{R_1 R_2}}. \tag{15.47}$$

Vaughan [2] and Siegman [3] even defined the Airy finesse by its approximation of Eq. (15.47),

$$\widehat{F}_{Airy} \overset{?}{:=} \pi\frac{\sqrt[4]{R_1 R_2}}{1-\sqrt{R_1 R_2}} \approx \frac{\Delta\nu_{FSR}}{\Delta\nu_{Airy}}, \tag{15.48}$$

thereby depriving this parameter of its lucid meaning. Since the definition of Eq. (15.48) does not comply with the Taylor criterion, it is denoted by a question mark. Saleh and Teich [7, 8] also proposed Eq. (15.48) for the Airy finesse, but from their derivation it remains unclear whether they consider it as a definition or as an approximation of Eq. (15.45).

15.4.4 Response to Frequency-Dependent Reflectivity

In the previous Sections we described a Fabry-Pérot resonator whose mirror reflectivities are independent of frequency. We showed that the Airy distribution is nothing else but the sum of its underlying mode profiles. Now we consider the mirror reflectivities as general functions of frequency, $R_i(\nu)$, such that the photon-decay time $\tau_c(\nu)$ of Eq. (15.3) becomes a function of frequency. As a result, the spectral line shapes $\tilde{\gamma}_q\ (\nu)$ of Eq. (15.11), the mode profiles $\gamma_{q,\,emit}(\nu)$ of Eq. (15.36) and all other mode profiles, as well as the Airy distribution $A_{emit}(\nu)$ of Eq. (15.37) and all other Airy distributions, are spectrally modified. In Eqs. (15.12) and (15.13), $\Delta\nu_c$ turns into a local function of frequency, thereby losing its meaning as the FWHM linewidth. Nevertheless, all Airy distributions fundamentally remain the sums of their corresponding mode profiles. Consequently, even for frequency-dependent

reflectivities $R_i(\nu)$ we can calculate the spectral line shape $\tilde{\gamma}_q(\nu)$ and mode profile $\gamma_{q,\,emit}(\nu)$ of each mode directly from Eqs. (15.11) and (15.36), respectively, and obtain all other mode profiles via the simple scaling factors of Eq. (15.39).

15.5 Summary

The understanding that the Airy distribution describing the spectral transmission of a Fabry-Pérot resonator physically originates in the sum of mode profiles of the longitudinal resonator modes has fundamental consequences. The resonator losses are related to the linewidth of the Lorentzian lines rather than the linewidth of the Airy distribution. Hence, a new parameter, the Lorentzian finesse, becomes important. Once the internal resonance enhancement, equaling the generic Airy distribution that characterizes the light intensity that is forward circulating inside the resonator, is known, all other Airy distributions of back-circulating, transmitted, back-transmitted, and total emitted light intensity can be derived by simple scaling factors. Furthermore, in the case of frequency-dependent mirror reflectivities, the deformed spectral line shapes and mode profiles of the underlying modes can be derived from the same simple equations. Also in this generalized situation, each sum of mode profiles generates the corresponding Airy distribution.

Acknowledgments The authors thank Cristine C. Kores and Dimitri Geskus for their contributions and acknowledge financial support by the ERC Advanced Grant "Optical Ultra-Sensor" No. 341206 from the European Research Council.

References

1. Fabry C, Pérot A (1899) Theorie et applications d'une nouvelle methode de spectroscopie interferentielle. Ann de Chim et de Phys 16:115
2. Vaughan JM (1989) The Fabry-Pérot interferometer. Adam Hilger, Bristol/Philadelphia, ch. 3
3. Siegman AE (1986) Lasers. University Science Books, Mill Valley, ch. 11
4. Svelto O (2010) Principles of lasers, 5th edn. Springer, New York, pp 142–146, ch. 4.5.1
5. Svelto O (2010) Principles of lasers, 5th edn. Springer, New York, pp 169–171, ch. 5.3
6. Saleh BEA, Teich MC (2007) Fundamentals of photonics, 2nd edn. Wiley-Interscience, Hoboken, pp 571–572
7. Saleh BEA, Teich MC (2007) Fundamentals of photonics, 2nd edn. Wiley-Interscience, Hoboken, pp 254–257, ch. 7.1B
8. Saleh BEA, Teich MC (2007) Fundamentals of photonics, 2nd edn. Wiley-Interscience, Hoboken, pp 62–66, ch. 2.5B
9. Eichhorn M, Pollnau M (2015) Spectroscopic foundations of lasers: spontaneous emission into a resonator mode. IEEE J Sel Top Quantum Electron 21:9000216
10. Ismail N, Kores CC, Geskus D, Pollnau M (2016) Fabry-Perot resonator: spectral line shapes, generic and related Airy distributions, linewidths, finesses, and performance at low or frequency-dependent reflectivity. Opt Express 24:16366

11. Koppelmann G (1969) Multiple-beam interference and natural modes in open resonators. In: Wolf E (ed) Progress in optics, vol 7. North Holland, Amsterdam/London, pp 1–66, ch. 1
12. Bayer-Helms F (1963) Analyse von Linienprofilen. I Grundlagen und Messein-richtungen. Z Phys 15:330
13. Juvells I, Carnicer A, Ferré-Borrull J, Martín-Badosa E, Montes-Usategui M (2006) Understanding the concept of resolving power in the Fabry-Perot interferometer using a digital simulation. Eur J Phys 27:1111

Chapter 16
Performance of Nd^{3+} As Structural Probe of Rare-Earth Distribution in Transparent Nanostructured Glass-Ceramics

Rolindes Balda, Giulio Gorni, José J. Velázquez, María J. Pascual, Alicia Durán, and Joaquín Fernández

Abstract Nanostructured glass-ceramics obtained by the adequate heat treatment of a Nd^{3+}-doped glass with composition SiO_2-Al_2O_3-Na_2O-LaF_3 have been investigated by several techniques. X-ray diffraction (XRD) and high resolution transmission electron microscopy (HR-TEM) show that the precipitated nanocrystals are LaF_3 with a crystal size between 9 and 13 nm. Furthermore, energy dispersive X-ray (EDX) analysis shows the incorporation of Nd^{3+} ions into the LaF_3 nano-crystals. A detailed optical characterization clearly shows that Nd^{3+} ions in glass-ceramics are incorporated in both crystalline and amorphous phases. Steady-state and time-resolved site-selective laser spectroscopies allow to isolate unambiguously the emission of Nd^{3+} ions in LaF_3 nanocrystals which shows extremely well defined spectra, similar to those obtained for pure LaF_3 crystal.

Keywords Glass-ceramics · Neodymium · Site-selective laser spectroscopy

16.1 Introduction

The search for new rare earth (RE)-doped materials is still a challenge of great interest for a wide range of photonics applications as well as for scientific basic research. For example, fiber lasers and amplifiers emitting at selected wavelengths

R. Balda · J. Fernández
Departamento de Física Aplicada I, Escuela Superior de Ingeniería, Universidad del País Vasco UPV-EHU, Bilbao, Spain

Materials Physics Center CSIC-UPV/EHU, San Sebastián, Spain
e-mail: rolindes.balda@ehu.eus

G. Gorni · J. J. Velázquez · M. J. Pascual · A. Durán
Instituto de Cerámica y Vidrio (CSIC), Madrid, Spain

B. Di Bartolo et al. (eds.), *Quantum Nano-Photonics*, NATO Science for Peace and Security Series B: Physics and Biophysics,
https://doi.org/10.1007/978-94-024-1544-5_16

in the continuous or pulsed time domain are of paramount importance for bioimaging, optical biosensors, light activated therapy, and telecommunications [1–5]. In particular, RE-doped oxyfluoride glass-ceramics containing one or more crystalline phases embedded in the glass matrix, combine the low phonon energy, optical transparency, and RE ions solubility of fluoride crystals with the good mechanical, thermal, and chemical properties of oxide glasses [6, 7].

The first transparent glass-ceramic (TGC) based on aluminosilicate glass doped with Er^{3+} and Yb^{3+} ions was developed by Wang and Ohwaki in 1993 [8]. It was observed that, exciting Yb^{3+} ions at 970 nm, the green-red upconversion emission from Er^{3+} ions was 100 times more intense than observed from fluoride glass, which suggested the segregation of Yb^{3+} and Er^{3+} ions in the $Pb_xCd_{1-x}F_2$ nano-crystals (NCs). Since then, different RE-doped oxyfluoride glass ceramics mainly based on silicate glass matrices and other fluoride crystal phases, such as LaF_3 [9–11], CaF_2 [12, 13], BaF_2 [14, 15], etc. have been proposed as active media for solid state lasers, optical amplifiers, phosphors or to enhance the efficiency of photovoltaic cells [16, 17].

The rare-earth ions, referred to as the lanthanides, comprise the series of elements in the sixth row of the periodic table after lanthanum from cerium to ytterbium. These atoms are usually incorporated in crystalline or amorphous hosts as trivalent ions and occasionally as divalent ions. The optical activity of the RE ions in solids occurs mainly between electronic states within the 4f configuration. These transitions are parity forbidden and may be partially allowed by crystal field interactions mixing states of different parity. The result is that the transitions between 4f states are weak, with oscillator strengths of the order of 10^{-6}, and radiative lifetimes in the micro and miliseconds range. The long lifetime plays an important role in increasing the probability of sequential excitations in the excited states of a single ion as well as in permitting ion-ion interactions in the excited states to allow energy transfer.

Energy levels in rare-earth ions are labeled according to their angular momentum and spin quantum numbers using terms symbols such as $^4I_{11/2}$, or $^4F_{3/2}$. Here the capital letter refers to the total orbital angular momentum of the ion, the superscript is the spin multiplicity, given as $2S + 1$, where S is the total spin angular momentum. The subscript refers to the total angular momentum of the ion and is determined using the Russell-Saunders coupling scheme [18]. These levels represent the energy levels of a free ion. However, when the ion is in a host, electron-host interactions further split these levels into Stark sublevels, due to the effect of the electric field of the matrix (crystal field effect), which is quite small since the 4f orbitals are shielded from the environment by the filled 5 s and 5p sub-shells. Nevertheless, the crystal field (CF) induced by the host is what determines the shape of the absorption and emission spectra of RE ions. When comparing the spectra of RE ions in crystals and glasses, the absorption and emission bands are narrow with well resolved Stark components, even at room temperature, in the case of crystals where RE ions occupy a well defined crystal field site. On the contrary, the spectra of RE

ions in an amorphous matrix like a glass, present an inhomogeneous broadening due to the different sites occupied by the ions in the host and thus, different crystal fields. As a consequence the Stark structure of RE spectra in glasses is only partially resolved even at low temperature. On the other hand, the symmetry and strength of the CF also affect the splitting of the levels. Moreover, the probability of radiative and nonradiative transitions is strongly affected by the host matrix.

Among rare-earth ions, Nd^{3+} has been recognized as one of the most efficient RE ions for solid-state lasers in crystals and glasses due to its intense $^4F_{3/2} \rightarrow {}^4I_{11/2}$ emission at around 1.06 μm [19]. Besides the interest of Nd^{3+} ions in the field of IR optical amplification, this ion can also be used as a probe for local ordering due to the close relation between its spectroscopic properties and the local structure and bonding at the ion site [19, 20].

In this work, we show how steady-state and time-resolved site-selective laser spectroscopies allow to isolate unambiguously the emission of Nd^{3+} ions occupying La^{3+} sites in the LaF_3 nanocrystals precipitated in transparent oxyfluoride glass-ceramics obtained by the adequate heat treatment of a Nd^{3+}-doped glass with composition SiO_2-Al_2O_3-Na_2O-LaF_3, from that produced by the Nd^{3+} ions sitting in the glass matrix. A strong reduction of the lifetimes of Nd^{3+} in the crystalline phase is observed for concentrations higher than 0.1% and attributed to the much higher concentration of Nd^{3+} in nanocrystals with respect to glass matrices.

16.2 Structural Characterization

Glasses of composition $55SiO_2$–$20Al_2O_3$-$15Na_2O$-$10LaF_3$ doped with 0.1, 0.2, 0.5, 1 and 2 Nd^{3+} (in mol %) have been prepared by melting-quenching by using as raw materials: SiO_2 (Saint-Gobain, 99.6%), Al_2O_3 (Panreac), Na_2CO_3 (Sigma Aldrich, >99.5%), LaF_3 (Alfa Aesar, 99.9%), and NdF_3 (Alfa Aesar, 99.99%). The batches were calcined at 1200 °C for 2 h, melted at 1650 °C for 1.5 h, and then quenched onto a brass mould. Glasses were melted again for 30 min and quenched onto a cold (−10 °C) brass mould. All the glasses were annealed at 600 ° C for 30 min to eliminate residual stresses. From now on, glass samples will be labelled by G0.1, G0.2, G0.5, G1 and G2, for Nd^{3+} concentrations equal to 0.1, 0.2, 0.5, 1, and 2, respectively, while corresponding glass-ceramics will be denoted by GCx.

Glass-ceramic samples were obtained by heat treatments of glass pieces at 620 °C for 1, 3, 5, 20, 40, 80 h, 660 °C-20 h, and 680 °C-20 h using a heating rate of 10 °C/min [21]. Glass sheets (1 cm × 1 cm × 2 mm) were treated and then polished for optical characterization. One glass lamella for each composition was not treated and used as reference glass for comparison with the corresponding glass-ceramics. The heat-treated samples were milled, sieved (<63 μm) and characterised by XRD (Bruker D8 Advance). XRD diffractograms were acquired in the 10–70° range, with

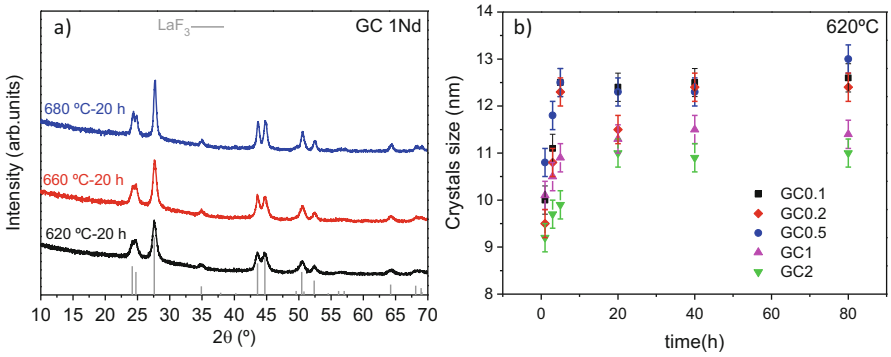

Fig. 16.1 (**a**) XRD diffractograms of GC1 samples heat treated at 620 °C-20 h, 660 °C-20 h, and 680-20 h. (**b**) Crystals size for the samples doped with different NdF_3 concentrations treated at 620 °C

0.02° step and 1 s acquisition for each step. The crystals size was calculated using the Scherrer equation [22]:

$$D = \frac{0.94\lambda}{\cos\,\theta\sqrt{B_m^2 - B_i^2}} \tag{16.1}$$

where λ is the wavelength (1.54056 Å – CuKα_1), B_m the FWHM of the LaF_3 peak (111) and θ its diffraction angle. Factor 0.94 corresponds to spherical crystals. Pseudo-Voigt function has been used to fit diffraction peak parameters. The instrumental broadening B_i has been also taken into account using NaF powder properly milled and sieved (<63 μm).

Figure 16.1a shows the XRD diffractograms of GC1 samples heat treated at 620 °C-20 h, 660 °C-20 h, and 680-20 h. On the bottom the LaF_3 peaks are given (JCPDS 00-032-0483) as reference. For all the compositions, only LaF_3 crystals precipitate in the glass matrix, but the crystal growth kinetics slows down as Nd^{3+} content increases. The inset shows the crystal size after 20 h of treatment at 620, 660, and 680 °C. Figure 16.1b shows the crystals size of GCs heat treated at 620 °C for all the Nd^{3+} concentrations. As can be seen the crystal size increases during the first 5 h reaching a constant value independent on the time of treatment. On the other hand as Nd^{3+} concentration increases the crystal size becomes smaller. LaF_3 nanocrystals grow from 10 nm to 12.5 nm during the first 5 h for the G0.1 glass, but grow less than 1 nm for G2 glass. This may be explained on consideration of the higher T_g of G2 glass. For 660 °C-20 h heat treatment bigger crystals are formed but a similar trend as for 620 °C is maintained [21].

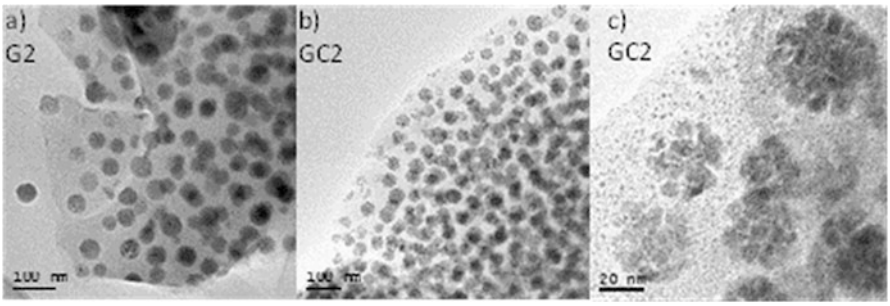

Fig. 16.2 HR-TEM of G2 glass (**a**) and GC2 heat treated at 620 °C-40 h (**b**) and (**c**)

TEM samples of glasses and glass-ceramics were prepared using sieved powders of size <63 μm. High resolution electron microscopy (HR-TEM), including Scanning Transmission Microscopy-High Angle Annular Dark Field (STEM-HAADF) and X-Ray Energy Dispersive Spectroscopy (EDXS), were recorded on a JEOL 2100 field emission gun transmission electron microscope, operating at 200 kV and providing a point resolution of 0.19 nm. The TEM is equipped with an EDXS energy dispersive X-ray spectrometer (INCA x-sight, Oxford Instruments). EDXS analysis was performed in STEM mode, with a probe size of 1 nm. TEM analysis clearly demonstrates the formation of nanocrystals in the heat treated samples. As an example, Fig. 16.2a shows the micrograph of the glass sample doped with 2 mol% of NdF_3 where phase separation droplets are observed. The main size of the droplets in the glass is around 35 nm.

The micrographs of the sample treated at 620 °C-40 h (Fig. 16.2b, c) show the formation of NCs inside the droplets. The main size of the droplets is similar to the glass sample and the average crystal size is around 10 nm in agreement with the values obtained from the diffractograms.

The incorporation of Nd^{3+} ions into the NCs has been demonstrated by Energy Dispersive X-ray (EDX) spectroscopy. As can be seen in Fig. 16.3, the crystallized droplets show an excess of La, F, and Nd, whereas Si is confined mostly at the interface between the droplets which leads to the formation of a barrier around them. The barrier formation should occur during the first 20 h of treatment since LaF_3 crystals grow up to this time, and constant values are stabilized for longer times. The yellow line is the scanning line. The incorporation of Nd^{3+} into crystals of LaF_3 is clearly visible from the EDX curves.

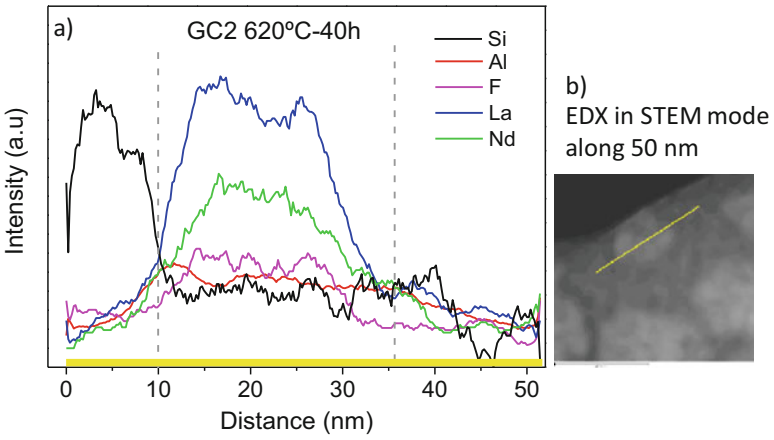

Fig. 16.3 (**a**) EDX of the GC2 620 °C-40 h sample. The yellow line indicates the scanning line. (**b**) STEM image of the droplets used for the EDX measurements. The yellow line represents the same as in (**a**)

16.3 Absorption and Emission Properties of Nd^{3+} Ions

16.3.1 Absorption Properties

Figure 16.4a shows the absorption coefficient for the glass and GC samples treated at 620 °C-20, 620 °C-40 h, and 660 °C-20 h doped with 2 mol% the bands observed in the spectra correspond to transitions from the fundamental level ($^4I_{9/2}$) to each of the excited levels of Nd^{3+} ions. The glass sample presents the characteristic inhomogeneously broadened absorption bands. However, in the case of the GC samples, better resolved absorption bands are observed indicating the incorporation of Nd^{3+} ions in the LaF_3 nanocrystals precipitated during the heat treatments. Figure 16.4b presents in more detail the absorption band of the hypersensitive transition and the bands around 750 and 800 nm for different glass and GC samples. As can be seen, in the case of the GC samples the bands present a more resolved structure and a reduction of the inhomogeneous broadening.

The absorption spectra have been used to calculate the radiative lifetime of the $^4F_{3/2}$ excited J manifold, the branching ratios, and the radiative transition probabilities of fluorescence transitions to the lower lying ^4I_J manifolds, according to the Judd-Ofelt (JO) theory [23, 24]. The experimental oscillator strengths of the absorption bands originating from the $^4I_{9/2}$ ground state have been calculated for the samples doped with 2 mol% by using the expression:

$$f_{\exp} = \frac{mc}{\pi e^2 N} \int_{band} \alpha(\nu) d\nu \tag{16.2}$$

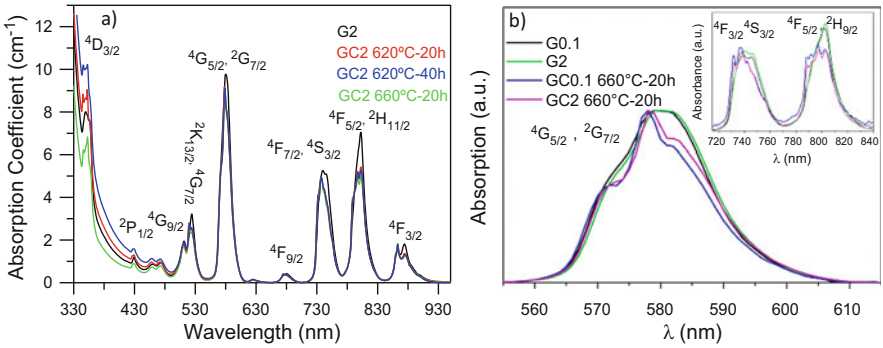

Fig. 16.4 (**a**) Absorption coefficient for the glass and GC samples doped with 2 mol% of NdF_3. (**b**) Enlarged views of absorption bands corresponding to the $^4I_{9/2} \rightarrow {}^4G_{5/2}$, $^2G_{7/2}$ and (inset) $^4I_{9/2} \rightarrow {}^4F_{7/2}$, $^4S_{3/2}$ and $^4I_{9/2} \rightarrow {}^4F_{5/2}$, $^2H_{9/2}$ for G0.1, G0.2, GC01, and GC2

where m and e are the electron mass and charge respectively, c is the light velocity, N is the number of ions per unit volume, and $\alpha(\nu)$ is the absorption coefficient. The experimental f values have been used to calculate the Ω_t parameters corresponding to the JO theory. In the framework of this theory the radiative electric-dipole transitions within the $4f^n$ configuration from the initial state |a J>, to the final state |b J′ > can be described in terms of the oscillator strength by using:

$$f_{cal}\left(aJ;bJ'\right) = \frac{8\pi^2 m\nu}{3h\left(2J+1\right)e^2 n^2}\left[\chi_{ed} S_{ed}\left(aJ;bJ'\right)\right] \tag{16.3}$$

where m is the mass of the electron, ν is the frequency of the transition, h the Planck's constant, J is the total angular momentum of the initial state (J = 9/2 in Nd^{3+}), e the electron charge, and n is the refractive index of the host $\chi_{ed} = [n(n^2 + 2)^2]/9$ is the effective field correction at a well-localized center in a medium of refractive index n. S_{ed} is the line strength for electric-dipole transitions expressed by:

$$S_{ed} = e^2 \sum_{t=2,4,6} \Omega_t \left|\left\langle aJ \left\| U^{(t)} \right\| bJ' \right\rangle\right|^2 \tag{16.4}$$

where $<|| U^{(t)} ||>$ are the double-reduced matrix elements of the unit tensor operators which are considered to be independent of the host matrix and Ω_t are the JO parameters. We have used the values reported by Carnall et al. for Nd^{3+} ions in LaF_3 [25]. The best set of Ω_t parameters can be determined by a least-squared fitting of the calculated and experimental oscillator strengths. The JO parameters obtained from the fitting are displayed in Table 16.1 for the glass and glass-ceramic samples doped with 2 mol% of NdF_3. The values of the root mean square (r.m.s.) indicate a good agreement between the experimental and calculated oscillator strengths.

Table 16.1 Judd-Ofelt parameters and r.m.s. deviation for glass and glass-ceramic samples doped with 2 mol% NdF_3

Sample	Ω_2 ($\times 10^{-20}$)	Ω_4 ($\times 10^{-20}$)	Ω_6 ($\times 10^{-20}$)	r.m.s.
Glass	3.23	6.23	5.03	5.35×10^{-7}
GC2–620 °C-20 h	2.85	5.57	4.37	5.25×10^{-7}
GC2–620 °C-40 h	2.82	5.48	4.31	5.16×10^{-7}
GC2–660 °C-20 h	2.89	5.45	4.17	5.35×10^{-7}

The value of Ω_2 in the GC samples is lower than in the glass sample, which means that the heat treatment induces a reduction in the degree of covalency in the rare-earth site. It is well known that Ω_2 is most sensitive to local structure and its value is indicative of the amount of covalent bonding between RE ions and ligand anions [26]. The decrease of Ω_2 further confirms the incorporation of Nd^{3+} ions into the fluoride NCs. Moreover, the sum of the JO parameters decreases for the GC sample due to the decrease of covalency of the chemical bond between the Er^{3+} ion and the ligand anions [27]. This is in accordance with reported results that predict that the sum decreases in the oxide > oxyfluoride > fluoride sequence. In addition, the Ω_2 parameter is closely related to the hypersensitive transitions. The more intense the hypersensitive transition is, the larger the Ω_2 value. The oscillator strength of this transition is reduced from 1796×10^{-8} in the glass to 1609×10^{-8}, 1581×10^{-8}, and 1591×10^{-8} in the GC 620 °C C-20 h, GC 620 °C-40 h, and GC 660 °C-20 h samples respectively, which confirms that the ligand field around Nd^{3+} ions has changed as a consequence of the heat treatment and crystallisation process.

The spontaneous emission probabilities from the $^4F_{3/2}$ level to the $^4I_{15/2,\ 13/2,\ 11/2,\ 9/2}$ ones can be calculated from the JO parameters. The radiative transition probability from the initial J to the terminal J′ manifold is given by:

$$A\left(aJ;bJ'\right) = \frac{64\pi^4\nu^3}{3h\left(2J+1\right)c^3}\left[n\frac{\left(n^2+2\right)^2}{9}S_{ed}\right] \tag{16.5}$$

where n is the refractive index, ν is the frequency of the transition and J' is the terminal manifold.

The radiative lifetime of an emitting level is related to the total spontaneous emission probability from this level by:

$$\tau_R = \left\{\sum_{bJ'} A\left(aJ;bJ'\right)\right\}^{-1} \tag{16.6}$$

The emission branching ratio can be obtained from the transition probabilities by using:

$$\beta = \frac{A\left(aJ;bJ'\right)}{\sum\limits_{bJ'} A\left(aJ;bJ'\right)} \tag{16.7}$$

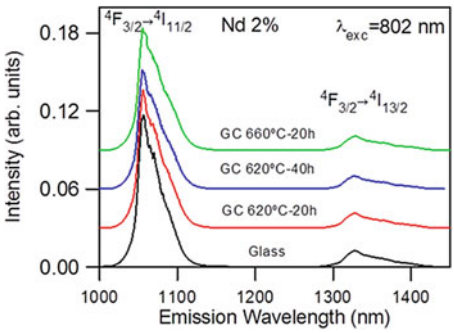

Fig. 16.5 Room temperature emission spectra for the glass and GC samples doped with 2 mol% of NdF_3

16.3.2 Fluorescence Properties

The $^4F_{3/2}\rightarrow^4I_{11/2,13/2}$ steady-state fluorescence spectra were measured at room temperature for all samples by exciting with a Ti-sapphire laser at 802 nm in resonance with the $^4I_{9/2}\rightarrow^4F_{5/2},^2H_{9/2}$ absorption band. The fluorescence was analyzed with a 0.25 monochromator, and the signal was detected by a Hamamatsu H10330A-75 photomultiplier and finally amplified by a standard lock-in technique. As an example, Fig. 16.5 shows the emission for the samples doped with 2 mol%. As can be seen in this figure, the emission is inhomogeneously broadened due to site-to-site variations in the local ligand field. Since the $^4F_{3/2}\rightarrow^4I_{11/2}$ emission band is slightly asymmetric an effective linewidth was determined by integrating the fluorescnce lineshape and dividing by the intensity at the peak fluorescence emission wavelength. The stimulated emission cross-section can be determined from spectral parameters using [28],

$$\sigma_p\left(\lambda_p\right) = \frac{\lambda_p^4}{8\pi cn^2\Delta\lambda_{eff}} A\left[\left(^4F_{3/2}\right);\left(^4I_{11/2}\right)\right] \tag{16.8}$$

where λ_p is the peak fluorescence wavelength, n is the refractive index, $\Delta\lambda_{eff}$ is the effective linewidth of the $^4F_{3/2}\rightarrow^4I_{11/2}$ transition, and $A[(^4F_{3/2});(^4I_{11/2})]$ is the radiative transition probability for this transition.

The stimulated emission cross-section for the $^4F_{3/2}\rightarrow^4I_{11/2}$ transition is presented in Table 16.2 together with the effective fluorescence linewidth ($\Delta\lambda_{eff}$), refractive index (n), and peak position (λ_p). The peak position remains unchanged for the GC samples and the effective linewidth slightly increases with the heat treatment. This, together with the lower radiative transition probability for the $^4F_{3/2}\rightarrow^4I_{11/2}$ emission for the heat treated samples, leads to smaller stimulated

Table 16.2 Room temperature emission properties of Nd^{3+} (2 mol%) in the glass and glass-ceramic samples

Sample	n	λ_p(nm)	$\Delta\lambda_{eff}$ (nm)	σ_p (pm^2)
Glass	1.523	1057	35.95	2.8
GC2–620 °C-20 h	1.525	1057	37.16	2.4
GC2–620 °C-40 h	1.526	1057	37.60	2.3
GC2–660 °C-20 h	1.526	1057	38.94	2.2

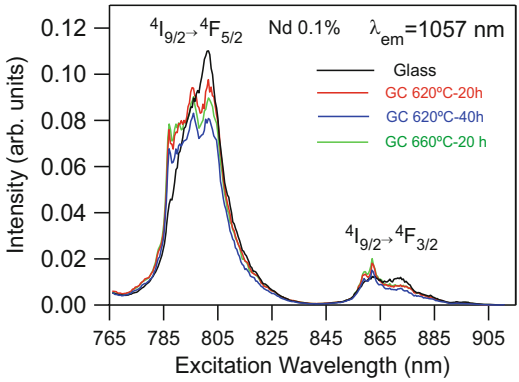

Fig. 16.6 Room temperature excitation spectra for the glass and GC samples doped with 0.1 mol% of NdF_3

emission cross-sections for the GC samples. The stimulated emission cross-section in these samples is in the range of the values found in silicate glasses (0.9–3.6 pm^2) [19].

The steady-state emission spectra present similar spectral features for all concentrations and heat treatments; however the excitation spectra of the GC samples doped with 0.1 0.2, and, 0.5 mol% performed in the 765–905 nm spectral range monitored at 1057 nm show, superimposed to the broad $^4I_{9/2}\rightarrow{}^4F_{5/2,3/2}$ bands of the glass, a fine structure which confirms the partial incorporation of Nd^{3+} ions in the NCs. As we shall see in the next section in the samples doped with 1 and 2 mol% the main contribution to the spectra belong to the Nd^{3+} ions in the amorphous environment. As an example Fig. 16.6 shows the excitation spectrum for the samples doped with 0.1 mol% of NdF_3.

16.3.3 Lifetime Results

The decays of the $^4F_{3/2}$ state were obtained by exciting with a pulsed Ti-sapphire laser at 802 nm in the $^4I_{9/2}\rightarrow{}^4F_{5/2}$ absorption band at 295 K by using a Ti-sapphire laser pumped by a pulsed frequency doubled Nd:YAG laser (9 ns pulse width). The decays of the samples doped with 0.1 and 0.2 mol% can be described to a good approximation by a single exponential function whereas the decays of the samples

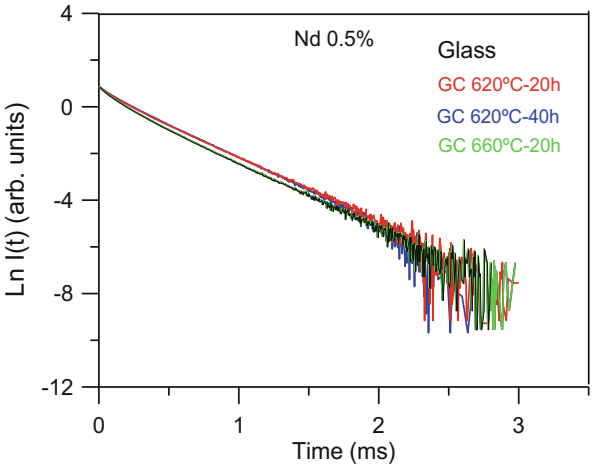

Fig. 16.7 Semilogarithmic plot of the room temperature experimental decays from the $^4F_{3/2}$ state for the samples doped with 0.5 mol% of NdF_3. The decays were obtained by exciting at the $^4I_{9/2} \rightarrow {}^4F_{5/2}$ transition and monitored at 1057 nm

Table 16.3 Experimental lifetimes of the $^4F_{3/2}$ level obtained under excitation at 802 nm collecting the luminescence at 1057 nm as a function of Nd^{3+} concentration and heat treatment

Sample	0.1%	0.2%	0.5%	1%	2%	τ_R (μs)
Glass	343	298	268	192	143	345
GC2–620 °C-20 h	382	350	308	251	187	390
GC2–620 °C-40 h	385	354	310	254	191	395
GC2–660 °C-20 h	388	359	315	254	197	398

The radiative lifetime is shown in the last column

with higher Nd^{3+} concentrations deviate from a single exponential and the lifetime decreases. As an example, Fig. 16.7 shows the logarithmic plot of the experimental decays of the $^4F_{3/2}$ level for the sample doped with 0.5 mol% of NdF_3 at room temperature. Table 16.3 displays the lifetime values for all samples. The lifetime value for the samples with concentrations higher than 0.1 mol% corresponds to the average lifetime defined by

$$\langle \tau \rangle \frac{\int I(t)dt}{I_0}$$

where I(t) is the intensity at time t. According to the value of the radiative lifetime the quantum efficiencies ($\eta = \tau_{exp}/\tau_R$) are around 99 and 41% for the glass samples doped with 0.1 and 2 mol% respectively. This reduction of the quantum efficiency as concentration increases indicates the presence of non-radiative cross-relaxation processes such as ($^4F_{3/2}$, $^4I_{9/2}$)→ ($^4I_{15/2}$, $^4I_{15/2}$).

The lifetime of the GC samples is longer than the lifetime of the glass samples for all concentrations which suggests a fluoride environment for Nd^{3+} ions according with their incorporation in the nanocrystalline phase.

The lifetime of an emitting level is governed by a sum of probabilities of several competing processes: radiative decay, nonradiative decay by multiphonon relaxation and by energy transfer to other ions.

$$\frac{1}{\tau_{\exp}} = \frac{1}{\tau_R} + W_{NR} = \frac{1}{\tau_R} + W_{MPH} + W_{ET} \tag{16.9}$$

where W_{NR} is the nonradiative probability. This nonradiative probability can be due to multiphonon relaxation, which depends on the host matrix, and/or energy transfer which is dependent on ion concentration. Nonradiative decay by multiphonon emission is expected to be small in this case because the energy difference between $^4F_{3/2}$ and $^4I_{15/2}$ levels is around 5500 cm^{-1} and the highest phonon energy is about 1000 cm^{-1}. This corresponds to more than 5 phonons, which indicates that the multiphonon relaxation process is weak and can be neglected in this case. Hence at low concentration (0.1%) the experimental lifetime, which is single exponential, should approach the radiative lifetime. As the concentration rises, the lifetime decreases, which indicates that Nd-Nd relaxation processes such as ($^4F_{3/2} \rightarrow {}^4I_{15/2}$) ($^4F_{3/2} \rightarrow {}^4I_{11/2}$) processes in which two ions exchange energy, play an important role [29].

16.4 Site-Selective Spectroscopy

The $^4F_{3/2} \rightarrow {}^4I_{11/2}$ transition of Nd^{3+} ions can show variations in peak wavelength, linewidth, and spectral profile depending on pumping wavelength due to the site-to-site variation of the local field acting on the ions. To obtain further information about the different environments for Nd^{3+} ions in these glass-ceramics, we have performed site-selective spectroscopy by using a Ti-sapphire ring laser with a narrow bandwidth (0.08 cm^{-1}) as an excitation source for the $^4I_{9/2} \rightarrow {}^4F_{5/2}$ transition. Figure 16.8a shows the normalized emission spectra obtained by exciting at 786 and 802 nm for the GC sample doped with 0.2 mol% of NdF_3 treated at 620 °C-40 h. As can be observed in this figure the shape, peak position, and linewidth of the emission band change depending on the excitation wavelength, which indicates that Nd^{3+} ions are in different crystal field sites. The spectrum obtained by exciting at 786 nm shows a more resolved structure which indicates a crystalline environment for Nd^{3+} ions, whereas the one obtained under excitation at 802 nm shows the inhomogeneous broadened band similar to the glass sample. Moreover, the excitation spectra obtained by collecting the luminescence at 1039 and 1057 nm also show the presence of different environments for Nd^{3+} ions. Figure 16.8b shows the normalized excitation spectra for the same GC sample doped with 0.2 mol% of NdF_3. The spectrum monitored at 1039 nm presents narrower and well-resolved peaks corresponding to Nd^{3+} ions in the NCs. As concentration increases the spectra become broader and less resolved. Similar results are obtained for the three heat treatments, which indicates that after a 20 h treatment at 620 °C the Nd^{3+} ions are incorporated in the NCs.

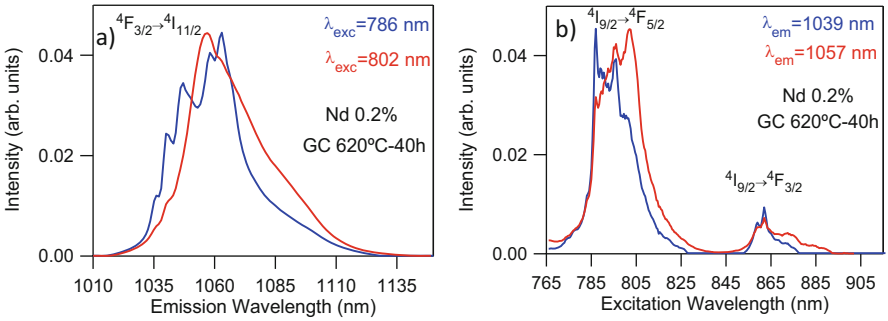

Fig. 16.8 (**a**) Room temperature normalized emission spectra obtained under excitation at 786 (blue) and 802 (red) nm for the GC treated at 620 °C-40 h sample doped with 0.2 mol% of NdF_3. (**b**) Normalized excitation spectra obtained by collecting the luminescence at 1039 and 1057 nm for the GC treated at 620 °C-40 h sample doped with 0.2 mol% of NdF_3

To clearly identify the emission from the Nd^{3+} ions in the NCs, the emission and excitation spectra have been measured at low temperature, in order to minimize the overlapping of the contributions from Nd^{3+} in the crystalline and amorphous phases due to the thermal population of the higher energy Stark components of the ground and excited states. The low temperature (9 K) excitation spectra are presented in Fig. 16.9 for the GC samples doped with 0.2 and 1 mol% treated at 620 °C-40 h. As observed in the spectra obtained at 1039 nm, the low energy band corresponding to the $^4I_{9/2}\rightarrow{}^4F_{3/2}$ doublet narrows and defines into two single components as expected for a well defined crystal field site. Moreover, the $^4I_{9/2}\rightarrow{}^4F_{5/2}$ band is composed of narrow and well resolved peaks which indicate that the spectra obtained at 1039 nm correspond to Nd^{3+} ions in the LaF_3 nanocrystals whereas the spectra obtained at 1055 nm show broad bands similar to those found in the glass samples. On the other side, the relative intensity of the contributions from Nd^{3+} ions in the NCs and in the amorphous matrix changes as Nd^{3+} concentration increases. At low concentrations, the higher intensity corresponds to Nd^{3+} in the crystalline phase.

In order to confirm if the features shown by the excitation spectra monitored at 1039 nm can be definitely related to the Nd^{3+} ions in the NCs, site-selective steady-state, emission spectra for the $^4F_{3/2}\rightarrow{}^4I_{11/2}$ transition were recorded by exciting at 786 and 802 nm. Figure 16.10 shows the emission spectra at 9 K obtained under excitation at 786 and 802 nm for the GC samples doped with 0.2 and 1 mol%. Different spectral features are observed depending on the excitation wavelength. The spectrum obtained under excitation at 786 nm shows sharp peaks, one at 1039 nm not overlapping with the emission spectrum obtained by exciting at 802 nm. This spectrum corresponds to the one obtained in pure LaF_3 crystals [30, 31]. The sharp peaks disappear and the spectrum becomes broader and similar to that found in the glass sample for 802 nm excitation. These results indicate that at 786 nm Nd^{3+} ions in the crystalline phase are excited. As concentration increases,

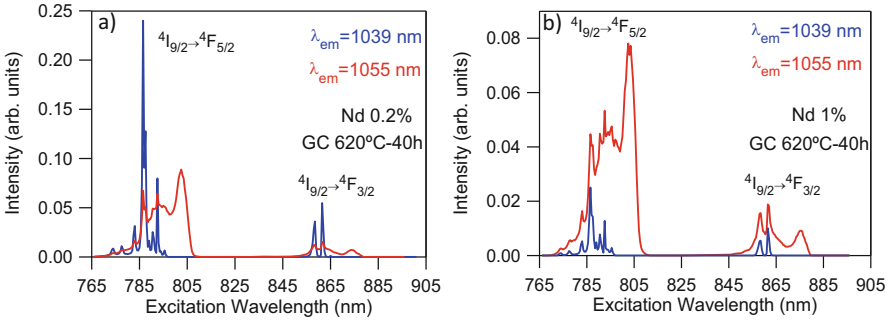

Fig. 16.9 Low temperature excitation spectra obtained by collecting the luminescence at 1039 (blue) and 1055 nm (red) for the GC samples doped with (**a**) 0.2 and (**b**) 1 mol% of NdF_3

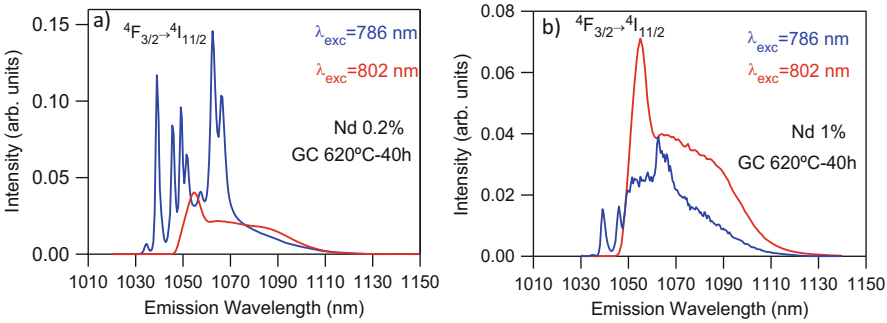

Fig. 16.10 Low temperature emission spectra obtained under excitation at 786 (blue) and 802 nm (red) for the GC samples doped with (**a**) 0.2 and (**b**) 1 mol% of NdF_3

the emission from Nd^{3+} ions in the NCs decreases and the spectra become broader and with less resolved peaks. Similar emission spectra are obtained by exciting the $^4I_{9/2}\rightarrow{}^4F_{3/2}$ band at 861.5 and 876 nm.

Furthermore, the existence of different environments for Nd^{3+} ions is also reflected by the lifetimes of the $^4F_{3/2}$ state. Lifetime measurements of the $^4F_{3/2}$ state were performed by exciting the samples at 786 and 802 nm by using a Ti-sapphire laser pumped by a pulsed frequency doubled Nd:YAG laser (9 ns pulse width), and collecting the luminescence at 1039 and 1055 nm respectively. If Nd^{3+} ions are incorporated in the LaF_3 NCs, the lifetime values should depend on the excitation and emission wavelengths. Under excitation at 786 nm and collecting the luminescence at 1039 nm the decay is single exponential with a lifetime of 688 μs for the GC sample doped with 0.1% whereas by exciting at 802 nm and collecting the luminescence at 1055 nm the lifetime is 336 μs. The longer lifetime corresponds to the Nd^{3+} ions incorporated in the NCs. Table 16.4 shows the lifetime values as a function of Nd^{3+} concentration for the GC samples treated at 620 °C-40 h. As can be seen, the Nd^{3+} lifetime in the crystalline phase is strongly reduced as concentration increases being 98 μs for the GC sample doped with 1 mol%.

Table 16.4 Experimental lifetimes, at low temperature, of the $^4F_{3/2}$ level obtained under excitation at 786 and 802 nm collecting the luminescence at 1039 and 1055 nm respectively

%NdF_3	λ_{exc} = 786 nm	λ_{exc} = 802 nm
	τ_{exp} (μs)	τ_{exp} (μs)
0.1	688	336
0.2	462	337
0.5	188	332
1	98	295

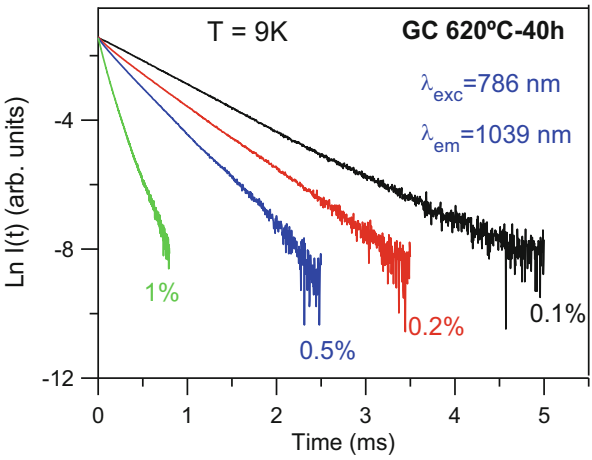

Fig. 16.11 Semi-logarithmic plot of the experimental decays from the $^4F_{3/2}$ state obtained under excitation at 786 nm collecting the luminescence at 1039 nm for the GC samples doped with 0.1, 0.2, 0.5, and 1 mol% of NdF_3

Figure 16.11 shows the semi-logarithmic plot of the experimental decays of the $^4F_{3/2}$ level for the samples doped with 0.1, 0.2, 0.5, and 1 mol% of NdF_3 under selective excitation (786 nm) and emission (1039 nm) wavelengths at which it is possible to separate the Nd^{3+} contribution in the crystalline phase.

As can be observed in Table 16.4 and Fig. 16.11 there is a strong quenching of the Nd^{3+} lifetimes in the LaF_3 nanocrystals, being much less relevant in the amorphous phase. This behaviour is likely explained by a high diffusion of Nd^{3+} ions from the glass matrix to the LaF_3 nanocrystals, as confirmed in the same system doped with Tm^{3+} studied by XANES with Synchrotron radiation [32].

16.5 Conclusions

Transparent oxyfluoride nano-glass-ceramics containing LaF_3 crystals with a crystal size between 9–13 nm have been obtained after proper heat treatments at T_g + 20–80 °C as confirmed by X-ray diffraction (XRD) and high resolution transmission electron microscopy (HR-TEM). A detailed optical characterization clearly shows that Nd^{3+} ions in glass-ceramics are incorporated in both crystalline and amorphous phases. The low temperature site-selective emission and excitation spectra, together with the different lifetime values of the $^4F_{3/2}$ state depending on the excitation

and emission wavelengths, allow to isolate unambiguously the emission from Nd^{3+} ions in the LaF_3 nanocrystals and to correlate the spectroscopic properties with the structural properties. As the Nd^{3+} concentration is increased beyond 0.1 mol%, a stronger quenching of lifetime is observed for Nd^{3+} ions inside LaF_3 crystals than for those dispersed in the glass matrix. This strong concentration quenching is explained by the much higher concentration of Nd^{3+} ions in the crystalline phase compared to the one in the glass matrix.

Acknowledgments This work was supported by the Spanish Government MEC under Projects MAT2013-48246-C2-2-P and MAT2013-48246-C2-1-P and the University of the Basque Country PPG17/07.

References

1. Blasse G, Grabmaier BC (1994) Luminescent materials. Springer, New York
2. Downing E, Hesselink L, Ralston J, Macfarlane R (1996) A three-color, solid-state, three-dimensional display. Science 273:1185–1189
3. Desurvire E (1994) Erbium-doped fiber amplifiers: principles and applications. Wiley, New York
4. Wang F, Han Y, Lim CS, Lu Y, Wang J, Xu J, Chen H, Zhang C, Hong M, Liu X (2010) Simultaneous phase and size control of upconversion nanocrystals through lanthanide doping. Nature 463:1061–1065
5. Huang X, Han S, Huang W, Liu X (2013) Enhancing solar cell efficiency: the search for luminescent materials as spectral converters. Chem Soc Rev 42:173–201
6. de Pablos-Martin A, Ferrari M, Pascual MJ, Righini GC (2015) Glass-ceramics: a class of nanostructured materials for photonics. Rivista del Nuovo Cimento 38:311–369
7. Fedorov PP, Luginina AA, Popov AI (2015) Transparent oxyfluoride glass ceramics. J Fluor Chem 172:22–50
8. Wang Y, Ohwaki J (1993) New transparent vitroceramics codoped with Er^{3+} and Yb^{3+} for efficient frequency upconversion. J. App Phys Lett 63:3268–3270
9. Chen D, Yu Y, Huang P, Lin H, Shan Z, Wang Y (2010) Color-tunable luminescence of Eu^{3+} in LaF_3 embedded nanocomposite for light emitting diode. Acta Mater 58:3035–3041
10. Luo Q, Qiao X, Fan X, Yang H, Zhang X, Cui S, Wang L, Wang G (2009) Luminescence behavior of Ce^{3+} and Dy^{3+} codoped oxyfluoride glasses and glass ceramics containing LaF_3 nanocrystals. J Appl Phys 105:043506
11. Velazquez JJ, Rodriguez VD, Yanes AC, del-Castillo J, Mendez-Ramos J (2010) Increase in the Tb^{3+} green emission in SiO_2-LaF_3 nano-glass-ceramics by codoping with Dy^{3+} ions. J Appl Phys 108:113530
12. Secu M, Secu CE, Polosan S, Aldica G, Chica C (2009) Crystallization and spectroscopic properties of Eu-doped CaF_2 nanocrystals in transparent oxyfluoride glass-ceramics. J Non-Cryst Solids 355:1869–1872
13. Sun X, Gu M, Huang S, Jin X, Lui X, Liu B, Ni C (2009) Luminescence behavior of Tb^{3+} ions in transparent glass and glass-ceramics containing CaF_2 nanocrystals. J Lumin 129:773–777
14. Qiao X, Fan X, Wang M (2006) Luminescence behavior of Er^{3+} in glass ceramics containing BaF_2 nanocrystals. Scripta Mater 55:211–216
15. Luo Q, Fan X, Qiao X, Yang H, Wang M, Zhang X (2009) Eu^{2+}-doped glass ceramics containing BaF_2 nanocrystals as a potential blue phosphor for UV-LED. J Am Ceram Soc 92:942–944

16. Goncalves MC, Santos LF, Almeida RM (2002) Rare-earth-doped transparent glass ceramics. CR Chimie 5:845–854
17. de Pablos-Martín A, Durán A, Pascual MJ (2012) Nanocrystallisation in oxyfluoride systems: mechanisms of crystallisation and photonic properties. Int Mater Rev 57:165–186
18. Russell HN, Saunders FA (1925) New regularities in the spectra of the alkaline earths. Astrophys J 61:38–69
19. Weber MJ (1990) Science and technology of laser glass. J Non-Cryst Solids 123:208–222
20. Jacobs RR, Weber MJ (1976) Dependence of the $^4F_{3/2} \rightarrow {}^4I_{11/2}$ induced-emission cross section for Nd^{3+} on glass composition. IEEE J Quantum Electron QE-12:102–111
21. Gorni G, Velázquez JJ, Mather GC, Durán A, Chen G, Sundararajan M, Balda R, Fernández J, Pascual MJ (2017) Selective excitation in transparent oxyfluoride glass-ceramics doped with Nd^{3+}. J Eur Ceram Soc 37:1695–1706
22. Cullity D (1978) Elements of X-ray diffraction. Addison-Wesley, Reading
23. Judd BR (1962) Optical absorption intensities of rare-earth ions. Phys Rev 127:750–761
24. Ofelt GS (1962) Intensities of crystal spectra of rare-earth ions. J Chem Phys 37:511–520
25. Carnall WT, Crosswhite H, Crosswhite HM (1977) Energy level structure and transition probabilities of the trivalent lanthanides in LaF_3. Argonne National Laboratory, Argonne
26. Nachimuthu P, Jagannathan R (1999) Judd-Ofelt parameters, hypersensitivity, and emission characteristics of Ln^{3+} (Nd^{3+}, Ho^{3+}, and Er^{3+}) ions doped in PbO-PbF_2 glasses. J Am Soc 82(2):387–392
27. Mason SF, Peacock RD, Stewart B (1975) Ligand-polarization contributions to the intensity of hypersensitive trivalent lanthanide transitions. Mol Phys 30:1829–1841
28. Krupke WF (1974) Induced emission cross-sections in neodymium laser glasses. IEEE J Quantum Electron QE-10:450–457
29. Erhmann PR, Campell JH (2002) Nonradiative energy losses and radiation trapping in neodymium-doped phosphate laser glasses. J Am Ceram Soc 85:1061–1069
30. Dmitruk MV, Kaminskii AA (1968) Stimulated emission from LaF_3-Nd^{3+} crystal lasers. Sov Phys JET 26(3):531–533
31. Hong JQ, Zhang LH, Zhang PX, Wang YQ, Hang Y (2015) Growth, optical characterization and evaluation of laser properties of Nd: LaF_3 crystal. J Alloy Comp 646:706–709
32. de Pablos-Martín A, García MA, Muñoz-Noval A, Castro GR, Pascual MJ, Durán A (2014) Analysis of the distribution of Tm^{3+} ions in LaF_3 containing transparent glass-ceramics through X-ray absorption spectroscopy. J Non-Cryst Solids 384:83–87

Chapter 17
Research on the Yb^{3+} Ion Activated Cubic Molybdates and Molybdato-Tungstates for Optical Transparent Ceramics

M. Guzik, M. Bieza, E. Tomaszewicz, Y. Guyot, and G. Boulon

Abstract As widely known, un-doped and rare earth-doped molybdates and tungstates are promising group which have attracted great attention in wide branches of optical material application not only as laser hosts but also as phosphors and scintillators. Most of laser host materials have been obtained as single crystals by Czochralski method. However, the materials in the form of transparent ceramics have comparable or even better important properties than single crystals.

Nowadays, a challenge is to obtain a high quality optical material based on new polycrystalline ceramics applied for laser sources, scintillators and phosphors and to improve manufacturing methods. Nevertheless, only few compositions of cubic transparent ceramics are actually well-developed, these include rare earth (RE^{3+})-doped garnets (Nd^{3+}/Yb^{3+}-doped $Y_3Al_5O_{12}/Lu_3Al_5O_{12}$, Ce^{3+} – doped $Y_3Al_5O_{12}$, fluorides (Yb^{3+}-doped CaF_2), RE^{3+}-doped sesquioxides (Nd^{3+}/Yb^{3+}-doped Lu_2O_3, Sc_2O_3, Y_2O_3) and also perovskite type BMT ($Ba(MgZrTa)O_3$) and un-doped spinel ($MgAl_2O_4$).

This is why our attention is focused on fabrication of new rare-earth doped molybdates or tungstates in the form of polycrystalline ceramics, unknown until now in the literature. The manufacture of ceramics takes less time, even only few days in contrast to 4–6 weeks to grow crystals by using the Czochralski method. In comparison with single crystals it is possible to receive samples highly activated by rare earth ions and of large size ceramics in much cheaper way without using

M. Guzik (✉) · M. Bieza
Faculty of Chemistry, University of Wrocław, Wrocław, Poland
e-mail: goguzik@poczta.fm

E. Tomaszewicz
Department of Inorganic and Analytical Chemistry, West Pomeranian University of Technology, Szczecin, Poland

Y. Guyot · G. Boulon
Univ Lyon, Université Claude Bernard Lyon1, CNRS, Institut Lumière Matière, Villeurbanne, France

B. Di Bartolo et al. (eds.), *Quantum Nano-Photonics*, NATO Science for Peace and Security Series B: Physics and Biophysics,
https://doi.org/10.1007/978-94-024-1544-5_17

expensive iridium or rhenium crucibles. Indeed, two conditions must be fulfilled to obtain transparent ceramics: the compounds should crystallize in the cubic system and the size of the crystallites must be in the order of tens of nanometers.

We present and discuss the structural (XRD and SEM analysis) and spectroscopic properties of three types of materials representing the family of Yb^{3+}-doped molybdates and molybdato-tungstates synthesized by the high-temperature solid-state reaction for future new optical ceramics crystallizing in the cubic system: $La_2Mo_2O_9$ /La_2MoWO_9 /Y_6MoO_{12}. Yb^{3+} rare earth ions has been selected since they can be substitute with trivalent La^{3+} and Y^{3+} cations and then can play the role of a structural probe and, in addition, can be used as laser ions in these materials.

17.1 Introduction

The rapid development of technology stimulates interest in substances that as a result of excitation can efficiently emit light-phosphor materials but also new high power efficient laser materials. Among inorganic matrices very well known, extensively studied and efficient as phosphors, scintillators and laser materials are tungstates and molybdates because of their thermal and chemical stability. In the literature, the most investigated groups are $CaWO_4$ and $MgWO_4$ as phosphors, as well as $ZnWO_4$, $CdWO_4$, and $PbWO_4$ as scintillators [1–8]. Additionally, Nd^{3+}-doped $CaWO_4$ was the first continuously operating crystal laser reported in 1961. Well known laser materials are $MRE(WO_4)_2$ (M = alkali metal, RE = Y, Gd, Lu) doped with optically active trivalent rare-earth ions such as Nd, Dy, Ho, Er, Tm, or Yb. Both Nd^{3+}- and Yb^{3+}-doped KGd $(WO_4)_2$ and KY $(WO_4)_2$ crystals became very important laser materials for near-infrared region [9–12]. Also, phosphors like Eu-doped $MgWO_4$, [13] Eu-doped $ZnWO_4$, [14] or Ce-doped MWO_4 (M = Ca, Sr, Ba) phosphors [15] have been recently published. Moreover, like for the tungstate family, un-doped and rare earth-doped $MMoO_4$ (M = Ca, Sr, Ba, Pb, and Cd) also form a wide class of materials used in different fields such as scintillators, phosphors, photoconductive and photocatalytic materials, as can be seen in these mentioned references as well as therein [16–24].

Our scientific program involves with trivalent rare earth ions doped $CdMoO_4$ scheelite-type cadmium molybdate. As an example, materials with the chemical formula of $Cd_{1-3x}Eu_{2x}\square_xMoO_4$ (cationic vacancy is denoted by $\square$) was investigated as a strong, pure, red-emitting phosphor for white light emitting diodes (WLEDs) by taking advantage of the Eu^{3+} spectroscopic probe ion to analyze in detail the structural properties as a continuation of our previous analysis on both, $Cd_{1-3x}Nd_{2x}\square_xMoO_4$ and $Cd_{1-3x}Yb_{2x}\square_xMoO_4$ characterized by very strong emission in the NIR region [25–27].

In last years increasing interest of development of the ceramic laser materials has been observed as the most important innovation of laser material fabrication technology. The polycrystalline ceramics possess many advantages in comparison to single-crystals; large size, a great number of varieties of shapes, better mechanical strength, higher content of doping activators, lower temperature of synthesis, less

time consuming, cheaper manufacturing process, and ability to engineer profiles and structures, which, moreover, do not require expensive equipment [28–31].

Indeed, two conditions must be fulfilled to obtain transparent ceramics: the compounds should crystallize in the cubic system and the size of the crystallites must be in the order of tens of nanometers. The above-mentioned advantages of the production of transparent ceramics are the reasons why a tendency to replace single crystals by transparent ceramics is observed. Surprisingly, today available rare earth (RE^{3+}) luminescent ions doped cubic optical transparent ceramics used as laser sources or phosphors for lighting are limited to a very small number.

Until now, only few transparent ceramics are known as optical materials with oxides (garnets, sesquioxides, spinels) and fluorides. Especially, we can mention the following references for laser materials:

- Nd^{3+}-doped $Y_3Al_5O_{12}$ garnets [32] In fact, Nd^{3+}:YAG ceramics has been fabricated and used to demonstrate an output power at 1.06 μm of 67 [33] and > 100 kW, [34] respectively.
- Yb^{3+}-doped $Y_3Al_5O_{12}$ ceramics [35, 36]
- Yb^{3+}-doped Y_2O_3 ceramics made by hot pressing of high submicron purity coprecipitated powder for high power solid-state lasers exploiting hosts with higher thermal conductivity than YAG [31]
- Nd^{3+}-doped Lu_2O_3 sesquioxide ceramics fabricated by Hot Isostatic Pressure (HIP) procedure [37]. Laser oscillation has been observed in hot pressed 10% Yb^{3+}-doped Lu_2O_3 ceramics [38]
- Nd^{3+}-doped Lu_2O_3 sesquioxide ceramics fabricated by the Spark Plasma Sintering (SPS) procedure [39, 40]
- Nd^{3+}, Yb^{3+}-co-doped SrF_2 laser ceramics [41]

Due to many advantages of rare earth-doped molybdate and tungstate compounds which fit several requests for optical materials, such as good mechanical strength, thermal property and chemical stability, our research was carried out toward new cubic ceramic optical materials different from those already known. The main objective is to succeed the challenge of synthesis of some rare earth ions (Ce^{3+}, Nd^{3+}, Eu^{3+}, Yb^{3+})-doped cubic tungstate and molybdate inorganic materials accompanied by structural and spectroscopic characterizations, within the expected goal of future innovative optical transparent ceramics.

The RE-doped $La_2Mo_2O_9$ molybdates crystallizing in monoclinic and cubic system were very little studied as the luminescent materials, while there are well-known as fast oxide-ion conductors and have been examined for catalytic applications [42, 43]. Only few articles reported optical properties of $La_2Mo_2O_9$ activated by the rare earth ions. However, the authors did not consider the complexity of crystal structure of both α-$La_2Mo_2O_9$ and β-$La_2Mo_2O_9$ phases and very easily pointed out on the cubic system without any prove, like for example analysis of the pseudo cubic reflection in the XRD patterns, which is an indicator of the cubic phase in $La_2Mo_2O_9$ molybdate.

We have started with Nd^{3+}-doped $La_2Mo_2O_9$ as described in two previous papers [44, 45] and have demonstrated that Nd^{3+}-doped monoclinic structure (α-

form) were observed for the concentration of Nd^{3+} ion up to 15 mol%. Pure cubic phase (β-form), necessary to get transparent ceramics, was obtained when the Nd^{3+} content had reached 50 mol%. However, in such a case of phases with high concentration of Nd^{3+} ions, unfavorable and very strong concentration quenching process takes place due to the clustering of Nd^{3+} ions and energy transfer by both down- and up-conversion processes. Continuing research, we have noticed that the partial substitution of Mo^{6+} ions by tungsten W^{6+} ones (ratio 1:1) can stabilize the cubic phase of mixed Yb^{3+}-doped La_2MoWO_9 molybdato-tungstate [46, 47]. We investigated also the influence of Yb^{3+} ions amount on $La_2Mo_2O_9$ structure, morphology and photoluminescence [48]. Detailed analysis of Yb^{3+}-doped $La_2Mo_2O_9$ shown that in some cases, as for 3 mol% of Yb^{3+}, it is cubic and could serve to produce transparent ceramics from the cubic nano-powders. It is worth to note that the Yb^{3+} luminescence in $La_2Mo_2O_9$ as Near Infra-Red (NIR) emitting optical material has never been reported up to now, so this is also one reason for our interest in this composition as laser material, but also because we can play with the presence of the $^2F_{7/2} \leftrightarrow {}^2F_{5/2}$ 0-phonon line of Yb^{3+} ion used as a structural probe in solids. The complexity of the $La_2Mo_2O_9$ crystal structure bring some difficulties in the interpretation of the spectroscopic results. Micro-crystalline samples obtained by high-temperature solid-state reaction characterized by higher crystallinity of material, and thus by more intense luminescence, were selected to perform the fundamental investigations of optical properties. Finally, the nano-powder obtained by the combustion method containing 3 mol% of Yb^{3+} ion was used to obtain Yb^{3+}-doped $La_2Mo_2O_9$ in the form of first translucent ceramics [48].

Recently we discovered that RE^{3+}-doped Y_6MoO_{12} molybdates easily crystallize in the cubic form and may be more beneficial relative to the solid solutions investigated by us [49]. Until now novel, yellow, brown and brick-red colored compositions activated by Sm^{3+}, Pr^{3+} or Nd^{3+} ions yttrium molybdates have been reported as high near infrared reflecting pigments due to their excellent optical property of reducing the heat build-up effectively [50–52]. A large number of rare earth based NIR refractive pigments are proposed as alternatives to traditional transition metal oxides pigments because of their low toxicity. Also a few articles on Eu^{3+}-doped Y_6MoO_{12} and mixed $Y_6Mo_{1-x}W_xO_{12}$, $Y_6(W,Mo)(O,N)_{12}$ or $Lu_6Mo(W)O_{12}$ phosphors have been reported recently [53–57]. The advantages of this matrices we can find also in the localization of the CT band shifted to the blue region with respect to the other molybdates or tungstates of tetragonal-coordinated $W(Mo)O_4$ groups. Indeed, the four-fold coordination (MO_4 groups; M = Mo, W) present in the scheelite-type structure shows the charge transfer bands (CTBs) of MO_4 groups located in the UV region, and thus near-UV or blue light cannot be utilized to excite rare earth activators through the host lattices. Compared with MO_4 groups, sixth-fold coordination (MO_6 groups) can efficiently absorb near-UV light by the ($O^{2-} \rightarrow M^{6+}$) CTBs and transfer the excitation energy to the activator [58]. These Eu^{3+}-doped compounds have been investigated in the frame of exploring of near-UV/blue light excited color-conversion phosphors in an expectation of obtaining white light with high color rendering index and low color temperature, namely,

warm white light. It is worth noting that the Yb^{3+} luminescence in Y_6MoO_{12} has never been reported before us and this is why we present solid solutions of this material as a very promising NIR emitting optical materials for phosphors and lasers with some hope to obtain them in the nearest future in the form of transparent ceramic due to their cubic structure.

In this review we would like to summarize some results on the Yb^{3+} ion activated cubic molybdates and molybdato-tungstates for optical transparent ceramics which have been presented as a lecture at the Erice's school. There are presented the detailed structural and spectroscopic studies performed by using complementary techniques as XRD, SEM with EDS, high-resolution low-temperatures absorption and emission with site selective excitation, which together brought very precious information. We are pointing out the advantages and disadvantages of the analyzed host lattices. Finally, we present also some results obtained for the first translucent ceramics.

17.2 Experimental Section

17.2.1 Sample Preparation

17.2.1.1 Synthesis of Yb^{3+}-Doped $La_2Mo_2O_9$

A series of micro-crystalline Yb^{3+}-doped $La_2Mo_2O_9$ molybdates with various concentrations of Yb^{3+} ion (x = 0, 0.5, 1, 2, 3, 4, 5, 6, 7, 8, 9, 10, 15 and 25 mol%) were successfully synthesized by a high-temperature solid-state reaction. The stoichiometric quantities of high purity commercial powders of La_2O_3, (99.999%, Stanford Materials), Yb_2O_3 (99.995%, Stanford Materials), MoO_3 (99.95%, Alfa Aesar) were used as initial reactants in this synthesis. Both rare-earth oxides were previously calcined at 850 °C in air in two 12-h heating stages to remove adsorbed moisture and carbon dioxide. The starting materials weighed in suitable molar proportion were mixed together and homogenized thoroughly by grinding in an agate mortar. All initial mixtures $Yb_2O_3/Y_2O_3/MoO_3$ were transferred into corundum crucibles and heated in air in the five stages: 600 °C/6 h, 700°C/6 h, 900°C/12 h, 1000°C/12 h and 1100°C/12 h. After each heating stage, Yb^{3+}-doped materials were slowly cooled to room temperature and then reground in an agate mortar with acetone for better reactivity.

The synthesis of Yb^{3+}-doped $La_2Mo_2O_9$ can be described by the following equation:

$$(1 - x/2)\ La_2O_{3(s)} + x/2\ Yb_2O_{3(s)} + 2\ MoO_{3(s)} = La_{2-x}Yb_xMo_2O_{9(s)} \tag{17.1}$$

17.2.1.2 Synthesis of Yb^{3+}-Doped La_2MoWO_9

The procedure performed for La_2MoWO_9 was very similar. However, the initial mixtures $Yb_2O_3/Y_2O_3/MoO_3/WoO_3$ were heated in air only in one stage at 1100 °C during 2 h. The micro-powder was obtained according to the reaction:

$$(1 - x/2)\ La_2O_{3(s)} + x/2\ Yb_2O_{3(s)} + MoO_{3(s)} + WO_{3(s)} = La_{2-x}Yb_xMoWO_{9(s)} \quad (17.2)$$

17.2.1.3 Synthesis of Yb^{3+}-Doped Y_6MoO_{12}

A series of micro-crystalline molybdates with chemical formula of $Y_{6\text{-}x}Yb_xMoO_{12}$ (later labelled as Yb^{3+}-doped Y_6MoO_{12}) with different concentration of optically active ion were synthesized by a high-temperature solid state reaction method. The concentration of the activator was set to 0.1, 1, 3, 5, 10, and 20 mol%, calculated in respect to Y^{3+} substitution. Commercial powders of Y_2O_3 (99.999%, Stanford Materials), Yb_2O_3 (99.995%, Stanford Materials), MoO_3 (99.95%, Alfa Aesar) were used as the starting reactants for synthesis of Yb^{3+}-doped Y_6MoO_{12} solid solutions. Before the synthesis, RE oxides were calcined at 850 °C, with two 12-h heating stages to remove adsorbed moisture and carbon dioxide. Weighed in appropriate molar ratios, the oxides were homogenized by grinding in an agate mortar. Next, as-prepared $Yb_2O_3/Y_2O_3/MoO_3$ mixtures were heated in corundum crucibles, in air, with 6-h annealing stages, and at temperatures from 550 to 750 °C. In next step, all samples were sintered with 12-h stages and at temperatures from 800–1000 °C. Finally, all ceramic materials were annealed at 1200, 1400, 1500 and 1550 °C for 6-h stages. After each heating stages the samples were cooled slowly down to ambient temperature, and for better reactivity, ground in an agate mortar. Several regrinding and heating sequences at the temperatures mentioned above were necessary to obtain appropriate and high-purity products. The synthesis of the solutions was started at a relatively low temperature (550 °C) due to the low melting point of MoO_3 (*ca.* 760 °C) and the possible mass loss caused by evaporation of this oxide. The phase composition of the samples was controlled by using powder X-ray diffraction (XRD). The pure and doped RE_6MoO_{12} phases can arise at 1500 °C. For this reason, it was absolutely necessary to apply so high temperature of annealing. The synthesis of samples under study can be described by the following equation:

$$(3\text{–}1/2x)\ Y_2O_3 + 1/2x\ Yb_2O_3 + MoO_3 = Y_{6-x}Yb_xMoO_{12} \quad (17.3)$$

17.2.1.4 Fabrication of Yb^{3+}-Doped $La_2Mo_2O_9$ and La_2MoWO_9 Translucent Ceramics

For the preparation of first translucent ceramics the cubic 3 mol% Yb^{3+}-doped $La_2Mo_2O_9$ and 3 mol% Yb^{3+}-doped La_2MoWO_9 nano-crystalline powders were used. This powders were prepared by combustion method according to previous paper [47]. Appropriate amounts of nano-powders was transferred to form and pressed under atmospheric pressure of 4 atm. during 5 min. Then, a white tablets was sintered at 1200 °C/6 h in vacuum atmosphere. In result a light yellowish (yellow-orange) (translucent ceramics, presented on the picture in the Sect. 17.4 of this paper, was obtained. Attempts to obtain transparent ceramics were carried out only for 3 mol% Yb^{3+}-doped $La_2Mo_2O_9$ and 3 mol% Yb^{3+}-doped La_2MoWO_9.

17.2.2 Apparatus

XRD Phase Analysis Room temperature (RT) powder XRD method was used to identify the phase purity and the crystal structure of solid solutions. X-ray diffraction patterns were collected over the angular range $2\Theta = 10–90°$ in continuous scanning mode with the scan rate of 0.008° per step on a D8 ADVANCE powder diffractometer with nickel-filtered Cu Kα radiation ($\lambda = 1.5418$ Å) and a Vantec detector, as well as on EMPYREAN II diffractometer (PANalytical) using Cu $K\alpha_{1,2}$ radiation ($\lambda = 1.5418$ Å) within $2\Theta = 10–70°$ range with a scan rate 0.008° per step and a counting time of 4 s per step. XRD patterns were analyzed by *HighScore Plus 4.0* software and lattice parameters were calculated using the least squares refinement procedure by *POWDER* software [59].

Density Measurements The density of samples under study was measured on a Ultrapycnometer 1000 Quantachrome Instruments (model Ultrapyc 1200e, USA) using argon (99.999%) as a pycnometric gas.

Scanning Electron Microscopy (SEM) The particle size and surface morphology of the Yb^{3+}-doped micro-powders and translucent ceramics were studied by scanning electron microscopy (SEM) using Hitachi S-3400N equipped with an energy dispersive X-ray spectroscopy EDS detector Thermo Scientific Ultra Dry. The powders were coated with thin gold alloy layer to facilitate conductivity, while the ceramics was analyzed without the gold coating.

Emission and Excitation Measurements The steady state emission spectra were measured using a SpectraPro 750 monochromator, equipped with a Hamamatsu R928 photomultiplier and a 1200 l/mm grating blazed at 500 nm. A 450 W xenon arc lamp was used as the excitation source. It was coupled with a 275 mm excitation monochromator which used a 1800 l/mm grating blazed at 250 nm. The excitation spectra were corrected for the excitation light intensity while the emission spectra were corrected for the instrument response. The measurements were taken at room

temperature (RT). **Site selective excitation and time resolved spectroscopy** (or Fluorescence Line Narrowing) was performed at 77 K in a nitrogen cryostat (or quartz dewar). A tuneable laser (EKSPLA OPO NT342B, 7 ns, 10 Hz) was used for scanning the excitation wavelength around 465 and 580 nm. The fluorescence was collected with an optical fiber and analysed with the help spectrometer equipped with a 1200 l/mm grating blazed at 500 nm, coupled to intensified charge coupled device (ICCD) camera (Shamrock 303 and iStar from Andor Technology).

Luminescence Decay Measurements The luminescence decay curves were recorded under pulsed laser excitation (OPO laser, EKSPLA NT342, 10 Hz, 7 ns), the fluorescence intensity around 1.06 μm being detected with a R1767 Hamamatsu photomultiplier through a HRS1 Jobin-Yvon monochromator equipped with a 1 μm blazed grating and coupled to a LECROY LT 342 digital oscilloscope. The luminescence decay curves were recorded at RT and 77 K.

17.3 Results and Discussion

17.3.1 Yb^{3+}-Doped $Y_2Mo_2O_9$ and Yb^{3+}-Doped Y_2MoWO_9 Micro-powders

17.3.1.1 Structural Analysis

As we reported in the articles devoted to $La_2Mo_2O_9$ molybdate activated by Nd^{3+} ions, dilanthanum molybdate with the formula of $La_2Mo_2O_9$ shows a reversible polymorphic transformation at 555 °C (determined during controlled heating of $La_2Mo_2O_9$ sample) from low-temperature α-phase (monoclinic structure) to high-temperature β-phase (cubic structure) [44, 45].

The monoclinic structure of $La_2Mo_2O_9$ phase with unit cell parameters: $a = 14.325(3)$ Å, $b = 21.482(4)$ Å, $c = 28.585(6)$ Å, β=90.40(3)°, V = 8796(3) Å^3, Z = 48, S.G. $P2_1$ was characterized based on small clear crystals by Evans et al. [60]. This structure is very complex and does not resemble the typical inorganic oxide due to the presence of 312 crystallographically independent atoms: 48 La, 48 Mo and 216 O. It corresponds to the 2 × 3 × 4 superstructure of the cubic structure of high-temperature $La_2Mo_2O_9$ phase. Both La^{3+} and Mo^{6+} cations have mixing oxygen coordination. The La^{3+} cations are found in irregular geometries containing different coordination numbers, between 6 and 12 oxygen anions, and 30 out of the 48 independent La^{3+} cations possess 9 oxygen anions. In turn, the Mo^{6+} cations occur in the three local coordination: tetrahedral, trigonal bipyramidal and octahedral.

The crystallographic data of cubic structure of high-temperature $La_2Mo_2O_9$ phase based on single crystal were presented by Alekseeva et al. [61]. The X-ray diffraction measurements were performed at 33 K to obtain the following unit-cell parameters: $a = 7.1377(2)$ Å, $\alpha=\beta=\gamma = 90°$, V = 363.64(2) Å^3, Z = 2, S.G.

$P2_13$. In contrast to the monoclinic structure, both of La^{3+} and Mo^{6+} coordination polyhedra are not be precisely determined because of partially occupied positions by the ions. The analysis of structure showed 15 oxygen anions surround La^{3+} cation and 7 oxygen anions are in the environment of Mo^{6+} cation. Moreover the interatomic distances between metal and oxygen vary from 2.3 to 2.93 Å for La-O and from 1.53- to 1.97 Å for Mo-O [62].

Hou et al. have also studied the cubic structure features of high-temperature $La_2Mo_2O_9$ modification using ab initio MD simulations. In contrast to previous results reported by Alekseeva, there were different data on the geometry optimization calculation. An important conclude of their research is that the all structure consists of mixture of coordinated cation sites. Molybdenum creates MoO_4 tetrahedra and MoO_5 trigonal bipyramids, while the lanthanum cations create much complex polyhedra, because La^{3+} cations are surrounded by seven or eight oxygen anions, forming LaO_7 and LaO_8 polyhedra. However, all Mo cations do not share common oxygens and are isolated by lanthanum polyhedra. In contrast to molybdenum polyhedra, there was noticed that three LaO_8 polyhedra and one LaO_7 polyhedra are connected together by sharing oxygen ions, forming complex network in three dimensions [63].

In case of Yb^{3+}-doped $La_2Mo_2O_9$ solid solutions, is expected that the Yb^{3+} ions occupy the same crystallographic positions as La^{3+} ones. The substitution of La^{3+} ions (1.10 Å for CN = 7 and 1.16 Å for CN = 8) by much smaller Yb^{3+} ones (0.925 Å for CN = 7, and 0.985 Å for CN = 8) and the same oxidation state (+3) does not require of a charge compensation and prevents to the formation of cationic holes.

Figure 17.1 shows the room temperature XRD patterns of the Yb^{3+}-doped samples obtained after the final sintering stage with the reference patterns of monoclinic (ICSD #172479) as well as cubic modification (ICSD #420672) of $La_2Mo_2O_9$ within the 2θ range of 10–70°.

If we look at XRD patterns from ICSD for the monoclinic (ICSD #174279) and the cubic (ICSD #420672) phases we could have an impression that that the positions of the diffraction lines for both phases are the same. However, the reflections for the monoclinic system have a more complex profiles. As an example in the insert of Fig. 17.1 we present the most informative pseudo-cubic [321] peak at 47Θ48° 2θ angle, which by change of the profile allows to determine the monoclinic (peak split into few components) or cubic (only one component of much broad and symmetrical peak) structure. The content of La_2O_3-MoO_3-Yb_2O_3 initial mixtures, total concentration of Yb^{3+} ions in final doped materials, calculated lattice parameters, calculated and experimental values of density for the identified Yb^{3+}-doped $La_2Mo_2O_9$ and Yb^{3+}-doped La_2MoWO_9 materials with detailed analysis of diffractograms were reported recently [46, 48]. It is observed that when the initial Yb^{3+} content is small, *i.e.* 0.5–2 mol%, the product of reaction between three metal oxides is only $La_{2-x}Yb_xMo_2O_9$ solid solution with monoclinic structure of $La_2Mo_2O_9$. We should not forget that Yb^{3+} ion (CN = 7 ionic radius – 0.925 Å, CN = 8 ionic radius – 0.985 Å) has much smaller ionic radius than La^{3+}

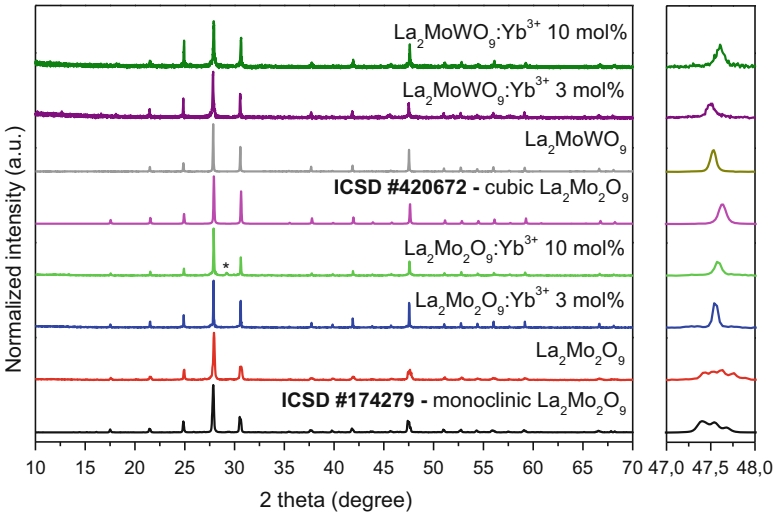

Fig. 17.1 X-ray powder diffraction patterns of monoclinic and cubic Yb^{3+} – doped molybdates and molybdato-tungstates

one (CN = 7 ionic radius – 1.10 Å and CN = 8 ionic radius – 1.16 Å). XRD measurements of the sample obtained by heating the mixture comprising initially 1 mol% of Yb_2O_3 (3 mol% Yb^{3+}, $x = 0.06$) show the presence of one solid phase, *i.e.* $La_{2-x}Yb_xMo_2O_9$ solid solution with cubic symmetry. At the concentration range over 4 mol% Yb^{3+}, two solid phases are found, *i.e.* cubic modification of $La_{2-x}Yb_xMo_2O_9$ and monoclinic Yb_2MoO_6 occurring in the samples on treatment. Starting from the sample with the concentration of 4 mol% Yb^{3+} the lattice parameters are very close to each other and to the *a* parameter calculated for cubic modification of $La_{2-x}Yb_xMo_2O_9$ ($x = 0.06$) [48]. An unexpected mixture of two phases: cubic molybdate of $La_2Mo_2O_9$ (ICSD #420672) and additional phase of Yb_2MoO_6 (ICSD #99574) is seen for the sample with concentration of Yb^{3+} equal 10 mol% (in Fig. 17.1 green line). The above observations clearly indicate that solubility limit of Yb^{3+} in $La_2Mo_2O_9$ is not higher than 4 mol%. Thus, in the case of obtained Yb^{3+}-doped materials it is observed that a substitution of La^{3+} ions by Yb^{3+} ones does not stabilize a cubic modification of $La_{2-x}Yb_xMo_2O_9$ within wide concentration range of dopant. It is only seen in the case of 3 mol% ($x = 0.06$). The experimental results show that for obtaining the Yb^{3+}-doped materials with cubic symmetry in all concentration range of activator by using the high-temperature solid-state reaction, the partial substitution of Mo^{6+} ions by W^{6+} ones is necessary.

17.3.1.2 Morphology and Particle Size by SEM Analysis

Figure 17.2 shows the SEM (Scanning Electron Microscope) micrographs of Yb^{3+}-doped $La_2Mo_2O_9$ molybdates with different content of the active ion. Due to the many stages of sintering at high temperature the grains formed micro-crystallites with a grain size in the range from 5 to even 15 μm. The overview pictures show that the good quality materials formed only for the materials containing small amount of activator. The powders with concentration of Yb^{3+} ions from 0.5 to 3 mol% are composed from homogeneous spherical shape of grains, with slight aggregation and a boundary between the microcrystals of powders clearly seen. Occasionally, on the surface of the grains one can see a few white grains of much smaller sizes of the order of several nanometers, very rich in Yb^{3+} ions, as indicated the EDS analysis. With increasing concentration of Yb^{3+} ions, the single particles are agglomerated into bigger clusters with irregular shape of micro-meter size. For higher concentration of Yb^{3+} ions the agglomerates form the sintered irregular blocks of size even 50–70 μm. However, at high magnification it is seen that on the surface of the big Yb^{3+}-doped $La_2Mo_2O_9$ grains, the second phase in form of cube-shaped crystals is created. The SEM micrographs and the energy dispersive X-ray (EDS) analysis indicate existing of two phases starting from 4 mol% of Yb^{3+} ions, thus morphology of Yb^{3+}-doped $La_2Mo_2O_9$ strongly depends on the amount of Yb^{3+} ions. From the Fig. 17.2 we see that the second phase occurs quite extensively, and the EDS analysis reveals very high content of Yb^{3+} ions in the cube-shaped crystals. The correlation of the results obtained from two applied methods (XRD patterns and SEM micrographs – EDS analysis) allows us supposed that this second Yb^{3+}- rich phase correspond to the monoclinic Yb_2MoO_6 phase, as postulated in the previous section (17.3.1.1 Structural analysis). Formation of the second phase is probably due to the small solubility limit of Yb^{3+} ions (3 mol%) in Yb^{3+} – doped $La_2Mo_2O_9$. The presence of La^{3+} ions in the results from EDS analysis is due to the measurement technique. The cube-shaped phase of Yb_2MoO_6 is located on the surface of Yb^{3+}-doped $La_2Mo_2O_9$, so electrons during analysis penetrate also the $La_2Mo_2O_9$ phase.

For the cubic Yb^{3+}-doped La_2MoWO_9 molybdato-tungstate micro-powders the phenomenon of second Yb_2MoO_6 phase formation was not observed [46].

17.3.1.3 Absorption Spectra

In order to investigate the absorption properties of Yb^{3+}-doped $La_2Mo_2O_9$, the measurements at room temperature and 4.2 K have been performed. As an example, in Fig. 17.3 we present the spectra obtained for 4 mol% of Yb^{3+} ion. High-resolution absorption spectra present four broad lines corresponding to $^2F_{7/2}(1) \rightarrow {}^2F_{5/2}$ (5,6,7) electronic transitions and to vibronic ones. The half-widths and positions of them practically do not change with decreasing the temperature: 1 → 5 (973.3 nm at RT, 972.5 nm at 4.2 K), 1 → 6 (944 nm at RT, and 946 nm at 4.2 K), 1 → 7 (926 nm at both temperature) and vibronic transitions at 963, 904 nm and 912 nm

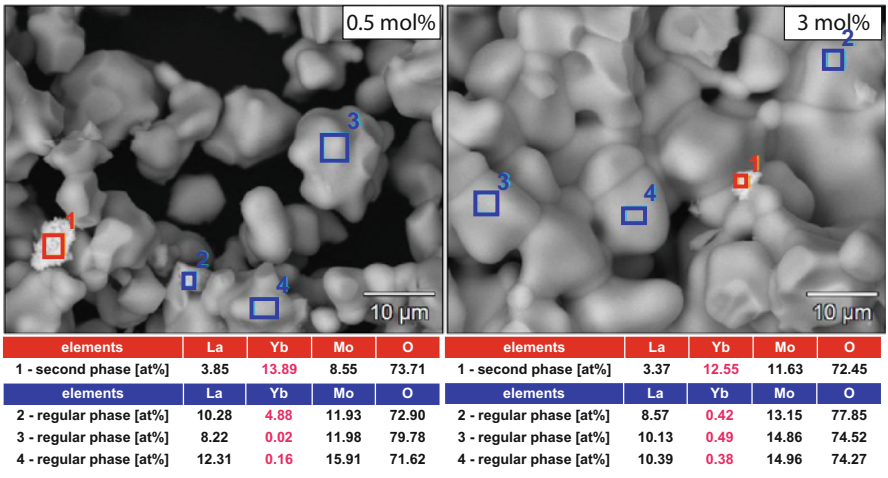

elements	La	Yb	Mo	O
1 - second phase [at%]	3.85	13.89	8.55	73.71
2 - regular phase [at%]	10.28	4.88	11.93	72.90
3 - regular phase [at%]	8.22	0.02	11.98	79.78
4 - regular phase [at%]	12.31	0.16	15.91	71.62

elements	La	Yb	Mo	O
1 - second phase [at%]	3.37	12.55	11.63	72.45
2 - regular phase [at%]	8.57	0.42	13.15	77.85
3 - regular phase [at%]	10.13	0.49	14.86	74.52
4 - regular phase [at%]	10.39	0.38	14.96	74.27

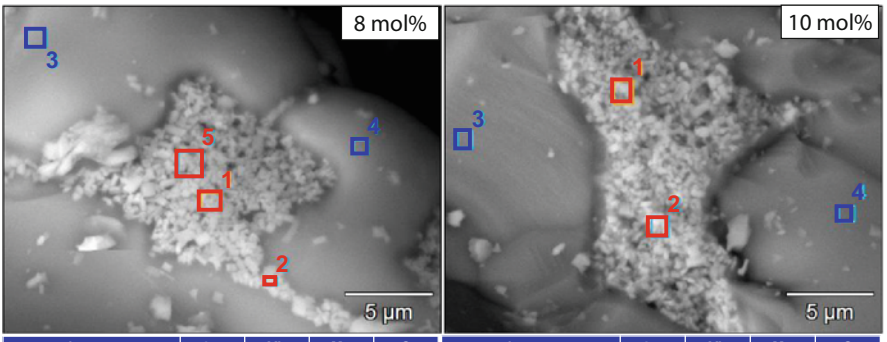

elements	La	Yb	Mo	O
3 - regular phase [at%]	10.52	0.72	15.23	73.53
4 - regular phase [at%]	6.80	0.51	11.25	81.44
1 - second phase [at%]	4.49	6.87	11.16	77.48
2 - second phase [at%]	7.65	3.04	13.24	76.07
5 - second phase [at%]	4.44	9.00	12.13	74.43

elements	La	Yb	Mo	O
3 - regular phase [at%]	10.20	0.85	14.75	74.20
4 - regular phase [at%]	8.73	0.62	13.42	77.22
1 - second phase [at%]	3.77	10.18	13.05	73.00
2 - second phase [at%]	3.99	10.03	12.86	73.12

Fig. 17.2 SEM micrographs and EDS elemental analysis of Yb^{3+}-doped $La_2Mo_2O_9$ molybdates

at RT and 910 nm at 4.2 K. When the temperature decreases, the absorption lines should narrow. In this case only broad well-formed 0-phonon is slightly narrowing. Broad lines still recorded at 4.2 K suggest a large disordering of active ions in the structure. We already proposed the existence of such a disorder in the structure for the similar compositions of $La_2Mo_2O_9$ dilanthanum dimolybdate doped with Nd^{3+} ions as well as for Yb^{3+}-doped mixed La_2MoWO_9 molybdato-tungstates [32, 37]. Here, as we can see from the Table 17.1 [42] the difference between the ionic radii of La^{3+} and Yb^{3+} is bigger than in case of La^{3+} and Nd^{3+} ions, so the disorder in the framework may also be bigger.

In turn, not presented here, room temperature absorption spectra recorded for molybdates with cubic structure (3–10 mol% Yb^{3+}-doped $La_2Mo_2O_9$) are similar

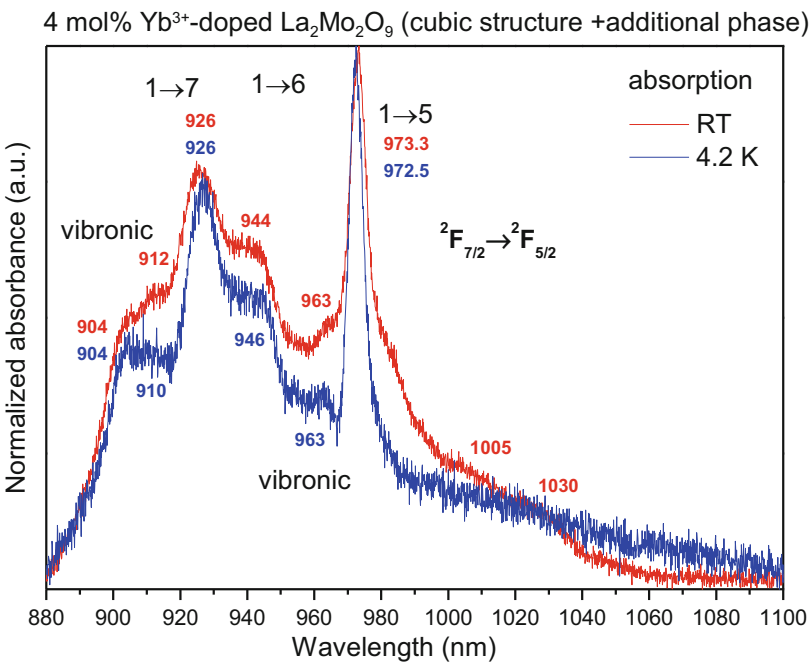

Fig. 17.3 Absorption spectra of 4 mol% Yb^{3+}-doped $La_2Mo_2O_9$ molybdates recorded at RT and 4.2 K

Table 17.1 Ionic radii of La^{3+}, Nd^{3+} and Yb^{3+} according to CN coordination number [62]

	La^{3+} [Å]	Nd^{3+} [Å]	Yb^{3+} [Å]
CN = 7	1.1	–	0.925
CN = 8	1.16	1.109	0.985
CN = 9	1.216	1.163	1.042

as for monoclinic samples (0.5–2 mol%) and present the broad, well-separated and contain only one component of 0-phonon line (1 → 5). Nevertheless, the calculated value of full width at half maximum (FWHM) is equal 196.5 cm^{-1} (3 mol% of Yb^{3+}) [48]. It may be due to the second, hidden component which suggests the multisite character of Yb^{3+} ions. These results are consistent with studies on Yb^{3+}-doped La_2MoWO_9, which demonstrated also one and broad 0-phonon line, most probably related to the existence of two main LaO_8 and LaO_7 polyhedra in the structure of La_2MoWO_9 molybdato-tungstates [46, 47]. In the whole series of Yb^{3+}-doped $La_2Mo_2O_9$ molybdates with the cubic structure the values of the FWHM of 0-phonon line systematically decrease with increasing the concentration of Yb^{3+} ion from 196.5 cm^{-1} (3 mol%) to 106 cm^{-1} (10 mol%). The intensity of the lines corresponding to 1 → 7 and 1 → 6 transitions in the 875–960 nm spectral range increases with higher concentration of Yb^{3+} up to 10 mol% of Yb^{3+} ions [48]. For high concentration of the activator the intensity of the line at 925 nm

corresponds to the 1 → 7 electronic transition is almost equal to intensity of the 0-phonon line. Moreover, the room temperature absorption spectra revealed the additional two additional absorption bands correspond to transition from second (2) and third (3) Stark sublevel of the ground state $^2F_{7/2}$ to the lowest higher sublevel (5) of the excited state $^2F_{5/2}$, which are located at 1006 nm (2 → 5) and 1030 nm (3 → 5), respectively.

To see the effect of introduction of W^{6+} ion into the $La_2Mo_2O_9$ matrix on the optical properties we present in Fig. 17.4 the room (Fig. 17.4a) and low (Fig. 17.4b) absorption spectra of 8 mol% Yb^{3+}-doped $La_2Mo_2O_9$ (cubic + additional phase) and 10 mol% Yb^{3+}-doped La_2MoWO_9 (cubic phase). Comparison of two similar systems: Yb^{3+}-doped $La_2Mo_2O_9$ molybdates and Yb^{3+}-doped mixed La_2MoWO_9 molybdato-tungstates lead to conclusion that at room and low temperatures, the absorption lines for $La_2Mo_2O_9$ are slightly shifted into higher energies and also that for La_2MoWO_9 molybdato-tungstates the spectra are less structured, so the larger disorder in the structure caused by substitution of one Mo^{6+} ion (i.r. – 0.59 Å) by one W^{6+} one (i.r. – 0.6 Å) is well seen. A big difference is the spectral shape observed for Yb^{3+}-doped $La_2Mo_2O_9$ and Yb^{3+}-doped La_2MoWO_9 especially at 4.2 K is a consequence of the presence of stoichiometric Yb_2MoO_6 second phase in 8 mol% Yb^{3+}-doped $La_2Mo_2O_9$. In both cases, the most intense absorption band is 0-phonon line with one broad distinct component, much broader for La_2MoWO_9. The values of full width at half maximum (FWHM) of 0-phonon line are quite different, around two times bigger for Yb^{3+}-doped $La_2Mo_2WO_9$ (97 cm^{-1}) than in

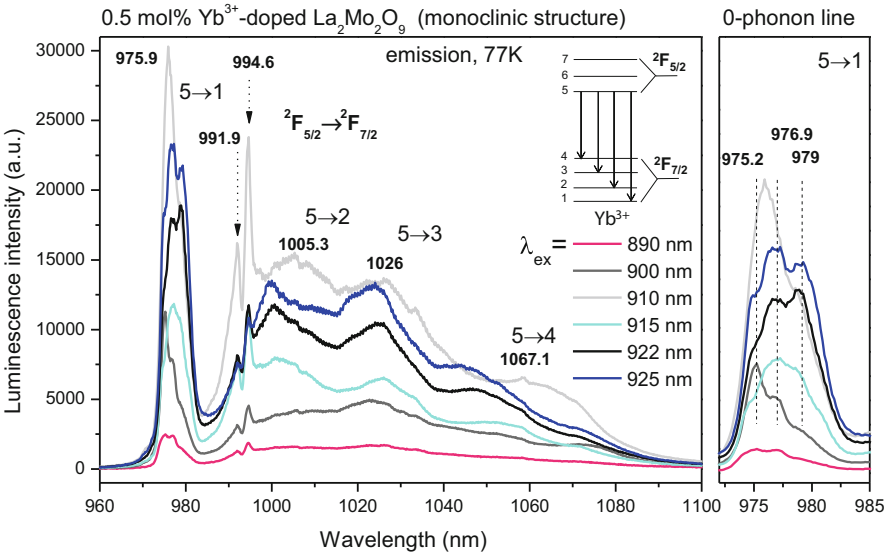

Fig. 17.4 Site selective emission spectra of 0.5 mol% Yb^{3+}-doped $La_2Mo_2O_9$ solid solution, measured at 77 K under different excitation wavelengths of the Ti-sapphire laser

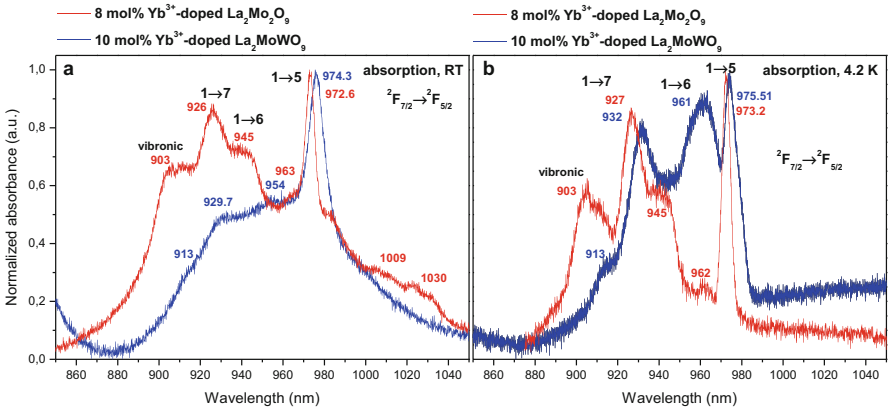

Fig. 17.5 Room (**a**) and low temperature (**b**) absorption spectra of 8 mol% Yb^{3+}-doped $La_2Mo_2O_9$ (cubic structure + additional phase, red line) and 10 mol% Yb^{3+}-doped La_2MoWO_9 (cubic structure, blue line)

case of Yb^{3+}-doped $La_2Mo_2O_9$ (56 cm^{-1}). Based on the results, it can be concluded that the partial substitution of Mo^{6+} ion by W^{6+} once in Yb^{3+}-doped La_2MoWO_9 leads to larger disorder in the structure, although the ionic radii of the two transition metals is quite similar.

17.3.1.4 Emission Spectra

Presented in Figs. 17.5 and 17.6 site selective emission spectra recorded by using a tunable Ti-Sapphire laser were used to determine the spectroscopic properties of Yb^{3+}-doped $La_2Mo_2O_9$ materials and to compare the differences in photoluminescence properties of molybdates crystallizing in the monoclinic (0–2 mol%) and the cubic system (3–10 mol% Yb^{3+}). On the low temperature emission spectra of 0.5 mol% Yb^{3+}-doped $La_2Mo_2O_9$ with monoclinic structure (Fig. 17.5) it is easy to notice the complex structure of emission bands in the near infrared region 970–1090 nm. The most intense is called 0-phonon line and corresponds to the 5 → 1 transition in resonance with the 1 → 5 absorption line. This line is used as a reference for the spectroscopy of Yb^{3+}-doped materials. Only one component of the 0-phonon line is expected at low temperature for the same crystallographic sites of Yb^{3+} ions in the structure. In Fig. 17.5 with changing the excitation wavelengths from 890 nm to 925 nm it is observed here that the 0-phonon line splits into three components located at around 975.2 nm, 976.9 nm and 979 nm. These results indicate the different distribution of Yb^{3+} ions in the monoclinic structure of molybdates what is strongly related with crystal structure discussed in Sect. 17.3.1.1: According to Evans the La^{3+} cations are found in irregular geometries containing different coordination numbers, between 6 and 12 oxygen anions, and 30 out of the 48 independent La^{3+} cations possess coordination number 9. In

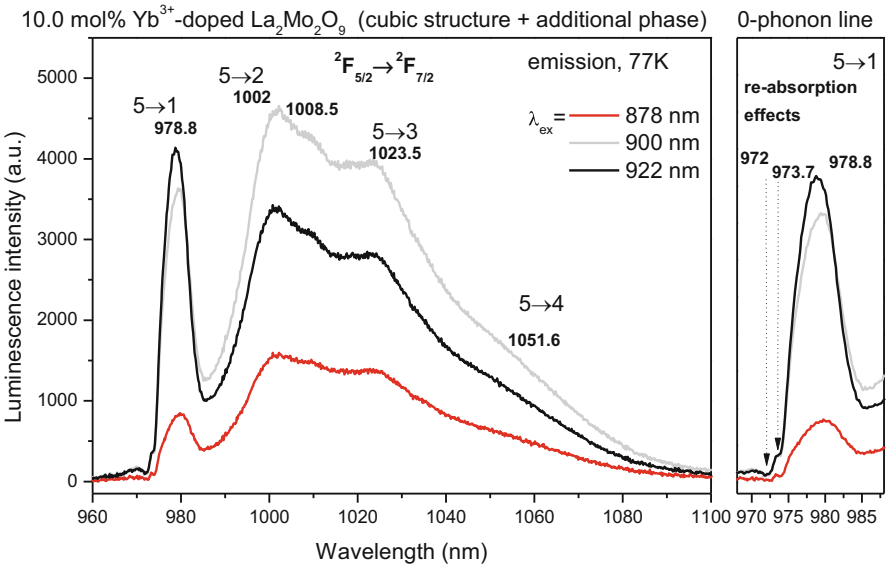

Fig. 17.6 Site selective emission spectra of 10 mol% Yb^{3+}-doped $La_2Mo_2O_9$ molybdate, measured at 77 K under different excitation wavelengths of the Ti-sapphire laser

turn, the Mo^{6+} cations occur in the three local coordination: tetrahedral, trigonal bipyramidal and octahedral [60]. Let's remind that in the monoclinic Nd^{3+}-doped $La_2Mo_2O_9$ obtained by us, at least two types of Nd^{3+} sites have been assigned with two coordination numbers of LaO_7 and LaO_8 [44, 45].A reasonable assignment might be that Yb^{3+} dopant reveals another coordination number like for example LaO_9, according to Evans possible to exist in this complex structure [60].

Despite the 0-phonon line, on the emission spectra of Yb^{3+} ions are expected three other emission bands corresponding to $^2F_{5/2}$ (5) → $^2F_{7/2}$ (2,3,4) electronic transitions. Usually they show the highest intensities with the electronic transitions than vibronic transitions. In case of emission spectra of monoclinic molybdates three expected intense lines with attributed transitions of Yb^{3+} ions are located at 1005.3 nm (5 → 2), 1026 nm (5 → 3) and 1067 nm (5 → 4) nm, respectively. Additionally, the two narrow components of emission lines at 991.9 and 994.6 nm are only recorded in the sample containing 0.5 mol% and more visible under $\lambda_{ex} = 910$ nm from the tunable Ti-sapphire laser. At this moment it is hazardous to assign them to Yb^{3+} ion and might be associated with an impurity only present in this specific sample. The photoluminescence intensity increases rightly with the change of excitation wavelengths from 890 nm to 925 nm in agreement with the profile of the absorption lines in Fig. 17.4.

Moreover, a continuous shift of the emission line corresponding to 5 → 4 transition occurs by changing excitation wavelength from 925 nm to 890 nm. This is another probe of the presence of multisites inside the molybdate lattice.

The emission spectra at low temperature of 10 mol% Yb^{3+}-doped $La_2Mo_2O_9$ by pumping with Ti-sapphire laser are presented in Fig. 17.6. In case of molybdates

with cubic structure are observed much broader emission lines with clearly noticeable positions at 978.8 nm (5 → 1), 1002 nm (5 → 2), 1023.5 nm (5 → 3) and 1051.6 nm (5 → 4).

The shape and the number of emission lines stay the same with changing the excitation wavelengths. The dominant features of the emission spectra recorded under laser diode excitation $\lambda_{ex} = 878$ and 900 nm are much intense emission lines attributed to 5 → 2 and 5 → 3 transitions than the 0-phonon line. We think that re-absorption phenomenon of the 0-phonon line 5↔1 occurs largely in such case. This results indicate evident differences for cubic molybdates from the monoclinic structure. Although the 0-phonon line is not split, the calculated value of full width at half maximum (FWHM) of this line is large, around 80.3 cm^{-1}, which indicates a distribution of un-equivalent sites. Moreover, the 0-phonon line has asymmetrical shape which is the most visible under $\lambda_{ex} = 900$ nm and 922 nm by pumping with a tuneable Ti-sapphire laser, leading to the hypothesis of two or three main environments of Yb^{3+} ions in this cubic lattice. Additionally, another re-absorption effect is observed on the emission spectra of Fig. 17.6 at 972 nm. It is probably the result of the high concentration of Yb^{3+} ions in Yb_2MoO_6 as seen in Fig. 17.2 for the morphology study.

We wanted to know the concentration dependence of Yb^{3+} ions on photoluminescence properties of molybdates and then we have recorded the low temperature emission spectra under the same laser diode excitation at $\lambda_{ex} = 405$ nm into the charge transfer band of the molybdate group (Figs. 17.7 and 17.8).

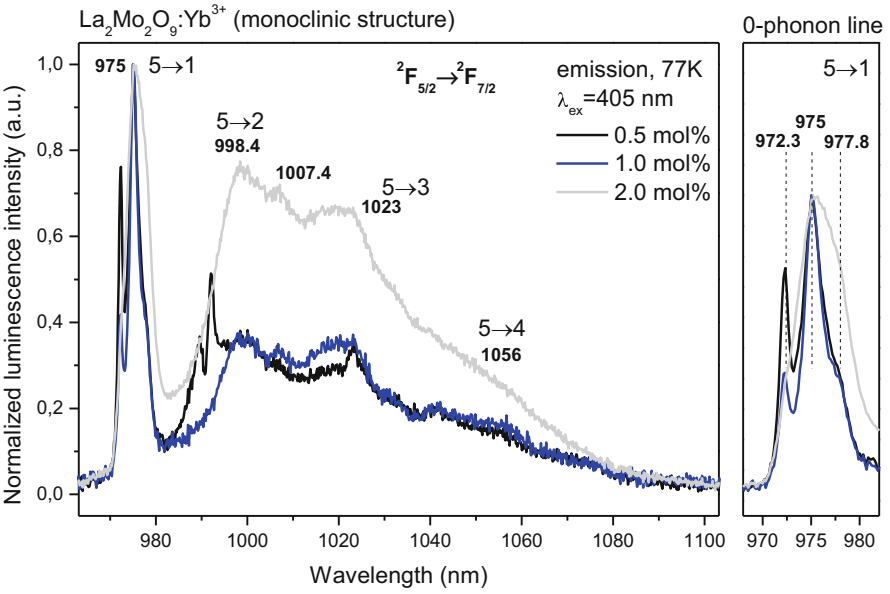

Fig. 17.7 Emission spectra of $La_2Mo_2O_9:Yb^{3+}$ 0.5, 1 and 2 mol% solid solutions crystallizing in the monoclinic system, measured at 77 K under laser diode excitation $\lambda_{ex} = 405$ nm into the charge transfer band of the molybdate group

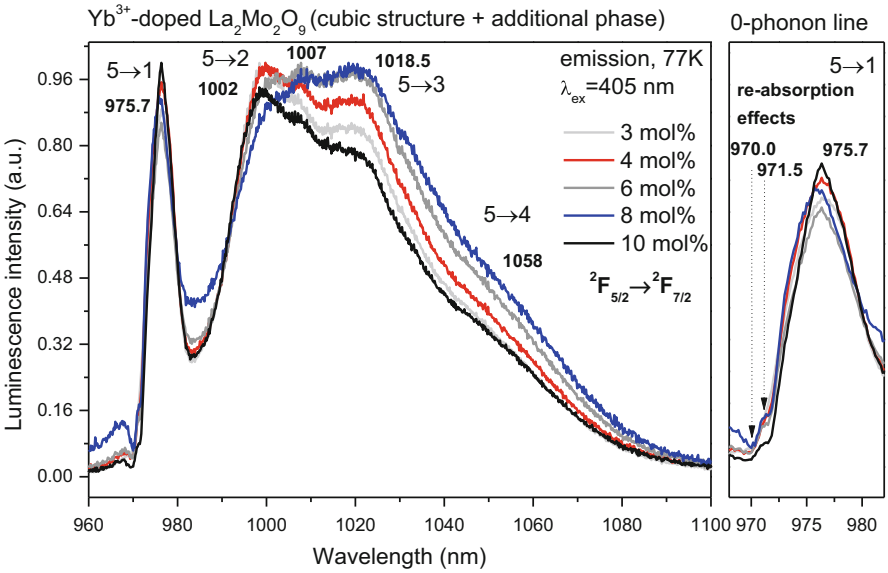

Fig. 17.8 Emission spectra of $La_2Mo_2O_9$:Yb^{3+} 3–10 mol% materials crystallizing in the cubic system, measured at 77 K under laser diode excitation $\lambda_{ex} = 405$ nm into the charge transfer band of the molybdate group. The values of wavelengths are mentioned for 8 mol% of Yb^{3+}

The 0.5 mol% of Yb^{3+}-doped $La_2Mo_2O_9$ molybdate with monoclinic structure shows two abnormal additional lines located at 989.6 nm and 992.1 nm which are still noticeable, under the laser diode excitation at $\lambda_{ex} = 405$ nm. As only this 0.5 mol % is concerned we have observed these two lines belong to a stoichiometric Yb_2MoO_6 phase characterized by the smallest white points, less than 1 μm, in the SEM photo of Fig. 17.5. The splitting of the 0-phonon line into three components (972.3 nm, 975 nm and 977.8 nm) are visible only for the lowest concentrations 0.5 and 1 mol% of Yb^{3+}-doped $La_2Mo_2O_9$ molybdates. However, the profile of this 0-phonon line is questionable in the following way. Instead to assign the sharp line at 972.3 nm to one component belonging to one special site symmetry or polyhedral coordination, we also can imagine there is a hole between 972.3 and 975 nm due to the reabsorption from the Yb^{3+} rich phase as can be seen in Fig. 17.2.

It should be a way to measure the absorption line of this Yb^{3+} segregation in the sample. In such hypothesis, it seems we can keep the resolution of three components of the 0-phonon line in Fig. 17.7 connected with three polyhedra in the monoclinic structure as already interpreted previously from the absorption spectra. When concentration of Yb^{3+} ions increases, the structured shape of the 0-phonon line disappears in the new cubic structure. Moreover, the large full width at half maximum (FWHM) of this line equals to 77.6 cm^{-1} suggests at least two or three slightly un-equivalent crystallographic sites occupied by the Yb^{3+} in substitution of La^{3+} ions of the cubic phase.

Based on the results, both monoclinic and cubic structures are pointed out in Yb^{3+}-doped $La_2Mo_2O_9$ molybdates. The substitution of Yb^{3+} ions on several types of La^{3+} sites causes the broadening of all emission lines suggesting a disordering of the Yb^{3+} ions in the host structure. The spectral resolution of the monoclinic phase is much higher than the cubic one. More especially, three main configurations of sites are detected in the monoclinic phase and most probably in the cubic phase which might be connected with three coordination numbers.

17.3.1.5 Some Comparison Between Cubic Structure of Yb^{3+}-Doped $La_2Mo_2O_9$ and Yb^{3+}-Doped Mixed La_2MoWO_9

In order to compare spectroscopic properties of two quite similar cubic systems: Yb^{3+}-doped $La_2Mo_2O_9$ and Yb^{3+}-doped La_2MoWO_9 were set together low and room temperature emission spectra recorded under Ti-sapphire laser (Fig. 17.9). For both samples, the most intense emission broad line on emission spectra corresponds to the similar 0-phonon line ($^2F_{5/2}$ (5) $\rightarrow$ $^2F_{7/2}$ (1) transition). The calculated value of full width at half maximum (FWHM) of the 0-phonon line is around 73.7 cm^{-1} for 3 mol% Yb^{3+}-doped $La_2Mo_2O_9$ and 72.2 cm^{-1} for 3 mol% Yb^{3+}-doped La_2MoWO_9, which suggests multisite disordered distribution of Yb^{3+} ions in both of structures. The room temperature and 77 K emission spectra shows weakly

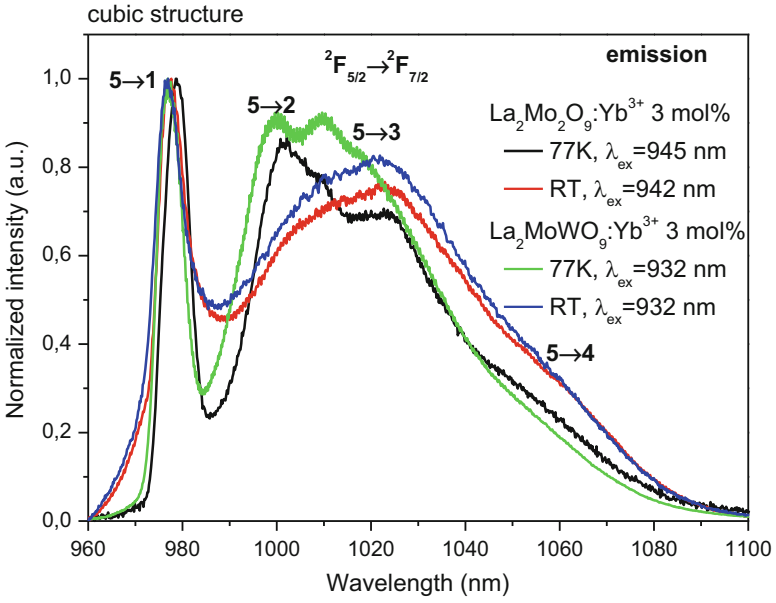

Fig. 17.9 Emission spectra of 3 mol% Yb^{3+}-doped $La_2Mo_2O_9$ and 3 mol% Yb^{3+}-doped La_2MoWO_9 solid solutions under selected excitation lines of the Ti-sapphire laser

separated broad emission bands. Successfully, along with the temperature drop to 77 K, the three emission bands located at 1000 nm (5 → 2), 1020 nm (5 → 3) and 1060 nm (5 → 4) for Yb^{3+}-doped La_2MoWO_9 and 1000.8 nm (5 → 2), 1024.4 nm (5 → 3) and 1047.8 nm (5 → 4) for Yb^{3+}-doped $La_2Mo_2O_9$ were observed.

17.3.1.6 Yb^{3+} Energy Level Diagram in $La_2Mo_2O_9$

In order to evaluate the crystal field splitting of $^2F_{5/2}$ and $^2F_{7/2}$ multiplets of Yb^{3+} ions in Yb^{3+}-doped $La_2Mo_2O_9$ is recorded low temperature absorption spectra (4.2 K) and emission spectra (77 K). The low temperature measurements are necessary to determine exact location of absorption and emission lines in contrast to the room temperature measurements which are not structured enough.

The energy levels scheme of Yb^{3+} ion in $La_2Mo_2O_9$ was drawn in Fig. 17.10. The value of total splitting levels equal 10,795 cm^{-1} for 8 mol% Yb^{3+}-doped $La_2Mo_2O_9$:Yb^{3+} is slightly bigger then 10,730 cm^{-1} in case of 10 mol% Yb^{3+}-doped La_2MoWO_9. The partial substitution of Mo^{6+} ions by W^{6+} ones (in ratio 1:1) promote a bit smaller splitting of multiplets of Yb^{3+} ions.

As can be seen from the Figs. 17.11 and 17.12, the position of the 0-phonon line on absorption and emission spectra are not the same. One most probable interpretation of this evident difference is the re-absorption effect associated with the resonance of absorption and emission lines. Two reasons can be involved: first, the presence of the second Yb_2MoO_6 phase with high concentration of Yb^{3+} ions giving rise to a hole in the 0-phonon line. Secondly, inside the main structure, where

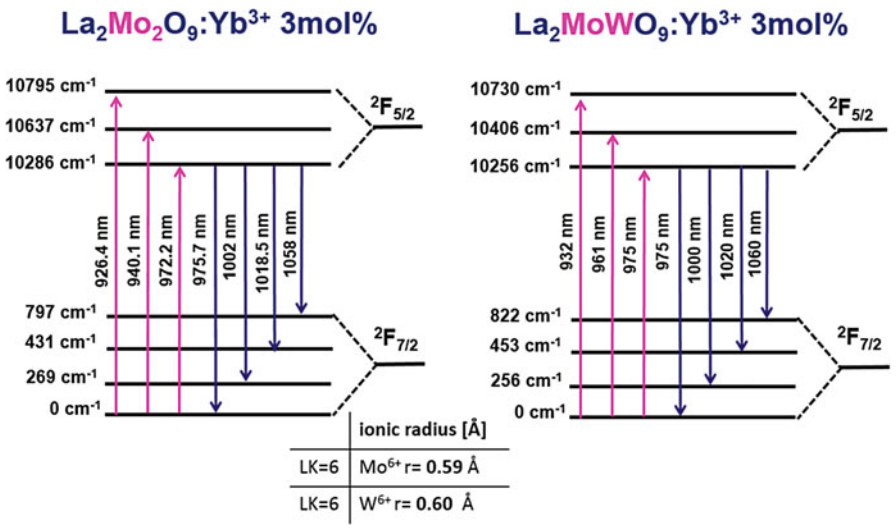

Fig. 17.10 Low temperature Stark splitting levels of Yb^{3+} ions calculated from the experimental data

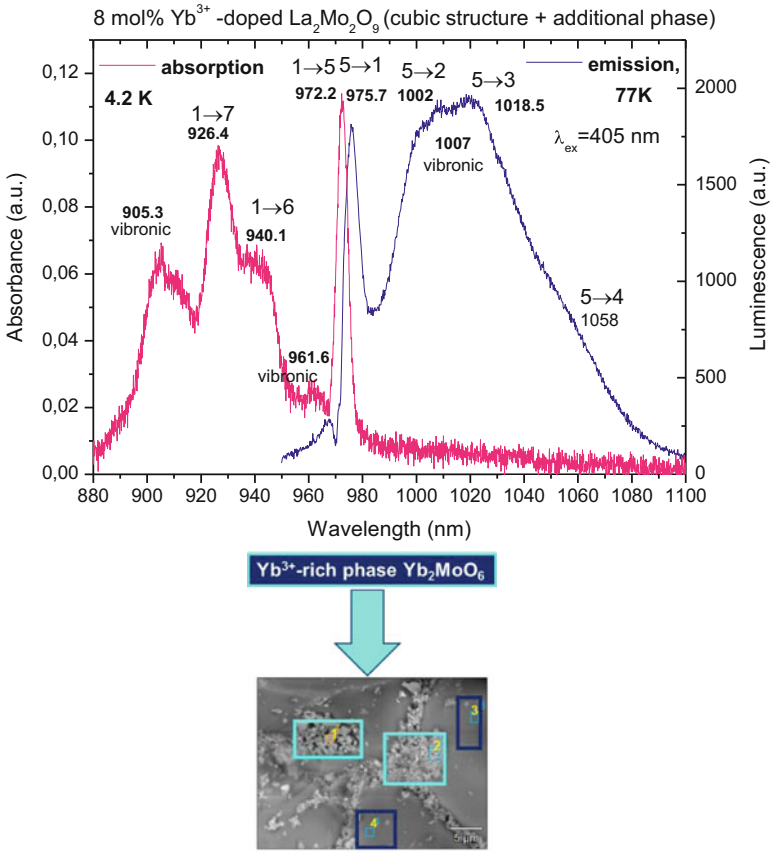

Fig. 17.11 Superposition of the absorption spectra at 4.2 K, emission spectra at 77 K of 8 mol% Yb^{3+}-doped $La_2Mo_2O_9$ cubic molybdate under laser diode excitation $\lambda_{ex} = 405$ nm (CT band)

multisites occur, a deformation of the profile of the 0-phonon line emission spectrum showing an overlapping between the absorption line of one of the three centers with the total emission spectrum.

Additionally, to compare the Stark splitting levels of Yb^{3+} ions and also re-absorption phenomena in $La_2Mo_2O_9$ and La_2MoWO_9 [47, 48] was reminded the low temperature superposition of absorption and emission spectra for 10 mol% Yb^{3+}-doped La_2MoWO_9 (Fig. 17.12).

17.3.1.7 Decay Analysis

Figure 17.13 presents collected decay profiles of Yb^{3+}-doped $La_2Mo_2O_9$ series of molybdates with large range of activator concentration (0.5–10 mol% Yb^{3+}) recorded at room temperature. The decay times were recorded under pulsed OPO

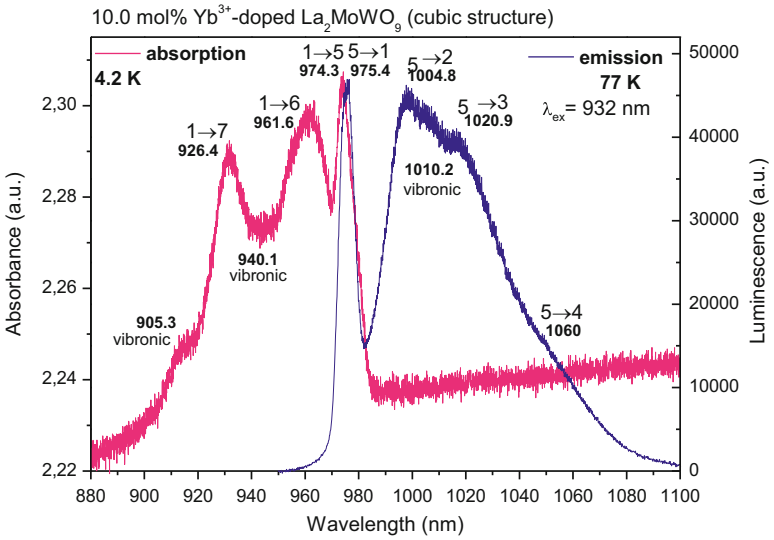

Fig. 17.12 Superposition of the absorption spectra at 4.2 K, emission spectra at 77 K of 10 mol% Yb^{3+}-doped mixed La_2MoWO_9 cubic molybdato-tungstates under Ti-sapphire laser excitation

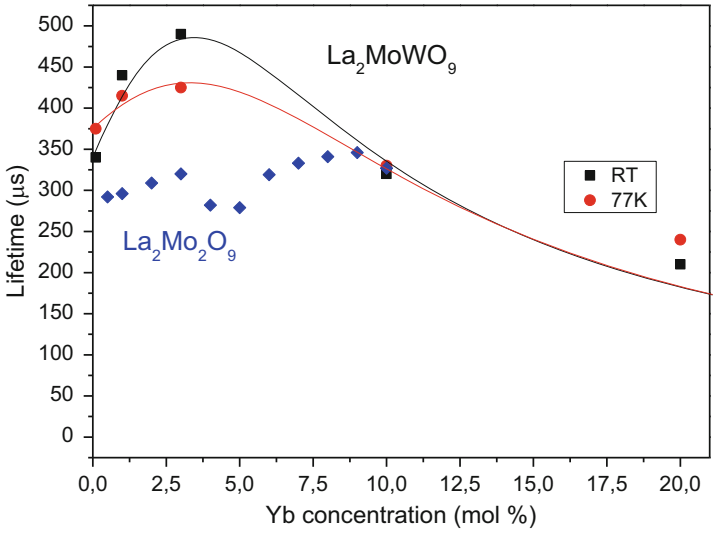

Fig. 17.13 Comparative concentration dependence of experimental decay times in Yb^{3+}-doped $La_2Mo_2O_9$ and Yb^{3+}-doped La_2MoWO_9 with different concentration of Yb^{3+} ions

laser laser pulsed excitation under $\lambda_{ex} = 975$ nm by monitoring $^2F_{5/2} \rightarrow {}^2F_{7/2}$ luminescence at $\lambda_{em} = 1030$ nm for the Yb^{3+}-doped $La_2Mo_2O_9$. These decays are considered as exponential profiles with an excellent approximation. Only the

points for the first μs deviate from the exponential as a result of an energy transfer between multisite Yb^{3+} ions. The values of the experimental lifetimes strongly depend on amount of Yb^{3+} ions as shown in Fig. 17.13. Among the whole series a slight increase of decay times is observed with approaching to 320 μs for 3 mol% Yb^{3+}. Then, the clearly visible reduction of value lifetimes is noticed for 4 and 5 mol%, which may be caused by the appearance of a new cubic phase. Above 5 mol% of Yb^{3+} ions, the decay lifetimes increase again from 319 μs up to 346 μs related to 6 and 9 mol% and increase again up to the slightest reduction to 327 μs for 10 mol%. There is evident correlation between the structural change from the monoclinic form ($Yb^{3+} \leq 2$ mol%) to the cubic form ($Yb^{3+} \geq 3$ mol%) and the decay lifetimes. An increase of Yb^{3+} ions contributes to the resonant diffusion process between the Yb^{3+} ions in all compounds and manifests as self-trapping phenomenon so that Fig. 17.13 shows the same behavior of the self-trapping effect for the two phases till 10 mol% of Yb^{3+} ions. The change of monoclinic and cubic structures indicates irregular changes of lifetimes has been compared with Yb^{3+}-doped $La_2Mo_2WO_9$ solid solutions which was described by the two usual phenomena of self-trapping effect and self-quenching effect [47]. Respectively, for the same activator concentrations are noticeable much longer decay lifetimes for Yb^{3+}-doped La_2MoWO_9 than for Yb^{3+}-doped $La_2Mo_2O_9$ solid solutions. It can suggest less number of resonant transitions of the $^2F_{5/2} \leftrightarrow {}^2F_{7/2}$ 0-phonon line and so shorter distances of light between the grains of Yb^{3+}-doped $La_2Mo_2O_9$: solid solutions.

17.3.1.8 Comparative Analysis of 3 mol% Yb^{3+}-Doped $La_2Mo_2O_9$ and 3 mol% Yb^{3+}-Doped La_2MoWO_9 Ceramics

First translucent ceramics of 3 mol% Yb^{3+}-doped $La_2Mo_2O_9$ and 3 mol% Yb^{3+}-doped La_2MoWO_9 ceramics have been successfully fabricated. The comparison turns out in favor of Yb^{3+}-doped mixed La_2MoWO_9. The structural and spectroscopic differences are also significant for these materials. Figure 17.14 presents SEM images with the EDS elemental analysis performed for 3 mol% Yb^{3+}-doped $La_2Mo_2O_9$ and 3 mol% Yb^{3+}-doped La_2MoWO_9 micro-ceramics sintered at 1200 °C/6 h in vacuum. For both cases the images indicate inhomogeneous morphology consisted of quite large grains with circular shape and much smaller, white points mostly accumulated at the grain boundaries (Fig. 17.21). According to the EDS analysis, the white points contain higher amount of Yb^{3+} ions than at the grains surface. The identification of this additional phase (white points) is very difficult due to the lack in crystallographic data base of standard corresponding to this phase. The performed analysis of morphology for both ceramics shows the troubles with obtaining transparent ceramics contained only one pure phase of Yb^{3+}-doped $La_2Mo_2O_9$ or Yb^{3+}-doped La_2MoWO_9. From Fig. 17.14 we see that La_2MoWO_9 ceramics is less yellow and characterized by better translucency.

Figure 17.15 presents comparison of room temperature and 4.2 K absorption spectra of Yb^{3+}-doped $La_2Mo_2O_9$ and Yb^{3+}-doped La_2MoWO_9 ceramics pre-

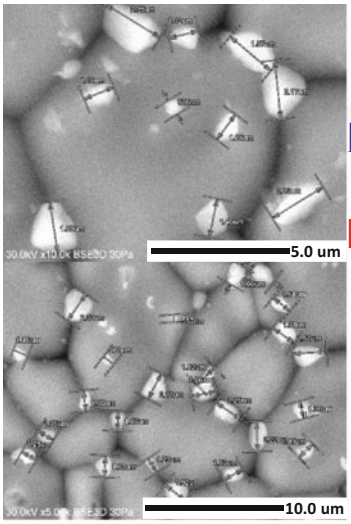

$La_2Mo_2O_9$: Yb^{3+} 3 mol% ceramics

elements	La	Yb	Mo	O
regular grain [at%]	11.20	0.28	15.16	73.36
regular grain [at%]	11.71	0.41	15.75	72.13
elements	**La**	**Yb**	**Mo**	**O**
white point [at%]	9.84	4.94	14.07	71.16
white point [at%]	8.80	3.54	12.84	74.81

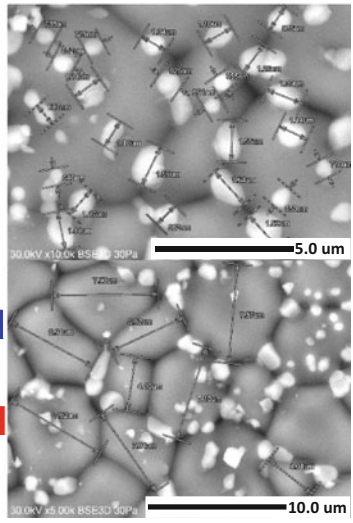

La_2MoWO_9:Yb^{3+} 3 mol% ceramics

elements	La	Yb	Mo	W	O
regular grain [at %]	10.79	1.03	7.60	6.85	73.74
regular grain [at %]	11.63	1.19	7.84	7.35	71.99
elements	**La**	**Yb**	**Mo**	**W**	**O**
white point [at %]	7.71	11.73	3.78	6.27	70.51
white point [at %]	8.01	9.67	4.41	6.25	71.66

Fig. 17.14 SEM images with the EDS elemental analysis performed for 3 mol% Yb3^{3+}-doped $La_2Mo_2O_9$ and 3 mol% Yb^{3+}-doped Yb^{3+}-doped La_2MoWO_9 micro-ceramics sintered at 1200 °C/6 h in vacuum

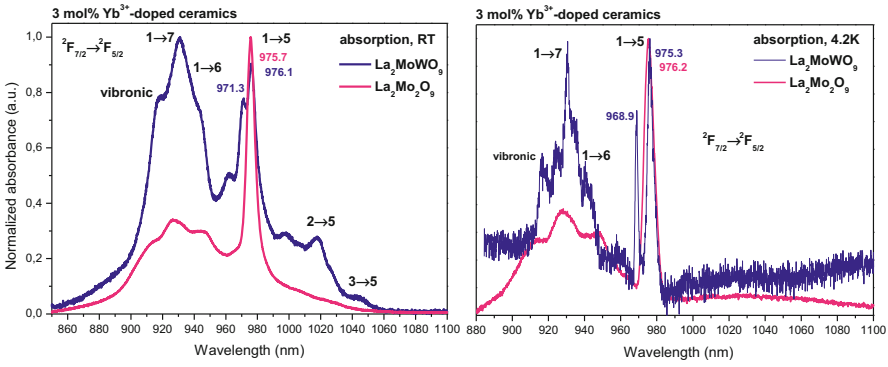

Fig. 17.15 Room and low temperature (4.2 K) absorption spectra of 3 mol% Yb^{3+}-doped $La_2Mo_2O_9$ and 3 mol% Yb^{3+}-doped La_2MoWO_9 sintered micro-ceramics

pared in the same annealing conditions at 1200 °C/6 h in vacuum. The room temperature absorption spectra reveals clearly visible differences of shape and number of components in the 850–1100 nm spectral range. Going to the low temperature absorption spectra, the differences are more pronounced. Only in case of Yb^{3+}-doped La_2MoWO_9, the intense 0-phonon line (1 → 5 transition) has two components, one at 968.9 nm at 4.2 K caused by the presence of the stoichiometric Yb_2MoO_6 in white points of Fig. 17.14 (11.73 at% and 9.67 at.% respectively) and another one at 976.2 nm at 4.2 K in the regular phase of Yb^{3+}-doped La_2MoWO_9. Therefore, on absorption spectra of Yb^{3+}-doped $La_2Mo_2O_9$ is visible only one component of 0-phonon line at 976.2 nm at 4.2 K. It is worth note that the 0-phonon line is relatively wide and a full width at half maximum (FWHM) equals to 72 cm^{-1} for molybdate and 44 cm^{-1} for molybdato-tungstate system. It may be suggest different distribution of the crystallographic Yb^{3+} sites in both structures. Additionally, even at low temperature absorption bands of Yb^{3+}-doped La_2MoWO_9 are more structured by existence of additional components primarily in the 900–970 nm spectral range.

The luminescence properties of 3 mol% Yb^{3+}-doped $La_2Mo_2O_9$ and 3 mol% Yb^{3+}-doped La_2MoWO_9 ceramics were investigated by using selective lines of Ti-sapphire laser in Fig. 17.16. The spectra were measured both at room and 77 K. As we can see, the common graph of emission spectra for Yb^{3+}-doped $La_2Mo_2O_9$ revealed mostly the same shape emission lines recorded at low temperature by changing the excitation wavelength and quite similar emission spectra at room temperature with the most intense and broad 0-phonon line at 977 nm as well as weakly resolved (5 → 2, 5 → 3, 5 → 4) emission lines in the 980–1080 nm spectral region. In contrast to that, the low temperature (77 K) emission spectra of 3 mol% Yb^{3+}-doped La_2MoWO_9 demonstrated the splitting of 0-phonon line into two components at 975 nm and 978 nm that affirmed the multisite character of Yb^{3+} ions most probably related to the two main YbO_7 and YbO_8 polyhedra.

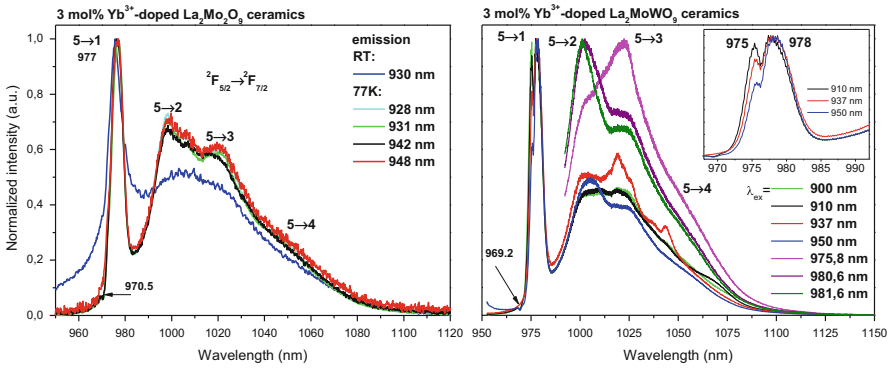

Fig. 17.16 Site selective emission spectra of 3 mol% Yb^{3+}-doped $La_2Mo_2O_9$ and 3 mol% Yb^{3+}-doped La_2MoWO_9 sintered micro-ceramics, measured under different excitation lines of the Ti-sapphire laser

Also changes in the intensity ratio of the emission lines strongly dependent on the excitation wavelengths. Additionally, the emission spectra of 3 mol% Yb^{3+}-doped La_2MoWO_9 includes one hole at 969.2 nm as signature of the reabsorption line corresponding to the additional 0-phonon line in the absorption spectra at 4.2 K presented in Fig. 17.15. This absorption line is associated with the unknown tetragonal Yb^{3+}-rich phase, which is observed as white points on the grain boundaries in Fig. 17.14 [46, 47]. In the case of the excitation line at 937 nm, we observed more than three bands in the range from 990 to 1100 nm, which should correspond to transitions from the lowest Stark level of the $^2F_{7/2}$ excited state (5) to Stark levels 2, 3, or 4. The multiplicity of emission lines point out a multisite character of the samples.

17.3.1.9 Conclusion for Yb^{3+}-Doped $La_2Mo_2O_9$/Mixed La_2MoWO_9 Cubic Materials

The structural studies for the first group: $La_2Mo_2O_9$ activated by Yb^{3+} dopants from 0.5 mol% to 25 mol% reveal the low solubility limit of 3 mol% Yb^{3+} ions in the $La_2Mo_2O_9$ host lattice. A small quantity of active ions ($\leq$2 mol% of Yb^{3+}) leads to obtain the pure monoclinic structure, while when the amount of Yb^{3+} ions is above 3 mol%, the mixture of two phases, the cubic structure of Yb^{3+}-doped $La_2Mo_2O_9$ and the additional phase of monoclinic stoichiometric Yb_2MoO_6, was detected. Depending on the concentration of Yb^{3+} ions, the obtained molybdates have different morphology. If the amount of dopant is less than 3 mol% good quality homogeneous particles, mostly in spherical shape are observed. In case of higher concentration of Yb^{3+} ions the irregular clusters of grains without visible grain boundaries covered by a second phase in the form of cube-shaped crystals are present. This second phase is corresponding to the monoclinic stoichiometric Yb_2MoO_6 phase. The low temperature emission spectra of Yb^{3+} probe ions-doped $La_2Mo_2O_9$ show three components of 0-phonon line for monoclinic molybdates and broad but not resolved 0-phonon line for cubic molybdates. Both results indicate the multisite character of Yb^{3+} ions in each of main un-equivalent sites of the $La_2Mo_2O_9$ structure which are consistent with research performed for Yb^{3+}-doped mixed La_2MoWO_9. Consequently, it can be assumed that the environment of all Yb^{3+} ions can be distinguished as, first of all, two types of polyhedra YbO_7 and YbO_8 like in Yb^{3+}-doped La_2MoWO_9 and secondly by a third type of YbO_9 polyhedron. Our results are confirmed by the decay time measurements. Summing up the results, it is evident strongly influence of the concentration of Yb^{3+} ions and type of crystallographic system on the luminescence properties.

In view of continuous research on application of the cubic molybdates or tungstates as cubic laser ceramics, the new Yb^{3+}-doped $La_2Mo_2O_9$ are less promising candidates in contrast to the Yb^{3+}-doped mixed La_2MoWO_9, which stabilize the pure cubic system in a whole concentration range (0.1–20 mol%). Also all the samples are very homogeneous.

We have shown that Yb^{3+} rare earth is a probe ion. It gives a new deeper contribution of the complex structure of both La_2MoO_9 and La_2MoWO_9 molybdate families. Our approach is similar with the analysis we have previously done with Nd^{3+} ion, which can be also used as a structural probe one. More generally we should bring all contributions to the knowledge of these crystallographic structures from the spectroscopic properties of rare earth optical ions. In this way, the spectroscopy of Eu^{3+} rare earth probe ion should bring complementary results in the next step.

First translucent ceramics of 3 mol% Yb^{3+}-doped $La_2Mo_2O_9$ and 3 mol% Yb^{3+}-doped La_2MoWO_9 ceramics have been successfully fabricated. The comparison turns out in favor of Yb^{3+}-doped mixed La_2MoWO_9. The structural and spectroscopic differences are also significant for these materials. SEM images with the EDS elemental analysis show for both cases inhomogeneous morphology consisted of quite large grains with circular shape and much smaller, white points mostly accumulated at the grain boundaries which contain higher amount of Yb^{3+} ions than at the grains surface. So, in both cases we deal with phase segregation in first translucent ceramics.

17.3.2 Yb^{3+}-Doped Y_6MoO_{12}

17.3.2.1 Structure Characterization

Basing on the article of Fournier [64] from 1970 devoted to deep research on Ln_2O_3-MoO_3 systems and Ln_6MoO_{12} phases, we know that Y_6MoO_{12} ($3Y_2O_3$:MoO_3) can exist in two forms: until 1480 °C – low temperature orthorombic phase and above 1500 °C – high temperature face cantered, cubic (Z = 4) structure, which is very stable. The compositions with chemical formula Ln_6MoO_{12} previously investigated by Aikten [65] and Bartram [66] were attributed to the cubic and orthorhombic structures. Fournier et al. have repeated the investigations by preparing the samples at 1350 °C, excepting the Y_6MoO_{12} and Er_6MoO_{12} obtained at 1500 °C. Thanks to this research which we know that stoichiometric molybdates with La, Pr, Nd, Sm, Eu, Gd, Tb, Dy and Ho crystallize in the cubic phase already at 1350 °C [64]. The three last lanthanides *i.e.* Tm, Yb and Lu do not give the cubic Ln_6MoO_{12} phase event at 1525 °C. Maybe this transformation could be possible at much higher temperature. It is necessary to add that all information on the structure of Ln_6MoO_{12} described by Fournier based on the refinements of XRD powder patterns and in the literature there is no information of crystal structure from the single crystals of Y_6MoO_{12}. This is why it is a great need to obtain samples in the form of single crystals.

Nevertheless, the crystal structure of Y_6WO_{12} crystalized in the rhombohedral system (S.G. R3 and Z = 3 for the R-centered setting) from the Rietveid refinement reported by Diot [67] can be helpful to discussion of Y_6MoO_{12} structure. Obtained at 1300 °C/24 h ternary oxides of Y_6WO_{12} crystallize with a three-dimensional

rhombohedral structure closely related to that of the binary oxides Ln_7O_{12} and deriving from the ideal fluorite structure. In this case the yttrium ion is sevenfold coordinated with Y-O bond length ranging from 2.19 to 2.70 Å. The coordination polyhedron may be described as a mono-capped trigonal prism. The tungsten atom is located at the center of a WO_6 octahedron with unique W-O distances of 1.98 and 1.92 Å. In the crystal structure of Y_6WO_{12}, W atoms occupy 3a (0, 0, 0) octahedral sites with six O atoms around them, forming slightly deformed WO_6 octahedra, while Y atoms occupy 18f (x, y, z) sites and they are coordinated to three O1 atoms and four O2 atoms, having C_1 point symmetry. The WO_6 and YO_7 polyhedra are connected each other by sharing corners and edges [67]. It is important to notice that at the temperature 1200 °C/12 h the Y_6WO_{12} represents the hexagonal system. According to the literature, [66, 68, 69] Y and Mo ions be distributed randomly in the cationic sublattice, and O ions and O vacancies should be distributed randomly in the anionic sublattice. An ordered distribution of Mo and O vacancies will result in a related hexagonal phase. For the isostructural Y_6WO_{12}, the disordered cubic fluorite phase is considered to be metastable. As regard to Y_6MoO_{12}, a coexistence of cubic and hexagonal phases was obtained from solid-state reaction, while the only cubic phase was observed from the chemical solution method [54]. This indicates that the stability of the cubic phase is equivalent or surpassing that of the hexagonal phase.

The Yb^{3+}-doped Y_6MoO_{12} micro-powders were characterized by XRD method to verify the phase purity. Figure 17.17 plots experimental results as a function of the Yb^{3+} concentration compared with the simulated XRD pattern of cubic Y_6MoO_{12} (ICSD#30-1456) from the database of inorganic crystal structures [31]. It is obvious that all the diffraction peaks of these samples are in good agreement with the pure Y_6MoO_{12} and no other phases as impurities can be detected. This result indicates that the Yb^{3+} ions were completely incorporated into the Y_6MoO_{12} host lattice without making significant changes to the crystal structure. As the ionic radius of Yb^{3+} ($r = 0.925$ Å, $CN = 7$) is smaller that of Y^{3+} ($r = 0.96$ Å, $CN = 7$), we suppose that Yb^{3+} ions occupy Y^{3+} sites. The un-doped and Yb^{3+}-doped Y_6MoO_{12} crystallize as disordered cubic fluorite phase with a space group of Fm-3 m and the lattice constants are calculated to be $a = 5.29$ Å. From literature we know also that the fluorite structure is capable to construct superstructures with its flexible nature [29, 31].

The lattice parameter calculated basing on the indexing powder diffraction patterns were reported recently [49]. The substitution of Y^{3+} ions by smaller Yb^{3+} leads to systematic decrease in the lattice parameters, thus we observed linear dependence of lattice constant vs. Yb^{3+} content for cubic Yb^{3+}-doped Y_6MoO_{12}. Furthermore, using the pycnometric method, an experimental density of each obtained solution was determined. The unit cell parameter and the volume calculated for each analyzed solution satisfy the Vegard law [49].

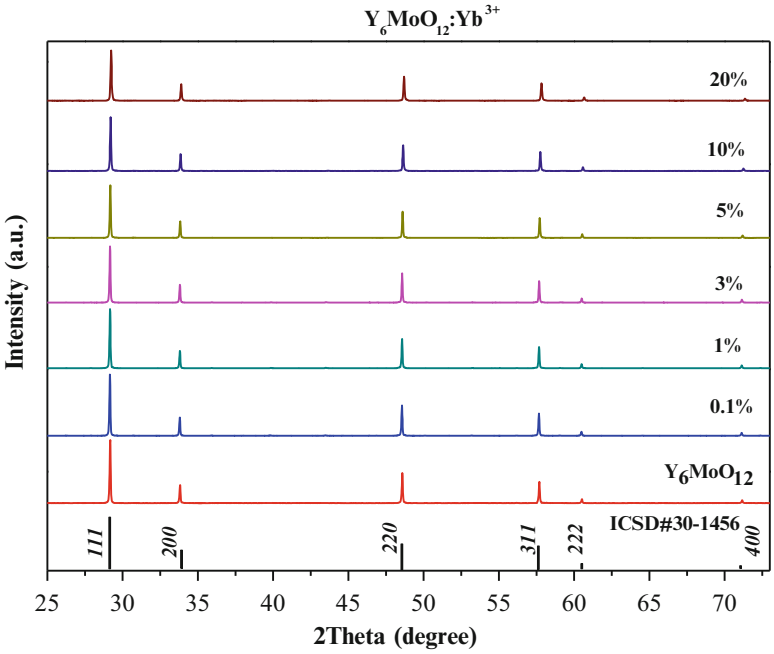

Fig. 17.17 X-ray powder diffraction patterns of Y_6MoO_{12} and Yb^{3+}-doped Y_6MoO_{12} solid solutions with different contents of the Yb^{3+} optically active ions

17.3.2.2 Morphology and Particle Size by SEM

According to very high sintering temperatures (1550 °C) applied in the solid-state reaction to obtain pure cubic phase the grains formed micro-crystallites with a grain size in the range from 0.5 to even 8 μm. A large impact on the size has also the fact that the reactions do not occur quickly and violently as in the case of the combustion method.

As an example in Fig. 17.18 we present the SEM (Scanning Electron Microscope) micrographs Y_6MoO_{12} compound and Yb^{3+}-doped Y_6MoO_{12} solid solutions with a different content of the active ion. The overview pictures show a good quality materials. Aggregates composed of grains and a type of boundary between the microcrystals of powders with different concentrations of Yb^{3+} ions can be seen. The overview pictures show separated particles and loose clusters. However, they create also the bigger forms by aggregation of the smaller grains of irregular forms. For Yb^{3+}-doped Y_6MoO_{12} solid solutions no second phase formation was observed, the samples are very homogeneous.

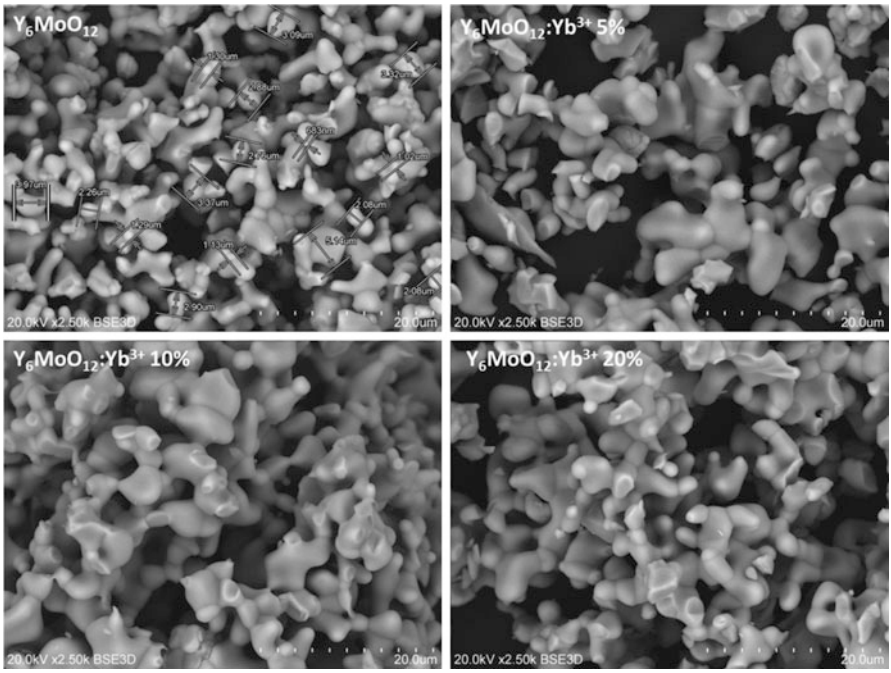

Fig. 17.18 SEM micrographs of Y_6MoO_{12} and Yb^{3+}-doped Y_6MoO_{12} solid solutions

17.3.2.3 Absorption Spectra

The relative energy of the Yb^{3+} Stark levels was investigated by optical absorption (4.2 K) and photoluminescence (77 K) measurements in near infrared region (NIR). Fig. 17.19 presents the absorption spectra for 20 mol% Yb^{3+} in Y_6MoO_{12} recorded at room and liquid helium temperatures. At RT the spectra consist of broad weakly resolved bands located between 850 nm and 1100 nm corresponding to the transition from the $^2F_{7/2}$ ground state of Yb^{3+} to the three Stark components of the $^2F_{5/2}$ excited state. The absorption line relates to the so-called zero phonon line, from the lowest Stark component to the $^2F_{7/2}$ (1) ground state to the lowest Stark level of the $^2F_{5/2}$ (5) is located at around 976 nm and it is the strongest absorption line. The others lines corresponding to the $^2F_{7/2}$ (1) → $^2F_{5/2}$ (6) and to $^2F_{7/2}$ (1) → $^2F_{5/2}$ (7) transitions are at room temperature not very well formed. Going to the low temperature we are able to distinguish four components located at 875, 905, 920 and 949 nm, respectively. We supposed that the bands of highest intensities at 920 and 949 nm originated from (1) → $^2F_{5/2}$ (7) and $^2F_{7/2}$ (1) → $^2F_{5/2}$ (6) transitions respectively and those at 875 and 905 nm might possess the vibronic character, the same as the line of small intensity at 963 nm.

The measurements performed at 4.2 K should lead to narrowing and better resolution of the main electronic Stark components, however it is not case for

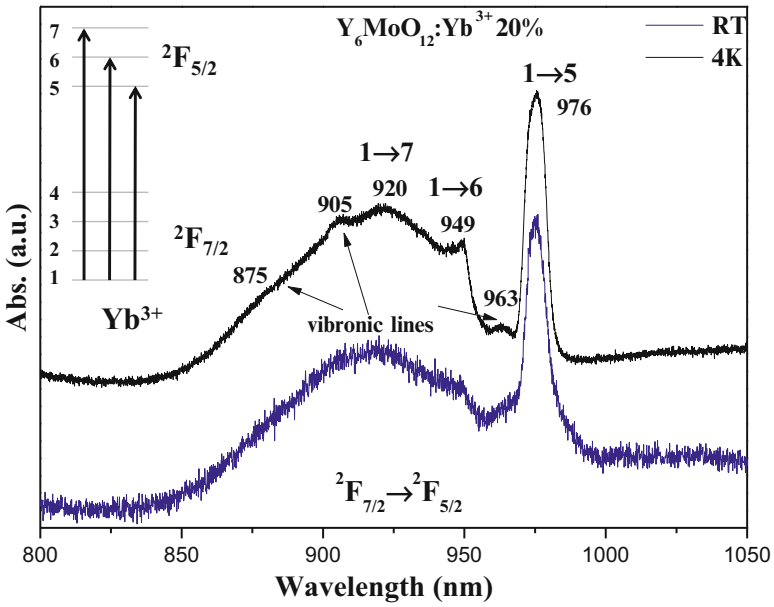

Fig. 17.19 Absorption spectra of Yb^{3+}-doped Y_6MoO_{12} solid solution recorded at room and liquid helium temperatures

Y_6MoO_{12} host lattice. As the ionic radius of Yb^{3+} (r = 0.925 Å, CN = 7) is slightly smaller that of Y^{3+} (r = 0.96 Å, CN = 7), we supposed that the Yb^{3+} ions introduced to the network occupy the Y^{3+} site. There is not a very large difference in the ionic radii, so that the disorder in the structure will not be significant. It will be at least smaller than in case when we substitute the La^{3+} ion (r = 1.1 Å, CN = 7) by the Yb^{3+} one [47].

According to the crystal-field theory of Kramer's ions, the maximum of allowed components splitting for J = 5/2 state is three; therefore, for one symmetry site the absorption spectrum at liquid helium temperature should be resolved into three bands. The 0-phonon line is a sharp one and contains only one component at 4.2 K. The total splitting of the excited $^2F_{5/2}$ state 624 cm^{-1} is similar like that observed for some other matrices like sesquioxides (about 793 cm^{-1}) [70], $K_5Bi(MoO_4)_4$ molybdates [71] orthohosphates (750–800 cm^{-1}) [72] but much larger than we reported recently for La_2MoWO_9 474 cm^{-1} [47] and 454 cm^{-1} for $CdMoO_4$ [26]. The interest of high splitting is clear for solid state lasers with a near 4-levels scheme.

17.3.2.4 Concentration Dependence and Excitation Wavelength Dependences of the Photoluminescence Spectra

The emission spectra of Y_6MoO_{12} activated with different concentrations of Yb^{3+} ion registered at room temperature under λ_{ex} = 915 nm of a Ti- Sapphire laser are

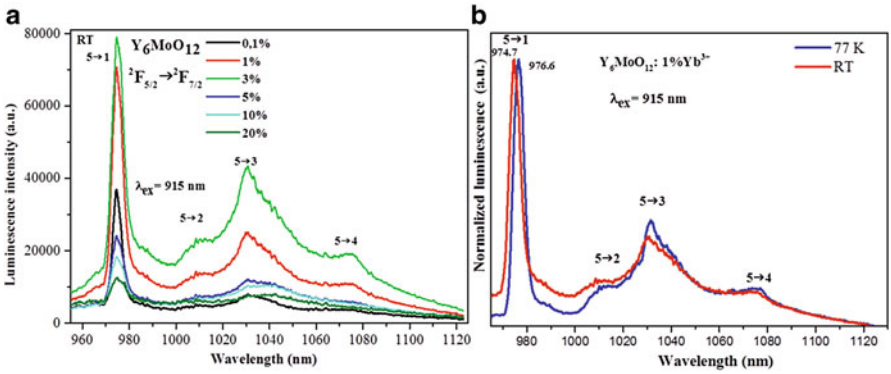

Fig. 17.20 Room temperature (RT) emission spectra of Yb^{3+}-doped Y_6MoO_{12} solid solutions with different concentrations of Yb^{3+} activator

plotted in Fig. 17.20a. The studied materials exhibit the usual luminescence lines in the near-infrared region from the $^2F_{5/2} \rightarrow {}^2F_{7/2}$ transitions of Yb^{3+} ions. At RT the lines are broad, however it is possible to distinguish the four components corresponding to the transitions from the lowest Stark level of the $^2F_{5/2}$ excited state (5) to each of the four Stark levels of the $^2F_{7/2}$ state (1, 2, 3, 4), respectively.

The (5 → 1) component is located at around 975–977 nm. In case of Y_6MoO_{12} solid solutions we can distinguish the lines at 974.7 nm (5 → 1), 1010 nm (5 → 2), 1030 nm (5 → 3) and 1075 nm (5 → 4). Starting from 5 mol% up to 20 mol% one can distinguish a second component of the 0-phonon (5 → 1) line located at 977 nm indicating a second type of Yb^{3+} site in this matrix. The maximum concentration of Yb^{3+} ions in this host lattice where the luminescence intensity is the highest was set at 3 mol%. For this sample, and also for 1 mol%, we can observe also very low components at 965 nm and 987 nm, which may correspond to vibronic transitions. Going to the 4.2 K the shape of the emission spectra stay the same although we should observe the narrowing of the lines. Very slight narrowing of the lines was also observed in the absorption spectra presented in the previous paragraph indicating some disorder degree of the active ions in the host. A clear change observed in the emission spectra of low Yb^{3+} concentration (1%) with decreasing temperature is the shifting of the 0-phonon line from 974.7 nm at RT to 976.6 nm at 4.2 K (see Fig. 17.20b). The multisite distribution of Yb^{3+} ions in Y_6MoO_{12} solid solution as a probe of some disorder can be seen by the temperature dependence of both, the unusual slight shift of the 0-phonon line in luminescence spectra, and almost the same half-widths at half maximum (FWHM) of this 0-phonon line (54 cm^{-1} at 77 K and 59 cm^{-1} at RT). Low temperature emission spectra recorded under site selective excitation of Ti-sapphire laser are presented in Fig. 17.21 for 1% Yb^{3+}. The spectra are normalized to show the differences in the shape of lines under different excitation wavelength. Nevertheless, we have performed also the comparison of the luminescence intensity of all samples by recording the spectra under the same conditions. The highest intensity has been observed for 5 → 3

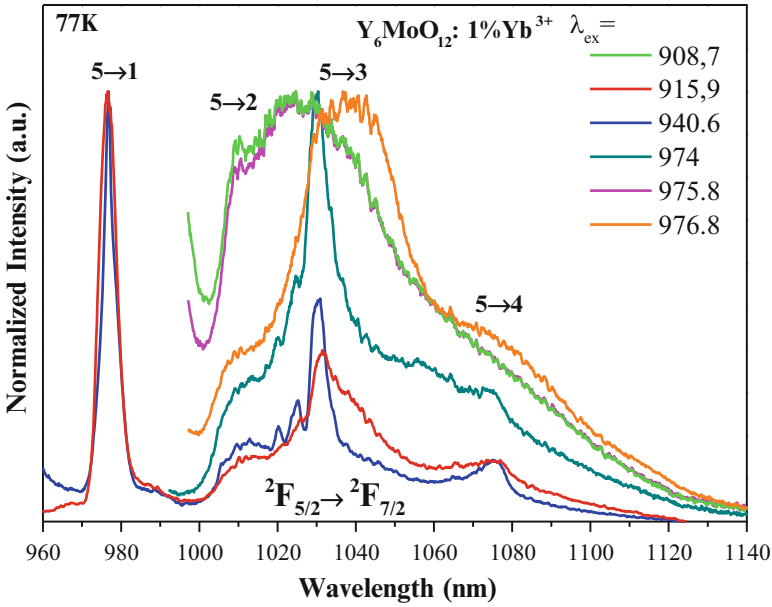

Fig. 17.21 Low temperature emission spectra of 1 mol% Yb^{3+}-doped Y_6MoO_{12} solid solution under site selective excitations of Ti-sapphire laser

transition at 1030 nm (the laser line when materials are used as laser source) under 974 nm pumping. It is between 2.8 times and 7 times more higher than for any other excitation lines of the tunable Ti-sapphire. The position of zero-phonon line from the absorption spectra stay in good agreement with that from the emission. Under the excitation of 915.9 nm four lines are clearly resolved. The main lines corresponding to the four Stark emission components are located at 976 nm (5 → 1), 1010 nm (5 → 2), 1030 nm (5 → 3) and 1075 nm (5 → 4), respectively. Under excitation at 940.6 nm the additional weak components at 1020 nm and 1025 nm is the result of electron– phonon coupling with M–O modes. When the excitation wavelength changes we can especially observe the shifting of the 5 → 3 transition to higher energy wavelengths i.e. at 1025 nm for excitation 908.7 nm and 975.8 nm or to infrared region (1037 nm) for excitation at 976.8 nm confirming the distribution of Yb^{3+} ions in, at least, three non- equivalent sites in the lattice. In addition, these bands start to be broad and the shifting from 1025 nm to 1037 nm is a result of changing the excitation line of only of 1 nm. We suppose in the case of Y_6MoO_{12} we observe the main distribution of Yb^{3+} ions under excitation at 915.9, 940.6 and 974 nm respectively, giving the highest intensity of the usual laser line at 1030 nm. We obtain similar well resolved spectra and two slightly distorted symmetry sites of Yb^{3+} ions for other excitations yielding the shifted lines observed at 1025 and 1037 nm.

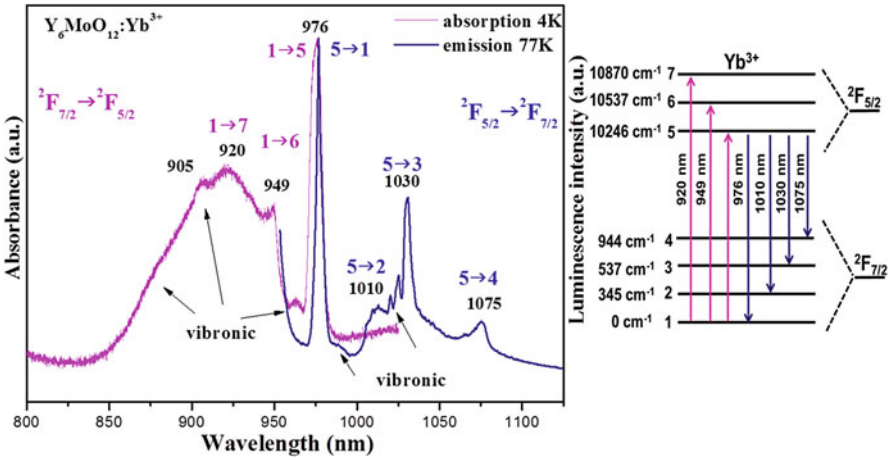

Fig. 17.22 Absorption and emission spectra at low temperatures and Stark splitting levels of Yb^{3+} ion

17.3.2.5 Yb^{3+} Energy Level Diagram in Y_6MoO_{12}

Figure 17.22 presents the low temperature absorption and emission spectra of 10 mol% Yb^{3+}-doped Y_6MoO_{12} which allowed to propose the drawn energy level scheme of Yb^{3+} ion in this matrix. An energy level diagram can be derived from low temperature measurements. The splitting both of ground state as well as the excited state is quite large if we compare with other cubic matrix recently reported by us *i.e.* Yb^{3+}-doped La_2MoWO_9.

17.3.2.6 Decay Analysis

The decay curves of x% Yb^{3+}-doped Y_6MoO_{12} solid solutions (x-0.1-50) were obtained under laser pulsed excitation at 940 nm (some of them at 980 nm) in the $^2F_{7/2}$ (1) → $^2F_{5/2}$ (6) absorption line and by monitoring 1030 nm $^2F_{5/2}$ (5) → $^2F_{7/2}$(2) emission. Table 17.2 summaries the decay times for Yb^{3+}-doped Y_6MoO_{12} with different concentration of Yb^{3+} ions recorded at room and low temperatures. The decays curves (not shown here) are exponential at low temperature for most of samples while at room temperature only for the lowest concentration (0.1 mol%) the decay curve keep the exponential shape with a fitted lifetime of about 285 μs at room temperature and 340 μs 77 K corresponding to the radiative lifetime. For the concentration of 3 and 5% energy transfer occurs between centers. Then, for the concentration above 10% self-quenching phenomena is predominant. When we compare Yb^{3+}-doped Y_6MoO_{12} solid solutions with another cubic composition evaluated recently by us as Yb^{3+}-doped La_2MoWO_9 and also with tetragonal Yb^{3+}-doped $CdMoO_4$ solid solution, we clearly see the difference [47, 73] concerning

Table 17.2 Luminescence decays times of cubic Yb^{3+}-doped Y_6MoO_{12} solid solutions recorded at room temperature and 77 K, $\lambda_{ex} = 940$ nm (some of them at 980 nm) and $\lambda_{em} = 1030$ nm

	0.1%	1%	3%	5%	10%	20%	50%
RT (μs)	285	250	128	45	17	6.5	1.5
77 K (μs)	340	340	275	112	32	11	2

the usual self-trapping process which is not observed in this matrix. Only the self-quenching process appears here. For investigated previously micro-crystallites, also obtained by the high temperature solid state method, with similar grain sizes the transfer of energy between the Yb^{3+} ions i.e. self-trapping process was easily observed due to short distances between Yb^{3+} ions where resonant diffusion occurs (3.66 Å in $CdMoO_4$ and 3.15 Å in La_2MoWO_9). It means that in Yb^{3+}-doped Y_6MoO_{12} the unknown distance between Yb^{3+} ions should be much higher than these values to reduce this process.

17.3.2.7 Conclusion on Yb^{3+}-Doped Y_6MoO_{12} Cubic Material

Other investigated group is Yb^{3+}-doped Y_6MoO_{12} solid solutions crystallizing as disordered cubic fluorite phase with a space group of Fm-3 m and the calculated lattice constants 5.29 Å. This material is thermally stable up to 1500 °C. All micro-powders obtained by high-temperature solid state reaction possess the yellow colour. The SEM images showed relatively big grains with the average size of few micrometers (0.5–8 μm) due to the high temperature (1550 °C) of synthesis. All the samples are very homogenous without other phase segregation and no significant change of the grain size with changing the activator concentration is observed. Relatively broad absorption lines in NIR region suggest disordering of the active ions in the structure. This phenomena is smaller than for cubic Yb^{3+}-doped La_2MoWO_9 molybdato-tungstates, what is a consequence of the smallest difference of ionic radii between Yb^{3+} (0.925 Å, CN = 7) and Y^{3+} (0.96 Å) ions in Yb^{3+}-doped Y_6MoO_{12} than between Yb^{3+} (0.925 Å) and La^{3+} (1.1 Å) ions in Yb^{3+}-doped La_2MoWO_9. Well formed in low temperature absorption spectra electronic transitions point out only one symmetry site in Yb^{3+}-doped Y_6MoO_{12}, but we observe also many vibronic components, what make very difficult the interpretation of the spectra. The NIR emission spectra recorded at RT are characterized by broad lines, and it is possible to distinguish four components corresponding to the transitions from the lowest Stark level of the $2F_{5/2}$ excited state (5) to each of the four Stark levels of the $^2F_{7/2}$ state (1, 2, 3, 4), respectively. Also in this case the band are assisted by the vibronic transitions. Very slight narrowing of the emission lines like in the absorption spectra is indicating a disorder of the active ions in the host. The multisite character in Yb^{3+}-doped $Y6MoO_{12}$ has been confirmed by the shifting of the 0-phonon line from 974.7 nm at RT to 976.6 nm at 4.2 K under the same excitation at 915 nm. Another evidence for the multisite character can be found in the site selective excitation spectra, where

change of excitation lines results in three different spectra. Thus, we observe three types of Yb^{3+} site symmetry, one main distribution of Yb^{3+} ions and two slightly distorted sites. Basing on the low temperature absorption and emission energy level diagram has been proposed. When we compare with other cubic matrix recently reported by us, i.e. Yb^{3+}-doped La_2MoWO_9, one can notice the advantage of the largest splitting both of the $^2F_{7/2}$ ground state as well as the $^2F_{5/2}$ excited one with Y_6MoO_{12} molybdate what is an important property in laser materials. The decays curves are exponential at low temperature for most of samples while at room temperature only for the lowest concentration (0.1 mol%) the decay curve keep the exponential shape with a fitted lifetime of about 285 μs and 340 μs 77 K corresponding to the radiative lifetime. When the concentration of Yb^{3+} ions increases the usual energy transfer occurs between centers so that the self-quenching phenomena is predominant. We didn't observe any self-trapping effect in this matrix meaning higher distances between Yb^{3+}- Yb^{3+}) ions than in cubic Yb^{3+} – doped La_2MoWO_9 and tetragonal Yb^{3+}-doped $CdMoO_4$ previously analyzed by us.

Concluding, the first studies have shown many advantages of this material and in the step of our program we will prepare the nano-powdered samples to succeed the fabrication in the form of transparent optical ceramics.

17.4 General Conclusion

A purpose of the paper is to summarize the first results obtained for Yb^{3+}-doped molybdates and molybdato-tungstates synthesized by the high-temperature solid-state reaction and crystallizing in the cubic system: $La_2Mo_2O_9$ /La_2MoWO_9 /Y_6MoO_{12} for future new transparent optical ceramics. We investigate the correlation between structural and spectroscopic properties of mentioned above compositions. Yb^{3+} rare earth dopant has been used as a structural probe in addition of the intrinsic interest to be a laser ion.

This probe ion gives a new deeper contribution of the complex structure of both La_2MoO_9, La_2MoWO_9 and Y_6MoO_{12} molybdate families. Our approach is similar with the analysis we have previously done with Nd^{3+} laser ion, which can be also used as a structural probe one. More generally we should bring all contributions to the knowledge of these crystallographic structures from the spectroscopic properties of rare earth optical ions. In this way, the spectroscopy of Eu^{3+} rare earth probe ion should bring complementary results in the next step.

The first studies of Yb^{3+}-doped Y_6MoO_{12} have shown many advantages of this material and in the step of our program we will prepare the nano-powdered samples to succeed the fabrication in the form of transparent optical ceramics.

The research is under progress to get high quality optical transparent ceramics from the technique of sintering nano-crystalline powders by using both the fast SPS (Spark Plasma Sintering) and known HIP (Hot Isostatic Pressing) techniques.

Acknowledgements The authors would like to thank for the financial support from National Science Center of Poland for the grant HARMONIA 8 No UMO-2016/22/M/ST5/00546 and also the Minister of Science and Higher Education in Poland and in France for the Grant POLONIUM for scientific exchange between Institute Light Matter (ILM), University Claude Bernard Lyon1, in France and Faculty of Chemistry, University of Wroclaw in Poland. Moreover, the financial support from the French Embassy in Warsaw (French Government scholarship for research stage for M. Guzik in Lyon) is gratefully acknowledge.

References

1. Dey S, Ricciardo RA, Cuthbert HL, Woodward PM (2014) Metal-to-metal charge transfer in AWO_4 (A = Mg, Mn, Co, Ni, Cu, or Zn) compounds with the wolframite structure. Inorg Chem 53:4394–4399
2. Feldmann C, Justel T, Ronda CR, Schmidt PJ (2003) Inorganic luminescent materials: 100 years of research and application. Adv Funct Mater 13:511–516
3. Brixner LH (1987) New X-ray phosphors. Mater Chem Phys 16:253–281
4. Mikhailik VB, Kraus H, Miller G, Mykhaylyk MS, Wahl D (2005) Luminescence of $CaWO_4$, $CaMoO_4$, and $ZnWO_4$ scintillating crystals under different excitations. J Appl Phys 97:083523
5. Mikhailik VB, Kraus H, Kapustyanyk V, Panasyuk M, Prots Y, Tsybulskyi V, Vasylechko L (2008) Structure, luminescence and scintillation properties of the $MgWO_4$-$MgMoO_4$ system. J Phys Condens Matter 20:365219
6. Kobayashi M, Ishii M, Harada K, Usiki Y, Okuno H, Shimizu H, Yazawa T (1996) Scintillation and phosphorescence of $PbWO_4$ crystals. Nucl Instrum Method Phys Res Sect A 373:333–346
7. Kaminskii A, McCray CL, Lee HR, Lee SW, Temple DA, Chyba TH, Marsh WD, Barnes JC, Annanenkov AN, Legun VD et al (2000) High efficiency nanosecond Raman lasers based on tetragonal $PbWO_4$ crystals. Opt Commun 183:277–287
8. Nikl M, Nitsch K, Polak K, Mihokova E, Dafinei I, Auffray E, Lecoq P, Reiche P, Uecker R, Pazzi GP et al (1996) Slow components in the photoluminescence and scintillation decays of $PbWO_4$ single crystals. Phys Status Solidi B 195:311–323
9. Pujol MC, Mateos X, Sole R, Massons J, Gavalda J, Solans X, Dias F, Aguilo M (2002) Structure, crystal growth and physical anisotropy of $KYb(WO_4)_2$, a new laser matrix. J Appl Crystallogr 35:108–112
10. Boulon G, Metrat G, Muhlstein N, Brenier A, Kokta MR, Kravchik L, Kalisky Y (2003) Efficient diode-pumped Nd:$KGd(WO_4)_2$ laser grown by top nucleated floating crystal method. Opt Mater 24:377–383
11. Brenier A, Bourgeois F, Metrat G, Muhlstein N, Boulon G (2001) Spectroscopic properties at 1.351 μm of Nd^{3+}-doped $KY(WO_4)_2$ and $KGd(WO_4)_2$ single crystals for Raman conversion. Opt Mater 16:207–211
12. Kaminskii AA (1981) Laser crystals: their physics and properties. Springer, Berlin/Heidelberg/New York
13. Feng X, Feng W, Xia M, Wang K, Liu H, Deng D, Qin X, Yao W, Zhu W (2016) Co-precipitation synthesis, photoluminescence properties and theoretical calculations of $MgWO_4$:Eu^{3+} phosphors. RSC Adv 6:14826–14831
14. Zhang WJ, Feng WL, Nie YM (2015) Photoluminescence properties of red europium doped calciumtungstate phosphors for blue-pumped light-emitting diodes. Optik 126:1341–1343
15. Feng WL, Tao CY, Wang K (2015) Synthesis and photoluminescence of tetravalent cerium-doped alkaline-earth-metal tungstate phosphors by a co-precipitation method. Spectrosc Lett 48:381–385
16. Itoh M (2012) Luminescence study of self-trapped excitons in $CdMoO_4$. J Lumin 132: 645–651

17. Sczancoski JC, Bomio MDR, Cavalcante LS, Joya MR, Pizani PS, Varela JA, Longo E, Li S, Andrés JA (2009) Morphology and blue photoluminescence emission of $PbMoO_4$ processed in conventional hydrothermal. J Phys Chem C 113:5812–5822
18. Minowa M, Itakura K, Moriyama S, Ootani W (1992) Measurement of the property of cooled lead molybdate as a scintillator. Nucl Instrum Method Phys Res Sect A 320:500–503
19. Hizhnyi YA, Nedilko SG (2003) Investigation of the luminescent properties of pure and defect lead tungstate crystals by electronic structure calculations. J Lumin 102−103:688–693
20. Kudo A, Steinberg MA, Bard J, Campion A, Fox MF, Mallouk TE, Webber SE, White JM (1990) Photoactivity of ternary lead-group VIB oxides for hydrogen and oxygen evolution. Catal Lett 5:61–66
21. Sczancoski JC, Cavalcante LS, Joya MR, Varela JA, Pizani PS, Longo E (2008) $SrMoO_4$ powders processed in microwave- hydrothermal: synthesis, characterization and optical properties. Chem Eng J 140:632–637
22. Sczancoski JC, Cavalcante LS, Marana NL, da Silva RO, Tranquilin RL, Joya MR, Pizani PS, Varela JA, Sambrano JR, Siu L et al (2010) Electronic structure and optical properties of $BaMoO_4$ powders. Curr Appl Phys 10:614–624
23. Thongtem T, Kungwankunakorn S, Kuntalue B, Phuruangrat A, Thongtem S (2010) Luminescence and absorbance of highly crystalline $CaMoO_4$, $SrMoO_4$, $CaWO_4$ and $SrWO_4$ nanoparticles synthesized by co-precipitation method at room temperature. J Alloys Compd 506:475–481
24. Feng W, Lin H, Liu H (2015) Photoluminescence and crystal-field analysis of Pr^{3+}-doped $SrMoO_4$ phosphors. Z Naturforsch 70(1a):11–16
25. Guzik M, Tomaszewicz E, Guyot Y, Legendziewicz J, Boulon G (2015) Structural and spectroscopic characterizations of new $Cd_{1-3x}Nd_{2x}€_xMoO_4$ scheelite-type molybdates with vacancies as potential optical materials. J Mater Chem C 3:40574069
26. Guzik M, Tomaszewicz E, Guyot Y, Legendziewicz J, Boulon G (2016) Spectroscopic properties, concentration quenching and Yb^{3+} site occupations in vacancied scheelite-type molybdates. J Lumin 169:755–764
27. Guzik M, Tomaszewicz E, Guyot Y, Legendziewicz J, Boulon G (2015) Eu^{3+} luminescence from different sites in a scheelite- type cadmium molybdate red phosphor with vacancies. J Mater Chem C 3:8582–8594
28. Boulon G (2012) Fifty years of advances in solid-state laser materials. Opt Mater 34:499–512
29. Sanghera J et al (2011) Transparent ceramics for high-energy laser systems. Opt Mater 33: 511–518
30. Sanghera J, Kim W, Villalobos G, Shaw B, Baker C, Frantz J, Sadowski B, Aggarwal I (2013) Ceramic laser materials: past and present. Opt Mater 35:693–699
31. Ikesue A, Aung YL (2008) Ceramic laser materials. Nat Photonics 2:721–727
32. Ikesue A, Kinoshita T, Kamata K, Yoshida K (1995) Fabrication and optical properties of high-performance polycrystalline Nd:YAG ceramics for solid-state lasers. J Am Ceram Soc 78(4):1033–1040
33. Heller A (2006) Transparent ceramics spark laser advances. Sci Technol Rev:10−17
34. Bishop A (2009) Northrop Grumman scales new heights in electric laser power, achieves 100 kW from a solid-state laser. Globe Newswire 18
35. Takaichi K, Yagi H, Lu J, Shirakawa A, Ueda K, Yanagitani T, Kaminskii AA (2003) Yb^{3+}-doped $Y_3Al_5O_{12}$ ceramics – a new solid-state laser material. Phys Status Solidi 200(1):R5–R7
36. Esposito L, Epicier T, Serantoni M, Piancastelli A, Alderighi D, Pirri A, Toci G, Vannini M, Anghel S, Boulon G (2012) Integrated analysis of non-linear loss mechanisms in Yb:YAG ceramics for laser applications. J Am Ceram Soc 32(10):2273–2281
37. Lu J et al (2002) Promising ceramic laser material: highly transparent Nd^{3+}:Lu_2O_3 ceramic. Appl Phys Lett 81:4324–4326
38. Sanghera J, Kim W, Baker C, Villalobos G, Frantz J, Shaw B, Lutz A, Sadowski B, Miklos R, Hunt J, et al. (2011) Laser oscillation in hot pressed 10% Yb^{3+}:Lu_2O_3 ceramic. Opt Mater 33(5):670–674

39. An L, Ito A, Zhang J, Tang D, Goto T (2014) Highly transparent Nd^{3+}:Lu_2O_3 produced by spark plasma sintering and its laser oscillation. Opt Mater Exp 4(7):1420–1426
40. Toci G et al (2015) Nd^{3+}-doped Lu_2O_3 transparent sesquioxide ceramics elaborated by the spark plasma sintering (SPS) method. Part 2: First laser output results and comparison with Nd^{3+}-doped Lu_2O_3 and Nd^{3+}-Y_2O_3 ceramics elaborated by a conventional method. Opt Mater 41:12–16
41. Li W, Mei B, Song J (2015) Nd^{3+}, Yb^{3+}-codoped SrF_2 laser ceramics. Opt Mater 47:108–111
42. Georges S, Goutenoire F, Altorfer F, Sheptyakov D, Fauth F, Suard E, Lacorre P (2003) Thermal, structural and transport properties of the fast oxide-ion conductors La-xRxMo2O9 (R=Nd,Gd,Y). Solid State Ionics 161:231–241
43. Kuang W, Fan Y, Yao K, Chen YJ (1998) Preparation and characterization of ultrafine rare earth molybdeum complex oxide particles. J Solid State Chem 140:354–360
44. Guzik M, Bieza M, Tomaszewicz E, Guyot Y, Boulon G (2014) Development of Nd^{3+}-doped monoclinic dimolybdates $La_2Mo_2O_9$ as optical materials. Z Naturforsch 69b:193–204
45. Guzik M, Bieza M, Tomaszewicz E, Guyot Y, Zych E, Boulon G (2015) Nd^{3+} dopant influence on the structural and spectroscopic properties of microcrystalline $La_2Mo_2O_9$ molybdate. Opt Mater 41:21–31
46. Bieza M, Guzik M, Tomaszewicz E, Guyot Y, Lebbou K, Zych E, Boulon G (2017) Toward optical ceramics based on cubic Yb^{3+} rare earth ion-doped mixed molybdato-tungstates: Part I – Structural characterization. J Phys Chem C 121:13290–13302
47. Bieza M, Guzik M, Tomaszewicz E, Guyot Y, Boulon G (2017) Toward optical ceramics based on Yb^{3+} rare earth ion-doped mixed molybdato-tungstates: Part II – Spectroscopic characterization. J Phys Chem C 121:13303–13313
48. Bieza M, Guzik M, Tomaszewicz E, Guyot Y, Boulon G (2017) Yb^{3+} rare earth structural probe and correlation between morphology and spectroscopic properties in $La_2Mo_2O_9$. Comparative analysis with mixed cubic La_2MoWO_9 translucent ceramics. J Eur Ceram Soc 38:3217–3234
49. Bieza M, Guzik M, Tomaszewicz E, Guyot Y, Boulon G (2017) Cubic Yb^{3+}-activated Y_6MoO_{12} micro-powder e optical material operating in NIR region. Opt Mater 63:3–12
50. Zhao X, Zhang Y, Huang Y, Gong H, Zhao J (2015) Synthesis and characterization of neodymium doped yttrium molybdate high NIR reflective nano pigments. Dyes Pigments 116:119–123
51. Zhang X, Zhang Y, Gong H, Zhao X, Wang C, Zhu H (2013) Synthesis, characterization and optical properties of $Y_{6-x}Sm_xMoO_{12+\sigma}$ composite/compounds pigments with high near-infrared reflectance. Adv Mater Res 602–604:102–106
52. George G, Vishnu VS, Reddy MLP (2011) 6. The synthesis, characterization and optical properties of silicon and praseodymium doped Y_6MoO_{12} compounds: Environmentally benign inorganic pigments with high NIR reflectance. Dyes Pigments 88:109–115
53. Li H, Pu X, Yin J, Wang X, Yao NSM, Jeong JH (2016) Effect of crystallite size and crystallinity on photoluminescence properties and energy transfer of Y_6MoO_{12}:Eu. J Am Ceram Soc 99(3):954–961
54. Li H, Yang HK, Moon BK, Choi BC, Jeong JH, Jang K, Lee HS, Yi SS (2011) Investigation of the structure and photoluminescence properties of Eu^{3+} ion-activated $Y_6W_xMo_{(1-x)}O_{12}$. J Mater Chem 21:4531–4537
55. Li H, Noh HM, Moon BK, Choi BC, Jeong JH, Jang K, Lee HS, Yi SS (2013) Wide-band excited $Y_6(WMo)_{0.5}O_{12}$:Eu red phosphor for white light emitting diode: structure evolution, photoluminescence properties, and energy transfer mechanisms involved. Inorg Chem 52:11210–11217
56. Li H, Yang HK, Moon BK, Choi BC, Jeong JH, Jang K, Lee HS, Yi SS (2011) Crystal structure, electronic structure, and optical and photoluminescence properties of Eu(III) ion-doped $Lu_6Mo(W)O_{12}$. Inorg Chem 50:12522–12530
57. Chevire F, Clabau F, Larcher O, Orhan E, Tessier F, Marchand R (2009) Tunability of the optical properties in the $Y_6(W,Mo)(O,N)_{12}$ system. Solid State Sci 1:533–536

58. Yu RJ, Shin DS, Jang K, Guo Y, Noh HM, Moon BK, Choi BC, Jeong JH, Yi SS (2014) Photoluminescence properties of novel host-sensitized Y_6WO_{12}:Dy^{3+} phosphors. J Am Ceram Soc 97:2170–2176
59. Taupin AA (1973) Powder-diagram automatic-indexing routine. J Appl Crystallogr 6:380–−385
60. Evans IR, Howard JAK, Evans JSO (2005) The crystal structure of α-$La_2Mo_2O_9$ and the structural origin of the oxide ion migration pathway. Chem Mater 17:4074–4077
61. Alekseeva OA, Verin IA, Sorokina NI, Novikova NE, Kolesnikova DS, Voronkova VI (2010) Crystal structure of the metastable cubic βms phase of $La_2Mo_2O_9$ single crystal at T = 33 K. Kristallografiya 55:213–219; Crystallogr Rep 55:199−205
62. Shannon RD (1976) Revised effective ionic radii and systematic studies of interatomic distances in halides and chalcogenides. Acta Crystallogr Sect A Cryst Phys Diffr Theor Gen Crystallogr 32:751–767
63. Chun-Ju H, Xu Z, Chang-Song L, Xian-Ping W, Qian-Feng F (2008) Crystal structure of β-$La_2Mo_2O_9$ from first principles calculation. Chin Phys Lett 25:3342–3345
64. Fournier JP, Fournier J, Kohlmuller R (1970) Étude des systómes La_2O_3 – MoO_3, Y_2O_3 – MoO_3 et des phases Ln_6MoO_{12}. Bulletin de la Societe Chimique de France 12:4277
65. Aitken AE, Bartram SF, Juenke EF (1949) Crystal chemistry of the rhombohedral $MO_3{\cdot}3R_2O_3$ compounds. Inorg Chem 3(7):949
66. Bartram SF (1966) Crystal structure of the rhombohedral $MO_3{\cdot}3R_2O_3$ compounds (M = U, W, or MO) and their relation to ordered R_7O_{12} phases. Inorg Chem 5(5):749–754
67. Diot N, Benard-Rocherulle P, Marchand R (2000) X-ray powder diffraction data and rietveid refinement for Ln_6WO_{12}(Ln=Y, Ho). Powder Diffr 15(4):220
68. Yoshimura M, Ma J, Kakihana M (1998) Low-temperature synthesis of cubic and rhombohedral Y_6WO_{12} by a polymerized complex method. J Am Ceram Soc 81(10):2721–2724
69. Apostolov ZD, Sarin P, Haggerty RP, Kriven WM (2013) In-situ synchrotron X-ray diffraction study of the cubic to rhombohedral phase transformation in Ln_6WO_{12} (Ln = Y, Ho, Er, Yb). J Am Ceram Soc 96(3):987–994
70. Boulon G, Laversenne L, Goutaudier C, Guyot Y, Cohen-Adad MT (2003) Radiative and non-radiative energy transfers in Yb^{3+}-doped sesquioxide and garnet laser crystals from a combinatorial approach based on gradient concentration fibers. J Lumin 102/103:417–425
71. Canibano H, Boulon G, Palatella L, Guyot Y, Brenier A, Voda M, Balda R, Fernandez J (2003) Spectroscopic properties of new Yb^{3+}-doped $K_5Bi(MoO_4)_4$ crystals. J Lumin 102–103: 318–326
72. Legendziewicz J, Cybinska J, Guzik M, Boulon G, Meyer G (2008) Comparative study of crystal field analysis in Pr^{3+} and Yb^{3+}-doped K_2LaX_5 (X = Cl-, Br-) ternary halides and Yb^{3+}-doped $A_3Lu(PO_4)_2$ (A = Na^+, Rb^+) double phosphates. Charge transfer band observations of Yb^{3+}-doped systems. Opt Mater 30:1655–1666
73. Guzik M, Tomaszewicz E, Guyot Y, Legendziewicz J, Boulon G (2016) Spectroscopic properties, concentration quenching and Yb^{3+} site occupations in vacancied scheelite-type molybdates. J Lumin 169:755–764

Part II
Short Seminars

Quantum Key Distribution Over Free Space

Fabian Beutel, Jasper Rödiger, Nicolas Perlot, Ronald Freund, and Oliver Benson

Abstract Quantum key distribution (QKD) enables the creation of a common secret key between two remote parties that are connected by a quantum channel. In the time-frequency (TF)-QKD scheme, Alice encodes her bits either in the arrival time (Pulse Position Modulation) or in the center frequency (Frequency Shift Keying) of weak laser pulses. We have successfully implemented the TF-QKD scheme by using mostly off-the-shelf telecom components and avalanche photodiodes operating at 1550 nm. With our setup we achieve secret-key rates of more than 400 kbit/s back-to-back and 80 kbit/s over a 25 km fiber spool. Furthermore, we have tested our scheme over an outdoor free-space test range of 390 m in the Berlin city center and are currently in the process of extending it to longer outdoor test ranges.

Keywords Quantum key distribution · Time-frequency · bb84

Time-frequency quantum key distribution Quantum key distribution (QKD) provides means to securely transfer keying material between two parties, backed by the fundamental laws of quantum physics. While the traditional BB84 protocol uses different polarization orientations as bases for the signal encoding, the use of modulation in time or frequency has previously been proposed as a promising alternative. In this so called time-frequency (TF-) QKD protocol, pulses are either encoded using pulse-position modulation (PPM) or frequency-shift keying (FSK).

F. Beutel (✉) · J. Rödiger
AG Nanooptik, Humboldt-Universität zu Berlin, Berlin, Germany

Fraunhofer Heinrich Hertz Institute, Berlin, Germany
e-mail: fabian.beutel@uni-muenster.de

N. Perlot · R. Freund
Fraunhofer Heinrich Hertz Institute, Berlin, Germany

O. Benson
AG Nanooptik, Humboldt-Universität zu Berlin, Berlin, Germany

B. Di Bartolo et al. (eds.), *Quantum Nano-Photonics*, NATO Science for Peace and Security Series B: Physics and Biophysics,
https://doi.org/10.1007/978-94-024-1544-5_18

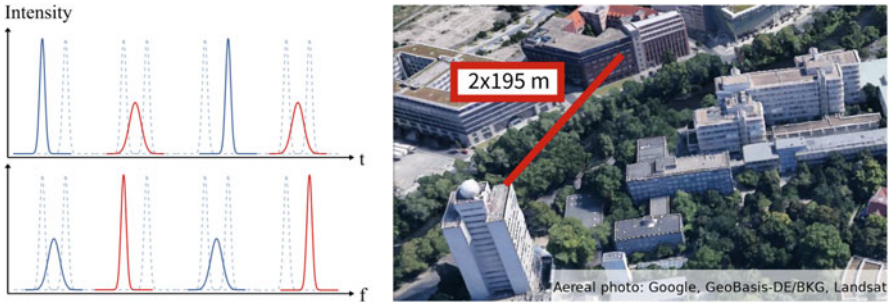

Fig. 1 Left: Pulse forms of PPM pulses (blue) and FSK pulses (red) in both, time and frequency domains. Measuring in the wrong basis leads to a loss of information. Right: Aerial view of the free-space transmission testbed

Due to the time-frequency uncertainty and similar to traditional BB84 protocols, measuring in the wrong basis increases the uncertainty in the other basis, hence information encoded therein is deleted (Fig. 1). One advantage of the TF-protocol is the ability to encode more than one symbol per basis. Since no polarization encoding is used, it remains a candidate for the implementation of multiplexing like bidirectional communication.

Implementation and results We have implemented the TF-QKD protocol in the laboratory using mostly standard telecom-components and avalanche photo-diodes (APDs) as single-photon detectors at 1550 nm wavelength. With strongly attenuated laser pulses on average less than one photon per pulse is being sent and the decoy-state method can easily be integrated. We measured the quantum bit error rate (QBER) as well as the achieved raw-key rates depending on the transmission line and pulse widths used. Considering a simple intercept-resend eavesdropping attack we were able to numerically calculate bounds for secret-key rates. With the back-to-back setup we achieved secret-key rates of about 400 kbit/s. Over a dispersion compensating single-mode fiber of 25 km length, secret key rates of about 80 kbit/s could be achieved. Transmissions over a free-space link connecting two buildings in the Berlin city center over a distance of 390 m yielded secret-key rates of 5 kbit/s. In these experiments, multiplexing techniques as well as further substantial reduction of transmission losses are yet to be explored and hence there exists great potential for future increase in these key rates. Because PPM and FSK are well-established coding techniques in classical communication and because of the demonstrated ability to implement secure quantum communication with mostly off-the-shelf telecom components, the TF-QKD protocol is a promising candidate for both, free space and fiber-based QKD implementations.

References

1. Beutel F, Rödiger J, Perlot N, Benson O, Freund R (2016) Evaluation of time-frequency QKD over different transmission channels. QCrypt conference poster, Washington D.C.
2. Leifgen M, Elschner R, Perlot N, Weinert C, Schubert C, Benson O (2015) Practical implementation and evaluation of a quantum key distribution scheme based on the timefrequency uncertainty. Phys Rev A 92(4). https://doi.org/10.1103/PhysRevA.92.042311
3. Beutel F (2017) Implementation and evaluation of time-frequency quantum key distribution over free space. Master's thesis, Humboldt-Universität zu Berlin

Modelling of Coloured Metal Surfaces by Plasmonics Nanoparticles

Antonino Calà Lesina, Jean-Michel Guay, Arnaud Weck, Pierre Berini, and Lora Ramunno

Abstract Metallic nanoparticles (NPs) dispersed in glass have been used since Romans times to color glasses [1]. With the recent development of metasurfaces, metallic and dielectric nanostructures have been proposed to color surfaces [2]. The excitation of resonant modes in the nanostructures is responsible for selective absorption of the incident light, thus causing the color creation. Top-down techniques based on lithography allow achieving highly saturated colors with a high resolution due to the deterministic patterning, but they are not suited for large-scale applications, such as the coloring of large surfaces. Furthermore, lithographic techniques are not suited to create metallic nanostructures on a substrate of the same metal. Metal nanostructures on metal can generate colors if their shape can support a localized surface plasmon resonance (LSPR). For example, this is valid for NPs of spherical shape slightly embedded on the substrate. In fact, when the embedding increases the resonance condition vanishes (an embedding increase corresponds to a transition from a spherical shape to a hemispherical shape) and the color disappears. This configuration has never been investigated theoretically. We recently proposed a bottom-up laser technique in the picosecond regime to create NPs on the metallic surface (laser-induced nanostructures) through a process of ablation and re-deposition, which is suited for mass production [3]. By tuning the laser properties, it is possible to control the NPs such that their size and density fall in the range of

A. Calà Lesina (✉) · J.-M. Guay · L. Ramunno
Department of Physics and Centre for Research in Photonics, University of Ottawa, Ottawa, Canada
e-mail: antonino.calalesina@uottawa.ca

A. Weck
Department of Physics and Centre for Research in Photonics, University of Ottawa, Ottawa, Canada

Department of Mechanical Engineering, University of Ottawa, Ottawa, Canada

P. Berini
Department of Mechanical Engineering, University of Ottawa, Ottawa, Canada

School of Electrical Engineering and Computer Science, University of Ottawa, Ottawa, Canada

B. Di Bartolo et al. (eds.), *Quantum Nano-Photonics*, NATO Science for Peace and Security Series B: Physics and Biophysics,
https://doi.org/10.1007/978-94-024-1544-5_19

dimensions supporting LSPR, thus producing colors. This is shown in the palette realized on silver at the Royal Canadian Mint in Fig. 1a [3]. SEM images of these colored metallic surfaces reveal the presence of NPs of two sizes, i.e., medium and small, with radii R_m and R_s, respectively. Based on this information, we simulated the optical response of silver NPs distributed on a flat silver surface by using an in-house parallel 3D-FDTD code running on IBM BlueGene/Q (SOSCIP). Medium NPs were embedded by 30% of their radius, while small NPs were embedded by 0.5–3.5 nm. The simulation domain was discretized with a space-step from 0.125 to 0.5 nm to achieve convergent results, and we arranged the NPs following a hexagonal lattice in the xz-plane with a center-to-center inter-distance of D_m and D_s for medium and small NPs, respectively. In order to apply periodic boundary conditions, we needed D_m/D_s to be an integer number. We modeled silver using the Drude+2CP model [4]. In Fig. 1b we show the field distribution at 390 nm for an xz-plane cut through the center of the small NPs. By averaging the reflectance over the embedding level of the small NPs, we obtained the average reflectance curves and the associated colors shown in Fig. 1c. The averaging washes out the effect of the small NPs, thus highlighting the major role in the color formation played by the medium NPs. The simulated palette in Fig. 1c reveals the same qualitative transition from blue to yellow observed in the experimental palette in Fig. 1a, thus identifying plasmonic resonances in arrangements of NPs as responsible for color creation.

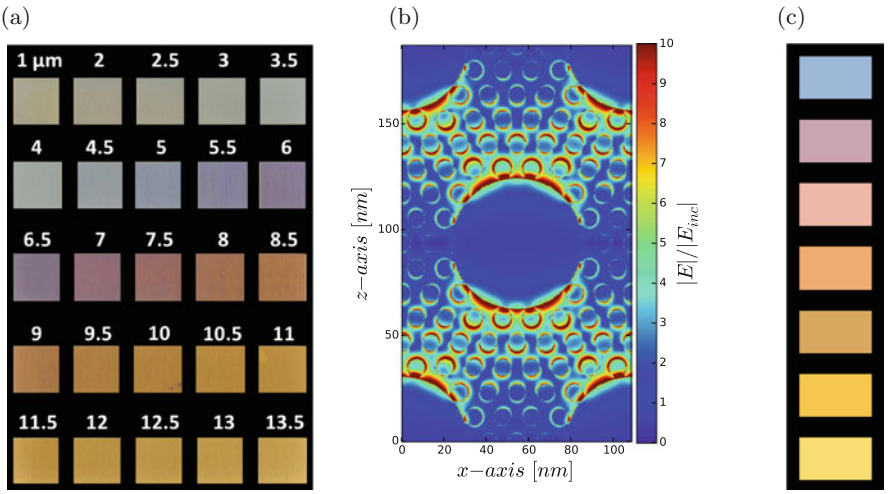

Fig. 1 (**a**) Colored squares produced by picosecond laser processing by changing the line spacing, L_s, in steps of 0.5 µm (as marked above each square) for a laser fluence of $\phi = 1.29$ J/cm^2 and a marking speed of $v = 100$ mm/s. (**b**) Field distribution at 390 nm, xz-view, revealing a plasmonic resonance. (**c**) Simulated colors for $R_m = 36$ nm, $R_s = 4$ nm, increasing D_m (from 81 to 139 nm), and decreasing D_s (from 16.2 to 10.7 nm) (top to bottom)

References

1. Barber DJ, Freestone IC (1990) An investigation of the origin of the color of the Lycurgus cup by analytical transmission electron-microscopy. Archaeometry 1:33–45
2. Zhao Y, Zhao Y, Hu S, Lv J, Ying Y, Gervinskas G, Si G (2017) Artificial structural color pixels: a review. Materials 10:944
3. Guay J-M, Calà Lesina A, Côté G, Charron M, Poitras D, Ramunno L, Weck A (2017) Laser-induced plasmonic colours on metals. Nat Commun 8:16095
4. Calà Lesina A, Vaccari A, Berini P, Ramunno L (2015) On the convergence and accuracy of the FDTD method for nanoplasmonics. Opt Express 23:10481

Exciton Dynamics of Colloidal Semiconductor Quantum Well Stacks

Onur Erdem, Burak Guzelturk, Murat Olutas, Yusuf Kelestemur, and Hilmi Volkan Demir

Abstract Colloidal semiconductor nanoplatelets (NPLs) have recently emerged as a new class of colloidal nanocrystals. NPLs are quasi two-dimensional nanocrystals having atomically flat surfaces and have unique properties such as narrow photoluminescence (PL) emission (∼10 nm) and giant oscillator strength. NPLs can be self-assembled into stacks. These are one-dimensional superstructures that can contain tens or hundreds of NPLs in one chain.

We studied how stacking modifies the optical properties of NPLs.

We found that PL quantum yield and exciton lifetime are reduced with increased degree of stacking in NPL ensembles. Moreover, we showed that temperature-dependent behavior of stacked NPLs is significantly different than the nonstacked ones. We developed two statistical models that account for the ultra-fast nonradiative energy transfer within stacked NPL chains as well as nonemissive subpopulation of NPLs in the ensemble to explain the aforementioned changes when NPLs are stacked.

Colloidal nanoplatelets (NPLs) are solution-processed quantum wells with magic sized vertical thickness of few nm's and lateral sizes of 10–100 nm. Since the lateral sizes are typically larger than the exciton Bohr radius, the quantum confinement in these nanostructures is strong only in the vertical direction. This leads to unique

O. Erdem · B. Guzelturk · M. Olutas · Y. Kelestemur
Department of Electrical and Electronics Engineering, Department of Physics, UNAM – Institute of Materials Science and Nanotechnology, Bilkent University, Ankara, Turkey

H. V. Demir (✉)
Department of Electrical and Electronics Engineering, Department of Physics, UNAM – Institute of Materials Science and Nanotechnology, Bilkent University, Ankara, Turkey

Luminous! Center of Excellence for Semiconductor Lighting and Displays, School of Electrical and Electronic Engineering, School of Physical and Materials Sciences, School of Materials Science and Nanotechnology, Nanyang Technological University, Singapore, Singapore
e-mail: volkan@fen.bilkent.edu.tr

B. Di Bartolo et al. (eds.), *Quantum Nano-Photonics*, NATO Science for Peace and Security Series B: Physics and Biophysics,
https://doi.org/10.1007/978-94-024-1544-5_20

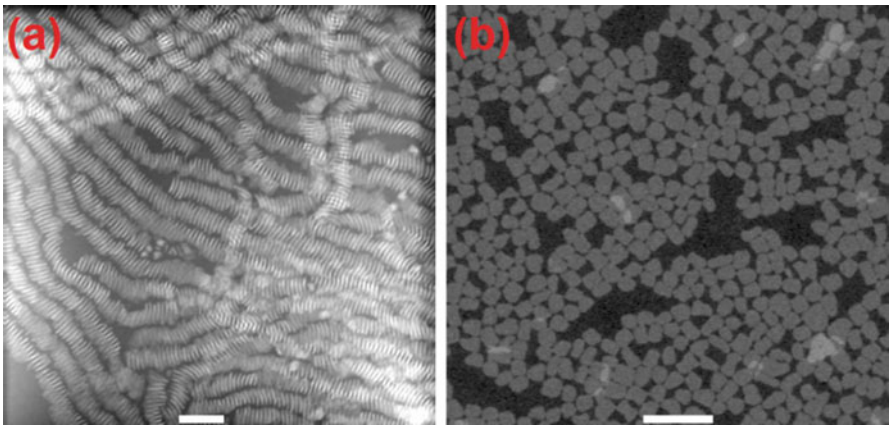

Fig. 1 Transmission electron microscopy images of (**a**) stacked and (**b**) nonstacked nanoplatelets. Scale bars are 50 nm (Demir Group)

properties in the NPLs including narrow photoluminescence (PL) emission (< 10 nm) and giant oscillator strength transition.

NPLs can assemble themselves into one-dimensional long chains, which are commonly referred to as stacks (Fig. 1a). When stacked, the NPLs are aligned face to face, standing on their edges instead of lying flat on the substrate (Fig. 1b). We observed that stacking strongly modifies the optical properties of the NPLs. For instance, the PL lifetime and quantum yield (QY) of the NPLs and the are reduced with increasing degree of stacking [1]. Moreover, the increase in QY with decreasing temperature is suppressed when the NPLs are in stacked formation [2].

To account for these modifications we developed two mathematical models making use of the fact that there is ultra-fast exciton transfer between neighboring NPLs of a stack, which leads to increased hole trapping in defected NPLs. The first one constructs and solves a set of rate equations to determine the lifetime of the exciton decay [1]. The second approach treats the movement of the excitation between the NPLs as a random walk and utilizes Markov chains to estimate the exciton lifetime and QY of the stacks. Using experimental data, the rates of energy transfer and exciton recombination are calculated and used in the construction of state transition matrices [2]. Using this model, we are able to calculate the changes in QY and PL lifetimes with temperature. Both models show good agreement with the experimental data.

References

1. Guzelturk B, Erdem O, Olutas M, Kelestemur Y, Demir HV (2014) Stacking in colloidal nanoplatelets: tuning excitonic properties. ACS Nano 8(12):12524–12533
2. Erdem O, Oluras M, Guzelturk B, Kelestemur Y, Demir HV (2016) Temperature-dependent emission kinetics of colloidal nanoplatelets strongly modified by stacking. J Phys Chem Lett 7(3):548–554

InAsP Quantum Dots in InP Nanowire Waveguides as Sources of Quantum Light

James R. Godfrey, Golnaz Azodi, James A. H. Stotz, and James M. Fraser

Abstract Quantum dots, a 3D analogue of the quantum potential well, have recently become a commonplace tool for production of non-classical light (Buckley S, Rivoire K, Vu J: Rep Prog Phys 75:126503, 2012; Lodahl P, Mahmoodian S, Stobbe S: Rev Mod Phys 87:347–400, 2015). Self-assembled quantum dots have a host of obstacles associated with their use for generation of non-classical light, including non-deterministic dimensions (and thus emission wavelength), generation of a 'wetting layer' and generally non-uniform surroundings, and emission through large solid angles (Buckley S, Rivoire K, Vu J: Rep Prog Phys 75:126503, 2012). Recent developments in quantum dot growth have allowed for deterministic control of quantum dot dimensions on the scale of 2 nm, for the quantum dots to be grown within tapering wire-shaped nanocavities (nanowire), and intimate control over various physical properties of the quantum dot and nanowire (Dalacu D, Kam A, Guy Austing D, Wu X, Lapointe J, Aers GC, Poole PJ: 2009 Nanotechnology 20:395602; Dalacu D, Mnaymneh K, Wu X, Lapointe J, Aers GC, Poole PJ, Williams RL: Appl Phys Lett 98:251101, 2011; Dalacu D, Mnaymneh K, Lapointe J, Wu X, Poole PJ, Bulgarini G, Akopian N, Hocevar M, Bavinck MB, Verheijen MA, Bakkers EPAM, Kouwenhoven LP, Zwiller V, Reimer ME: Nano Lett 12:5919–5923, 2012). The nanowire geometry highly directionalizes the photoluminescence of the quantum dot over a broad range of wavelengths, allowing for high extraction efficiencies, provides stable and uniform surroundings (Dalacu D, Mnaymneh K, Lapointe J, Wu X, Poole PJ, Bulgarini G, Akopian N, Hocevar M, Bavinck MB, Verheijen MA, Bakkers EPAM, Kouwenhoven LP, Zwiller V, Reimer ME: Nano Lett 12:5919–5923, 2012; Reimer ME, Bulgarini G, Akopian N, Hocevar M, Bavinck MB, Verheijen MA, Bakkers EPAM, Kouwenhoven LP, Zwiller V: Nat Commun 3:737, 2012). Depending on the choice of excitation scheme, the quantum dot within the nanowire can be used as a source of single photons (Dalacu D, Mnaymneh K, Wu X, Lapointe J, Aers GC, Poole PJ, Williams RL: Appl Phys

J. R. Godfrey (✉) · G. Azodi · J. A. H. Stotz · J. M. Fraser
Queen's University, Kingston, ON, Canada
e-mail: lncs@springer.com

B. Di Bartolo et al. (eds.), *Quantum Nano-Photonics*, NATO Science for Peace and Security Series B: Physics and Biophysics,
https://doi.org/10.1007/978-94-024-1544-5_21

Lett 98:251101, 2011; Dalacu D, Mnaymneh K, Lapointe J, Wu X, Poole PJ, Bulgarini G, Akopian N, Hocevar M, Bavinck MB, Verheijen MA, Bakkers EPAM, Kouwenhoven LP, Zwiller V, Reimer ME: Nano Lett 12:5919–5923, 2012; Reimer ME, Bulgarini G, Akopian N, Hocevar M, Bavinck MB, Verheijen MA, Bakkers EPAM, Kouwenhoven LP, Zwiller V: Nat Commun 3:737, 2012) or entangled photon pairs through the radiative biexciton cascade (Versteegh MAM, Reimer ME, Jöns KD, Dalacu D, Poole PJ, Gulinatti A, Giudice A, Zwiller V: Nat Commun 5:5298, 2014).

We have discussed the growth of InAsP quantum dots embedded in InP nanowires, their geometric and optical properties, and their ability as a bright and highly-efficient source of highly-indistinguishable single photons and polarization-entangled photon pairs.

Keywords Quantum optics · Single photon sources · Quantum communication

References

1. Buckley S, Rivoire K, Vu J (2012) Engineered quantum dot single-photon sources. Rep Prog Phys 75:126503
2. Lodahl P, Mahmoodian S, Stobbe S (2015) Interfacing single photons and single quantum dots with photonic nanostructures. Rev Mod Phys 87:347–400
3. Dalacu D, Kam A, Guy Austing D, Wu X, Lapointe J, Aers GC, Poole PJ (2009) Selective-area vapour-liquid-solid growth of InP nanowires. Nanotechnology 20:395602
4. Dalacu D, Mnaymneh K, Wu X, Lapointe J, Aers GC, Poole PJ, Williams RL (2011) Selective-area vapor-liquid-solid growth of tunable InAsP quantum dots in nanowires. Appl Phys Lett 98:251101
5. Dalacu D, Mnaymneh K, Lapointe J, Wu X, Poole PJ, Bulgarini G, Akopian N, Hocevar M, Bavinck MB, Verheijen MA, Bakkers EPAM, Kouwenhoven LP, Zwiller V, Reimer ME (2012) Ultraclean emission from InAsP quantum dots in defect-free wurtzite InP nanowires. Nano Lett 12:5919–5923
6. Reimer ME, Bulgarini G, Akopian N, Hocevar M, Bavinck MB, Verheijen MA, Bakkers EPAM, Kouwenhoven LP, Zwiller V (2012) Bright single-photon sources in bottom-up tailored nanowires. Nat Commun 3:737
7. Versteegh MAM, Reimer ME, Jöns KD, Dalacu D, Poole PJ, Gulinatti A, Giudice A, Zwiller V (2014) Observation of strongly entangled photon pairs from a nanowire quantum dot. Nat Commun 5:5298

Diamond Nanophotonic Circuits

W. Hartmann, P. Rath, and W. H. P. Pernice

Abstract Ordinary quantum optic experiments often reach a very high complexity very quickly, filling up whole optical tables with free space optic components. Integrating quantum optics on a nanophotonic chip not only reduces the size of a normally several square meters sized experiment to a few millimeters, but also provides high scalability and stability. One very promising material for such nanophotonic circuits is thin-film diamond due to its relatively high refractive index of 2.4 and very high Young's modulus of around 1100 GPa. Therefore, we present a complete approach for quantum applications based on diamond nanophotonic circuits, comprising single photon sources, superconducting single photon detectors and optomechanical phase-shifters.

References

1. Rath P (2013) Diamond-integrated optomechanical circuits. Nat Commun 4:1690
2. Rath P (2014) Diamond electro-optomechanical resonators integrated in nanophotonic circuits. APL 105:251102
3. Peruzzo A (2014) A variational eigenvalue solver on a photonic quantum processor. Nat Commun 5:4213
4. Poot M (2014) Broadband nanoelectromechanical phase shifting of light on a chip. APL 104:061101

W. Hartmann (✉) · W. H. P. Pernice
Institute of Physics, University of Münster, Münster, Germany

CeNTech – Center for Nanotechnology, University of Münster, Münster, Germany
e-mail: wladick.hartmann@uni-muenster.de

P. Rath
Qorvo Inc., Greensboro, NC, USA

B. Di Bartolo et al. (eds.), *Quantum Nano-Photonics*, NATO Science for Peace and Security Series B: Physics and Biophysics,
https://doi.org/10.1007/978-94-024-1544-5_22

Superchiral Near Fields in Photonic Crystal Waveguides

Isabelle Palstra and Dolfine Kosters

Abstract Highly accurate sensing of chiral molecules is crucial in drug development as one mirror image of a chiral molecule (enantiomer) can be toxic while the other is healing. The rate of absorption for a chiral molecule is different for left- and right-handed circularly polarized light (LCPL, RCPL), and this interaction asymmetry can be used to probe chirality. This interaction asymmetry is typically very weak, but it can be enhanced when light becomes superchiral [1], i.e. the field has an optical chirality (C) that is larger than that of circularly polarized light. Here we show that a conventional silicon photonic crystal waveguide (PhCW) has a near field with superchiral hotspots and we propose to use this superchirality to make an on-chip sensing device. A conventional PhCW has a zero net optical chirality, as the optical chirality is antisymmetric in every mirror plane and conventional PhCWs have several mirror symmetries. The symmetries were broken by shifting the rows of holes closest to the waveguide. The resulting chiral PhCW and a conventional PhCW are shown in Fig. 1. The near fields of this chiral PhCW exhibit superchiral hotspots far stronger than that of the conventional one, and the net chirality is nonzero.

I. Palstra (✉)
Center for Nanophotonics, AMOLF, Amsterdam, The Netherlands
e-mail: i.palstra@amolf.nl

D. Kosters
Department of Quantum Nanoscience, Kavli Institute of Nanoscience, Delft, The Netherlands
e-mail: n.d.kosters@tudelft.nl

B. Di Bartolo et al. (eds.), *Quantum Nano-Photonics*, NATO Science for Peace and Security Series B: Physics and Biophysics,
https://doi.org/10.1007/978-94-024-1544-5_23

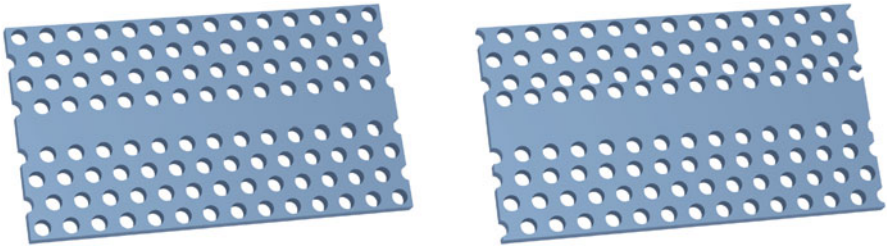

Fig. 1 A regular PhCW (left), and a symmetry-broken or chiral PhCW (right)

Reference

1. Tang Y, Cohen AE (2010) Optical chirality and its interaction with matter. Phys Rev Lett 104:163901-1–4

Neodymium Doped Luminescent Composites Derived from the Sols Based on Carboxylic Acids

M. V. Rudenko, A. V. Mudryi, T. I. Orekhovskaya, and N. V. Gaponenko

Abstract Luminescent structures presented monocrystalline silicon and porous anodic alumina with neodymium doped yttrium alumina composites YAC:Nd that were formed by sol-gel route from different sols. Structure, phase composition and luminescence of the obtained structures were investigated. Photoluminescence spectra of structures containing YAC:Nd carry emission bands caused by electron transitions of neodymium. Thin emission bands structure of all samples occurs due to Stark effect appearance.

Keywords Luminescence · Yttrium alumina composites · Sol-gel · Neodimium

Yttrium aluminum garnets and perovskites doped with lanthanides are widely used as active components of solid-state lasers, X-ray scintillators, light emitting phosphors in liquid crystal displays and cathode luminescence devices. One of the most promising methods of obtaining YAC is sol-gel method. Various precursors and approaches to the synthesis of the amorphous phase make it possible to influence the crystallization temperature, the final size of the crystallites, dispersion, purity and other material properties [1]. The use of carboxylic acids is rather promising.

In this work we used the nitric acid salts of yttrium and neodymium, aluminum isopropoxide, lactic and citric acids and butyl alcohol as solvents. Xerogels were synthesized on silicon substrates and structures of porous anodic alumina (PAA) formed on silicon after annealing at 1000 °C.

The X-ray diffraction spectrum of the xerogel powder obtained from the citric acid sol contains diffraction lines corresponding to the cubic crystalline $Y_3Al_5O_{12}$ (PDF-82-0575). The same weak diffraction lines are resolved for the xerogel films

M. V. Rudenko (✉) · T. I. Orekhovskaya · N. V. Gaponenko
Belarusian State University of Informatics and Radioelectronics, Minsk, Belarus

A. V. Mudryi
National Academy of Sciences of Belarus, Scientific and Practical Materials Research Center, Minsk, Belarus

B. Di Bartolo et al. (eds.), *Quantum Nano-Photonics*, NATO Science for Peace and Security Series B: Physics and Biophysics,
https://doi.org/10.1007/978-94-024-1544-5_24

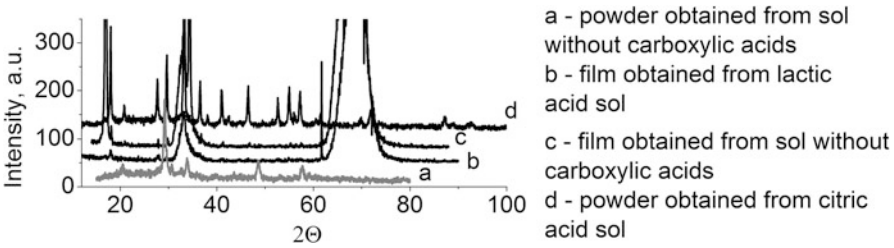

Fig. 1 X-ray diffraction patterns of neodymium-doped YAC obtained from different sols

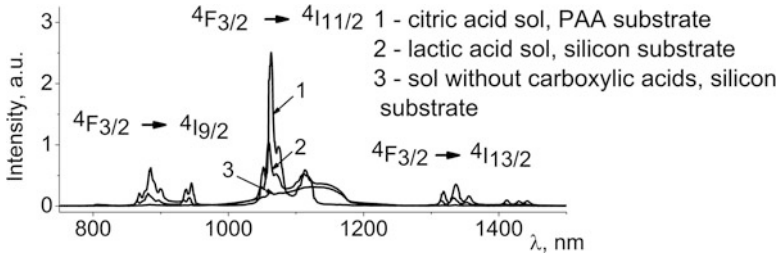

Fig. 2 The luminescence spectra of neodymium-doped YAC xerogels obtained from different sols. Excitation wavelength is 325 nm

formed on monocrystalline silicon. The average crystal powder size of the xerogel powders synthesized from citric acid and lactic acid sols were 25 and 9.5 nm, respectively (Fig. 1).

The samples reveal strong room temperature photoluminescence with the characteristic Stark splitting of the luminescence bands of trivalent neodymium ions [2] presented on Fig. 2. Spectra of xerogels formed on monocrystalline silicon also contain luminescence band of silicon, which slows down when using the lactic acid sols.

The sol-gel derived YAC powders are presently more developed than thin films, although the last have also found practical application [3]. The use of lactic acid in the sol composition allows the reduction of side phases formation of YAG xerogel thin films on monocrystalline silicon and generation of highly dispersed YAC powders.

References

1. Mathur S (2006) Structural and optical properties of highly Nd-doped yttrium aluminum garnet ceramics from Alkoxide and Glycolate precursors. Amer Cer Soc 89(6):2027–2033
2. Rudenko MV (2016) Luminescence of terbium and neodymium ions in yttrium aluminum garnet Xerogels on porous anodic alumina. J Appl Spectr 83(1):121–125
3. Greer J Laser-deposition of high luminance thin film phosphors. MRS Proc 345. https://doi.org/10.1557/PROC-345-281(1994

Vibrational Properties of Ge-Sb-Te Phase-Change Alloys Studied by Temperature-Dependent IR and Raman Spectroscopy

K. Shportko and M. Wuttig

Abstract This work is focused on the vibrational properties of Ge-Sb-Te phase-change alloys. We report on the systematic compositional dependencies of the intensities of the bands in Raman spectra of amorphous Ge-Sb-Te alloys. We have also studied the change of the anharmonicity upon crystallization of Ge-Sb-Te alloys using temperature-dependent IR and Raman spectroscopy.

1 Introduction

Ge-Sb-Te phase-change alloys are employed as active elements in optical data storages and are promising for new generation of the electronic memory devices [1]. Upon crystallization, their visible and infrared dielectric properties change dramatically due to the formation of resonant bonds [2]. A fundamental understanding of the properties of the phase change alloys has important implications for the optimization of materials for the next generation of storage media. This work is aimed to study vibrational properties of the amorphous and crystalline Ge-Sb-Te alloys.

2 Results

Three amorphous Ge-Sb-Te alloys have been investigated using IR and Raman spectroscopy: $GeSb_2Te_4$, $Ge_2Sb_2Te_5$, and $Ge_3Sb_2Te_6$. Gaussian decomposition of the obtained Raman spectra of amorphous Ge-Sb-Te has been performed [3]. Observed Raman bands at around 124, 213 and 264 cm^{-1} are ascribed to the A_1

K. Shportko (✉)
V.E. Lashkaryov Institute for Semiconductor Physics of NAS of Ukraine, Kyiv, Ukraine
e-mail: konstantin@shportko.com

M. Wuttig
I. Institute of Physics (IA), RWTH University of Technology Aachen, Aachen, Germany

B. Di Bartolo et al. (eds.), *Quantum Nano-Photonics*, NATO Science for Peace and Security Series B: Physics and Biophysics,
https://doi.org/10.1007/978-94-024-1544-5_25

mode (shoulder at 125 cm^{-1}) and antisymmetric stretching modes (bands at 213 and 264 cm^{-1}) of $GeTe_{4-n}Ge_n$ (n = 1, 2) corner-sharing tetrahedra. The broad band around 70 cm^{-1} is assigned to Γ_3(E) vibrational mode involving threefold coordinated Te atoms. The strongest band in the Raman spectra of amorphous Ge-Sb-Te samples results from the superposition of two bands. The first one at 150 cm^{-1} is directly linked to the Sb_2T_3 content in the Ge-Sb-Te samples. It is partly linked to Sb-Te vibrations in the defective octahedral configurations of Sb atoms and $SbTe_3$ pyramidal units. The second superposing band at 162 cm^{-1} corresponds to the vibrations in Ge-based defective octahedra. In $Ge_2Sb_2Te_5$, and $Ge_3Sb_2Te_6$ samples the band at 162 cm^{-1} linked to the GeTe content gains its intensity, while other one at 150 cm^{-1} representing the modes of $SbTe_3$ units significantly loses it. The shoulder at around 125 cm^{-1} does not gain much intensity. The band at around 125 cm^{-1} becomes more visible in the spectra of Ge-Sb-Te with higher Ge content mainly due to the weakening of the $SbTe_3$ linked band at 150 cm^{-1}[4].

Analysis of the Raman and FIR spectra of studied alloys at different temperatures has shown that phonons' frequencies in the crystalline samples are more temperature dependent than those in amorphous samples. The crystalline state of phase-change materials shows higher thermal atomic displacements and a more pronounced anharmonic behavior in the crystalline phase [5]. Crystalline Ge-Sb-Te alloys form a distorted rock-salt structure with high concentration of vacancies. Obtained results reveal that the lattice anharmonicity in crystalline Ge-Sb-Te depends on both, vacancy concentration and vacancy order [6].

3 Conclusions

We report on the systematic compositional dependencies of the intensities of the bands in Raman spectra of amorphous Ge-Sb-Te. These dependencies correlate with evolution of concentration of the different structural units in amorphous Ge-Sb-Te alloys. We have shown that the FIR and Raman spectra of Ge-Sb-Te are sensitive to the change in bonding mechanism upon crystallization. Obtained results confirm the more anharmonic behavior of the crystalline state of Ge-Sb-Te.

References

1. Wuttig M (2008) Phase-change materials: Towards a universal memory?. Nat Mater 4:265–266
2. Shportko K, Kremers S, Woda M et al (2008) Phase-change materials: vibrational softening upon crystallization and its impact on thermal properties. Nat Mater 7:653–658
3. Shportko K, Ruekamp R, Klym H (2015) CoRa: an innovative software for Raman spectroscopy. J NANO-Electron Phys 7:3005
4. Shportko K, Revutska L, Paiuk O, Baran J, Stronski A, Gubanova A, Venger E (2017) Compositional dependencies in the vibrational properties of amorphous GeAs-Se and Ge-Sb-Te chalcogenide alloys studied by Raman spectroscopy. Opt Mater (Amst) 73:489–496

5. Matsunaga T, Yamada N, Kojima R et al (2011) Resonant bonding in crystalline phase-change materials. Adv Funct Mater 21:2232–2239
6. Shportko K, Wuttig M (2015) Vibrations properties of Ge-Sb-Te phase change alloys at different temperatures. In: Fesenko OM (ed). 3rd International Research and Practice Conference "Nanotechnology and nanomaterials: Nano-2015", p. 252, Eurosvit, Lviv

Size Dependence of the Coupling Strength in Plasmon-Exciton Nanoparticles

Felix Stete, Phillip Schoßau, Wouter Koopman, and Matias Bargheer

Abstract The coupling between molecular excitations and nanoparticles leads to promising applications. It is for example used to enhance the optical cross-section of molecules in surface enhanced Raman scattering, Purcell enhancement or plasmon enhanced dye lasers. In a coupled system new resonances emerge resulting from the original plasmon (ω_{pl}) and exciton (ω_{ex}) resonances as

$$\omega_{\pm} = \frac{1}{2}(\omega_{pl} + \omega_{ex}) \pm \sqrt{\frac{1}{4}(\omega_{pl} - \omega_{ex})^2 + g^2}, \tag{1}$$

where g is the coupling parameter. Hence, the new resonances show a separation of $\Delta = \omega_+ - \omega_-$ from which the coupling strength can be deduced from the minimum distance between the two resonances, $\Omega = \Delta(\omega_+ = \omega_-)$.

Among the most frequent systems which exhibit a plasmon-exciton coupling are core-shell particles with a plasmonic core and an excitonic shell. These have been shown to possess various coupling strengths. However the dependence of the coupling strength on the nanoparticle size has not yet been investigated experimentally. Theoretical models have predicted an increase in the coupling strength for decreasing particle sizes [1], but this has not yet been confirmed in

F. Stete (✉)
Institut für Physik & Astronomie, Universität Potsdam, Potsdam, Germany

School of Analytical Sciences Adlershof (SALSA), Humboldt-Universität zu Berlin, Berlin, Germany
e-mail: stete@uni-potsdam.de

P. Schoßau · W. Koopman
Institut für Physik & Astronomie, Universität Potsdam, Potsdam, Germany

M. Bargheer
Institut für Physik & Astronomie, Universität Potsdam, Potsdam, Germany

Helmholtz Zentrum Berlin, Berlin, Germany

B. Di Bartolo et al. (eds.), *Quantum Nano-Photonics*, NATO Science for Peace and Security Series B: Physics and Biophysics,
https://doi.org/10.1007/978-94-024-1544-5_26

experiments. This fact is rooted in the technique that is mostly used to determine the coupling strength. Usually authors tune the plasmon resonance in their nanoparticles and deduce the coupling strength from Eq. (1). However this plasmon tuning is often realized by changing the particle size. With this technique an actual size dependence cannot be investigated; on the contrary, the size dependence even has to be neglected to deduce a constant value Ω.

This contribution presents an experimental study of the particle size dependence of the coupling strength. We deduce the coupling strength of core-shell nanorods with four different sizes by tuning the plasmon resonance over the exciton resonance and fitting Eq. (1) to the hybrid resonance positions. We tuned the plasmon resonances by changing the particles environment via layer-by-layer deposition of polyelectrolytes [2], a technique where the particle shape does not have to be changed. We investigated gold nanorods with transversal diameters of 10 nm, 25 nm, 40 nm and 50 nm. The coupling strength reaches from 115 meV for the biggest particles to 227 meV for the smallest particles.

The values follow a simple relation: The coupling strength between N emitters and a plasmonic cavity is given by

$$\Omega = \frac{\sqrt{N}\mu E_{vac}}{\hbar} \tag{2}$$

Here μ denotes the transition dipole moment of an emitter whereas E_{vac} represents the electric vacuum field given by

$$E_{\mathrm{vac}} = \sqrt{\frac{\hbar\omega}{2\epsilon\epsilon_0 V}} \tag{3}$$

Three assumptions need to be made: First, N scales with the particle surface A as the dye forms a monolayer on the particle; second, the mode volume V is equal to the physical volume of the particles V_{phys} (a valid assumption for small particles [3]); third, we regard the aspect ratio a/c equal for all four particle sizes. The three assumptions lead to a coupling dependence on the transversal diameter a of

$$\Omega \propto \sqrt{\frac{A}{V_{phy}}} = \frac{1}{\sqrt{a}}. \tag{4}$$

As will be presented our experimental data agrees very nicely with this model.

References

1. Antosiewicz TJ, Apell Sp, Shegai T (2014) Plasmon–exciton interactions in a core–shell geometry: from enhanced absorption to strong coupling. ACS Photon 1:454–463D.C.
2. Stete F, Koopman W, Bargheer M (2017) Signatures of strong coupling on nanoparticles: revealing absorption anticrossing by tuning the dielectric environment. ACS Photon 4:1669–1676
3. Koenderink AF (2010) On the use of Purcell factors for plasmon antennas. Opt Lett 35:4108–4210

Introduction to Shock Wave-Boundary Layer Interaction and Unstart in Supersonic Inlets

Hasan Tabanli and K. Bulent Yuceil

Abstract A supersonic aircraft is designed to exceed the speed of sound in its normal flight configurations. Supersonic aircrafts are affected by shock waves which are prime importance in air intakes whose purpose is to provide a stable, uniform, low-loss, subsonic flow to the engine face at all flight conditions. Oblique shock waves are an efficient form of compression; however, they interact with the boundary layer forming on the inlet walls. The shock-induced adverse pressure gradient can trigger large-scale separation, resulting in significant total pressure loss and flow distortion. Furthermore, the unsteady aspects of separated shock-wave/boundary-layer interactions (SWBLI) can cause large structural loads and may even lead to inlet unstart. During unstart, the original inlet shock system can eventually take the form of a detached bow shock that resides upstream of the inlet entrance. The unstart process can be severe with high transient pressure loads and it can lead to a loss of engine thrust. In order to eliminate or reduce the effects of these interactions their characteristics must be analyzed and active/passive control techniques must be employed.

Keywords Supersonic inlet · Shock-wave/boundary-layer interactions · Unstart

Brief Literature Summary Since the 1940s, many experimental and computational studies have been performed to better understand the SWBLI and unstart phenomena. A. Fage, and R.F. Sargent studied shock wave and turbulent boundary layer phenomena near the smooth flat plate by means of traverses made with pitot and static pressure probes, surface tubes and direct shadow and Topler striation photographs [1]. A. McCabe performed experiments on the interaction of the shock wave generated by a wedge in a supersonic wind tunnel with the turbulent boundary layer on the side wall [2]. S.M. Bogdonoff and A.H. Solarski obtained data in the

H. Tabanli (✉) · K. B. Yuceil
Department of Astronautical Engineering, Istanbul Technical University, Istanbul, Turkey
e-mail: hasantabanli@itu.edu.tr

B. Di Bartolo et al. (eds.), *Quantum Nano-Photonics*, NATO Science for Peace and Security Series B: Physics and Biophysics,
https://doi.org/10.1007/978-94-024-1544-5_27

form of static and pitot pressure distributions and shadow and Schlieren photographs for shock wave with a turbulent boundary layer on a flat wall at approximately M = 3 [3]. T. Handa, M. Masuda and K. Matsuo investigated the three-dimensional flow structure induced by normal shock wave/turbulent boundary layer interaction in a constant area rectangular duct by a laser-induced-fluorescence method [4]. R.A. Humble, G.E. Elsinga, F. Scarano and B.W. van Oudheusen carried out an experimental study to investigate the three-dimensional instantaneous structure of an incident shock wave/turbulent boundary layer interaction at Mach 2.1 using tomographic particle image velocimetry [5]. S. Sun and R. Guo proposed a highly curved serpentine inlet and experimentally studied. In this study a single array of vortex generators (VGs) employed within the inlet to improve the flow uniformity and the effects of mass flow ratio, free stream Mach number, angel of attack and yaw on the performance of inlet instrumented with VGs were obtained [6]. S. Lee, E. Loth and H. Babinsky investigated various vortex generators which include ramp, split-ramp and a new hybrid concept *ramped-vane* under normal shock conditions with a diffuser at Mach number of 1.3 [7]. W.R. Hawkins and E.J. Marquart performed a supersonic wind tunnel tests to investigate the start/unstart characteristics of a two dimensional generic inlet design [8]. J.L. Wanger, K.B. Yuceil, A. Valdivia, N.T. Clemens and D.S. Dolling experimentally investigated the dynamics of unstart of an inlet/isolator model in a Mach 5 flow [9].

References

1. Fage A, Sargent R (1947) Shock-wave and boundary-layer phenomena near a flat surface. In: Proceedings of the royal society of London A: mathematical, physical and engineering sciences. http://rspa.royalsocietypublishing.org/content/190/1020/1
2. McCabe A (1966) The three-dimensional interaction of a shock wave with a turbulent boundary layer. Aeronaut Q 17:231–252
3. Bogdonoff SM, Solarski A (1951) A preliminary investigation of a shockwave-turbulent boundary layer interaction. In: Princeton university NJ James Forrestal research center. http://www.dtic.mil/dtic/tr/fulltext/u2/a800233.pdf
4. Handa T, Masuda M, Matsuo K (2005) Three-dimensional normal shock wave/boundary layer interaction in a rectangular duct. AIAA J 43:2182–2185
5. Humble R, Elsinga G, Scarano F, Van Oudheusden B (2009) Three-dimensional instantaneous structure of a shock wave/turbulent boundary layer interaction. J Fluid Mech 622:33–62
6. Shu S, GUO RW (2006) Serpentine inlet performance enhancement using vortex generator based flow control. Chinese J Aeronaut 19:10–17
7. Lee S, Loth E, Babinsky H (2011) Normal shock boundary layer control with various vortex generator geometries. Comput Fluids 49:233–246
8. Hawkins W, Marquart E (1995) Two-dimensional generic inlet unstart detection at mach 2.5–5.0. https://doi.org/10.2514/6.1995-6019
9. Wagner J, Yuceil K, Valdivia A, Clemens N, Dolling D (2009) Experimental investigation of unstart in an inlet/isolator model in mach 5 flow. AIAA J 47:1528–1542

Investigation of the White Light Emission from Er/Nd/Yb Rare Earth Oxides at Vacuum and Atmospheric Pressure

Sevcan Tabanli, Gonul Eryurek, and Baldassare Di Bartolo

Abstract We present the production of white light emission with the monochromatic infrared light excitation of erbium oxide (Er_2O_3), ytterbium oxide (Yb_2O_3), and neodymium oxide (Nd_2O_3) nano-crystalline powders at atmospheric (1 Atm) and vacuum (0.03 mbar) pressures. We synthesized the rare-earth oxide nano-crystalline powders by thermal decomposition technique. The crystal structure and morphological properties were determined by X-Ray Diffraction (XRD) and high-resolution transmission electron microscope (HRTEM). The optical region emission spectra of rare earth oxide powders measured in the 400–900 nm wavelength region at 1 atm and 0.03 mbar pressure. Luminescence spectra upon 808 nm, and/or 975 nm diode laser excitation were carried out at room temperature. The white light (WL) emission properties, color quality parameters were investigated at atmospheric and vacuum pressures. **Synthesis Procedure** We synthesized the rare-earth oxide nano-crystalline powders by thermal decomposition technique. For synthesis, rare-earth nitrate salts were used as precursors. Alginic acid sodium salt was used for gelation [1]. Details on the preparation method were described in some previous works [2, 3]. **Results and Discussion** *Structural and Morphological Properties* X-ray diffraction (XRD) patterns were collected by Bruker AXS D8 diffractometer. According to JCPDS (Joint Committee for Powder Diffraction Data), the peak positions observed in the XRD pattern of Yb_2O_3, Nd_2O_3, and Er_2O_3 powders corresponded well with

S. Tabanli (✉) · G. Eryurek
Department of Physics Engineering, Istanbul Technical University, Istanbul, Turkey

Department of Physics, Boston College, Newton, MA, USA
e-mail: tabanlisevcan@itu.edu.tr

B. D. Bartolo
Department of Physics, Boston College, Newton, MA, USA

B. Di Bartolo et al. (eds.), *Quantum Nano-Photonics*, NATO Science for Peace and Security Series B: Physics and Biophysics,
https://doi.org/10.1007/978-94-024-1544-5_28

Card# 01-074-1981, Card# 01-070-2152, Card# 01-074-1983, respectively. The peak positions of Nd_2O_3 powder correspond well with $Nd_2O_2(CO_3)$ crystalline phase is originated from the combination of alginic acid and nitrate salt of neodymium during the synthesis process [3, 4]. The morphological properties were investigated by a Jeol 2100F model high resolution transmission electron microscope (HRTEM). The particle sizes are in good agreement with the results obtained from XRD measurements. *Spectroscopic Measurements* The optical region emission spectra upon 808 nm, and/or 975 nm diode laser excitation were carried out at room temperature. For vacuum pressure, the samples were mounted in a closed chamber pumped by a vacuum pump. Both at vacuum and atmospheric pressures, bright white light was observed under 808 nm laser excitation for Nd_2O_3, Er_2O_3 nano powder, and under 975 nm laser excitation for Yb_2O_3, Er_2O_3. We also observed some additional overlapping anti-Stokes type emissions at vacuum pressure. The white emission behavior of Nd_2O_3 at two different pressures are given as an example in Fig. 1.

Keywords Thermal decomposition method · White light production · Upconversion · Nanocrystal · Rare-earth oxide

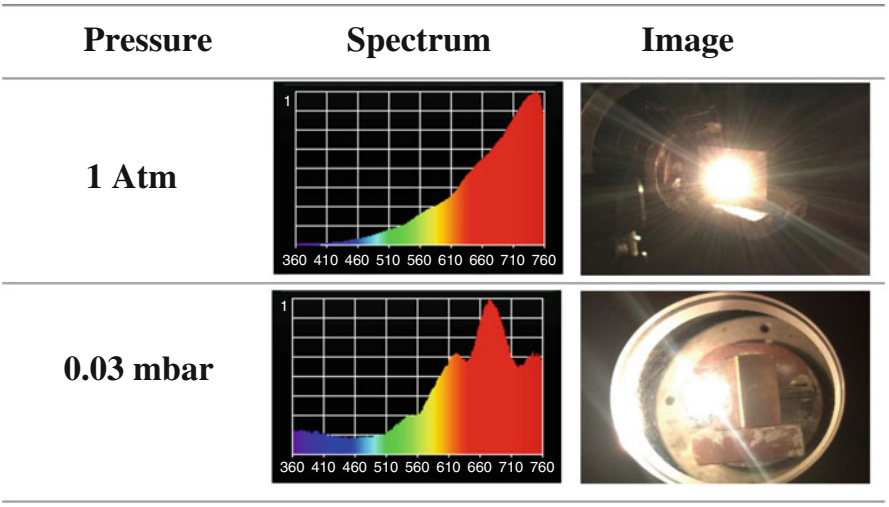

Fig. 1 The white emission behavior of Nd_2O_3 at two different pressures under 808 nm laser excitation

Acknowledgements This work was supported by Istanbul Technical University Scientific Research Projects Department (ITU BAP, project number 39283). The author, Sevcan Tabanli, is grateful to The Scientific and Technological Research Council of Turkey for granting a scholarship (TUBITAK, 2211C) for her Ph.D. studies.

References

1. Stavgianoudaki N, Papathanasiou KE, Colodrero RM et al (2012) Crystal engineering in confined spaces. A novel method to grow crystalline metal phosphonates in alginate gel systems. CrystEngComm 14:5385–5389
2. Tabanli S, Eryurek G, Di Bartolo B (2017) White light emission from Er_2O_3 nano-powder excited by infrared radiation. Opt Mater 69:207–213
3. Tabanli S, Bilir G, Eryurek G (2017) Optical properties and Judd-Ofelt analysis of Nd_2O_3 nanocrystals embedded in polymethyl methacrylate. J Rare Earths. https://doi.org/10.1016/j.jre.2017.07.010
4. Zhang Y, Jin L, Sterling K, Luo Z, Jiang T, Miao R, Guild C, Suib SL (2015) Potassium modified layered $Ln_2O_2CO_3$ (Ln:La, Nd, Sm, Eu) materials: efficient and stable heterogeneous catalysts for biofuel production. Green Chem 17:3600–3608

Carbon Nanotubes as Integrated Electrically Driven Light Source

N. Walter, S. Khasminskaya, and W. H. P. Pernice

Abstract A main component enabling integrated quantum optics and quantum-information is an integrated single photon source (Eisaman MD, Fan J, Migdall A, Polyakov SV: Rev Sci Instrum 82(7):71101, 2011). The usual work horse of quantum optic sources, parametric down-conversion, is hard to integrate due to the non-compatibility with most photonic material systems used in integrated photonics. This problem has sparked the development of novel approaches to generate non-classical light on-chip, e.g. the use of nano-emitters as trapped ions, molecules, SiV, Quantum dots, etc. Most of these emitters are excited optically which requires additional external or internal lasers and subsequent filtering of the pump light which is hard to achieve on-chip (Aharonovich DE, Toth M: Nat Photonics 10(10):631–641, 2016). Another obstacle for the large-scale integration of these emitters is the need to align them within the photonic circuit on a chip. For most sources this can be done via a 'pick-and-place'-technique, which is a delicate and time-consuming method.

Here, we present our work on semi-conducting single walled carbon nanotubes (sc-SWCNTs) as an integrated light source (Khasminskaya S, Pyatkov F, Flavel BS, Pernice WH, Krupke R: Adv Mater 26(21):3465–3472, 2014; Pyatkov F et al Nat Photonics 10(6):420–427, 2016). The use of electroluminescent or incandescent light from the sc-SWCNT omits the need of optical pumping and therefore avoids spectral filtering schemes. Furthermore, sc-SWCNTs can be assembled to photonic structures in a directed fashion on a wafer-scale using dielectrophoresis (Vijayaraghavan A et al: Nano Lett 7(6):1556–1560, 2007). The electroluminescence spectrum from the sc-SWCNTs exhibits antibunching which indicates non-classical light emitted from these sources, measured directly on-chip in an all integrated photonic circuit (Khasminskaya S et al: Nat Photonics 1–19, 2016).

N. Walter (✉) · W. H. P. Pernice
Institute of Physics, University of Muenster, Muenster, Germany
e-mail: n.walter@uni-muenster.de

S. Khasminskaya
Institute of Nanotechnology, Karlsruhe Institute of Technology, Karlsruhe, Germany

B. Di Bartolo et al. (eds.), *Quantum Nano-Photonics*, NATO Science for Peace and Security Series B: Physics and Biophysics,
https://doi.org/10.1007/978-94-024-1544-5_29

References

1. Eisaman MD, Fan J, Migdall A, Polyakov SV (2011) Invited review article: single-photon sources and detectors. Rev Sci Instrum 82(7):71101
2. Aharonovich DE, Toth M (2016) Solid-state single-photon emitters. Nat Photonics 10(10):631–641
3. Khasminskaya S, Pyatkov F, Flavel BS, Pernice WH, Krupke R (2014) Waveguide-integrated light-emitting carbon nanotubes. Adv Mater 26(21):3465–3472
4. Pyatkov F et al (2016) Cavity-enhanced light emission from electrically driven carbon nanotubes. Nat Photonics 10(6):420–427
5. Vijayaraghavan A et al (2007) Ultra-large-scale directed assembly of single-walled carbon nanotube devices. Nano Lett 7(6):1556–1560
6. Khasminskaya S et al (2016) Fully integrated quantum photonic circuit with an electrically driven light source. Nat Photonics, vol. to be publ, no. September 1–19

Part III
Posters

Plasmonic Metasurfaces for Nonlinear Structured Light

Antonino Calà Lesina, Pierre Berini, and Lora Ramunno

Abstract Nonlinear optical processes can be enhanced at the nanoscale by exploiting plasmonic field enhancement [1]. Recently, hybrid metallic/dielectric nanostructures have been proposed to boost the nonlinear emission [2], but separating the nonlinear contributions from metal and dielectric is not easy in experiments. This led us to study the third harmonic generation (THG) from a gold dipole nanoantenna containing a nonlinear dielectric nanoparticle in its gap [3], such to delineate the design conditions to have the nonlinear emission dominating in the gap material or in the metal. The control of polarization and phase of the THG emitters is also required to shape the nonlinear far-field. In [4], a so called "butterfly nanoantenna" (Fig. 1a) is proposed to precisely control the polarization and phase of the linear field in the gap, which is used to drive the emission from a nonlinear gap material. The nonlinear emitter localized in the gap behaves as an ideal source, with its polarization oriented along the polarization of the linear field (red arrow in Fig. 1a), and the nonlinear phase ϕ_{NL} is related to the linear phase ϕ_L by $\phi_{NL} = n \cdot \phi_L$, where n is the order of the nonlinearity ($n = 3$ for THG). The scheme in Fig. 1b shows how to design a nonlinear metasurface by placing the red arrows, i.e., the nanoantennas, in a square lattice at locations (r, ϕ), and progressively rotating them by $\theta = \theta_0 + \gamma\phi$, where θ_0 is the orientation along the positive x-axis, and γ is the number of full rotations of the nanoantenna per 2π. The control of the nonlinear phase is achieved by exploiting the Pancharatnam-Berry phase [5], which allows us to excite the metasurface by circularly polarized light and to obtain a vortex beam carrying orbital angular momentum (OAM) due to spin-orbit coupling [6]. Moreover, using a nonlinear process allows us to structure light at frequencies that would not be accessible via the linear response of plasmonic devices, and that are spectrally separated from the incoming radiation, leading to highly pure states. Our approach is demonstrated by large-scale FDTD simulations on an IBM BlueGene/Q

A. Calà Lesina (✉) · P. Berini · L. Ramunno
Department of Physics and Centre for Research in Photonics, University of Ottawa, Ottawa, ON, Canada
e-mail: antonino.calalesina@uottawa.ca

B. Di Bartolo et al. (eds.), *Quantum Nano-Photonics*, NATO Science for Peace and Security Series B: Physics and Biophysics,
https://doi.org/10.1007/978-94-024-1544-5_30

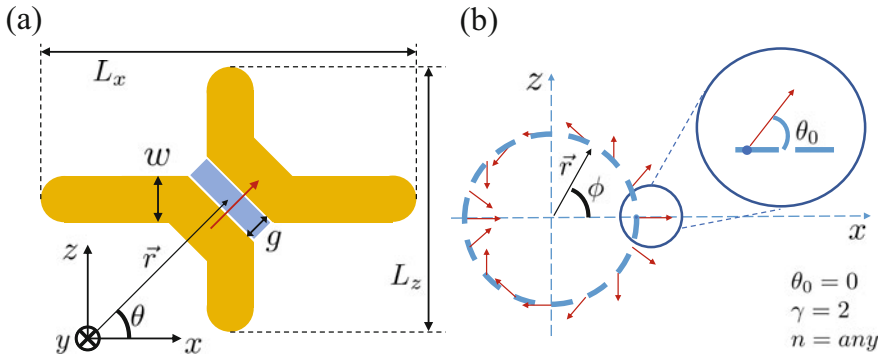

Fig. 1 (**a**) Butterfly nanoantenna. (**b**) Arrangement of nanoantennas in a metasurface

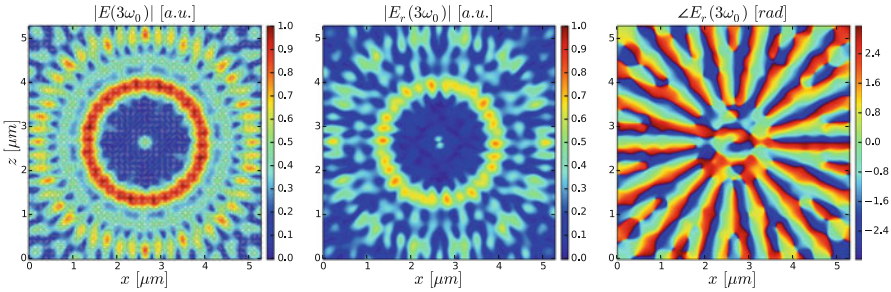

Fig. 2 Nonlinear far-field beam for $\gamma = 8$ carrying OAM state of $l = 17$

supercomputer (SOSCIP). In Fig. 2, we show the THG far-field beam obtained for a metasurface with $\gamma = 8$, by applying the Fraunhofer diffraction formula to the nonlinear near-field. The OAM state of the innermost intensity ring, figuring as a phase term $e^{il\phi}$ in the far-field electric field, is given by $l = 1 + (n-1)\gamma = 17$. This beam synthesis framework is general and can be scaled to create highly pure nonlinear vectorial beams of arbitrary complexity, such as Laguerre-Gaussian beams with high OAM state [4].

References

1. Kauranen M, Zayats AV (2012) Nonlinear plasmonics. Nat Photon 6:737–748
2. Aouani H et al (2014) Third-harmonic-upconversion enhancement from a single semiconductor nanoparticle coupled to a plasmonic antenna. Nat Nanotechnol 9:290–294
3. Calà Lesina A, Berini P, Ramunno L (2017) Origin of third harmonic generation in plasmonic nanoantennas. Opt Mater Express 7(5):1575–1580
4. Calà Lesina A, Berini P, Ramunno L (2017) Vectorial control of nonlinear emission via chiral butterfly nanoantennas: generation of pure high order nonlinear vortex beams. Opt Express 25(3):2569–2582
5. Li G et al (2015) Continuous control of the nonlinearity phase for harmonic generations. Nat Mater 14:607–612
6. Karimi E et al (2014) Generating optical orbital angular momentum at visible wavelengths using a plasmonic metasurface. Light Sci Appl 3:e167

Cell Poration of Fixed and Live Cells by Phase Shaped Femtosecond Pulses

Gabriel Campargue, Bastian Zielinski, Sébastien Courvoisier, Cristian Sarpe, Luigi Bonacina, Thomas Baumert, and Jean-Pierre Wolf

Abstract In femtosecond optical transfection and nanosurgery, cell survival critically depends on phototoxicity. It is therefore of primary importance to optimize the laser-cell interaction in order to increase the membrane poration efficiency while reducing collateral cell damage. Baumert group studied the impact of spectral phase modulation of femtosecond for machining on glass substrate. They demonstrated that the use of third order phase pulses (Airy pulses) could modulate the photon-interaction leading to holes of higher aspect ratio, compared to those produced by femtosecond bandwidth limited pulses. Following this approach, we showed that optimally shaped temporal Airy pulses display better performances also on fixed biological samples. In fact, Airy pulses can increase the cell membrane poration efficiency for a lower peak intensity and a similar energy per pulse than bandwith limited femtosecond pulses. We also discuss results from a live cell experiment. We set up a protocol where we investigate cells poration efficiency and cell viability as a function of pulse spectral phase. Hence, we present a protocol based on the use of three fluorophores to assess cells viability at different time points after poration.

G. Campargue (✉) · S. Courvoisier · L. Bonacina · J.-P. Wolf
GAP Biophotonics, University of Geneva, Geneva, Switzerland
e-mail: gabriel.campargue@unige.ch

B. Zielinski · C. Sarpe · T. Baumert
Institute of Physics, University of Kassel, Kassel, Germany

B. Di Bartolo et al. (eds.), *Quantum Nano-Photonics*, NATO Science for Peace and Security Series B: Physics and Biophysics,
https://doi.org/10.1007/978-94-024-1544-5_31

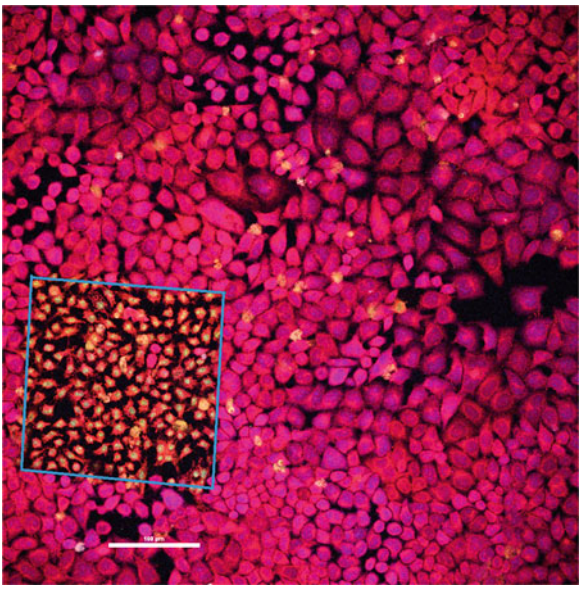

Fig. 1 Fixed cancer cells imaged by non-linear microscopy. Red: cells alive one hour after poration. Green/yellow: cell with porated membrane (either dead or laser porated). The blue square outlines the sample region where laser poration was performed. Scalebar = 100 μm

On-Chip Nonlinear Optics in Silicon Rich Nitride Photonic Crystal Cavities

Marco Clementi, D. Kapil, F. Gardes, and M. Galli

Abstract Photonic crystal (PhC) nanocavities allow to confine light with ultra high quality (Q) factors to wavelength-sized mode volumes, with a strong enhancement of light-matter interaction. Although these features make PhC cavities a promising platform for integrated nonlinear optical components, the usual materials of photonic fabrication (specifically silicon and gallium arsenide) suffer from parasitic effects such as two-photon absorption (TPA) and free-carrier absorption (FCA), which limit the benefits of integration. In this work we show how a novel material, silicon rich nitride [1], can be successfully employed for the fabrication of air membraned PhC cavities reaching ultra high Q factor at telecom wavelength. We fabricated samples with line-width modulated geometry, approaching a theoretical value (from FDTD simulations) of $Q_{th} = 520,000$. We then measured the cavities with resonant scattering technique [2], determining a maximum experimental value $Q_{exp} = 122,000$. We later studied the spectral behaviour of the cavity at a regime of optical bistability [3]. The resulting analysis of the thermo-optic resonance shift as a function of input power suggests the absence of TPA and TPA-related FCA. In order to confirm the suitability of this material for nonlinear optical signal processing, we designed and fabricated far-field optimized samples [4] with heterostructure geometry. Far-field optimization allows to dramatically increase the coupling of the cavity to focused laser beams, thus increasing the available intracavity optical power. In this experimental configuration we observed second (SHG) and third (THG) harmonic generation even at low CW input power (as low as a fraction of milliwatt). These results confirm the suitability of silicon rich nitride as a potential platform for efficient integrated nonlinear optical devices based upon PhC nanocavities in a fully CMOS compatible approach.

M. Clementi (✉) · M. Galli
Department of Physics, University of Pavia, Pavia, Italy
e-mail: marco.clementi01@universitadipavia.it

D. Kapil · F. Gardes
Optoelectronics Research Centre, University of Southampton, Southampton, UK

B. Di Bartolo et al. (eds.), *Quantum Nano-Photonics*, NATO Science for Peace and Security Series B: Physics and Biophysics,
https://doi.org/10.1007/978-94-024-1544-5_32

Keywords Photonic crystal cavities · Silicon rich nitride · Integrated nonlinear optics

References

1. Lacava C, Stankovic S, Khokhar AZ, Bucio TD, Gardes FY, Reed GT, Richardson DJ, Petropoulos P (2017) Si-rich silicon nitride for nonlinear signal processing applications. Sci Rep 7(1):22
2. Galli M, Portalupi SL, Belotti M, Andreani LC, O'Faolain L, Krauss TF (2009) Light scattering and Fano resonances in high-Q photonic crystal nanocavities. Appl Phys Lett 94(7):071101
3. Barclay PE, Srinivasan K, Painter O (2005) Nonlinear response of silicon photonic crystal microresonators excited via an integrated waveguide and fiber taper. Opt Exp 13(3):801–820
4. Portalupi SL, Galli M, Reardon C, Krauss TF, O'Faolain L, Andreani LC, Gerace D (2010) Planar photonic crystal cavities with far-field optimization for high coupling efficiency and quality factor. Opt Express 18:16064–16073

Mechanical Activity: The Elastic Counterpart of Optical Activity

T. Frenzel, M. Kadic, and M. Wegener

Abstract Recent advances in 3D-printing technologies enable more and more sophisticated designs of artificial materials, so called metamaterials. Thereby, properties well beyond the limits of ordinary Cauchy mechanics can be achieved [1]. In our work, we design, fabricate and characterize chiral micropolar mechanical metamaterials, that show mechanical activity – the elastic analogue of optical activity [2]. Finite-element band structure calculations indicate, that the lowest two transversal modes are circular polarized. In addition, the degeneracy of these modes is lifted and the relative phase velocities differ by up to 5%. Hence, the polarization vector of linear polarized waves would rotate when propagating through such media. To unambiguously identify effects originating from chirality, static experiments have been performed showing a twist upon pushing onto a bar. This rotational degree of freedom is absent in ordinary Cauchy mechanics. The necessary sliding boundary conditions have been realized experimentally by putting a right handed structure on top of left handed structure. Thereby, the face between these two structures is free to rotate and rotation angles exceeding 2 per percent strain have been measured. Additionally, the micropolar theory predicts a breakdown of scalability due to the presence of a local length scale [3]. Intuitively, this lenght scale can be associated with the substructure of the material, like the distance between atoms or the lattice

T. Frenzel (✉)
Institute of Applied Physics, Karlsruhe Institute of Technology, Karlsruhe, Germany
e-mail: Frenzel@kit.edu

M. Kadic
Institute of Applied Physics, Karlsruhe Institute of Technology, Karlsruhe, Germany

Institut FEMTO-ST, CNRS, Universit de Bourgogne Franche-Comt, Besanon, France

Institute of Nanotechnology, Karlsruhe Institute of Technology, Karlsruhe, Germany

M. Wegener
Institute of Applied Physics, Karlsruhe Institute of Technology, Karlsruhe, Germany

Institute of Nanotechnology, Karlsruhe Institute of Technology, Karlsruhe, Germany

B. Di Bartolo et al. (eds.), *Quantum Nano-Photonics*, NATO Science for Peace and Security Series B: Physics and Biophysics,
https://doi.org/10.1007/978-94-024-1544-5_33

constant a of an artificial material. Therefore, the crucial experiments are probing the twist per strain and the effective Young's modulus as a function of L/a, with L being the sidelength of the sample.

References

1. Wegener M (2002) Metamaterials beyond optics. Science 342:939
2. Lakhtkia A, Varadan VV (1988) Elastic wave propagation in noncentrosymmetric, isotropic media: dispersion and field equations. J Appl Phys 63:5246
3. Eringen AC (1999) Microcontinuum field theories: I. Foundations and solids. Springer Science & Business Media, New York

Highly Compact and Scalable Waveguide-Integrated Single Photon Spectrometer Based on Tailored Disorder

W. Hartmann, P. Varytis, K. Busch, and W. H. P. Pernice

Abstract The understanding of the underlying physics of randomly disordered systems has been subject to many different studies, especially in the field of integrated photonics. It has been shown (Redding B, Liew SF, Sarma R, Cao H: Nat Photonics 7:746, 2013) that for certain applications randomly disordered photonic systems have major advantages in comparison to conventional systems. One such application is an on-chip integrated spectrometer. Conventional spectrometer designs are based on ring resonators, so-called arrayed waveguide grating or echelle gratings. Those designs are prone to fabrication errors and exhibit a very large footprint.

Here we utilize the unique properties of randomly oriented scatterers to build a highly broadband and narrow linewidth, yet low footprint on-chip integrated spectrometer. In combination with integrated superconducting nanowire single-photon detectors (Pernice WHP, Schuck C, Minaeva O, Li M, Goltsman GN, Sergienko AV, Tang HX: Nat Commun 3:1325, 2012) this device will be able to resolve optical spectra on the single photon level which is interesting for instance for single-photon spectroscopy or quantum wavelength multiplexing.

References

1. Redding B, Liew SF, Sarma R, Cao H (2013) Nat Photonics 7:746
2. Pernice WHP, Schuck C, Minaeva O, Li M, Goltsman GN, Sergienko AV, Tang HX (2012) Nat Commun 3:1325

W. Hartmann (✉) · W. H. P. Pernice
Institute of Physics, University of Münster, Münster, Germany

CeNTech – Center for Nanotechnology, University of Münster, Münster, Germany
e-mail: wladick.hartmann@uni-muenster.de

P. Varytis · K. Busch
Institute of Physics, Humboldt-University Berlin, Berlin, Germany

Max-Born Institute, Berlin, Germany

B. Di Bartolo et al. (eds.), *Quantum Nano-Photonics*, NATO Science for Peace and Security Series B: Physics and Biophysics,
https://doi.org/10.1007/978-94-024-1544-5_34

Symmetry Breaking and Active Fano Resonance Tuning in Dolmen Nanostructures

G. R. S. Iyer, C. T. Ellis, A. J. Giles, J. G. Tischler, and J. D. Caldwell

Abstract Polar-dielectrics have garnered a lot of attention as an alternative to the metal plasmons to support sub-diffractional confinement of light in the mid-infrared to THz regime due to their very low optical losses (Caldwell JD, Lindsay L, Giannini V, Vurgaftman I, Reinecke TL, Maier SA, Glembocki OJ: Nanophotonics 4(44), 2015). The surface phonon polariton (SPhP) in SiC, a polar dielectric, is formed when the optical phonon vibration in the crystal lattice couple with the incident radiation. Recently coupled phononic SiC nanostructures have received enormous attention both in basic research and applied research (Caldwell JD, Glembocki OJ, Francescato Y, Sharac N, Giannini V, Bezares FJ, Long JP, Owrutsky JC, Vurgaftman I, Tischler JG, Wheeler VD, Bassim ND, Shirey LM, Kasica R, Maier SA: Nano Lett 13:3690, 2013; Ellis CT, Tischler JG, Glembocki OJ, Bezares FJ, Giles AJ, Kasica R, Shirey LM, Owrutsky JC, Chigrin DN, Caldwell JD: Sci Rep 6(32959), 2016). In this work, we fabricate a metasurface in the form of SiC nanostructured dolmen structures from a 4H-SiC substrate, which enables creation of new optical modes via periodicity induced symmetry breaking that are active in the Reststrahlen band region (window between the transverse and longitudinal optical phonons). The polarisation dependent far field studies reveal that the nanostructures exhibit very strong dipolar and quadrupolar resonances and the interaction between the radiant, broader dipolar modes with the narrow, sub-radiant quadrupolar modes gives rise to a unique asymmetric Fano type of resonance. By controlling the geometry and spacing of the features in the dolmen we notice that the resonances can be highly tunable, resulting in exceptional optical properties highly desirable to enhance the performance of various nanophotonic applications.

G. R. S. Iyer (✉) · C. T. Ellis · A. J. Giles · J. G. Tischler
U.S. Naval Research Laboratory, Washington, DC, USA
e-mail: swathiiyer.ganjigunteramaswamy.ctr.in@nrl.navy.mil

J. D. Caldwell
U.S. Naval Research Laboratory, Washington, DC, USA

Electrical and Mechanical Engineering, Vanderbilt University, Nashville, TN, USA

B. Di Bartolo et al. (eds.), *Quantum Nano-Photonics*, NATO Science for Peace and Security Series B: Physics and Biophysics,
https://doi.org/10.1007/978-94-024-1544-5_35

Keywords Surface phonon polaritons · Strongly coupled systems · Fano resonance

References

1. Caldwell JD, Lindsay L, Giannini V, Vurgaftman I, Reinecke TL, Maier SA, Glembocki OJ (2015) Nanophotonics 4(44)
2. Caldwell JD, Glembocki OJ, Francescato Y, Sharac N, Giannini V, Bezares FJ, Long JP, Owrutsky JC, Vurgaftman I, Tischler JG, Wheeler VD, Bassim ND, Shirey LM, Kasica R, Maier SA (2013) Nano Lett 13:3690
3. Ellis CT, Tischler JG, Glembocki OJ, Bezares FJ, Giles AJ, Kasica R, Shirey LM, Owrutsky JC, Chigrin DN, Caldwell JD (2016) Sci Rep 6(32959)

Pump-Profile Engineering for Spatial- and Spectral-Mode Control in Two-Dimensional Colloidal-Quantum-Dot Spasers

Robert C. Keitel, Jian Cui, Stephan J. P. Kress, Boris le Feber, Ario Cocina, Karl-Augustin Zaininger, and David J. Norris

Abstract In the initial proposal of the spaser – a source of coherent, intense, and narrow-band surface plasmons – colloidal quantum dots were envisioned as an ideal gain medium for compensation of the significant losses intrinsic to plasmonics. However, many spasers shown to date have required a single material to both serve as a gain medium and define the plasmonic cavity, a design that prevents the use of quantum dots or other colloidal nanomaterials. In addition, these concepts are inherently challenging for integration in a larger plasmonic circuit.

We have recently established a new class of spasers in which the gain medium and cavity are decoupled by combining both top-down and bottom-up fabrication. Our devices consist of planar plasmonic Fabry-Perot-type cavities, defined by aberration-corrected block reflectors placed precisely on an ultrasmooth silver substrate, that are then filled with colloidal quantum dots. Photoexcitation yields high-quality-factor (Q∼1000) multimode spasing within the gain envelope of the quantum-dot emission spectrum.

In contrast to many conventional laser sources, our cavity design allows direct access to the full active region due to its two-dimensional nature. Consequently, the device can be pumped not only in its entirety with a spatially uniform beam, but with arbitrary 2D pump profiles generated by a spatial light modulator. In combination with the extremely high quality factors, this gives us unprecedented access to the physics of spaser modes. Using well-defined excitation patterns, we are thus able to isolate the contributions of specific modes, both transverse and longitudinal.

R. C. Keitel (✉) · J. Cui · S. J. P. Kress · B. le Feber · A. Cocina · K.-A. Zaininger · D. J. Norris
OMEL, ETH Zürich, Zürich, Switzerland
e-mail: keitelr@ethz.ch

B. Di Bartolo et al. (eds.), *Quantum Nano-Photonics*, NATO Science for Peace and Security Series B: Physics and Biophysics,
https://doi.org/10.1007/978-94-024-1544-5_36

With analytical calculations of the spasing modes based on gaussian beam analysis as a starting point for well-defined excitation patterns, we are able to bias the mode competition adaptively in favor of specified transverse modes. We thereby experimentally verify the applicability of conventional laser theory to spasers. Our technique of spatially modulated pumping allows efficient characterization of 2D spasers and thus paves the way towards engineering of devices with optimized device footprint for on-chip applications.

Hybridizing Whispering Gallery Modes and Plasmonic Resonances in a Photonic Meta-device for Bio-sensing Applications

Carolin Klusmann

Abstract High-Q dielectric whispering gallery mode (WGM) resonators emerged as promising sensing-platforms which enable ultra-sensitive detection of e.g. nanoparticles (NPs) [1] or single molecules [2]. Measuring the shift in the resonance wavelength of a high-Q dielectric whispering gallery mode (WGM) resonator induced upon changing the dielectric environment is thereby a prime sensing strategy. To increase the sensitivity of dielectric WGM resonators, strategies have to be developed to push the optical mode further outside the resonator to enhance its interaction with the surrounding.

This contribution has presented a novel approach to improve the sensing capabilities of optical microresonators. We have studied theoretically and numerically a photonic meta-device consisting of a dielectric microdisk resonator decorated with a large number of randomly distributed and densely arranged gold nanoparticles. By relying on metamaterial concepts, we have considered the layer of gold NPs surrounding the resonator as a homogenous medium to which effective properties are assigned. This effective treatment allows for an efficient tuning of its properties and is the key to investigate resonator systems with huge NP densities.

Careful spectral tuning of the plasmonic resonance relative to the WGM increases the sensitivity to a notable extent at an acceptable simultaneous decrease of the quality factor [3]. We have demonstrated that dielectric WGM resonators with ultra-thin homogeneous metal coatings with thicknesses <15 nm can be well mimicked with our effective medium approach. By replacing ultra-thin metallic films with NP composites hybrid devices with comparable optical properties can be

C. Klusmann (✉)
Institute of Applied Physics, Karlsruhe Institute of Technology, Karlsruhe, Germany
e-mail: carolin.klusmann@kit.edu

B. Di Bartolo et al. (eds.), *Quantum Nano-Photonics*, NATO Science for Peace and Security Series B: Physics and Biophysics,
https://doi.org/10.1007/978-94-024-1544-5_37

fabricated with ease via self-assembly techniques. In contrast to the challenging fabrication of ultra-thin, ultra-smooth metallic coatings on micron-sized non-planar dielectric substrates, our metamaterial-inspired approach is robust against fabrication imperfection as the only critical parameter is the NP density.

References

1. Swaim JD, Knittel J, Bowen WP (2013) Appl Phys Lett 102:183106
2. Vollmer F, Arnold S (2008) Nat Methods 5:591–596
3. Klusmann C, Suryadharma RNS, Oppermann J, Rockstuhl C, Kalt H (2017) J Opt Soc Am B 34:D46–D55

Three-Dimensional Chiral Photonic Crystals in the THz Regime Exhibiting Weyl Points with Topological Charges

Julian Köpfler, Christian Kern, Ming-Li Chang, Che Ting Chan, and Martin Wegener

Abstract Recently, the existence of multiple Weyl points was theoretically shown for chiral woodpile photonic crystals [1]. These Weyl points carry topological charges and thus lead to the emergence of backscattering-immune gapless surface states, making the photonic crystal a topological photonic insulator. The proposed photonic crystal structure consists of chirally stacked rods made of a perfect electric conductor (PEC), forming a hexagonal lattice. The structure parameters are designed to obtain isolated Weyl points in the THz regime. Polymer structures are fabricated using three-dimensional laser lithography and subsequently coated with silver via polymer sensitization and electroless deposition. For a silver film thickness well above the skin depth of the THz radiation, a material optically comparable to a bulk PEC can be realized. Measurements of the angle resolved transmission spectra using photoconductive antennas as THz sources and detectors will be carried out soon. From these spectra one can obtain the band structure and hence show the existence of the Weyl points.

Reference

1. Chang M, Xiao M, Chen W, Chan CT (2017) Multiple Weyl points and the sign change of their topological charges in woodpile photonic crystals. Phys Rev B 95:12

J. Köpfler (✉)
Institute of Applied Physics, Karlsruhe Institute of Technology (KIT), Karlsruhe, Germany
e-mail: julian.koepfler@student.kit.edu

C. Kern · M. Wegener
Institute of Applied Physics, Karlsruhe Institute of Technology (KIT), Karlsruhe, Germany

Institute of Nanotechnology, Karlsruhe Institute of Technology (KIT), Eggenstein-Leopoldshafen, Germany

M.-L. Chang · C. T. Chan
Physics Department, Hong Kong University of Science and Technology, Hong Kong, China

B. Di Bartolo et al. (eds.), *Quantum Nano-Photonics*, NATO Science for Peace and Security Series B: Physics and Biophysics,
https://doi.org/10.1007/978-94-024-1544-5_38

Three-Dimensional Fluorescent Security Features Fabricated via 3D Laser Lithography

Frederik Mayer, Stefan Richter, Phillip Hübner, Toufic Jabbour, and Martin Wegener

Abstract In the field of optical security features, which are commonly used to protect products or documents against forgery, there is an ongoing race between researchers developing new security features and counterfeiters finding new methods to fake them. Thus, security features continuously need to be improved.

Today's optical security features are usually based on planar (2D) fabrication techniques. To further improve the level of counterfeiting security, we have recently proposed, fabricated and characterized three-dimensional fluorescent security features, which are 3D-printed by Direct Laser Writing [1]. These security features consist of a non-fluorescent support structure, into which different fluorescent markers containing CdSSe/ZnS quantum dots with different emission wavelengths can be printed in any arbitrary pattern. Thus, data can be stored in the security feature. The structures can be read out by optical sectioning methods. We use confocal laser scanning microscopy, and show fluorescence images as well as well as 3D-reconstructions calculated from the whole fluorescence image stack.

Reference

1. Mayer F, Richter S, Hübner P, Jabbour T, Wegener M (2017) 3D fluorescence-based security features by 3D laser lithography. Adv Mater Technol 2(11):1700212

F. Mayer (✉) · M. Wegener
Institute of Nanotechnology (INT), Karlsruhe Institute of Technology (KIT), Karlsruhe, Germany

Institute of Applied Physics (APH), Karlsruhe Institute of Technology (KIT), Karlsruhe, Germany
e-mail: frederik.mayer@kit.edu

S. Richter · P. Hübner
Carl Zeiss AG, Jena, Germany

T. Jabbour
Carl Zeiss AG, Oberkochen, Germany

B. Di Bartolo et al. (eds.), *Quantum Nano-Photonics*, NATO Science for Peace and Security Series B: Physics and Biophysics,
https://doi.org/10.1007/978-94-024-1544-5_39

Strong Coupling Effects Between IR-Inactive Zone Folded LO Phonon and Localized Surface Phonon Polariton Modes in SiC Nanopillars

Michael A. Meeker, Chase T. Ellis, Joseph G. Tischler, Alexander J. Giles, Orest J. Glemboki, Dmitry N. Chigrin, Francisco J. Bezares, Richard Kasica, Loretta Shirey, and Joshua D. Caldwell

Abstract While plasmonics have a broad range of technological applications including infrared photovoltaics and photodetectors, plasmonic metals are subject to high optical losses in the long-wave infrared spectral regime. In order to reduce optical losses in the infrared, alternatives to plasmonic metals are being explored. One promising alternative employs polar dielectric materials, which exhibit a highly-reflective, optically-metallic spectral band (Reststrahlen band), bounded by the LO and TO optical phonons, and are capable of supporting plasmonic-like resonance in the infrared. In polar dielectrics, plasmonic-like resonances, known as surface phonon polariton (SPhP) resonances, arise from a coupling between incident light and collective oscillations of bound lattice charges, which are mediated by the optical phonons. In this study, we have examined the SPhP resonances of SiC nanopillars with constant height of 950 nm and width in the range of 200–400 nm, as a function of their aspect ratio (AR=Length/Width=0.5–16). As the nanopillar width is decreased, we have found that localized SPhP resonances redshift towards

M. A. Meeker (✉) · C. T. Ellis · J. G. Tischler · A. J. Giles · O. J. Glemboki · L. Shirey
J. D. Caldwell
U.S. Naval Research Laboratory, Washington, DC, USA
e-mail: michael.meeker.ctr@nrl.navy.mil

D. N. Chigrin
Institute of Physics (IA), RWTH Aachen University, Aachen, Germany

F. J. Bezares
IFCO-The Institute of Photonic Sciences, Barcelona, Spain

R. Kasica
Center for Nanoscale Science and Technology, National Institutes of Standards and Technology, Gaithersburg, MD, USA

B. Di Bartolo et al. (eds.), *Quantum Nano-Photonics*, NATO Science for Peace and Security Series B: Physics and Biophysics,
https://doi.org/10.1007/978-94-024-1544-5_40

the zone folded LO (ZFLO) phonon that is normally not infrared active. However, as localized SPhP resonances are spectrally tuned through the ZFLO mode, we have found that the latter mode becomes infrared active. Furthermore, reflectance measurements have revealed strong coupling between the ZFLO and both the monopolar and dipolar localized SPhP resonances.

Measuring the Intensity Profile of Arbitrary Shaped Laser Foci Using Confocal Microscopy

Tobias Messer, Patrick Müller, and Martin Wegener

Abstract 3D printing is an emerging field both on the macro and the nano scale. Especially while working in the nano scale, there are a lot of limiting factors for resolution. One way to improve it, is the usage of two-photon absorption in combination with the STED mechanism – well known from super-resolution microscopy. In this scheme, two lasers are used. One laser with a common Gaussian focus excites the photoresist via two-photon absorption, leading to polymerization, while a second laser with a different wavelength suppresses this reaction. The phase of the second laser is modified such way that a focus shape with a spot of zero intensity, e.g. a donut-shaped focus, arises. While not having a conceptual limit, the experimentally achievable resolution of this approach can be limited by shape deviations of the intensity profile of the second laser focus. Therefore, we are proofing the widely used method of measuring the profile via scattering from gold beads (100 nm size) by comparing it to measurements of the fluorescence signal of quantum dots (6 nm size) using confocal detection.

T. Messer (✉)
Institute of Applied Physics, Karlsruhe Institute of Technology (KIT), Karlsruhe, Germany
e-mail: tobias.messer@student.kit.edu

P. Müller · M. Wegener
Institute of Applied Physics, Karlsruhe Institute of Technology (KIT), Karlsruhe, Germany

Institute of Nanotechnology, Karlsruhe Institute of Technology (KIT), Eggenstein-Leopoldshafen, Germany

B. Di Bartolo et al. (eds.), *Quantum Nano-Photonics*, NATO Science for Peace and Security Series B: Physics and Biophysics,
https://doi.org/10.1007/978-94-024-1544-5_41

3D Cubic Buckling Mechanical Metamaterials

Alexander Münchinger, Tobias Frenzel, Muamer Kadic, and Martin Wegener

Abstract Current concepts for shock absorbers are based on destructive deformation or viscoelasticity. In the latter case the absorbers are reusable but the amount of absorbed energy heavily depends on the loading speed. Frenzel et al. have introduced a concept using buckling mechanical instabilities to realize a reusable shock absorber working independently of the loading conditions [1]. They presented proof-of-principle structures with a uniaxial hexagonal lattice, being able to absorb shocks along this axis.

We extend this idea to a cubic structure, being able to absorb energy from shocks of any direction. The structure is fabricated using three-dimensional direct-laser writing. The produced samples show energy absorption along all axes probed, including the principal axes. Unfortunately, it turns out, that the viscoelasticity of the used photoresist is quite large. Hence, we cannot observe the predicted effect in our samples.

A. Münchinger (✉) · T. Frenzel
Institute of Applied Physics, Karlsruhe Institute of Technology (KIT), Karlsruhe, Germany
e-mail: uycsv@student.kit.edu

M. Kadic
Institute of Applied Physics, Karlsruhe Institute of Technology (KIT), Karlsruhe, Germany

Institute of Nanotechnology, Karlsruhe Institute of Technology (KIT), Eggenstein-Leopoldshafen, Germany

Institut FEMTO-ST, Université de Bourgogne Franche-Comté, Besançon, France

M. Wegener
Institute of Applied Physics, Karlsruhe Institute of Technology (KIT), Karlsruhe, Germany

Institute of Nanotechnology, Karlsruhe Institute of Technology (KIT), Eggenstein-Leopoldshafen, Germany

B. Di Bartolo et al. (eds.), *Quantum Nano-Photonics*, NATO Science for Peace and Security Series B: Physics and Biophysics,
https://doi.org/10.1007/978-94-024-1544-5_42

Reference

1. Frenzel T, Findeisen C, Kadic M, Gumbsch P, Wegener M (2016) Tailored buckling microlattices as reusable light-weight shock absorbers. Adv Mater 28:5865–5870

Light Absorbing Diamond for Solar Energy Conversion

S. Orlando, A. Bellucci, M. Girolami, M. Mastellone, and D. M. Trucchi

Abstract High-temperature solar cells are possible by exploiting the Photon-Enhanced Thermionic Emission (PETE) concept, which represents a novel and very attractive mechanism for the exploitation of solar radiation, especially if concentrated, and characterized by promisingly high conversion efficiency (>50%). PETE converters rely on the concept that engineered semiconductor photocathodes can provide a very efficient electron emission, induced by hot-electrons produced by photons with sufficient energy, combined to a thermionic emission, sustained by the high temperatures induced by every other thermalization process. Ultrashort pulse laser-assisted surface nanotexturing combined to surface-hydrogenation, aimed at achieving negative electron affinity conditions and a work function as low as 1.7 eV with a nitrogen-doping of the emitting-layer, have been proposed as a radically new and potential effective PETE cathode completely based on chemical-vapour-deposited (CVD) diamond, able to operate up to temperatures of 800 °C. CVD diamond is transparent to solar radiation due to its wide bandgap, consequently "black diamond" technology, based on ultrashort laser treatment, was developed for drastically increase its absorption coefficient and photogeneration capability under sunlight irradiation [1]. The final p/i/n structure merges the technologies of surface texturing by fs-laser [2], boron-implantation for formation of buried p-type layer [3], and laser-induced graphitic microchannels [4], to form an innovative

S. Orlando (✉)
Consiglio Nazionale delle Ricerche – Istituto di Struttura della Materia (CNR – ISM), Tito Scalo, PZ, Italy
e-mail: stefano.orlando@pz.ism.cnr.it

A. Bellucci · M. Girolami · M. Mastellone · D. M. Trucchi
Consiglio Nazionale delle Ricerche – Istituto di Struttura della Materia (CNR – ISM), Rome, Italy

B. Di Bartolo et al. (eds.), *Quantum Nano-Photonics*, NATO Science for Peace and Security Series B: Physics and Biophysics,
https://doi.org/10.1007/978-94-024-1544-5_43

defect-engineered black diamond cathode for the conversion of concentrated solar radiation operating at high temperature. Ongoing extension of the technology to polycrystalline films for large area scale-up and to thin single crystal films for an optimized performance has been discussed.

References

1. Calvani P et al (2016) Carbon 105:401
2. Bellucci A et al (2016) Appl Surf Sci 380:8
3. Bellucci A et al (2016) IEEE Trans Nanotechnol 15:862
4. Girolami M et al (2017) Carbon 111:48

Nonlinear Response and Strong Coupling of Surface Phonon Polaritons

Nikolai Passler, Ilya Razdolski, Sandy Gewinner, Wieland Schöllkopf, Simone De Liberato, Christopher Gubbin, Joshua Caldwell, Martin Wolf, and Alexander Paarmann

Abstract Analogous to surface plasmon polaritons in metals, polar dielectrics support surface phonon polaritons (SPhP) in the mid infrared (MIR) spectral region. In contrast to their plasmonic counterpart, however, SPhPs exhibit much longer lifetimes, and hence constitute a promising alternative in the development of nanophotonics. Employing an MIR free-electron laser, we here experimentally reveal resonant second harmonic generation from SPhPs, excited in the Otto geometry for prism coupling. In a second system featuring an ultrathin layer on top of the SPhP active material, we observe strong coupling of the bulk SPhP to the epsilon near zero mode supported by the thin layer. Our experimental findings are corroborated using a specifically developed matrix formalism for anisotropic multilayer wave propagation.

Keywords Strong coupling · Surface phonon polariton · Epsilon near zero mode · Second harmonic generation

Surface Phonon Polaritons (SPhP) are recently investigated as an alternative building block for mid-infrared (MIR) nanophotonic applications, promising to possibly solve the intrinsic loss problem of plasmonics [1]. SPhPs arise in polar dielectrics due to IR-active phonon resonances leading to negative permittivity between transverse and longitudinal optical phonon frequencies, a region called the Reststrahlen band. SPhPs exhibit tremendous field enhancements [2, 3], driving

N. Passler (✉) · I. Razdolski · S. Gewinner · W. Schöllkopf · M. Wolf · A. Paarmann
Fritz-Haber-Institute, Berlin, Germany
e-mail: passler@fhi-berlin.mpg.de

S. De Liberato · C. Gubbin
University of Southampton, Southampton, UK

J. Caldwell
Vanderbilt University, Nashville, TN, USA

B. Di Bartolo et al. (eds.), *Quantum Nano-Photonics*, NATO Science for Peace and Security Series B: Physics and Biophysics,
https://doi.org/10.1007/978-94-024-1544-5_44

the lattice atoms into a strongly non-linear regime. Hence, SPhPs might grant a frequency-tunable access to vibrational-driven transient material phases.

In contrast to plasmon polaritons in metals, the limitation of the SPhP dispersion to the Reststrahlen region leads to strong modulation of the dielectric response around SPhP frequencies. In consequence, combining different polar dielectrics with overlapping Reststrahlen bands leads to a variety of phenomena such as mode-splitting, index-sensing, and wave-guiding [4], allowing for the construction of new hybrid materials with custom-designed polaritonic response.

Here, we use linear and nonlinear MIR spectroscopy [5] for studying SPhPs in SiC and AlN, employing Otto-type prism coupling. The air gap in the Otto geometry is steered by white light interferometry, granting extrinsic control over the critical conditions of the SPhP excitation [6]. Our experiments employ the intense, tunable and narrowband MIR pulses from the FHI free-electron laser, revealing the resonant second harmonic generation (SHG) arising from the optical field enhancement associated with propagating SPhPs at the SiC/air interface [3].

Furthermore, we place a nanoscale thin layer of AlN onto SiC, leading to strong coupling and mode-splitting of the SiC SPhP and the AlN ultrathin film polariton. Specifically, we show that the coupling strength can be tuned intrinsically using different AlN layer thicknesses, and extrinsically using modulation of the radiative losses of the SPhP by varying the air gap. These experimental observations are corroborated with simulations using a specifically developed matrix formalism for anisotropic multilayer wave propagation [4], providing a detailed understanding as well as predictability of the linear and non-linear properties of SPhPs in polar dielectric heterostructures.

References

1. Caldwell J et al (2015) Low-loss, infrared and terahertz nanophotonics using surface phonon polaritons. Nano 4(1):44–68
2. Razdolski I et al (2016) Resonant enhancement of second-harmonic generation in the mid-infrared using localized surface phonon polaritons in subdiffractional nanostructures. Nano Lett 16(11):6954–6959
3. Passler NC et al (2017) Second-harmonic generation from critically coupled surface phonon polaritons. ACS Photonics 4(5):1048–1053
4. Passler NC, Paarmann A (2017) Generalized 4 × 4 matrix formalism for light propagation in anisotropic stratified media: study of surface phonon polaritons in polar dielectric heterostructures. J Opt Soc Am B 34:2128–2139
5. Paarmann A et al (2015) Second harmonic generation spectroscopy in the reststrahl band of SiC using an infrared free-electron laser. Appl Phys Lett 107:081101
6. Pufahl K et al (2017) Controlling nanoscale air-gaps for critically coupled surface polaritons by means of non-invasive white-light interferometry (In preparation)

Grating Couplers in Silicon-on-Insulator: The Role of Photonic Guided Resonances on Lineshape and Bandwidth

Marco Passoni, Dario Gerace, Lee Carroll, and Lucio Claudio Andreani

Abstract In this work we focus on the problem of the bandwidth of 1D grating couplers in the standard Silicon On Insulator (SOI) platform, consisting of a 220 nm silicon layer on top of an SiO2 cladding (typical thickness around 2 um) on a silicon substrate.. Grating couplers offer a viable solution to the problem of fiber-to-chip light coupling in integrated silicon photonics [1], and understanding the mechanism underlying their operation could give useful hints on increasing their performances. We analyse 1D grating couplers by means of numerical simulations with the 2D FDTD method. We consider different sizes of the incoming light beam, defined by the Mode Field Diameter (MFD), and we propose for the bandwidth a model based on two contributions. The first, of Gaussian lineshape, comes from the *k*-space Fourier broadening of the incident field and dominates for small MFD (the typical MFD of single mode fibers used in telecommunication is about 10 μm and falls in this regime). The second, of Lorentzian lineshape, comes from the intrinsic broadening of the photonic mode propagating inside the gratings above the cladding light line [2], and dominates for large MFD ($>\approx 50\,\mu$m). When both contributions are comparable we see that the coupling spectrum results in a Voigt lineshape. This is clearly seen in Fig. 1, where we plot the coupling spectra of the same grating structure for different values of the MFD. The evolution of the spectrum from purely Gaussian to purely Lorentzian, passing through a Voigt, is evident.

Multi-objective particle swarm optimisation [3] of selected small footprint grating couplers is then used to locate the Pareto fronts along which the highest coupling efficiency is achieved for a given bandwidth. The optimization is carried on for 4 different values of the MFD by changing the positions and widths of each single

M. Passoni (✉) · D. Gerace · L. C. Andreani
Department of Physics and CNISM, University of Pavia, Pavia, Italy
e-mail: marco.passoni01@universitadipavia.it

L. Carroll
Tyndall National Institute, Cork, Ireland

B. Di Bartolo et al. (eds.), *Quantum Nano-Photonics*, NATO Science for Peace and Security Series B: Physics and Biophysics,
https://doi.org/10.1007/978-94-024-1544-5_45

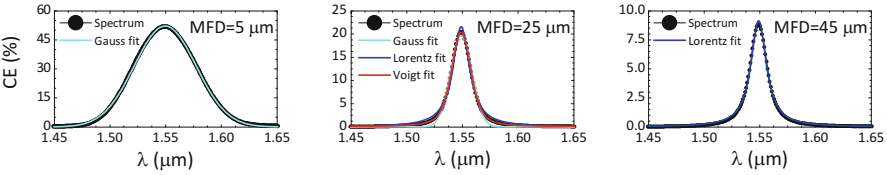

Fig. 1 Coupling spectra for different values of the MFD keeping every other grating parameter fixed

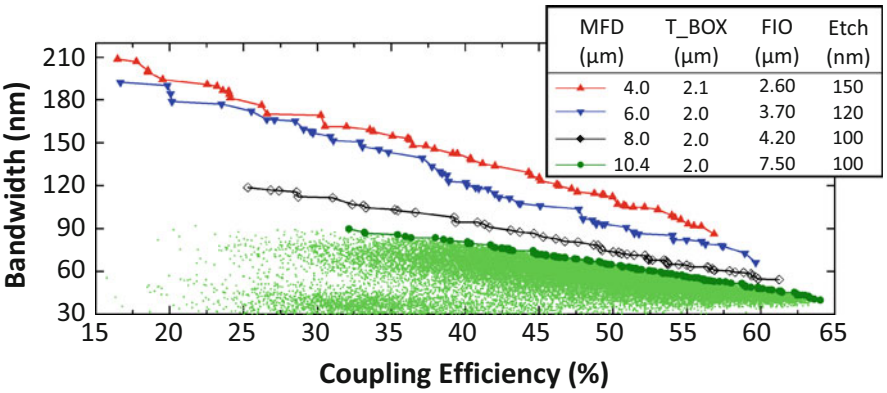

Fig. 2 Calculated Pareto fronts for 4 different values of the MFD. For the 10.4 μm MFD we plot (light green) also all the points of each structure analyzed in the optimization algorithm, to help the reader visualizing the Pareto front as a true physical front

groove in the grating. The starting point of each optimization is the chirped grating configuration (namely a grating with fixed period but with increasing grooves' widths) that maximizes the coupling efficiency for a given MFD. This approach identifies several high-efficiency 220 nm SOI grating coupler designs with 1 dB bandwidths exceeding 100 nm. The Pareto fronts for all 4 values of footprint are presented in Fig. 2.

References

1. Taillaert D, Bienstman P, Baets R (2004) Compact efficient broadband grating coupler for silicon-on-insulator waveguides. Opt Lett 29(23):2749–2751
2. Fan S, Joannopoulos JD (2002) Analysis of guided resonances in photonic crystal slabs. Phys Rev B 65(23):235112
3. Tripathi PK, Bandyopadhyay S, Pal SK (2007) Adaptive mufti-objective particle swarm optimization algorithm. In: IEEE congress on evolutionary computation, 2007. CEC 2007. IEEE, pp 2281–2288
4. Passoni M, Gerace D, Carroll L, Andreani LC (2017) Grating couplers in silicon-on-insulator: the role of photonic guided resonances on lineshape and bandwidth. Appl Phys Lett 110(4):041107

Aluminum Plasmonics: Fabrication and Characterization of Broadly Tunable Plasmonic Surfaces for Plasmon Molecule Strong-Coupling and Fluorescence Enhancement

Siim Pikker, Shen Boxuan, Kosti Tapio, Gerrit Groenhof, and Jussi Toppari

Abstract Our work based on previous studies [1, 2] confirms, that simple aluminum nanostructures can be utilized as effective plasmonic resonators over a broad range of frequencies and wavelengths. The nanostructured surfaces, fabricated by electron-beam lithography demonstrated relatively narrow-band resonances and are suitable for various plasmonic applications ranging from metal enhanced fluorescence to strong-coupling [1–5] experiments. We represent data for molecule-plasmon coupling near the strong coupling limit and demonstrate that these aluminum structures do act as fluorescence increasing substrates. In this work, we used two different types of dyes. We studied the narrow band j-aggregate forming TDBC with almost no Stokes-shift and a recently developed large Stokes-shift dye commercially available under the name ATTO 490LS. Anti-crossing behavior was observed for both dyes, but a clear Rabi split for the ATTO 490LS was not fully reached. We observed a Rabi split of more than 160 meV for the TDBC sample (Fig. 1) and enhanced selectively the fluorescence of the ATTO 490LS dye more than 3.5 times.

S. Pikker (✉) · S. Boxuan · K. Tapio · G. Groenhof · J. Toppari
Department of Physics, Nanoscience Center, University of Jyväskylä, Jyväskylä, Finland
e-mail: siim.x.pikker@jyu.fi

B. Di Bartolo et al. (eds.), *Quantum Nano-Photonics*, NATO Science for Peace and Security Series B: Physics and Biophysics,
https://doi.org/10.1007/978-94-024-1544-5_46

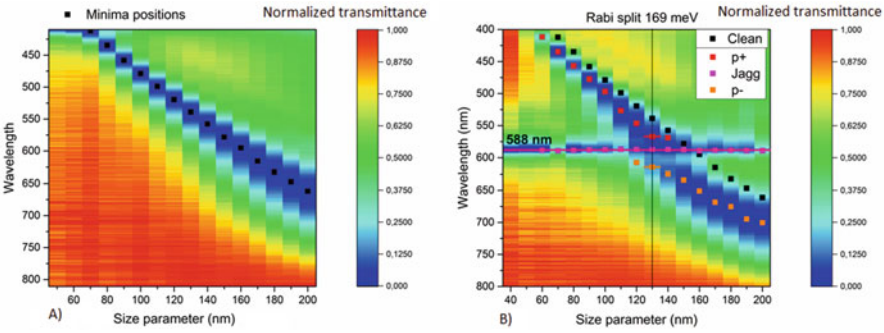

Fig. 1 (**a**) Normalized transmittance spectra for nanostructures with different nanoparticle sizes producing a dispersion relation. (**b**) Same structures covered with a 30–35 nm thick PVA layer doped with TDBC dye j-aggregates. The thin film induces a redshift and Rabi split of 169 meV to the dispersion curve

References

1. Eizner E, Avayu O, Ditcovski R, Ellenbogen T (2015) Nano Lett 15:6215. https://doi.org/10.1021/acs.nanolett.5b02584
2. Li J, Ueno K, Uehara H, Guo J, Oshikiri T, Misawa H (2016) J Phys Chem Lett 7:2786. https://doi.org/10.1021/acs.jpclett.6b01224
3. Törmä P, Barnes WL (2015) Rep Prog Phys 78:13901. https://doi.org/10.1088/0034-4885/78/1/013901
4. Baieva S, Hakamaa O, Groenhof G, Heikkilä TT, Toppari JJ (2017) ACS Photon 4:28. https://doi.org/10.1021/acsphotonics.6b00482
5. Koponen MA, Hohenester U, Hakala TK, Toppari JJ (2013) Phys Rev B 88:85425. https://doi.org/10.1103/PhysRevB.88.085425

3D Metamaterials with Negative Thermal Expansion and Negative Effective Compressibility

Jingyuan Qu, Muamer Kadic, Andreas Naber, Alexander Gerber, Frederik Mayer, and Martin Wegener

Abstract Materials with negative thermal expansion are desired for controlling thermal stresses, but unusual in nature. With two-component metamaterials it is possible to tune the thermal expansion from positive over zero to negative values, even if both components have positive thermal expansion. Using gray-tone laser lithography we fabricate three-dimensional two-component polymer microlattices, exhibiting zero or negative thermal expansion [1].

Similarly, poroelastic metamaterials can have a negative effective compressibility [2]. By using the high compressibility of air or vacuum, only one constituent solid component is needed here. At an elevated pressure, the effective metamaterial volume increases, while the volume defined by the constituent solid still decreases. Thus the metamaterial with this counterintuitive property is still stable.

The thermal expansion and effective compressibility of fabricated samples are measured by cross-correlating optical images taken at different temperatures or pressure respectively. The results ar in good agreement with numerical calculations.

References

1. Qu J, Kadic M, Naber A, Wegener M (2017) Sci Rep 7:40643
2. Qu J, Kadic M, Wegener M (2017) Appl Phys Lett 110:171901

J. Qu (✉) · F. Mayer · M. Wegener
Institute of Applied Physics, Karlsruhe Institute of Technology (KIT), Karlsruhe, Germany

Institute of Nanotechnology, Karlsruhe Institute of Technology (KIT), Karlsruhe, Germany
e-mail: jingyuan.qu@kit.edu

M. Kadic
Institute of Applied Physics, Karlsruhe Institute of Technology (KIT), Karlsruhe, Germany

Institut FEMTO-ST, CNRS, Université de Bourgogne Franche-Comté, Besançon, France

A. Naber · A. Gerber
Institute of Applied Physics, Karlsruhe Institute of Technology (KIT), Karlsruhe, Germany

B. Di Bartolo et al. (eds.), *Quantum Nano-Photonics*, NATO Science for Peace and Security Series B: Physics and Biophysics,
https://doi.org/10.1007/978-94-024-1544-5_47

Colloidal Spherical Silver Nanoparticles Based Plasmon Enhanced Fluorescence for Rapid Quantitative Point-of-Care Testing Fluorescent Immunoassay Development

Andrei Ramanenka, Svetlana Vaschenko, Olga Kulakovich, Alina Muravitskaya, Dmitry Guzatov, Anatoly Lunevich, Yuri Glukhov, and Sergey Gaponenko

Abstract One of the promising applications of plasmon enhancement of fluorescence is the development of rapid quantitative point-of-care testing devices based on fluorescent immunoassays, for which it is crucial to increase the desired fluorescent signal for small analyte concentrations. In this work, we investigated plasmonic enhancement of fluorescence by colloidal spherical silver nanoparticles (Ag np-s) and polyelectrolyte spacer based multilayered plasmonic nanostructures for FITC-labeled bovine serum albumin (BSA) model protein, FITC-labeled alpha-fetoprotein (AFP) antibodies and prostate specific antigen (PSA) sandwich immunoassay for developing of rapid quantitative point-of-care testing fluorescent immunoassay. Bottom-Up Layer-by-layer electrostatic deposition technique for sample preparation was used with alternatively charged PDADMAC/PSS polyelectrolytes as a spacer to prevent fluorescence quenching. Ag np-s free area of samples was used as a control. Negatively charged Ag np-s with mean diameters 42 nm and 55 nm and dispersion 25–30 nm were synthesized by citrate reduction method of $AgNO_3$. Fluorescence enhancement for FITC-labeled model protein (BSA), AFP antibodies and PSA sandwich immunoassay using Ag np-s containing nanostructures was observed. Maximal fluorescence enhancement factor (∼7-fold) was observed for BSA-FITC for optimal 3,3–

A. Ramanenka (✉) · O. Kulakovich · A. Muravitskaya · S. Gaponenko
Stepanov Institute of Physics, National Academy of Sciences of Belarus, Minsk, Belarus
e-mail: a.ramanenka@ifanbel.bas-net.by

S. Vaschenko
Chemistry Department, Belarusian State University, Minsk, Belarus

D. Guzatov
Physical-Technical Department, Yanka Kupala Grodno State University, Grodno, Belarus

A. Lunevich · Y. Glukhov
ELTA Ltd., Moscow, Russia

B. Di Bartolo et al. (eds.), *Quantum Nano-Photonics*, NATO Science for Peace and Security Series B: Physics and Biophysics,
https://doi.org/10.1007/978-94-024-1544-5_48

6,6 nm spacer thickness (3–5 polyelectrolyte layers) and nanostructures with bigger Ag np-s average diameter (55 nm). The feasibility of detection of clinically important concentrations for PSA antigen in range 1–100 ng/ml was demonstrated. Comprehensive modeling of fluorescence enhancement factor in system 'one spherical silver nanoparticle – one fluorophore' including excitation light field enhancement, fluorophore radiative and nonradiative rates modification, excitation light polarization, fluorophore position and its dipole moment orientation was made. Satisfactory agreement between the theory and the experiment was observed. The prototype of point-of-care testing device based on silicon photodiode with integrated preamplifier and blue laser diode (450 nm) was proposed and developed.

Keywords Plasmon-enhanced fluorescence · Spherical silver nanoparticle · Polyelectrolyte · Fluorescein isothiocyanate · Fluorescent immunoassay · Point-of-care testing · Alpha-fetoprotein · Prostate specific antigen

Synthesis and Photoluminescence of Strontium Titanate Xerogels Doped with Terbium, Ytterbium and Europium

M. V. Rudenko, T. F. Raichenok, N. V. Mukhin, and N. V. Gaponenko

Abstract Terbium, ytterbium and europium doped strontium titanate thin films and undoped strontium titanate powder were synthesized using sol-gel method. Xerogel was deposited by spin-on technic on monocrystalline silicon and porous anodic alumina substrates formed on monocrystalline silicon. Structure and photoluminescence of obtained films were investigated. Doped strontium titanate xerogel films show photoluminescence spectra with emission bands caused by electron transitions of relevant rare earth dopant. The broad photoluminescence band of the undoped $SrTiO_3$ powder at 300–400 nm is detected.

The doping of materials having perovskite structure with rare earth elements (REE) is prospective for the creation of effective phosphors. Strontium titanate, $SrTiO_3$ with a perovskite structure has found wide application in the manufacture of electronic components. The introduction of various rare-earth elements into strontium titanate makes it possible to observe strong luminescence in the blue, green or red spectral ranges [1]. In this connection, the study of luminescence in a wide band gap material such as strontium titanate doped with REE receive interest in the development of new functional materials for optoelectronics and lighting engineering [2]. In addition, the high radiation stability of strontium titanate is of considerable interest for the creation of X-ray converters [1]. Strontium titanate properties depend not only on its chemical composition, but also on its structure, shape and grain size [3]. Sol-gel synthesis of strontium titanate films is of particular interest, since this technology is low cost and allows tailoring the

M. V. Rudenko (✉) · N. V. Gaponenko
Research Laboratory of Nanophotonics, Belarusian State University of Informatics and Radioelectronics, Minsk, Belarus

T. F. Raichenok
B.I. Stepanov Institute of Physics, National Academy of Sciences of Belarus, Minsk, Belarus

N. V. Mukhin
Saint Petersburg Electrotechnical University "LETI", Saint Petersburg, Russia

B. Di Bartolo et al. (eds.), *Quantum Nano-Photonics*, NATO Science for Peace and Security Series B: Physics and Biophysics,
https://doi.org/10.1007/978-94-024-1544-5_49

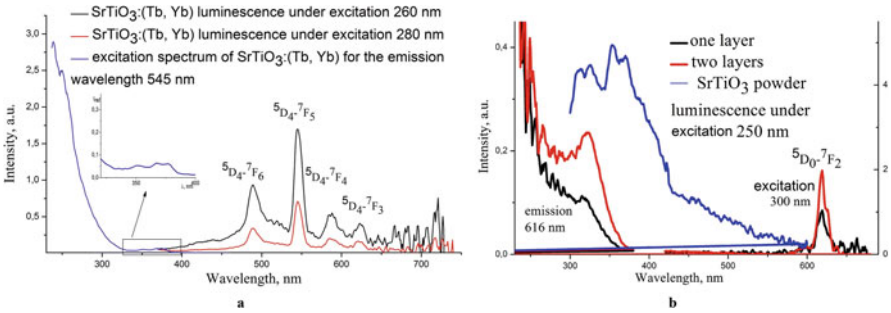

Fig. 1 The excitation and luminescence spectra of the structures of $SrTiO_3$:(Tb, Yb)/PAA/silicon and $SrTiO_3$:Eu/silicon and $SrTiO_3$ powder

morphology of the host and variation concentration of the doping impurities. This occurs when individual template formatting has been modified. In this case, under no circumstances should the changes be saved to the document template.

The xerogels doped with REE (Tb, Yb, Eu) were synthesized on monocrystalline silicon and in porous anodic alumina (PAA) formed on silicon by sol-gel route from sols based on titanium isopropoxide, nitric acid salts of strontium and REE and ethylene glycol monomethyl ether. The use of highly ordered PAA as a carrier matrix for nanoclusters makes it possible to achieve anisotropy of the propagation of light within such a structure and provides an increase in the luminescence intensity due to anisotropic density of photonic states for the emission modes and multiply scattering of exciting light [4, 5]. The PL and PL excitation spectra of the obtained structures were detected by the spectrofluorometer CM2203. A high pressure xenon arc lamp 150 Watt was used as an excitation source. The PL spectra in Fig. 1a, contain the main peaks belonging to the trivalent terbium, corresponding to the transitions $^5D_4 \rightarrow {}^7F_6$, $^5D_4 \rightarrow {}^7F_5$, $^5D_4 \rightarrow {}^7F_4$, $^5D_4 \rightarrow {}^7F_3$ with the most intensive band at 545 nm. The ratios of the components were Sr:(Tb + Yb) = 2.5 and Tb:Yb = 2:1. With a decrease in the excitation wavelength the luminescence intensity increases.

The excitation and PL spectra of $SrTiO_3$:Eu xerogel formed on monocrystalline silicon after annealing at 750 °C contain intensive PL peak at 618 nm corresponding to the transition $^5D_0 \rightarrow {}^7F_2$ of the trivalent europium (Fig. 1b). Sequential deposition of the second layer promotes an increase in the luminescence intensity. The broad PL band of the undoped $SrTiO_3$ powder at 300–400 nm associated probably with oxygen vacancies [6] matches the $SrTiO_3$:Eu excitation band (Fig.1b). One and two layered $SrTiO_3$:Eu xerogel films with high porosity and about 350 and 510 nm thick respectively are shown in Fig. 2. The films are characterized with high porosity contrary to previously fabricated undoped $SrTiO_3$ xerogels synthesized using another solvents [7].

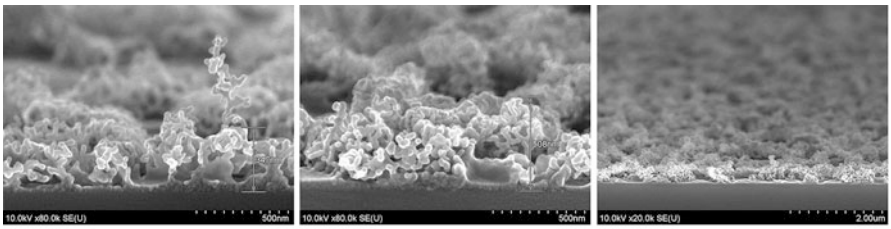

Fig. 2 The SEM images of one (**a**) and two layered (**b** and **c**) $SrTiO_3$:Eu xerogel films

The described porous $SrTiO_3$:Eu xerogel films of structures are prospective for optoelectronic devices through multiple scattering in a porous structure, which contributes to obtaining the optimum luminescent properties.

References

1. Hill N (2000) J Phys Chem B 104:6694
2. Zhang W, Yin Z, Zhang M (2000) Appl Phys A Mater Sci Process 70:93
3. Rudiger A, Schneller T, Roelofs A, Tiedke S, Schmitz T, Waser R (2005) Appl Phys A Mater Sci Process 80:1247
4. Gaponenko NV (2001) Synth Met 124(1):125–130
5. Lutich AA, Gaponenko SV, Gaponenko NV, Molchan IS, Sokol VA, Parkhutik V (2004) Nano Lett 4:1755
6. Kan D (2005) Nat Mater 4:816
7. Sohrabi Anaraki H, Gaponenko NV, Rudenko MV, Guk AF, Zavadskij SM, Golosov DA, Kolosnitsyn BS, Kolos VV, Pyatlitskij AN, Turtsevich AS (2014) Semiconductors 48:1685

Integration of Single Photon Sources with Nano-photonic Circuits

P. Schrinner and C. Schuck

Abstract Quantum information processing technologies are expected to have a revolutionary impact on cryptography, communication and computing. Whereas feasibility has already been shown, industrial applications face scalability as a major hurdle. Advanced CMOS fabrication is a promising tool to realize large-scale quantum photonic circuits on silicon [1–4].

We consider such a system, where single photons are manipulated in nano-photonic waveguide devices. The implementation consists of single photon sources (SPS), nano-photonic circuits and single photon detectors. In this work we aim on coupling nano-scale quantum emitters to photonic crystal cavities to create deterministic, pure and on-demand SPS. We present simulations that show that up to 50% of the emitters radiation can be collected into a single guided mode within realistic alignment precision. Additionally, a large number of photonic crystal cavity devices can be tested through rapid prototyping employing nano-fabrication routines and automated fiber-optic measurement capabilities. The spectral and statistical properties of quantum emitters will be investigated with a custom built confocal microscope. Several positioning techniques will be investigated for achieving optimal coupling between a quantum emitter and an optical waveguide. Integration of single-photon sources with SNSPDs linked via nanophotonic circuits on a silicon chip will then constitute a key step towards scalable quantum information processing.

P. Schrinner (✉) · C. Schuck
Center for Nanotechnology, WWU Münster, Münster, Germany
e-mail: schrinner@uni-muenster.de

B. Di Bartolo et al. (eds.), *Quantum Nano-Photonics*, NATO Science for Peace and Security Series B: Physics and Biophysics,
https://doi.org/10.1007/978-94-024-1544-5_50

References

1. Shalaev V et al (2017) OME 7(1):111
2. Thompson M et al (2016) IEEE 22(6):6700113
3. Aharonovich I et al (2016) NP 10:631–641
4. Schuck C et al Nat Commun 7:10352
5. Schuck C et al Sci Rep 3:1893

Vibrational Properties of Ge-Sb-Te Phase-Change Alloys Studied by IR and Raman Spectroscopy at Different Temperatures

K. Shportko and M. Wuttig

Abstract Ge-Sb-Te phase-change alloys are employed as active elements in optical data storages and are promising for new generation of the electronic memory devices (Wuttig M, Nat Mater 4:265–266, 2008). Upon crystallization, their visible and infrared dielectric properties change dramatically due to the formation of resonant bonds (Shportko K, Kremers S, Woda M, Lencer D, Robertson J, Wuttig M, Nat Mater 7(8):653–658, 2008).

In this work we report on the systematic compositional dependencies of the intensities of the bands in Raman spectra of amorphous Ge-Sb-Te alloys. These dependencies correlate with evolution of concentration of the different structural units in amorphous Ge-Sb-Te alloys. Obtained compositional trends may enable one to predict vibrational properties of other amorphous Ge-Sb-Te chalcogenides. We have also studied the change of the anharmonicity upon crystallization of Ge-Sb-Te alloys, and the influence of vacancy concentration and vacancy ordering on the anharmonicity. The temperature-dependent IR and Raman study of vibrational modes directly reveals a correlation between anharmonicity and vacancy concentration and ordering.

References

1. Wuttig M (2008) Nat Mater 4:265–266
2. Shportko K, Kremers S, Woda M, Lencer D, Robertson J, Wuttig M (2008) Nat Mater 7(8):653–658

K. Shportko (✉)
V.E. Lashkaryov Institute for Semiconductor Physics, National Academy of Sciences of Ukraine, Kyiv, Ukraine
e-mail: konstantin@shportko.com; kostiantyn.shportko@rwth-aachen.de

M. Wuttig
I. Institute of Physics (IA), RWTH University of Technology, Aachen, Germany

B. Di Bartolo et al. (eds.), *Quantum Nano-Photonics*, NATO Science for Peace and Security Series B: Physics and Biophysics,
https://doi.org/10.1007/978-94-024-1544-5_51

Fock States Engineering with Single Atom Laser

Vladislav P. Stefanov

Abstract On the basis of quantum stochastic trajectories approach it is shown that the state of the single atom laser under the action of sequence of pulses of coherent pumping can be Fock state.

A single atom in a high-Q cavity is a key model for a number of quantum optics applications. It was demonstrated [1] that the system with appropriate parameters acts as a simplest laser: single atom laser (SAL). In [2], by means of stochastic quantum trajectories method [3, 4] it has been shown that continuous measurement of quantum jumps connected with the intracavity field decay, atomic decay, or incoherent pumping of the atom, results in fixing the SAL in a state with specific number of excitations. In the present paper, the possibilities of generation of Fock states are predicted for SAL with coherent pumping and imperfect quantum jumps detection, followed by coherent feedback pulses.

The model of the system is a two-level atom in a high-Q cavity interacting with a single field mode via the Jaynes-Cummings Hamiltonian $H_{JC} = \hbar g(a^{\dagger}\sigma_{-} + a\sigma_{+})$, where g is the interaction constant, σ_{+}, σ_{-} are atomic transition operators and $a^{\dagger}$, a are field creation and annihilation operators. The field and atomic decay rates $2k$ and Γ are taken into account through the corresponding Lindblad superoperators $2L(x)\rho = 2x\rho x^{\dagger} - x^{\dagger}x\rho - \rho x^{\dagger}x$. The coherent pump is described by the interaction operator

$$V = \frac{E_0}{2}(\mathcal{D}_{ge}\sigma_{-} + \mathcal{D}_{eg}\sigma_{+}), \tag{1}$$

where $\mathcal{D}_{ge} = \mathcal{D}_{eg} = \mathcal{D}$ is the dipole transition moment of atom and E_0 is the amplitude of the pumping field.

V. P. Stefanov (✉)
B.I.Stepanov Institute of Physics of NAS of Belarus, Minsk, Republic of Belarus
e-mail: v.p.stefanov@mail.ru

B. Di Bartolo et al. (eds.), *Quantum Nano-Photonics*, NATO Science for Peace and Security Series B: Physics and Biophysics,
https://doi.org/10.1007/978-94-024-1544-5_52

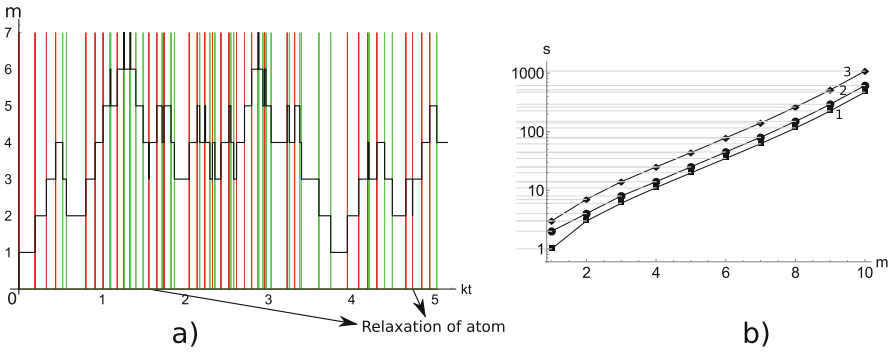

Fig. 1 System parameters: $2g = 2\pi * 68\,\text{MHz}$, $\Gamma = 2\pi * 2.6\,\text{MHz}$, $k = 2\pi * 4.1\,\text{MHz}$, $d = E_0\mathcal{D}/(2\hbar k) = 20000$. (**a**) Quantum trajectory with the detection of decay clicks. Black line is the evolution of excitation number m (photon number plus unity if atom occupiers excited state); red lines indicate $\pi/2$ pulses; green lines represent the times of field decay detecting; orange lines represent the times of atom decay detecting and immediately after their detection runs $\pi/2$ pulse. (**b**) The quantity of relaxation acts for obtaining the m excitation level with probability 1–90%, 2–95%, 3–99.5%

If the experimental setup allows to monitor continuously the moments of detection clicks due to the atomic and field decay, one can increase the field excitation efficiency by the switching on of the $\pi/2$ pulses in needed time after detection of a click. By the method an arbitrary Fock state with some probability can be generated (see Fig. 1a). For example, for SAL parameters [1] the ten-photons Fock state can be generated with probability 99.5% in (see Fig. 1b).

References

1. Boca A, Miller R, Birnbaum KM, McKeever J, Kimble HJ (2004) Observation of the vacuum Rabi spectrum for one trapped atom. Phys Rev Lett 93:23. https://doi.org/10.1103/PhysRevLett.93.233603
2. Kilin SYa, Stefanov VP (2017, November) Quantum state engineering with single atom laser. J Phys Conf Ser 917(6): 062020. IOP Publishing
3. Kilin SYa (1990) Quantum optics: fields and their detection. Navuka i tehnika, Minsk, pp 123–140
4. Carmichael HJ (1993) Quantum trajectory theory for cascaded open systems. Phys Rev Lett 70:15. https://doi.org/10.1103/PhysRevLett.70.2273

Signatures of Strong Coupling on Nanoparticles: Revealing Absorption Anticrossing by Tuning the Dielectric Environment

Felix Stete, Wouter Koopman, and Matias Bargheer

Abstract The electromagnetic coupling of molecular excitations to plasmonic nanoparticles offers a promising method to manipulate the light-matter interaction at the nanoscale. Plasmonic nanoparticles foster exceptionally high coupling strengths, due to their capacity to strongly concentrate the light-field to sub-wavelength mode volumes. A particularly interesting coupling regime occurs, if the coupling increases to a level such that the coupling strength surpasses all damping rates in the system. In this so-called strong-coupling regime hybrid light-matter states emerge, which can no more be divided into separate light and matter components. These hybrids unite the features of the original components and possess new resonances whose positions are separated by the Rabi splitting energy $\hbar\Omega$. Detuning the resonance of one of the components leads to an anticrossing of the two arising branches of the new resonances ω_+ and ω_- with a minimal separation of $\Omega = \omega_+ - \omega_-$.

A popular approach for achieving strong light-matter coupling on nanoparticles is the fabrication of hybrid core-shell particles with a noble-metal core and a molecular shell. Several hybrid nanoparticles that allegedly show strong-coupling have been presented in recent literature [1–3]. In several cases these claims have however been challenged as an unambiguous determination of the coupling regime is difficult [4, 5]. Most often, evidence for strong coupling is deduced from a peak splitting

F. Stete (✉)
Institut für Physik & Astronomie, Universität Potsdam, Potsdam, Germany

School of Analytical Sciences Adlershof (SALSA), Humboldt-Universität zu Berlin, Berlin, Germany
e-mail: stete@uni-potsdam.de

W. Koopman
Institut für Physik & Astronomie, Universität Potsdam, Potsdam, Germany

M. Bargheer
Institut für Physik & Astronomie, Universität Potsdam, Potsdam, Germany

Helmholtz Zentrum Berlin, Berlin, Germany

B. Di Bartolo et al. (eds.), *Quantum Nano-Photonics*, NATO Science for Peace and Security Series B: Physics and Biophysics,
https://doi.org/10.1007/978-94-024-1544-5_53

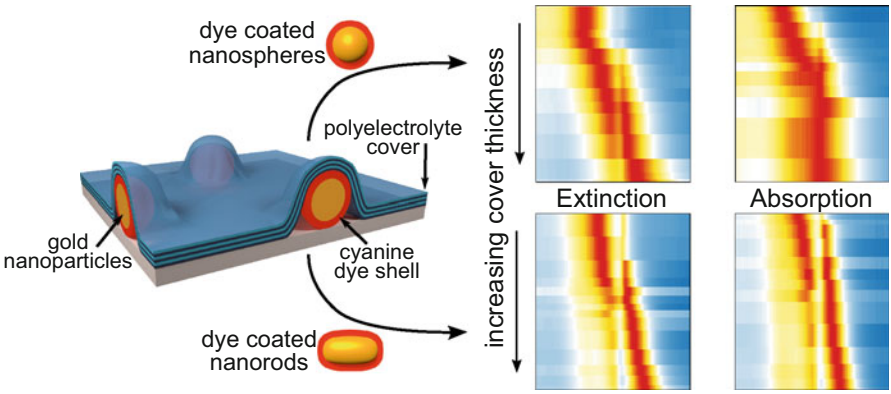

Fig. 1 A model sample is shown on the left side. The cover thickness can be varied to tune the plasmon resonance. The upper row shows the results of extinction and absorption measurements for coated nanospheres, where the absorption does not show an anticrossing. The lower row presents the extinction (left) and absorption (right) spectra for the coated gold nanorods. Here both spectra show an anticrossing indicating strong coupling

or anticrossing in extinction or scattering spectra. However situations can occur where the extinction spectrum does show a peak splitting although the system is not strongly coupled. Therefore several authors discussed that absorption and fluorescence are the only reliable quantities to determine the presence of strong-matter coupling [3–5].

Additionally, the anticrossing (and with that the coupling strength) is usually obtained by changing the size of the metal cores and thus the plasmon resonance position. This is, however, a problematic approach since the coupling strength changes with the particle size [5].

This contribution presents two examples of core-shell nanoparticles, both with a shell of the J-aggregate forming cyanine dye TDBC and a gold core. In one case gold nanospheres were used, in the other gold nanorods. The resonances were tuned by changing the particles environment on a substrate by layer-by-layer deposition of thin polyelectrolyte films replacing air and thus shifting the plasmon resonance without changing the particle size (see Fig. 1). The extinction spectra of both systems show an anticrossing indicating a regime of strong coupling. However true absorption spectra reveal an anticrossing only for the rods suggesting they are strongly coupled whereas the spheres are rather in a regime of induced transparency. Parts of the work have recently been published [6].

References

1. Fofang NT, Park T-H, Neumann O, Mirin NA, Nordlander P, Halas NJ (2008) Plexcitonic nanoparticles: plasmonExciton coupling in nanoshell-J-aggregate complexes. Nano Lett 8:3481–3487
2. Balci S, Kocabas C, Küçüköz B, Karatay A, Akhüseyin E, Gul Yaglioglu H, Elmali A (2014) Probing ultrafast energy transfer between excitons and plasmons in the ultrastrong coupling regime. Appl Phys Lett 105:51105
3. Melnikau D, Esteban R, Savateeva D, Sánchez-Iglesias A, Grzelczak M, Schmidt MK, Liz-Marzán LM, Aizpurua J, Rakovich YP (2016) Rabi splitting in photoluminescence spectra of hybrid systems of gold nanorods and jaggregates. J Phys Chem Lett 7:354–362
4. Zengin G, Gschneidtner T, Verre R, Shao L, Antosiewicz TJ, Moth-Poulsen K, Käll M, Shegai T (2016) Evaluating conditions for strong coupling between nanoparticle plasmons and organic dyes using scattering and absorption spectroscopy. J Phys Chem C 120:20588–20596
5. Antosiewicz TJ, Apell Sp, Shegai T (2014) Plasmon–exciton interactions in a core–shell geometry: from enhanced absorption to strong coupling. ACS Photon 1:454–463
6. Stete F, Koopman W, Bargheer M (2017) Signatures of strong coupling on nanoparticles: revealing absorption anticrossing by tuning the dielectric environment. ACS Photon 4:1669–1676

Solid State Synthesis, Structural and Up-Conversion Properties of Yb^{3+}/Er^{3+} and $Yb^{3+}/Tm^{3+}/Er^{3+}$ Doped $La_2Ti_2O_7$ Phosphors

Sevcan Tabanli, Murat Erdem, Burak Canturk, Ayhan Mergen, and Gonul Eryurek

Abstract In this work, Yb^{3+}/Er^{3+} co-doped and $Yb^{3+}/Tm^{3+}/Er^{3+}$ tri-doped $La_2Ti_2O_7$ phosphors were synthesized by solid-state reaction method. The phases of the powders were identified using the X-Ray Diffraction (XRD) technique. The purity of the $La_2Ti_2O_7$ phosphors were tested by energy dispersive spectroscopy (EDS). The photoluminescence properties of $La_2Ti_2O_7$ phosphors were investigated in the range of 400–850 nm wavelength under 975 nm laser excitation at room temperature. Presence of Tm^{3+} ion in the tri-doped powder effects the UC-emission processes observed in the powders co-doped with Yb^{3+}/Er^{3+}.

Synthesis Procedure Yb^{3+}/Er^{3+} co-doped and $Yb^{3+}/Tm^{3+}/Er^{3+}$ tri-doped $La_2Ti_2O_7$ phosphors were synthesized by solid-state reaction. La_2O_3, TiO_2, Yb_2O_3, Er_2O_3, Tm_2O_3 powders were mixed using ball-milling for 20 h, followed by calcination of the resulting mixture at 180 °C (2 h). The samples were heated at a constant heating rate of 300 °C/h to 1350 °C. The concentration of Yb^{3+} ion was fixed at 2 mol% while the concentration of Er^{3+} ion was varied 0.5 mol%, 1 mol%, 1.5 mol% for co-doped phosphors. For tri-doped phosphors, the concentration of Yb^{3+} and Tm^{3+} ions were fixed at 2 mol% and 1 mol%, respectively, while the concentration of Er^{3+} ion was varied 0.5 mol%, 1 mol%, 1.5 mol%.

Results and Discussion *Structural and Morphological Properties* The phases of the powders were identified using the XRD technique. All the diffraction peaks are well indexed to the monoclinic phase of $La_2Ti_2O_7$ structure (JCPDS Card #028-

S. Tabanli (✉) · G. Eryurek
Department of Physics Engineering, Istanbul Technical University, Istanbul, Turkey
e-mail: tabanlisevcan@itu.edu.tr

M. Erdem
Department of Physics, Marmara University, Istanbul, Turkey

B. Canturk · A. Mergen
Department of Material and Metallurgy Engineering, Marmara University, Istanbul, Turkey

B. Di Bartolo et al. (eds.), *Quantum Nano-Photonics*, NATO Science for Peace and Security Series B: Physics and Biophysics,
https://doi.org/10.1007/978-94-024-1544-5_54

0517) [1]. From Scherrer equation, the average crystallite sizes of the powders were estimated around 50 ± 4 nm. The surface morphology, micro-structure and phase detection of powders were performed by scanning electron microscopy measurements. The purity of the $La_2Ti_2O_7$ phosphors were tested by EDS. *Photoluminescence Properties* The photoluminescence properties of $La_2Ti_2O_7$ phosphors were investigated in the range of 400–850 nm wavelength under 975 nm laser excitation for ≈1 W pumping power at room temperature. The strong visible UC emission were observed from Yb^{3+}/Er^{3+} co-doped $La_2Ti_2O_7$ phosphors in the green and red spectral regions (Fig. 1) which are localized at around 523 nm, 550 nm, 658 nm, and 801 nm associated with the $^2H_{11/2} \rightarrow {}^4I_{15/2}$, $^4S_{3/2} \rightarrow {}^4I_{15/2}$, $^4F_{9/2} \rightarrow {}^4I_{15/2}$, and $^4I_{9/2} \rightarrow {}^4I_{15/2}$ transitions of Er^{3+}, respectively [7, 8]. The UC emission spectra of $Yb^{3+}/Tm^{3+}/Er^{3+}$ tri-doped $La_2Ti_2O_7$ phosphors have the same peaks with co-doped phosphors except for a peak, which localized at around 813 nm associated with the $^3H_4 \rightarrow {}^3H_6$ transition of Tm^{3+}. Presence of Tm^{3+}ion in the tri-doped powder effects the UC-emission processes observed in the powders co-doped with Yb^{3+}/Er^{3+}.

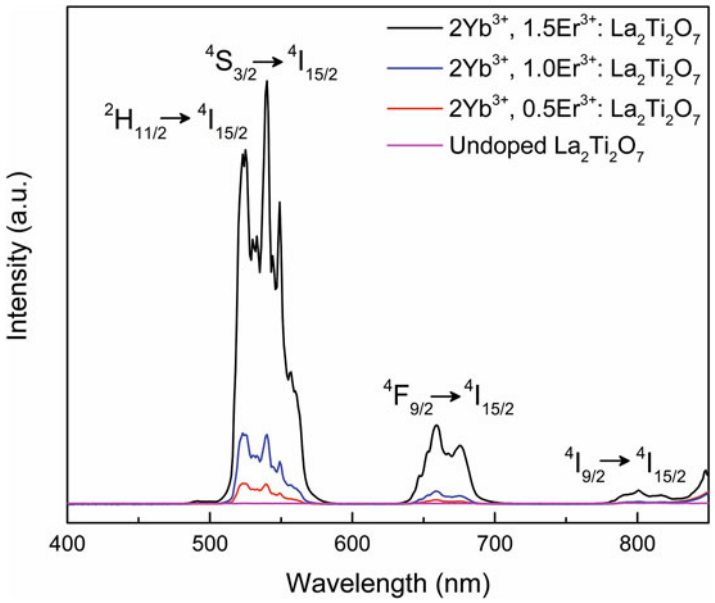

Fig. 1 The UC emission spectra of Yb^{3+}/Er^{3+} co-doped $La_2Ti_2O_7$ phosphors under 975 nm laser excitation for ≈1 W pumping power

Acknowledgements We express our condolences for the sudden loss of Prof. Ayhan Mergen who was one of the authors. It was an honor to have known such a great person and he will be greatly missed by all of us.

References

1. Cheng H, Lu Z, Liu Y et al (2011) Sol-gel synthesis and photoluminescence characterization of $La_2Ti_2O_7 : Eu^{3+}$ nanocrystals. Rare Metals 30:602–606
2. Tabanli S, Bilir G, Eryurek G (2017) Color tunable up-conversion emission from $Er^{3+} : Y_2O_3$ nanoparticles embedded in PMMA matrix. J Lumin 182:146–153
3. Erdem M, Erguzel O, Ekmekci MK, Orucu H et al (2015) Bright white up-conversion emission from solgel derived $Yb^{3+}/Er^{3+}/Tm^{3+} : Y_2SiO_5$ nanocrystalline powders. Ceram Int 41:12805–12810

Static and Tunable Devices for Terahertz Focusing and Beam Steering

Silvia Tofani, Walter Fuscaldo, Alessandro Galli, and Romeo Beccherelli

Abstract The electromagnetic radiation with wavelengths between 0.1 and 1 mm, and frequencies between 0.3 and 3 THz, is usually called "terahertz radiation". In this band, photons have energies in the milli-electronvolt range and interact with systems that have picosecond lifetimes and energetic transitions between 1.24 and 12.4 meV (Jepsen PU, Cooke DG, Koch M Laser Photonics Rev. https://doi.org/10.1002/lpor.201000011). Currently, numerous practical applications for optoelectronic THz systems are studied, but their progress has closely been linked to the more general development of a well-established technology. In this context, two different types of devices for THz-wave control will be presented: polymeric zone plates (ZPs) as THz lenses, and leaky-wave antennas (LWAs) based on nematic liquid crystals (LCs) for THz beam steering.

ZPs are circular diffraction gratings with radially increasing line density. The basic properties of ZPs were already described by J. L. Soret in 1875 (Soret JL, Ann Phys Chem 156, 1875), and they are commonly employed for extreme UV and hard X-ray focusing. ZPs are able to focus THz waves with a theoretical resolution comparable to the radiation wavelength and a theoretical diffraction efficiency of about 40%, but both these goals are difficult to reach in practice. Some considered implementations are: (i) to employ a multilevel ZP; (ii) to employ two stacked binary ZPs instead of a conventional single-layer binary ZP lens (double-sided ZP) (Tofani S, Zografopoulos DC, Missori M, Beccherelli R.

S. Tofani (✉)
Dipartimento di Ingegneria dell'Informazione, Elettronica e Telecomunicazioni,"Sapienza" Università di Roma, Rome, Italy

Istituto per la Microelettronica e Microsistemi, Consiglio Nazionale delle Ricerche, Rome, Italy
e-mail: tofani@diet.uniroma1.it; silvia.tofani@artov.imm.cnr.it

W. Fuscaldo · A. Galli
Dipartimento di Ingegneria dell'Informazione, Elettronica e Telecomunicazioni,"Sapienza" Università di Roma, Rome, Italy

R. Beccherelli
Istituto per la Microelettronica e Microsistemi, Consiglio Nazionale delle Ricerche, Rome, Italy

B. Di Bartolo et al. (eds.), *Quantum Nano-Photonics*, NATO Science for Peace and Security Series B: Physics and Biophysics,
https://doi.org/10.1007/978-94-024-1544-5_55

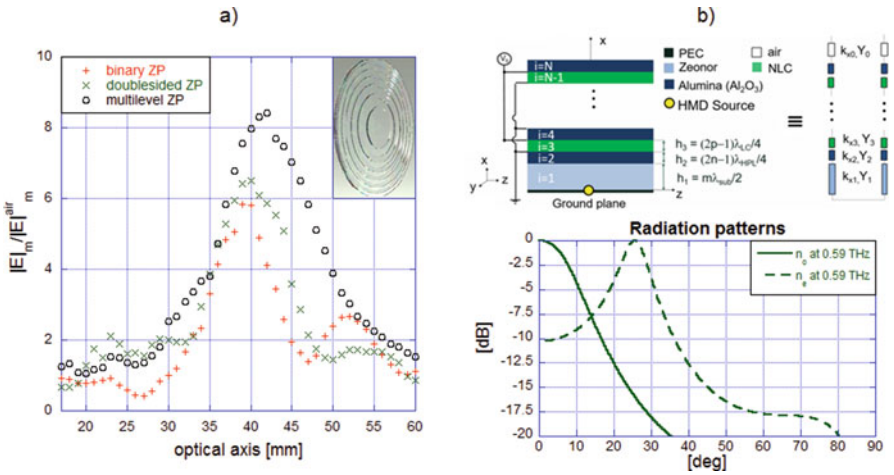

Fig. 1 (**a**) Focal length of three different ZP layouts; (**b**) Scheme of a FPC-LWA, its equivalent network, and radiation patterns showing different pointing angles by changing the LC refractive index through a bias voltage

IRMMW-THz, 2016. https://doi.org/10.1109/IRMMW-THz.2016.7758664); (iii) to substitute conventional THz ZP materials with low-loss polymers. In order to compare these solutions, the ZP focusing properties have preliminarily been investigated by simulating their behavior through a commercial software employing the finite element method. A binary ZP, a double-sided ZP, and a 4-level ZP have consequently been fabricated by molding a 2 mm thick polymeric slab. Their focusing properties have been characterized by means of a THz time domain spectrometer in transmission mode, as shown in Fig. 1a. The double-sided ZP is able to focalize THz E-field increasing it ($|E|_m$) more than 6 times, if compared with E-field in absence of lens ($|E|^{air}_m$), and showing better performance than a conventional binary ZP.

With the aim to design an antenna able to operate the beam steering of THz radiation at a fixed frequency, a Fabry-Perot cavity LWA (FPC-LWA) based on LCs has been developed and designed. The structure consists of a multilayered stack of alternating layers, placed above a grounded dielectric slab. Specifically, the alternation of tunable LC low-permittivity and of high-permittivity dielectric layers, with thicknesses suitably fixed at odd multiples of a quarter wavelength in the medium, produces a resonance condition, which makes it possible to obtain a narrow radiated beam at broadside (Jackson DR, Oliner AA, Ip A, IEEE Trans Antennas Propag. https://doi.org/10.1109/8.233128). By applying a common bias voltage to the LC layers, the resonance condition and the fundamental leaky-mode propagation constant change, with consequent beam steering capability.

The investigation on the antenna behavior has been driven by developing a suitable circuit model for the dispersive analysis of planar structures including anisotropic layers. A transverse equivalent network can be derived and, by imposing

the resonance condition, complex-mode dispersion equations are obtained. The fundamental TE and TM leaky-mode wavenumbers are found by numerically searching for the improper complex roots of the characteristic equation. This piece of information allows us to achieve the LWA basic radiative features (pointing angle and beam width) as a function of the bias voltage. The results deriving from this analysis have been corroborated and validated by rigorous *ad hoc* numerical simulations of a realistic FPC-LWA layout, which takes into account also fabrication constraints, at the operating frequency 0.59 THz (Fig. 1b) (Fuscaldo W, Tofani S, Zografopoulos DC, Baccarelli P, Burghignoli P, Beccherelli R, Galli A, IEEE Antenn Wirel Propag Lett. https://doi.org/10.1109/LAWP.2017.2695324). Other promising configurations of tunable THz FCP-LWAs are currently under investigation.

References

1. Jepsen PU, Cooke DG, Koch M Laser Photonics Rev. https://doi.org/10.1002/lpor.201000011
2. Soret JL (1875) Ann Phys Chem 156
3. Tofani S, Zografopoulos DC, Missori M, Beccherelli R (2016) IRMMW-THz. https://doi.org/10.1109/IRMMW-THz.2016.7758664
4. Jackson DR, Oliner AA, Ip A IEEE Trans Antennas Propag. https://doi.org/10.1109/8.233128
5. Fuscaldo W, Tofani S, Zografopoulos DC, Baccarelli P, Burghignoli P, Beccherelli R, Galli A IEEE Antenn Wirel Propag Lett. https://doi.org/10.1109/LAWP.2017.2695324

List of Participants

Erice, Sicily, Italy: July 20 – August 4, 2017

1. Diana Adliene
   Kaunas University of Technology
   Kaunas, Lithuania
   diana.adliene@ktu.lt
2. Javier Aizpurua
   CSIC/DIPC
   San Sebastian, Spain
   http://cfm.ehu.es/nanophotonics
   aizpurua@ehu.es
3. Steve Arnold
   Polytechnic Institute of NYU
   Brooklyn, NY, 11201, USA
   sa1577@nyu.edu
4. Rolindes Balda
   University of the Basque Country
   Bilbao, Spain
   rolindes.balda@ehu.es
5. Oliver Benson
   Humboldt Universität
   Berlin, Germany
   oliver.benson@physik.hu-berlin.de
6. Fabian Beutel
   Westfälische Wilhelms-Universität Münster
   CeNTech – Center for Nanotechnology
   Münster, Germany
   fabian.beutel@uni-muenster.de

B. Di Bartolo et al. (eds.), *Quantum Nano-Photonics*, NATO Science for Peace and Security Series B: Physics and Biophysics,
https://doi.org/10.1007/978-94-024-1544-5

7. Georges Boulon
Laboratoire de Physico-Chimie des Materiaux Luminescents
Université Claude Bernard- Lyon I
Villeurbanne Cedex, France
georges.boulon@univ-lyon1.fr
8. John W. Bowen
The University of Reading
Reading, UK
j.bowen@reading.ac.uk,
cybjb@cyber.reading.ac.uk
9. Antonino Cala' Lesina
Department of Physics
University of Ottawa
Ottawa, ON, Canada
Antonino.Calalesina@uottawa.ca
10. Joshua Caldwell
Mechanical Engineering Department
Vanderbilt University
Nashville, TN, USA
josh.caldwell@vanderbilt.edu
11. Gabriel Campargue
Faculté des Sxciences
Section de Physique
Genève, Switzerland
gabriel.campargue@unige.ch
12. Maura Cesaria
IMM-CNR: Institute of Microelectronics and Microsystems
Lecce, Italy
Università degli Studi di Firenze, Sesto Fiorentino, Florence, Italy
maura.cesaria@le.infn.it, maura.cesaria@bc.edu
13. Federico Chiossi
Department of Physics
University of Padova
Padova, Italy
federico.chiossi@phd.unipd.it
14. Marco Clementi
Deparment of Physics,
University of Pavia
27100 Pavia, Italy
marco.clementi01@universitadipavia.it
15. John Collins
Department of Physics
Wheaton College
Norton, MA, USA
jcollins@wheatonma.edu

16. Paul Corkum
    Department of Physics
    University of Ottawa
    Ottawa, ON, Canada
    pcorkum@uOttawa.ca
17. Baldassare Di Bartolo (Co-Director of the Institute)
    Department of Physics
    Boston College
    Chestnut Hill, MA, 02467, USA
    dibartob@bc.edu
18. Hilmi Volkan Demir
    Bilkent University, Turkey
    volkan@fen.bilkent.edu.tr
19. Onur Erdem
    UNAM – National Nanotechnology Research Center
    Bilkent University
    06800 Ankara, Turkey
    onur.erdem@bilkent.edu.tr
20. Joaquín Fernández
    University of the Basque Country
    Bilbao, Spain
    joaquin.fernandez@ehu.es
21. Tobias Frenzel
    Karlsrhue Institute of Technology
    Karlsruhe, Germany
    tobias.frenzel@kit.edu
22. Sergei Gaponenko (Co-director of the Institute)
    National Academy of Sciences
    Institute of Physics
    Minsk, Belarus
    nanoscience@tut.by
23. James Godfrey
    Department of Physics, Engineering Physics, and Astronomy
    Queen's University
    Kingston, ON, Canada
    11jrkg@queensu.ca
24. Małgorzata Guzik
    University of Wrocław
    Wrocław, Poland
    goguzik@poczta.fm
25. Wadislaw Hartman
    Karlsruhe Institute of Technology
    Karlsruhe, Germany
    wladick.hartmann@uni-muenster.de

26. Swathi Iyer
Naval Research Laboratory
Washington, DC, 20375, USA
swathiiyer.ganjigunteramaswamy.ctr.in@nrl.navy.mil
27. Robert Keitel
ETH Zürich
Zürich, Switzerland
keitelr@student.ethz.ch
28. Caroline Klusmann
Institute of Applied Physics
Karlsrhue Institute of Technology
Karlsruhe, Germany
carolin.klusmann@kit.edu
29. Julian Köpfler
Karlsrhue Institute of Technology
Karlsruhe, Germany
julian.koepfler@student.kit.edu
30. Antonino La Francesca
Medfield, MA, 02052, USA
ninolf@hotmail.com
31. Frederik Mayer
Karlsrhue Institute of Technology
Karlsruhe, Germany
frederik.mayer@kit.edu
32. Eric Mazur
School of Engineering and Applied Sciences; Harvard University
Cambridge, MA, 02138, USA
mazur@physics.harvard.edu
33. Michael Meeker
U.S. Naval Research Laboratory
Electronics Science & Technology Division, code 6814
Washington, DC, USA
michael.meeker.ctr@nrl.navy
34. Tobias Messer
Karlsrhue Institute of Technology
Karlsruhe, GERMANY
tobias.messer@student.kit.edu
35. Alexander Münchinger
Karlsrhue Institute of Technology
Karlsruhe, Germany
uycsv@student.kit.edu
36. Lukas Novotny
ETH Zurich, Photonics Laboratory
Zurich, Switzerland
lnovotny@ethz.ch

37. Stefano Orlando
CNR- ISM
Tito Scalo (PZ), Italy
stefano.orlando@pz.ism.cnr.it
38. Isabelle Palstra
Center for Nanophotonics AMOLF
University of Amsterdam
Amsterdam, The Netherlands
I.Palstra@amolf.nl
39. Nikolai Passler
Department of Physical Chemistry
Fritz Haber Institute
Max Planck Society
Berlin, Germany
passler@fhi-berlin.mpg.de
http://www.fhi-berlin.mpg.de/pc/latdyn/
40. Marco Passoni
Department of Physics
University of Pavia
Pavia, Italy
marco.passoni01@universitadipavia.it
41. Wolfram Pernice
Karlsruhe Institute of Technology
Karlsruhe, Germany
wolfram.pernice@googlemail.com
42. Siim Pikker
Department of Physics
University of Jyväskylä
Jyväskylä, Finland
siim.x.pikker@jyu.fi
43. Fabrizio Pinto
Izmir University of Economics
Izmir, Turkey
fabriziopinto2013@gmail.com
44. Markus Pollnau
Department of Materials and Nano Physics
School of Information and Communication Technology
KTH – Royal Institute of Technology
Kista, Sweden
m.pollnau@utwente.nl
45. Jingyuan Qu
Karlsrhue Institute of Technology
Karlsruhe, Germany
jingyuan.qu@kit.edu

46. Andrei Ramanenka
Stepanov Institute of Physics
The National Academy of Sciences of Belarus
Minsk, Belarus
andrew_romanenko@mail.ru
47. Lora Ramunno
Department of Physics
University of Ottawa
Ottawa, ON, Canada
lora.ramunno@uOttawa.ca
48. Maryia Rudenko
Belarusian State University of Informatics and Radioelectronics
Research Laboratory of Nanophotonics
Minsk, Belarus
rudmash@gmail.com
49. Philip Schrinner
University of Muenster
Muenster, Germany
schrinner@uni-muenster.de
50. Kostiantyn V. Shportko
V. E. Lashkarayov Insritute for Semiconductor Physics
National Academy of Sciences of Ukraine
Kyiv, Ukraine
konstantin@shportko.com,
kostiantyn.shportko@rwth-aachen.de
51. Elpidio Silvestri
Lungotevere Pietra Papa 21
00146 Roma, Italy
elpidio.silvestri@alice.it
52. Luciano Silvestri
Department of Physics
Boston College
Chestnut Hill, MA, USA
silveslu@bc.edu
53. Felix Stete
Institute of Physics and Astronomy
University of Potsdam
Potsdam, Germany
stete@uni-potsdam.de
54. Vadislav Stefanov
Stepanov Institute of Physics
The National Academy of Sciences of Belarus
Minsk, Belarus
v.p.stefanov@mail.ru

55. Mark I. Stockman
Department of Physics and Astronomy
Georgia State University
Atlanta, GA, USA
mstockman@gsu.edu
56. Hasan Tabanli
Istanbul Technical University
Istanbul, Turkey
hasantabanli@gmail.com
57. Sevcan Tabanli
Istanbul Technical University
Department of Physics Engineering
Istanbul, Turkey
tabanlisevcan@itu.edu.tr
sevcantabanli@gmail.com
http://akademi.itu.edu.tr/tabanlisevcan/
58. Silvia Tofani
Department of Information Engineering
Electronics, and Telecommunications
University of Rome La Sapienza
Institute for Microelectronics and Microsystems
National Research Council (CNR-IMM)
Rome, Italy
tofani@diet.uniroma1.it
silvia.tofani@artov.imm.cnr.it
59. Robert Tomala
Polish Academy of Sciences
Institute of Low Temperature and Structure Research
Department of Excited State Spectroscopy
Wroclaw, Poland
R.Tomala@int.pan.wroc.pl
60. Nicolai Walter
Westfälische Wilhelms-Universität Münster
Physikalisches Institut
CeNTech – Center for Nanotechnology
Münster, Germany
n.walter@uni-muenster.de
61. Martin Wegener
Karlsrhue Institute of Technology
Karlsruhe, Germany
martin.wegener@kit.edu
62. Jean-Pierre Wolf
Faculté des Sciences
Biophotonics Group
Gèneve, Switzerland
jean-pierre.wolf@unige.ch

63. Vanessa Wood
Institut für Integrierte Systeme
ETH Zürich, ETZ J86
Zürich, Switzerland
wood@iis.ee.ethz.ch

Index

B. Di Bartolo et al. (eds.), *Quantum Nano-Photonics*, NATO Science for Peace and Security Series B: Physics and Biophysics,
https://doi.org/10.1007/978-94-024-1544-5

O